BERGISCHE
UNIVERSITÄT
WUPPERTAL

Bergische Universität Wuppertal
Fakultät für Mathematik und Naturwissenschaften

A Mesoscopic Computer Model for Reinforcement in Filled and Strain-Crystallizing Elastomers

Lena Tarrach

Dissertation zur Erlangung des akademischen Grades
Doktor der Naturwissenschaften (Dr. rer. nat.)
im Fach Physik

Dezember 2024

Abstract

In this thesis, a mesoscopic model for reinforcement in filled and strain-crystallizing elastomers is developed and applied to study their mechanical behavior from small deformations to failure. For this purpose, the model for strain-induced crystallization (SIC) proposed by Plagge & Hentschke [1] is combined with the model for filler in rubber designed by Viktorova *et al.* [2]. The utilization of the so-called morphology generator (MG) produces model elastomer networks containing finely or coarsely dispersed filler.

The unfilled non-crystallizing model networks obey Neo-Hookean behavior according to the theory of rubber elasticity and the modeling of the polymer chains as freely-jointed. For unfilled crystallizing model networks, the stress-stretch and crystallinity-stretch curves align with experimental observations. In particular, the typical plateau of the stress and the characteristic hystereses of both of the curves attributed to SIC can be observed. Snapshots of the model network show that layers of crystalline model polymer chains aligned with the stretching direction evolve perpendicularly to the direction of the deformation until crystalline strands traverse the polymer network.

In filled model networks, the Payne effect can be observed at small deformations and it is attributed to breaking of filler-filler bonds in this model. At larger deformations, the stress is amplified which is advanced if the filler is finely dispersed compared to coarsely dispersed filler and if the filler content is increased. The filler particles are tightly bound in aggregates, while mainly the model polymer chains bear the load. Thus, these polymer chains predominantly strain-crystallize. The onset of SIC also shifts to smaller stretches when the filler content is increased as it is observed in experiments. Simultaneously, the plateau of the stress and the hysteresis vanish.

Furthermore, the model is extended by a rupture criterion for the model polymer chains to investigate their rupture behavior. The threshold value for rupture, which is the so-called critical free energy density, is defined based on the analysis of free energy density histograms and by the comparison of the relation of the tensile strength and the elongation at break of crystallizing and non-crystallizing model networks with experimental observations.

For a suitable choice of the critical free energy density, both the tensile strength and the elongation at break of crystallizing model networks are enhanced compared to non-crystallizing model networks. These quantities are also raised when the filler is finely dispersed. With increasing filler content, the elongation at break decreases as expected. In contrast to experimental observations, the tensile strength of poorly filled networks is reduced compared to the unfilled networks and it only increases beyond a minimum. If the filler content reaches the percolation threshold, the model networks do not fail because a percolating structure is formed.

Although large fractions of filler-filler bonds break and polymer-filler bonds weaken, the formation of holes is initiated by rupture of model polymer chains which is promoted in filled networks by stress amplification. Failure of the model networks originates from the growth of these holes due to the same effect. As expected, SIC particularly evolves at the boundaries of the holes.

Under cyclic deformation, the fatigue in terms of stress softening can be observed. Wöhler curves indicate that the fatigue life is enhanced by SIC. As the filler content increases, the fatigue life is reduced first and, then, increases for small filler contents. For larger filler contents, failure of the model networks is not detected.

Contents

1. Introduction

This thesis describes a mesoscopic computer model for the investigation of reinforcement of strain-crystallizing elastomer networks containing particulate fillers. Reinforcement means that the material becomes 'stiffer' and a greater 'force' is required to damage or break the material. Both 'stiffer' and 'force' are momentarily convenient colloquial terms, which will be refined as we go along.

Strain-induced crystallization (SIC) manifests itself via crystallites, roughly 10 nm in linear dimension, which form reversibly in response to large local stresses. The diameter of active filler particles is comparable. Contrary to the aforementioned crystallites, however, filler particles are permanent. Nevertheless, both, reversible crystallites and permanent particles, serve or are thought to serve essentially the same purpose - material reinforcement. The former 'particles' are present in the material due to its chemical nature, whereas the latter particles are added during the manufacturing process of the rubber material.

The material in the context of this thesis is foremost filled natural rubber (NR). The predominant use, which we have in mind, is the use of NR in vehicle tires. Lability versus stability is not the only distinguishing feature of the crystallites and the particles. They are also distinguished by the structural and dynamic properties of their superstructures or networks inside the polymer matrix. The purpose of this thesis is it to shed light on the common and distinguishing properties of the reversible crystallites and the inert particles as well as their superstuctures in the context of rubber reinforcement.

Strength can be understood as the stress σ, which is proportional to the force per area, required to deform the material until a certain stretch λ is reached. The cartoon in Figure 1.1 illustrates a frequently reoccurring computer experiment in this thesis. A, in this case, cylindrical piece of material of length L is subject to a force f acting uniformly throughout its cross section A, i.e. $\sigma = f/A$, causing the elongation ΔL, i.e. $\lambda = 1 + \Delta L/L$. Measuring stress versus stretch yields a non-linearly increasing stress-stretch curve, whose non-linearity depends partly on the experiment itself but mainly on the chemical nature and structure of the sample. Moreover, strength of a material can be also understood as resistance to crack propagation and its ability to withstand rupture at high deformations which is quantified by its tensile strength and elongation at break. In particular the latter quantities will be examined in this thesis. From a broader perspective, mechanical durability in terms of fatigue might also be considered as strength and will be studied as well. However, the resistance of rubber to cutting and chipping will not be addressed. Tensile tests of model networks into which an artificial hole has been initially inserted have been investigated in [3, 4].

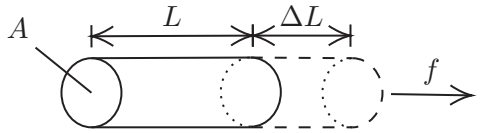

Figure 1.1.: Stretching a cyclindrical piece of material.

NR is indispensable for industrial applications such as tires, conveyor belts or damping elements due to its outstanding mechanical properties. It is harvested from the

rubber tree *Hevea Brasiliensis* and became useful with the discovery of vulcanization, i.e. the chemical cross linking of the polyisoprene chains in NR, by Charles Goodyear in 1839. NR possesses a considerable tensile strength of 28 MPa and can be stretched up to 8 times its relaxed length [5]. Wide Angle X-Ray Scattering (WAXS) experiments performed during uniaxial stretching of NR show its unique ability for SIC [6]. At stretches of 300 % or greater polymer backbones of NR align along the direction of the elongation and crystallites of linear dimension of approximately 10 nm emerge in domains of large strain [7–9]. The process of SIC is reversible and depends on temperature and strain rate. Other synthetic rubbers such as isoprene rubber (IR), which is the synthetic analogue of NR, are inferior to NR in both their mechanical properties and their ability for SIC. It is mainly this observation which is responsible for the believe in the importance of SIC for reinforcement. For example, the comparison of stress-stretch curves of NR and IR, e.g. in [10], shows that the stress at fixed stretch is higher for NR. The stress-stretch behavior of strain-crystallizing rubber is characterized by a plateau of the stress starting at the onset of SIC which indicates softening. However, softening is followed by strain-hardening which is observable as a steep incline of the stress. In addition, the typical hysteresis of SIC can be observed not only in the crystallinity but also in the stress-stretch curves.

Particulate fillers, such as Carbon Black (CB) or silica, are added to the rubber matrix in order to enhance the mechanical properties of NR as well as those of other elastomers [11]. The diameter of these solid particles is of order of 10 nm [5, 11] and thus comparable to the size of strain-induced crystallites. The impact of filler on the compound depends on temperature, the type of the filler particle itself accompanied by its specific properties and on the filler loading [12–15]. Filler particles act reinforcing on rubber already at small deformations which is indicated by a strongly elevated elastic modulus compared to unfilled rubber. This is an important difference to SIC. However, much of this modulus increase in filled versus unfilled rubber disappears when the strain, i.e. $\lambda - 1$, exceeds 0.5 (or 50 %) [15, 16]. This is called the Payne effect [11, 17]. It occurs in a strain range which is still far below the onset strain for SIC. Hence, if we want to compare reversible crystallites to inert filler particles, we must realize that inert filler particles act differently in different strain domains, i.e. their 'filler network structure' is different - something our model must include. Strain-induced crystallites self-organize in response to local strain, whereas much of the filler network structure is due to mixing of filler and elastomer when the material is made.

Beyond the aforementioned Payne Effect, there are a number of important experimental observations which the model should reproduce. At larger deformations, the stress at fixed stretch in filled NR is amplified compared to unfilled NR [18–23]. Moreover, the onset of SIC in filled rubber is shifted towards smaller stretches compared to pure rubber because filler particles enhance the local strain [18–21]. In addition, the characteristic hysteresis tightens and the typical plateau of the stress vanishes with increasing filler content, while the incline which represents hardening becomes even more pronounced [18]. The tensile strength increases with increasing filler content until a maximum is reached and decreases beyond [13, 14, 24–27]. However, the elongation at break decreases already for smaller filler content [26–28].

Comparing the change of the stress-stretch behavior of rubber at intermediate to large deformations due to SIC and due to the inclusion of filler suggests that both have a similar reinforcing effect in this strain regime. A common explanation is that both appear to act like additional cross links in addition to the physical and chemical cross links in the polymer matrix [22]. Nevertheless, on a microscopic scale, SIC enhances the conformational freedom of the amorphous polymer chain segments, while filler particles restrict the mobility of the polymer chains [18]. This suggests that both reinforcement

mechanisms must be of different nature. Hence, one needs to understand why crystallites appear to act like more or less fixed anchoring points for the chains in the polymer network, even though, on a microscopic level, the 'anchors' possess considerable translational freedom.

A difficulty when modeling SIC in rubber is that SIC is a cooperative phenomenon involving many polymer chain segments. Hence, a fully atomistic model is computationally too expensive. Numerous simulations of pure rubber have been conducted on the continuum level by applying finite element methods to hyperelastic material models [29–31]. But these models do not include SIC explicitly and they obviously do not capture the cooperative behavior of the chain segments involved in SIC.

Furthermore, filled rubber is often simulated at small deformations far below the onset of SIC or over a larger range of deformations without the consideration of SIC (e.g. [32, 33]). For the simulation in the latter case, constitutive models are commonly applied which are based on continuum mechanical approaches and do not include SIC [34–36]. The importance of the polymer-filler interface and the filler properties for the resistance to fracture is revealed in molecular dynamics (MD) simulations [37, 38]. Nevertheless, approaches for the simulation of fracture of pure and filled polymer often do not incorporate SIC as well or they do not cover the impact of the filler loading and the filler network structure on the tensile strength [39–43].

An example for an approach combining the simulation of SIC and filler is the constitutive model by Dargazany *et al.* [44]. Although the polymer-filler interaction is taken into account in this study, fillers are modeled as rigid particles such that their inner structure is neglected. Another example are the coarse-gained MD simulations by Chen *et al.* [45] for the investigation of *cis*-polyisoprene nanocomposites. In this work, SIC is defined by a certain chain orientation, but not explicitly included into the model. In both of the examples, large deformations which cause failure of the material are not considered.

Here, a coarse-grained model for SIC, which has been introduced by Plagge & Hentschke [1] and studied further in [3, 4], is presented in an extended form. The original model is based on the theory proposed by Flory [46]. Coarse-graining means that monomer units of the material are combined into larger elements possessing an effective free energy. Because the free energy is non-uniformly distributed, which is in contrast to mean-field theories [**Hentschke2021**, 44, 47–49], the crystalline segments are enabled to organize into labile non-equilibrium structures via local free energy minimization in response to global deformation.

This model for SIC is combined with the so-called morphology generator (MG), a Monte-Carlo (MC) algorithm originally developed by Viktorova *et al.* [2] which generates different types of dispersions, i.e. 'fine', 'coarse' or 'network-like', of filler in a rubber matrix. The MG is based on the interface tensions of the components and allows to take filler flocculation in the post-mixing stages of the composite into account. The molecular level, represented by the interface tensions, is connected to the dynamical properties on the macroscopic scale by a bead-spring model. This means that both filler and polymer are modeled as coarse-grained spherical volume elements and that polymer-polymer, filler-filler and polymer-filler bonds are modeled by harmonic interactions with different parameters, respectively. This model for filled rubber was originally constructed for the simulation of the dynamic moduli of rubber which are obtained from oscillatory shearing at small amplitudes. Therefore, SIC was not considered. However, the model reproduces the aforementioned Payne effect which is characteristic for filled rubber. In addition, because of the sufficient inclusion of local properties of the model composites, this model is capable of providing insights into the

contributions of each constituent to crack initiation [38].

Hence, while the model developed in this work includes both SIC and filler, it permits to study one without the other as well as both in combination inside an otherwise unaltered matrix structure at all strains - an advantage which experimental systems do not offer.

The motivation for investigating reinforcement by SIC and filler in NR is, first, the theoretical interest for understanding reinforcement mechanisms in general. Secondly, since NR nanocomposites play an unique role in the industry, understanding how their mechanical properties are related to their microscopic structure facilitates targeted design of alternative or new materials. Thus, the objective of this thesis is to investigate the differences in reinforcement by SIC and by filler as well as their interplay by analyzing the mechanical behavior of crystallizing and non-crystallizing model NR networks with variable filler content in the entire range of deformations - from small stretches to failure.

The focus is on the study of two-dimensional model networks due to computational effort for the simulations and the simplicity to visualize them. With the preknowledge gained from two-dimensional networks, three-dimensional networks are investigated. Plagge & Hentschke [1] report that the model for SIC in elastomers yields stress-stretch and crystallinity-stretch curves which feature the characteristic behavior of strain-crystallizing elastomers in accordance with experimental data. In particular, the stress-stretch curves of crystallizing model networks show the typical plateau and incline beyond it. In addition, the crystallinity-stretch curve shows a hysteresis which induces an attendant hysteresis of the stress. These observations have been validated in [3, 4] and are recalled in this thesis. For the extension of the model for filled networks, the MG and the newly introduced filler-filler and polymer-filler bonds have been parametrized by comparing the morphologies and the mechanical behavior with experimentally obtained data. Filled model networks have been studied first at small deformations where SIC does not occur and thus is neglected. The derivative of the stress-stretch curve, which is proportional to the elastic modulus, is elevated compared to the case of unfilled networks dependent on the filler content as expected. Comparing the derivatives for variable filler morphologies implies that finely dispersed filler reinforces the composite more than lumpy filler. In addition, the Payne effect can be observed as the filler content exceeds the percolation threshold. Here, it is mainly caused by breaking of filler-filler bonds. At larger deformations, the stress-stretch curves of filled non-crystallizing and crystallizing model networks show that the stress at fixed stretch increases with increasing filler content. Filler affects SIC in the model networks also as expected. The onset of SIC is shifted towards smaller stretches with increasing filler content, while the typical plateau in the stress-stretch curve vanishes and the hysteresis of the stress-stretch and the crystallinity-stretch curve tightens. In contrast to [3, 4] where a force and a crystallinity threshold have been applied to make model polymer chains break, a critical free energy density is employed here. This is motivated by the notion that the formation and propagation of 'damage' requires the temporary local storage of energy. A suitable range for the critical free energy density is derived from the comparison of free energy density histograms of stable unfilled crystallizing and non-crystallizing model networks. The final values are deduced from the additional analysis of the rupture behavior of crystallizing and non-crystallizing model networks with variable filler content for variable critical free energy density. Based on this, tensile strength and elongation at break are investigated for crystallizing and non-crystallizing model networks with variable filler content for different filler morphologies. For all of the tested filler morphologies, the tensile strength of the unfilled networks does not

agree with experimental observations since it is higher than for any other filler content. This particular weakness of the present model will be discussed in some detail. The relation of the tensile strength and elongation at break of the crystallizing networks to that of the non-crystallizing networks strongly depends on the choice of the critical free energy density. The behavior of the elongation at break dependence on the filler content is consistent with experimental observations. In particular, the type of filler dispersion determines the dependence of tensile strength on filler content. For finely dispersed filler, the tensile strength increases with increasing filler content as expected. Based on experimental observations, it is expected that the tensile strength decreases beyond a certain filler content. This, however, is not observed here. Since the inclusion of filler causes stress amplification as the extension of model polymer chains located between adjacent filler aggregates is promoted, rupture of model polymer chains is these domains is also fostered. Hole formation in the model elastomer networks is initiated by rupture of model polymer chains, but not filler-filler or polymer-filler bonds. Although SIC does not totally prevent failure of the model elastomer networks, it impedes the rupture process because strain-induced crystallites particularly evolve at the boundaries of the holes. During cyclic deformation of the model elastomer networks, stress softening can be observed. Wöhler curves indicate that the fatigue life is enhanced by SIC and that is optimized for very small filler content or for filler content above the percolation threshold. Nevertheless, it will be pointed out that the study of fatigue by employing the presented model requires for further analysis.

The thesis is structured as follows. Chapter 2 serves as an introduction to the mechanical properties of elastomers reinforced by SIC and filler by presenting experimental observations and simple models. In order to set the scene, essential mechanical properties of elastomers in general and NR in particular are described. The quantities which define the strength of rubber such as the stress σ and the elastic modulus E are introduced. Additionally, reinforcement by SIC and by filler in terms of the aforementioned quantities are explained. Moreover, properties of cross links and fillers as well as their impact on rubber are elucidated. After the consideration of a phenomenological model for the viscoelastic behavior of rubber, the so-called time-temperature superposition is discussed. Based on experimentally obtained moduli and stress-stretch curves, the characteristics of the mechanical behavior of filled and strain-crystallizing rubber are outlined. In chapter 3, the fundamental physical principles for the model of NR employed here are compiled. An expression for the stress is derived from the theory of elasticity. The forces of the model polymer chains are obtained from the theory of rubber elasticity which is then combined with the model for SIC proposed by Flory [46]. In a theoretical analysis, the resulting expressions for the free energy and the forces of semi-crystalline model polymer chains are investigated with respect to the impact of SIC on the mechanical behavior and for the subsequent definition of a rupture criterion for the model polymer chains. In addition, the modeling of filler-filler and polymer-filler bonds is elucidated. With regard to the functionality of the MG, which is applied to disperse the filler inside the rubber matrix, the concepts of wettability and work of adhesion are introduced by considering the surface tension. The simulation algorithm is explained in chapter 4 where the so-called morphology generator for setting up filled model NR networks plays a special role. Regarding the filler morphologies, a remark on percolation of filler is made. In chapter 5, the results of the investigations on strength and reinforcement of NR are presented which rely on the study of two- and three-dimensional filled and strain-crystallizing model networks with variable filler content. First, the stress-stretch behavior of unfilled model networks as well as the impact of SIC on their behavior are validated by taking the results in [1, 3, 4] into account. Secondly, the morphology generator is set up for the simulation of

filled networks. The bonds in filled networks are parameterized based on an analysis of the mechanical behavior, in particular at small deformations, for variable parameter settings. Subsequently, the mechanical behavior of filled model networks at small stretches is examined for the Payne effect. At higher stretches, the impact of filler on SIC is investigated by assessing stress-stretch and crystallinity-stretch curves. As a next step, a critical free energy density is introduced as a rupture criterion for the model polymer chains in the context of simulated tensile testing. The rupture behavior of crystallizing and non-crystallizing model networks with variable filler content is evaluated with regard to their mircrostructure. In addition, the tensile strength and the elongation at break are studied. Finally, fatigue of the model networks is investigated via simulated Wöhler curves. In chapter 6, the main results of this thesis are summarized and an outlook is given.

Parts of the results obtained in course of this work and presented in this thesis are published in the following articles:

- Tarrach, L. & Hentschke, R. A mesoscopic computer model for reinforcement in filled and strain-crystallizing elastomer networks. *Computational Materials Science* **246,** 113374. doi:10.1016/j.commatsci.2024.113374 (2025),
- Tarrach, L. & Hentschke, R. Development of a Mesoscopic Computer Model for Reinforcement in Filled and Strain-Crystallizing Elastomer Networks, in: *Constitutive Models for Rubbers XIII*. (ed Dal, H.) 87-92 (CRC Press, 2025)
- Tarrach, L. Hentschke, R. & Weilert, J. Modelling Study of Reinforcement and Rupture in Strain-Crystallizing Elastomer Networks. *Kautschuk Gummi Kunststoffe KGK* **3**, 62-71 (2023)
- Tarrach, L. Modeling study of tensile strength of filled and strain-crystallizing elastomers. (accepted for the IRC 2024 special issue of *Macromolecular Symposia*)

The following conference papers have also resulted from parts of this work:

- Tarrach, L. & Hentschke, R. Modeling study of tensile strength of filled and strain-crystallizing elastomers. *International Rubber Conference IRC 2024*, Istanbul, Turkey
- Tarrach, L. & Hentschke, R. Modeling Study of Filler Reinforcement in Elastomers: From Small Strains to Failure. *Fall Rubber Colloquium KHK 2024*, Hannover, Germany
- Tarrach, L. & Hentschke, R. Development of a Mesoscopic Computer Model for Reinforcement in Filled and Strain-Crystallizing Elastomer Networks. *European Conference on Constitutive Models for Rubbers ECCMR 2024*, Istanbul, Turkey
- Tarrach, L. & Hentschke, R. Model-Based Approach to Reinforcement in Filled and Strain-Crystallizing Elastomer Networks. *RubberCon 2023*, Edinburgh, UK
- Tarrach, L. Hentschke, R. & Weilert, J. Modelling Study of Reinforcement and Crack Formation in Strain-Crystallizing Elastomer Networks. *Fall Rubber Colloquium KHK 2022*, online

2. Elastomers - Materials Combining Elasticity with Strength

This section describes the material studied in this thesis, including its relevant physical properties. In particular, it is elucidated how the mechanical strength of elastomers is affected by the inclusion of filler particles and by strain-induced crystallization (SIC). For this purpose, relevant experimental observations are summarized. In addition, a short overview on approaches to modeling and simulation of filled and strain-crystallizing elastomers is provided.

2.1. What are Elastomers?

An Elastomer is a certain type of polymer. The International Union of Pure and Applied Chemistry (IUPAC) defines polymers as "A substance composed of macromolecules."[51] and a macromolecule as "A molecule of high relative molecular mass, the structure of which essentially comprises the multiple repetition of units derived, actually or conceptually, from molecules of low relative molecular mass."[51]. Thus, polymers are large molecules consisting of repeating elementary units called monomers. They can be classified into three categories according to their molecular structure: thermoplastics, duroplasts or thermosets and elastomers [5]. Besides, these categories can be distinguished by the temperature dependence of their mechanical properties [5]. In particular, the glass transition temperature is an important quantity. For temperatures below the glass transition, a polymeric material is glassy and rigid, which means that it is solidified in an amorphous or disordered state. If the temperature is increased, the material softens and the polymer chains inside become flexible and movable. The turning point of the mechanical behavior defines the glass transition temperature. Above the glass transition temperature, the material and the molecules inside it are highly flexible. The mobility of the polymer chains is just restricted by entanglements. In contrast to the glassy state, a crystalline state is ordered. It does not occur in every kind of polymer and, if it occurs, only crystalline domains form within the amorphous material [52]. In the latter case, a polymer is called semi-crystalline. Thermally induced crystallization usually occurs below the glass transition temperature of the amorphous domains and involves the arrangement of the polymer chains into ordered structures. The melting temperature of the crystalline domains is usually situated above the glass transition. At this point, the crystallites vanish. The material becomes disordered and it starts to flow.

Thermoplastics are linear or branched polymers which are amorphous or semi-crystalline with a glass transition above room temperature. Therefore, they are rigid at room temperature, but they melt at sufficiently high temperature. As mentioned above, "melting", in this context, means that the material starts to flow. Examples for thermoplastics are polymethyl methacrylate (PMMA) used for plexiglas®, polyethlene therephthalate (PET) applied in fibers for clothing or food containers and polyvinyl chloride (PVC) used for pipes.

Duroplasts are amorphous polymer networks with a high network density. As for thermoplastics, the glass transition is above room temperature such that they are rigid

at room temperature, but, in contrast to thermoplastics, they cannot melt and decompose instead at high temperature. Moreover, they are deformed in the region of plastic deformation at room temperature such that the deformation remains permanently. Examples for duroplasts are polyurethanes applied for insulation, polyimides used for medical tubing or vinyl ester resins applied for fiber reinforcement.

Elastomers are amorphous polymers characterized by their glass transition below 0 °C and their network structure with a low network density compared to duroplasts. Therefore, they are flexible and elastic at room temperature ("rubber"). Elastomers behave viscoelastic. On the one hand, there is a viscous contribution to a deformation which is irreversible and leads to dissipation of heat. On the other hand, the elastic contribution is reversible and accounts for the storage of deformation energy. For example, polyisoprene and polybutadiene are elastomers.

Because of their viscoelasticity, the mechanical behavior of elastomers is strongly dependent on temperature. Both the mechanical behavior at certain temperature and the categorization of polymers can be deduced from plots of the shear modulus versus temperature [5]. Such a schematic plot is depicted in Figure 2.1 for an elastomer. In domain (I), the polymer is in its glassy state and behaves energetically elastic. The material is rigid. In interval (II), the glass transition takes place at the glass transition temperature T_g which is defined as the inflection point of the curve. The polymer chains become movable and the material becomes flexible. Region (III) is called "rubber plateau" and the range of application for elastomers. Their elasticity is determined by entropy. In domain (IV), the elastomer thermally decomposes.

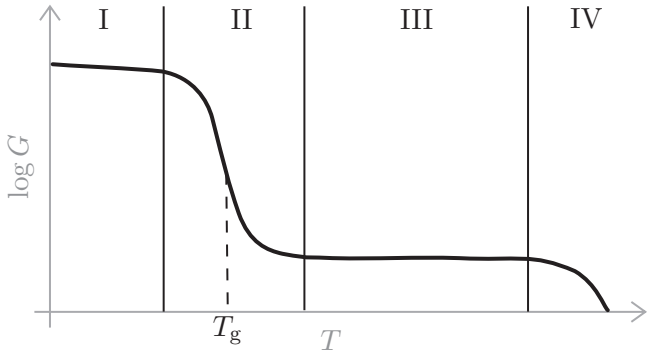

Figure 2.1.: Schematic plot of the logarithm of the shear modulus $\log G$ versus temperature T for elastomers. T_g indicates the glass transition temperature.

This work focuses on natural rubber (NR) which mainly consists of *cis*-1,4-polyisoprene. The glass transition temperature of NR is around −60 °C [53, 54] It should not be confound with its isomer *trans*-1,4-polyisoprene, so-called gutta percha, which is a thermoplastic. Both of them are illustrated in Figure 2.2.

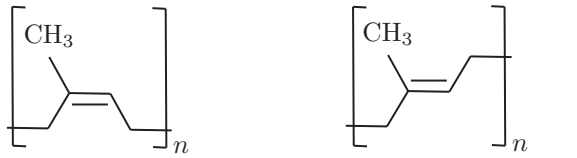

cis-1,4-polyisoprene *trans*-1,4-polyisoprene

Figure 2.2.: Chemical structure of *cis*- and *trans*-1,4-polyisoprene.

The polyisoprene content in NR originates from polycondensation within the sap of the rubber tree *Hevea Brasiliensis* [52]. The residues are fats and proteins. For the production of NR, rubber latex is harvested from the bark of the rubber tree, which

mainly grows on plantations in South America and Asia [5]. By coagulation, rolling and drying, the latex is manufactured to sheets which are the basis for further processing.

NR just became applicable with the discovery of vulcanization by Charles Goodyear in 1839 [5] which improves its mechanical properties. For vulcanization conventionally, sulfur is added to the polymer and the mixture is heated up such that sulfur bridges serving as chemical cross links between the polymer chains are established and a network structure is formed. Accelerators are required to speed up the opening of the S_8-rings in which sulfur is present. Also other chemicals such as peroxides can be used for curing. In addition to chemical cross links, physical entanglements can generate a network-like structure. However, in the context of this work, 'cross link' means chemical cross link.

Due to its stereoregularity and possible other factors like its non-rubber content, e.g. proteins, NR possesses the ability to show strain-induced crystallization (SIC). During stretching, the polymer backbones align along the stretching direction such that crystallites are formed reversibly at stretches of around $300 - 400\,\%$ in highly strained regions of the material [7–9]. The crystallites possess a linear dimension of approximately 10 nm and melt if the stress is released. Wide-Angle X-ray scattering (WAXS) experiments indicate a relation between the ability of NR for SIC and its mechanical properties [6].

Moreover, polyisoprene can be synthesized from isoprene monomers. They originate from petroleum and are polymerized in a chain-growth reaction in solution with Ziegler-Natta catalysts. The synthetic analogue of the natural product is called isoprene rubber (IR).

Nevertheless, NR and IR differ in their properties. NR contains nearly $100\,\%$ of *cis*-content, while IR consists of approximately $98\,\%$ of *cis*-1,4-polyisoprene [54]. The glass transition temperature of IR is shifted towards slightly higher temperature compared to that of NR [53, 54]. IR is inferior in mechanical properties such as tensile strength which is attributed to a smaller extend of SIC compared to NR.

Furthermore, note that the term "rubber" usually refers to the compound material of polymer and additives after processing. Additives are used to improve the processing and the properties of the material. For example, reinforcing fillers such as silica or carbon black (CB) are added to the rubber matrix. This is in particular necessary for applications for which enormous strength is required. Another commonly used term for filled rubber is "composite". NR is of special importance because of its high elasticity, durability and tensile strength. It is used in for instance truck tires, conveyor belts or for dampers.

2.2. Strength and Reinforcement of Elastomers

In the course of this work, the terms "strength" and "reinforcement" are frequently used. Strength is understood as the stress σ required to stretch the material until a certain elongation described by the stretch λ is reached. In the range of small or intermediate stretches, this can be translated to the elastic modulus E of the material, which is proportional to the gradient of the stress-stretch curve. Unless noted otherwise, the materials considered here posses isotropic elasticity, i.e. $E = 3G$, where G is the shear modulus. These quantities are affected by the viscoelastic properties of elastomers and irreversible processes within the material. Reinforcement means an increase of the stress at fixed stretch. To generate reinforcement, for instance structural modifications are applied to the material by cross links or filler, but SIC is also considered to act reinforcing. In fact it is the interplay between filler and SIC which

is the main topic of this thesis. Furthermore, the term "tensile strength" is defined as the maximum stress the material can resist during stretching before it breaks.

As it will be discussed later, the theory of rubber elasticity [55–60] yields for the stress:

$$\begin{aligned}\sigma &= k_\mathrm{B}Tn_\nu\left(\lambda-\frac{1}{\lambda^2}\right)\\ &\approx 3k_\mathrm{B}Tn_\nu\varepsilon, \quad \lambda = 1+\varepsilon \approx 1,\end{aligned}$$

where n_ν denotes the density of chains, which is proportional to the cross link density. Hence, the shear modulus at small deformation is given as:

$$G_0 = k_\mathrm{B}Tn_\nu. \tag{2.1}$$

If a small volume fraction ϕ of filler particles is added to the pure rubber, hydrodynamic reinforcement leads to an increase of the modulus [61]:

$$G = G_0\left(1+\frac{5}{2}\phi\right). \tag{2.2}$$

This equation has been formulated initially by Einstein [62, 63] in the context of viscosity of liquids and has been later generalized to elastomers by Guth [64]. Although, experiments indicate that the modulus depends on the size of the filler particles [15, 65, 66], this is not included in Equation 2.2. There are various extensions of Equation 2.2 including higher orders of ϕ [67–75]. Since the basic idea of 'hydrodynamic reinforcement' by filler remains the same, they will not be discussed here.

Note that, when talking about filler particles, minimum aggregates are meant. They are formed by primary particles, but are not broken up into them during processing and mixture. The linear dimension of the minimum aggregates is proportional to that of the primary particles [76]. These minimum aggregates are the filler particles which build breakable aggregates and agglomerates.

A dependence of G on the particle size may be incorporated by considering the anchor points of the polymer chains on the surface of a filler particle as bonds which act like cross links in the bulk rubber. This idea relies on the observation of analogous behavior of rubber with variable filler content and rubber with variable cross link density [18]. In the picture applied here, a part of the rubber matrix, which contains cross links, is replaced by a filler particle which provides anchor points on its surface instead. Equation 2.1 suggests that the linear dependence of the modulus on the cross link density may also hold for filled rubber. Therefore, the excess modulus, which describes reinforcement by filler, is proportional to the change of the cross link density, i.e.:

$$\Delta G \equiv G - G_0 \propto \frac{A_\mathrm{f}}{V},$$

where $A_\mathrm{f} = N_\mathrm{f}a_\mathrm{f}$ is the total filler surface area, which is given by the product of the number N_f of primary filler particles and the surface area a_f of a single filler particle, and V denotes the volume of the material. The total volume of filler within the material is given by $V_\mathrm{f} = N_\mathrm{f}v_\mathrm{f}$, where v_f is the volume of a single particle. Assuming that filler particles are of spherical shape, the particle size is given by its radius R and it holds $a_\mathrm{f} \propto R^2$ and $v_\mathrm{f} \propto R^3$. Since $N_\mathrm{f}v_\mathrm{f}/V = \phi$, the excess modulus fulfills:

$$\Delta G \propto \frac{N_\mathrm{f}v_\mathrm{f}}{V}\frac{a_\mathrm{f}}{v_\mathrm{f}} \propto \frac{\phi}{R}. \tag{2.3}$$

This idea also involves the phenomenon that sufficiently large filler particles, approximately in the μm-range, lead to a decrease of the modulus instead of an increase. This happens if the number of bonds on the filler surface becomes smaller than the number of cross links replaced by the filler particle, i.e.:

$$n_c v_f > \frac{a_f}{a} \quad \Rightarrow \quad R \gtrsim \frac{1}{n_c a},$$

where n_c is the cross link density and a is the area of an anchor point. Equation 2.3 is validated by experimental data. (c.f. for example Figure 10.12 in [77]).

The previous thoughts rely on the consideration of isolated filler particles. However, filler particles aggregate into agglomerates and build networks. If the structure of filler inside the rubber is taken into account and the limit of infinitely small deformation is considered, the excess modulus behaves like

$$\Delta G \sim \phi^y.$$

The exponent y can be obtained from the assumption of a fractal-like filler distribution. In practice, mixing of filler and rubber limits the occurrence of a fractal distribution beyond a length ξ. On a larger scale, there occur filler voids[1] which are "destroyed" in the mixing process (i.e. macroscopically the filler is homogeneously distributed).

The assumption is justified since fillers embedded into a rubber matrix behave like aggregated colloids which can be considered as stochastic mass fractals [78]. This is validated by experiments [79, 80] and simulations [81]. The formation of aggregated colloids can be modeled for instance via cluster-cluster aggregation [82, 83].

As illustrated in Figure 2.3, a volume $V = L^3$ is considered which consists of cells of volume ξ^3. Since the number of filler particles is proportional to the volume for a homogeneous filler distribution, it holds:

$$N_f / N_\xi \propto L^3 / \xi^3.$$

The number N_ξ of filler particles inside the cell fulfills:

$$N_\xi \sim \xi^{d_f},$$

where $d_f < 3$ denotes the fractal dimension [77, 84, 85].

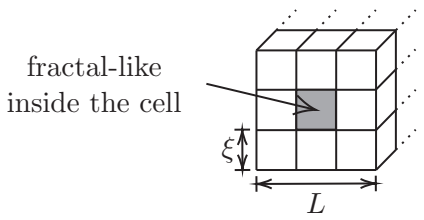

Figure 2.3.: Illustration of a cubic volume divided into cubic cells with fractal-like filler distribution.

This yields for the filler volume fraction in the entire volume:

$$\phi \propto \frac{N_\xi}{\xi^3} \sim \frac{\xi^{d_f}}{\xi^3} = \xi^{d_f - 3}.$$

[1] Neglecting this yields that $\phi \sim L^{d_f - 3} \to 0$ as $L \to \infty$ for system with homogeneous filler distribution. Here, $L^3 = V$ is the volume, which contains filler, and $d_f < 3$ denotes the fractal dimension. This is not realistic.

Consequently, one finds:

$$\frac{1}{A_\xi} = \frac{1}{\xi^2} \sim \phi^{\frac{2}{3-d_\mathrm{f}}}$$

with $A_\xi = \xi^2$ as cross sectional area of the cell. The left hand side can be understood as a measure for the density of filler-filler contacts passing through the cross section of the cell. On average, there are L^2/A_ξ surfaces of fractal cells in the cross section of the entire volume. Since filler-filler contacts may also be interpreted as cross links, the stress is proportional to the product $1/A_\xi \cdot L^2/A_\xi$, which describes the density of filler-filler contacts in the cross section of the entire volume. Hence, a relation for the modulus can be obtained by dividing the product through L^2:

$$\Delta G \sim \frac{1}{A_\xi}\frac{L^2}{A_\xi}\frac{1}{L^2} \sim \phi^{\frac{4}{3-d_\mathrm{f}}}. \tag{2.4}$$

Note that this relation is only valid above the percolation threshold, but the $1/R$-dependence derived above remains valid. Thus, the result for the exponent is:

$$y = \frac{4}{3-d_\mathrm{f}}. \tag{2.5}$$

One can find $3.3 \leq y \leq 4.5$ for different models for fractal aggregation [86]. This result for the exponent is consistent with that obtained by cluster-cluster aggregation (CCA) models [77, 87, 88] and experimental data if it is plotted appropriately [89–91]. CCA yields $y = (3 + d_{\mathrm{f,B}}) / (3 - d_\mathrm{f}) \approx 3.5$, where $d_{\mathrm{f,B}} \approx 1.3$ denotes the fractal dimension of the cluster backbone and $d_\mathrm{f} = 1.78$ [77, 87].

If filler is randomly distributed, the probability for a filler particle located in a cell of a cubic lattice to find a neighbor in an adjacent cell is qN_f/L^3, where q denotes the coordination number of the lattice. Since the number of pairs formed is proportional to N^2/L^3, the density of pairs is proportional to $N^2/L^6 = \phi^2$. Thus, it holds for the excess modulus:

$$\Delta G \sim \phi^2. \tag{2.6}$$

Experiments on filled elastomers used by the tire industry produce exponents from 2 to the y-values mentioned above. For example, Klüppel *et al.* [92] found $y = 3.5$ for volume fractions $\phi > 0.1$ of CB N300 in rubber.

But why is a filler-filler contact reinforcing? Originally, it was thought that the atomic interactions between two adjacent filler particles could be the cause [93]. The attractive energy of them is concerned as van der Waals interaction between two spheres of radius R with surface-to-surface distance $d \ll R$ [94]. It is given as

$$W = -\frac{AR}{12d}, \tag{2.7}$$

where A denotes the Hamaker constant[2] [95]. However, closer study shows that the Hamaker constants are too small to cause pronounced reinforcement [96] (cf. Figure 3 in [97]).

Nevertheless, neighboring filler particles do not just interact directly. Rather, they may be considered as a part of a filler network strand as depicted in the left sketch of Figure 2.4. The filler particles are 'coated' with a layer of polymer which binds to their

[2]For CB particles, the Hamaker constant amounts to $A \approx 10^{-19}$ J under the assumption that the main contribution is due to the oxygen layer on the particle surface [93].

surfaces. Thus, it is the 'bound rubber' which ultimately causes the reinforcement of a filler-filler contact.

Since the filler particles within a network strand do not contribute to the extension during deformation, the extension must arise from the gaps between them. The strain $\varepsilon_{\text{local}}$ in these areas is strongly amplified according to

$$\varepsilon_{\text{local}} = \frac{D}{d}\varepsilon, \quad \frac{D}{d} \gg 1, \tag{2.8}$$

compared to the macroscopic strain $\varepsilon = \lambda - 1$. Here, D is the diameter of a filler particle and d the width of the gap between adjacent filler particles. This is illustrated in Figure 2.4. Consequently, the stress required to reach a given strain is increased in comparison to an unfilled network as long as no large voids are formed.

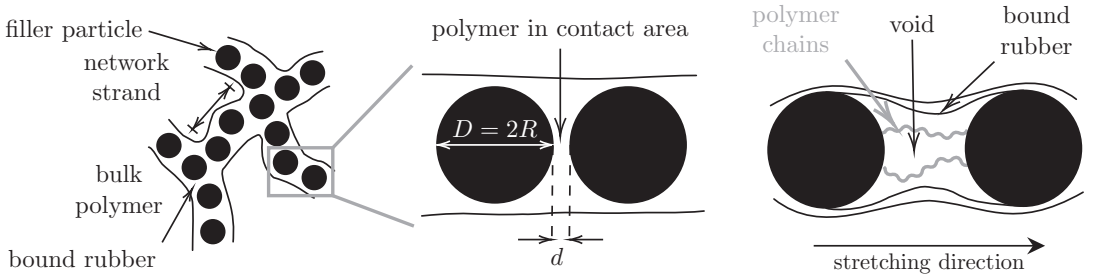

Figure 2.4.: Sketches of the contact region between two filler particles inside a strand of a filler aggregate embedded into the polymer matrix. The figures on the left and in the center show the undeformed state, while the right figure depicts the stretched state.

Note that this model for a filler-filler contact explains, and in fact is supported by, the Payne effect. Due to the filler network structure and the interaction of filler particles, the modulus is comparatively high at small strain. However, if the strain is increased, the modulus decreases between $0.1 - 1\,\%$ and $10\,\%$ of strain [15, 16], which can be observed in the data shown in Figure 2.17. This is called the Payne effect and is caused by the disruption of the filler network. Because of the deformation, voids form between adjacent filler particles within a network strand as illustrated in Figure 2.4. The temperature dependence of the Payne effect indicates that monomolecular reactions take place [17]. This means that bonds, for instance hydrogen bonds or attachments of polymer chains on the surface of filler particles, dissociate reversibly [98]. Figure 2.5 shows a sketch of the behavior of the modulus G dependent on the logarithm of the strain $\log \varepsilon$. It also depicts further contributions to the modulus of a filled elastomer network. The hydrodynamic contributions are according to Equation 2.2. While the hydrodynamic effects and the contribution of bound rubber are approximately independent of the strain, the contribution of the filler network is strongly strain-dependent.

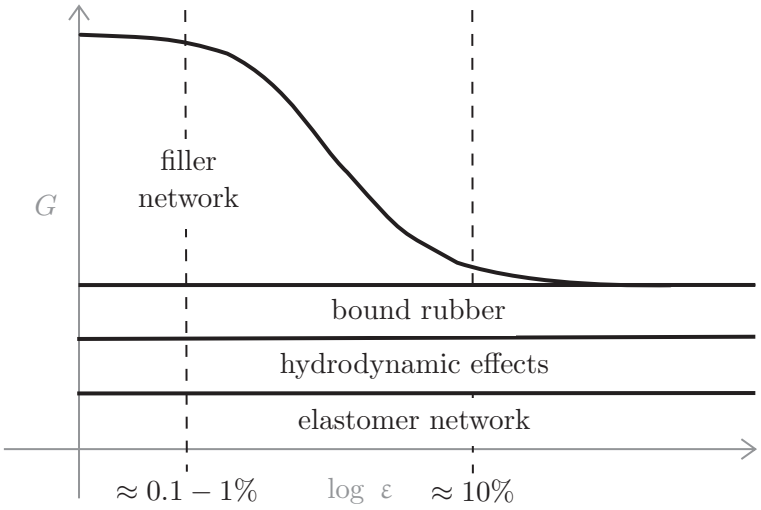

Figure 2.5.: Illustration of the storage modulus μ of filled rubber dependent on the logarithm of the strain $\log \varepsilon$.

At stretches beyond the decrease due to the Payne effect, the strength of the filled elastomer is determined by load-bearing polymer chain segments which are located between filler particles, cross links or both of them. This is depicted in Figure 2.6. Load-bearing chains between filler particles can be formed out of chains which are adsorbed on the filler surface. During stretching, they can slip over the surface such that the stress is locally redistributed which reinforces the material [11, 99].

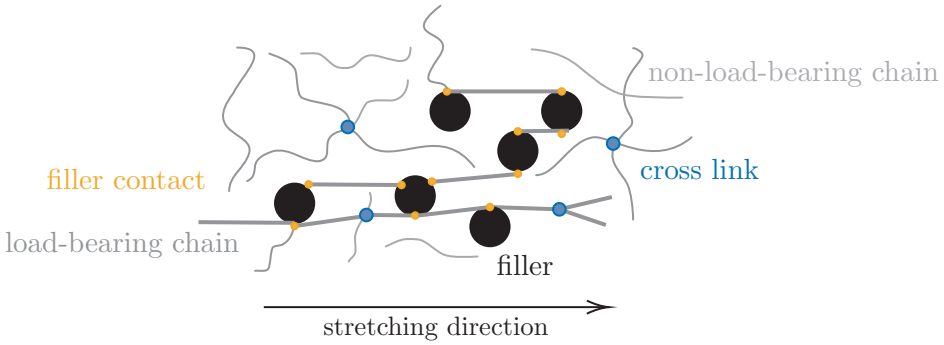

Figure 2.6.: Illustration of load-bearing polymer chain segments within filled rubber.

SIC begins at stretches of around 100 % in filled NR and around 300 % in unfilled NR [18]. In Wide Angle X-ray Diffraction (WAXD) patterns, it is indicated by Bragg peaks evolving from the amorphous halo, which is attributed to the amorphous phase, during the deformation (cf. Figure 9 in [6]). Those spots associated with the crystallographic (200), (120) and (002) planes are of highest intensity [6]. Although the lattice parameters are experimentally calculated by using the Bragg equation, it is still unclear whether the crystallographic structure of the strain-induced crystallites in NR is orthorhombic or monoclinic [6]. Furthermore, the crystallite size perpendicular to a (hkl) plane can be computed from the WAXD data by inserting the full width at half maximum of the corresponding Bragg peak into the Scherrer equation [6]. In addition, the orientation angle of the crystallites can be deduced from the half width at half height of the Bragg peak. Based on the scattering intensity of the amorphous halo I_a and the intensity of the diffraction peaks I, the crystallinity χ is experimentally

obtained via [100]:

$$\chi = \frac{I_\mathrm{a} - I}{I_\mathrm{a}} \cdot 100.$$

Experimental data indicates that the process of SIC is separated into nucleation and growth of crystallites. Oriented chains serve as nuclei for strain-induced crystallites [101]. Gros *et al.* [102] explain that the bundle-like structure of the nuclei is not only caused by the reduction of the entropy due to the deformation but principally by a decrease of the surface energies due to the structure. During the deformation a shish-kebab structure evolves in which chains attach to the aligned chains by back folding such that spherulites form perpendicularly to the stretching direction. However, the formation of this crystal structure is impeded by cross links in vulcanized rubber [7, 103]. The crystal structure depends on temperature and strain which means that this lamellar structure transitions to a fibrillar structure at sufficiently high strain [6, 104].

In contrast to filler particles which limit the mobility of the polymer chains, SIC increases the conformational entropy of the amorphous chain segments by restricting the conformation of the crystalline chain segments to the alignment along the stretching direction [46]. A sketch of a crystallite surrounded by amorphous chain segments is depicted in Figure 2.7. The comparison of the stress-stretch behavior of IR and NR, as it is shown in Figure 2.14, indicates reinforcement by SIC, since NR has a higher ability for SIC than IR. Alignment of chains along the external strain direction, analogous to the load-bearing chains between filler particles - especially if their number is increased by the aforementioned 'slip'-mechanism - increases the strength along this direction. Thus, there is an analogy here between filled elastomers and those showing SIC.

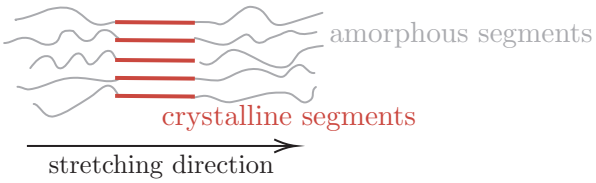

Figure 2.7.: Illustration of crystallites which formed due to SIC and are surrounded by amorphous segments.

Another aspect of reinforcement is resistance to crack formation and attendant failure of the material. Filled elastomers and strain-crystallizing elastomers are similar in this respect because both filler particles and crystallites impede crack formation and propagation to a first approximation. In particular, both filler addition and SIC increase the tensile strength of the elastomers. However, the cause for this may be quite different. Filler particles, i.e. minimum aggregates, usually do not break. Thus, a crack must circumvent these particles, which means a longer path and therefore a larger energy needed for crack propagation. This of course depends on the polymer-filler interface strength. In principle, this is also true for crystallites. But in addition, they are surrounded by a 'soft shell' due to the larger conformational freedom of the amorphous chain segments surrounding the crystallites. Propagating a crack along or inside this shell again requires additional energy. Another point is the formation energy (or enthalpy) of the crystallites themselves, which upon formation must be provided by the external forces.

Reinforcement (not including catastrophic failure) by SIC dominates in the range of high stretches, while reinforcement by filler also plays an important role in the range of small stretches and decreases due to the Payne effect with increasing stretch. Nevertheless, the remaining contributions to filler reinforcement persist such that they for

instance can also increase the tensile strength compared to unfilled rubber. Although the crystallites are of different nature than filler particles, both of them are often interpreted in the same way in the literature, i.e. as if they act like additional cross links [22]. If both phenomena are comparable, one may ask whether reinforcement by SIC is determined by interactions or hydrodynamic effects. Understanding of reinforcement requires for separating both phenomena and analyzing the interplay and the differences between both of them.

Besides due to the viscoelastic behavior of elastomers, strength of the material and reinforcement depend on the rate or frequency of loading, temperature and the history of the sample due to the viscoelastic behavior of rubber. The latter aspect will be covered in section 2.4, where the stress-stretch behavior of rubber is discussed. A phenomenological model for the time dependence will be provided in subsection 2.4.1. In section A.1, a model for the temperature dependence which bridges the molecular level with the macroscopic behavior of the material will be discussed. A relation between time and temperature regarding the mechanical behavior of rubber will be derived in subsection 2.4.2. Moreover, the dependence of SIC itself on temperature and strain-rate will be part of in section 2.4.

2.3. Cross Links and Fillers in Elastomers

When discussing strength and reinforcement of elastomers, microstructural changes of the material play an important role. On the one hand, this can be intrinsic changes due to SIC. On the other hand, the changes can be induced by processing of the material, for instance varying the cross link density or embedding filler into the rubber matrix.

There are chemical and physical "cross links" in a network. When talking about cross links in this work, the chemical ones are meant, while the physical ones are called entanglements subsequently. Both of them are illustrated in Figure 2.8. They are expected to act reinforcing since they restrict the mobility of the polymer chains due to the generated network structure.

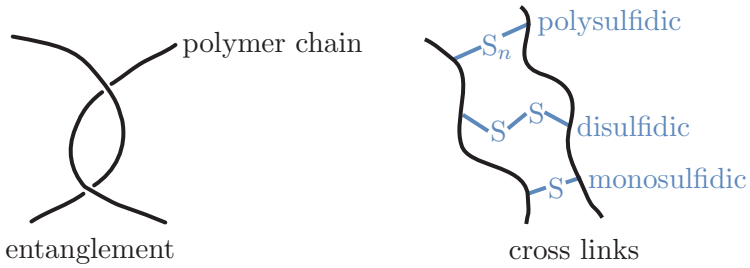

Figure 2.8.: Illustration of entanglements and cross links between two polymer chains. The cross links are drawn as sulfur bridges where monosulfidic, disulfidic and polysulfidic are distinguished.

Entanglements occur if the polymer chains are sufficiently long. The transition can be observed in the viscosity at a critical molecular weight M_c of the polymer [105–107]. Below this threshold, the viscosity increases linearly and can be explained by the Rouse model, but, beyond the threshold, the viscosity inclines according to a power law. This behavior just became explainable by entanglements. Furthermore, the frequency- or time-dependent storage moduli of polymers with sufficiently high molecular weight show a plateau between the glass transition and the region of viscous flow in contrast to the moduli of polymers with low molecular weight. Also the plateau modulus is explained

by entanglements which generate a network structure that is stable at high frequencies since their release requires for a huge number of changes in the conformations [107].

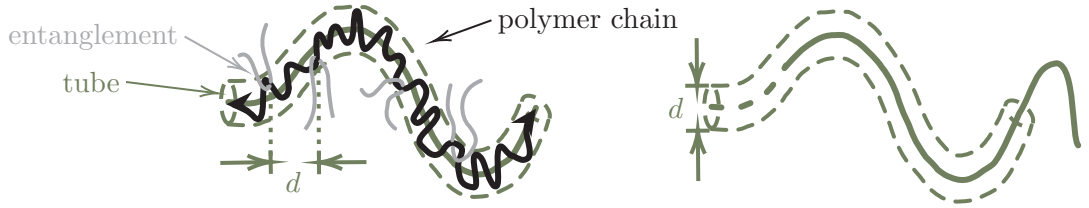

Figure 2.9.: Illustration of the tube model. On the left, the polymer chain is trapped in the tube. On the right, the chain has partly left the tube towards the right such that the original tube partly disappears.

For the purpose of a quantitative description, the tube model [58] has been introduced. In this picture, the polymer is confined within a tube which restricts the possible conformations of the chain segments to this volume [107]. It is assumed that this constraint is equivalent to the restriction of possible conformations due to entanglements. The tube model is illustrated in Figure 2.9. The tube diameter d measures the so-called entanglement length which is the mean distance between two entanglements:

$$d = a\sqrt{N_\mathrm{e}}.$$

This equation originates from the assumption that the chain segment between two entanglements which itself consists of N_e segments of length a is a Gaussian chain. Movements of the chain within the tube are not constrained such that the N_e segments between two entanglements can move freely and, thus, their motion can be described by the Rouse model. This yields different eigenmodes and relaxation times for the chain segments [107]. Due to the restriction of the chain, the longest relaxation time $\tau_\mathrm{e} \propto N_\mathrm{e}^2 \propto d$ is shorter than the longest relaxation time of the Rouse model for an entire free chain. Just for times larger than τ_e, the entanglements affects the motion of the chain. The motion is constrained to the diffusion of the chain along its contour and fluctuations perpendicularly to it which are limited by the tube. The movement is called reptation. It is presumed now that, for viscous flow, the chain has to leave the tube, which means that all entanglements are released. Consequently, the time-dependent storage modulus reaches a plateau value after a sufficiently long time:

$$G_\mathrm{e} = \frac{\rho RT}{M_\mathrm{e}} \propto \frac{1}{N_\mathrm{e}},$$

where ρ denotes the mass density, R is the ideal gas constant, T the temperature and M_e the molecular weight of the chain segments between two entanglements. It is expected that more flexible polymer chains are more likely to entangle with adjacent chains. Hence, the number N_e of chain segments between two entanglements decreases such that the plateau modulus increases [107]. For NR, plateau modulus has been experimentally determined to be $G_\mathrm{e} = 0.58\,\mathrm{MPa}$, the entanglement molar mass has been obtained as $M_\mathrm{e} = 3890\,\mathrm{g/mol}$ and tube diameter as $d = 51.4\,\text{Å}$ [108].

Moreover, the critical molecular weight for the occurrence of entanglements is related to the mean molecular weight M_e of the chain segment between two entanglements as follows:

$$M_\mathrm{c} \approx 2M_\mathrm{e}.$$

Consequently, the critical molecular weight can be computed from the experimentally obtained plateau value of the storage modulus. Nevertheless, note that, first, the

model relies on the presumption of equally distributed molecular weight. Secondly, the considerations hold for uncured samples, otherwise chemical cross links additionally contribute to the modulus. Although entanglements limit the number of possible chain conformations and, therefore, affect the mechanical behavior of the elastomer, the polymer chains are not as fixed as by chemical cross links and they are able to slip [77]. For polyisoprene, values of $M_c = 10\,000\,\mathrm{g/mol} - 15\,000\,\mathrm{g/mol}$ are reported [109].

Cross links in NR as well as in other elastomers are established during vulcanization by the formation of sulfur bridges between the polymer chains. This process, discovered by Charles Goodyear in 1839, made elastomers relevant for applications because it improves their mechanical properties. Since sulfur is present in form of S_8-rings which inertly open up, accelerators are required [5]. If high elasticity of the vulcanizate is required, 0.25 phr to 7 phr of sulfur are used. Conventional sulfur-accelerator systems for curing of rubber contain $2 - 3.5$ phr of sulfur and $0.5 - 1$ phr of accelerator. Besides, there are also efficient and semi-efficient sulfur-accelerator systems. The ingredients are added to the rubber and the mixture is heated up afterwards for the reaction. The vulcanization temperatures for conventional sulfur-accelerator systems must not exceed 160 °C in order to avoid so-called reversion [5]. In NR, sulfur bridges usually bond to the methylene groups adjacent to the double bonds of the isoprene monomers [5]. Peroxides can be used as an alternative for sulfur, but both the reaction properties and the properties of the resulting vulcanizate differ [5]. The process of vulcanization determines the cross link density and, thus, the mesh size of the generated network structure. However, the cross link density does not increase linearly with the amount of sulfur. The sulfur bridges can be monosulfides, disulfides or polysulfides. In addition, the sulfur may form a ring which cycles back to the chain at which it started. Therefore, the cross link density is difficult to adjust and it may be inhomogeneous. Besides, there may remain unbound parts of sulfur in the material. Furthermore, the structure of the cross links, which also determines the mechanical properties of the vulcanizate, is affected by the vulcanization temperature and vulcanization time. In NR, conventional sulfur-accelerator systems generate disulfidic and polysulfidic cross links, but no monosulfidic [5].

The cross link density refers to the amount of monomers associated with a cross link which is usually measured in units of $\mathrm{mol/cm^3}$. As shown above, it is related to the molecular weight between two cross links.

The mesh size of vulcanized NR can be estimated for a given mass fraction of sulfur and it is in general given as follows:

$$a = N_{\mathrm{link}} l_{\mathrm{m}},$$

where N_{link} denotes the number of monomers in a link, i.e. a polymer chain which connects two cross links, and l_{m} is the length of a monomer. The number of monomers per cross link is related to the number of monomers in a link by

$$\frac{N_{\mathrm{m}}}{N_{\mathrm{c}}} = f \frac{N_{\mathrm{link}}}{2},$$

where N_{m} is the total number of monomer and N_{c} is the number of cross links established during vulcanization. The functionality f of a cross link, i.e. the number of links connected to the cross link, is set to be 4 subsequently. For the right hand side of the equation, it is presumed that half of the monomers in a link are assigned to the considered cross link, while the remaining number of monomers belongs to an adjacent cross link. The number of cross links N_{c} is the ratio of the total number of sulfur atoms N_{S} and the number $N_{\mathrm{S,c}}$ of sulfur atoms within a sulfur bridge. The total number of

monomers and the total number of sulfur atoms are both computed from the ratio of the total mass of NR M_{NR} or sulfur M_{S} and the mass of a monomer m_{m} or sulfur atom m_{S} respectively. Consequently, the number of monomers between two cross links is given as:

$$N_{\mathrm{link}} = 2\frac{N_{\mathrm{S,c}}}{f}\frac{M_{\mathrm{NR}}}{m_{\mathrm{m}}}\frac{m_{\mathrm{S}}}{M_{\mathrm{S}}}. \tag{2.9}$$

The weight of an isoprene monomer amounts to $m_{\mathrm{m}} = 68.1170\,\mathrm{g/mol}$ [110] and the weight of a sulfur atom is $m_{\mathrm{S}} = 32.065\,\mathrm{g/mol}$ [111]. On average, a sulfur bridge in a conventional vulcanization system consists of $N_{\mathrm{S,c}} = 5$ sulfur atoms [5]. Presuming that NR is vulcanized with 1 phr of sulfur, i.e. $M_{\mathrm{NR}}/M_{\mathrm{S}} = 100$, yields $N_{\mathrm{link}} \approx 118$. With the length of an isoprene monomer $l_{\mathrm{m}} \approx 3\,\text{Å} - 5\,\text{Å}$, this corresponds to a mesh size of $a \approx 34.5\,\mathrm{nm} - 59.0\,\mathrm{nm}$.

Since vulcanization generates effectively longer chains if ends of different chains are linked, branched structures or indeed a network, the viscosity is increased and thus the moduli are affected [107]. A network is just generated if the cross link density exceeds the percolation threshold or gelation point, but there might remain free chains. The percolation threshold is indicated by the viscosity diverging towards infinitely large values [107]. Analogously to the case of entangled polymer chains, the storage modulus of vulcanized polymers converges towards a plateau value after sufficiently long time. Both cross links and entanglements contribute to the plateau modulus:

$$\lim_{t\to\infty} G(t) \equiv G = G_{\mathrm{x}} + G_{\mathrm{e}} = \rho RT\left(\frac{1}{M_{\mathrm{x}}} + \frac{1}{M_{\mathrm{e}}}\right),$$

where G_{x} denotes the contribution to the plateau modulus due to chemical cross links and M_{x} and M_{e} are the molecular weights between two cross links and between two entanglements respectively. The molecular weights can be related to the cross link density p_{x} and the entanglement density p_{e} respectively:

$$p = \frac{2}{f}\frac{m_{\mathrm{M}}}{M},$$

where f is the functionality of a cross link or entanglement and m_{M} the molecular weight of the monomers. This yields for the plateau modulus:

$$G = \rho RT\frac{f}{2}\frac{1}{m_{\mathrm{M}}}\left(p_{\mathrm{x}} + p_{\mathrm{e}}\right). \tag{2.10}$$

If the storage modulus of a vulcanized polymer is measured in the region of rubber elasticity dependent on time or frequency, this equation allows for the computation of the cross link density.

The cross link density can be experimentally obtained from stretching or swelling experiments. On the one hand, according to the theory of rubber elasticity which can be applied to stretching, the elastic modulus is proportional to the cross link density. On the other hand, it is often obtained by applying the phenomenological Mooney-Rivlin equation for the stress σ:

$$\sigma = 2\left(C_1 + \frac{C_2}{\lambda}\right)\left(\lambda - \frac{1}{\lambda^2}\right),$$

where C_1 and C_2 are constants [5, 107]. This equation is only applicable in the intermediate range of stretches for $\lambda < 2$. The constant C_1 is related to the shear modulus G as follows:

$$2C_1 = G = \frac{\rho RT}{M_{\mathrm{x}}},$$

where M_x denotes the molar mass of a chain segment between two cross links. A Mooney-Rivlin plot, i.e. plotting $\sigma/2\left(\lambda-\lambda^{-2}\right)$ versus $1/\lambda$, yields C_1 from which the cross link density can be derived.

To extract the cross link density from equilibrium swelling, the Flory-Rehner equation [112] is applied :

$$\rho\frac{v_s}{M_x}=\frac{\ln\left(1-\phi_p\right)+\phi_p+\chi\phi_p^2}{\phi_p^{1/3}-\phi_p/2},$$

where v_s is the molecular volume of the solvent, ϕ_p denotes the volume fraction of polymer in the mixture and χ is the Flory-Huggins parameter for the interaction of solvent and polymer network which can be for instance obtained from measurements of the osmotic pressure.

It is found in experiments that the cross link density affects SIC in NR [8]. The onset stretch of SIC is approximately independent of the cross link density. However, the crystallite dimensions decrease with increasing cross link density and the crystallite volume declines with increasing cross link density at high cross link density, but it varies just slowly at small cross link densities. The region in which the behavior changes coincides with the density of physical entanglements. In addition, the crystallization rate shows a maximum in the vicinity of the density of physical entanglements. Chenal *et al.* [8] explain their observation in a picture in which crystallite nuclei are generated by stretched chains which align along the stretching direction and folding of surrounding chains leads to crystal growth. In samples with a small cross link density, the formation of nuclei is not promoted and occurs rather occasionally. In samples with a high cross link density, nucleation is advanced, but crystal growth due to chain folding is inhibited because the cross links restrict the mobility of the chains.

Filler particles are added to the rubber matrix during mixing or compounding. Essentially, this is the first step when rubber is made, while the vulcanization, mentioned before, is the last step. The reinforcement ability of filler particles is characterized by their physicochemical properties such as surface structure, surface area, dispersibility and surface-chemical properties [98]. These properties also determine the filler network morphology. Filler network morphologies can be observed by transmission electron microscopy (TEM). The smallest units of filler are so-called primary particles which are spherically shaped [107]. Their size is usually in the nanometer-range and, dependent on the filler type, of order of the mesh size of cross-linked rubber.

In industry, carbon black (CB) and silica are used most commonly as reinforcing filler. A certain nomenclature for different types of CB, which is presented in Table 2.1, has been introduced by American Society of Testing Materials (ASTM) [98, 113]. The first digit refers to the vulcanization speed which is normal "N" or slow "S". The latter three digits are related to the diameter of the primary particles. Typical CB types are designated by indicating the primary particle size with the first numeral, repeating this number in the second numeral and keeping the last digit as zero [114]. Primary particles of active types of CB are smaller than those of inactive CB types. Silica tends to aggregate and thus it is difficult to disperse it in the rubber matrix. This inhibits its reinforcing properties. Nevertheless, employing the silane coupling agent bis(triethoxysilylpropyl)tetrasulfide (TESPT) and using specific preparations leads to reinforcement [98].

Table 2.1.: ASTM numbers for CB classification, corresponding primary particle diameter D and name of standard CB in a category. The information in this table is taken from [98] and from Table 2 in [114].

ASTM number	D/nm	standard CB	
900-999	201-500	Medium Thermal (MT)	N990
800-899	101-200	Fine Thermal (FT)	N880
700-799	61-100	Semi-Reinforcing Furnace (SRF)	N770
600-699	49-60	General Purpose Furnace (GPF)	N660
500-599	40-48	Fast Extrusion Furnace (FEF)	N550
400-499	31-39	-	
300-399	26-30	High Abrasion Furnace (HAF)	N330
200-299	20-25	Intermediate Super Abrasion Furnace (ISAF)	N220
100-199	11-19	Super Abrasion Furnace (SAF)	N110
000-099	1-10	-	

The primary particles build larger filler aggregates. Due to their structure, the aggregates possess an effective volume which is higher than their actual volume. The effective volume determines how the surrounding elastomer matrix is deformed. Therefore, reinforcement must rather originate from the aggregates than from the primary particles themselves [98]. Primary particles of CB for instance consist of layers of graphite and aggregate to irregular, branched structures, which are mechanically stable [98, 107]. However, the structure of CB aggregates depends on the CB type. While some tend to form comparatively short linear chains of a small number of primary particles, others bond with a lot of primary particles to larger, branched aggregates. In contrast to CB, aggregates formed by silica-based filler are not mechanically stable [107]. If the filler content is sufficiently high, larger agglomerates build. Dependent on the structure of an agglomerate, so-called trapped or occluded rubber is surrounded by filler particles such that it is shielded from mechanical stress and the effective filler content is increased [107]. The agglomerates can be destructed due to mechanical deformation of the material, but also bond again afterwards [107]. If the filler content is above the percolation threshold, a filler network is formed. For CB, the percolation threshold can be obtained by conductivity measurements [107]. Percolation of filler will be discussed further in subsubsection 5.2.1.

The filler content is usually given in "phr" which means *parts per hundred rubber* and refers to the mass fraction, but not to the volume fraction of filler in the composite. The volume fraction ϕ can be computed from the mass fraction "phr" as follows:

$$\phi = \frac{V_\mathrm{f}}{V} = \frac{m_\mathrm{f}/\rho_\mathrm{f}}{m_\mathrm{f}/\rho_\mathrm{f} + m_\mathrm{p}/\rho_\mathrm{p}} = \frac{\mathrm{phr}/\rho_\mathrm{f}}{\mathrm{phr}/\rho_\mathrm{f} + 100/\rho_\mathrm{p}}, \tag{2.11}$$

where $\rho_\mathrm{f} = m_\mathrm{f}/V_\mathrm{f}$ and $\rho_\mathrm{p} = m_\mathrm{p}/V_\mathrm{p}$ denote the densities of filler and polymer, i.e. NR in this case, respectively. In two-component systems, it holds $V = V_\mathrm{f} + V_\mathrm{p}$. Rewriting Equation 2.11 yields:

$$\mathrm{phr} = \frac{\phi}{1-\phi}\frac{\rho_\mathrm{f}}{\rho_\mathrm{p}} \cdot 100 \tag{2.12}$$

Typically, the filler content in rubber amounts to 20 to 80 phr. This corresponds to a volume fraction of $\phi = 0.09 - 0.29$ according to Equation 2.11 under the presumption of $\rho_\mathrm{p} = 1\,\mathrm{g/cm^3}$ and $\rho_\mathrm{f} = 2\,\mathrm{g/cm^3}$ which are consistent with the densities of rubber and CB. Assuming that the aggregate size is approximately 50 nm to 500 nm, the mean distance between two aggregates can be estimated to be 10 nm to 400 nm which is of order

of the so-called gyration radius of polyisoprene [107]. This indicates that the polymer might act as a junction between aggregates such that the mechanical properties are affected [107]. In the discussion of the interplay between elastomers and fillers, it is commonly referred to so-called bound rubber. This part of the rubber matrix cannot be extracted from it by swelling with a good solvent at room temperature due to adsorption on the filler surface [11]. Therefore, it is a measure for the surface activity of filler particles and for their reinforcing effect. Nevertheless for most of the measurement methods, particularly the gel content of NR can be misinterpreted as bound rubber.

Fei *et al.* [115] have measured the cross link densities of NR with variable content of CB N330 and variable sulfur content. Their data suggests that CB does not affect the chemical cross links density. The density of entanglements is independent of the sulfur content, but it is elevated by the inclusion of filler. In addition, the total cross link density is increased. These increases are attributed to the adsorption of polymer chains on the filler surface or chemical bonds between each other which restricts their mobility.

The viscoelastic properties of the compound change, when fillers are added to rubber [11]. Due to hydrodynamic effects, the viscosity and thus the Young's modulus is increased by reducing the volume fraction of the polymer. Besides, the filler geometry affects the viscosity. The higher the effective volume of the filler is, the higher is the viscosity of the compound. The viscosity is also determined by adsorption of rubber on the filler surfaces, since the attachment of a segment of a polymer chain on a filler surface limits the mobility of the entire chain. This leads to the formation of bound rubber, which results in an enlarged effective volume of the filler particles. The amount of adsorbed rubber increases with the interfacial area per volume and the strength of the polymer-filler interaction. Another effect induced by inserting filler is polymer gelation. Moreover, filler flocculation increases the viscosity of the compound by magnifying the effective filler volume. Wang & Morris [11] state that the formation of filler agglomerates is superior to the effect of adsorption.

The increase of Young's modulus of the compound because of the inclusion of filler into vulcanized rubber is theoretically described by the Guth-Gold equation [67, 68]:

$$G = G_0 \left(1 + 2.5\phi + 14.1\phi^2\right), \tag{2.13}$$

where G_0 is the shear modulus of the unfilled sample and ϕ the filler volume fraction [11]. The terms up to linear order of ϕ account for hydrodynamic reinforcement according to Equation 2.2. However, this equation is in practice not applicable without further modifications since it relies on the assumption of, for example, spherical filler particles, non-interacting particles and ideal dispersion [11]. Consequently, this equation has been further modified for example by replacing the filler volume fraction by the effective filler volume fraction [116] in order to take the filler structure into account. Nevertheless, this equation has for example been tested on CB and silica filled NR [117].

In Figure 2.10, the orders of magnitude inside a rubber specimen are summarized. The size of the specimen is on the macroscopic scale and amount to several centimeters. The size of filler agglomerates or a filler network is up to the millimeter range. The filler agglomerates are composed of connected aggregates which dimension amounts up to a micrometer. The filler aggregates are build up by filler particles. The mesh size of the polymer network, into which the filler network is embedded is even smaller then the filler aggregates. The linear dimension of strain-induced crystallites is similar to the size of a filler particle. When going to even smaller sizes, the atomistic scale is reached. The values given here refer to CB filled NR. They depend on both the polymer and the filler type.

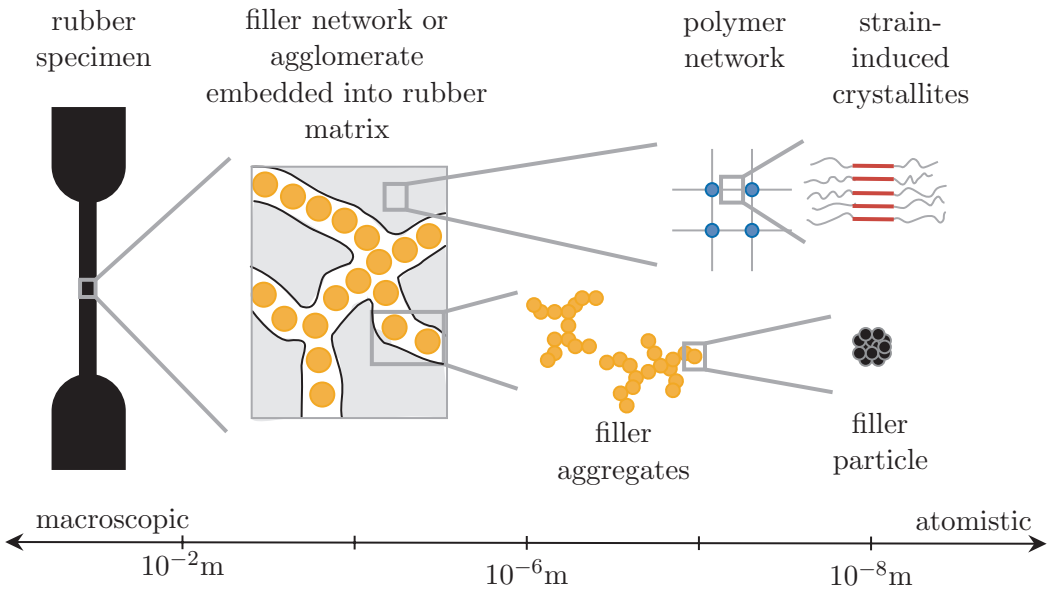

Figure 2.10.: Illustration of the orders of magnitude in a rubber specimen. Note that such a dumbbell-shaped specimen is usually deformed along the vertical axis such that strain-induced crystallites align along this direction.

2.4. Stress-Stretch Behavior of Elastomers

During the investigations, stress-stretch curves for the model networks will be obtained. Therefore, it is clarified in this section what stress-strain behavior is expected for both unfilled and filled NR because it will be focused on this elastomer. While experimental observations are described and explained, the governing effects are pointed out.

The stress-stretch behavior of NR is governed by its ability to strain-crystallize. This leads to stress relaxation and a characteristic hysteresis. These phenomena will be explained subsequently. Stress-stretch curves are obtained by tensile tests. The sample is deformed by applying a force and the strain response is measured. The force usually acts uniaxially. The deformation is conducted at a fixed strain rate and temperature. Tensile tests in particular give access to the Young's modulus which is given by the slope of the stress-strain curve in the linear region, the load capacity which is called yield strength, the strength before distortion which is determined by the so-called the yield point, the ductility which is given by the elongation at break, the toughness which is the energy required to break the sample and can be obtained from the area under the curve, as well as the tensile strength [118].

Nevertheless, it is of common interest from in an industrial point of view to characterize rubber by its moduli which are obtained from Dynamic Mechanical Analysis (DMA) [118]. As it will be explained during the discussion of the theory of rubber elasticity in section 3.3, DMA is more convenient than tensile tests in this context. However, these quantities are related to the stress-stretch behavior as will be discussed in the following. DMA is performed by periodically applying a stress to the material and measuring its strain response.

2.4.1. A Simple Model for Viscoelasticity

Due to the viscoelastic behavior of elastomers, DMA of rubber reminds of the driven harmonic oscillator known from classical mechanics [119]. Usually, the shear amplitudes are comparatively small and, therefore, in the region of linear response of the material.

In order to describe the viscoelastic properties of rubber and to predict its moduli, the Kelvin-Voigt model can be considered for small frequencies [119]. The two basic elements are a spring accounting for the elastic behavior and a dashpot accounting for the viscous behavior, which are combined as shown in Figure 2.11. The stress σ_G and the strain u_G at a spring with shear modulus G are, in the linear region, related by Hooke's law

$$\sigma_G = G u_G,$$

while the stress σ_η and the strain rate $\dot{u}_\eta$ at a dashpot with viscosity coefficient η are related by

$$\sigma_\eta = \eta \dot{u}_\eta,$$

which is in general valid for Newtonian fluids and also holds within the harmonic approximation. The former equation describes the elastic contribution and the latter the dissipative contribution to the stress. The Kelvin-Voigt model is an arrangement of a spring and a dashpot in parallel. The total stress σ and the total strain u of this arrangement are given by

$$\begin{aligned} \sigma &= \sigma_G + \sigma_\eta, \\ u &= u_G = u_\eta. \end{aligned}$$

Inserting the relations from above into the equation for σ yields

$$\sigma = G u + \eta \dot{u}. \tag{2.14}$$

Equation 2.14 can be solved for σ and u by a complex ansatz considering a phase factor δ which accounts for dissipation and friction:

$$\begin{aligned} \sigma &= \sigma_0 \mathrm{e}^{i(\omega t + \delta)} \\ u &= u_0 \mathrm{e}^{i\omega t}. \end{aligned}$$

The amplitudes of the stress and the strain are denoted as σ_0 and u_0, respectively. The frequency of the periodic deformation is ω. Inserting the ansatz into Equation 2.14 leads to

$$G^* \equiv \frac{\sigma_0}{u_0} \mathrm{e}^{i\delta} = G + i\omega\eta, \tag{2.15}$$

where $G^* = G' + iG'' = \sigma/u$ is defined as the complex modulus. The real part G' is the storage modulus, while the imaginary part G'' is the loss modulus. From the moduli, so-called $\tan\delta = G''/G'$, the damping, can be derived, which is a measure for energy dissipation due to internal effects. For example, if a sinusoidal stress is applied to a rubber sample for DMA, the detected strain is also sine-shaped, but it is shifted in phase by δ. Since the stress amplitude is known and both the strain amplitude and the phase factor can be measured, the moduli and the damping can be computed.

It holds for the Kelvin-Voigt model:

$$\begin{aligned} G' &= G, \\ G'' &= \omega\eta, \\ \tan\delta &= \tau_{\mathrm{KV}}\omega, \end{aligned}$$

where $\tau_{\mathrm{KV}} = \eta/G$ is a relaxation time [119]. These formulae can be fitted to experimental data for obtaining the parameters G and η. Obviously, the storage modulus

accounts for elastic processes within the material and the loss modulus accounts for dissipative processes.

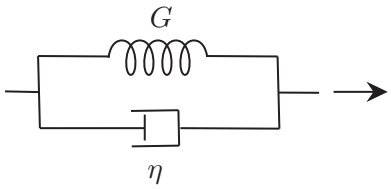

Figure 2.11.: Illustration of the Kelvin-Voigt model.

That the Kelvin-Voigt model includes dissipative processes is an important aspect. In Figure 2.12, plots of the normalized stress versus the normalized strain are depicted for sinusoidal excitation where the relation between excitation and response is linear, like for the Kelvin-Voigt model, and the stress is shifted with respect to the strain by the phase δ. These plots show a hysteresis dependent on the phase. In general, the hysteresis is quantified by the work required for a strain cycle:

$$w = \oint \sigma \, du. \tag{2.16}$$

For the Kelvin-Voigt model, it holds:

$$w = \pi G'' u_0^2,$$

which highlights that the hysteresis is caused by dissipative processes. As depicted in the plot, it vanishes for $\delta = 0$ and is maximized for $\delta = \pi/2$. Note that the dissipative processes involved in the hysteresis of the Kelvin-Voigt model are not further specified. They are all unified in the abstract viscosity η.

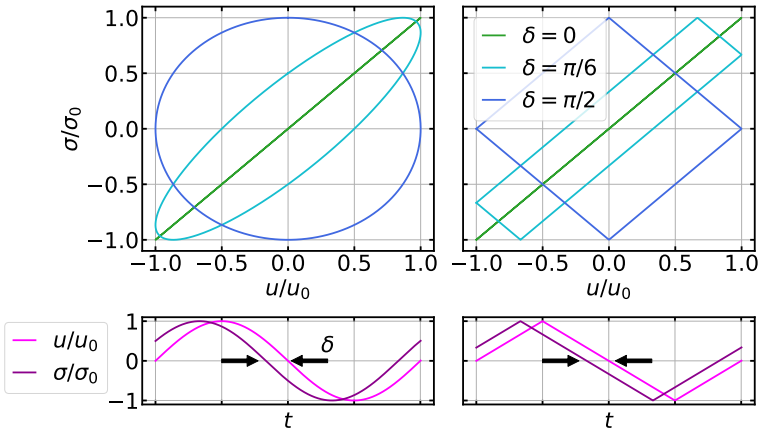

Figure 2.12.: Stress-strain curves for sinusoidal and triangular excitation for different phase shifts δ with linear relation to the response. The hysteresis, i.e. the area enclosed by the curves, yields the work required for a strain-cycle. In addition, the normalized stress and the normalized strain are plotted against time in arbitrary units.

The occurrence of a hysteresis in plots of stress versus strain for strain cycles agrees with experimental observations like in Figure 2.14. In stretching experiments which are considered in this work, the stress is not applied according to a sine function but rather according to a triangle function. The stress-strain relation for a linear relation between excitation and response in this case is also depicted in Figure 2.12. The stress-strain curves and thus the hystereses are of different shape in comparison to the case

of sinoidal excitation. A striking difference is that the linear relation between stress and strain for triangular excitation. A reason is that the molecular structure of the material is neglected. The polymer chains disentangle during stretching. In addition, both cross links and entanglements affect the mechanical behavior since they restrict the mobility of the polymer chains at sufficiently high deformations. In filled rubber, the non-linear behavior at small deformations is determined by the filler network structure and its interaction with the polymer. SIC also contributes to the hysteresis of strain-crystallizing rubber, which in particular depends on the deformation rate and on temperature. Indeed, a dependence of the hysteresis on the frequency of the deformation is predicted by the Kelvin-Voigt model. Furthermore, the stress-strain relations provided by the Kelvin-Voigt model are independent of the history of the sample. In contrast, experimental data shows that rubber behaves different if it has already been deformed. Another reason for the distortion of the curve in an experimental context is the slippage of the sample from the clamps at large deformations.

Besides the Kelvin-Voigt model, there are several other combinations of springs and dashpots applied for the description of the mechanical behavior of materials. For example, the Maxwell model is composed of a spring and a dashpot which are arranged in series. It is suitable for the description of the moduli and damping of rubber at high frequencies. Another example is the Zener model, which is a combination of the Maxwell model and the Kelvin Voigt model.

2.4.2. A Relation between Time and Temperature Dependence

For the Kelvin-Voigt model presented in the previous section, the shear moduli depend on the product of frequency and viscosity which includes a temperature dependence. Thus, the moduli at different frequencies ω_1 and ω_2 are identical if the temperatures T_1 and T_2 are chosen such that:

$$\omega_1 \eta\left(T_1\right) = \omega_2 \eta\left(T_2\right) \tag{2.17}$$

This is for example useful to generate data for frequency ranges that cannot be reached by a measurement device, but by varying the temperature instead. A so-called master curve can be obtained by shifting the data along the frequency axis. This principle is called time-temperature superposition [107, 120].

The dependence of the viscosity on temperature is empirically given by the Doolittle relation [121]:

$$\eta\left(T\right) \propto \exp\left[A / v_{\mathrm{f}}\left(T\right)\right], \tag{2.18}$$

where A is a constant and $v_{\mathrm{f}}\left(T\right)$ denotes the so-called free volume [120]. The latter quantity is obtained from a Taylor expansion up to leading order in T around $T_1 = T_{\mathrm{r}}$ which serves as reference temperature:

$$v_{\mathrm{f}}\left(T\right) = v_{\mathrm{f}}\left(T_{\mathrm{r}}\right) + \alpha\left(T - T_{\mathrm{r}}\right), \tag{2.19}$$

where α is a constant. With the help of these relations, an equation for the shift factor for the frequency can be derived:

$$\begin{aligned} a_T \equiv &= \frac{\eta\left(T\right)}{\eta\left(T_{\mathrm{r}}\right)} \\ &= \exp\left[-\frac{A}{v_{\mathrm{f}}\left(T_{\mathrm{r}}\right)} \cdot \frac{\left(T - T_{\mathrm{r}}\right)}{v_{\mathrm{f}}\left(T_{\mathrm{r}}\right)/\alpha + \left(T - T_{\mathrm{r}}\right)}\right]. \end{aligned} \tag{2.20}$$

This expression is called WLF-equation according to Williams, Landel and Ferry [122]. For a sequence of temperatures T, the shift factor is determined by fitting the parameters $A/v_\mathrm{f}(T_\mathrm{r})$ and $v_\mathrm{f}(T_\mathrm{r})/\alpha$ in the WLF-equation. The shifted frequency ω can be computed from the reference value ω_r via

$$\omega = \frac{1}{a_T}\omega_\mathrm{r}.$$

In Figure 2.13, the construction of a master curve for the storage modulus via time-temperature superposition with the help of the shift factor is illustrated. The data for the storage modulus obtained in the small interval of frequencies but at various temperatures is translated to the master curve for a fixed reference temperature. It is convenient to plot the data for the moduli in a log-log plot where log refers to the logarithm to base 10 but not the natural logarithm. Furthermore, the principle of time-temperature superposition is applied to data for other frequency-dependent quantities such as the damping.

In [123], experimentally obtained master curves for the moduli and the damping of CB filled NR can be found with shift factors determined from the WLF-equation as well as from the approach via the Arrhenius relation which is presented in section A.1. Note that it is not obvious that the principle of time-temperature superposition can be applied to filled rubber since the inclusion of filler affects the viscosity.

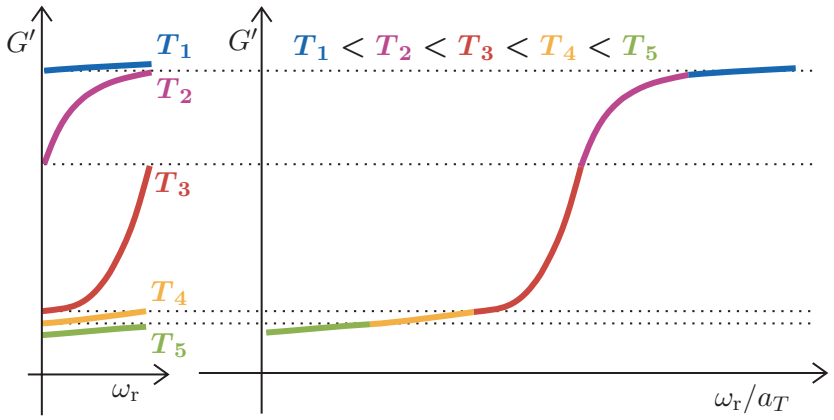

Figure 2.13.: Illustration of a master curve of the storage modulus obtained with the help of the shift factor.

2.4.3. Characteristics of Stress-Stretch Curves of NR

Typical stress-stretch curves for unfilled NR and synthetic isoprene rubber (IR) are presented in Figure 2.14. The data has been experimentally obtained by Toki *et al.* [10]. It has to be remarked that stress-stretch curves for elastomers are both temperature and strain rate dependent. In general, IR consists of around $93-98\,\%$ *cis*-1,4-polyisoprene, which is less than for NR, and it does not contain impurities [11]. The IR employed in the study by Toki *et al.* [10] is IR-2200 contains $98.5\,\%$ *cis*-content.

Considering the unvulcanized samples, the stress-strain curve for NR stands out because it possesses a hysteresis and a remaining permanent set in contrast to that for IR. These features remind of the stress-stretch curves for vulcanized rubber. Therefore, the hysteresis in NR is attributed to a pseudo-end-linked network which only occurs in NR due to additional functional groups [10, 124, 125]. The hysteresis phenomenon will be discussed in detail later in this section. For both samples, the stress rapidly increases at low strain. For IR, the stress tends to decrease beyond the so-called yield stress because of the rearrangement of entanglements and their dissociation [11]. Although both kinds

of rubber are able to strain-crystallize in general due to their *cis*-1,4-stereoregularity, only NR shows SIC at the considered temperature of 25° C. Coincidentally with the onset of SIC, the stress-stretch curve levels of in a plateau or shoulder. On the one hand, SIC enables relaxation of the amorphous chains which leads to softening. On the other hand, the crystallites can be interpreted as new cross links which increase the stress [46]. At first appearance, the increase of the stress in NR beyond softening can be ascribed to the pseudo-end-linked network since a network structure restricts the extensibility of the polymer chains, such that its limit is approached at lower strain. Nevertheless, strain-hardening [126] might be the dominating effect which is because of rearrangements in the sample caused by SIC and crystallites which act like additional cross links.

In comparison to uncured samples, vulcanized samples contain chemical cross-links, which generate a network structure, in addition to physical entanglements. Contrary to vulcanized IR, the shoulder, which indicates SIC, vanishes for NR. This is attributed to its dependence on the network density [10]. Furthermore, the stress-stretch curves for NR and IR overlap at small strain and there is no permanent remaining set for both of the samples. In particular for the NR sample, the stress decreases slower during release than it has risen during stretching. This observation can be attributed to the so-called inverse-yielding effect [127]. Albouy *et al.* [127] have studied this phenomenon in NR dependent on the cross link density. Beyond the first decline of the stress, a neck which has formed propagates through the sample such that the stress becomes approximately constant. When the neck disappeared, the stress decreases further and remaining crystals melt. However, this phenomenon requires that the maximum stretch and the crystallinity are sufficiently high. The incline of the stress in the regime of high stretch can be attributed to the strain-hardening effect [126]. Zhang *et al.* [126] have observed this self-reinforcement due to structural changes in peroxide-vulcanized IR, which are in particular associated with SIC.

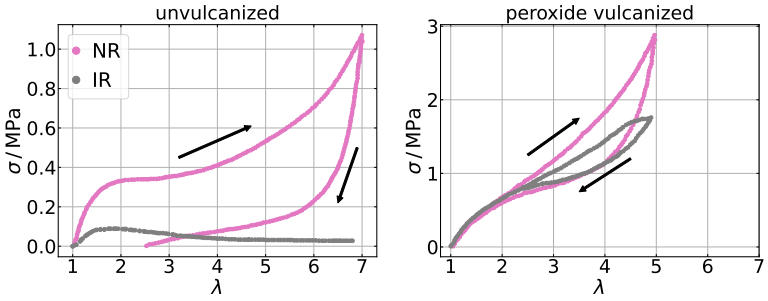

Figure 2.14.: Experimentally obtained stress-stretch curves for unfilled NR and IR at 25 °C and a deformation rate of 10 mm/min. The data is extracted from Figures 2 and 7 in [10]. Adapted with permission from Reference [10]. Copyright 2013 American Chemical Society.

In further experimental works, SIC in NR and in IR has been directly compared by analyzing stress and crystallinity. The crystallinity is mainly experimentally studied by wide-angle X-ray scattering (WAXS) using synchrotron radiation. At low strain rates, the ability of IR for SIC is hindered because it is branched along its backbone and possesses a lower stereoregularity [128, 129]. Thus, the equilibrium melting temperature is decreased. At high strain rates, both materials appear to have the same ability for SIC since the chain extension dominates SIC in this region [129]. It has been found that the onset of SIC and the end point of the plateau of the stress-stretch curve can be superposed with the help of a translation factor [129, 130]. The same holds for the crystalllinity-stretch curves in the hardening region. The hardening effect in IR is

thought to be not as pronounced as in NR due to smaller crystallinity [130]. However, the orientation and the size of the crystallites during deformation appear identical in both cases which emphasizes the similarity of the crystallization processes. Besides, the plateau of the stress for IR is twice as long as for NR [130].

At $-25\,^{\circ}\mathrm{C}$, crystallization in IR is suppressed compared to NR which is indicated by a lower crystallization rate and attributed to its non-*cis* content [131]. At $-50\,^{\circ}\mathrm{C}$, the crystallinity in NR is higher at any stretch than in IR as it is at $+25\,^{\circ}\mathrm{C}$ [132]. In particular, the onset of SIC is situated at lower stretches for NR. The crystallite sizes in NR and IR are approximately equal and independent of the stretch. The orientation of the crystallites in NR is smaller and the disorder is higher than in IR which is attributed to impurities and the pseudo-network in NR. Both may, on the one hand, hamper the alignment of the crystallites along the stretching direction and, on the other hand, promote SIC in NR rather than its stereoregularity does [132].

Chen *et al.* [133] investigated the impact of the mass fraction of non-rubber components, i.e. phospholipids and proteins, and interaction strengths of hydrogen and non-hydrogen bonds on the structure, dynamical and mechanical behavior of NR by coarse-grained molecular dynamics simulations. They did not include filler particles. A single NR chain in their model is composed of a phosphate group at the one end, cis-1,4-polyisoprene and polypeptide at the other end. The end groups and each polyisoprene unit are represented by beads which are connected by harmonic potentials and a harmonic bending potential is considered. Phospholipids and proteins are also modeled as beads, but they are linked to the phosphate groups and polypeptide, respectively, or to beads of their kind via hydrogen bonds. Thus, clusters of non-rubber components form which act like cross links. The Lennard-Jones potential is applied for non-bonded interaction between polyisoprene units, for the hydrogen bonds and for interactions of the polyisoprene units with phospholipids and proteins, i.e. non-hydrogen bonds. SIC is not explicitly incorporated into the model, but identified by analyzing the orientation of chain segments. They simulate NPT-ensembles of 100 identical NR chains consisting of 331 beads with variable number of phospholipids and proteins at 298 K and 0.1 MPa. The authors report that the clusters of phospholipids and proteins restrict the mobility of the NR chains due to adsorption of the chains and their physical structure. They find that the alignment of the chains along the stretching direction and SIC are enhanced by strong hydrogen bonds and high mass fraction of phospholipids and proteins. In addition, the stress at fixed stretch is increased.

In general, SIC shows a dependence on strain rate and temperature. The retardation of the nucleation of crystallites suggests that SIC is strongly strain rate dependent, in particular the onset stretch [134]. Increasing the strain rate shifts the onset of SIC towards higher stretches [7, 134]. In addition, the relaxation due to SIC, which is indicated by the plateau of the stress-stretch curve, and the hardening decrease due to lower crystallinity [7, 134]. Candau *et al.* [134] find that the onset of SIC decreases with increasing so-called induction time, which is associated with strain rate, until a critical time is reached above which the onset of SIC is approximately time-independent. The authors assume retarded nucleation and instantaneous crystal growth such that, under quasi-static conditions, the onset of SIC is controlled by the stretching ratio [134]. For higher strain rates, the onset of SIC is determined by diffusion of the macromolecules. Candau *et al.* [135] derived a characteristic time for SIC from cyclic deformation of vulcanized NR with variable pre-stretches for variable frequencies at room temperature. The stretch $\lambda = 4$ marks the onset of SIC for stretching under quasi-static conditions. The characteristic time for pre-stretches $\lambda > 4$ is constant around 20 ms. For pre-

elongation $\lambda = 4$, the characteristic time is multiple times larger because of superposing thermal crystallization.

With increasing temperature, the onset stretch of SIC increases [136]. According to time-temperature superposition in elastomers, the onset stretch of SIC shows a minimum at certain temperature which is shifted towards higher temperature with increasing strain rate [134]. Candau *et al.* [136] have studied the impact of temperature on SIC and on melting of those crystallites in vulcanized NR by WAXS. During SIC, the behavior of the size of the crystallites dependent on the crystallinity is independent of temperature [136]. Cooling down a stretched sample from 80 °C to room temperature shows a behavior of the crystallite size dependent on the crystallinity index very similar to that for SIC.

The process of SIC also depends on the cross link density, the type of cross linker and the structure of the cross links. Stress-stretch and crystallinity-stretch curves for vulcanized NR with different cross link densities are depicted in Figure 2.15. If the cross link density is varied, the onset of SIC is unaffected [7, 101, 128], but the crystallinity at certain stretch decreases with increasing cross link density [7]. Tosaka *et al.* [128] point out that the melting temperature of the crystallites depends on the deformation entropy which itself, according to the theory of rubber elasticity which will be discussed in section 3.3, depends on the cross link density. In order to overcome this discrepancy between experimental observation and theory, the authors separate fully stretched short chains and long coiled chains in the network. The former are thought serve as crystallite nuclei, while the backfolded chains lead to crystal growth. The separation of these components yields to a contribution to the deformation entropy of the crystallite nuclei which depends on the cross link density and another contribution of the coiled chains which is independent of the cross link density. The Young's modulus and the stress at certain stretch in general increase with increasing cross link density [7, 101]. In addition, the plateau of the stress-stretch curve associated with SIC vanishes with increasing cross-link density [7]. For high cross link densities, the upturn of the stress of NR is shifted towards smaller stretches [7, 101]. Sainumsai *et al.* [101] report that the upturn of the stress and SIC are apparently not directly related. Since the crystallinity and simultaneously the stress of unvulcanized NR are significantly smaller than those of vulcanized NR, Sainumsai *et al.* [101] conclude that the contribution of SIC to the amplification of the stress in vulcanized NR is small.

Ikeda *et al.* [137] have compared SIC in peroxide-vulcanized NR and sulfur vulcanized NR and report a different impact on SIC. While increasing the network chain density in sulfur-vulcanized NR leaves the onset stretch of SIC unaffected, it decreases the onset of SIC in peroxide-vulcanized NR. The crystallite size depends also differently on the cross link density for both types of cross linker. However, the crystallization rate shows the same behavior in both cases. Their investigations suggest that peroxide-vulcanization generates a homogeneous network, but sulfur-vulcanization leads to domains of high and low cross link density. The comparison of the tensile properties indicated that those of peroxide-vulcanized NR are directly related to SIC, while the networks structure dominates in sulfur-vulcanized NR before the onset of SIC. The authors report that the domains of high cross link density act like reinforcing filler particles [137].

The behavior of the stress and of the crystallinity are similar for various dominating cross link structures, i.e. monosulfidic, disulfidic or polysulfidic [101]. In particular, the onset stretch of SIC appears to be independent of the cross link structure.

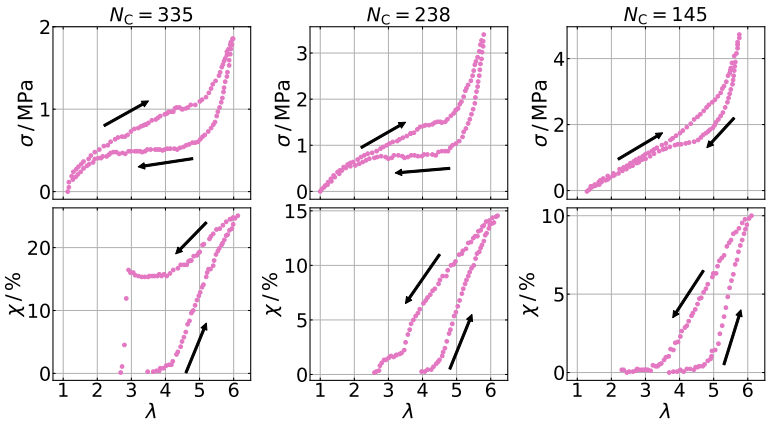

Figure 2.15.: Experimentally obtained stress-stretch and crystallinity-stretch curves for unfilled vulcanized NR with different cross link densities at 23° C. N_C denotes the number of monomers between two cross links, i.e. small N_C corresponds to high cross link density. The data is extracted from Figure 8 in [7]. Adapted with permission from Reference [7]. Copyright 2003 American Chemical Society.

As pointed out in section 2.3, embedding filler into the polymer matrix affects the mechanical properties of the compound. Exemplary stress-stretch curves for filled vulcanized rubber are shown in Figure 2.16. The curves have been obtained by Rault *et al.* [22] for vulcanized NR at a strain rate of $0.033\,\mathrm{s}^{-1}$. They examined both unfilled and filled samples containing 20, 40 and 50 phr of CB N375 as filler. Rault *et al.* point out that the maximum strain $\lambda = 4$ is the strain at which SIC approximately starts in the unfilled sample, while SIC begins at lower stretches in the filled samples [22]. The authors report that the filler particles serve as nuclei for SIC because the chains are extremely strained around them compared to other regions in the material [22]. Their ^{2}H NMR experiments enabled them to observe stress relaxation in the amorphous domains [22]. However, Poompradub *et al.* [19] disagree with the interpretation of filler particles as nuclei for SIC.

At small deformations, filler aggregates and agglomerates cannot be destructed and trapped rubber, which is situated within agglomerates, is not deformed [11]. Therefore, the stress increases. With growing strain, but still at small deformations, the so-called Payne effect [17] occurs [11, 98]. It can be observed more pronounced in the behavior of the storage modulus of the compound dependent on the stretch as shown in Figure 2.17. Since shearing is convenient in this context, the storage modulus approaches the shear modulus for such small deformations. Note that in the case of stretching the analogous quantity to the shear modulus is the elastic modulus or Young's modulus. Initially, polymer chains are adsorbed on the filler surface. During deformation of the sample, chain segments which connect two filler particles are stretched to a higher extend than the macroscopic stretch due to strain amplification. Hence, elastic energy is stored in the extended chains and the storage modulus is high. With increasing stretch, according to a model proposed by Dannenberg [99], the polymer chains slip off the filler particle such that the mobility of the chain segment between the filler particles is enhanced [98]. The chains are adsorbed or desorped alternately and reversibly such that the modulus decreases. Finally, this leads to a homogenization of the length of the chain segments which link the filler particles. Thus, the modulus becomes approximately constant. These rearrangements in the material cause the mechanical hysteresis. In this range of deformations, SIC does not contribute to the hysteresis since it begins at higher stretches.

Apart from that, it must be remarked that the curves presented in Figure 2.17 mimic different properties of both considered types of filler [15]. They differ in the

surface area and surface free energy, which are both higher for CB N134 than for CB N330. For CB N134 and CB N330, the surface free energy is significantly decreased by graphitization, while the size of the filler particles and filler morphology are preserved [15]. Furthermore, Tunnicliffe *et al.* [15] report that the filler on the scale of at least 1 μm is similarly well dispersed in any sample. Hence, the data indicates that the storage modulus decreases with decreasing surface area and with increasing surface free energy.

Going back to Figure 2.16, the stress-stretch behavior in the range of intermediate deformations is governed by the destruction of filler agglomerates such that the slope of the stress-strain curve reaches its minimum [11]. The behavior of the stress at higher stretches is determined by the non-Gaussian behavior of the polymer chains, i.e. their finite extensibility, and SIC [11]. Furthermore, polymer-filler interaction is a determining factor in filled vulcanizates for this stretch range. Besides, the stress-stretch curves depicted in Figure 2.16 show that the stress grows with filler content and that it decreases with increasing temperature.

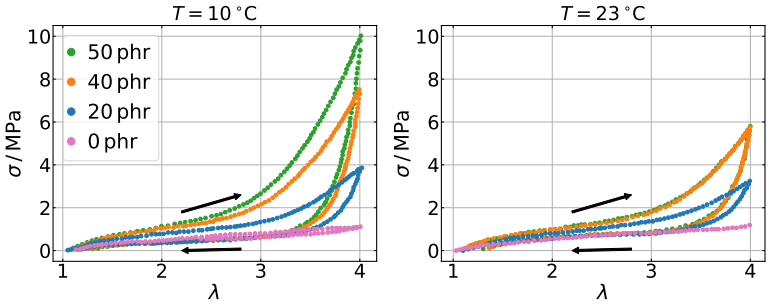

Figure 2.16.: Experimentally obtained stress-stretch curves at different temperatures for unfilled NR and NR containing different mass fractions of CB N375 as filler. The data is extracted from Figure 2 in [22]. Adapted with permission from Reference [22]. Copyright 2006 American Chemical Society.

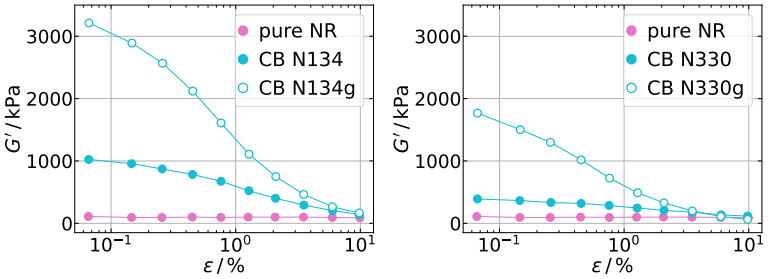

Figure 2.17.: Experimentally obtained data for the storage moduli of unfilled, CB filled and graphitized-CB filled NR. CB of the types N134 and N330 has been used to a volume fraction of 0.2 which is equivalent to a mass fraction of 50 phr of unmodified filler. The data is extracted from Figure 3 in [15]. The letter g refers to the graphitized samples and ε denotes the dynamic shear strain. The data points are connected for the eye, but this does not have any physical meaning. Adapted with permission from Reference [15]. Copyright 2014 John Wiley and Sons.

The direct comparison of the stress-stretch behavior of filled and unfilled vulcanizates leads to the concept of a strain-amplification factor because the stress-stretch curves are shifted towards smaller stretches with increasing filler content, i.e. the stress at fixed stretch is amplified [18, 21, 138, 139]. Harwood & Payne [139] state that the magnitude of the strain amplification factor scales with the reinforcement ability of

the filler. An exemplary plot is depicted in Figure 2.18. Since softening in all of the samples occurs to a similar extend, Harwood *et al.* [140] conclude that changes in the rubber phase dominate this effect. Due to the incorporation of filler into the rubber matrix, the rubber matrix is non-uniformly deformed [22, 139]. The strain is increased in the vicinity of filler particles compared to the bulk where it is like in unfilled rubber [18].

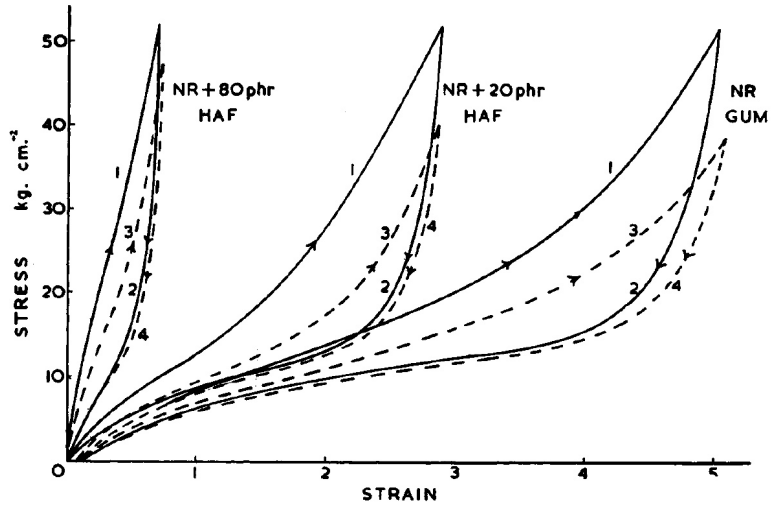

Figure 2.18.: Experimentally obtained stress-stretch curves for filled and unfilled NR vulcanizates. CB N330 (High Abrasion Furnace (HAF)) has been used as filler. Reprinted with permission from Reference [140]. Copyright 2003 John Wiley and Sons.

The study of Trabelsi *et al.* [18] contains elementary WAXS investigations where the amplification factor is obtained for the comparison of different quantities such as stress and crystallinity:

$$A_X = \frac{\epsilon}{\epsilon_\mathrm{f}} = \frac{\lambda - 1}{\lambda_\mathrm{f} - 1}, \tag{2.21}$$

where ϵ and ϵ_f denote the strains for the unfilled and filled sample at which the quantity X is identical. Figure 2.19 shows the stress-stretch curves and the crystallinity-stretch curves for filled and unfilled NR obtained by Trabelsi *et al.* [18]. The crystallite orientation $\delta\psi_{1/2}$ and the crystallite size l_{002} are also plotted. Filled NR containing 50 phr of carbon black N375 has been examined. The volume concentration of filler amounts to 20 %. The data has been measured at a strain rate of 1 mm/min after the fourth strain-cycle.

The plateau in the stress-stretch curve for the filled sample is significantly shorter and the upturn beyond the plateau is steeper than in the unfilled sample. This is explained by considering the polymer-filler interfaces as multifunctional cross links [18]. The onset of SIC is located at smaller macroscopic stretch in the filled sample than in the unfilled sample [18, 19]. Investigations by Candau *et al.* [21] indicate that the local onset stretch for SIC is identical for both filled and unfilled NR, but not the macroscopic stretch of the sample. This suggests that the local chain density of the first emerging crystalline segments must be equal [21]. In addition, Candau *et al.* [21] report a decreasing local stretch for melting of the crystallites with decreasing amount of filler which is explained by the increasing crystallite size. The increase of the crystallinity during stretching is linear in both cases [18]. However, the shape of the curves differs during contraction which indicates a difference in the melting process of the crystals [18]. Furthermore,

the crystallinity-stretch curve for the unfilled sample shows a much more distinctive hysteresis.

Poompradub *et al.* [19] observe domains of highly oriented, crystalline chains and coiled, amorphous chains in the samples in filled rubber like it is typical for SIC. It can be observed in Figure 2.19 that the size of the crystallites in the filled sample of approximately 9 nm is smaller than in the unfilled sample, where it amounts to around 20 nm. Poompradub *et al.* [19] explain this decrease of the size of the crystallites in filled sampled compared to unfilled samples by the occurrence of highly crystalline domains between adjacent filler particles due to large strain in these regions. The orientation of the crystallites is significantly higher in the unfilled sample. Trabelsi *et al.* [18] suggest that this originates from the elastomer-filler interface which hinders the chain mobility. In addition, the inclusion of filler increases the orientational fluctuation of the crystallites [19].

Furthermore, Candau *et al.* [21] investigated self-heating due to viscoelastic dissipation of the samples at high deformation frequency. Self-heating is amplified in the filled sample due to friction at the rubber-filler interface [21]. Therefore, the authors conclude the crystallinity decreases and crystallites disappear at higher stretch.

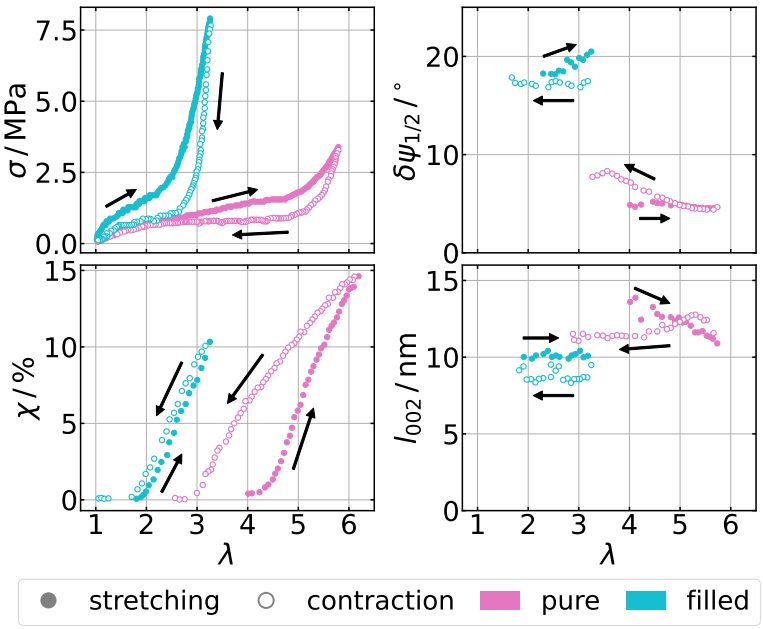

Figure 2.19.: Experimentally obtained stress-strain curves and the crystallinity-strain curves for filled and unfilled NR, where χ denotes the crystallinity. The crystallite orientation $\delta\psi_{1/2}$ and the crystallite size l_{002} are also plotted. The data is extracted from Figure 2 in [18]. Adapted with permission from Reference [18]. Copyright 2003 American Chemical Society.

There are also works in which CB and silica as filler for NR have been compared. For instance, Chenal *et al.* [20] investigated the impact of the filler surface and the filler structure on SIC by WAXS experiments. Spratte *et al.* [23] examined unfilled, CB filled, and silica filled, with and without silane coupling agent, NR samples by surface temperature measurements instead of WAXS. The results for the onset of SIC and the alignment of the crystallites which agree with other works are similar for CB and silica [20, 23]. However, Spratte *et al.* [23] report the highest maximum crystallinity for the CB filled sample followed by the silica/silane sample. The authors point out that the maximum crystallinity scales with the stress, but they cannot conclude that strain amplification is the only effect governing SIC. The results by Chenal *et al.* [20] indicate

that the crystallization rate (cf. Figure 9 in [20]) and the crystallite size depend on the effective cross links density. Spratte *et al.* [23] also note that polymer-filler interfaces act like additional cross links which increases the stress and, therefore, decreases the maximum crystallinity.

There are further experimental works which address the relation of SIC and the inclusion of filler. Besides particulate fillers, for example the impact of organoclays on NR is studied and compared to conventionally filled NR in [141]. Their crystallinity-strain curves indicate that the crystallization process is divided into the rearrangement of the organoclays and the actual onset of SIC. An enhanced reinforcement is attributed to the reorganization. In consistency with the results for filled NR, SIC in the nanocomposites begins at lower strain than in unfilled NR. In addition, the crystallinity of the nanocomposites reaches higher values. The behavior of nanocomposites compared to conventionally filled NR is ascribed to the increased interfacial interactions.

In the light of the demand to produce sustainable materials, the work of Candau *et al.* [142] is based on the idea of recycling ground tire rubber (GTR) by generating NR/GTR composites. The GTR particles appeared to act like filler such that they enhanced reinforcement. Barrera & Tardiff [143] examined eggshell filled NR composites in comparison with CB filled NR and maintained similar properties.

Comparing the curves for the vulcanized samples presented in Figure 2.14 with the stress-stretch curves in Figure 2.16 suggests that the reinforcement mechanism due to SIC is the same as that due to filler. Since IR shows SIC to a smaller extend than NR does, IR imitates the effect of smaller filler content. However at a first glance, a higher extend of SIC implies a higher degree of stress-softening. As previously mentioned, NR apparently contains a pseudo-network in addition to the network structure generated by vulcanization and the strain-induced crystallites act like new cross links. This causes the steeper upturn of the stress at high stretches which is apparently affected by the ability for SIC. Also the inclusion of filler particles increases the modulus and the stress at fixed stretch. In addition, this is in common with the effect of increasing the cross link density. However, strain-induced crystallites just occur at intermediate stretches, but filler particles are permanently embedded into the rubber matrix. Therefore, they already affect the mechanical behavior at small deformations due to rearrangements as depicted in Figure 2.17. Furthermore, it appears like the plateau of the stress-stretch curve associated with SIC vanishes for higher ability for SIC according to Figure 2.14 and for filled networks compared to unfilled networks according to Figure 2.19.

The stress-stretch curves presented up to this point show the stress of the material during one strain cycle. Nevertheless, the stress-stretch curves depend on the history of the rubber sample. Indeed, this is a difficulty in material modeling. Deforming a vulcanizate over several strain cycles yields stress-stretch curves as presented in Figure 2.20. The curves display the so-called Mullins effect [140, 144] or stress softening [145]. It can be observed that the stress during stretching in the first strain cycle of the cyclic deformation behaves identically like the stress for the simple tensile test. During recovery, the stress-stretch curve draws a hysteresis. A non-vanishing deformation of the sample remains. From this point, the next strain cycle starts, but the stress does not follow the behavior of the first cycle. The stress during stretching is smaller now than before due to softening. This is a kind of self-reinforcement mechanism. For the following cycles with identical maximum stretch, this effect vanishes until a steady state is reached. However, if the maximum stretch is increased, the stress during stretching is still smaller than for earlier strain cycles until the first maximum

stretch is reached. Afterwards, the stress continues like the stress for the simple tensile test. During recovery, a hysteresis occurs again. For following strain cycles with the same maximum stretch, the stress indicates softening as previously. If the maximum stretch is increased, softening becomes more pronounced. Mullins softening can be reversed by heating or swelling [145]. If Mullins effect is unwanted for measurements during tensile tests, it is eluded by pre-stretching for several strain-cycles.

Besides, Diani *et al.* [145] report that Mullins effect has been observed in filled polymer networks or unfilled networks which contain crystallites or are able to strain-crystallize, such as pure NR. Nevertheless, almost all of the physical interpretations of the Mullins effect rely on effects of filler particles and do not take the effect in unfilled crystallizable rubber into account. Possible explanations are, for example, detachment of polymer from the filler surface or rupture of polymer chains which link two filler particles. The latter idea has been proposed by Bueche [146]. Bueche explains that pure rubber does not feature Mullins softening because of the arrangement of the entanglements and cross links in order to minimize the forces and to avoid overstretching when the rubber is stretched. However, this physical interpretation does not incorporate the recovery of softening. Thus, another idea for the explanation is slippage of the polymer chains over the filler surface such that bonds are destructed and new bonds are established. This interpretation is supported by measurements of a constant cross link density [147]. Nevertheless based on the analysis of the volume expansion, other authors declare the destruction of the filler network as the origin of Mullins softening [148], but this is irreversible. Moreover, the Mullins effect is explained by disentanglements arising from local non-affine deformation of the networks [149]. Apart from that, a macromolecular model for the interpretation of the Mullins effect has been developed by Fukahori which assumes a double-layer structure of rubber around the filler particles [150]. The inner layers consist of rigid bound rubber which sticks to the filler surface during deformation, while the outer layers of bound rubber build a network structure during the first stretching although they are constrained in motion. If the sample experiences the same stretch as before, the polymer matrix bears the stress. But if the maximum stretch is exceeded, the network of bound rubber holds the stress. Diani *et al.* [145] highlight that this model cannot explain softening in unfilled crystallizing rubber since the crystals melt during recovery.

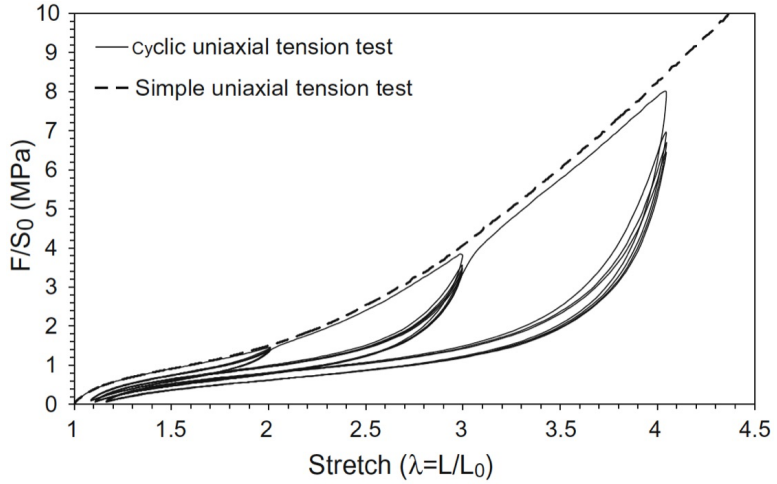

Figure 2.20.: Experimentally obtained stress-stretch curves for styrene-butadiene rubber (SBR) filled with 50 phr of CB. For the cyclic deformation, the maximum stretch is increased every 5 cycles. Reprinted with permission from Reference [145], Copyright (2009), with permission from Elsevier.

At this point it must be highlighted that all of the stress-stretch curves for NR show a hysteresis. At different stretches, different effects contribute to this hysteresis. Progressively, the hysteresis due to SIC will be of special importance, but it must be clarified which other phenomena are involved and whether they have to be incorporated into the model for strain-crystallizing elastomer networks. Experimentally, hysteresis can be studied by temperature measurements using an infrared camera [151].

One contribution to hysteresis is softening due to the Mullins effect. In addition, the viscoelastic behavior of rubber and the alignment of the polymer chains at higher stretches are associated with hysteresis [140]. SIC dominates the hysteresis at large stretches [140]. Viscoelasticity is already considered in the Kelvin-Voigt model presented in subsection 2.4.1, but the hysteresis predicted by this phenomenological model for uniaxial stretching is of different shape because in particular SIC and the inclusion of filler particles are neglected. In vulcanized NR for high strain rates, the hysteresis is entirely attributed to SIC [7]. Trabelsi *et al.* [7] report that the hysteresis of the crystallinity is caused by the supercooling which is the difference between the crystallization and the melting temperature and depends on the stretch. In this context, it might rather be referred to "super-straining". If SIC was an equilibrium phenomenon, the hysteresis would vanish. Therefore, the model for strain-crystallizing elastomers must include SIC as a non-equilibrium phenomenon in order to generate the hysteresis. Le Cam [152] report that the hysteresis of pure NR caused by SIC originates entirely from microstructural changes, i.e. chains align and SIC induces topological constraints for the amorphous chains located in the vicinity of the crystals. As SIC is promoted with increasing stretch, the topological constraints accumulate. During the deformation, the mechanical energy is converted into elastic energy for the rearrangements and, at sufficiently high stretches, stored in strain-induced crystallites with a certain rate. Since the rate for the change of the crystallinity during melting is different as SIC continues, the hysteresis occurs.

In filled rubber, a hysteresis occurs even at low stretches which is caused by rearrangements of the polymer chains and at higher stretches by destruction of the filler aggregates. The hysteresis can significantly vary with the filler type [140]. A comparison of models for the prediction of the hysteresis loss in filled rubber at small deformation in presented in [153].

2.5. Rupture and Tensile Strength of Elastomers

Another aspect of strength of rubber is its tensile strength which will be also investigated in course of the study of the model networks. Therefore, observations addressing the rupture behavior of rubber as well as experimentally obtained data for the tensile strength σ_t and the elongation at break λ_t of rubber are described.

From a theoretical point of view, fracture of polymeric materials can be described by the fracture energy. The first approach was developed by Griffith [154]. According to that, crack growth must minimize the energy, but this process increases the surface energy of the crack and requires for work which overcompensates attractive forces between molecules. Therefore, the energy of the crack surface has to be smaller than the elastic energy stored in the material in order to facilitate crack growth. This is characterized by the tearing energy:

$$T = -\frac{\partial W}{\partial A}, \tag{2.22}$$

where ∂W denotes the change of the stored energy and ∂A is the change of the area of the crack surface [155]. The tearing energy is a material property [155]. In the rupture

criterion by Griffith, T is solely associated with surface energy. Taking only the rupture of atomic bonds in an isoprene monomer into account, yields a tearing energy which is more than an order of magnitude smaller than experimentally obtained values for vulcanized NR [156]. Therefore, additional energy contributions must be involved which are proportional to the increase of the cut length and which depend on the shape of the crack tip [157]. The latter determines the deformation in the vicinity of the crack tip. In addition to the rupture of a single bond at the crack tip, Lake & Thomas [156] include the work applied to the bonds in the polymer chain segment which connects two cross links on either side of the crack tip and which is located at the crack tip in the plane of crack propagation in their calculation of the limiting value of the tearing energy. For simplification of their calculation, the authors neglect the deformation of the other chains in the vicinity of the crack tip. The authors assume that the diameter of the crack tip is limited by the end-to-end distance this chain segment [156]. However, since the tearing energies predicted by the model proposed by Lake & Thomas [156] are still smaller than experimentally measured values, recently, Deng *et al.* [158] presented a new model for fracture in polymer networks. SIC is not taken into account. Instead of the tearing energy, the authors studied the intrinsic fracture energy which is given by the integral of the nominal stress over the sample height. The intrinsic fracture energy increases with increasing non-linearity of the mechanical behavior of the chains. [158]. Deng *et al.* [158] report that energy release and dissipation from chains located multiple layers away from the crack tip contribute to the fracture energy. Other approaches to assess the strength of rubber based on fracture energy are discussed for example in [159] and [160]. Elmukashfi [161] proposes a method to determine the critical tearing energy required for crack propagation which is based on the change of the elastically stored energy instead of the total stored energy by subtracting the dissipated contributions.

Another quantity which is usually referred to in the context of the characterization of fracture toughness is the J-integral [162, 163]:

$$J = \int_{\Gamma} \left(w n_k - \sigma_{ij} n_j \frac{\partial u_i}{\partial x_k} \right) d\Gamma, \tag{2.23}$$

where Γ is a path around the crack tip starting at one crack surface and ending at the other, w denotes the strain energy density, σ_{ij} is an element of the stress tensor, u_i is the displacement in direction i, and n_k and n_j are components of an unit vector normally and outward directed on the contour. A two-dimensional field of deformation is considered. The strain energy density is given by:

$$w = \int_{0}^{\varepsilon} \sigma_{ij} \, d\varepsilon_{ij},$$

where ε_{ij} are elements of the strain tensor. This is just a generalized form of Equation 2.16. The first term of the J-integral accounts for internal work during the deformation, while the second term stands for external work involving traction and the displacement gradient along the axis of the crack. The J-integral is path-independent for homogeneous materials and it equals the tearing energy for ideal non-linear elastic deformation. However, rubber is not homogeneous and dissipation occurs at certain deformations causing path-dependence of the J-integral. The tearing energy and the J-integral have been compared for CB-filled NR for example in [164].

The initiation and propagation of cracks in NR can for instance be observed via scanning electron microscopy (SEM). Small Angle X-ray Scattering (SAXS) is also used for the observation of cavitation [165]. In specimens into which no notch has been cut

initially, cracks are initiated by flaws which already existed in the material. This is usually studied in the context of fatigue. Flaws originate from impurities and the inclusion of rigid particles rather than from pre-existing voids [166, 167]. In particular, large CB agglomerates embedded in the rubber matrix induce flaws. However, not every flaw causes failure of the material. In the case studied by Huneau *et al.* [167], the bonding within the CB agglomerates is stronger than that at the interface and they have a spherical structure prohibiting the covering by bound rubber. Huneau *et al.* [167] propose two stages of fatigue crack initiation caused by CB agglomerates: First, the rubber matrix detaches from a pole of the particle. Second, the cavity opens up to the sides. These steps are associated with the interface between particle and rubber matrix. Afterwards, a crack can grow, but this just happens if the size of the cavity becomes larger than that of the particle. Saintier *et al.* [166] observe this process at weak interfaces like the one between rubber and SiO_2. The polymer is completely removed from the surface of the included rigid particle. The authors distinguish this so-called decohesion process from cavitation which means the spontaneous formation of voids [166].

Crack propagation is often studied by using specimens into which a crack has been cut initially. The specimen is then stretched along the direction perpendicular to the orientation of the crack. In the context of fatigue life, the samples are deformed for multiple cycles. The dependence of the crack growth resistance of NR on temperature is associated with the temperature dependence of SIC [168]. Moreover, the so-called R-ratio, which is $R = P_{\min}/P_{\max}$ with P as a loading parameter like stress or strain, determines the propagation direction of the crack and can even prohibit crack growth [168].

One of the characteristic phenomena for crack propagation in NR is crack blunting which means that the crack tip is not sharp but flattened [169–171]. Around the crack tip, a semi-crystalline zone evolves, which is flattened in the stretching direction [170–172]. This semi-crystalline zone prevents crack propagation [170–172]. It is larger in filled NR than in unfilled NR at fixed stretch because the inclusion of filler amplifies the local strain and thus promotes SIC [172]. In unfilled NR, directly around the crack tip, Trabelsi *et al.* [171] found a zone of constant maximum crystallinity which is enclosed by a transition zone in which the crystallinity decreases with increasing distance from the crack tip and lines of constant crystallinity are observed. According to these observations, a fixed crystallinity corresponds to a constant local stretch [171]. Simultaneously, the orientation of the crystallites is constant in the zone of maximum crystallinity and decreases in the transition region. The area of the total semi-crystalline region increases like the stretch squared [171]. The molecular orientation in the crack tip region increases with increasing filler content and remains approximately constant beyond a certain filler content [170]. Lee & Donovan [170] attribute this observation to biaxial stress in front of the crack surface instead of uniaxial stress as it is attendant in the bulk. Increasing the CB content increases both the size of the semi-crystalline zone as well as the crystallinity inside this zone at fixed crack driving force [170]. Since deformation energy is stored in strain-induced crystallites, energy dissipation is enhanced in filled NR and, thus, the energy required for crack growth and rupture increases with CB content [170].

Another characteristic observation regarding crack propagation in NR is crack branching which means that the initial crack splits up at a certain point and this happens several times. Branches evolve after blunting of the primary crack [173]. Crack branching occurs under so-called non-relaxing conditions, which means that that the load during cyclic deformation is always larger zero, but not under relaxing conditions [174]. SEM images obtained by Saintier *et al.* [174] show a fractal-like pattern in which secondary

cracks are of smaller size. Since all of these subsequent cracks propagate simultaneously, much more energy is dissipated such that the crack growth rate is smaller than for the propagation of a single crack [174]. Therefore, crack branching provides an explanation for the fatigue life of NR [174]. Crack branching results from the structural anisotropy due to SIC [173, 174]. The cracks circumvent the crystallites. Under non-relaxing conditions, strain-induced crystallites accumulate at the crack tip because some of them remain until the next loading cycle [174]. Hamed *et al.* [173] relate the occurrence of crack branching to the increase of tearing energy for NR compared to butadiene rubber (BR) which shows SIC to a smaller extend. Furthermore, strain-induced crystallites appear to act like reinforcing fillers during the process of crack propagation [175, 176]. In other filled polymers, the crack growth slows down as the crack tip reaches a filler aggregate because the crack circumvents it and increases again until it reaches the next aggregate [177].

In unfilled NR, the crack rather propagates along the direction of the orientation of the initially inserted crack, while, in filled NR, the cracks emerging during crack branching orient along the direction of loading [172]. In unfilled NR, cavitation in the crack tip region occurs before SIC [172]. Therefore, unfilled rubber is weakened before it can be strengthened by SIC. Since the order of the processes is reversed in filled NR, the semi-crystalline zone around the crack tip can grow until the onset of cavitation [172]. Indeed, the damage zone in unfilled NR corresponds to the semi-crystalline zone, but in filled NR the damage zone is concentrated around the crack tip and embedded into the larger semi-crystalline zone. Due to the orientation of the crystallites, the material is reinforced along the direction of the initially inserted crack, but it is weakened along the stretching direction [172]. Thus, the crack splits.

However, Xiang *et al.* [172] point out that the process of cavitation depends on the properties of the filler as well as the preparation of the rubber matrix. In addition, the authors conclude from their observations that there must be an optimum CB content at which the onset strain of cavitation is maximized and the volume fraction of cavities is minimized. Schneider *et al.* [168] find that the cracking resistance in silica-filled NR is enhanced compared to CB-filled NR due to finer aggregate size. In addition, the crack propagation rate decreases with increasing filler content because of the shift of the onset of SIC towards smaller stretches, but beyond a certain filler content cavitation is initiated at smaller stretch [168].

The tensile strength and the elongation at break allow to measure strength and reinforcement. They are usually determined from a uniaxial deformation. These tensile tests yield stress-stretch curves such as depicted in Figure 2.21. The elongation at break is the maximum stretch which the material resists until it fails. At this point, the stress-stretch curves terminate. The tensile strength is the value of the corresponding stress. Both quantities depend on the ability of the rubber for SIC and on the filler. In particular, the tensile strength and the elongation at break of NR are significantly larger than those of IR which shows SIC to a smaller extend. Exemplary values are given in Table 2.2 and further values can be found for instance in [131]. Another evidence for the importance of SIC is the sharp decrease of the tensile strength when temperature becomes sufficiently large such that SIC is suppressed [13, 131].

Table 2.2.: Experimentally obtained values for the tensile strength σ_t and elongation at break ε_t of NR and IR.

	σ_t/MPa	ε_t/%	T	strain rate	reference
NR	18	1100	21 °C	55 mm/min	[178]
IR	1.2	139	21 °C	55 mm/min	[178]

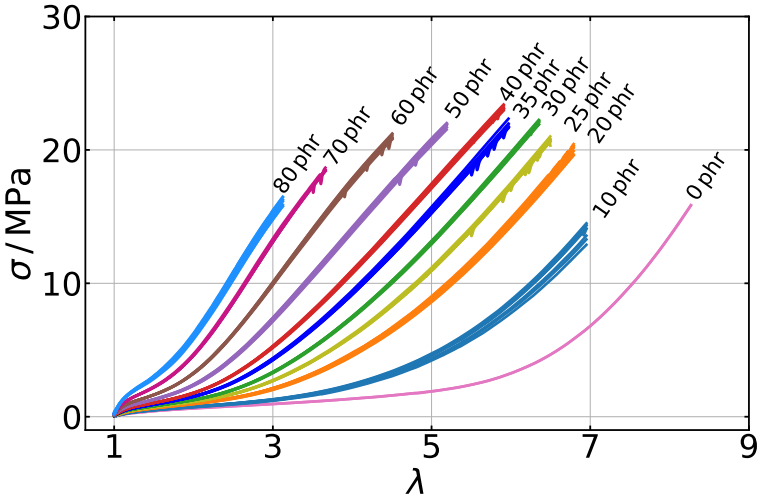

Figure 2.21.: Stress-stretch curves of CB N121 filled NR. The data has been obtained from a uniaxial tensile test at room temperature with a strain rate of 500 mm/min. For each filler content, stress-stretch curves of several specimens with the same composition are depicted. The compositions of the rubbers are listed in Table A.1. The data has been provided by Dr. Frank Fleck from Continental Reifen Deutschland GmbH and is printed with permission.

The experimental data for the tensile strength and elongation at break of unfilled and CB N121 filled NR are extracted from Figure 2.21 and plotted in Figure 2.22 versus filler content. With the exception of the tensile strength for the smallest considered filler content, the tensile strength is increased by the inclusion of filler into the rubber matrix. Instead of a decrease of the tensile strength for the inclusion of a small volume fraction of filler, other authors also report an increase [13, 14, 24, 26, 27]. However, the observation of a maximum of the tensile strength agrees with other experimental data. Beyond this maximum, the tensile strength decreases. SEM images show that the filler agglomerates are formed with increasing filler content because filler-filler interaction is preferred over filler-rubber interaction [24]. The initial increase of the tensile strength is attributed to the increase of the length of the interface available for rubber-filler interaction which causes reinforcement [14, 26]. But then, the so-called dilution effect due to the filler volume counteracts resulting in the decrease of the tensile strength [14, 26]. The filler particles are not well dispersed or wetted by rubber [24, 26]. This means that an optimum ratio between surface area and volume of the filler must exist regarding the anchor points provided by the filler. For illustration, one can think of a spherical particle which is included into a cross linked polymer network as depicted in Figure 2.23 [120]. Part of the bulk polymer containing cross links is replaced by the particle volume, but new bonding sites on the particle surface are generated. The filler content of maximum tensile strength depends on temperature and on the type of filler [13, 14, 24, 25]. Under certain conditions, the location of the maximum tensile strength coincides with the percolation threshold of the filler.

The elongation at break decreases already at small filler content because the filler stiffens and embrittles the composite [26, 28]. This is consistent with the observations in other works [26–28].

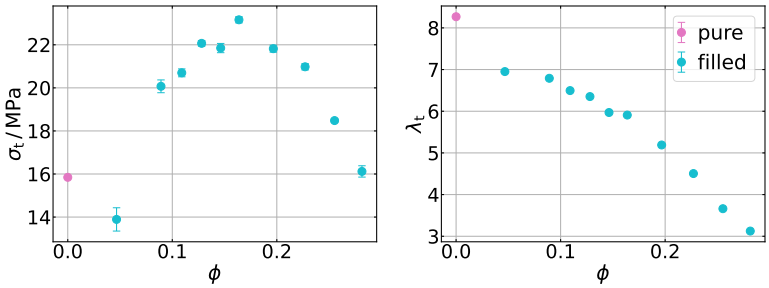

Figure 2.22.: Tensile strength and elongation at break of CB N121 filled NR versus filler volume fraction ϕ. The data has been obtained as averages from the stress-stretch curves shown in Figure 2.21. The error bars are given by the standard deviations. The mass fractions of filler corresponding to the volume fractions are listed in Table 2.3.

Table 2.3.: Mass fractions m_f and corresponding volume fractions ϕ of filler for the data plotted in Figure 2.22 and Figure A.3. The conversion is independent of the CB type. The data has been provided by Dr. Frank Fleck from Continental Reifen Deutschland GmbH and is printed with permission.

m_f / phr	10	20	25	30	35
$\phi / 10^{-2}$	4.668	8.919	10.906	12.807	14.63
m_f / phr	40	50	60	70	80
$\phi / 10^{-2}$	16.377	19.667	22.707	25.525	28.145

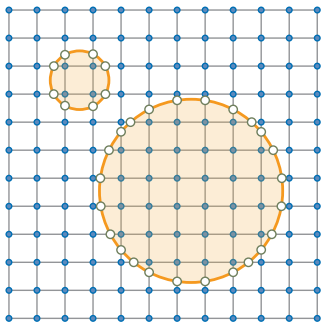

Figure 2.23.: Illustration of the replacement of cross links (blue dots) in the bulk polymer network by anchor points (open dots) for polymer chains (grey lines) on the filler surface for different sizes of spherical filler particles (orange circles).

In Figure 2.24, the tensile strength and the elongation at break are plotted for different types of CB. According to their surface areas obtained by the so-called Brunner Emmet Teller (BET) analysis, these filler types can be arranged as follows: CB N121 > CB N339 > CB N660. The surface areas measured by this method include the additionally accessible surface area due to surface structures like branches or pores. Therefore, a higher surface area means more interaction sites for the polymer [179].

In accordance with Figure 2.22, the tensile strength for each of the filled samples is higher than for the unfilled sample and the elongations at break are smaller. It

is expected at room temperature that the tensile strength decreases with decreasing surface area [13]. This is also observed here for a filler mass fraction of 50 phr, but, for 40 phr of filler, a maximum of the tensile strength occurs at intermediate surface area.

Further experimental data for the tensile strength and elongation at break of NR filled with various contents of different filler is included in Table A.3 in section A.2. It shows that the exact values of these quantities depend on the experimental conditions, in particular temperature and strain rate. In addition, the tensile strength and the elongation at break are affected by vulcanization and the cross link density which is associated with the included mass fraction of sulfur.

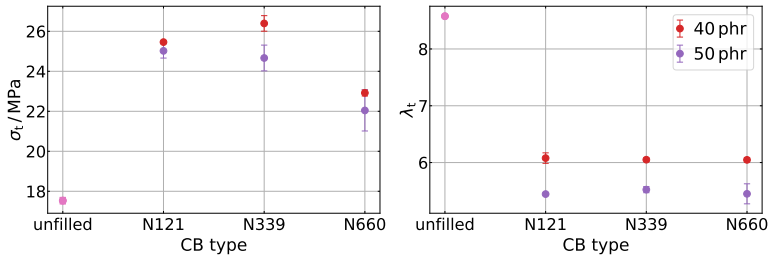

Figure 2.24.: Tensile strength and elongation at break of CB-filled NR for different CB types arranged according to descending surface area. The data has been obtained as averages from the stress-stretch curves shown in Figure A.4. The error bars are given by the standard deviations.

In addition, different types of CB possess different surface activity [14]. The compatibility between filler and polymer can be measured by their surface tensions [179]. Enhanced rubber-filler interaction increases the tensile strength, but decreases the elongation at break since the mobility of the polymer chains is limited [180, 181]. Its importance can be revealed by surface modifications [14]. For example, CB can be graphitized to weaken the polymer-filler interaction and silica is usually coated with silane so advance the polymer-filler interaction. Ideally, the filler surface is wetted with rubber. If the polymer chains slip over the filler surface due to weak interaction, they to not foster rearrangements of the filler which would reinforce the composite [175]. Note that the tensile strength σ_t of an elastic material into which a cut has been inserted can be theoretically related to the elastic modulus E as follows:

$$\sigma_\mathrm{t} = \sqrt{\frac{T_c E}{\pi c}},$$

where T_c denotes the fracture energy and c is the cut length [175]. Therefore, the impact of filler on the modulus affects the tensile strength and the considerations made in section 2.2 with that regard are also important here.

Furthermore, the tensile strength and the elongation at break depend on the structure formed by the filler inside the rubber matrix, which also varies with the filler type, and on the filler dispersion which is mainly determined by the manufacturing of the material. The structure of the filler, or in general its shape, affects the tensile strength and elongation at break due to hydrodynamic effects and occluded rubber [175, 179]. In particular, nano-particles with a rod-like shape, i.e. high aspect ratio, increase the amount of bound rubber compared to spherical particles [182]. Due to their geometry, they offer more interaction sites. Rod-like particles assemble in domains in which they align along the major axis contributing to reinforcement, but this effect is impeded when the filler loading becomes too high [182].

The tensile strength is advanced by finely dispersed filler, while the elongation at break is reduced [183]. Choi *et al.* [183] relate the dispersion to the content of a cure

accelerator in silica-filled NR and, thus, explain this by an increased effective cross link density. Tensile strength is reduced if the filler is badly dispersed due to larger aggregates which cause the formation of crack precursors [184]. The tensile strength is also decreased if the size of the filler particles themselves is comparatively large [175].

Besides, the impact of the filler on the tensile strength on NR is affected by temperature because of the interplay with SIC [13]. Under the absence of SIC, increasing the area of the filler surface increases the tensile strength [13]. In addition, the tensile strength is reduced at elevated temperature because slippage and debonding of polymer chains from the filler surface occur more easily [175].

In Figure A.2, the stress-stretch curves for NR filled with the different types of CB from Figure 2.24 are plotted for further filler contents. The tensile strength and elongation at break extracted from this plot are plotted versus filler content in Figure A.3. However, the data does not provide further insights.

As already indicated above, fatigue is another aspect that must be discussed in the context of rupture of elastomers. It gives insights into the reliability of the material. Experimentally, the fatigue life is studied by cyclic deformation of a specimen. A comprehensive review addressing fatigue of rubber is the one by Tee *et al.* [185]. Even though fatigue life is of high interest for applications of rubber for example due to safety reasons, there are is no universal definition of fatigue life [185]. For instance, the fatigue life is quantified by failure or the growth of a crack up to a certain size. So-called predictors are tried to be established for predicting the life time. The life time can be modeled by strain-based, stress-based or energy-based predictors [166, 185, 186]. They are derived from the so-called crack nucleation or from the so-called crack growth approach.

In the former case, it is convenient to apply different stress amplitudes with fixed mean stress periodically to multiple identical samples and to obtain the fatigue life, usually in terms of the number of the deformation cycle in which the sample fails [187, 188]. Plotting the stress amplitudes versus the corresponding fatigue lives in a log-log or semilog plot yields a so-called S-N curve or Wöhler curve. The range of the number of cycles is divided into low-cycle and high-cycle fatigue. For polymers, the slope of the curve is smaller in the low-cycle domain than in the high-cycle region [189]. Typically, the curves decrease linearly in the so-called finite life region until they transition into a nearly horizontal line which indicates the so-called infinite life region [187]. The point of the transition is the fatigue limit or endurance limit [187]. However, since polymers can show thermal and mechanical fatigue, the curves could be misinterpreted. Besides, note that the Wöhler curves for polymers are strongly frequency-dependent [189]. In addition, the fatigue life data is usually widely scattered because of structural differences of the samples or different testing conditions and, thus, statistical methods are required for the evaluation [187–189].

As an alternative to stress-controlled testing, experiments are conducted for which the applied stretch is controlled [188]. Commonly, the number of cycles until incipient cracking is measured in this case as the fatigue life. A schematic representation of such a Wöhler curve for filled NR is depicted in Figure 2.25. The relation between the strain and the fatigue life in the shown range is linear. Note that the fatigue life reaches up to multiple thousands of strain cycles.

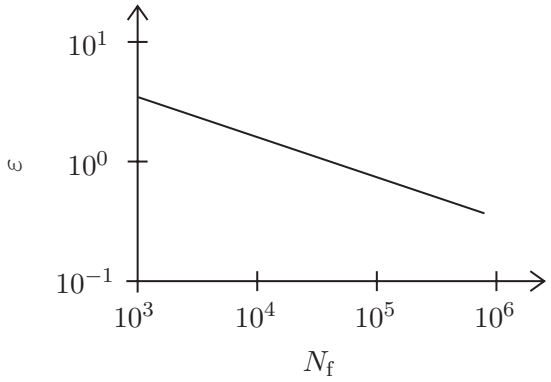

Figure 2.25.: Illustration of a Wöhler curve of filled NR. Here, the strain ε is plotted versus the crack nucleation life N_f. This sketch is inspired by the experimental data shown in Figure 5 in [190].

For the crack growth approach, the crack growth rate $\mathrm{d}c/\mathrm{d}N$ which describes the change of the length of a crack per strain cycle is measured [155, 185]. The crack already exists or it is cut initially into the sample. The crack growth rate is plotted versus the energy release rate which is equivalent to the tearing energy [155]. An illustration of the so-called Paris-Erdogan plot for filled NR is depicted in Figure 2.26. As crack growth is initiated, the crack growth rate is constant first, but then it transitions into a range in which it increases according to a power law until the material fails. At this point the critical tearing energy is reached for which the crack growth rate becomes infinitely large. There are approaches to predict the fatigue life based on crack growth by using a critical tearing energy or a critical J-integral [155, 185, 191]. Besides, the critical tearing energy can be obtained from the study of both the crack growth rate and the tearing energy which is obtained from stretching an initially cut specimen [192].

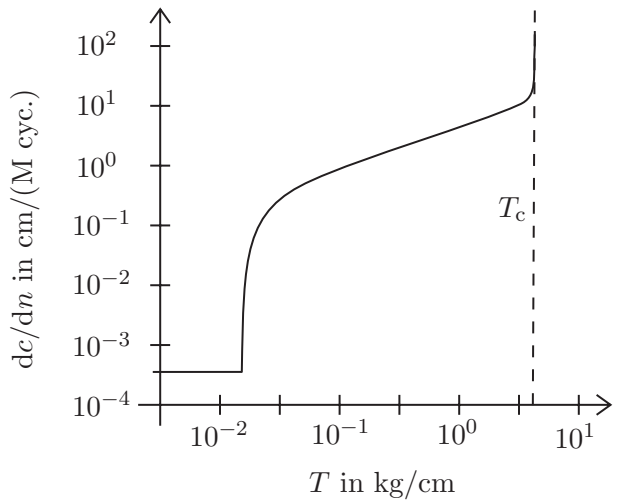

Figure 2.26.: Illustration of the crack growth rate $\mathrm{d}c/\mathrm{d}n$ depending on the tearing energy T for vulcanized NR. The critical tearing energy T_c is indicated by the dashed line. This sketch is inspired by the experimental data shown in Figure 3 in [193].

For rubbers, especially if they show SIC, the fatigue life is advanced by applying a R-ratio larger zero [190]. Failure of the samples is caused by cracks emerging from intrinsic flaws of the material and their growth rate depends on individual properties such as size and orientation [190]. The growth of a crack to a critical size contributes to 20 % of the fatigue life of NR [166, 186]. Cracks propagate comparatively slowly [186].

Steck *et al.* [194] investigated the effect of cross-link density, filler loading, and

polymer-filler interaction on the modulus and fatigue threshold of filled rubber. Enhancement of both properties is achieved by so-called stress deconcentration, but the underlying structural requirements differ. To increase the modulus, the polymer chains must be entangled and the filler particles must percolate. However, the fatigue threshold is increased if the polymer chains are long, the filler particles are clustered and the polymer-filler interaction is strong. If the friction between the polymer chains is low, the stress deconcentrates over the entire chain and rupture of a bond dissipates the entire energy stored in the bonds of the chain. This picture is analogous to that in [158]. In a cluster of rigid particles, the stress is transmitted between polymer and particles by strong polymer-filler interaction and the gaps between the particles. If a crack impinges on such a particle cluster, the energy stored in the gaps between the particles is dissipated. This phenomenon is independent of the percolation threshold. In order to achieve both an enhanced modulus and increased fatigue threshold, the authors suggest to construct a polymer network consisting of long, densely entangled chains with low friction and containing a percolated filler network with strong polymer-filler interaction.

Beurrot-Borgarino *et al.* [195] studied the evolution of SIC in CB-filled NR during fatigue. If the minimum applied stretch is below the threshold of melting, all crystallites melt and the maximum crystallinity decreases with increasing number of strain cycle. For the first cycles, both the number and the volume of the crystallites decreases, but, afterwards, only the volume decreases. If the minimum applied stretch is above the melting threshold the crystallinity increases with progressive cycles of deformation. In this case, one part of the crystallites entirely melts and their volume decreases with increasing strain cycle, while the others persist and accumulate further volume. Besides, Beurrot-Borgarino *et al.* [195] state that the micro-structure of the amorphous domains must be modified by the occurrence of SIC under cyclic loading and this may cause the durability of NR.

2.6. Modeling and Simulation of Filled and Strain-Crystallizing Elastomers

This section is dedicated to give a short overview on modeling and simulation approaches for filled and strain-crystallizing elastomers. Computer simulations are useful as a complement to experimental studies because they provide unbiased insights. Idealizations applied in simulations enable the focus on essential properties. For example, impurities of NR can be neglected, but other features can be tuned in an unaltered environment. Therefore, relations between the microscopic structure, i.e. its elements and their features, and macroscopic physical properties can be identified. Most of the simulation studies consider either filler reinforcement or reinforcement by SIC and the investigations are limited to a certain range of deformations.

A general introductory overview on modeling and simulation of polymers on the molecular level is provided by Gartner & Jayaraman [196]. Molecular Dynamics (MD) simulations are a strong tool in context of mechanical reinforcement because they enable relating the behavior and material structure on the microscopic scale with the mechanical properties. In MD simulations, the trajectories of 'particles', i.e. atoms or molecules, are computed by the numerical solution of Newton's equations of motions. Typically, polymers are modeled via coarse grained bead-spring models. In these models, several monomers of a polymer chains are confined to a bead and linked to the adjacent elements in the polymer chain by a harmonic-like potential. However, atomistic approaches are also utilized. For coarse-grained modeling, they can be used

complementary to derive the parameters for the effective interaction potentials via the so-called inverse Boltzmann method (see for example [197] and [198]). Uddin & Ju [198] developed a constitutive model for NR based on this approach. Distributions of the bond length and bond angle as well as the radial distribution function for NR are obtained from atomistic MD simulations and inserted into the potentials for their coarse-grained model which relies on statistical thermodynamics. In particular, this is an advantage over the application of the freely-jointed chain model which involves to a Gaussian distribution of the bond length that is not valid in general. From the coarse-grained model, a continuum formulation for the stress-stretch behavior is derived by fitting the so-called Arruda-Boyce model.

In particular, filled rubber is often studied at small shear or uniaxial deformations, for instance up to strains of $\varepsilon = 100\,\%$, due to the occurrence of the Payne effect. Coarse-grained, but also atomistic, MD simulations show an increase of the elastic modulus when filler is included into the rubber matrix [2, 199–201]. The dominant contribution to the decrease of the modulus due to the Payne effect is the destruction of the filler network [197, 200, 202]. The mechanical strength is enhanced by stronger interaction of nanoparticles causing the formation of a filler network and restricting the mobility of the polymer chains [200]. In addition, the nanoparticles induce orientation of the bonds inside the polymer chains [200].

MD simulations of polymer nanocomposites at larger deformations usually do not consider SIC at all or do not involve it explicitly. The stress is amplified by increasing the filler content [33, 45, 203, 204]. In addition, the interaction and contacts between polymer and filler are crucial for reinforcement [33, 45, 200].

Zhang *et al.* [204] performed a comprehensive study of the impact of filler morphology, filler shape and interaction strength on the mechanical behavior of composites. The authors obtained the stress-stretch behavior, the resistance to crack propagation and the fatigue performance. Ellipsoidal particles enhance the resistance to external deformations compared to spherical particles since their aspect ratio hinders their translational or rotational movement during the deformation which is induced by load-bearing polymer chains. Simulation of unfilled, non-crystallizing polymer networks demonstrates that the polymer chains rearrange themselves during stretching [205]. They transition from randomly coiled conformations via elongation to the alignment along the stretching direction. In filled polymer networks, enhanced interaction conditions between polymer and filler promote the orientation of polymer chains along the stretching direction [204]. The strength increased by rough particles compared to smooth particles because they provide more interaction sites. Zhang *et al.* [204] report that for weak interactions and smooth spherical filler particles, the stress is reduced independent of the filler content compared to unfilled systems because the rubber does not bind to the filler, but the filler aggregates bind to each other, and, thus, the polymer network structure is damaged. The results obtained by Zhang *et al.* [204] give some clue about the importance of carbon nanotubes (CNT) for reinforcement.

The comparison of aggregated and dispersed filler by Hagita *et al.* [202] shows that the stress is larger in the former case because the number of contacts between nanoparticles is larger. Aggregated filler also promotes the alignment of bonds in the polymer chains [202]. This observation is contrary to that made by Morozov *et al.* [206] who applied a finite-element type model. The authors report that randomly distributed filler reinforces the material to the highest extend compared to regularly arranged or clustered filler.

In [45], Chen *et al.* have developed the molecular model proposed in [133] further

for the investigation of the stress-strain behavior of polymer nanocomposites. SIC is not included explicitly into the model but defined via the orientation of the chains. The authors report that reinforcement is caused by orientation of the rubber chains due to the nano-particles and dissipation due to slippage of the chains on the particle surface. Thus, decreasing the size of the filler particles at fixed filler loading enhances the mechanical properties. These observations are in accordance with the results in [33] and in [203]. However, larger particles provide more sites for the adsorption of rubber beads. Moreover, Chen *et al.* [45] find that, for strong interfacial interaction of polymer and filler, the filler particles aggregate which makes them poorly dispersed, while they are well dispersed for weak interaction compared to polymer-polymer interaction. However, the number of polymer beads adsorbed on the nano-particle surface saturates at a certain interaction strength. For well dispersed filler, the stress increases with increasing interaction strength until a certain point is reached above which the stress remains unaltered. First, the particles are enabled to adsorb more polymer beads, but, for higher interaction strength, SIC and energy dissipation dominate the mechanical behavior to variable extend.

An example for combining the simulation of filler and SIC is the work by Dargazany *et al.* [44]. The authors use a mean field theory for the simulation of filled strain-crystallizing rubber. They extended a network evolution model [207] in which the strain energy is computed by separating the pure rubber network and the polymer-filler network. The polymer chains are considered as freely-rotating with non-Gaussian statistics. Fibrillar crystallites and spherulites can form, where fibrillar structures act as nuclei for folding chains. The rubber network behaves ideally elastically, while it is presumed that the polymer-filler network causes damage. Shorter polymer chains detach from the filler during network relaxation. Filler aggregates in this model are randomly distributed rigid volume elements which means that their deformation is not taken into account.

The investigations at comparatively small deformations based on MD simulations give already insights into the initiation of cracks inside the material [37, 38, 197]. Pavlov & Khalatur [201] report that the inclusion of filler induces more defects compared to unfilled systems. Hagita *et al.* [37] find that voids form in the polymer bulk if the interaction between polymer and nanoparticle is attractive, and that they form at the interface if the interaction is repulsive.

Fracture and the tensile strength of pure and filled polymeric systems are also studied by computer simulations. Commonly, the impact of the filler loading and the filler structure inside the rubber matrix is not investigated in detail or SIC is not considered. The atomistic scale is useful for the study of fracture since it is capable of bond dissociation and the importance of interactions in general. MD simulations often include rupture by cutting off bonding or non-bonding interactions beyond a certain distance [39, 41, 205, 208, 209]. Also probabilistic approaches for bond dissociation in polymeric systems are used which depend on the bond length [210]. Another approach to model dissociation of bonds is to apply a potential like the Morse potential (e.g. [43]) for the bonds which already involves this phenomenon.

Simulations confirm that the tensile strength tends to increase with increasing filler content until a maximum is reached [43, 211]. Fracture initiates from the formation of multiple small voids which then grow until they merge into larger voids [43, 205, 208, 211]. In unfilled polymer networks, the local density of chains is increased during stretching due to their alignment along the stretching direction which promotes more efficient packaging [205]. The conformations of the chains vary dependent on the local network topology and in particular due to the presence of cross links and

entanglements. Thus, the system becomes inhomogenous and voids form due to bond dissociation if chains cannot be elongated even more. Nevertheless, surrounding chains get more conformational freedom and the network can be stretched even more until it is torn apart. In filled systems, depending on local weakness of the system, voids form either at the polymer-filler interface or in the rubber bulk [211]. David *et al.* [43] report that, for silica-filled polybutadiene, sulfur bonds are the weakest bonds and they are located at the polymer-filler interface and in chemical cross links. This agrees with the simulation results by Payal *et al.* [205] for unfilled polybutadiene where the breaking bonds are predominantly sulfur bonds. The comparison of the impact on fracture by the inclusion of "smooth" and grafted silica nanoparticles into polyisoprene by Yuan *et al.* [209] allows to further study the importance of the polymer-filler interface. Note that grafting enhances the compatibility between polymer and silica as particular filler. The authors explain the softening of polyisoprene by smooth silica with weak interaction between polymer and filler which promotes the aggregation of nanoparticles, with the induced inhomogeneity that impedes the arrangement of the polymer chains along the tensile direction and with the reduction of the number of entanglements.

As already indicated above, another approach for the simulation of filled and strain-crystallizing rubber are finite element methods (FEM), but they rather consider the continuum than the molecular scale [212, 213]. Thus, they cannot capture molecular mechanisms. Overall, MD simulations are advantageous for the study of reinforcement mechanisms in rubber. They reveal the importance of the filler properties and the polymer-filler interface. The microscopic features of SIC can be captured as well. However, coarse-graining is feasible for modeling of SIC since multiple chain segments which are involved in this phenomenon must be considered. Models for SIC often rely on mean-field theories in which the cooperativeness of the chain segments is neglected [44, 46–49, 214]. In addition, SIC is often treated as equilibrium phenomenon in contrast to its nature (e.g. [215]).

Khiêm *et al.* [216] present a model for SIC under dynamic loading which is fitted to their data obtained from uni- and biaxial deformation in [217]. Dynamic loading means that no relaxation of the network takes place during the deformation which is in contrast to quasi-static loading. The network is decomposed in strands between permanent cross links. Static and free strands are distinguished where the former crystallize in equilibrium while the latter can crystallize out of equilibrium. Nucleation and growth of the crystallites are separated where both processes generate different crystal morphologies. For non-equilibrium crystallization, the crystals emerge and melt spontaneously which is determined by a characteristic time. The non-equilibrium crystallization process can be understood as diffusion of chain segments into nuclei [216]. In order to consider the Mullins effect and rate dependence in filled rubber, the polymer-filler network is separated in an equilibrium and a non-equilibrium network which involve rate-independent and rate-dependent damage respectively. This model enables the authors to separate contributions of equilibrium and non-equilibrium phenomena, in particular SIC, for the explanation of the behavior of the stress and dissipation. The authors conclude that it is necessary to study SIC simultaneously from equilibrium and non-equilibrium perspective.

3. Physical Principles of a Material Model for Filled Natural Rubber

In this chapter, the physical principles underlying the material model for filled and strain-crystallizing elastomers are introduced. The macroscopic stress of a material is defined according to elasticity theory. First, it is related to the microscopic properties of a polymer network by the theory of rubber elasticity under the consideration of the conformational entropy of individual polymer chains. On this basis, a theory for strain-induced crystallization (SIC) is introduced according to the model proposed by Flory [46] which has been developed further by Plagge & Hentschke [1]. By studying the forces, the expected mechanical behavior of such model elastomers is elucidated. Furthermore, the extension of the model by introducing a rupture criterion for model polymer chains based on their free energy is discussed. Finally, modeling of filler particles and their interactions is described. In particular, the physical concepts of surface free energies and surface tension underlying the algorithm for the generation of different filler morphologies inside the rubber matrix are explained.

3.1. Stress

During the deformation of a material out of its equilibrium state, the molecules inside are displaced [119, 218]. The molecular interactions cause internal restoring forces which are in range of the order of intermolecular distances and, thus, short from the continuum mechanical perspective. The total resulting force $\vec{f}$ on a volume V of the material is given by the integral of the force density $\vec{F}$, i.e. the force per volume element:

$$\vec{f} = \int \vec{F}\,\mathrm{d}V. \tag{3.1}$$

Due to Newton's action-reaction law, the forces inside the volume compensate each other such that the resulting force is given by the forces acting on the surface of the volume. Therefore, Equation 3.1 can be rewritten as an integral over the surface by applying Gauss' integral theorem. The definition of the Cauchy stress tensor $\sigma_{ik}^{(\mathrm{C})}$ allows to express the i-th component of the force density as divergence:

$$F_i = \frac{\partial \sigma_{ik}^{(\mathrm{C})}}{\partial x_k}, \tag{3.2}$$

where x_k is the k-th coordinate and the Einstein summation notation is applied. The index k refers to the direction of the normal vector on a surface element of the volume. If i and k are equal, the components of the Cauchy stress tensor correspond to the normal stresses. Otherwise, they are called shear stresses.

Inserting Equation 3.2 into Equation 3.1 and applying Gauss' integral theorem yields for the i-th component of the force:

$$f_i = \int \frac{\partial \sigma_{ik}^{(\mathrm{C})}}{\partial x_k}\,\mathrm{d}V = \oint \sigma_{ik}\,\mathrm{d}A_k, \tag{3.3}$$

where A_k is the k-th component of the normal vector on a surface element of the volume directed outwards.

In the course of this thesis, the deformation of a piece of rubber along the z-direction will be considered. In this case, the Cauchy stress tensor is of diagonal form. Its component $\sigma_{zz}^{(\mathrm{C})}$ is determined by the force f_z which is necessary for the deformation according to Equation 3.3. Since rubber is incompressible, its volume is conserved during the deformation. This is included in terms of an internal hydrostatic pressure p of the material [1]. Requiring that the stresses on the surfaces orthogonal to the direction of the deformation vanish, it holds:

$$p = \sigma_{xx}^{(\mathrm{C})} = \sigma_{yy}^{(\mathrm{C})}. \tag{3.4}$$

The Einstein summation notation does not apply here because the component indices are designated explicitly. Since this internal pressure contributes also to the stress along the z-direction, the normal stress $\sigma_{zz}^{(\mathrm{C})}$ is given by:

$$\sigma_{zz}^{(\mathrm{C})} = \frac{f_z}{A_z} - p. \tag{3.5}$$

For the comparison of the stress with other data, it is convenient to compute the stress with respect to the original cross section A_0 of the specimen. This yields the so-called engineering stress:

$$\sigma \equiv \frac{A_z}{A_0}\sigma_{zz}^{(\mathrm{C})} = \frac{1}{A_0}f_z - \frac{1}{A_0}\frac{A_z}{A_x}f_x.$$

In an equilibrated undeformed sample, the engineering stress vanishes because of vanishing forces.

3.2. Freely-Jointed Chain Model

For the computation of the engineering stress given by Equation 3.6, the restoring force of the material has to be obtained which is determined by forces on the microscopic scale, i.e. forces of polymer chains and filler particles. On the one hand, it would cost immense computational effort to compute these forces on the scale of smallest elements like atoms or monomers. On the other hand, this scale is irrelevant for the phenomena which will be studied subsequently. Therefore, coarse graining will be used. Atoms or monomers are condensed to larger units which represent their effective properties.

The polymer chains connecting two cross links in the elastomer network are modeled as so-called freely-jointed chains which consist of rod-like segments without orientation correlation [55]. This is illustrated in Figure 3.1. Each segment represents a certain number of monomers. The segments do not interact and none of the spatial directions is preferred over the others.

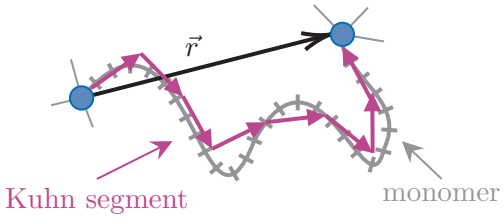

Figure 3.1.: Illustration of a polymer chain connecting two crosslinks. The chain has the end-to-end vector $\vec{r}$. Several monomers are unified in a Kuhn segment which build up the corresponding freely-jointed chain.

The separation between two monomers in a polymer chain with no or negligible orientation correlation is quantified by the so-called Kuhn length b [55, 219, 220]. Accordingly, a polymer chain can be divided into n Kuhn segments of length b in order to model it as freely-jointed chain. The Kuhn length of *cis*-polyisoprene is $b_{\mathrm{cis-PI}} = 9.34\,\text{Å}$ [108] which corresponds to the length of 2 to 2.5 monomers.

The contour length of the freely-jointed chain which corresponds to its maximum end-to-end distance r is:

$$r_{\max} = nb. \tag{3.6}$$

Because of the random orientation of the Kuhn segments, the mean end-to-end vector is:

$$\langle \vec{r} \rangle = 0. \tag{3.7}$$

However, it holds for the mean-square end-to-end vector:

$$\langle \vec{r}^2 \rangle = \left\langle \left(\sum_{i=1}^{n} \vec{b}_i \right) \left(\sum_{j=1}^{n} \vec{b}_j \right) \right\rangle = \sum_{i=1}^{n} \sum_{j=1}^{n} \langle \vec{b}_i \vec{b}_j \rangle \tag{3.8}$$

$$= b^2 \sum_{i=1}^{n} \sum_{j=1}^{n} \langle \cos\left(\vartheta_{ij}\right) \rangle \tag{3.9}$$

$$= nb^2, \tag{3.10}$$

where $\vec{b}_i$ is the bond vector of Kuhn segment i with $|\vec{b}_i| = b$ and ϑ_{ij} denotes the angle between the bond vectors of segments i and j [55]. The last equality holds because of the absence of orientation correlation of the segments in the freely-jointed chain by definition. Therefore, the mean of the cosine is not vanishing only if $i = j$.

Note that this model is a strong idealization since there are constraints for the bond angles and torsion angles of real polymer chains. They are taken into account in the so-called rotational isomeric state model in which the mean-square end-to-end vector contains the so-called characteristic ratio as an additional factor. For non-ideal polymer chains, the characteristic ratio is larger than one and can be considered as a measure for their stiffness.

Furthermore, the freely-jointed chain model describes a single polymer chain. Subsequently, it will be used for the computation of the mechanical behavior of a network consisting of cross linked freely-jointed chains. This is the Neo-Hookean material model and the corresponding elastic restoring force obeys the incompressible Neo-Hookean law. This model is applied for the elastomer network studied in the course of this thesis.

3.3. Rubber Elasticity

In the following, the elastic restoring force of a network composed of freely jointed chains is obtained from the theory of rubber elasticity. The elastic restoring force is the force required to deform the material. It is derived from the Helmholtz free energy

$$F = E - TS, \tag{3.11}$$

where E denotes the internal energy given by the first law of thermodynamics, T is the temperature and S denotes the entropy. For the deformation of the network, work in terms of changing the volume V and the elongation L of the network has to be done [55]. Therefore, it holds for the total differential of the Helmholtz free energy:

$$\mathrm{d}F = \left(\frac{\partial F}{\partial T}\right)_{V,L} \mathrm{d}T + \left(\frac{\partial F}{\partial V}\right)_{T,L} \mathrm{d}V + \left(\frac{\partial F}{\partial L}\right)_{T,V} \mathrm{d}L \tag{3.12}$$

$$= -S\mathrm{d}T - p\mathrm{d}V + f\mathrm{d}L, \tag{3.13}$$

where p denotes the pressure and f the retraction force of the network. It has an energetic and an entropic contribution:

$$f = \left(\frac{\partial E}{\partial L}\right)_{T,V} - T\left(\frac{\partial S}{\partial L}\right)_{T,V} = f_E + f_S. \tag{3.14}$$

Both contributions can be separated by using the so-called Flory construction, for which the retraction force is plotted versus temperature and the interception of the tangent with the f-axis is obtained. Since the entropic part contributes f_S with more than 90 % for rubbers, the energetic contribution f_E is negligible and vanishes for ideal networks [55]. Rubber is called entropic elastic. Therefore, the conformational entropy of a single freely-jointed chain is computed first and applied to the derivation of the elastic entropy of an entire network in order to obtain the elastic restoring force.

3.3.1. Conformational Entropy

Before the conformational entropy of a polymer chain is discussed, the general concept of entropy is described. An isolated large system containing a smaller subsystem is considered [60, 221]. Both can only exchange energy with each other. A certain internal energy E of the subsystem can be realized by a number $\Omega(E)$ of microstates of the subsystem. For example, if the subsystem is filled with a gas of particles, a microstate can be defined by a set of positions and velocities of the particles. Different particle positions and velocities can yield the same internal energy.

By definition, it holds in statistical mechanics:

$$\beta \equiv \frac{\mathrm{d}\ln(\Omega(E))}{\mathrm{d}E}. \tag{3.15}$$

If the mean value of the internal energy is computed, one can conclude:

$$\beta = \frac{1}{k_\mathrm{B}T}, \tag{3.16}$$

where k_B is Boltzmann's constant. In thermodynamics, temperature is defined by the following relation:

$$\frac{\partial S}{\partial E} = \frac{1}{T}, \tag{3.17}$$

where S denotes the entropy. Combining the above equations yields for the entropy

$$S = k_\mathrm{B} \ln\left(\Omega\left(E\right)\right). \tag{3.18}$$

The entropy describes the lack of information in a system. In the example of the gas, the lack of information refers to the information regarding one microstate due to the number of possible alternative combinations of particle positions and velocities.

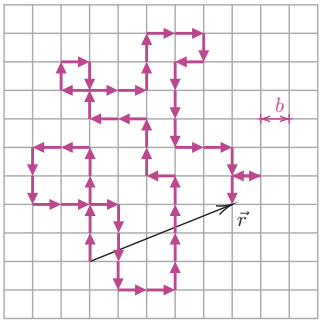

Figure 3.2.: Illustration of a polymer chain as path on a lattice with lattice constant b. The end-to-end vector $\vec{r}$ of the chain is drawn in.

The conformational entropy of a polymer chain denotes the entropy associated with its shape. For simplicity, a polymer chain is idealized as a random path on a simple cubic lattice with lattice constant b as depicted in Figure 3.2. The lattice constant is determined as the length of uncorrelated successive chain segments. Therefore, this picture is a variation of the freely-jointed chain model and the lattice spacing is associated with the Kuhn length.

Such a polymer chain consisting of n segments has the end-to-end vector

$$\vec{r} = (r_x, r_y, r_z)^\mathsf{T} = \left(\sum_{m=1}^{n} x_m, \sum_{m=1}^{n} y_m, \sum_{m=1}^{n} z_m\right)^\mathsf{T}. \tag{3.19}$$

The probability for a certain end-to-end distance r of the polymer chain is

$$p\left(r\right) = \frac{\Omega\left(r\right)}{\sum\limits_{r'} \Omega\left(r'\right)}, \tag{3.20}$$

where $\Omega\left(r\right)$ denotes the number of different paths on the lattice for a polymer chain consisting of n segments with the end located in a radius r around the other end. The sum in the denominator accounts for all possible paths for the polymer chain consisting of n segments including all possible end-to-end distances r'.

This probability enables to relate entropy to the shape of the polymer chain:

$$S\left(r\right) = k_\mathrm{B} \ln\left(\Omega\left(r\right)\right) \tag{3.21}$$

$$= k_\mathrm{B} \ln\left(p\left(r\right)\right) + \underbrace{k_\mathrm{B} \ln\left(\sum_{r'} \Omega\left(r'\right)\right)}_{=\text{const.}}. \tag{3.22}$$

The last term is constant because n is fixed. The conformational entropy is the difference of the entropy for the case that the polymer chain is widened and that the end of the polymer chain ties back to its start:

$$S(r) - S(0) = k_\mathrm{B} \ln p\left(r\right) - k_\mathrm{B} \ln p\left(0\right). \tag{3.23}$$

Hence, the probability $p(r)$ that the polymer chain has the end-to-end distance r has to be obtained. Since the components of the end-to-end vector are independent of each other, the probability factorizes:

$$p\left(r\right) = p\left(r_x\right) p\left(r_y\right) p\left(r_z\right). \tag{3.24}$$

For the calculation of the probabilities for the components, the central limit theorem is applied because the polymer chain describes a random path on the lattice. A random variable Z_n is constructed from random variables s_m. It holds:

$$Z_n = \frac{1}{\sqrt{n}\sigma_s}\left(\sum_{m=1}^{n} s_m - n\mu_s\right), \tag{3.25}$$

where $\mu_s = \langle s \rangle$ denotes the expectation value of the random variables s_m and $\sigma_s^2 = \langle s^2 \rangle - \langle s \rangle^2$ is their variance. The central limit theorem states that, for large n, Z_n obeys a Gaussian distribution:

$$f\left(Z_n\right) = \frac{1}{\sqrt{2\pi}} \exp\left(-\frac{Z_n^2}{2}\right) \quad \text{for } n \to \infty. \tag{3.26}$$

However, the central limit theorem yields also good approximations for smaller n. In the context of the polymer chain on the lattice, s_m is the contribution of the m-th Kuhn segment to a certain component of the end-to-end vector $\vec{r}$. For the x-component, it holds that $x_m \in \{-b,b,0\}$ with $p(-b) = p(b) = 1/6$ and $p(0) = 2/3$ in 3D. The probabilities arise from the fact that, if $x_m = 0$, the corresponding contribution to one of the other coordinates is non-zero, i.e. $y_m = \pm b$ or $z_m = \pm b$. Thus, $\mu_x = 0$ and $\sigma_x = \sqrt{b^2/3}$. This leads to

$$Z_n = \frac{1}{\sqrt{n}\sigma_x}\left(\sum_{m=1}^{n} x_m - n\mu_x\right) = \sqrt{\frac{3}{nb^2}} r_x. \tag{3.27}$$

Then, the normalized probability $p(r_x)$ according to the central limit theorem is:

$$p(r_x) = \sqrt{\frac{3}{2\pi n b^2}} \exp\left(-\frac{3}{2}\frac{r_x^2}{nb^2}\right). \tag{3.28}$$

Repeating these steps for the remaining components of the end-to-end vector $\vec{r}$ yields with Equation 3.24:

$$p(r) = \left(\frac{3}{2\pi n b^2}\right)^{\frac{3}{2}} \exp\left(-\frac{3}{2}\frac{r_x^2 + r_y^2 + r_z^2}{nb^2}\right) \tag{3.29}$$

$$= \left(\frac{3}{2\pi n b^2}\right)^{\frac{3}{2}} \exp\left(-\frac{3}{2}\frac{r^2}{nb^2}\right). \tag{3.30}$$

The end-to-end distance of the freely-jointed chain obeys a standard Gaussian distribution. By inserting Equation 3.30 into Equation 3.22, the conformational entropy is obtained as [55, 58, 60]

$$S(r) - S(0) = -\frac{3}{2} k_\mathrm{B} \frac{r^2}{nb^2}. \tag{3.31}$$

Since the number of possible paths for the polymer chain on the lattice is reduced when it is stretched to a larger end-to-end distance, its conformational entropy decreases.

3.3.2. Elastic Entropy

The conformational entropy of an individual freely-jointed chain according to Equation 3.31 is now applied for the computation of the elastic entropy of an entire network of polymer chains. The polymer chain segments connecting two cross links are now defined as freely-jointed chains.

In the following, a network is going to be stretched along the z-direction by a factor $\lambda_z = \lambda$. Since rubber is incompressible, the volume is conserved:

$$V = l_x l_y l_z = \lambda_x l_x \cdot \lambda_y l_y \cdot \lambda l_z = l'_x l'_y l'_z = V', \tag{3.32}$$

where V is the volume of the undeformed network, l_x, l_y and l_z denote its side lengths and the primed quantities refer to the deformed state of the network. Accordingly, it holds:

$$\lambda_x = \lambda_y = \frac{1}{\sqrt{\lambda}}. \tag{3.33}$$

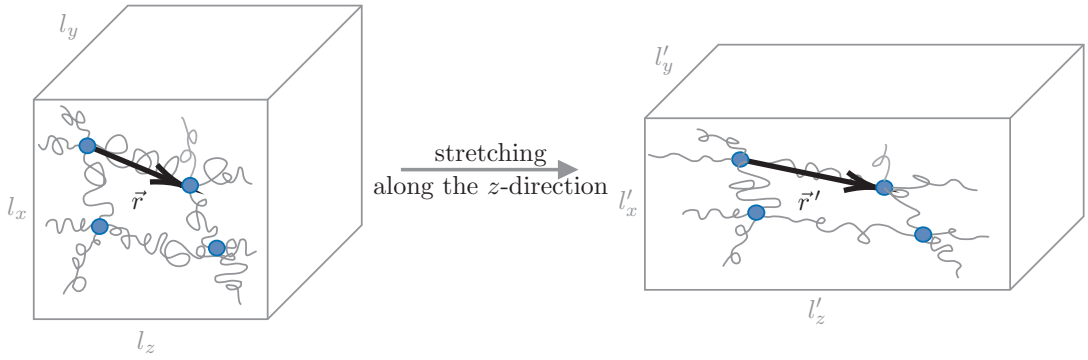

Figure 3.3.: Illustration of stretching a polymer network. The end-to-end vector of a chain as well as the side lengths of the volume of the network before and after the deformation are drawn. The blue dots are nodes of the network corresponding to cross links.

It is presumed now, that the positions of the cross links inside the network transform like the macroscopic volume during stretching. Therefore, the polymer chains are deformed analogously and an affine deformation is applied. The situation is illustrated in Figure 3.3. In addition, it is assumed that the mean-square end-to-end distance of the network chains is equal to that for free chains.

Based on this preliminary considerations, the elastic entropy is computed as the change of the total conformational entropy due to the deformation:

$$\Delta S = \sum_{i=1}^{\nu} S_i(r'_i) - \sum_{i=1}^{\nu} S_i(r_i), \tag{3.34}$$

where $S_i(r'_i)$ and $S_i(r_i)$ denote the entropy of chain i in the deformed and undeformed state of the network and ν is the total number of chains. Under the constraint that all of the chain segments in the network are composed of n Kuhn segments of Kuhn length b, the elastic entropy becomes:

$$\Delta S = \sum_{i=1}^{\nu} -\frac{3}{2} k_\mathrm{B} \frac{1}{nb^2} \left(r_i'^2 - r_i^2 \right) \tag{3.35}$$

$$= \sum_{i=1}^{\nu} -\frac{3}{2} k_\mathrm{B} \frac{1}{nb^2} \left[\left(\frac{1}{\lambda} - 1 \right) r_{i,x}^2 + \left(\frac{1}{\lambda} - 1 \right) r_{i,y}^2 + \left(\lambda^2 - 1 \right) r_{i,z}^2 \right]. \tag{3.36}$$

The sums over the squared components of the end-to-end vector are replaced by their averages multiplied by the total number of chains:

$$\Delta S = -\frac{3}{2} k_\mathrm{B} \frac{\nu}{nb^2} \left[\left(\frac{1}{\lambda} - 1 \right) \langle r_x^2 \rangle + \left(\frac{1}{\lambda} - 1 \right) \langle r_y^2 \rangle + \left(\lambda^2 - 1 \right) \langle r_z^2 \rangle \right]. \tag{3.37}$$

Since none of the spatial directions is preferred over the others for the freely-jointed chain, they contribute equally to the mean-squared end-to-end distance:

$$\langle r_x^2 \rangle = \langle r_y^2 \rangle = \langle r_z^2 \rangle = \frac{1}{3} \langle r^2 \rangle. \tag{3.38}$$

Hence, the elastic entropy is given as:

$$\Delta S = -\frac{1}{2} k_\mathrm{B} \frac{\nu}{nb^2} \left(\lambda^2 + \frac{2}{\lambda} - 3 \right) \langle r^2 \rangle \tag{3.39}$$

$$= -\frac{1}{2} k_\mathrm{B} \nu \left(\lambda^2 + \frac{2}{\lambda} - 3 \right), \tag{3.40}$$

where the last equality holds due to the consideration of the polymer chains as freely-jointed chains [56, 57, 59]. Equation 3.40 means that the entropy is reduced when the polymer network is stretched.

The elastic entropy of the polymer network is now applied for the derivation of its elastic restoring force f_el. For this purpose, the considerations made in the context of Equation 3.14 regarding the entropic elasticity of rubber have to be taken into account. It holds for the elastic restoring force of the network:

$$f_\mathrm{el} \equiv T \frac{\partial \Delta S}{\partial \lambda} = -k_\mathrm{B} T \nu \left(\lambda - \frac{1}{\lambda^2} \right). \tag{3.41}$$

Note that the stretch is a dimensionless quantity and, thus, this equation yields rather an energy than a force. However, it is useful to rewrite this expression as the stress of the network. For this purpose, the number of chains is expressed in terms of the density of chains $n_\nu = 2n_\mathrm{c}$ with n_c as the cross link density. The relation between the chain density and the cross link density is because each chain is linked to two cross links. Consequently, the stress is given by:

$$\sigma = k_\mathrm{B} T n_\nu \left(\lambda - \frac{1}{\lambda^2} \right). \tag{3.42}$$

The opposite sign is due to Newton's action-reaction law. Hence, this stress describes the force per area required to deform the network. The proportionality between the stress and temperature is characteristic for entropic elasticity [55]. Since the number of possible conformations decreases if a freely-jointed chain is stretched, the stress increases with increasing stretch.

Note that the stress given in Equation 3.42 is the engineering stress due to the derivative in Equation 3.41 with respect to λ. Whereas, the corresponding Cauchy or true stress would result from the derivative of the elastic entropy with respect to the actual box length in stretching direction. According to Equation 3.6, the two kinds of stresses can be transformed into each other by division or multiplication with λ in the case the uniaxial deformation under volume conservation.

Equation 3.42 is the Neo-Hookean law which transitions into Hooke's law for small deformations:

$$\sigma \approx 3 k_\mathrm{B} T n_\nu \left(\lambda - 1 \right). \tag{3.43}$$

Hooke's law and the Neo-Hookean law are plotted in Figure 3.4 in order to visualize the theoretical expectation for the mechanical behavior of a 3D-network consisting of cross linked freely-jointed chains. The stretch is $\lambda = 1.0$ if the sample is undeformed and it increases when the network is stretched. For small deformations, the stress σ according to the Neo-Hookean law behaves approximately linear and the curve overlaps with that corresponding to Hooke's law. This means that, in this range, the same force is required to deform a material obeying Hooke's law and another material which behaves according to the Neo-Hookean law. However, at larger deformations, the non-linearity of the Neo-Hookean law dominates and the stress is smaller compared Hooke's law which inclines linearly. Therefore, in this range, a smaller force is necessary to deform a Neo-Hookean material to the same extend as a material obeying Hooke's law. While the force required to gain a certain increase in stretch is constant for a material obeying Hooke's law, it becomes smaller with increasing stretch for a material with Neo-Hookean behavior.

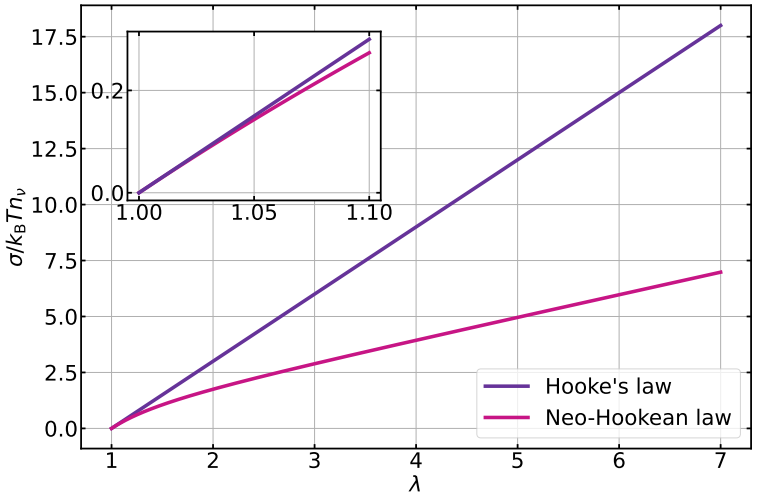

Figure 3.4.: Plot of the stress σ versus the stretch λ according to Hooke's law given in Equation 3.43 and according to the Neo-Hookean law given in Equation 3.42. The extract in the top left hand corner shows the curves in the range of small stretches.

Equation 3.42 is valid for 3D-networks. However, 2D-networks will also be considered during the studies conducted in this thesis. For the sake of completeness, the elastic restoring force for 2D-networks is derived now analogously to the 3D-case.

The conformational entropy of a freely-jointed chain in 2D is given by

$$S(r) - S(0) = -k_B \frac{r^2}{nb^2}$$

with $r^2 = r_x^2 + r_y^2$. Deforming a 2D-network consisting of such chains, where $\lambda_x = \lambda$ and $\lambda_y = 1/\lambda$, yields for the elastic entropy:

$$\Delta S = -\frac{1}{2} k_B \nu \left(\lambda^2 + \frac{1}{\lambda^2} - 2 \right).$$

Thus, the stress becomes

$$\sigma = k_B T n_\nu \left(\lambda - \frac{1}{\lambda^3} \right). \tag{3.44}$$

This is the Neo-Hookean law for 2D-networks.

Shear Deformation

Up to this point, uniaxial stretching of a network consisting of freely-jointed chains has been considered. This kind of deformation is in particular important to assess SIC. However, filled elastomers are usually also studied via shearing at small deformations for the dynamical-mechanical analysis (DMA) which has already been addressed in subsection 2.4.1 from a phenomenological point of view. Thus, theoretical considerations regarding rubber elasticity are discussed now for shear deformation and compared to the results for uniaxial deformation.

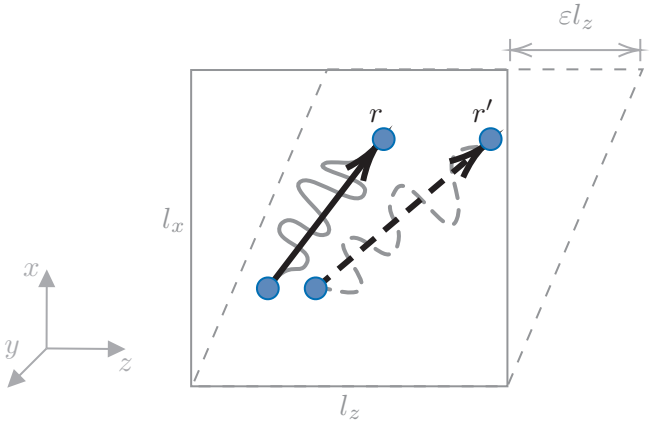

Figure 3.5.: Illustration of a shear deformation applied to a network of freely-jointed chains along the z-direction. The dashed lines indicate the sheared case.

Applying the theory of rubber elasticity to a shear deformation along the z-direction in 3D, as it is illustrated in Figure 3.5, yields the following transformation of the components of end-to-end vectors of the chains:

$$r'_x = r_x, \quad r'_y = r_y, \quad r'_z = r_z + \frac{r_x}{l_x} l_z \varepsilon,$$

where $\varepsilon = \lambda - 1$ denotes the strain amplitude. The coordinates of the nodes transform analogously. The change of the elastic entropy according to Equation 3.35 is for shearing given by:

$$\Delta S_{\text{shear}} = -\frac{3}{2} k_{\text{B}} \frac{1}{nb^2} \sum_{i=1}^{\nu} \left(\varepsilon^2 r_{x,i}^2 \frac{l_z^2}{l_x^2} + 2\varepsilon r_{x,i} r_{z,i} \frac{l_z}{l_x} \right).$$

Considering a cubic volume with $l_x = l_z$, it holds:

$$\begin{aligned} \Delta S_{\text{shear}} &= -\frac{3}{2} k_{\text{B}} \frac{\nu}{nb^2} \left(\varepsilon^2 \langle r_x^2 \rangle + 2\varepsilon \langle r_x r_z \rangle \right) \\ &= -\frac{1}{2} k_{\text{B}} \nu \varepsilon^2, \end{aligned} \tag{3.45}$$

where $\langle r_x^2 \rangle = nb^2/3$ and $\langle r_x r_z \rangle = 0$.

For stretching instead of shearing, the elastic entropy given in Equation 3.40 can be approximated in the limit of small strain as:

$$\Delta S_{\text{stretch}} \approx -\frac{3}{2} k_{\text{B}} \nu \varepsilon^2.$$

Deriving the corresponding stresses yields

$$\sigma_{\text{shear}} = \mu \varepsilon \tag{3.46}$$

$$\sigma_{\text{stretch}} = E \varepsilon, \tag{3.47}$$

where $\mu = k_B T\nu/V$ is the shear modulus and E the elastic modulus with $E = 3\mu$. The former relation has already been employed in the phenomenological model presented in subsection 2.4.1. The latter relation is known from elasticity theory and corresponds to Hooke's law given in Equation 3.43. At small deformations, the stress for uniaxial stretching behaves nearly linearly and just differs by a factor from the shear stress. Overall, this derivation shows that the non-linearity of the stress in the case of uniaxial stretching arises from the experimental geometry.

When rubber is studied at small deformations, the moduli are commonly measured in order to quantify reinforcement by filler. The derivative of the stress with respect to stretch or strain is proportional to the elastic or shear modulus. However, the derivative depends on the stretch for uniaxial deformation. For 3D-networks, taking the derivative of Equation 3.42 yields

$$\partial\sigma/\partial\lambda = k_B T n_\nu \left(1 + \frac{2}{\lambda^3}\right). \tag{3.48}$$

For the 2D-case, the relation is

$$\partial\sigma/\partial\lambda = k_B T n_\nu \left(1 + \frac{3}{\lambda^4}\right). \tag{3.49}$$

In both cases, the derivative decreases with increasing stretch. In order to avoid this and in particular to be able to observe the Payne effect, which is characteristic for filled rubber, without a superposing decrease, shear experiments are rather used than stretching experiments to obtain the dynamic modulus of rubber. For shearing, the derivative is constant over the entire range of strains.

3.4. Strain-Induced Crystallization

In this section, the model for strain-induced crystallization (SIC) is developed from the theory of rubber elasticity presented in section 3.3. The model is based on the theory by Flory [46] and has already been discussed by Plagge & Hentschke [1] as well as in [3].

The polymer chains connecting two cross links in a network are still considered as freely-jointed chains. SIC is treated as an equilibrium phenomenon although experimentally studied networks usually do not reach this equilibrium state [46]. Flory [46] presumes that crystalline chain segments, i.e. the corresponding polymer backbones, align along the stretching direction according to experimental observations. Crystallite nuclei form when neighboring chain segments attach to each other perpendicularly to the stretching direction due to thermal excitation [46]. These chain segments can belong to the same chain. The involved small changes of the entropy are neglected. If further chain segments of adjacent chains attach to a potential nucleus because their energy is minimized by this process, a crystal grows [46]. Since the conformation of the crystalline segments is restricted to the alignment along the stretching direction, the number of possible conformations for the remaining amorphous segments is increased. Therefore, the entropy reduction in the crystalline part competes with the entropy increase in the amorphous part. Hence, beyond a critical point at which the entropy gain is overcompensated by the entropy loss, crystallization is favorable.

Figure 3.6 depicts a semi-crystalline polymer chain. The crystalline segments are modeled as straight rods laying in between the amorphous parts. In addition, they are embedded into a crystal consisting of several crystalline segments which are attached to each other in a plane perpendicular to the stretching direction. The adjacent crystalline

chain segments can belong to neighboring chains or to the same chain due to chain-folding.

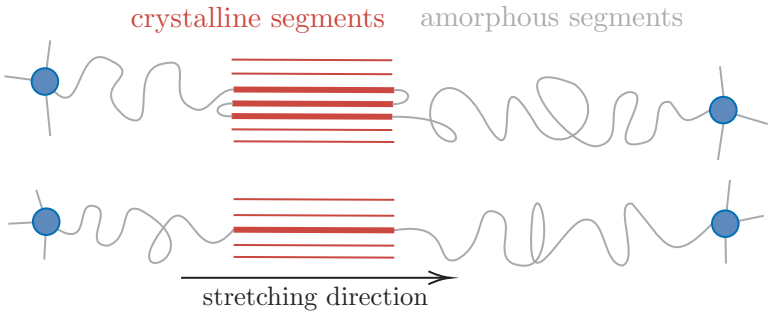

Figure 3.6.: Illustration of semi-crystalline polymer chains embedded into a crystal. The blue dots represent cross links of the polymer network.

In order to deal with crystallization of a polymer chain, it is convenient to derive its Gibbs free energy. The considerations made in section 3.3 with the Helmholtz free energy are still applicable. The Gibbs free energy is defined as:

$$G = E + pV - TS. \tag{3.50}$$

If a polymer chain or a network of multiple chains is deformed, the total differential is given by:

$$\mathrm{d}G = -\left(\frac{\partial G}{\partial T}\right)_{p,L} \mathrm{d}T + \left(\frac{\partial G}{\partial p}\right)_{T,L} \mathrm{d}p + \left(\frac{\partial G}{\partial L}\right)_{T,p} \mathrm{d}L \tag{3.51}$$

$$= -S\mathrm{d}T + V\mathrm{d}p + f\mathrm{d}L, \tag{3.52}$$

where L denotes the elongation and f is the retraction force.

For the derivation of the retraction force of a semi-crystalline polymer chain, the conformational entropy of a freely-jointed chain given in Equation 3.31 is adapted according to the considerations regarding SIC made above. The crystalline segments are treated as straight rod aligned with the stretching direction, which is in this case the z-axis. Since the conformation of the crystalline segments is fixed, only the amorphous chain segments contribute. Therefore, the conformational entropy of a semi-crystalline polymer chain i is written as:

$$S_\mathrm{c}\left(|\vec{r}_i - \vec{c}_i|\right) - S_\mathrm{c}\left(0\right) = -\frac{3}{2} k_\mathrm{B} \frac{\left(\vec{r}_i - \vec{c}_i\right)^2}{\left(n_i - n_{\mathrm{c},i}\right) b^2}, \tag{3.53}$$

where $n_{\mathrm{c},i} = c_i l_\mathrm{c}/b$ denotes the number of crystalline Kuhn segments and $\vec{c}_i = (0{,}0, c_i l_\mathrm{c})^\mathsf{T}$ is the end-to-end vector of the crystalline part with c as the number of crystalline segments and l_c as the length of a single crystalline segment [214]. Note that a crystalline segment consists of multiple Kuhn segments.

The corresponding Gibbs free energy of the semi-crystalline polymer chain derived from its conformational entropy is:

$$g_\mathrm{conf}\left(\vec{r}_i, c_i\right) = \frac{3}{2} \frac{\left(r_i - c_i l_\mathrm{c}\right)^2}{n_i - c_i l_\mathrm{c}}, \tag{3.54}$$

where $r_i = |\vec{r}_i|$ denotes the end-to-end distance of the chain. Energies are given in units of $k_\mathrm{B}T$ and lengths are given in units of the Kuhn length b. This equation does not involve any constraint regarding the orientation of the considered chain, but it presumed that the crystalline segments are oriented along the same direction.

In order to model SIC properly, the Gibbs free energy requires an additional contribution due to crystallization itself [1]:

$$g_{\text{cryst}}\left(\vec{r}_i, c_i, \{\vec{r}_j, c_j\}\right) = \theta_i c_i l_{\text{c}}, \tag{3.55}$$

where $\theta_i \equiv \theta\left(\vec{r}_i, \{\vec{r}_j, c_j\}\right)$ accounts for the change of the free energy when a crystalline segment is incorporated into a crystal and is defined as:

$$\theta\left(\vec{r}_i, \{\vec{r}_j, c_j\}\right) = \theta_0 - \eta \sum_{i \neq j} c_j \exp\left(-\frac{|\vec{r}_{\text{m},i} - \vec{r}_{\text{m},j}|}{R_0}\right). \tag{3.56}$$

Note that $\{\vec{r}_j, c_j\}$ is the set of all polymer chains $i \neq j$ in the network. The first term of Equation 3.56 is the free energy which has to be overcome to build a crystalline segment which means that work has to be done on the system for SIC. The second term represents the interaction of semi-crystalline links with strength η. The midpoint of link i is $\vec{r}_{\text{m},i}$ and R_0 denotes a characteristic distance. The exponential function is arbitrarily chosen [1]. Since it reduces the free energy of a semi-crystalline link, nucleation is taken into account. In general, the sum includes all links in the model network, but, in order to reduce the computational effort, the interaction will in practice be cut off beyond a certain distance. This is justified by the exponential decay.

Altogether, the total free energy of the semi-crystalline link is given by:

$$g\left(\vec{r}_i, c_i\right) \equiv g\left(\vec{r}_i, c_i, \{\vec{r}_j, c_j\}\right) = g_{\text{conf}}\left(\vec{r}_i, c_i\right) + g_{\text{cryst}}\left(\vec{r}_i, c_i, \{\vec{r}, c_j\}\right). \tag{3.57}$$

Taking the derivative with respect to $\vec{r}_i$ yields the force of the semi-crystalline link:

$$\vec{f}_i \equiv \vec{f}\left(\vec{r}_i, c_i\right) = -\frac{\partial g\left(\vec{r}_i, c_i\right)}{\partial \vec{r}_i} \tag{3.58}$$

$$= -3\frac{r_i - c_i l_{\text{c}}}{n_i - c_i l_{\text{c}}}\vec{e}_{r_i}, \tag{3.59}$$

where $\vec{e}_{r_i}$ is a unit vector oriented in the direction of link i.

In order to relate microscopic SIC to the macroscopic mechanical properties of a polymer network, the force of the semi-crystalline link given in Equation 3.59 can now be inserted into Equation 3.6. At a fixed stretch λ, it holds for the engineering stress [1]:

$$\sigma = \frac{1}{A_0}\left(\sum_{i \in A_z(\lambda)} f_{i,z} - \frac{A_z\left(\lambda\right)}{A_x\left(\lambda\right)} \sum_{i \in A_x(\lambda)} f_{i,x}\right), \tag{3.60}$$

where total force along a spatial direction is given by the sum over the components of the forces of all links which cross the corresponding boundary with a normal vector pointing in this direction. The z-component of the force of link i is denoted as $f_{i,z}$ and $f_{i,x}$ is the x-component. If a non-crystallizing network is considered, the stress obeys the Neo-Hookean material law.

Stretching a network of links under volume conservation by applying the deformation described in subsection 3.3.2 to an initially cubic volume yields:

$$A_x\left(\lambda\right) = l'_y l'_z = \frac{\lambda}{\sqrt{\lambda}} l_0^2 \quad \text{and} \quad A_z\left(\lambda\right) = l'_x l'_y = \frac{1}{\lambda} l_0^2$$

$$\Rightarrow \quad \frac{A_z\left(\lambda\right)}{A_x\left(\lambda\right)} = \lambda^{-\frac{3}{2}}, \tag{3.61}$$

where l_0 is the original side length. If a 2D-network is considered, which is initially of square shape, the original cross section becomes the original side length, i.e. $A_0 \to l_0$, and it holds:

$$A_x(\lambda) \to l'_z = \lambda l_0 \quad \text{and} \quad A_z(\lambda) \to l'_x = \frac{1}{\lambda} l_0$$
$$\Rightarrow \quad \frac{A_z(\lambda)}{A_x(\lambda)} \to \lambda^{-2}. \tag{3.62}$$

The ratio of the cross sections are different in the 2D- and in the 3D-case due to the applied deformation. Therefore, if $l_0 = 1$, the value of the stress for the 3D-case is systematically reduced dependent on attendant stretch. Note that, strictly speaking, the stress in the 2D-case possesses different units than in the 3D-case. It is a force per length instead of a force per area. Furthermore. the stresses can be translated to SI-units for the comparison with experimental data by considering *cis*-polyisoprene with Kuhn length $b = 9.34\,\text{Å}$ [108] at $T = 300\,\text{K}$. This yields approximately $\sigma = 1 \mathrel{\widehat{=}} 5\,\text{MPa}$ for the 3D-networks. Applying the same conversion to 2D-systems is justified because they represent extracts of 3D-systems for which the deformation is only applied to two of the spatial directions.

Another macroscopic quantity which is related to the microstructural properties of the material addressed here is the crystallinity which implicitly depends on the stretch:

$$\chi = \frac{\sum\limits_i c_i l_\text{c}}{\sum\limits_i n_i}, \tag{3.63}$$

where the sums include all links in the network [1]. The crystallinity at a certain stretch can be related with the corresponding stress.

3.4.1. Analysis of the Force

This subsection is devoted to deeper investigations of the force of links depending on their crystallinity.

Omitting the index i in Equation 3.59, the force can be rewritten as follows:

$$\vec{f} = -3\frac{r}{n} \cdot \frac{1 - \frac{c l_\text{c}}{r}}{1 - \frac{c l_\text{c}}{n}} \cdot \vec{e}_r. \tag{3.64}$$

The second factor describes how the force changes for different numbers of crystalline segments c in the considered link depending on its end-to-end distance r. An example is plotted in Figure 3.7. In the given units, the number of Kuhn segments in this link equals its contour length. The factor is constantly equal to 1 for a non-crystalline link. If the end-to-end distance of the link is smaller than its contour length, i.e. $r < n$, factor is smaller than 1 and the absolute value of the force decreases with increasing crystallinity. This causes softening of the model material by SIC. All curves intersect at the point $r = n$. Although $r \leq n$ is the physically relevant range, the end-to-end distance of a model polymer chain can exceed its contour length since finite chain extensibility is not included into the model. If the range $r > n$ is reached, the factor is larger than 1 and the force increases with increasing crystallinity. SIC then causes hardening of the model material. A potential approach for the implementation of finite chain extensibility into the model is described in section A.9.

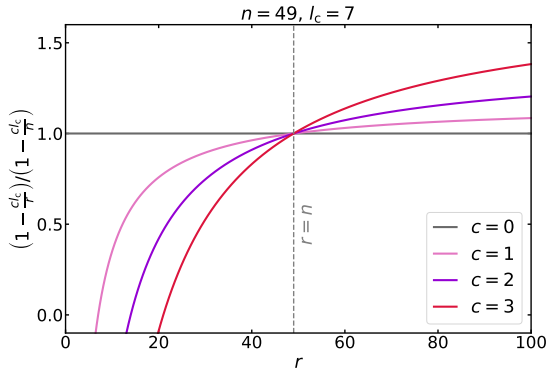

Figure 3.7.: Plot of the second factor of the force of a semi-crystalline link given in Equation 3.64 versus its end-to-end distance r for different numbers c of crystalline segments in this link. The number of Kuhn segments in this link is $n = 49$ and the length of a crystalline segment is $l_c = 7$.

Since Figure 3.7 involves specific values, for instance for the number of Kuhn segments in the link, the absolute value of the force of a link is generalized in terms of its extension r/n and its particular crystallinity cl_c/n:

$$f = 3\frac{\frac{r}{n} - \frac{cl_c}{n}}{1 - \frac{cl_c}{n}}. \tag{3.65}$$

This expression is plotted in Figure 3.8. As already indicated by the example, increasing the crystallinity of a link decreases the force below $r/n = 1$, while it increases the force above this threshold. The plot of the absolute value of the force depending on the crystallinity visualizes the non-linear relation. In particular, if the extension exceeds $r/n = 1$ and becomes even larger, the force is strongly amplified with increasing crystallinity. For very small extensions, the force is significantly reduced with growing crystallinity. However, small extensions and in particular the extension $r/n = 0$ can physically not be combined with high values of the crystallinity due to the assumption that crystalline segments can be treated as straight rods. Moreover, note that the crystallinity of a particular link with fixed number of Kuhn segments can only be discrete values because the number of crystalline segments can only be integers and it is restricted by the number of Kuhn segments.

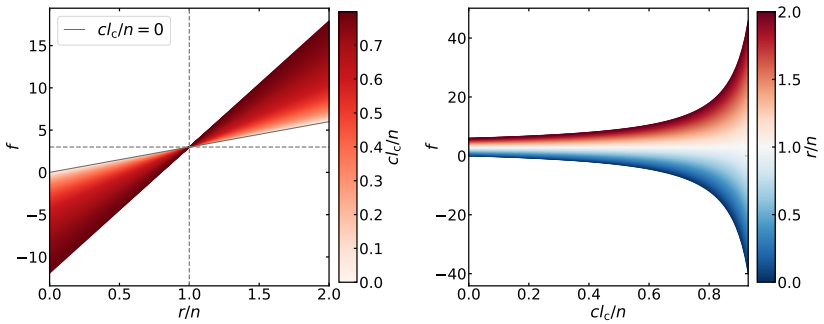

Figure 3.8.: Plot of the absolute value of the force f given in Equation 3.65 versus the extension r/n for different crystallinities cl_c/n and versus the crystallinity for various extensions. In the left plot, the value of the force at $r/n = 1$ is indicated by the dashed line.

Based on the considerations made above, crystalline links can be treated as springs with a smaller spring constant than non-crystalline links in the range of end-to-end

distances $r < n$. This allows for further analysis of possible arrangements of crystalline and non-crystalline links in a network structure. For this purpose, the forces of these springs are written as:

$$f_\mathrm{c} = k_\mathrm{c} u_\mathrm{c}, \tag{3.66}$$

$$f_\mathrm{nc} = k_\mathrm{nc} u_\mathrm{nc}, \tag{3.67}$$

where the index c refers to the crystalline link and nc to the non-crystalline link and $k_\mathrm{c} < k_\mathrm{nc}$. The spring constants are denoted by k_c and k_nc, respectively, while u_c and u_nc are the elongations. The springs can be arranged in series and in parallel as it is depicted in Figure 3.9. If the serial combination is deformed, the total elongation u is the sum of the individual elongations, but the force acting on each spring equals the total force:

$$f_\mathrm{s} = \frac{k_\mathrm{c} k_\mathrm{nc}}{k_\mathrm{c} + k_\mathrm{nc}} u. \tag{3.68}$$

When the parallel arrangement is stretched, the elongation of both springs equals the total elongation. The total force is then given by the sum of the individual forces:

$$f_\mathrm{p} = (k_\mathrm{c} + k_\mathrm{nc})\, u. \tag{3.69}$$

The systems (1)-(3) in Figure 3.9 depict possible arrangements of these combinations in a network structure. The system (1) is composed of two serial connections which are combined in parallel. This yields the total force:

$$f^{(1)} = 2 f_\mathrm{s}. \tag{3.70}$$

In combination (2), two crystalline links are serially connected and arranged in parallel with two serially connected non-crystalline links. The total force in this case is:

$$f^{(2)} = \frac{1}{2} f_\mathrm{p}. \tag{3.71}$$

The system (3) consists entirely of the same type of links, which are non-crystalline here. Two of them are connected in series and situated in parallel to the same serial combination. Hence, the total force is simply:

$$f^{(3)}_\mathrm{nc} = k_\mathrm{nc} u. \tag{3.72}$$

If all of the springs are replaced by crystalline links, the spring constant is exchanged accordingly.

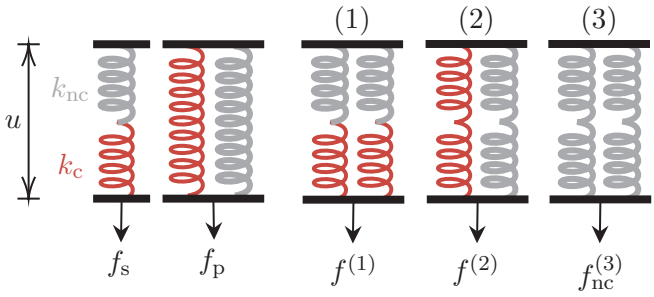

Figure 3.9.: Schematic representation of possible arrangements of springs representing crystalline (c) and non-crystalline (nc) links in a network structure. To each system, a force f applied to deform it to the elongation u. The combinations (1)-(3) are possible arrangements in a network structure.

The total forces of the systems (1)-(3) are related to each other as follows:

$$f^{(1)} = 4\frac{k_\mathrm{c}k_\mathrm{nc}}{(k_\mathrm{c}+k_\mathrm{nc})^2}f^{(2)} = 2\frac{k_\mathrm{c}}{k_\mathrm{c}+k_\mathrm{nc}}f_\mathrm{nc}^{(3)} = 2\frac{k_\mathrm{nc}}{k_\mathrm{c}+k_\mathrm{nc}}f_\mathrm{c}^{(3)}. \tag{3.73}$$

As an example, for $k_\mathrm{c} = k_\mathrm{nc}/2$, it holds:

$$f^{(1)} = \frac{8}{9}f^{(2)} = \frac{2}{3}f_\mathrm{nc}^{(3)} = \frac{4}{3}f_\mathrm{c}^{(3)}. \tag{3.74}$$

It follows:

$$f_\mathrm{c}^{(3)} < f^{(1)} < f^{(2)} < f_\mathrm{nc}^{(3)}. \tag{3.75}$$

Thus, the macroscopic force of a network is minimized either if all links are crystalline or if layers of crystalline and non-crystalline links evolve which alternate along the stretching direction. A model network is expected to organize itself in this way.

3.5. Rupture Criterion

Up to this point a model for polymer chains in a network has been discussed which does not involve rupture of them. In theory, they can be infinitely extended. This does not replicate the behavior of a real-world material at large deformations. In addition, the subsequent study of failure requires for the definition of a rupture criterion for links.

Since polymer chains are considered to be entropically elastic, the end-to-end distance of polymer chains is approximately limited to $r \leq n$. Nevertheless, real polymer chains can resist for end-to-end distances $r > n$ because, when the contour length is reached, the bond lengths between monomers are increased until it comes to failure, but this is a minor contribution. However, pulling the chemical bonds causes a steep increase of the force.

In the model, rupture of links will be included by the definition of a critical free energy density, which is the free energy of a link per Kuhn segment. Applying an energy based criterion is consistent with Griffith's approach discussed in section 2.5. If the free energy density of a link exceeds this threshold value the link breaks.

The critical free energy density must be selected such that the strength of crystalline links is higher that the strength of non-crystalline links as it is expected from experimental observations. In general, it must be sufficiently large such that it is approached at stretches at which domains of strain-induced crystallites have already formed. Then, crystalline links can persist higher stretches than non-crystalline links due to the free energy minimization. However, the force is also lowered by SIC if the end-to-end distance of a link is below its contour length. Consequently, the tensile strength of crystalline links would also be smaller than for non-crystalline links, but this is in contrast to experimental observations. Nevertheless, due to the specific modeling of links, the absolute value of their force increases with their crystallinity as their end-to-end distance exceeds their contour length. In order to take advantage of this specific modeling of links, the critical free energy density must be chosen such that it is reached when the end-to-end distance of crystalline links exceeds their contour length. In the following, these qualitative considerations are elaborated further.

According to Equation 3.57, the free energy density of a non-crystalline link is:

$$\frac{g}{n} = \frac{3}{2}\frac{r^2}{n^2}. \tag{3.76}$$

It increases quadratically with the end-to-end distance. Since rubber is entropically elastic, it is suitable to set the threshold value of the critical free energy density for rupture of links to $(g/n)_{\mathrm{crit}} = 1.5$. Thus, non-crystalline links break if their end-to-end distance reaches their contour length. Note that this relation is derived for the 3D-case. For the 2D-case, it would be $g/n = r^2/n^2$, but this relation is not applied in the simulation algorithm.

In order to make further considerations regarding the critical free energy density, Equation 3.57 is rewritten as follows:

$$\frac{g}{n} = \frac{3}{2}\frac{\left(\frac{r}{n} - \frac{cl_{\mathrm{c}}}{n}\right)^2}{1 - \frac{cl_{\mathrm{c}}}{n}} + \frac{cl_{\mathrm{c}}}{n}\theta, \tag{3.77}$$

where θ is given by Equation 3.56. This relation is plotted in Figure 3.10 for two different values of the penalty θ_0. The interaction of semi-crystalline links is neglected here by setting $\eta = 0.0$. Depending on the crystallinity of a particular link, it would lower the free energy density, whereas increasing the penalty raises it. With respect to the minimization of the free energy density, smaller crystallinities are preferred over higher crystallinities at small and at very large extensions. Thus, if the extension far exceeds $r/n = 1$ and leaves the physically relevant range, the strain-induced crystallinity would be preferentially reduced again. However, there is an interval around $r/n = 1$ in which the free energy density decreases with enhanced crystallinity compared to the non-crystalline case. Higher crystallinities are advantageous in this range. At lower crystallinity, the interval is more extended.

Now, the critical free energy density $(g/n)_{\mathrm{crit}} = 1.5$ is considered, which has been derived from the non-crystalline case. Due to the aforementioned interval, semi-crystalline links would reach this threshold value at larger extensions the higher their crystallinity is. Therefore, the elongation at break of a link or even a network of links is expected to be increased compared to the non-crystalline case. In particular, the critical free energy density is reached as the end-to-end distance exceeds the contour length, i.e. $r > n$. In this range, the force of a link increases with increasing crystallinity. Hence, the tensile strength of a semi-crystalline link or even of a semi-crystalline network of links is expected to also be enhanced compared to the non-crystalline case. Altogether, the value $(g/n)_{\mathrm{crit}} = 1.5$ is expected to be suitable as critical free energy density for rupture of links. However, only individual links have been considered and filler particles are not included into the model yet. Therefore, the behavior of a network of such links must be analyzed, also when it is filled. This is done in section 5.6.

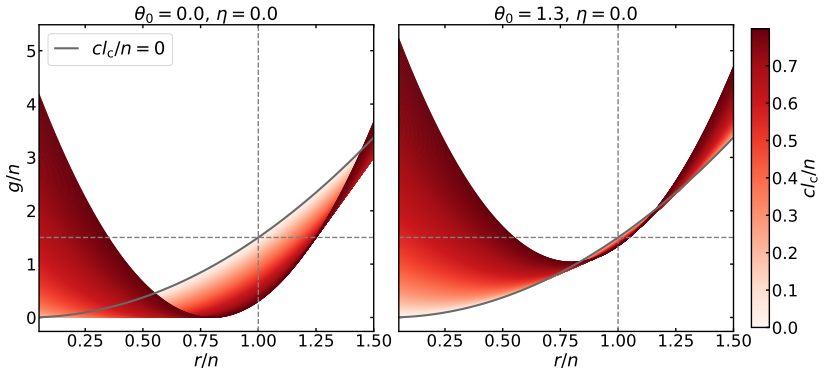

Figure 3.10.: Plot of free energy density g/n given in Equation 3.77 the extension r/n for different crystallinities cl_{c}/n. The free energy density of a non-crystalline link at $r/n = 1$ is indicated by the dashed line.

3.6. Filler Interactions

The previous sections have dealt with modeling of pure elastomer networks and SIC. This approach is complemented now by the inclusion of filler particles into the rubber matrix. For this purpose, the interactions of polymer with filler particles and between filler particles are discussed subsequently. This extension is based on the model for filled rubber developed by Viktorova *et al.* [2].

The filled model networks which are studied in course of this work are build up from so-called nodes, filler nodes and links. The nodes represent chemical cross links and are connected by the links which are the model polymer chains, while the filler nodes account for coarse-grained filler particles. Due to the inclusion of filler, new interactions must be defined. Filler-filler bonds and polymer-filler bonds describe the interaction between two filler nodes and between a cross link and a filler, respectively. They are modeled by harmonic potentials u_i which can be distinguished by their spring constant k_i [2]:

$$u_i \equiv u\left(\vec{r}_i\right) = \frac{1}{2} k_i \left(r_{0,i} - r_i\right)^2 . \tag{3.78}$$

where $r_{0,i}$ denotes the equilibrium end-to-end distance of bond i. The spring constant is given as follows:

$$k_i = \begin{cases} k^{\mathrm{ff}}, & r_i < R^{\mathrm{ff}} r_{0,i} \\ 0, & r_i \geq R^{\mathrm{ff}} r_{0,i} \end{cases} \quad \text{filler-filler bonds,}$$
$$k_i = \begin{cases} k^{\mathrm{pf}}, & r_i < R^{\mathrm{pf}} r_{0,i} \\ k^{\mathrm{pf}}_{\mathrm{weak}}, & r_i \geq R^{\mathrm{pf}} r_{0,i} \end{cases} \quad \text{polymer-filler bonds} \tag{3.79}$$

with R^{ff} and R^{pf} as factors which define cut-off radii for the interactions. Both types of bonds are not able to undergo strain-induced crystallization.

This modeling of filler-filler and polymer-filler bonds is motivated as follows: The attractive interactions between filler particles are determined by intermolecular van der Waals forces. They include dipole-dipole interactions of molecules, but no electrostatic contributions or chemical bonding [222]. To be more precise, dipole moments can be permanently present in molecules. Alternatively, they can be induced by fluctuations in the electron density due to quantum mechanical perturbations in molecules with symmetric atomic orbitals. Hence, the molecules interact via an attractive $1/r^6$-potential with R as the intermolecular distance. In the latter case, the resulting forces are called London dispersion forces [223]. For filler particles which are considered as identical spheres consisting of such molecules, the theory by Hamaker [224] yields an attractive $1/r$-potential at close distances which is stated in Equation 2.7. Here r denotes the distance between the spheres. These filler particles are considered as stable, in particular they do not further aggregate. Hence, there must be an repulsive contribution to the interaction. If the particles possess a polar surface, electrostatic interaction is involved. In contrast to silica, the polarity of the CB surface is negligible [11]. Additionally, steric repulsion[1] can, for instance, be described by the hard-sphere potential, but it is not convenient for computations. In addition, combining these attractive and

[1] Note that the repulsion of neutrally charged atoms or molecules is commonly modeled by a $1/r^{12}$-potential which accounts for the Pauli exclusion principle when electronic orbitals overlap. In the so-called Lennard-Jones (LJ) potential, this is combined with the attractive term associated with London forces. An advantage of the LJ-potential is that the repulsive term can be easily computed from the attractive term.

repulsive terms for non-polar filler yields a potential that contains a divergence. Moreover, depending on the filler type, filler aggregate may not be build up from direct filler contacts, but due to the surrounding rubber [11]. The filler particles embedded into a rubber matrix may be coated by a soft shell of polymer and form a joint shell with each other. Therefore, the repulsive interaction may be described by a more slowly decaying function instead of a step function.

The approximation of the filler-filler bonds by a harmonic potential is the simplest approach that can be made. In particular, it is computationally advantageous. Since it is presumed that the interaction between filler particles is predominantly short-ranged, in accordance with the Hamaker interaction, the filler-filler bonds are defined as reversibly breakable depending on their end-to-end distance. Thus, dissipation is incorporated into the model. It is expected that this breaking mechanism enables modeling of the Payne effect. A similar approach to modeling of the filler contact is the jump-in-jump-out model [97].

Moreover, the modeling of polymer-filler bonds involves slippage of polymer chains over the filler surface due to absorption and desorption because polymer-filler bonds can weaken reversibly. Although, polymer-filler interactions are predominantly physical, there may be a minor fraction of covalent bonds [225]. In particular, modifications of the filler surface, for instance by silanization or graphitization, can advance the strength of the interaction. These stronger interaction may also be included in this particular modeling of polymer-filler bonds. In addition, it accounts for effects like bound rubber. Furthermore, the harmonic potential preserves the linear elastic behavior of the network of freely-jointed chains at small deformations, which has been outlined earlier.

The parametrization of filler-filler and polymer-filler bonds will be discussed further in subsection 5.2.2. Note that the equilibirium end-to-end distances provide an estimation for the size of the coarse-grained filler particles in the model.

According to Equation 3.78, the force of bond i is given by:

$$\vec{f}_i = k_i \left(r_{0,i} - r_i\right) \vec{e}_{r_i}, \tag{3.80}$$

with the unit vector $\vec{e}_{r_i}$ pointing along the direction of the end-to-end vector of the bond with end-to-end distance r_i. This expression is inserted into Equation 3.60 for the computation of the engineering stress if the considered connection i is a filler-filler or a polymer-filler bond instead of a link.

3.6.1. Surface Tension

The interaction between polymer and filler included in Equation 3.78 refers to the mechanical response of a bond under deformation. However, the interaction of polymer and filler is already important during the production of a composite material. Their compatibility determines the filler morphology which itself affects the mechanical properties. The filler morphology is the dispersion of the filler particles inside the rubber matrix. If the compatibility between polymer and filler is bad, the filler particles preferentially aggregate. Otherwise, the filler particles are more likely to separate. In this work, the so-called Morphology Generator (MG) developed by Viktorova *et al.* [2] is applied to generate different filler dispersions. This algorithm models the flocculation of filler particles in the rubber matrix in the post mixing stages based on their surface free energies.

In this section, the concept of surface tension is elucidated and it is pointed out how it is related to intermolecular forces or interactions between different components. The compatibility between different materials is also addressed.

It is convenient to start from the total differential of the Gibbs free energy:

$$\mathrm{d}G = -S\mathrm{d}T + V\mathrm{d}p + \gamma\mathrm{d}A + \mu_i\mathrm{d}N_i, \tag{3.81}$$

where Einstein's summation convention applies. The term $\gamma\mathrm{d}A$ is the surface work with γ as the surface tension and $\mathrm{d}A$ as the change of the surface area. The term $\mu_i\mathrm{d}N_i$ accounts for chemical work, where μ_i is the chemical potential associated with the number N_i of particles of type i. This expression immediately yields for the surface tension:

$$\gamma = \left(\frac{\partial G}{\partial A}\right)_{T,p,\{N_i\}}. \tag{3.82}$$

It is the change of the total Gibbs free energy in response to a change of the surface area. In particular, it depends on temperature T, pressure p, and particle number N_i.

Note that the surface tension is given in units of energy per area or force per length which indicates its relation to microscopic forces. Moreover, the term "surface" usually refers to an interface in which a gas phase is involved. Otherwise the term "interface tension" is commonly used. However, in the following we shall not strictly adhere to this distinction.

Considering the interface of two bulk systems, for instance liquid and gas, the intermolecular forces at the interface differ from those in the bulk. Repulsive interactions which cause internal pressure are predominantly short-ranged and, thus, remain isotropic when an interface is involved [226]. Nevertheless, an asymmetry occurs perpendicularly to the interface as it is depicted in Figure 3.11. In order to establish mechanical equilibrium, the repulsive and attractive forces perpendicular to the interface must compensate each other. In parallel to the interface, the symmetry with respect to that attendant in the bulk is not broken. Phenomenologically, the attractive forces oriented in parallel to the interface are increased compared to those in the bulk, but still conserving the force balance [226]. These attractive forces are the stress at the surface and lead to positive surface tension.

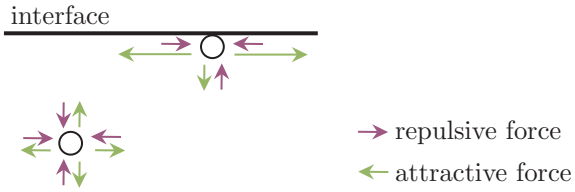

Figure 3.11.: Illustration of intermolecular forces in a material when an interface is involved.

During filler flocculation which is modeled by the MG, volume elements of the components are separated and combined with each other. If a piece of material is cut in half, two new surfaces are formed. The work required to overcome the molecular interactions is the so-called work of cohesion which is twice the surface tension of one of these new surfaces. For separating to different materials, which adjoin one another at an interface, to an infinitely large distance, the work of adhesion w has to be overcome. It is given by the Dupré-equation [227]:

$$w = \gamma_\alpha + \gamma_\beta - \gamma_{\alpha\beta}, \tag{3.83}$$

where γ_α and γ_β denote the surface tensions of material α and β, respectively, and $\gamma_{\alpha\beta}$ denotes the interface tension. The sum accounts for the work necessary to form new surfaces of each material. It is reduced then due to the interface.

When, for instance, a liquid drop is deposited on a solid surface, the change of the surface free energy G_s is determined by the work of adhesion:

$$\Delta G_\mathrm{s} = w \Delta A \tag{3.84}$$

with $G_\mathrm{s} = G - G_\mathrm{b}$, where G_b denotes the Gibbs free energy of the bulk. According to the principle of energy minimization and Equation 3.83, on the one hand, the liquid-solid interface is maximized if the interface tension is high or both the interface tension and the cohesive forces of the liquid are weak. In the ideal case, the entire surface of the solid is wetted by the liquid. On the other hand, the interface is minimized, if the interface tension is low compared to the surface tension of the liquid. In this case, the drop persists on the surface in a nearly spherical shape. An exemplary observation for this is the Lotus effect. Hence, the surface tension and the interface tension determine the compatibility between different materials. The ability of the liquid to wet the solid surface can be distinguished the contact angle ϑ. Wetting is illustrated in Figure 3.12.

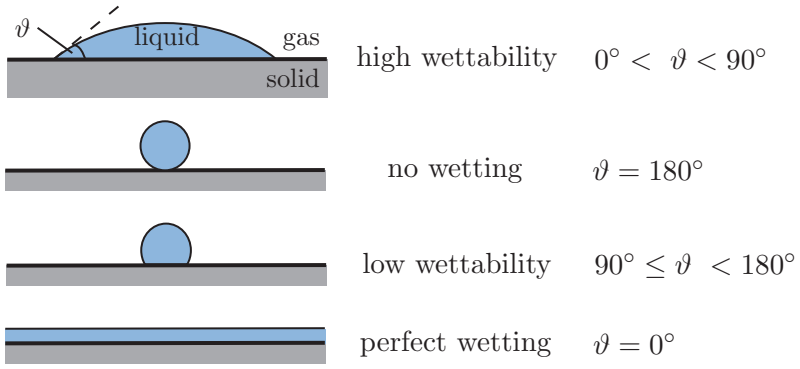

Figure 3.12.: Schematic illustration of wetting for different contact angles ϑ. A liquid drop is deposited on a solid surface. Depending on the surface tensions of the liquid and the solid, the drop adopts a shape ranging from a sphere to a flattened configuration resulting in different contact angles.

Moreover, in the MG, polymer and filler are treated as the liquid and the solid phase, respectively. The change of the Gibbs free energy of the surface when interfaces are created from the interchange of volume elements representing polymer and filler is implemented and will be discussed in the subsequent section. In this approach, experimentally obtained values for the surface tensions of polymer and filler will be applied. They are compiled in Table 4.1.

A common method for measuring surface tensions is the sessile drop method which is illustrated in Figure 3.13. A liquid drop is placed on a solid surface in a gas environment and spreads according to the aforementioned concept. As explained above, the vectors representing the surface tensions of each phase are directed tangential to the respective surfaces. Young's equation holds due to the force equilibrium in the three-phase contact point [227]:

$$\gamma_\mathrm{s} = \gamma_\mathrm{ls} + \gamma_\mathrm{l} \cos \vartheta, \tag{3.85}$$

where ϑ denotes the contact angle between liquid indicated by l and solid indicated by s. The interface tension γ_ls is usually approximated by applying so-called OWRK-theory after Owens & Wendt [228], Rabel [229] and Kaelble [230], which involves earlier considerations by Fowkes [231]:

$$\gamma_{\alpha\beta} = \gamma_\alpha + \gamma_\beta - 2 \left(\sqrt{\gamma_\alpha^\mathrm{d} \gamma_\beta^\mathrm{d}} + \sqrt{\gamma_\alpha^\mathrm{p} \gamma_\beta^\mathrm{p}} \right), \tag{3.86}$$

where $\gamma_\alpha = \gamma_\alpha^\mathrm{d} + \gamma_\alpha^\mathrm{p}$ and the indices d and p mark the dispersive and the polar part of the surface tensions of phases α and β, respectively, which are liquid and solid here. This approach is based on the form of the equations describing intermolecular forces. The separation of the contributions to the surface tension in this way can be difficult on the scale of microscopic interactions [60]. If the material possesses a comparatively large permanent dipole moment due to polar groups, the polar part of the surface tension is also dominant [60]. An example for this is water. However, the polar term vanishes otherwise if the polarizability of the material is also small. The dispersive part is governed by attractive van der Waals interactions because of quantum fluctuations in the electronic orbitals [60]. Inserting Equation 3.86 into Equation 3.85 and dividing by $\sqrt{\gamma_\mathrm{l}^\mathrm{d}}$ yields:

$$\frac{\gamma_\mathrm{l}}{\sqrt{\gamma_\mathrm{l}^\mathrm{d}}} \frac{1+\cos\vartheta}{2} = \sqrt{\gamma_\mathrm{s}^\mathrm{d}} + \sqrt{\frac{\gamma_\mathrm{l}^\mathrm{p}}{\gamma_\mathrm{l}^\mathrm{d}}} \sqrt{\gamma_\mathrm{s}^\mathrm{p}}. \tag{3.87}$$

The surface tension of the solid can be obtained via this equation from the measurement of the contact angle if the surface tension of the liquid is known. For this purpose, the left-hand side of Equation 3.87 must be plotted versus $\sqrt{\gamma_\mathrm{l}^\mathrm{p}/\gamma_\mathrm{l}^\mathrm{d}}$ and fitted linearly. The squares of the intercept and the slope of the resulting linear function are the dispersive and polar contribution to the surface tension of the solid respectively. Dividing by $\sqrt{\gamma_\mathrm{s}^\mathrm{d}}$ in the derivation yields an equation for obtaining the surface tension of the liquid instead.

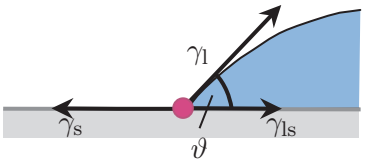

Figure 3.13.: Schematic illustration of the sessile drop method. An extract of the contact of the liquid drop with the solid substrate is shown. The three-phase contact point is highlighted by the pink dot.

An alternative to the sessile drop method for the measurement of the surface tension of a liquid is the Wilhelmy plate method. Its principle is illustrated in Figure 3.14. A plate with length l_1 and width l_2 is submerged into a liquid. The force acting on the plate is:

$$f = L\,\gamma_\mathrm{l} \cos\vartheta - V \Delta\rho\, g, \tag{3.88}$$

where $L = 2\,(l_1 + l_2)$ is the wetted perimeter of the plate, V denotes the volume of the liquid that is displaced by the plate, $\Delta\rho$ is the difference of the density of the liquid and the surrounding air and g is the acceleration of gravity [60]. The first term accounts for the force due to the surface tension of the liquid, whereas the second term represents the bouyancy. With this equation the surface tension of a liquid can be obtained from measurements of the force and the contact angle. Commonly, a platinum plate is used since the contact angle becomes zero due to its high surface free energy [60]. Often, this method is modified by slowly submerging the plate into the liquid and retracting it. The advancing and the receding angle which can be measured respectively differ. A contact angle hysteresis occurs.

For the measurement of the surface tension of fillers, an adhesive tape is covered with them [232]. According to the modified Wilhelmy method, this sample is submerged into a test liquid and both the advancing and the receding contact angle are measured.

The surface tension can then be computed according to Equation 3.87 for both contact angles and for the mean contact angle as well. The sessile drop method is not convenient for obtaining the surface tension of hydrophilic powders or granular matter because the deposited drop must be stable [232]. However, the surface tension of polymers can be obtained from both of the presented methods. Note that the these measurement methods are sensitive to inhomogeneity and contamination of the surface.

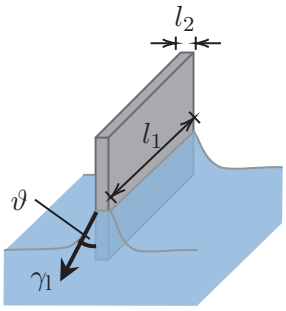

Figure 3.14.: Schematic illustration of the Wilhelmy plate method.

For the sake of completeness, it is useful to introduce the concept of so-called wetting envelopes at this point. The liquid drop on the solid surface is considered again. It is supposed that the disperse and the polar part of the surface tension of the liquid are fixed. The components of the surface tension of the solid can be expressed as [60]:

$$\gamma_s^d = R\cos\psi, \tag{3.89}$$
$$\gamma_s^p = R\sin\psi \tag{3.90}$$

with $0 \leq \psi \leq \pi/2$. Inserting this and Equation 3.86 into Equation 3.85 and solving for R yields:

$$R(\psi,\vartheta) = \left(\frac{\gamma_l^d + \gamma_l^p}{\sqrt{\gamma_l^d\cos\psi} + \sqrt{\gamma_l^p\sin\psi}}\right)^2 \frac{(\cos\vartheta+1)^2}{4}. \tag{3.91}$$

With this equation, the components of the surface tension of the solid can be obtained by varying ψ for fixed contact angle ϑ. It is convenient to plot γ_s versus γ_s^p. The analogous procedure can be conducted for obtaining the surface tension of the liquid if the surface tension of the solid is known [60]:

$$\gamma_l^d = R'\cos\psi', \tag{3.92}$$
$$\gamma_l^p = R'\sin\psi', \tag{3.93}$$
$$\Rightarrow \quad R'(\psi',\vartheta) = \left(\frac{\sqrt{\gamma_s^d\cos\psi'} + \sqrt{\gamma_s^p\sin\psi'}}{\cos\psi'+\sin\psi'}\right)^2 \frac{4}{(\cos\vartheta+1)^2}. \tag{3.94}$$

Figure 3.15 shows examples of wetting envelopes computed with this procedure. The total surface tension of the solid or the liquid is plotted versus its polar contribution. If the variable surface tensions are selected such that the data point in the plot lays on the iso-contact-angle line for $\vartheta = 0°$ or is enclosed by it, perfect wetting occurs. These kind of plots give rise to the compatibility of different materials.

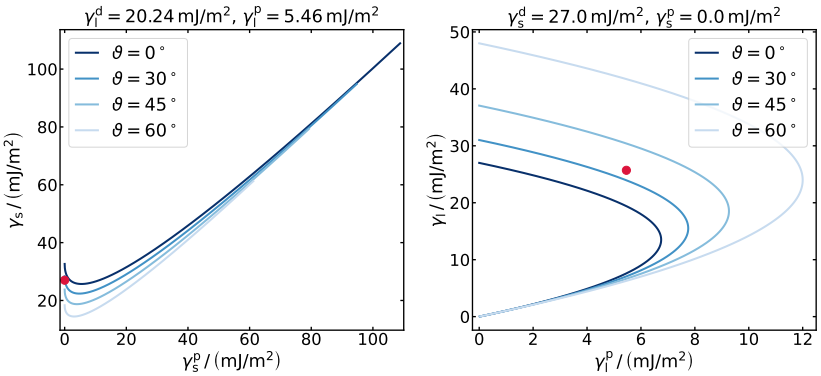

Figure 3.15.: Exemplary wetting envelopes. In the left panel, the values for the components of the surface tension of the liquid are values for NR taken from [233]. In the right panel, the components of the surface tension of the solid are values for CB N339 taken from [232]. The red dot in the left panel marks the data point for the surface tension of CB N339 applied in the right panel, while the red dot in the right panel is the corresponding data point for NR.

4. A Simulation Algorithm for the Mechanical Strength of Filled Natural Rubber

In the preceeding section, the physical concepts underlying the material model for filled and strain-crystallizing elastomers like NR have been discussed. In this section, these principles are implemented into the computer algorithm for the simulation of the mechanical behavior of these materials. First, it is described how the initial configuration of model elastomer networks is constructed from coarse-grained elements, so-called "nodes", "links", "filler", "filler-filler bonds" and "polymer-filler bonds". In particular, the working principle of the Morphology Generator (MG) for the simulation of filler flocculation which has been developed by Viktorova *et al.* [2] is outlined. Afterwards, the simulation of uniaxial stretching experiments in analogy to [1, 3] is elucidated and the default parametrization is stated.

4.1. Initial Configuration

Unfilled model networks consist of so-called "nodes" and "links". The former are points that represent chemical cross links, while the links are the polymer modeled as freely-jointed chains which connect the nodes. Figure 4.1 visualizes the steps performed when setting up a model network. Initially, N nodes are placed on a square lattice in 2D or on a simple cubic lattice in 3D with lattice spacing $d_\mathrm{i} = 7.0$. For the estimation of this particular value, the entanglement spacing of *cis*-polyisoprene, which is roughly 51.4 Å [108], is taken into account. In addition, it is thought that the linear dimension of strain-induced crystallites, which is around 10 nm, is related to the mesh size of the elastomer [7–9]. Treating the lattice spacing as square root of the mean-square end-to-end vector yields $n = 49$ for the number of Kuhn segments per link. This is equivalent to approximately 100 monomers which is consistent with experimental observations for NR [108].

The initial length l_i of the square or cubic simulation box is then given by:

$$l_\mathrm{i} = d_\mathrm{i}\, N^{\frac{1}{d}}, \tag{4.1}$$

where d denotes the dimension. To make the lattice more inhomogeneous, the nodes can be displaced by transforming their coordinates $x_{j,\alpha}$ according to a random factor:

$$x_{j,\alpha} \to x_{j,\alpha} + \kappa\, d_\mathrm{i} \cdot \mathrm{random}\,(-1.0,\, 1.0)\,, \tag{4.2}$$

where the index j refers to the node, the index α refers to the coordinate, κ denotes a parameter for the perturbation and the function random $(-1.0,\, 1.0)$ returns random numbers on the interval $[-1.0,\, 1.0]$ from a uniform distribution.

If filled networks are about to be studied, filler particles are included into the rubber matrix by assigning the type "filler" to a given fraction ϕ of nodes. Thus, the filler content in the model is comparable to the filler volume fraction in experimental samples, but not to the mass fraction. Note that the model filler particles are rather smallest non-breakable aggregates than primary filler particles. Initially, the particular filler nodes

are chosen at random according to the fraction ϕ. To modify the filler morphology inside the model network, the Morphology generator is applied. This algorithm will be explained in section 4.2.

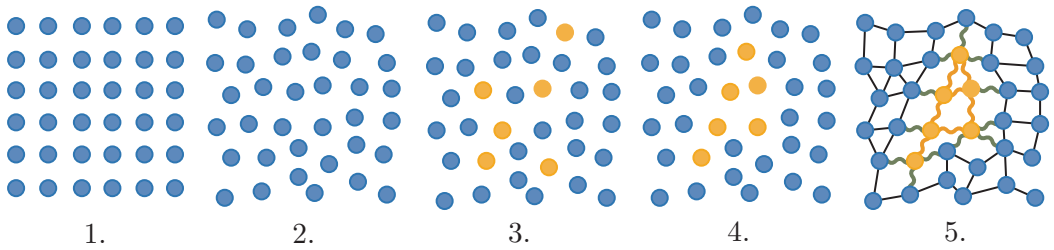

Figure 4.1.: Schematic illustration of setting up a 2D-model elastomer network. (1.) First, nodes, depicted as blue dots, are placed on a square lattice. (2.) This ideally lattice can be perturbed to generate a mode inhomogeneous structure. (3.) If the network must be filled, nodes are replaced at random by filler, which is drawn as orange dots, according to a given fraction. (4.) The morphology generator can be applied to adjust the filler dispersion. (5.) Finally, the links and bonds are established. Links are drawn as straight black lines, filler-filler bonds are orange wavy lines, and polymer-filler bonds are green wavy lines.

The last step for setting up the initial configuration is to establish links and bonds which are introduced due to the inclusion of filler. Filler nodes can either interact with another filler via a filler-filler bond or with a cross link via a polymer-filler bond. Based on a neighbor radius r_{con}, the connections are established:

$$r_{\mathrm{con}} = \frac{1}{2}\left(d_{\mathrm{i}} + \sqrt{2}\, d_{\mathrm{i}}\right) \approx \frac{1}{2} d_{\mathrm{i}} \cdot 2.41. \tag{4.3}$$

The neighbor radius is chosen such that, on an ideal unperturbed lattice, a (filler) node is connected to its $2\,d$ first nearest-neighbors. In this case, the distance to the first nearest neighbors is d_{i}, while the distance to its second nearest-neighbors is $\sqrt{2}\, d_{\mathrm{i}}$. The latter are excluded by r_{con}. If the parameter κ is small, this scheme of connections persists. For larger values of κ, (filler) nodes are linked to more or fewer adjacent (filler) nodes.

If two nodes of type cross link are connected, the free energy for the corresponding link is given by Equation 3.57. To further randomize the model networks, for each link i, the number of Kuhn segments n_i is randomly drawn from a Gaussian distribution with mean $\mu_n = 49$ and standard deviation $\sigma_n = \mu_n/5$. The choice of the mean reflects experimental observations for the number of monomers between two cross links in NR as stated above, while the choice of the distribution and its standard deviation are derived from experimental data for NR obtained by Miyaji *et al.* [234].

Depending on whether two filler or a cross link and a filler are connected, filler-filler and polymer-filler bonds are established with interaction according to Equation 3.78. Their equilibrium distances are defined based on pure polymer networks, which do not contain any filler nodes. Thus, for the initial relaxation of the network, the filler morphology is ignored. All links are considered as freely jointed chains with free energy given in Equation 3.57. Therefore, a number of Kuhn segments n_i is attributed to each link. After the initial relaxation, filler-filler and polymer-filler links replace some of the polymer-polymer links according to the generated filler morphology. Ideally, the stress of an unstretched, unfilled network equals the stress of an unstretched, filled network. Consequently, the force of a filler-filler of polymer-filler link must equal the force on the previous polymer-polymer link at its site. Therefore, the equilibrium end-to-end

distance of bond i is defined as follows:

$$r_{0,i} = r_i \left(1 - \frac{3}{k_i n_i}\right), \tag{4.4}$$

where r_i denotes the current end-to-end distance of the corresponding link and k_i denotes the spring constant of the filler-filler or polymer-filler bond below the cut-off distance.

4.1.1. Boundary Conditions

Since the volume of model material incorporated in the simulation is limited due to computational resources, surface effects must be considered. Applying periodic boundary conditions to mimic a bulk system can reduce them [235]. The concept of periodic boundary conditions is visualized in Figure 4.2 for the 2D-case. The original simulation box containing the real filled model elastomer network is located in the center. It is surrounded by an infinite amount of images of itself. Links and bonds which cross a boundary are continued by images in the adjacent box. Additionally, they are equivalent to those which enter the original volume on the opposite side. Each image, whether node, filler, link or bond, is located at the same position in its box as its original version in its current simulation box. If a real node or filler leaves the original volume, an image of it enters the original volume at the same place where the real version enters the adjacent box.

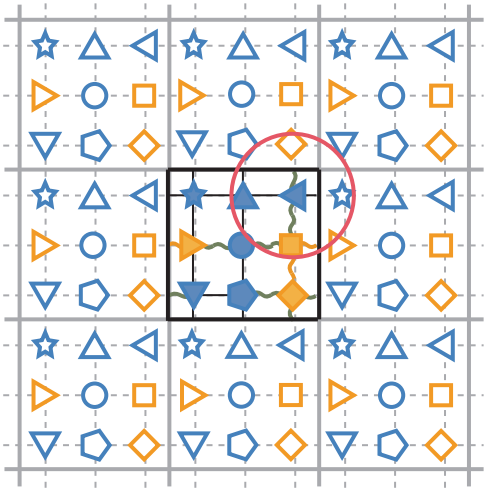

Figure 4.2.: Illustration of periodic boundary conditions. The original simulation box containing the real model elastomer network is surrounded by an infinite amount of images of itself. Images of links and bonds are unified by dashed lines, although their type is still identical to that of their original version.

The positions of nodes, filler, links and bonds are computed by using the minimum image convention:

$$x_{\alpha,\min} = x_\alpha - \text{round}\left(\frac{x_\alpha}{l_\alpha}\right) \cdot l_\alpha, \tag{4.5}$$

where x_α is the α-th coordinate of a node, a filler node, a link or a bond, respectively, l_α denotes the length of the simulation box along the α-direction and the function round() rounds its argument to an integer [235]. Equation 4.5 can be formulated for distances analogously. If the original node or filler has left the original simulation box, Equation 4.5 yields the position of the corresponding image that is located in the

original simulation box. According to the minimum image convention, the neighbors of a node or a filler, which must be located within a certain radius, can also be images instead of the real nodes or filler. In addition, they must not be located within the same simulation box. For example in Figure 4.2, the real node symbolized by the diamond and the real filler symbolized by the star are not located within the radius marked by the pink circle around the node symbolized by the triangle pointing to the left. However, when the minimum distances of the triangular node to the real diamond and to the real star the star is computed, Equation 4.5 yields the distances to the images located different images of the simulation box.

4.2. Morphology Generator

The morphology generator (MG), which has been proposed by Gundlach & Hentschke [236] and has been further developed by Viktorova *et al.* [2], is implemented for the simulation of filled elastomer networks. It is designed to capture the flocculation process in filled rubber in the post-mixing stages. The MG is based on a nearest-neighbor site-exchange Monte Carlo (MC) algorithm and relies on local equilibrium thermodynamics and the interface tension between the different components. Its original form is extensively studied in [237]. The components considered here are the original nodes, i.e. cross links, and so-called filler nodes, i.e. filler particles.

It is efficient to apply a MC algorithm since the trajectories of the nodes during the flocculation process are not of interest. The aim is only to minimize the Gibbs free energy with respect to the interfaces. The underlying concept of the MC method is that, if an experiment is repeated sufficiently often, the mean value of the measured data converges towards its expectation value. For example, a large number of rolls of a fair cubic dice will demonstrate that each number from 1 to 6 has an equal probability of occurring. This reveals that the mean value of all the numbers rolled is equal to their expectation value. In the case of the MG, an experiment corresponds to a certain configuration of node positions and the quantity of interest is the Gibbs free energy. At each MC step, configurations with different Gibbs free energies are generated out of each other by so-called moves, and, then, accepted or rejected based on the evaluation of the so-called Metropolis criterion. The Metropolis criterion incorporates a form of of importance sampling by taking the probability of a configuration into account which is derived from statistical mechanics. The general form of the Metropolis criterion is:

$$\min\left(1, \frac{p_{\text{new}}}{p_{\text{old}}}\right) \geq \text{random}\,(0,\, 1.0)\,, \tag{4.6}$$

where $p_{\text{new}}/p_{\text{old}}$ is the relative probability of the new and the old configuration [235]. If the probability of the new configuration is larger than that of the old configuration, the new one is accepted. However, if the probability of the old configuration is larger, acceptance of the new configuration is likely according to the ratio of both probabilities, also called transition probability, and determined by the random number. Thus, a Metropolis-MC algorithm generates a random path towards equilibrium. In analogy to the aforementioned ideal dice, the mean value of the Gibbs free energy computed by adding up the Gibbs free energies of each configuration along the path and dividing by the total number of MC steps will approach the expectation value if the number of MC steps is sufficiently large.

Figure 4.3 illustrates how the MG works. When the initially ideal square or cubic lattice of nodes has been randomly perturbed, a specific type, "cross link" or "filler", is

assigned to each node based on a given fraction of filler. Afterwards, a neighbor list for each node is set up with the help of a fixed radius r_{MG} containing its nearest neighbors. Thereafter, the MG is applied. At each MC step, a node is picked at random. In this example, it is the filler node which is framed by the pink circle. The surrounding nodes which are located within the grey circle are contained in the neighbor list of the selected node. Out of these neighboring nodes, the cross link, which is also framed by a pink circle, is chosen randomly. The positions of the selected nodes are about to be interchanged. By evaluating the Metropolis criterion, it is checked whether the new state would be favorable. In this case, interchanging the filler and the cross link minimizes the energy since the number of polymer-filler interfaces is reduced. Therefore, the new configuration is accepted. It is continued with the next MC step starting again from the random selection of node. In this algorithm, the interchange of node positions is the only move that is made. Moreover, the links, which connect the nodes, are not taken into consideration up to this point. They have to be included into the network in a next step of setting up the initial network.

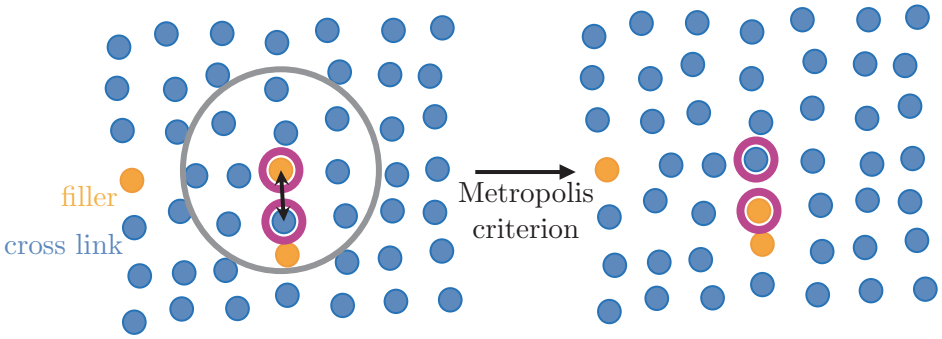

Figure 4.3.: Illustration of the functionality of the morphology generator.

As indicated above, the transition probability in Metropolis criterion applied in the MG is derived from statistical mechanics. In the case of the model elastomer networks, an ensemble with constant number of nodes N_α of type α, constant pressure p and constant temperature T is considered. The corresponding partition function is:

$$Q = \sum_{\mathrm{k}} \exp\left(-G_k\right), \tag{4.7}$$

where the sum runs over all possible configurations k and G_k denotes their Gibbs free energy in units of $k_{\mathrm{B}}T$. The probability for a configuration is then given as:

$$p_k \equiv p\left(G_k\right) = \frac{\exp\left(-G_k\right)}{\sum_{\mathrm{k}} \exp\left(-G_k\right)} \tag{4.8}$$

and the expectation value of the Gibbs free energy at equilibrium can be computed via:

$$G = \sum_{k} G_k \, p_k. \tag{4.9}$$

Thus, the relative probability which has to be inserted into the Metropolis criterion given by Equation 4.6 is:

$$\frac{p_{\mathrm{new}}}{p_{\mathrm{old}}} = \exp\left(\Delta W\right), \tag{4.10}$$

where $\Delta W = G_{\mathrm{old}} - G_{\mathrm{new}}$ denotes the change of the Gibbs free energy. Since the nodes in the model networks are enclosed by nodes of the same type and nodes of different

type, the change of the Gibbs free energy at equilibrium is determined by the change of the work of adhesion:

$$\mathrm{d}G = \gamma_j \mathrm{d}A_j \tag{4.11}$$

with A_j denoting the total area of contacts of type j and the Einstein summation convention applies here. This suggests:

$$\Delta W = \gamma_j \Delta A_j, \tag{4.12}$$

where $\Delta A_j = A_{j,\mathrm{old}} - A_{j,\mathrm{new}}$. With this quantity inserted into the Metropolis criterion, the MC algorithm drives the system towards equilibrium with respect to minimum Gibbs free energy.

In the filled elastomer networks investigated here, attendant parings are 'polymer-polymer' (pp), i.e. a contact of two nodes representing cross links, 'filler-filler' (ff) and 'polymer-filler' (pf). The corresponding interface tensions are computed via Equation 3.86 with α, $\beta \in \{\mathrm{p}, \mathrm{f}\}$. Accordingly, the contributions of polymer-polymer and filler-filler contacts vanish.

Furthermore, it is assumed that the contact area is equal for each contact. Hence, the total area of an interface is $A_j = a\, n_j$. As Viktorova *et al.* [2] have done, it is set $a/\left(k_\mathrm{B}T\right) = 0.421\,\mathrm{m}^2/\mathrm{mJ}$. For temperature $T = 300\,\mathrm{K}$, this means that the effective "contact area" is $a = 1.74 \cdot 10^{-21}\,\mathrm{m}^2$. It is $a = 2.33 \cdot 10^{-21}\,\mathrm{m}^2$ for $T = 400\,\mathrm{K}$. These values make sense, since the surfaces of the filler particles are not smooth but rough.

In practice, in each MC step, solely the neighbor lists of the two randomly selected nodes are considered. The number of polymer-filler interfaces in just these two neighbor lists before and after the swap of the positions is computed for the evaluation of the Metropolis criterion since the number of the remaining interfaces is not affected, i.e. constant. Therefore, the following expression is applied:

$$\Delta W = \gamma_\mathrm{pf} a \left(n_\mathrm{pf,old}^\mathrm{local} - n_\mathrm{pf,new}^\mathrm{local} \right). \tag{4.13}$$

Note that the sign depends on whether more polymer-filler contacts are destructed than created. According to Equation 4.6, the MG minimizes the number of polymer-filler interfaces.

Experimentally measured values for the dispersive and polar contributions to the surface tensions of polymer and filler, which will be inserted in the following, are compiled in Table 4.1.

The MC flocculation algorithm is implemented using the random number generator `ran2()` presented on page 282 in [238]. It is faster than the `C++ standard` random number generator and expected to yield "more random" numbers. Further parametrization of the MG is explained in subsection 5.2.1.

Table 4.1.: Experimentally obtained values for the disperse and polar parts γ^{d} and γ^{p} of the surface free energies of NR and different types of filler. Note that silica in the granulated form is considered and, if the Wilhelmy method is used, the values obtained for the mean contact angle is given. Coupsil 8113 is a type of silanized silica.

	$\gamma^{\mathrm{d}}/\left(\mathrm{mJ/m^2}\right)$	$\gamma^{\mathrm{p}}/\left(\mathrm{mJ/m^2}\right)$	$T/^{\circ}\mathrm{C}$	method	reference
NR	20.24	5.46	22	sessile drop	[233]
	15.9	6.1		sessile drop	[232]
	23.4	6.4		Wilhelmy	[232]
CB N121	28.1	0.0		Wilhelmy	[232]
CB N234	29.5	1.1		Wilhelmy	[232]
CB N339	27.0	0.0		Wilhelmy	[232]
CB N990	26.8	0.7		Wilhelmy	[232]
Silica VN3	18.7	22.7		Wilhelmy	[232]
Coupsil 8113	21.1	15.8		Wilhelmy	[232]

At this point, it is useful to make some considerations regarding role of the surface tensions for filler flocculation driven by the MG. In subsection 3.6.1, the concept of wettability has been introduced which is determined by the surface tensions of the materials that are brought in contact. Based on the wetting envelopes of NR shown in Figure 3.15, theoretical values of the surface tensions for potential filler particles can be obtained which cause perfect wetting. However, as outlined above, the MG relies on the change of the work of adhesion according to Equation 4.13 which is thought to determine filler flocculation [11].

For simplicity, two polymer-filler interfaces with unit area each are considered now. Interchanging the one of the polymer elements with the filler element at the second interface yields a polymer-polymer interface and a filler-filler interface. It holds for the change in work of adhesion:

$$\Delta w = -2w_{\mathrm{pf}} + w_{\mathrm{pp}} + w_{\mathrm{ff}}. \tag{4.14}$$

The work of adhesion for each kind of interface is given by Equation 3.83. Therefore, it holds:

$$\Delta w = 2\gamma_{\mathrm{pf}} = 2\left[\left(\sqrt{\gamma_{\mathrm{p}}^{\mathrm{d}}} - \sqrt{\gamma_{\mathrm{f}}^{\mathrm{d}}}\right)^2 + \left(\sqrt{\gamma_{\mathrm{p}}^{\mathrm{p}}} + \sqrt{\gamma_{\mathrm{f}}^{\mathrm{p}}}\right)^2\right]. \tag{4.15}$$

The tension of the polymer-filler interface is rewritten using Equation 3.86. If the polymer is NR again, a corresponding surface tension of potential filler can be obtained which leads to a fixed change in the work of adhesion. In this case, the solutions of Equation 4.15 for the components of the filler surface tensions describe a closed loop. For different Δw, the lines of change in the work of adhesion are plotted in Figure 4.4 together with the wetting envelopes of NR from Figure 3.15 and the experimentally obtained surface tensions of different types of filler given in Table 4.1.

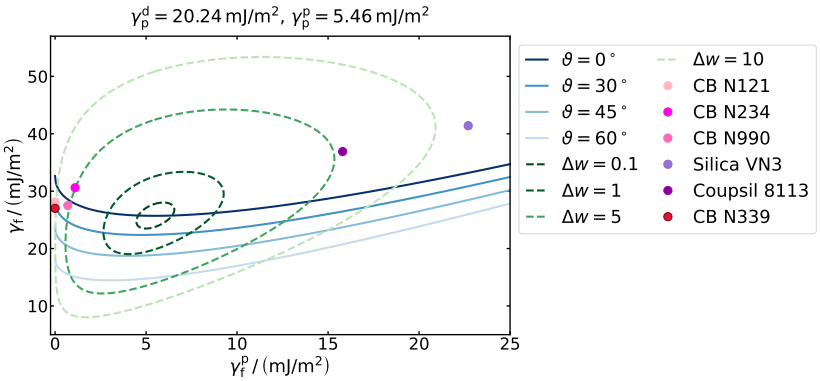

Figure 4.4.: Wetting envelope - work of adhesion plot for NR with the components of the surface tensions γ_p^d and γ_p^p given in the first row of Table 4.1. The iso-contact-angle lines are drawn as solid lines, while lines for constant change in the work of adhesion according to Equation 4.15 are dashed. For the different filler types, the data points are extracted from Table 4.1.

According to the Metropolis criterion applied in the MG, configurations that pair nodes of the same type are always accepted. Whereas, generated configurations that introduce new polymer-filler interfaces are more likely to be accepted if the change in the work of adhesion is comparatively small. In contrast, pairing nodes of the same type, which causes flocculation, is promoted if the interface tension is comparatively large. Correspondingly, in the example depicted in Figure 4.4, flocculation is advanced on the outer most lines of constant work of adhesion.

The experimentally obtained surface tension of CB N234 lays on the most inner line of constant work of adhesion compared to the other filler types. Therefore, the finest filler dispersion is expected. In addition, this data point is located within the region of perfect wetting like the data points for Silica VN3 and Coupsil 8113. While the former appears to be the outermost data point regarding the work of adhesion, the latter is close to the same line as CB N234. However, the polar contribution to the surface tension of Coupsil 8113 is larger than that of CB 234. This is a systematic difference between silica and CB. The data point for CB N339 is in close proximity to that for CB N234, but not located within the region of perfect wetting. For the other types of CB, the contact angle is within the region of good wetting and the change in the work of adhesion is comparatively large which suggests filler flocculation.

4.3. Flow Chart of the Algorithm

After setting up the initial configuration of a model elastomer network containing the filler content ϕ, its deformation is simulated featuring the process of SIC, as well as rupture of model polymer chains.

Because several length and time scales must be combined, Molecular Dynamics (MD) simulations are not suitable and phenomenological length scales are introduced. In addition to the macroscopic deformation of the entire model network, the node positions on the microscopic scale have to be adjusted for relaxation of the network. Moreover, segments of links possibly crystallize. Each process follows a different time scale:

$$\tau_{\mathrm{def}} \gg \tau_{\mathrm{relax}} \gg \tau_{\mathrm{cryst}}, \tag{4.16}$$

where τ denotes a characteristic time and the indices refer to deformation, relaxation and crystallization [1]. The characteristic time of SIC in NR is experimentally obtained to be of the order of milliseconds or even faster [135, 215]. This suggests that SIC of

polymer chains is restricted to their immediate environment [1]. Therefore, the energy minimization associated with SIC is separated from the relaxation of the entire network.

The algorithm which is applied here is similar to that used by Plagge & Hentschke [1] and has already been employed in [3]. When the initial configuration of the model network is set up, the simulation of the stretching experiment starts. Either uniaxial stretching or strain cycles can be simulated with a fixed maximum stretch $\lambda_{\max}$. The algorithm runs periodically through the steps visualized in Figure 4.5. First, the network is deformed by changing the stretch in a small increment $\Delta\lambda$. It is either stretched or contracted depending on the kind of experiment that is simulated. Immediately after setting up the initial network, this step is skipped. As a next step, the positions of the nodes and the filler are adapted in a global free energy minimization. A local free energy minimization follows in which it is checked whether forming or melting a crystal in a link minimizes its free energy. Filler-filler and polymer-filler bonds are unaffected. In Figure 4.5, the red line in the considered link indicates the crystalline segments, whereas the amorphous segments are drawn as wavy grey lines. Subsequently, it is checked whether a link fulfills the rupture criterion. In this approach, a link breaks if its free energy density given by Equation 3.77 exceeds the so-called critical free energy density $(g/n)_{\text{crit}}$. This threshold value for rupture of links will be defined in section 5.6. Finally, the engineering stress σ and the crystallinity χ are computed according to Equation 3.60 and Equation 3.63, respectively. If uniaxial stretching is simulated, the algorithm terminates at the stretch $\lambda = \lambda_{\max}$. Otherwise, if a strain cycle is simulated, the stretch is decreased as the maximum stretch is reached until the simulation box is again in its original shape. This means that the algorithm returns to the initial stretch $\lambda = \lambda_0$.

In the following, the deformation of the network and the free energy minimizations are elucidated in greater detail.

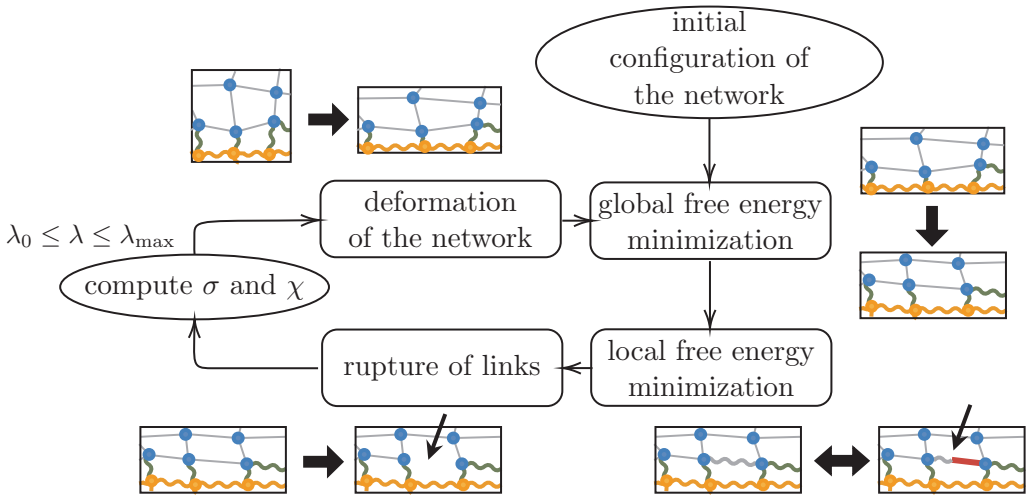

Figure 4.5.: Flow chart for the algorithm for the simulation of stretching experiments.

4.3.1. Deformation of the Network

Because rubber is considered to be incompressible, the model network is affinely stretched or contracted under volume conservation. Therefore, the following transformation is

applied to the side lengths of the simulation box:

$$l_{1,k+1} = \frac{\lambda_{k+1}}{\lambda_k} \cdot l_{1,k}, \tag{4.17}$$

$$l_{\alpha,k+1} = \left(\frac{\lambda_k}{\lambda_{k+1}}\right)^{\frac{1}{d-1}} \cdot l_{\alpha,k}, \quad 1 < \alpha \leq d. \tag{4.18}$$

Here, $l_{1,k}$ is the length of the simulation box along the principal direction of the stretch at the k-th value of the stretch λ_k. The index α refers to the remaining spacial directions determined by the dimension d. The positions of the nodes and filler are transformed analogously. For the initial state of the network, the stretch is $\lambda_0 = 1.0$. During the deformation, the stretch increment $\Delta\lambda$ is added or subtracted from the current stretch to obtain the subsequent stretch depending on whether stretching or contraction is simulated. It holds:

$$\Delta\lambda = |\lambda_{k+1} - \lambda_k|. \tag{4.19}$$

4.3.2. Global Free Energy Minimization

During the global free energy minimization, the positions of the nodes are adjusted in order to minimize the total Gibbs free energy G of the model network which is given by the sum of the Gibbs free energies of the links according to Equation 3.57 and the energies of filler-filler and polymer-filler bonds according to Equation 3.78:

$$G = \sum_{i=1}^{N(1-\phi)} g\left(\vec{r}_i, c_i\right) + \sum_{i=N(1-\phi)+1}^{N} u\left(\vec{r}_i\right). \tag{4.20}$$

The number of crystalline segments in a link c_i is held constant here. Note that $N(1-\phi)$ is the number of nodes that represent cross links in a network containing a fraction ϕ of filler.

FIRE Algorithm

In practice, the so-called FIRE algorithm proposed by Bitzek *et al.* [239] is employed for the relaxation. The abbreviation "FIRE" stands for "Fast Inertial Relaxation Engine"[239]. Originally, this algorithm was developed for the equilibration of atomic systems for which the application of MD methods is also very common. Although the FIRE algorithm relies on a MD integrator, its runtime can compete with that of other optimization methods like steepest decent or conjugate gradient which is faster than typical MD [239]. Essentially, the algorithm adjusts the velocities such that motion away from the potential minimum is immediately eliminated and Euler discretization is applied to the equations of motion.

In Figure 4.6, the flow chart of the FIRE algorithm is depicted. After the deformation of the network, the positions $\vec{x}$, the velocities $\vec{v}$ and forces $\vec{F}$ of all nodes must be computed. These vectors contain the corresponding data for all nodes and, thus, they are of size $d\,N \times 1$. For this calculation, the equations of motion are solved numerically by using the velocity-Verlet algorithm [240, 241]. This typical MD integrator originates from the series expansion of position and velocity. It holds:

$$\vec{x}_j\left(t + \Delta t\right) = \vec{x}_j\left(t\right) + \Delta t\, \vec{v}_j\left(t\right) + \frac{\Delta t^2}{2m_\mathrm{F}} \vec{F}_j\left(t\right) + \mathcal{O}\left(\Delta t^3\right), \tag{4.21}$$

$$\vec{v}_j\left(t + \Delta t\right) = \vec{v}_j\left(t\right) + \frac{\Delta t}{2m_\mathrm{F}} \left(\vec{F}_j\left(t\right) + \vec{F}_j\left(t + \Delta t\right)\right) + \mathcal{O}\left(\Delta t^2\right), \tag{4.22}$$

where $\vec{x}_j(t)$ is the position of node or filler j at time t, $\vec{v}_j(t)$ is the corresponding velocity and $\vec{F}_j(t)$ is the respective force and Δt denotes the time step, which is adaptable. Proceeding the integration of the equations of motion, the power P is calculated and the velocity is transformed by applying the parameter $\alpha_\mathrm{F} = \gamma_\mathrm{F}\,\Delta t$ with γ_F as a parameter which promotes movement towards the energy minimum. Bitzek *et al.* [239] explain the algorithm by the example of a blind skier. In this picture, the parameter γ_F introduces an acceleration along the direction of the steepest descent [239]. If the power is $P > 0$ and if the algorithm has been iterating for $N_\mathrm{F} > N_\mathrm{F,min}$ steps since the power was negative, the time step is increased by multiplying with a factor $f_\mathrm{F,inc}$ and the parameter α_F is decreased by multiplying with the factor $f_{\mathrm{F},\alpha}$. Otherwise, if the power is $P \leq 0$, the time step is reduced by multiplying with the factor $f_\mathrm{F,dec}$, all velocities are set to zero and the parameter α_F is set to its initial value α_start. Afterwards, convergence of the algorithm is examined by checking if the change of the total Gibbs free energy is small:

$$\Delta G_\mathrm{diff} = \frac{1}{\Delta t}\left(\frac{G_{k_\mathrm{F}}}{G_{k_\mathrm{F}-1}} - 1\right) < \Delta G_\mathrm{F} \tag{4.23}$$

with G_{k_F} as the total Gibbs free energy at the k_F-th iteration of the FIRE algorithm and ΔG_F as the maximum change of the total Gibbs free energy allowed for minimized Gibbs free energy. If this relation is fulfilled, the algorithm terminates and the network is relaxed. Otherwise, the algorithm runs again through these steps until the maximum number of iterations $N_\mathrm{F,max}$ is reached. The values of the parameters used in the FIRE algorithm are compiled in Table 4.2.

Table 4.2.: Parameters for the FIRE algorithm.

$N_\mathrm{F,max}$	$N_\mathrm{F,min}$	α_start	$f_{\mathrm{F},\alpha}$	Δt_start	Δt_max	$f_\mathrm{F,inc}$	$f_\mathrm{F,dec}$	m_F	ΔG_F
10^5	10	0.95	0.9	0.01	1.0	1.1	0.9	10.0	10^{-8}

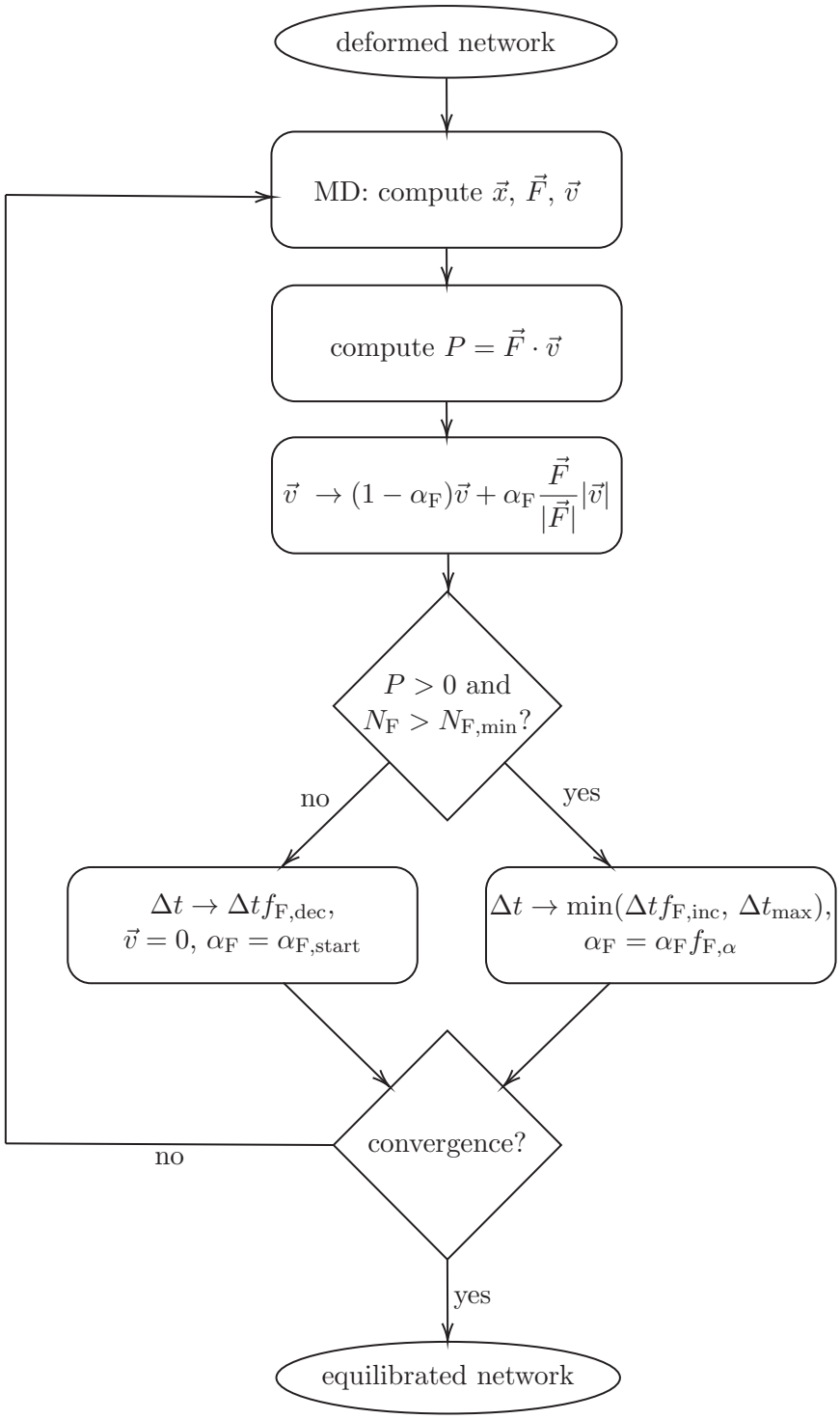

Figure 4.6.: Flow chart for the FIRE algorithm.

Calculation of the Interaction of Crystalline Segments

For the computation of the total Gibbs free energy and the forces, the interaction of crystalline segments in the links has to be calculated. The time for the computation is advanced by setting up a neighbor list. For this purpose, the prospective positions of the links at maximum stretch are obtained based on the initial configuration of the network by only applying the transformation used for the deformation of the network. Based on this state, links located within a radius r_neighbor around that of a certain link are added to its neighbor list. These fixed neighbor lists are used throughout the

simulation for the calculation of the interaction. In particular, if a link is oriented along the stretching direction, links become interaction partners which have the same direction and are adjacent to it perpendicularly to the direction of the deformation. The reason is that the distances between the links orthogonal to the direction of the deformation are reduced due to the applied transformation, while they are increased in parallel to this direction. Therefore, its is expected that crystalline layers emerge perpendicularly to the stretching direction. Note that the positions of the links are considered to be the positions of the midpoints of the lines that directly connect the nodes which are the endpoints of the link.

Moreover, a cut-off radius r_{cut} is introduced to neglect small contributions. According to the choice of the function in Equation 3.56 describing the interaction of semi-crystalline links, the contribution vanishes as $r_{\mathrm{cut}} = 7.0\,R_0$. Thus, the radius for finding neighboring links is set to $r_{\mathrm{neighbor}} = r_{\mathrm{cut}} + 1.0$. Note that, with respect to the initial lattice spacing, these values also enable interactions of semi-crystalline links already at small deformations.

4.3.3. Local Free Energy Minimization

Proceeding the global free energy minimization, the Gibbs free energy of each single link is minimized in the local free energy minimization with respect to SIC. Since only individual links are considered at this step instead of all of the links simultaneously, SIC is treated as a non-equilibrium phenomenon [1]. In principle, all links in the model networks are able to crystallize under strain, but SIC can also be prohibited. If SIC is allowed, it is checked for each link i separately whether establishing or melting a crystalline segment minimizes its free energy according to Equation 3.57 [1]:

$$g\left(\vec{r}_i, c_i \pm 1\right) < g\left(\vec{r}_i, c_i\right) \Rightarrow c_i \pm 1 \quad \text{if } c_i > 0 \text{ and } c_i l_{\mathrm{c}} < n_i. \tag{4.24}$$

This expression includes the condition for the number of the amorphous chain segments that $n_i - c_i l_{\mathrm{c}} \geq 1$. Therefore, the number of crystalline segments is restricted to integers in the interval $[0, (n_i - 1)/l_{\mathrm{c}}]$. A crystalline chain segment possesses the crystal length $l_{\mathrm{c}} = 7$. This means that it consists of 7 Kuhn segments. In WAXS experiments, the crystal length along the stretching direction is obtained to be approximately 10 nm [7–9]. It is limited by the mesh size of the network and appears to be constant for increasing strain since the crystals grow perpendicularly to the stretching direction. As mentioned above, the initial lattice spacing is $d_{\mathrm{i}} = 7.0$ here.

4.3.4. Parametrization

As a summary, the values of the parameters applied in the simulation of stretching experiments are listed in Table 4.3. Additionally, values of the parameters for the computation of the Gibbs free energy of the links according to Equation 3.57 are given. Originally, most of the parameters have been determined in [3].

In Figure 4.7, the meaning of the parameters describing a model polymer chain is visualized. Initially, the end-to-end distance r of the link is roughly the lattice spacing d_{i}. Perturbing the ideal square or cubic lattice causes small deviations. The link represents a polymer chain that is entirely amorphous which is indicated by the random coiled black line between the nodes. The number of Kuhn segments n of which the link consists is randomly drawn from a Gaussian distribution with mean $\mu_n = 49$ and standard deviation $\sigma_n = \mu_n/5$. This particular mean value of the number of Kuhn segments suggests that $\lambda_{\mathrm{max}} = 7.0$ is an appropriate choice for the maximum applied stretch since, on average, the links are expected to be extended to their contour length at this stretch. Although the contour length is a limit for the end-to-end distance of real

polymer chains, this finite extensibility is not incorporated into the model such that the links can be stretched further. If the link is stretched due to the deformation of the model network, its end-to-end distance increases and it can become semi-crystalline. It is assumed that the crystalline chain segments are strictly aligned with the stretching direction. In this example, the link contains $c = 2$ crystalline segments in the stretched state and each of them consists of $l_\mathrm{c} = 7.0$ Kuhn segments. Therefore, $n - cl_\mathrm{c}$ Kuhn segments remain amorphous. The number of crystalline segments in a link depends on the applied stretch.

Table 4.3.: Parameters for the simulations of stretching experiments.

κ	μ_n	σ_n	d_i	$\Delta\lambda$	l_c	θ_0	η	R_0	r_cut	r_neighbor
0.1	49	$\mu/5$	7.0	0.01	7.0	1.3	0.015	$0.5\,d_\mathrm{i}$	$7.0\,R_0$	$r_\mathrm{cut} + 1.0$

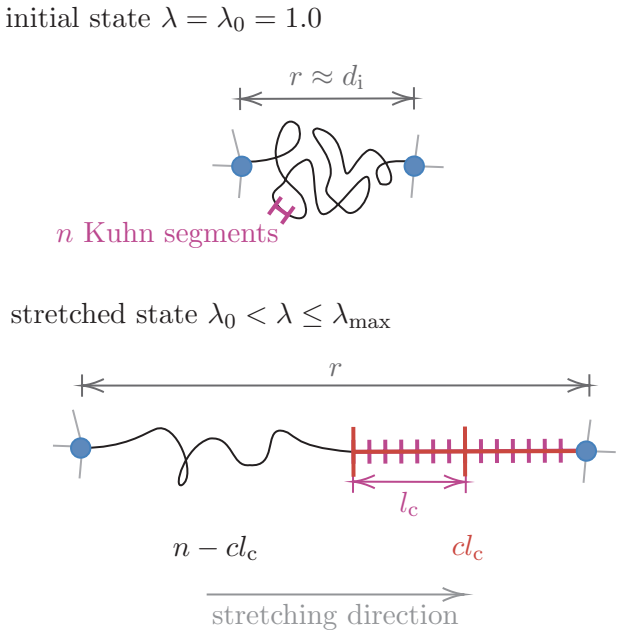

Figure 4.7.: Illustration for the parameters for model polymer chains in a network.

5. Effects of Strain-Induced Crystallization and Particulate Fillers on the Reinforcement of Natural Rubber

The simplest network which can be simulated with the model is an unfilled non-crystallizing network. Based on such a network, reinforcement by filler and SIC will be analyzed subsequently. Mainly, 2D-networks will be studied, but, based on this data, 3D-networks will be investigated.

It is expected from the theory of rubber elasticity that the stress-stretch curve of an unfilled non-crystallizing network behaves according to the Neo-Hookean law. For small stretches, it is expected to exhibit linear stress-stretch behavior according to Hooke's law.

First, stretching of 2D-networks consisting of $N = 5041$ nodes has been simulated. The corresponding stress-stretch curve is depicted in Figure 5.1. The data is averaged over 10 independent simulations and the error bars are given by the standard deviations. It is fitted with the expected relations. The corresponding fit parameters are listed in Table 5.1. Apparently, the Neo-Hookean law fits the data nicely. Moreover, the data is well described by Hooke's law at small deformations. That the obtained values for χ^2/ndf are smaller than the ideal value of 1.0 suggests that the errors are relatively large for these conditions, especially for the Neo-Hookean fit.

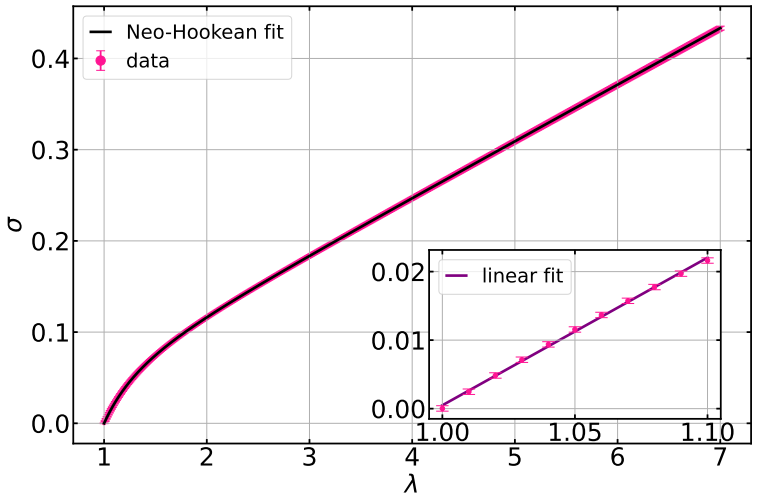

Figure 5.1.: Stress-stretch curves obtained from the simulations of stretching unfilled 2D-networks which consist of $N = 5041$ nodes. The data points are given as averages from 10 independent simulations and the error bars indicate the corresponding standard deviations. The data is fitted with a Neo-Hookean law and additionally with a linear function according to Hooke's law in the range of $\lambda \in [1.0, 1.1]$ The fit parameters are compiled in Table 5.1.

Table 5.1.: Parameters for the fitted functions in Figure 5.1.

Neo-Hookean fit: $\sigma(\lambda) = A\left(\lambda - \frac{1}{\lambda^3}\right) + B$		
A	B	χ^2/ndf
0.062 ± 0.001	$(1.577 \pm 0.034) \cdot 10^{-5}$	$3.340 \cdot 10^{-5}$
Linear fit: $\sigma(\lambda) = A\lambda + B$		
A	B	χ^2/ndf
0.215 ± 0.003	-0.215 ± 0.003	0.523

As a next step, the stress-stretch curves for 3D-networks consisting of $N = 5832$ nodes are obtained from the simulation of stretching such networks. The data is averaged over 10 simulations and the error bars are given by the standard deviations. The fit parameters are compiled in Table 5.2. Note that the Neo-Hookean law for 3D-networks is of different form than that for the 2D-case. The Neo-Hookean law fits the data properly in the entire range, while the data is well described by Hooke's law at small stretches. For both fitted functions, the values of χ^2/ndf are significantly smaller than the ideal value of 1.0. This suggests that the errors are large for the considered conditions. Furthermore, it is remarkable that the stress for the 3D-networks is an order of magnitude smaller than that for the 2D-networks.

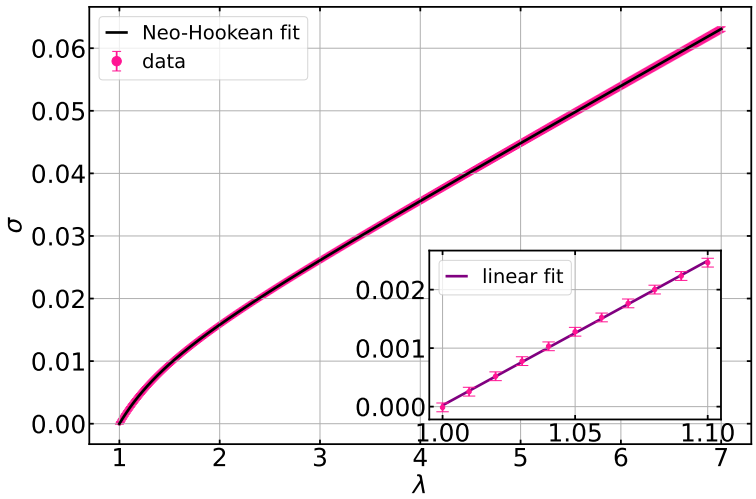

Figure 5.2.: Stress-stretch curves obtained from the simulations of stretching unfilled 3D-networks which consist of $N = 5832$ nodes. The data points are given as averages from 10 independent simulations and the error bars indicate the corresponding standard deviations. The data is fitted with a Neo-Hookean law and additionally with a linear function according to Hooke's law in the range of $\lambda \in [1.0, 1.1]$ The fit parameters are compiled in Table 5.2.

Table 5.2.: Parameters for the fitted functions in Figure 5.2.

Neo-Hookean fit: $\sigma(\lambda) = A\left(\lambda - \frac{1}{\lambda^2}\right) + B$		
A	B	χ^2/ndf
0.009 ± 0.001	$(-8.164 \pm 0.127) \cdot 10^{-6}$	$1.581 \cdot 10^{-4}$
Linear fit: $\sigma(\lambda) = A\lambda + B$		
A	B	χ^2/ndf
0.025 ± 0.001	-0.025 ± 0.001	0.085

5.1. Strain-Induced Crystallization in Unfilled Networks

As a first step towards the analysis of reinforcement mechanisms, unfilled crystallizing networks consisting of stable links are investigated in order to gain an understanding for the process of strain-induced crystallization (SIC) in the model networks and to check whether the results agree with experimental observations. This has already been discussed in the paper [4] and, in detail, in [3].

The stress-stretch curves of crystallizing and non-crystallizing 2D-networks are plotted in Figure 5.3 for an entire strain cycle together with the crystallinity-stretch curve for the crystallizing case. The simulated networks consist of $N = 5041$ nodes and the data is averaged over 10 simulations where the errors are given by the corresponding standard deviations. Overall, the shapes of the stress-stretch and crystallinity stretch curves for the crystallizing networks agree with experimentally obtained curves, e.g. in [7, 242].

At the beginning of stretching, the stress-stretch curves for the crystallizing and non-crystallizing networks overlap. At the onset stretch of SIC $\lambda \approx 3.5$, the stress in the crystallizing networks lowers compared to the non-crystallizing case and, then, continues. As the crystallinity increases steeper, the stress remains approximately constant. However at certain stretch, the stress rapidly increases again such that it intersects the stress-stretch curve for the non-crystallizing networks. In the context of experimental observations, this increase beyond the plateau is attributed to the strain-hardening effect [126]. Nevertheless, previous investigations have shown that the origin for this increase for the model networks is an artifact because ideal chains are employed [1, 3]. Since this model does not include finite chain extensibility, a chain can be extended to an end-to-end distance $r > n$ which exceeds its contour length, but this causes the increase of the stress. It must be highlighted here that the plateau and the incline of the stress beyond the plateau are characteristic features for strain-crystallizing rubber. At the maximum stretch $\lambda = 7.0$, both the stress and the crystallinity reach their maxima. The maximum crystallinity $\chi \approx 0.43$ indicates that most of the links oriented along the stretching direction are nearly completely crystalline. In contrast to the stress-stretch curve for the non-crystallizing network, that for the crystallizing network shows a hysteresis which is also observable in the crystallinity-stretch curve. An explanation for this is so-called "supercooling" or in this context "superstraining" which means that SIC is retarded by a nucleation energy barrier [1, 9]. In this model, the hysteresis is essentially caused by splitting the process of SIC of a link from the relaxation of the network. This relies on the consideration of SIC as a phenomenon of local equilibrium. During the contraction, the stress of the crystallizing networks slowly decreases. In the context of experiments, this observation is assigned to so-called "inverse yielding" [127]. Distinct crystalline and amorphous domains, which can propagate through it, occur in the sample during recovery.

In Figure 5.4, snapshots of a crystallizing 2D-network consisting of $N = 196$ nodes at certain stretches during a strain cycle are presented with the corresponding stress-stretch and crystallinity-stretch curve. The phenomena that can be observed here have already been discussed by Plagge & Hentschke [1]. Near the onset of SIC, semi-cystalline links occur randomly distributed over the network. As expected, the semi-crystalline links are oriented along the stretching direction. With increasing stretch, crystalline layers emerge which grow perpendicularly to the stretching direction. Simultaneously, the crystallinity increases steeper and the stress forms the plateau. At the maximum stretch, most of the links aligned along the stretching direction are approximately fully crystalline. During the contraction process, the crystallites melt and a hysteresis can be observed. Persisting crystalline links appear like highly crystalline and highly extended rods which press the non-crystalline links together. Crystalline and amorphous layers tend to alternate along the direction of the deformation during recovery. This is arrangement minimizes the macroscopic force and Plagge & Hentschke [1] call it a "microphase separation".

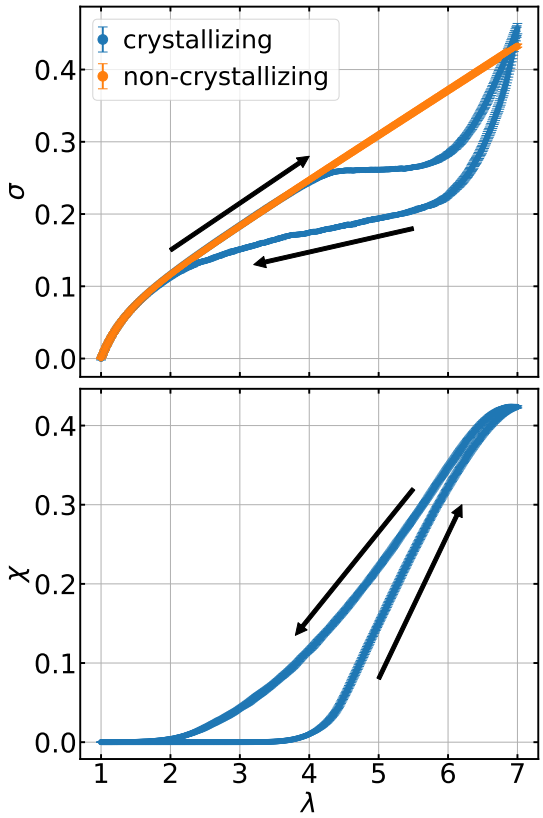

Figure 5.3.: Stress-stretch curves for crystallizing and non-crystallizing 2D-networks and crystallinity-stretch curve for the former. The data points are obtained as averages from 10 independent simulations of strain-cycles of 2D-networks consisting of $N = 5041$ nodes. The error bars depict the standard deviations. The black arrows indicate the stretching and the retraction process.

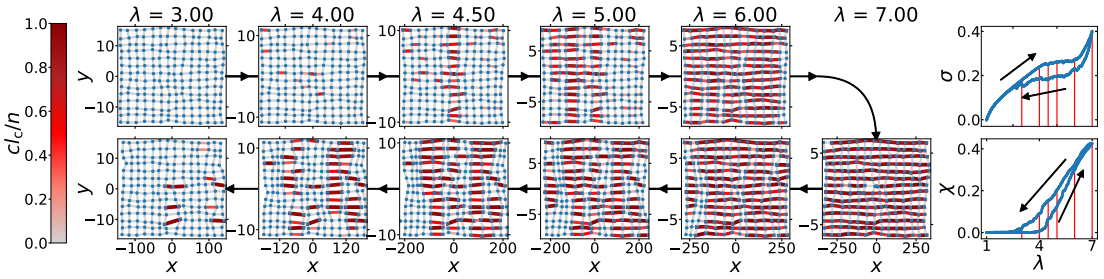

Figure 5.4.: Snapshots of a 2D-network which consists of $N = 196$ nodes at certain stretches λ during a strain cycle. The upper row represents the stretching process, while the lower row shows the contraction of the network. Each column corresponds to a specific stretch such that the plots share the x-axis. The direction of the deformation is along the x-axis. The scaling of the axes mimics the volume conservation. The blue dots stand for the cross links, while the crystallinity cl_c/n of each link is indicated according to the color bar. Links which cross the boundaries due to the periodic boundary conditions are not drawn. Moreover, the corresponding stress-stretch and crystallinity-stretch curves are depicted, where the vertical red lines mark the stretches at which the snapshots have been taken. The black arrows expose stretching and contraction of the network.

In Figure 5.5, stress-stretch and crystallinity-stretch curves for 3D-networks consisting of $N = 5832$ nodes are plotted analogous to the 2D-case. Overall, the curves are consistent with experimental observations and the observations which can be made here are analogous to the ones above. Nevertheless, the onset of SIC is shifted to slightly smaller stretches and the curves posses features that do not occur for 2D-networks. In particular before the stress continues in the characteristic plateau, it shows a kink. Simultaneously, the crystallinity makes a "jump". Plagge & Hentschke [1] suggest a phase transition as explanation for this behavior. Crystallite nuclei may trigger fast crystal growth such that the stress decreases which leads to temporary supercooling. Analogous behavior can be observed during the contraction process as the last crystallites vanish.

In Figure 5.6, snapshots of a crystallizing 3D-network during a strain-cycle are depicted with the corresponding stress-stretch and crystallinity-stretch curves. The network consists of $N = 216$ nodes. The observations which can be made here are analogous to the 2D-case, but the stress shows fluctuations in the region of the characteristic plateau and during contraction in the same regime of stretches. On the one hand Plagge & Hentschke [1] propose the phase transition which might cause the kink also as reason for this observation. However, on the other hand, this might originate from finite size effects.

Overall, the comparison of the observations for 2D- and 3D-networks justifies the subsequent focus on the 2D-case which captures essential features.

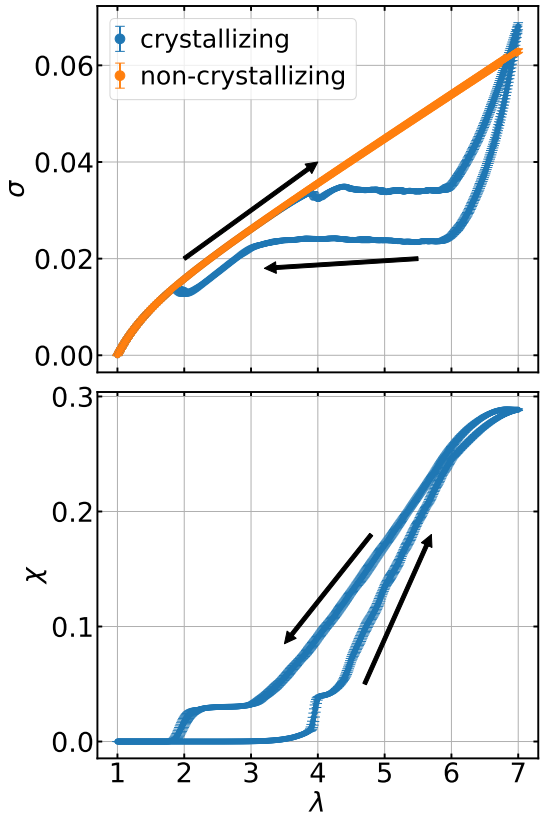

Figure 5.5.: Stress-stretch curves for crystallizing and non-crystallizing 2D-networks and crystallinity-stretch curve for the former. The data points are obtained as averages from 10 independent simulations of strain-cycles of 3D-networks consisting of $N = 5832$ nodes. The error bars depict the standard deviations. The black arrows indicate the stretching and the retraction process.

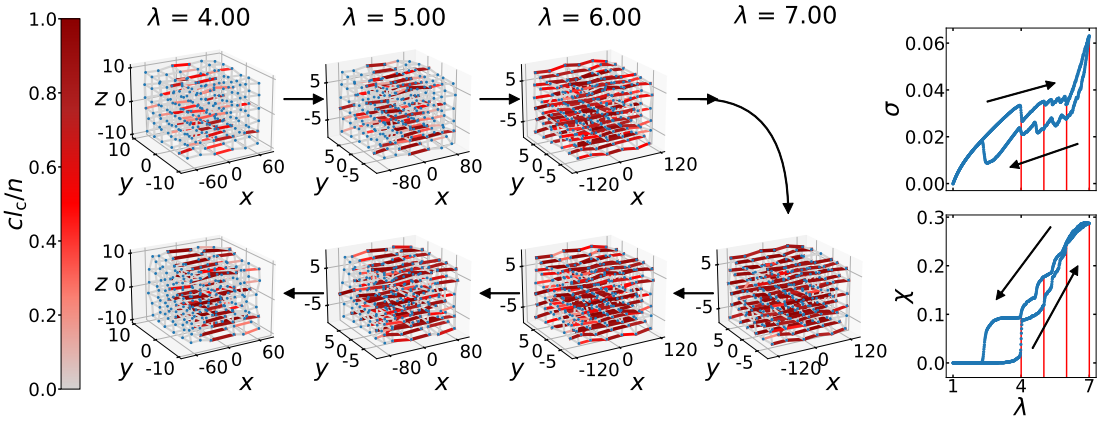

Figure 5.6.: Snapshots of a 3D-network which consists of $N = 216$ nodes at certain stretches λ during a strain cycle. The upper row represents the stretching process, while the lower row shows the contraction of the network. Each column corresponds to a specific stretch. The direction of the deformation is along the x-axis. The scaling of the axes mimics the volume conservation. The blue dots stand for the cross links, while the crystallinity cl_c/n of each link is indicated according to the color bar. Links which cross the boundaries due to the periodic boundary conditions are not drawn. Moreover, the corresponding stress-stretch and crystallinity-stretch curves are depicted, where the vertical red lines mark the stretches at which the snapshots have been taken. The black arrows expose stretching and contraction of the network.

5.2. Parametrization for the Simulation of Filled Networks

For the investigation of reinforcement in filled elastomer networks, the morphology generator (MG) and the filler-filler and polymer-filler bonds, which are introduced due to the inclusion of filler, must be parametrized.

5.2.1. Morphology Generator

The morphology generator must be configured in order to generate realistic filler morphologies. These are distributions of the filler particles inside the rubber matrix. Filler nodes may form agglomerates consisting of filler aggregates which are connected to each other such that a network is built. In the following, the impact of the radius of the neighbor list applied in the MG, the total number of MC steps through which the algorithm runs and the composition of filled NR are discussed.

As elucidated in section 4.2, the MG relies on the work of adhesion required for the formation of interfaces in the post-mixing stages of the compound. Therefore, experimentally obtained values for the surface tensions of NR and filler are inserted into the model. For NR, the components of the surface tension given in the first row of Table 4.1 are used throughout this work since they have also be applied in [2, 243]. As a filler, CB N339 is considered first.

Subsequently, snapshots of the networks during the morphology generation are examined. These are the counterpart to experimentally obtained transmission electron microscopy (TEM) images. In order to monitor the convergence of the algorithm, the total interfacial energy, which is similar to the work of adhesion, can be computed as follows at each MC step:

$$W = \gamma_{\mathrm{pf}} a n_{\mathrm{pf}}^{\mathrm{total}}. \tag{5.1}$$

In practice, the energy is saved at every MC step until the 50th MC step and at every 50th afterwards. This quantity is expected to decrease, while constant minimal energy is expected to occur if polymer and filler "phases" are separated like, for example, water and oil.

Moreover, the radius of the neighbor list for the MG is set to $r_{\mathrm{MG}} = 2.0\, d_{\mathrm{i}}$. Viktorova *et al.* [2] have chosen r_{MG} such that a node possesses 12-13 neighbors in the MG, but a face-centered cubic lattice (fcc) has been considered. This number of neighbors is consistent with liquid-like packed spheres. On the perturbed square 2D-lattice applied here, $r_{\mathrm{MG}} = 2.0\, d_{\mathrm{i}}$ corresponds to up to 12 adjacent nodes in the neighbor list of a node. For the perturbed sc 3D-lattices, this radius encompasses 32 nodes at maximum. In fact, on an ideal sc lattice, a node has only 8 neighbors in 2D and 26 neighbors in 3D because the potential next shell of neighboring nodes is screened by the first shell of neighbors. Since the neighbor lists for $r_{\mathrm{MG}} = 2.0\, d_{\mathrm{i}}$ contain a larger number of nodes than those employed by Viktorova *et al.* [2], coarser filler structures are expected to be generated with the same number of MC steps.

First, a 2D-network consisting of $N = 5041$ nodes and containing a fraction $\phi = 0.2$ of CB N339 is considered. In Figure 5.7, the total interfacial energy W according to Equation 5.1 is plotted versus the MC interchange attempts per node during the morphology generation. It shows the expected behavior indicating that the number of polymer-filler interfaces is minimized by pairing nodes of the same type. Constant minimum energy is not reached, but the morphology associated with this stage is also not desirable here. The snapshots of the network during the evolution are also shown in Figure A.5. Initially, the filler is finely dispersed all over the network. For these smaller fractions of filler, there is no highly developed filler network. After 1 MC interchange

attempt per node, the filler nodes still appear dispersed, but smaller aggregates have built. At this point, the total interfacial energy has already started to decrease. The aggregates grow with increasing number of MC steps. Finally, after $100 \cdot N$ MC steps, there are mainly separated filler aggregates but not a filler network. The filler structure is coarse. Optically, the difference between the morphologies after $10 \cdot N$ MC steps and $100 \cdot N$ MC steps is comparatively small. Correspondingly, the decrease of the total interfacial energy became slower in this range.

Note that, for instance, $10 \cdot N$ MC steps means the total number of MC steps which has been really applied to the network, whereas the number of MC steps per node refers to the resulting average number of interchange attempts. There may be nodes which have been involved in more or less interchange attempts. Here, both terms are used equivalently.

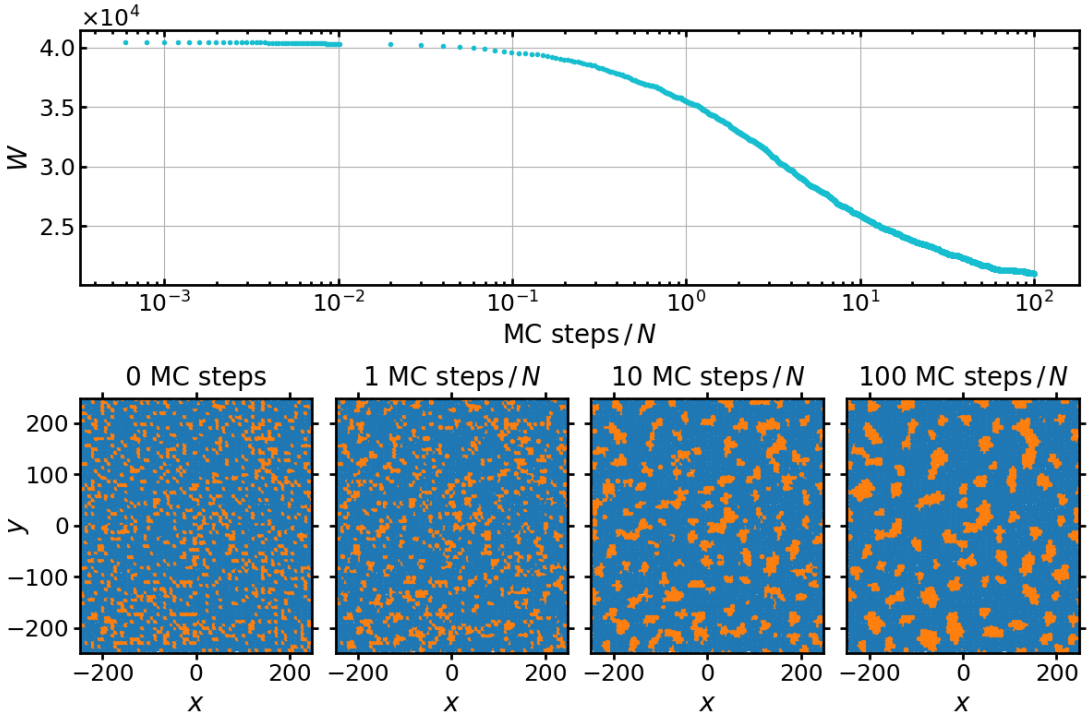

Figure 5.7.: Plot of the total interfacial energy W versus the MC interchange attempts per node during morphology generation and evolution of the filler morphology at different number of MC steps. A 2D-network consisting of $N = 5041$ nodes and containing a fraction $\phi = 0.2$ of filler has been simulated with $r_{\mathrm{MG}} = 2.0\, d_{\mathrm{i}}$. In the snapshots, the blue dots are cross links, while the orange dots indicate filler.

Increasing the filler content to $\phi = 0.4$ yields the morphologies in Figure 5.8. The observations which can be made here are analogous to the case $\phi = 0.2$, but the filler structure is more branched now. The additional snapshot at $5 \cdot N$ MC steps already shows coarser filler aggregates. With increasing number of MC steps, the polymer-filler interfaces appear to become more smooth. This causes less branching and further separation of the aggregates.

Viktorova *et al.* [2] report that, in their case, 50 MC interchange attempts per node are sufficient to generate a realistic filler morphology and that the aggregates lose their connectivity by increasing the number of MC steps. However, this number of 50 MC interchange attempts per node appears to be still too large here since separated filler aggregates with a smooth surface build instead of a branched filler structure. Therefore, the number of MC interchange attempts per node must be reduced here. Because of

the snapshots in Figure 5.7 and Figure 5.8, the optimum of the total number of MC steps for the morphology generation in 2D can be estimated to $10 \cdot N$. Optically, the filler structures are also consistent with experimentally obtained transmission electron microscopy (TEM) images presented by Klüppel [244]. Note that the formation of a filler network requires for a larger filler content as it will be outlined subsequently.

Additional plots for the evolution of the network structure during morphology generation for $r_{\mathrm{MG}} = 1.205\, d_{\mathrm{i}}$ can be found in section A.3. The radius for the neighbor list of the MG applied there corresponds to the radius in which the nearest neighbors, on average 4 in 2D, are located and it is used to set up the links in the network. With increasing r_{MG}, the size of the filler aggregates appears to increase. This effect is consistent with the observations by Viktorova [245]. However, by requiring realistic interaction ranges between the nodes, it still makes sense to set $r_{\mathrm{MG}} = 2.0\, d_{\mathrm{i}}$, which corresponds to approximately 12 neighbors in the neighbor list of a node.

Exemplary snapshots of 2D-networks consisting of $N = 5041$ nodes with variable filler content ϕ are plotted in Figure 5.9. These snapshots have been taken immediately after $10 \cdot N$ MC steps of morphology generation and it is $r_{\mathrm{MG}} = 2.0\, d_{\mathrm{i}}$. While the filler aggregates are isolated at small filler concentrations, they grow and connect with increasing filler content such that aggregates form. The filler content at which the first connected aggregate of filler particles occurs that traverses the polymer from one side of the network to its opposite is called the percolation threshold. In the 2D-model networks is approximately at $\phi = 0.5$.

With the Kuhn length of NR, the networks consisting of $N = 5051$ nodes, which have been shown up in this section, have a size of roughly 462 nm × 462 nm. Due to the initial configuration of the model networks, the linear dimension associated with a filler node representing a non-breakable aggregate or particle is nearly 10 nm. Hence, the size of the filler aggregates in Figure 5.9 for $\phi = 0.4$ is up to 100 nm. This is smaller than the linear dimension of typical agglomerates which is of the order of 10 µm to 100 µm.

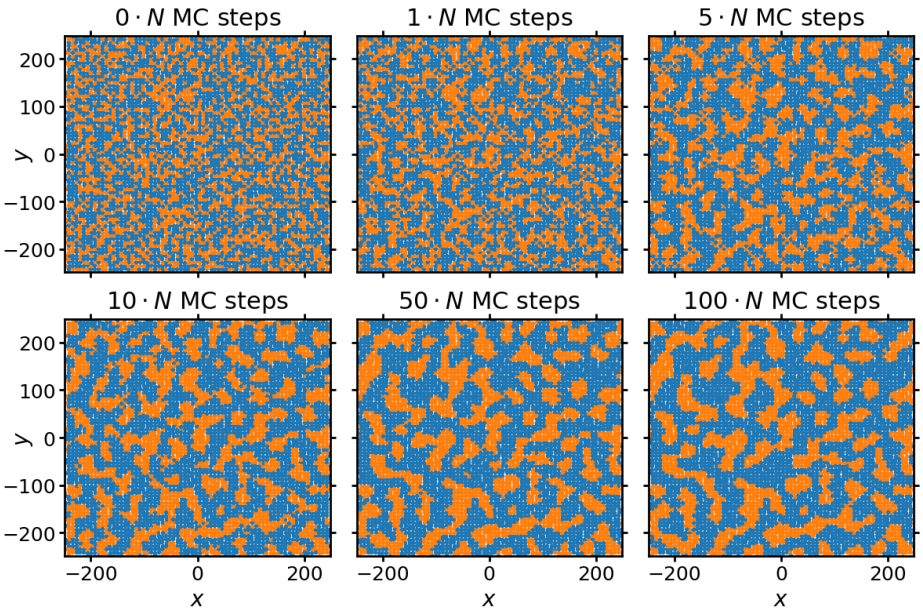

Figure 5.8.: Evolution of the filler morphology during the application of the morphology generator at different number of MC steps. The blue dots are cross links, while the orange dots indicate filler. 2D-networks consisting of $N = 5041$ nodes and containing a fraction $\phi = 0.4$ of filler have been simulated with $r_{\mathrm{morph}} = 2.0\, d_{\mathrm{init}}$.

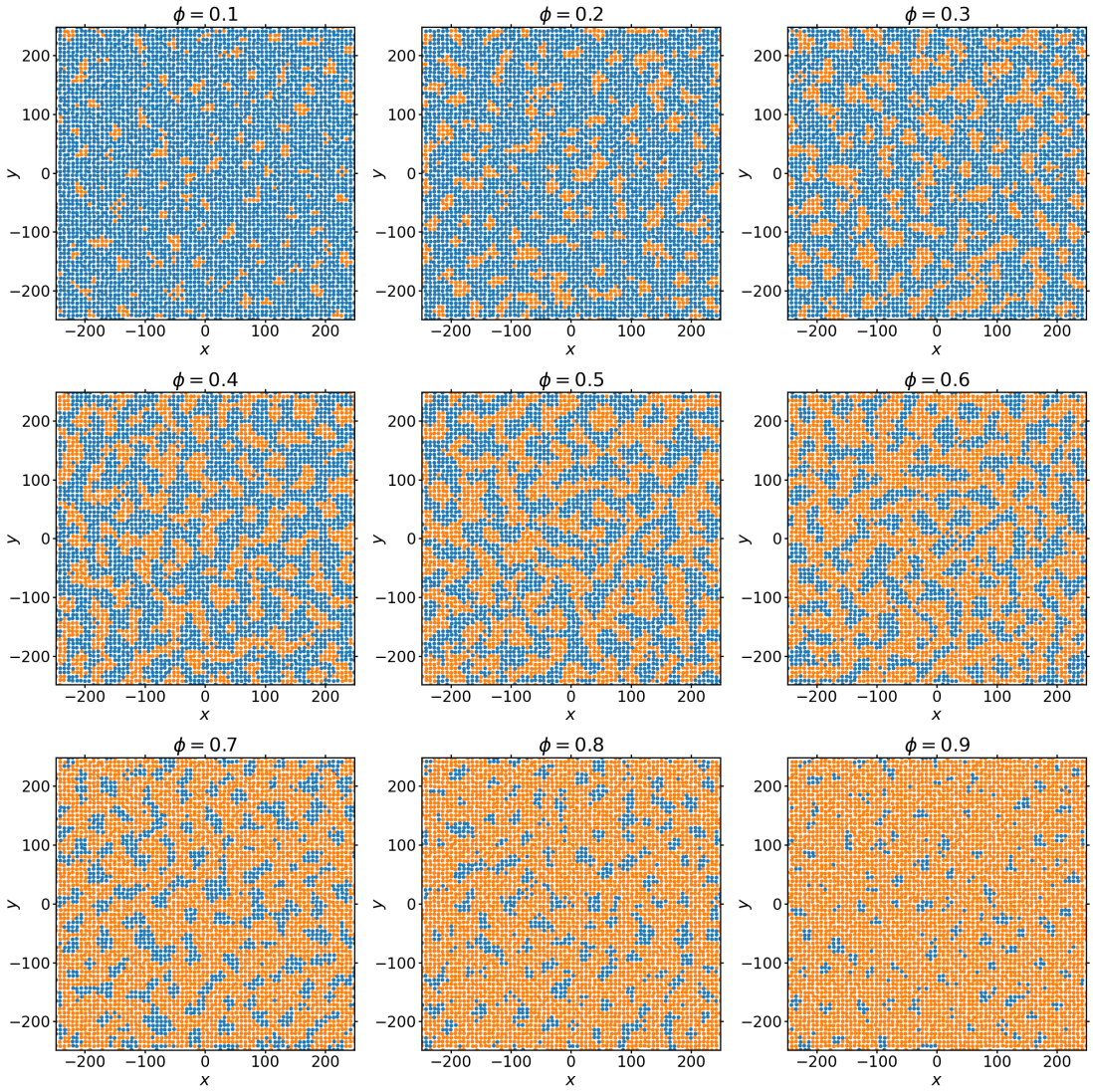

Figure 5.9.: Snapshots of examples for the initial 2D-networks consisting of $N = 5041$ nodes containing different filler content ϕ. The parameters for the morphology generator are set as given in Table 5.3. Cross links are marked by blue dots, while filler nodes are drawn as orange dots.

Up to this point, the surface tensions of CB N339 have been employed. Figure 5.10 shows snapshots after 10 MC steps/N of 2D-networks consisting of $N = 5041$ nodes and containing a fraction $\phi = 0.4$ of CB N234 and Silica VN3 in comparison to CB N339. Analogous plots for $\phi = 0.2$ can be found in Figure A.8. Optically, it is difficult to distinguish the morphologies for the different types of fillers. The aggregates of Silica VN3 appear to be finer and more branched than for the CBs and the aggregates formed by CB N339 appear to be coarser than for CB N234. Taking the exemplary wetting envelope - work of adhesion plot in Figure 4.4 into account, the overall similarities may be surprising since flocculation of CB N339 and Silica VN3 is expected to be promoted compared to CB N234 due to the associated work of adhesion. This is only observed by comparison of CB N339 and CB N234. Nevertheless, the wettability of CB N339 is expected to be worse than for the other types of filler. This makes flocculation more pronounced and, thus, aligns with the observed difference in the shape of the aggregates of Silica VN3. Furthermore, this observation agrees with data by Gundlach & Hentschke [236] who have examined a wetting envelope - work of adhesion plot and snapshots for filled NR similar to those considered here for NR filled with CB N339

and Silica VN3 (cf. Figure 5 in [236]).

However, this does not explain why Silica VN3 appears to be finer dispersed than CB N234 because the work of adhesion for CB N234 is smaller and both of the wettablilities are optimal according to Figure 4.4. Note that optical appearance only provides qualitative but not quantitative insights. Possibly, the application of the neighbor list in the MG and the chosen total number of MC steps contribute to this deviation of the expectation.

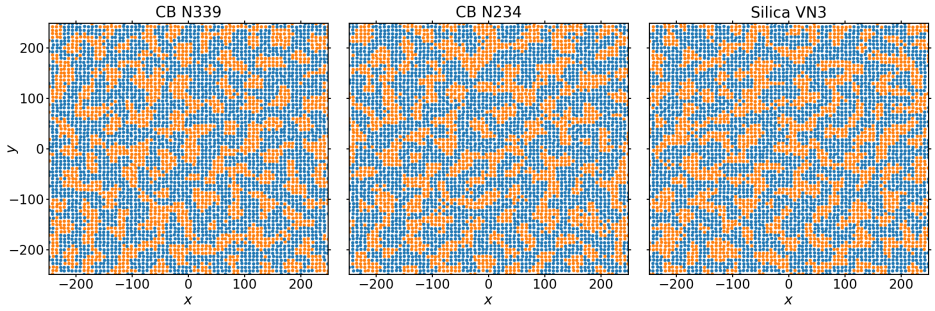

Figure 5.10.: Snapshots of 2D-networks after 10 MC steps/N of morphology generation for NR containing different types of filler with the surface tensions given in Table 4.1. The networks which have been simulated consist of $N = 5041$ nodes and contain a fraction $\phi = 0.4$ of filler.

Since the generated morphologies are very similar for different components with variable surface tensions, only CB N339 will be used in the following investigations and, thus, it is referred to as "filler". The morphology generated after $10 \cdot N$ MC steps will be called the one with coarsely dispersed filler in the case of 2D-networks. For the investigation of the impact of the filler morphology on the mechanical behavior of the model networks, so-called finely dispersed filler is that originating from the initial random distribution of the filler nodes in the model networks without applying the MG. As it can be observed in Figure 5.7 and Figure 5.8, the difference between these morphologies is more distinct than that resulting from the application of different types of filler. Furthermore, the parametrization of filler-filler and polymer-filler bonds which is subject of the next subsection does not distinguish different types of filler.

Overall, the filler morphology in this model rather depends on how the types of nodes are initially distributed and which nodes are selected at random in the MC flocculation algorithm than on the filler type. Thus, in agreement with [245], the radius of the neighbor list used in the MG and the extend to which the original simple cubic lattice is randomized affect the filler morphology. Nevertheless, the filler loading with respect to the percolation threshold is also crucial for the filler structure.

Altogether, it can be concluded that connected filler aggregates or filler networks, are generated in 2D if the number of MC interchange attempts per node is small and the amount of filler nodes is high. Both of the parameters are crucial for the generation of the filler structure.

The situation in 3D-networks is different. Networks consisting of $N = 5832$ nodes and containing a fraction $\phi = 0.2$ of filler have been simulated with $r_{\mathrm{MG}} = 2.0\, d_{\mathrm{init}}$. As indicated above, the filler is CB N339 here and the polymer is NR with the surface tension given in the first row of Table 4.1. Figure 5.11 shows the total interfacial energy W during morphology generation and mock TEM images of the 3D-network. These mock TEM images are plotted by plotting the y-coordinate of the filler nodes versus their x-coordinate and drawing the dots representing the nodes transparently. The z-direction is pointing into the plane of the image. Therefore, the more intense the color is at a certain point, the more filler nodes with similar x- and y coordinates are

located behind it along the z-axis.

As expected, the total interfacial energy W decreases during morphology generation. Initially, the filler is comparatively homogeneously distributed. The mock TEM images at 0 MC steps and after 1 MC steps/N are very similar and difficult to distinguish. As the MG proceeds, regions of high filler concentration build and voids emerge which do not contain filler at all. This effect advances with increasing number of MC steps. Although, it appears like the filler eventually percolates in the mock TEM images, the third dimension must be considered for a definite conclusion regarding that.

Supplemental TEM images at intermediate number of MC steps are added in Figure A.9. In Figure A.10, TEM images of 3D-networks containing a fraction $\phi = 0.4$ of filler are presented. Essentially, the observations are analogous to that for $\phi = 0.2$. Moreover, note that the filler distribution appears to be comparatively regular and ordered in any case, although the nodes have been randomly displaced during the set up of the initial configuration.

To ensure that a filler network can evolve for sufficiently high filler contents, the number of MC steps for morphology generation in 3D-networks is set to $50 \cdot N$ MC steps, analogous to the value applied by Viktorova *et al.* [2]. In Figure 5.12, a snapshot of such a network containing a fraction $\phi = 0.2$ of filler is presented after $50 \cdot N$ MC steps of morphology generation. It validates that the filler aggregates build a network structure.

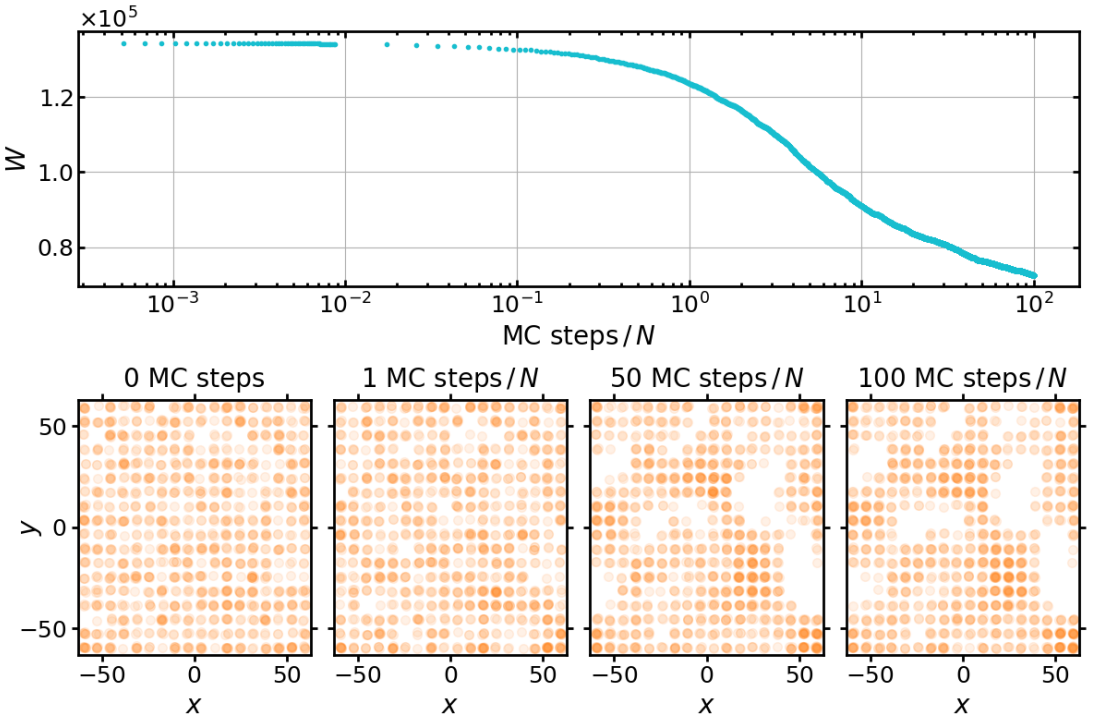

Figure 5.11.: Plot of the total interfacial energy W versus the MC interchange attempts per node during morphology generation and mock TEM images. 3D-networks consisting of $N = 5832$ nodes and containing a fraction $\phi = 0.2$ of filler have been simulated with $r_{\mathrm{MG}} = 2.0\, d_{\mathrm{i}}$. In the mock TEM images, only the filler nodes are plotted.

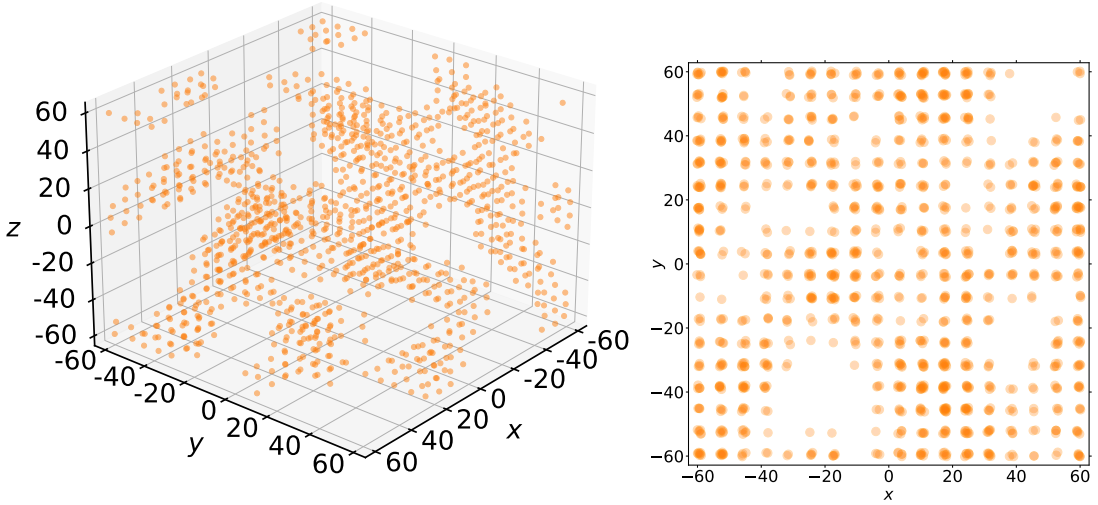

Figure 5.12.: Snapshot of a 3D-network after $50 \cdot N$ MC steps of morphology generation and corresponding mock TEM image. The network consists of $N = 5832$ nodes and contains a fraction $\phi = 0.2$ of filler.

Mock TEM images of 3D-networks consisting of $N = 5832$ nodes with variable filler content ϕ are presented in Figure 5.13. The MG has been applied for $50 \cdot N$ MC steps. As already indicated above, it is difficult to draw a conclusion regarding a potential filler network based on the mock TEM images. However, the data for $\phi = 0.1$ suggests that isolated aggregates of filler form. For larger filler contents, a filler network structure may evolve, but in particular for $\phi \geq 0.7$ it is difficult to distinguish the filler structure according to their mock TEM images. Taking Figure 5.12 into account, the percolation threshold of the 3D-model networks is probably situated at smaller filler contents than in the 2D-case.

Under the consideration of the results of this section, the parameters of the MG for the generation of different filler morphologies are subsequently set as summarized in Table 5.3. In analogy to the 2D-case, finely dispersed filler in 3D-networks is generated by only randomly distributing the filler particles in the model networks. If not stated differently, coarsely dispersed filler is used for the investigations of filled model elastomer networks.

Table 5.3.: Values of the parameters of the morphology generator for the generation of different filler dispersion.

d	designation of filler dispersion	MC steps/N	r_{MG}
2	finely dispersed	0	$2.0\,d_{\mathrm{i}}$
2	coarsely dispersed	10	$2.0\,d_{\mathrm{i}}$
3	finely dispersed	0	$2.0\,d_{\mathrm{i}}$
3	coarsely dispersed	50	$2.0\,d_{\mathrm{i}}$

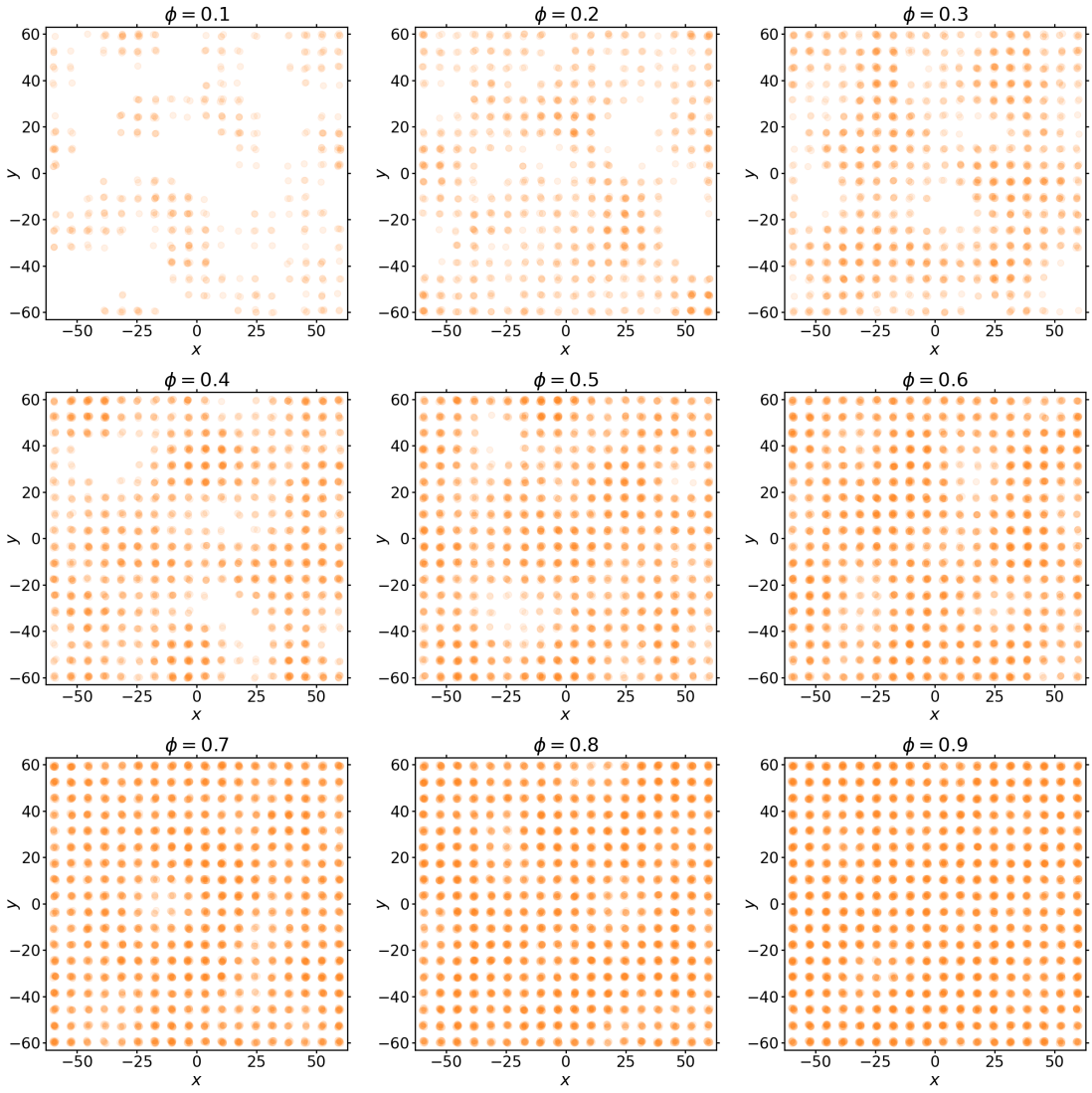

Figure 5.13.: Mock TEM images of examples for the 3D-networks consisting of $N = 5832$ nodes containing different filler content ϕ. The parameters for the morphology generator are set as given in Table 5.3. The TEM images rely on the configurations after the first relaxation of the networks. Filler nodes are drawn as orange dots, while cross links are not plotted.

Remark on Percolation

In Figure 5.9 and Figure 5.13, model elastomer networks are depicted for different filler contents ϕ in between 0.1 and 0.9. The observations made in these figures suggest that the formation of a filler network which traverses the polymer from one side of the network to the opposite depends on the filler content. Moreover, the threshold for this phenomenon apparently occurs at smaller filler content in the 3D-case than in the 2D-case. In the following, the differences between 2D- and 3D-networks and between the model networks and real elastomer networks are outlined

Realistic fractions of filler in a reinforced network are around $\phi = 0.2$, but elastomer networks in the real world are 3D. Real filler morphologies are networks of connected filler aggregates. They are percolating. The so-called percolation threshold defines the fraction of filler above which percolation of filler occurs, i.e. at which a cluster of filler nodes has built which covers an entire axis of a network.

Theoretically, the percolation threshold is obtained to be approximately 0.5927 for ideal 2D square lattices with coordination number of 4 and 0.3116 for 3D sc lattices with coordination number of 6 [246–248]. These values rely on the consideration of infinetly large lattices and the concentration at which the first infinitely large cluster occurs [247]. At fixed dimension, the percolation threshold decreases with increasing coordination number [248]. For instance, it amounts to 0.198 for the 3D fcc lattice, which has been employed for the investigations by Viktorova *et al.* [2]. Note that the percolation threshold is not well-defined for finite lattices [248].

Zhukov *et al.* [249] have investigated from a mathematical background what affects the value of the percolation threshold. They found that, in both 2D- and 3D-networks, increasing the number of links per node decreases the percolation threshold. In general, the percolation threshold is higher in 2D- than in 3D-networks at the same number of links per node. Moreover, spatial symmetries have an impact on the percolation threshold. In 2D-networks which possess symmetry, the percolation threshold is higher compared to random 2D-networks with the same number of links per node. The effects of the spatial symmetry as well as the number of links per node are stronger in 2D- than in 3D-networks. Here, the networks which have been generated up are highly symmetric and have a comparatively small network density, which explains the apparently high percolation thresholds.

Experimentally, percolation in polymer networks is studied by conductivity measurements. It is found that the percolation threshold depends not only on the filler content, but also on its size and shape as well as on the structure of the polymer matrix [250–253]. For instance, the percolation threshold is smaller for larger filler particles and filler particles with a higher aspect ratio, for example fibers compared to spherical particles [252]. Furthermore, agglomerated structures of filler reduce the percolation threshold due to the increased effective volume [252]. In addition, the ability of the filler particles to rearrange and their physical-chemical surface properties determine the percolation threshold [254–256]. In conductivity measurements on various CB filled polymers, Miyasaka *et al.* [257] observed that the percolation threshold increases with increasing polar part of the surface tension, although their data point for NR does not fit into the scheme. They also report an increase of the percolation threshold with increasing adhesion strength. Besides, the processing of the material affects the percolation properties since it determines the distribution and orientation of filler in the polymer matrix [252]. Note that, in the given references, percolation is mainly investigated in thermoplastics, but not in elastomers.

In Table 5.4, the percolation thresholds in NR obtained in experiments are listed for various types of filler as both mass and volume fraction. For the computation of the missing values, the density of polymer is estimated to be $\rho_\mathrm{p} = 1\,\mathrm{g/cm^3}$ and the density of filler $\rho_\mathrm{f} = 2\,\mathrm{g/cm^3}$. These densities are in consistent with those for rubber and CB respectively.

Azura *et al.* [24] performed electrical conductivity measurements on NR which has been filled with 0 phr to 50 phr of CB N220. They obtained the percolation threshold at 20 phr CB content. Omnès *et al.* [65] investigated NR samples which have been filled with CB N330 and CB N650. They performed swelling tests in order to obtain the percolation threshold. The percolation threshold amounts to a volume fraction of 7 % to 13 % in the case of CB N330 and 12.8 % to 18 % for CB N650. Omnès *et al.* attribute the difference in the values to the different properties of both fillers. CB N330 possesses higher specific surface. These volume fractions correspond to mass fractions between 0 phr and 45 phr. It can be concluded that the applied filler fractions in real

NR networks are around the percolation thresholds.

Table 5.4.: Experimentally measured percolation thresholds for various filler types embedded into NR matrices. Given mass fractions are converted to volume fractions with the help of Equation 2.11 and vice versa.

filler	percolation threshold	
	mass fraction	volume fraction
CB N220	20 phr [24]	9 %
CB N330	15 phr to 30 phr	7 % to 13 % [65]
CB N650	29 phr to 44 phr	12.8 % to 18 % [65]

Altogether, in the two-component networks simulated here, the filler fraction determines the percolation threshold predominantly. The physical-chemical properties and the size of the filler appear to play a secondary role. Initially, when the filler nodes are randomly distributed over the network, percolation is entirely governed by mathematical aspects such as networks density and spatial symmetry. The physical-chemical properties in terms of the surface tensions and the filler size are included into the model by the morphology generator. However, it has been observed that these properties are not the determining factors for the generated filler morphologies. Therefore, percolation in the model networks can be considered as predominantly mathematical phenomenon. In particular, this conclusion is consistent with the observations in the snapshots of 2D-network for variable filler content depicted in Figure 5.9.

5.2.2. Filler-Filler and Polymer-Filler Bonds

As a next step, reasonable values for the spring constants for the interaction energies of the filler-filler and the polymer-filler bonds given by harmonic potentials according to Equation 3.78 have to be obtained. The corresponding energies are proportional to the deflection from the equilibrium positions of the nodes. Analogously, the conformational part of the free energy of a polymer-polymer link can also be understood as harmonic energy, like for a spring, which is proportional to the extension of the polymer chain. For a non-crystalline link, the extension of the polymer chain is comparable to the displacement of the nodes in a harmonic potential from their equilibrium positions and the "spring constant" in this case is given as $k^{\mathrm{pp}} = 3$ according to Equation 3.57. In order to model amplified stress in filled networks compared to unfilled networks as observed in experiments, it must be set:

$$k^{\mathrm{pp}} = 3 \ll k^{\mathrm{pf}} \ll k^{\mathrm{ff}}. \tag{5.2}$$

Up to this point, various types of filler nodes are not distinguished. The filler morphology in the two-component networks is nearly independent of the filler type. However, different spring constants may be chosen according to different filler in order to model different interaction properties within the network. For instance, in a similar approach, Viktorova *et al.* [199] have varied the filler morphologies and the spring constants associated with different types of filler to study the dynamic moduli of filled polymer blends.

In previous simulations, the increment in the deformation has been set to $\Delta\lambda = 0.01$ [3]. Due to the application of an affine deformation to the positions of the nodes for the stretching step, filler-filler bonds are breaking immediately in the first stretching step

if $R^{\mathrm{ff}} = 1.01$ as it has been set by Viktorova *et al.* [2]. Meanwhile, polymer-filler links become weakly interacting at this point if $R^{\mathrm{pf}} = 1.01$. Hence, the Payne effect might not be as notable here as in the work of Viktorova *et al.* [2]. However, the limit of very slow deformation is considered in the following. It means that breaking of filler-filler bonds and the transition to weak interaction for polymer-filler links is separated from the global energy minimization by the FIRE algorithm, which adjusts the positions of the nodes directly after the deformation of the network. If the distance between two interacting filler nodes still exceeds the cut-off distance, the bond breaks, i.e. the interaction is set to zero. This is analogously performed for the transition to the weak interaction of polymer-filler links. The impact of the limit of slow deformation on the stress-stretch curves is stated in subsection A.4.1.

Subsequently, the stress in non-crystallizing networks is analyzed first regarding whether it mimics the phenomenology. For this purpose, 2D-networks consisting of $N = 5041$ nodes are simulated at variable filler content ϕ and the corresponding stress-stretch curves are examined. The parameters for the MG are set as given in Table 5.3 for coarsely dispersed filler. As a first approach, the spring constants are chosen as follows:

$$k^{\mathrm{ff}} = k^{\mathrm{pf}} = k^{\mathrm{pf}}_{\mathrm{weak}} = 4.$$

In addition, it is set $R^{\mathrm{ff}} = \infty$. Exemplary initial configurations of these networks are plotted in Figure 5.9.

At this point, a short justification is given for the particular definition of the equilibrium end-to-end distances of filler-filler and polymer-filler bonds which has been stated in section 4.1. Figure 5.14 shows the stress-stretch curves for variable filler content in the case that the equilibrium end-to-end distances are given by the initial distances between the corresponding nodes. Although the stress increases with increasing filler content at higher stretches, the stress tends to decrease with increasing ϕ at small stretches. In particular, the initial stress becomes negative and just intersects the stress-stretch curve for the unfilled sample after several stretch increments. This is contradictory to experimental observations, where embedding filler into the network increases the stress and the modulus due to hydrodynamic effects.

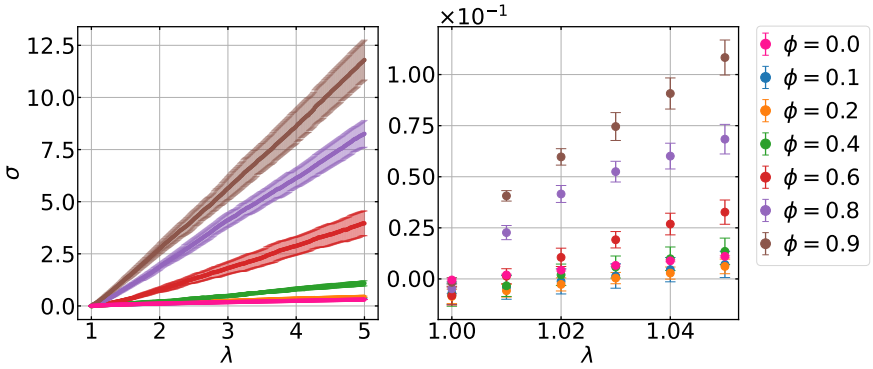

Figure 5.14.: Stress-stretch curves obtained as averages from 10 simulations of non-crystallizing 2D-networks consisting of $N = 5041$ nodes containing different fractions ϕ of filler. The MG ran through $10 \cdot N$ MC steps.

For further analysis, the initial stress and both the forces and extensions of polymer-filler and filler-filler bonds have been investigated dependent on their orientation. The

results are discussed in subsection A.4.2. The data does not allow for a definitive conclusion on whether a spatial direction is preferred over the others. In addition, the FIRE algorithm does not show a significant impact on the negative stress. Besides, the bonds are rather extended to $r > r_0$ than contracted. However, the definition of the equilibrium distances of the bonds contributes the initially negative stress. Therefore, this problem is solved by initially relaxing an unfilled polymer network and replacing some of the links by polymer-filler and filler-filler bonds according to the generated filler morphology such that the equilibrium end-to-end distances of the bonds are determined by the relaxed link. This is stated in section 4.1. Analogously, the stress-stretch curves of crystallizing networks are shifted by the mean initial stretch of unfilled networks subsequently.

Figure 5.15 shows the shifted stress-stretch curves for non-crystallizing 2D-networks consisting of $N = 5041$ nodes with variable content ϕ of CB N339. The stress increases with filler content at higher stretches. Also at small stretches, for comparatively high filler content, the stress is increased by embedding filler into the network as it is expected. However, if the filler content is $\phi \leq 0.4$, the data points for the unfilled networks lay within the error margin of the data for the filled networks at small stretches. The difference in the stresses for different ϕ increases with increasing stretch λ.

Moreover, as already observable in Figure 5.14, the stress-stretch curves for filled networks do not possess the same shape as the curve for the unfilled network. Apparently, there is a kink at a certain stretch above which the curves incline linearly, such that the curved shape of the stress-stretch curves gets lost. The stretch at which this kink occurs appears to decrease with ϕ. Figure 5.16 shows the ratio $L_{\mathrm{r>n}}/L$ of the number of links with end-to-end distances larger than their contour length, i.e. $r > n$, to the total number of links and bonds during stretching for variable filler content ϕ. Note that it would be more convenient to normalize by the total number of links. The plot indicates that the number of links with unphysical end-to-end distance $r > n$ tends increase with ϕ, particularly at smaller stretches. Therefore, there might be a correlation between the linear increase of the stress and the occurrence of links with $r > n$.

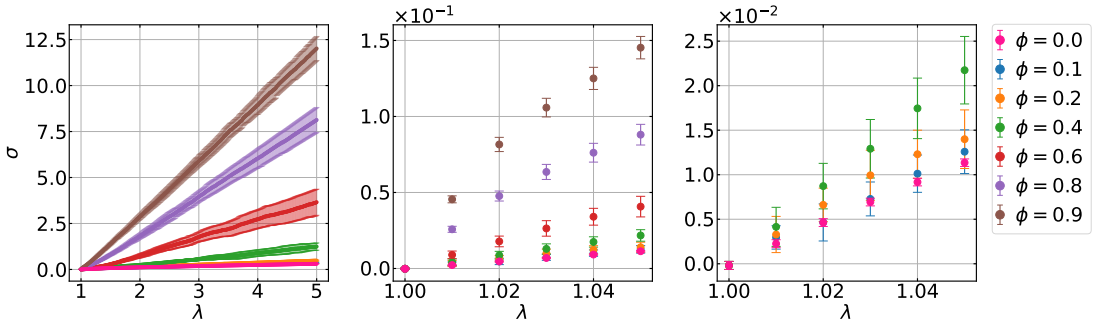

Figure 5.15.: Shifted stress-stretch curves obtained as averages from 10 simulations of non-crystallizing 2D-networks consisting of $N = 5041$ nodes with variable filler content ϕ. The morphology generator ran through $10 \cdot N$ MC steps.

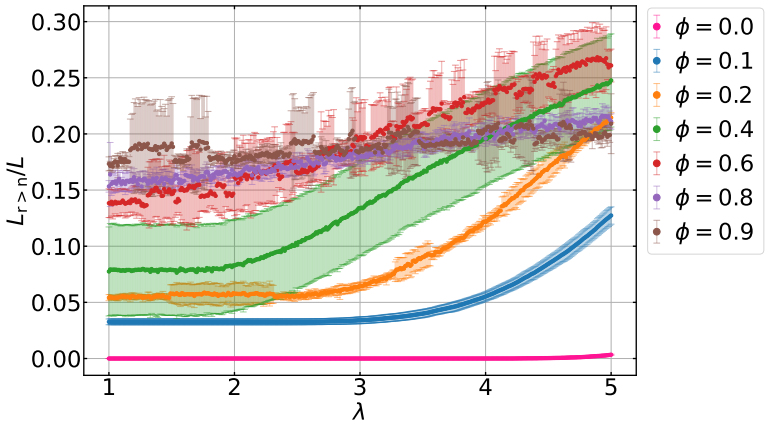

Figure 5.16.: Ratio of the number of polymer-polymer links with $r > n$ to the total number of links $L_{r>n}/L$ during stretching for variable content ϕ of CB N339 in 2D-networks consisting of $N = 5041$ nodes, where the morphology generator ran through $10 \cdot N$ MC steps. The data are obtained as averages from 10 simulations.

Starting from this point of information about the stress-stretch behavior of filled model elastomer networks, the spring constants will be specified in the following. It will be examined how their parametrization affects the mechanical properties. For this purpose, the relation between the derivative of the stress stretch curve $\partial\sigma/\partial\lambda$ which is proportional to the elastic modulus and the filler content is studied. According to experimental observations, the inclusion of filler particularly determines the mechanical behavior of the compound at small deformations. In this regime, the modulus of the material is commonly the quantity of interest. Note that, since SIC is negligible in this case, only non-crystallizing model networks will be investigated.

Below the percolation threshold, it is expected that $\partial\sigma/\partial\lambda \propto \phi^2$ [258]. Above the percolation threshold, $\partial\sigma/\partial\lambda \propto \phi^y$ holds, where $y \approx 3.5$ in the ideal case [77]. For this purpose, 2D-networks consisting of $N = 5041$ nodes with variable filler content ϕ are deformed until the maximum stretch $\lambda_{\text{max}} = 1.1$. The stress-stretch curve in this range is obtained by averages over 10 simulations each and fitted with a linear function according to Hooke's law, which holds for small stretches. The slope of the curve yields an approximation for the derivative $\partial\sigma/\partial\lambda$. Finally, $\partial\sigma/\partial\lambda$ is plotted dependent on ϕ and fitted with

$$\partial\sigma/\partial\lambda = A \cdot \phi^y + B. \tag{5.3}$$

This is done for different filler morphologies resulting from variation in the number of MC steps applied in their generation. The results are presented in Figure 5.17. However, the data point for $\phi = 0.0$ is not taken into account for the fits made here since considering it leads to the curves deviating from the behavior of most of the remaining data.

In the range of intermediate filler content, $\partial\sigma/\partial\lambda$ decreases with increasing number of MC steps for morphology generation. This indicates that the total number of polymer-filler and filler-filler bonds is reduced by morphology generation. However at low filler content, the data points obtained in particular for $10 \cdot N$ to $100 \cdot N$ MC steps for morphology generation overlap. This observations align with the behavior of the total interfacial energy and snapshots of the filler distributions during morphology generation which have been considered in the previous subsection. At high filler content, the differences increase, but the data points for for $30 \cdot N$ to $100 \cdot N$ MC steps for morphology generation still lay within each others error margin.

For low filler content, the curves fit the data very well. While the deviation from the data point for $\phi = 0.0$, which is not considered in the fit, is small, it is large for the

data points at $\phi = 0.9$, which lay above the curves. Due to their comparatively large error, the latter are weighted less than the other data in the fit. The curves indicate that $\partial\sigma/\partial\lambda$ decreases with increasing number of MC steps for morphology generation which indicates softening due to filler flocculation. Since the spring constants for filler-filler and polymer-filler bonds are identical and fixed, this behavior suggests that the total number of these types of bonds decreases with increasing number of MC steps. Furthermore, the obtained exponents y are consistent with the expected values. In particular, the result for $10 \cdot N$ MC steps fits the expectation for the ideal case.

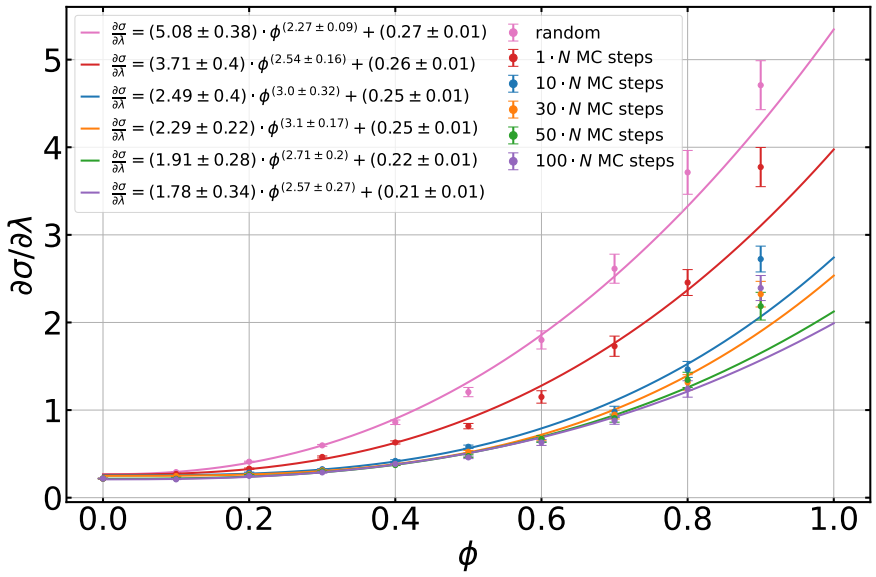

Figure 5.17.: $\partial\sigma/\partial\lambda$ versus ϕ for 2D-networks. "random" means that the filler nodes are randomly distributed all over the network, i.e. the morphology generator has not been employed.

Apart from that, the stress in filled 3D-networks in analyzed in the following. For this purpose, networks consisting of $N = 5832$ nodes are simulated with variable content ϕ of CB N339. The MG is parameterized as given in Table 5.3. Mock TEM images of such networks are presented in Figure 5.13.

The shifted stress-stretch curves are plotted in Figure 5.18. The observations, which can be made here, are analogous to the 2D-case. Nevertheless, the stress of the networks with $\phi = 0.1$ is smaller than that of the unfilled network at small stretches.

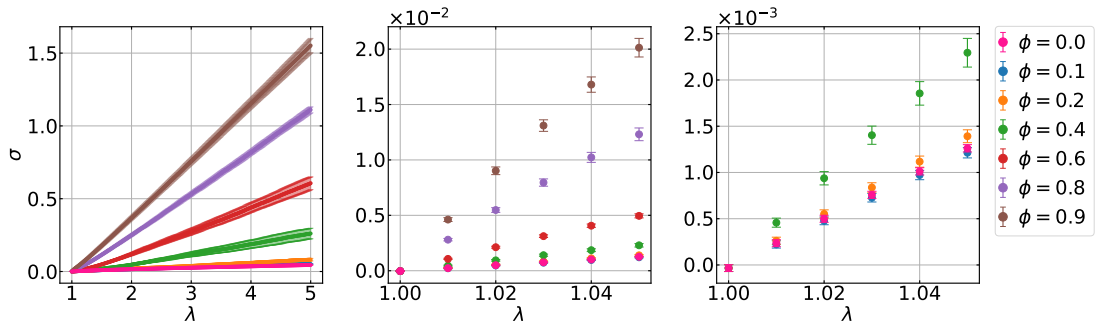

Figure 5.18.: Shifted stress-stretch curves obtained as averages from 10 simulations of non-crystallizing 3D-networks consisting of $N = 5832$ nodes with variable filler content ϕ. The morphology generator ran through $50 \cdot N$ MC steps.

Moreover, the derivative $\partial\sigma/\partial\lambda$ of the stress-stretch curve is investigated analogous to the case of 2D-networks and, thus, plotted in Figure 5.19 as a function of ϕ. Again, the data point for $\phi = 0.0$ is not taken into account for the fits. Additionally, the case of the morphology generation for $100 \cdot N$ MC steps is considered here.

With the exception of the data obtained for $50 \cdot N$ MC steps of morphology generation, $\partial\sigma/\partial\lambda$ decreases with increasing number of MC steps, but the curves for $30 \cdot N$ MC steps and $100 \cdot N$ MC steps approximately overlap. For the latter, the fitted curves deviate from the data points for $\phi = 0.9$. Moreover, the curve for $50 \cdot N$ MC steps only slightly differs from that for $10 \cdot N$ MC steps. Both of them appear to be able to describe also the data point for $\phi = 0.0$ although it is not considered in the fit. Analogous to the 2D-case, the decrease of the derivative with increasing number of MC steps indicates softening due to filler flocculation. The obtained values for the exponents y are consistent with the expectations.

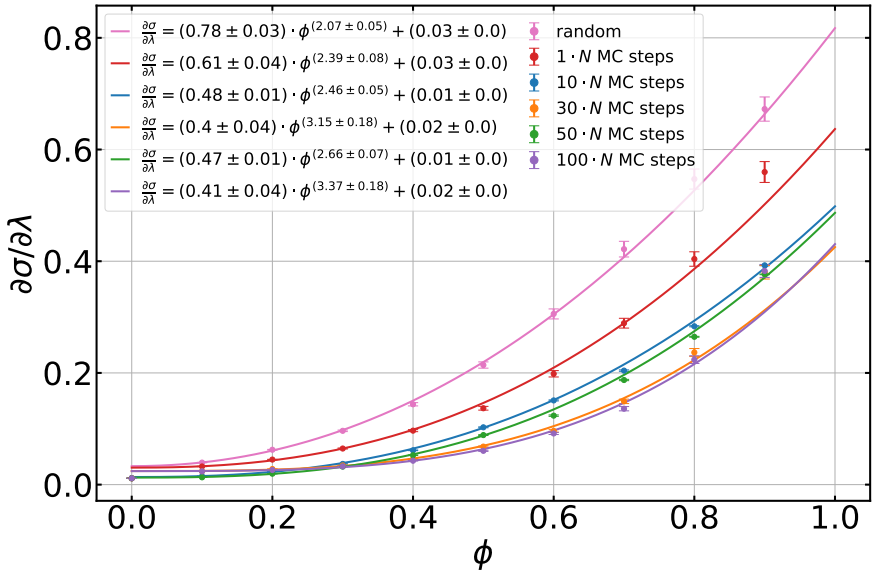

Figure 5.19.: $\partial\sigma/\partial\lambda$ versus ϕ for 3D-networks. "random" means that the filler nodes are randomly distributed all over the network, i.e. the morphology generator has not been employed.

Specification of the Spring Constants

Subsequently, the spring constants for filler-filler and filler-polymer interaction are specified according to Equation 5.2. The spring constant for polymer-filler interaction $k^{\mathrm{pf}} = 4.0$ is fixed, while k^{ff} and $k^{\mathrm{pf}}_{\mathrm{weak}}$ are to be determined. For this purpose, 2D-networks consisting of $N = 5041$ nodes are simulated with variable filler content ϕ. If not stated differently, the MG is applied for $10 \cdot N$ MC steps. As explained previously, $\partial\sigma/\partial\lambda$ is extracted from the stress-stretch curves in the region of small deformation. Equation 5.3 is fitted to each data set. The procedure is explained in detail in subsection A.4.3. In Figure 5.20, the main results are compiled. The corresponding parametrization of the interactions can be found in Table 5.6.

First, it is checked how the variation of $k \equiv k^{\mathrm{ff}} = k^{\mathrm{pf}} = k^{\mathrm{pf}}_{\mathrm{weak}}$ affects $\partial\sigma/\partial\lambda$ in the case $R^{\mathrm{ff}} = \infty$. In particular at filler content higher than the percolation threshold, it can be observed that $\partial\sigma/\partial\lambda$ increases with increasing k as it is expected. The plot of $\partial\sigma/\partial\lambda$ for $k = 4.0$ is used as a reference in order to analyze the effect of the following variation of the parameters.

As a next step, the spring constant for filler-filler interaction k^{ff} is varied, while it has

been set $k^{\mathrm{pf}} = k^{\mathrm{pf}}_{\mathrm{weak}} = 4.0$ and $R^{\mathrm{ff}} = \infty$. Here, it is required that $k^{\mathrm{ff}} > k^{\mathrm{pf}} = 4.0$. With increasing k^{ff}, $\partial\sigma/\partial\lambda$ tends to increase as expected. Figure 5.20 shows that $k^{\mathrm{ff}} = 5.0$ increases $\partial\sigma/\partial\lambda$ to a relatively high extend, especially at high filler content.

Afterwards, $k^{\mathrm{pf}}_{\mathrm{weak}}$ is varied, where it is set $R^{\mathrm{pf}} = 1.01$ and $k^{\mathrm{ff}} = k^{\mathrm{pf}} = 4.0$ and $R^{\mathrm{ff}} = \infty$. With increasing $k^{\mathrm{pf}}_{\mathrm{weak}}$, $\partial\sigma/\partial\lambda$ increases and Figure 5.20 shows that setting $k^{\mathrm{pf}}_{\mathrm{weak}} < 4.0$ lowers $\partial\sigma/\partial\lambda$. This behavior is expected. For sufficiently small $k^{\mathrm{pf}}_{\mathrm{weak}}$, the fitted functions describe the data well, but, for higher $k^{\mathrm{pf}}_{\mathrm{weak}}$, the curves deviate from the data points at high filler content as it can also be observed in Figure 5.20 for $k^{\mathrm{pf}}_{\mathrm{weak}} = 1.0$. For small $k^{\mathrm{pf}}_{\mathrm{weak}}$, the stress in the networks is not significantly amplified by small filler content in comparison to the unfilled network. In particular, the stress becomes smaller than in the unfilled network in certain cases particularly at small stretches. This is in contrast to the expectations. Viktorova *et al.* [2] have set this spring constant 4 orders of magnitude smaller than k^{pf}, but apparently it does not make sense to choose this parameter as small here. Furthermore for very small $k^{\mathrm{pf}}_{\mathrm{weak}}$, the exponents y become larger than the expected values.

Analyzing the effect of enabling rupture of filler-filler bonds by setting $R^{\mathrm{ff}} = 1.01$ and keeping $k = 4.0$ fixed does not affect the data significantly in contrast to decreasing $k^{\mathrm{pf}}_{\mathrm{weak}}$. Therefore, the polymer-filler bonds appear to be dominant compared to the filler-filler bonds. In Figure 5.20 at high filler content, the curve fitted to this data set lays above the curve for the data set with unbreakable filler-filler bonds. This is in contrast to the expectation. However, the data points in this region indicate a lowering of $\partial\sigma/\partial\lambda$.

Altogether, the obtained exponents y for the cases discussed up to this point lay within the expected range. Although the curves fit the data well for small filler content, they differ for high filler content due to comparatively large errors of the data in the latter region. Based on the investigations of the spring constants, in order to meet the relation between the spring constants given in Equation 5.2 and to model stress amplification, it is useful to parametrize the interaction between fillers and between polymer and filler by the parameters confined in Table 5.6. The plot of $\partial\sigma/\partial\lambda$ for this setting is also depicted in Figure 5.20. The curve fits the data well. With respect to the choices of the spring constants discussed above, the curve for this case is lowered to the highest extend. This might be attributed to the combination of the decreased spring constant $k^{\mathrm{pf}}_{\mathrm{weak}}$ and the rupture of filler-filler bonds. The obtained exponent y is comparatively small, but still consistent with the expected value $y = 2$ for networks with filler content below the percolation threshold. Due to their relatively small errors, the data in this region of the filler content determine the fitted function. In addition, the exponents obtained here are consistent with those determined by Viktorova *et al.* [2].

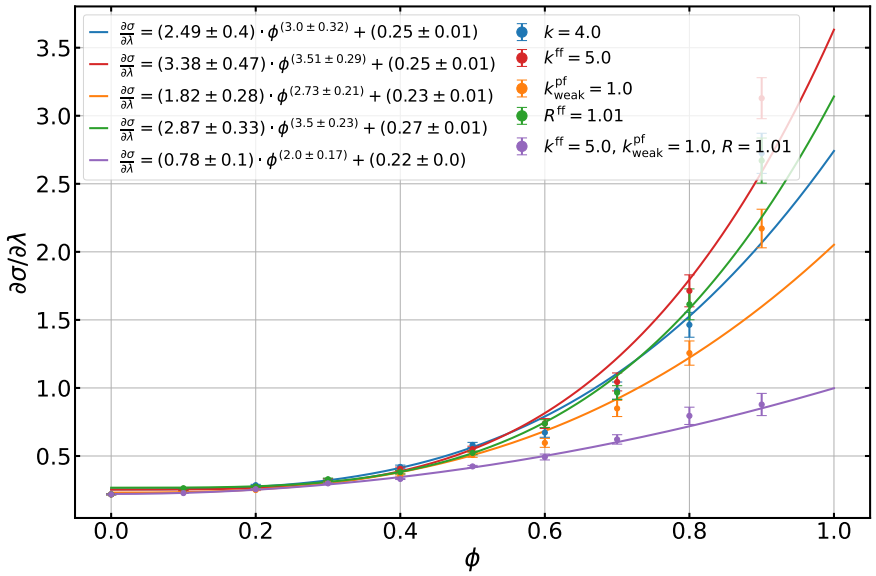

Figure 5.20.: $\partial\sigma/\partial\lambda$ versus ϕ for 2D-networks with variable configurations of the polymer-filler and filler-filler bonds. The morphology generator is parameterized as given in Table 5.3. The data points for $\phi = 0.0$ are not taken into account for the fits. In the legend, only the essential parameters are given with the full parameter settings compiled in Table 5.5.

Table 5.5.: Full parameter settings for Figure 5.20 and Figure 5.21.

legend item	k^{ff}	k^{pf}	$k^{\mathrm{pf}}_{\mathrm{weak}}$	R^{ff}	R^{pf}
$k = 4.0$	4.0	4.0	4.0	∞	∞
$k^{\mathrm{ff}} = 5.0$	5.0	4.0	4.0	∞	∞
$k^{\mathrm{pf}}_{\mathrm{weak}} = 1.0$	4.0	4.0	4.0	∞	1.01
$R^{\mathrm{ff}} = 1.01$	4.0	4.0	4.0	1.01	∞
$k^{\mathrm{ff}} = 5.0,\ k^{\mathrm{pf}}_{\mathrm{weak}} = 1.0,\ R = 1.01$	5.0	4.0	1.0	1.01	1.01

Table 5.6.: Parameters for the interaction between fillers and between polymer and filler obtained in this section.

k^{ff}	k^{pf}	$k^{\mathrm{pf}}_{\mathrm{weak}}$	R^{ff}	R^{pf}
5.0	4.0	1.0	1.01	1.01

Figure 5.21 shows the stress-stretch curves for $\phi = 0.1$ and $\phi = 0.5$ corresponding to the data presented in Figure 5.20. For $\phi = 0.1$ at low stretches, the stress does not appear to be significantly amplified, but it is rather consistent with the data for the unfilled network. However, at higher stretches, the stress becomes larger than for the unfilled network, but the data for the filled networks overlaps. For $\phi = 0.5$, the stress is significantly increased compared to the unfilled network already at small stretches for all of the choices of the spring constants. At small stretches, the stress for $k = 4.0$ overlaps with the data for $k^{\mathrm{ff}} = 5.0$, but at high stretches the latter rises even higher. At small stretches it appears like the impact of rupture of filler-filler bonds is similar to the weakening of polymer-filler bonds, but at high stretches the stress for $R^{\mathrm{ff}} = 1.01$ overlaps with the data for $k = 4.0$.

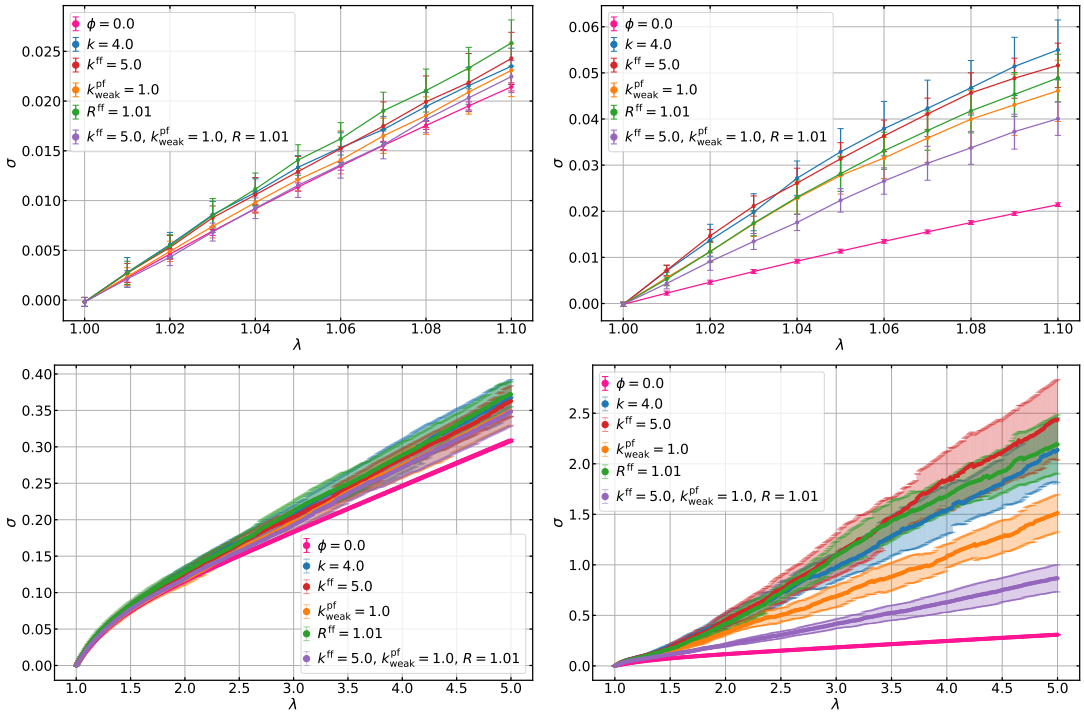

(a) $\phi = 0.1$ **(b)** $\phi = 0.5$

Figure 5.21.: Stress-stretch curves for 2D-networks with variable configurations of the polymer-filler and filler-filler bonds. The morphology generator is parameterized as given in Table 5.3. In the legend, only the essential parameters are given. The full parameter settings are compiled in Table 5.5. The upper plots show the region of small deformation extracted from the lower plots. The data points are connected for visualization, but this does not have any physical meaning.

5.3. Behavior of Filled Networks at Small Deformations

Since suitable values for the spring constants have been obtained, the mechanical behavior of filled networks at small deformations is analyzed. In particular, it is examined now whether the model involves the Payne effect.

Typically, the modulus of the material is investigated for this purpose via shear experiments. The model and the simulation algorithm employed here are based on uniaxial stretching. Because small deformations are applied now, the modulus is determined by the derivative of the stress-stretch curve and it is presumed to be constant for the unfilled networks. However, this is not true in general, in particular for stretching experiments as discussed in section 3.3 in the context of the theory of rubber elasticity on which the model relies. There is a decrease of the derivative with increasing stretch which will overlay the actual Payne effect if it is involved in the model. In order to avoid this, it is checked for the Payne effect by analyzing the difference of the derivative when the bonds are not cut off and the derivative when the bonds are cut off $(\partial\sigma/\partial\lambda)_\infty - \partial\sigma/\partial\lambda$ dependent on the stretch. The derivative when the bonds are not cut off $(\partial\sigma/\partial\lambda)_\infty \equiv \partial\sigma/\partial\lambda\left(R^{ff} = R^{pf} = \infty\right)$ must not show the Payne effect since it is expected to arise from the rupture or slippage of bonds and the destruction of the filler network. Therefore, the Payne effect must be indicated by an increase of the difference.

The derivative $\partial\sigma/\partial\lambda \equiv \partial\sigma/\partial\lambda\left(R^{ff}, R^{pf}\right)$ of the stress at comparatively small stretches λ is numerically approximated. For $\lambda = 1.0$, forward difference approximation is ap-

plied:

$$\partial\sigma/\partial\lambda\,(\lambda) = \frac{\sigma\,(\lambda+\Delta\lambda) - \sigma\,(\lambda)}{\Delta\lambda}. \tag{5.4}$$

The accuracy is of order $\Delta\lambda$. For the remaining derivatives, the central difference method with accuracy of order $\Delta\lambda^2$ is used:

$$\partial\sigma/\partial\lambda\,(\lambda) = \frac{\sigma\,(\lambda+\Delta\lambda) - \sigma\,(\lambda-\Delta\lambda)}{2\Delta\lambda}. \tag{5.5}$$

For the following data, the simulated networks are defined by the default parameters determined in the previous sections. The 2D-networks consist of $N = 5041$ nodes, while the 3D-networks consist of $N = 5832$ nodes. For filled networks, the morphology generator runs through $10 \cdot N$ MC steps or $50 \cdot N$ MC steps, respectively, such that the filler is coarsely dispersed. In both cases, the spring constants and cut off radii are set as given in Table 5.7. Note that the cut-off radii differ from the choice in the previous section. The case $R^{\mathrm{ff}} = R^{\mathrm{pf}} = 1.01$ is not considered because the investigations have shown that the simulation is not as sensitive to these cut-off radii. Supplemental information regarding that is included in section A.5. These cut-off radii for both the filler-filler and polymer-filler bonds are small compared to the choice of the stretch increment $\Delta\lambda = 0.01$. According to Figure 5.20, the general impact of this change of the cut-off radius must be small.

Table 5.7.: Default parameters for the interaction between fillers and between polymer and filler.

k^{ff}	k^{pf}	$k^{\mathrm{pf}}_{\mathrm{weak}}$	R^{ff}	R^{pf}
5.0	4.0	1.0	1.1	1.1

Figure 5.22 shows the numerical approximation of the derivative of the stress-stretch curve for an unfilled 2D-network. The errors of the data points are relatively large which is due to the numerical approximation. The data is fitted with

$$\frac{\partial\sigma}{\partial\lambda} = E_{0,\mathrm{2D}}\left(1 + \frac{3}{\lambda^4}\right)$$

according to the theory of rubber elasticity discussed in section 3.3, where $E_{0,\mathrm{2D}}$ is a constant which accounts for the elastic modulus. Analogously, the data for the 3D-networks depicted in Figure 5.23 is fitted with

$$\frac{\partial\sigma}{\partial\lambda} = E_{0,\mathrm{3D}}\left(1 + \frac{2}{\lambda^3}\right),$$

where $E_{0,\mathrm{3D}}$ refers to the elastic modulus. In both cases, the data decreases with increasing stretch as expected and the curves fit the data well. All of the data points lay on the curves except for the first at $\lambda = 1.0$ which probably deviated due to the different approximation method.

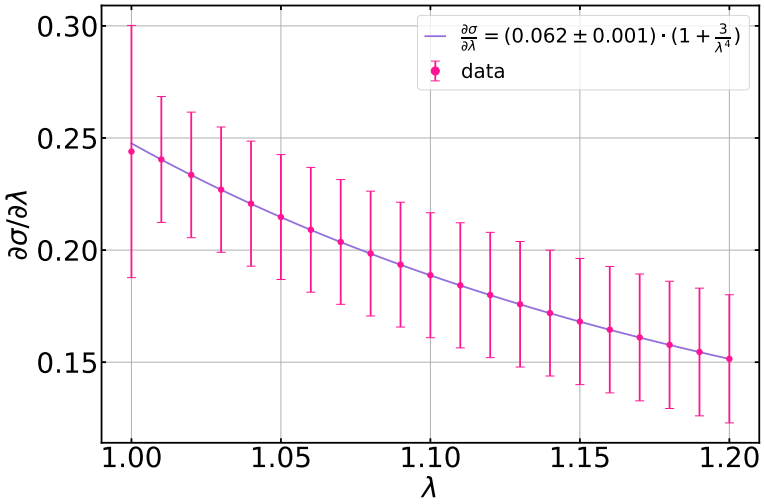

Figure 5.22.: Derivative $\partial\sigma/\partial\lambda$ of the stress-stretch curve versus λ for an unfilled 2D-network.

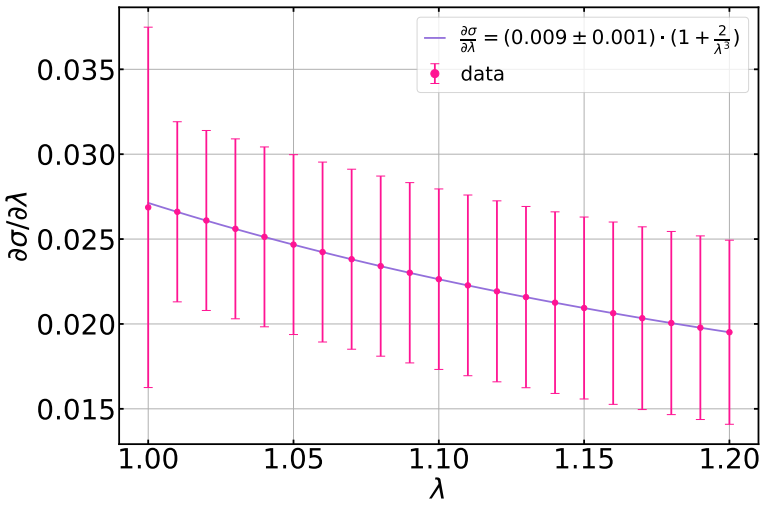

Figure 5.23.: Derivative $\partial\sigma/\partial\lambda$ of the stress-stretch curve versus λ for an unfilled 3D-network.

The differences $(\partial\sigma/\partial\lambda)_\infty - \partial\sigma/\partial\lambda$ of the numerically approximated derivatives for different filler content ϕ are depicted in Figure 5.24 for $R^{\mathrm{ff}} = R^{\mathrm{pf}} = 1.1$. For small filler content $\phi \leq 0.3$, the difference is approximately constant which means that the data does not show the Payne effect. The reason is that none or only a few of the filler-filler and polymer-filler bonds break if the filler content is very small. For $0.3 < \phi \leq 0.5$, the difference remains approximately constant in the region of stretches where the Payne effect is expected, i.e. $1 - 10\,\%$, but it scatters at higher stretches. The latter case coincides with the range of stretches in which filler-filler and polymer-filler bonds break. For $\phi \geq 0.6$, the data increases with increasing stretch from a difference of 0 until a plateau is reached. For high filler content, this happens in the range where the Payne effect is expected, but for smaller filler content, the increase occurs at higher stretches and it is not as steep. Figure A.25 indicates that the start of breaking of filler-filler and polymer-filler bonds decreases and the 'rate of bond breaking' increases with increasing filler content. However, the incline in the differences suggests that the Payne effect is incorporated into the model. The effect becomes more pronounced with higher filler content.

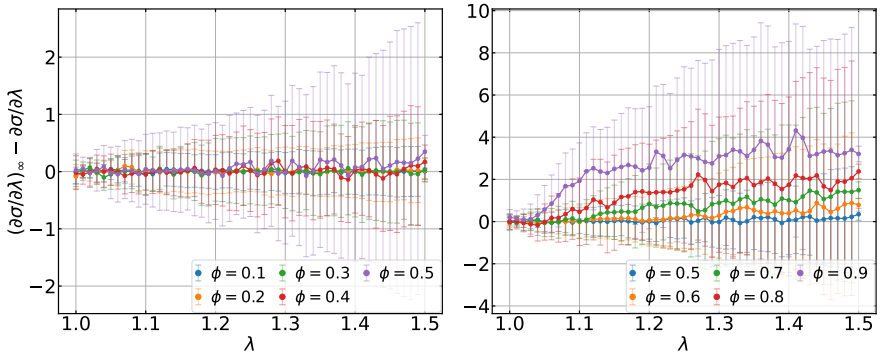

Figure 5.24.: $(\partial\sigma/\partial\lambda)_\infty - \partial\sigma/\partial\lambda$ versus λ for 2D-networks for variable filler content ϕ with $R^{\mathrm{ff}} = R^{\mathrm{pf}} = 1.1$. The data points are connected for the eye, but this does not have any physical meaning.

In order to examine which type of bonds causes the Payne effect, the cut-off radii are varied for fixed filler content $\phi = 0.9$. Both the original derivatives of the stress-stretch curves and the differences $(\partial\sigma/\partial\lambda)_\infty - \partial\sigma/\partial\lambda$ are plotted in Figure 5.25. First, it is remarkable that the derivative of the stress in any of the shown cases sharply decreases at small stretches. This decrease has also been observed for further cut-off distances larger than $R^{\mathrm{ff}} = R^{\mathrm{pf}} = 1.01$. Hence, the decrease may be of systematic origin. Until $\lambda = 1.03$ the derivatives overlap. Beyond this stretch, that for $R^{\mathrm{ff}} = R^{\mathrm{pf}} = \infty$ continues approximately constant. The derivative in the case $R^{\mathrm{ff}} = \infty$ and $R^{\mathrm{pf}} = 1.1$ behaves analogously, but the derivatives are smaller. If the filler-filler bonds are cut off and the polymer-filler bonds are not breakable, i.e. $R^{\mathrm{ff}} = 1.1$ and $R^{\mathrm{pf}} = \infty$, the derivative decreases further until it levels off. This data set overlaps with the derivative in the case that both types of bonds are breakable, i.e. $R^{\mathrm{ff}} = R^{\mathrm{pf}} = 1.1$. Furthermore, the observations on the differences of the derivatives agree with the ones on the derivatives themselves. Thus, what is observable in the data for the model networks and identified with the Payne effect is rupture of filler-filler bonds. Nevertheless, the number of filler-filler bonds is higher than the number of polymer-filler bonds in the model network due to the construction. These results agree with those obtained by Viktorova *et al.* [38] and they indicate that the Payne effect is suppressed if the filler is finely dispersed because of fewer filler-filler bonds. Besides during continuous stretching of the model network, the broken polymer-filler bonds are not as likely to establish again because the distance between the cross-link and the filler rather increases further.

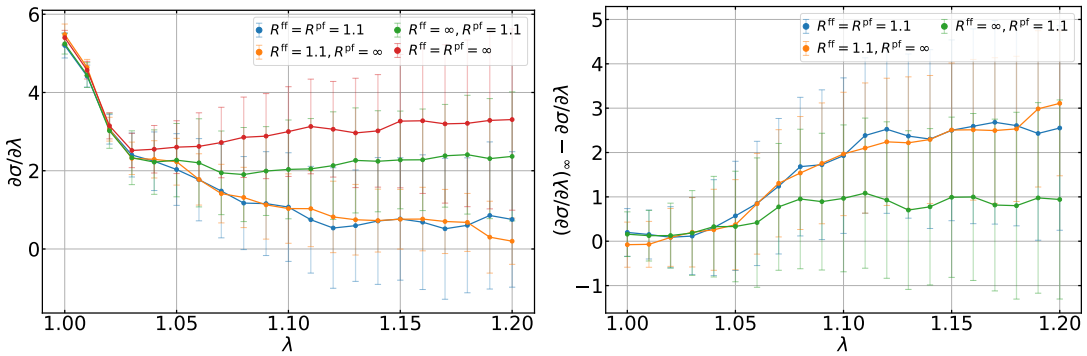

Figure 5.25.: $\partial\sigma/\partial\lambda$ and $(\partial\sigma/\partial\lambda)_\infty - \partial\sigma/\partial\lambda$ versus λ for 2D-networks with filler content $\phi = 0.9$ for variable cut-off radii R^{ff} and R^{pf}. The data points are connected for the eye, but this does not have any physical meaning.

Moreover, the derivative of the stress-stretch curve is investigated in order to check

whether the model includes stretch-independent contributions to the elastic modulus of filled elastomers which lead to reinforcement compared to unfilled networks. Figure 5.26 shows a plot of the derivative $\partial\sigma/\partial\lambda$ versus the stretch λ for different filler content ϕ. The error bars of the data are very large such that they do not allow for meaningful conclusions. For small filler content $\phi \leq 0.5$, there is no constant contribution to the derivative due to the inclusion of filler. However, if the filler content is increased, $\partial\sigma/\partial\lambda$ is significantly increased at small stretches. This effect occurs for $\phi \geq 0.5$, which is approximately the percolation threshold of the system. With increasing stretch, the derivative decreases. The decline of the derivative appears to become steeper with increasing filler content. Although this happens in a stretch range which is typical for the occurrence of the Payne effect, it cannot be identified with it but with a systematic phenomenon as discussed in the context of Figure 5.24. Beyond the decrease, the derivative approaches the derivative for the unfilled sample if the filler content is intermediately high, but it reaches a plateau for high filler content. The plateau emulates the expected constant contributions to the modulus of filled networks such as hydrodynamic reinforcement. Nevertheless, it rather originates from the parametrization of the bonds in the model network.

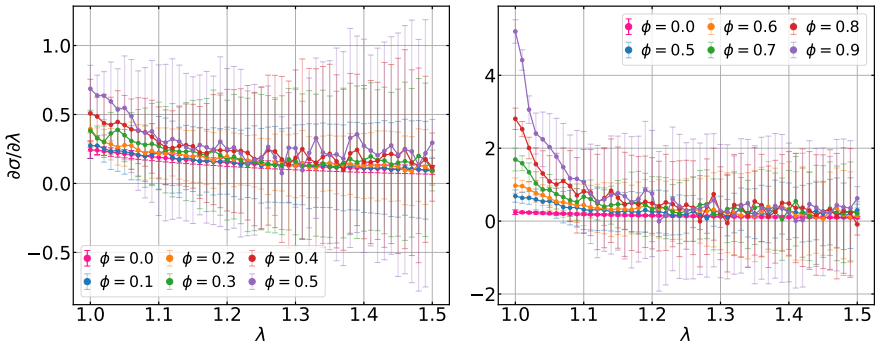

Figure 5.26.: $\partial\sigma/\partial\lambda$ versus λ for 2D-networks for variable filler content ϕ with $R^{\mathrm{ff}} = R^{\mathrm{pf}} = 1.1$. The data points are connected for the eye, but this does not have any physical meaning.

For the sake of completeness, it is also examined whether 3D-networks show the Payne effect. The differences of the derivatives $(\partial\sigma/\partial\lambda)_{\infty} - \partial\sigma/\partial\lambda$ are plotted in Figure 5.27 dependent on the stretch λ for variable filler content ϕ. Since a Payne-like effect has been observed in the 2D-case for $R^{\mathrm{ff}} = R^{\mathrm{pf}} = 1.1$, the cut-off radii are set to this value here. For small filler content $\phi \leq 0.6$, the Payne effect cannot be observed. However for $\phi = 0.5$, an approximately constant offset appears. For higher filler content, the difference shows an increase between $\lambda = 1.05$ and $\lambda = 1.1$ which indicates the Payne effect. In 2D, the filler content at which a Payne-like effect becomes observable approximately coincides with the percolation threshold of these networks. However in 3D, the threshold value of the filler content for the visibility of the increase is higher than the percolation threshold of these networks.

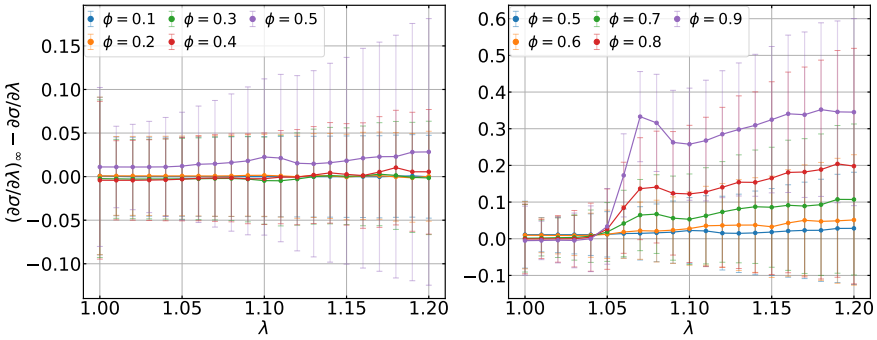

Figure 5.27.: $(\partial\sigma/\partial\lambda)_\infty - \partial\sigma/\partial\lambda$ versus λ for 3D-networks for variable filler content ϕ with $R^{\mathrm{ff}} = R^{\mathrm{pf}} = 1.1$. The data points are connected for the eye, but this does not have any physical meaning.

Moreover, it is examined which type of bonds cause the Payne-like effect in the case of 3D-networks. Procedure for this investigation is analogous to that followed in the 2D-case. Both the derivatives and the differences of the derivatives are plotted in Figure 5.28. As for the 2D-networks, a systematic decrease of the derivatives can be observed here. Beyond this decrease, the data for $R^{\mathrm{ff}} = R^{\mathrm{pf}} = \infty$ levels off and then tends to slightly incline. The data for $R^{\mathrm{ff}} = \infty$ and $R^{\mathrm{pf}} = 1.1$ features a dip at $\lambda = 1.06$ and overlaps with the data for $R^{\mathrm{ff}} = R^{\mathrm{pf}} = \infty$ again afterwards. The dip arises from rupture of polymer-filler bonds since the cut-off distance must be approached in this range of stretches. The data for $R^{\mathrm{ff}} = 1.1$ and $R^{\mathrm{pf}} = \infty$ and that for $R^{\mathrm{ff}} = R^{\mathrm{pf}} = 1.1$ overlap with each other also beyond the systematic decrease. This indicates that the filler-filler bonds dominate the behavior of the derivative for $R^{\mathrm{ff}} = R^{\mathrm{pf}} = 1.1$. The data steeply declines until a minimum with negative values of the derivative is reached at $\lambda = 1.07$. At this stretch, the extensions of the polymer-filler bonds and in particular the filler-filler bonds approach the cut-off distances. Afterwards, the data exhibits a local maximum before it behaves analogously to the other data sets.

The observations on the differences agree with the observations on the derivatives. The feature that the differences of the derivatives for $R^{\mathrm{ff}} = 1.1$ and $R^{\mathrm{pf}} = \infty$ and that for $R^{\mathrm{ff}} = R^{\mathrm{pf}} = 1.1$ increase and continue in a plateau larger zero validates the observation of a Payne-like effect which arises from the rupture of filler-filler bonds. This result is consistent with that for the 2D-networks.

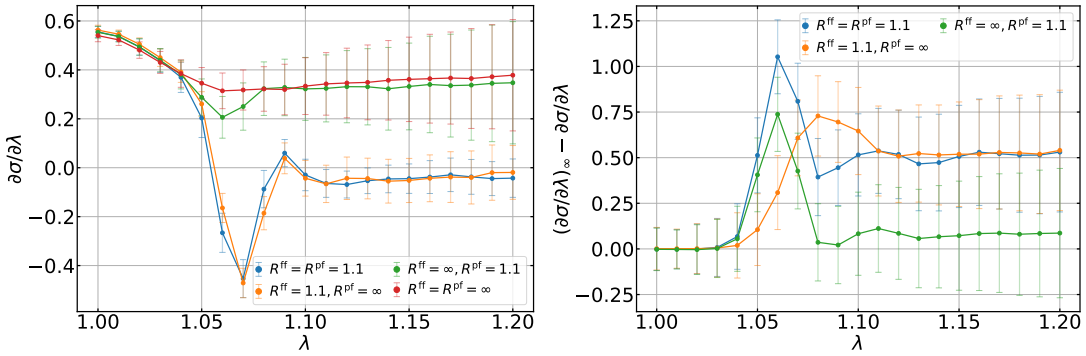

Figure 5.28.: $\partial\sigma/\partial\lambda$ and $(\partial\sigma/\partial\lambda)_\infty - \partial\sigma/\partial\lambda$ versus λ for 3D-networks with filler content $\phi = 0.9$ for variable cut-off radii R^{ff} and R^{pf}. The data points are connected for the eye, but this does not have any physical meaning.

5.4. Behavior of Filled Networks at Large Deformations

In the previous section, the mechanical behavior of filled network has been discussed at small deformations for which SIC does not occur. In this section, the stress-stretch curves of filled non-crystallizing model networks are investigated at larger deformations. The impact of the filler content and the filler dispersion is studied.

In Figure 5.29, stress-stretch curves of non-crystallizing 2D-networks containing variable filler content are depicted. The filler flocculated since the MG has been applied for $10 \cdot N$ MC steps. At small deformations and low filler content, the stress of the filled networks overlaps with the stress of an unfilled network. However, the stress is amplified at larger deformations by the inclusion of filler. As the filler content approaches the percolation threshold, the stress is already enhanced at small deformations. The occurrence of this strain-amplification effect caused by filler agrees with experimental observations. In the model networks, it is introduced by the parametrization of the spring constants of polymer-filler and filler-filler bonds. In addition, the stress appears to behave linearly at large deformations. Linear behavior is introduced by modeling polymer-filler and filler-filler bonds as harmonic springs.

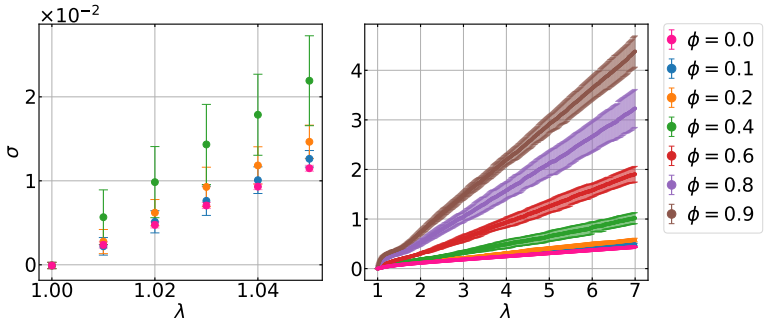

Figure 5.29.: Stress-stretch curves for stretching non-crystallizing 2D-networks consisting of $N = 5041$ nodes with variable filler content. The MG ran through $10 \cdot N$ MC steps. It has been set $R^{\mathrm{ff}} = R^{\mathrm{pf}} = 1.1$, $k^{\mathrm{ff}} = 5.0$, $k^{\mathrm{pf}} = 4.0$ and $k^{\mathrm{pf}}_{\mathrm{weak}} = 1.0$. The left panel shows an extract of the right at small deformations.

In order to analyze microscopic phenomena in these filled model networks further, Figure 5.30 is considered. The local stretch r/r_0 of the links is amplified compared to the macroscopic stretch λ. Simultaneously, the inclusion of filler promotes the extension of the links to end-to-end distances larger than their contour length, i.e. $r > n$, which can occur because finite chain extensibility is not included in the model. These effects enhance with increasing filler content, but they tend to saturate. Accordingly, the free energy density g/n of the links increases.

The fraction $L_{(r>n)}/L$ of links with end-to-end distances $r > n$ also increases with increasing filler content and increasing stretch. The onset of this phenomenon shifts towards smaller stretches. The fractions of reversibly weakened polymer-filler bonds and reversibly broken filler-filler bonds, i.e. $L_{\mathrm{pf,weak}}/L_{\mathrm{pf}}$ and $L_{\mathrm{ff,b}}/L_{\mathrm{ff}}$, increase with increasing filler content until $\phi = 0.6$ which is in the vicinity of the percolation threshold. For larger filler contents, the fraction of broken filler-filler bonds increases with filler content just for small stretches and, then, shows a kink. Beyond a cross-over region, the fraction of broken filler-filler bonds decreases with increasing filler content $\phi \geq 0.6$. At the maximum stretch, at least half of the filler-filler bonds are broken. In the 2D-networks simulated here, roughly half of the total number of links and bonds are oriented along the stretching direction. If the filler is ideally distributed over the network, none of the spatial directions is preferred and, thus, the orientation of the bonds

introduced due to the inclusion of filler must be equally distributed. Furthermore, the fraction of weakened polymer-filler bonds increases with increasing filler content until $\phi = 0.8$. The data for $\phi = 0.6$ and $\phi = 0.8$ converges at large stretch, while the data for $\phi = 0.9$ intersects the data for $\phi = 0.6$ and $\phi = 0.8$ such that the fraction of weakened polymer-filler bonds is smaller at maximum stretch for the maximum considered filler content. Analogous to broken filler-filler bonds, at least half of the polymer-filler bonds are weakened.

Apparently, the extension of polymer-filler and filler-filler bonds until softening or rupture, respectively, is preferred by the model networks over the extension of the links in particular at small deformations. Taking the parametrization into account, this minimizes the interaction energies. Nevertheless, more polymer-filler bonds are weakened compared to broken filler-filler bonds. At larger deformations, the extension of the links contributes even more. Above the percolation threshold of the filler, this effect is amplified. The extension of the links tends to be significantly preferred. A possible reason is that particularly the polymer-filler bonds have reached sufficiently large extension such that the energy is smaller if a link is extended further instead.

Regarding Figure 5.30, it must be remarked that the networks simulated here have been stretched only up to $\lambda_{\max} = 5.0$ instead of $\lambda_{\max} = 7.0$. The reason is that the occurrence of links with unphysical end-to-end distances $r > n$ is prevented for the unfilled case and limited for the filled networks. The occurrence of these end-to-end distances has been discussed further in [3].

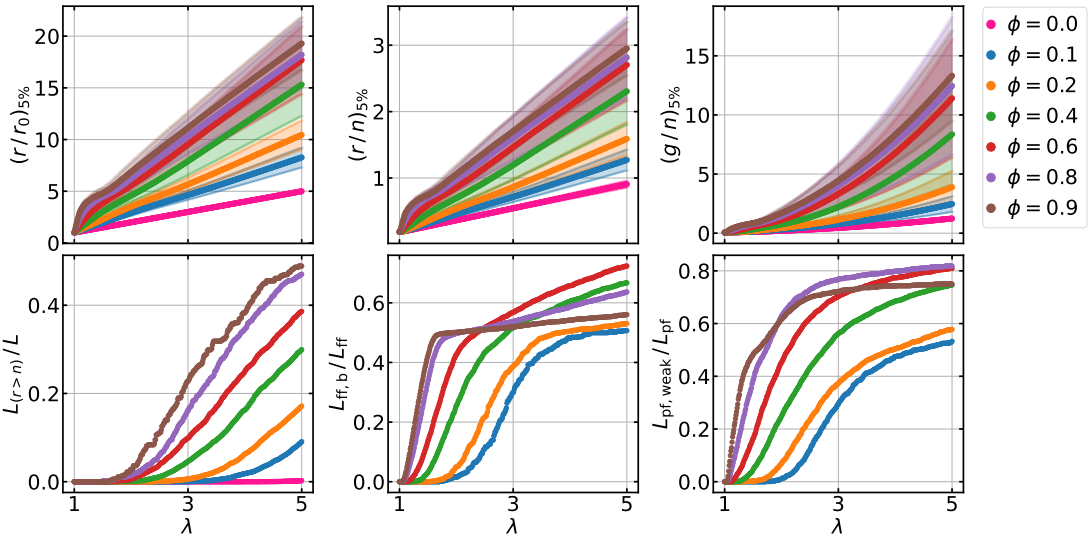

Figure 5.30.: Plots of stretch r/r_0, extension r/n, free energy density g/n of links versus the macroscopic stretch λ obtained as averages over the links with the top 5 % values in a non-crystallizing 2D-network consisting of $N = 5041$ nodes with filler content ϕ. The fraction $L_{(r>n)}/L$ of links with $r > n$, the fraction $L_{\mathrm{ff,b}}/L_{\mathrm{ff}}$ of reversibly broken filler-filler bonds and the fraction $L_{\mathrm{pf,weak}}/L_{\mathrm{pf}}$ of reversibly weakened polymer-filler bonds are also plotted versus the stretch λ. The MG was applied for $10 \cdot N$ MC steps and it has been set $R^{\mathrm{ff}} = R^{\mathrm{pf}} = 1.1$, $k^{\mathrm{ff}} = 5.0$, $k^{\mathrm{pf}} = 4.0$ and $k^{\mathrm{pf}}_{\mathrm{weak}} = 1.0$, i.e. the networks are configured analogously to those considered in Figure 5.29.

Analogously to Figure 5.29, stress-curves of non-crystallizing 2D-networks are plotted in Figure 5.31, but the filler is finely dispersed, i.e. randomly distributed since the MG not been applied, in this case. The stress is more amplified compared to the case of flocculated filler. A possible explanation is that the number of polymer-filler bonds is increased and this type of bonds can just weaken but not break. In contrast, if the

filler is flocculated, there are more filler-filler bonds which can break.

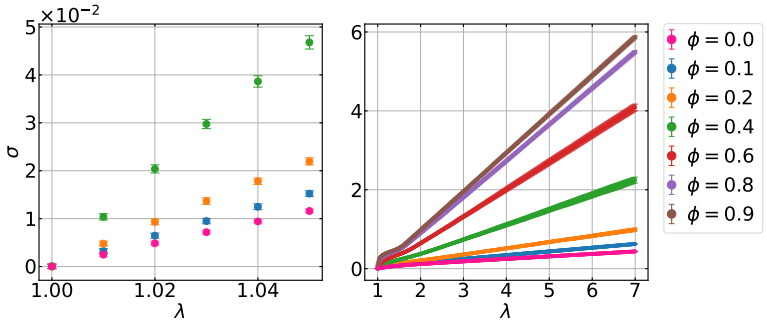

Figure 5.31.: Stress-stretch curves for stretching non-crystallizing 2D-networks consisting of $N = 5041$ nodes with variable filler content. The filler is randomly distributed. It has been set $R^{\mathrm{ff}} = R^{\mathrm{pf}} = 1.1$, $k^{\mathrm{ff}} = 5.0$, $k^{\mathrm{pf}} = 4.0$ and $k^{\mathrm{pf}}_{\mathrm{weak}} = 1.0$. The left panel shows an extract of the right at small deformations.

In Figure 5.32, corresponding data concerning the properties of the links is plotted. The observations for $\phi \leq 0.4$ are similar to the case of flocculated filler. The comparison of the exact values of these quantities for the different filler dispersions is not highly diagnostic because these values belong to a specific network configuration. However, the comparison shows trends and indicates the possibly different effect of the filler loading.

For $\phi = 0.6$, the stretch, the extension and the free energy density nearly overlap with the date for $\phi = 0.4$. Additionally, the fraction $L_{\mathrm{pf,weak}}/L_{\mathrm{pf}}$ of reversibly weakened polymer-filler bonds converges with the data for $\phi = 0.4$ at large stretches. The fraction $L_{(r>n)}/L$ of links with $r > n$ is still increased compared to the data for smaller filler content. The fraction $L_{\mathrm{ff,b}}/L_{\mathrm{ff}}$ of reversibly broken filler-filler bonds intersects the data for $\phi = 0.4$ and is reduced compared to that at large deformations.

For $\phi \geq 0.6$ or above the percolation threshold, the stretch, the extension and the free energy density are decrease with increasing filler content. Simultaneously, the fractions of weakened polymer-filler and broken filler-filler bonds at maximum stretch decrease with increasing filler content. For $\phi = 0.8$ and $\phi = 0.9$, the data also shows a cross over. In particular for $\phi = 0.9$, the fraction of weakened polymer-filler bonds and broken filler-filler bonds shows a plateau at large deformations. Nevertheless, the fraction of links with $r > n$ still increases with increasing filler content and with increasing stretch.

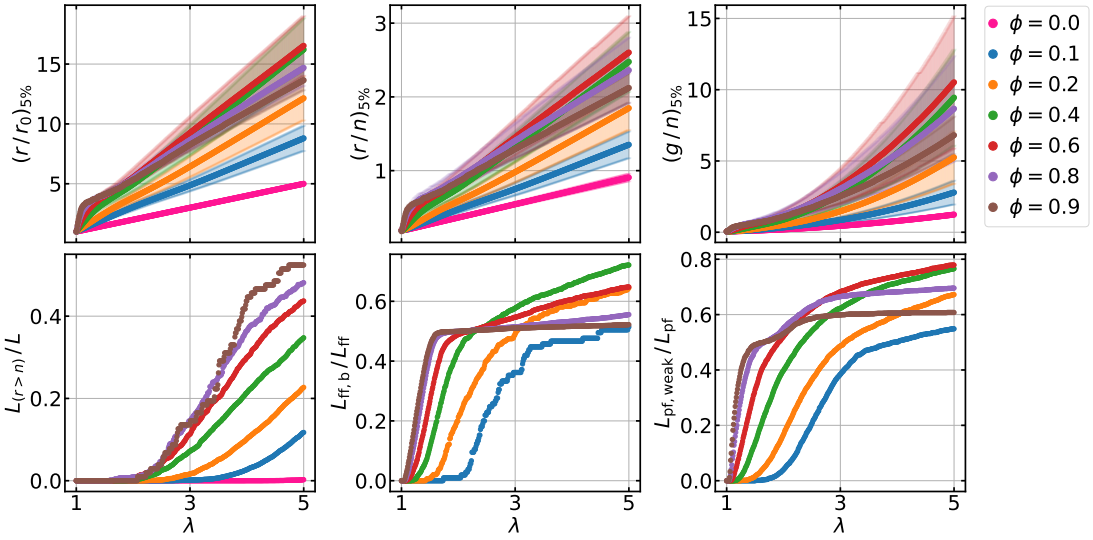

Figure 5.32.: Plots of stretch r/r_0, extension r/n, free energy density g/n of links versus the macroscopic stretch λ obtained as averages over the links with the top 5 % values in a non-crystallizing 2D-network consisting of $N = 5041$ nodes with filler content ϕ. The fraction $L_{(r>n)}/L$ of links with $r > n$, the fraction $L_{\mathrm{ff,b}}/L_{\mathrm{ff}}$ of reversibly broken filler-filler bonds and the fraction $L_{\mathrm{pf,weak}}/L_{\mathrm{pf}}$ of reversibly weakened polymer-filler bonds are also plotted versus the stretch λ. The filler is randomly distributed and it has been set $R^{\mathrm{ff}} = R^{\mathrm{pf}} = 1.1$, $k^{\mathrm{ff}} = 5.0$, $k^{\mathrm{pf}} = 4.0$ and $k^{\mathrm{pf}}_{\mathrm{weak}} = 1.0$, i.e. the networks are configured analogously to those considered in Figure 5.31.

In Figure 5.33, snapshots of non-crystallizing 2D-networks with flocculated and finely dispersed filler are depicted. The filler content $\phi = 0.2$ is below the percolation threshold, while $\phi = 0.8$ is located above. For $\phi = 0.2$ and $\lambda = 1.5$, polymer-filler bonds oriented perpendicularly to the stretching direction are weakened, in particular for the lumpy filler dispersion. However, polymer-filler bonds aligned with the stretching direction attach the cross links to the filler nodes. The filler-filler bonds bind the filler particles tightly to each other for both dispersions. The macroscopic stretch appears to be mainly applied to the links. These phenomena enhance with increasing stretch for both filler dispersions at $\phi = 0.2$. Cross links located in the vicinity of filler particles and aggregates concentrate around them and links situated between filler particles and oriented along the stretching direction are further extended.

For flocculated filler with $\phi = 0.8$ and at $\lambda = 1.5$, regions of filler nodes located between two domains of polymer along the stretching direction are compressed due to the extension of the links. The remaining filler-filler bonds which are aligned with the stretching direction already broke. This phenomenon advances as the stretch increases. The cross links connected to filler by polymer-filler bonds are tightly bound. For finely dispersed filler, filler nodes which are tightly bound to each other due to the extension of links are more distributed over the network according to the filler morphology. In particular at large deformations, a large number of polymer-filler bonds is also stretched such that these bonds weaken even if they are aligned perpendicularly to the stretching direction. Weakening of polymer-filler bonds is apparently promoted by stronger bonds which are located in their vicinity and preferentially not further extended. These observations explain the behavior of the fraction of weakened polymer-filler bonds discussed in the context of Figure 5.30 and Figure 5.32, particularly with respect to the fraction of broken filler bonds.

Moreover, the links apparently determine the stress-stretch relation for $\phi = 0.2$, while the linear behavior of the filler-filler bonds dominates the stress-stretch behavior for $\phi =$

0.8. The stress-stretch curves show a small hysteresis which is attributed to weakening and breaking of polymer-filler and filler-filler bonds respectively. The hysteresis appears to be more pronounced for randomly distributed filler than for flocculated filler.

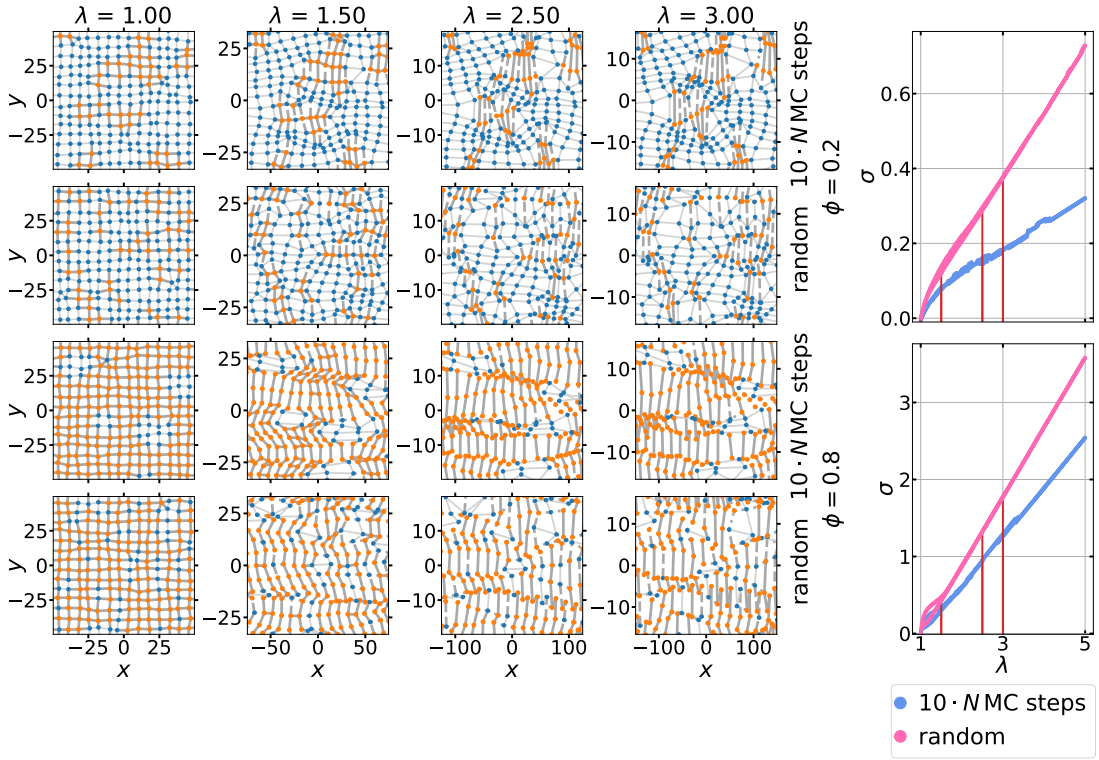

Figure 5.33.: Snapshots of extracts of non-crystallizing 2D-networks consisting of $N = 5041$ nodes containing different filler content ϕ with different filler dispersion. The stretching direction is the x-axis. Each column corresponds to a certain stretch λ during stretching and the plots share the x-axis. The corresponding stress-stretch curves for entire strain cycles are also plotted. The blue dots represent cross links and the orange dots represent filler. Links are indicated as lightgrey straight lines, while the other bonds are drawn in darkgrey if they are not weakened or broken. Weakened polymer-filler bonds are indicated by dashed lines and broken filler-filler bonds are not drawn.

In order to quantify the stress amplification effect of filler in non-crystallizing 2D-networks further, the so-called stress amplification factor is computed according to Equation 2.21. For this purpose, the stress of a network containing filler content ϕ is plotted against the corresponding stress of the unfilled network at each stretch. For lumpy and finely dispersed filler, this is depicted in Figure A.26 and in Figure A.27 respectively. In the interval $\lambda \in [2.0, 3.0]$, the a linear function is fitted to the data and its slope yields the corresponding stress-amplification factors. The fit parameters are compiled in Table A.4 and in Table A.5 respectively.

In Figure 5.34, the stress-amplification factors are plotted versus the filler content ϕ and fitted with the Guth-Gold relation

$$A_\sigma = A_0 + A_1\phi + A_2\phi^2. \tag{5.6}$$

This is according to the procedure employed by Trabelsi *et al.* [18] to experimental data for CB-filled NR. Their fit parameters are compiled in Table 5.8.

Table 5.8.: Parameters for fits of the Guth-Gold relation according to Equation 5.6 obtained by Trabelsi *et al.* [18] for CB-filled NR.

A_0	A_1	A_2
1	3.886	54.4968

The data for flocculated filler is well described by the Guth-Gold relation. Nevertheless, the reduced χ^2-value amounts to $\chi^2/ndf = 224.71$ which is larger than the ideal value of 1.0 because of the comparatively small errors of the data points which result from the small uncertainties of the underlying linear fits. The dimension of the considered networks, which determines the percolation threshold of the model, is one reason why the curve appears to be stretched along the ϕ-axis compared to that by Trabelsi *et al.* [18]. In addition, the values of the stress-amplification factors up to the percolation threshold are smaller.

The Guth-Gold relation does not fit the data for finely dispersed filler. The reduced χ^2-value $\chi^2/ndf = 2029.54$ is significantly too large. The data rather possesses a *s*-like shape. The Guth-Gold relation could be a good approximation up to the percolation threshold of $\phi = 0.5$ at which the data shows a transition. The region beyond coincides with the filler contents for which the fractions of weakened polymer-filler bonds and of broken filler-filler bonds show a kink and decrease with increasing filler content at sufficiently large stretch which lays in the considered interval. Comparing Figure 5.30 and Figure 5.32 again shows in particular a change of the behavior of the fraction of weakened polymer-filler bonds. This observation suggests that this bond type is crucial for stress amplification in the model networks.

The stress-amplification factors for finely dispersed filler are larger than for flocculated filler. The difference enlarges at intermediate filler contents. The composition of the total number of links and bonds depending on filler content for both considered filler dispersions is depicted in Figure 5.35. The number of polymer-filler bonds which can weaken but do not break is larger in the case of finely dispersed filler since the interface is reduced if the filler flocculates. If the filler content in the case of randomly distributed filler becomes sufficiently large, a threshold value must occur beyond which the number of polymer-filler bonds is not further increased in order to optimize filler reinforcement by finely dispersed filler compared to flocculated filler because larger aggregates, agglomerates or a network form. Here, this threshold appear to be in the vicinity of the percolation threshold. For flocculated filler, the number of polymer-filler bonds does not show such a strong dependence on the filler content. The amount of filler-filler bonds is rather increased with increasing filler content at the expense of links. Nevertheless, links in a filler reinforced network rather contribute to its strength because at large filler content they are further extended, while filler-filler bonds either bind filler nodes tightly to each other or break. Altogether, these observations indicate that the polymer-filler bonds dominate filler reinforcement of the model networks.

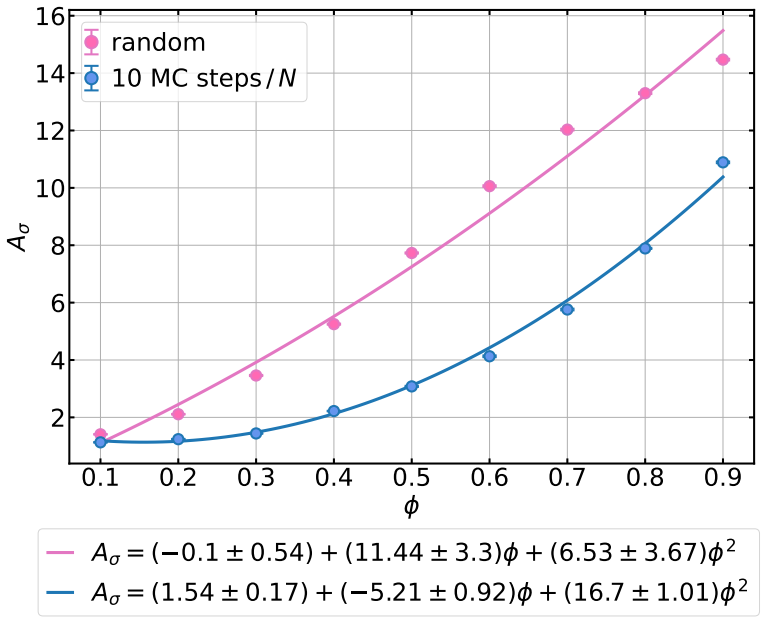

Figure 5.34.: Stress amplification factor A_σ versus filler content ϕ for non-crystallizing 2D-networks consisting of $N = 5041$ nodes for different filler morphologies, i.e. randomly dispersed filler and application of the MG for 10 MC steps/ N. The data is fitted according to the relation by Guth and Gold given in Equation 5.6.

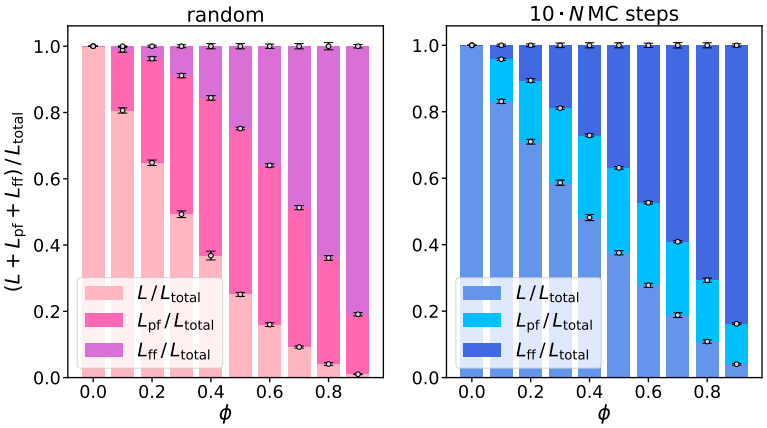

Figure 5.35.: Composition the total number of links and bonds L_{total} of 2D-model networks. The fractions of links L, polymer-filler bonds L_{pf} and filler-filler bonds L_{ff} are shown depending on the filler content ϕ. The data are obtained as averages from 10 independent networks consisting of $N = 5041$ nodes. The dots highlight the contribution of each connection type and their error bars indicate the corresponding standard deviations.

As a next step, non-crystallizing 3D-networks are investigated analogously to the 2D-case. In Figure 5.36, stress-stretch curves for networks containing flocculated filler are depicted. For small filler content $\phi \leq 0.2$, the stress-stretch data overlaps, in particular at small deformations. The stress of the networks with $\phi = 0.1$ even tends to be smaller than for the unfilled network. However, for larger deformations and in particular larger filler content, the stress is amplified by the inclusion of filler and the effect enhances with increasing filler content. This observation agrees with those for 2D-networks and with experimental observations. For the 3D-networks, the percolation threshold is located approximately between $\phi = 0.3$ and $\phi = 0.4$. Therefore, the stress-amplification effect

appears to be related to the percolation phenomenon.

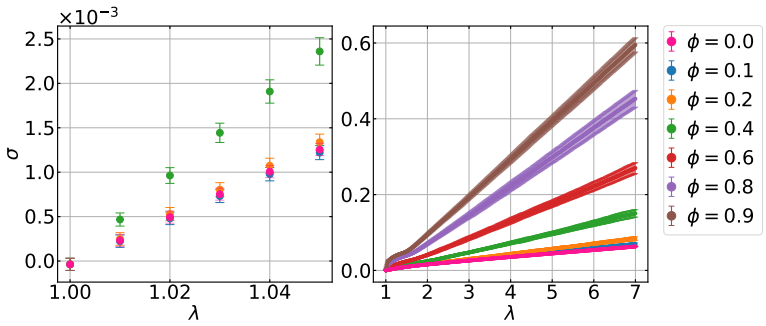

Figure 5.36.: Stress-stretch curves for stretching non-crystallizing 3D-networks consisting of $N = 5832$ nodes with variable filler content ϕ. The MG ran through $50 \cdot N$ MC steps. It has been set $R^{\mathrm{ff}} = R^{\mathrm{pf}} = 1.1$, $k^{\mathrm{ff}} = 5.0$, $k^{\mathrm{pf}} = 4.0$ and $k^{\mathrm{pf}}_{\mathrm{weak}} = 1.0$. The left panel shows an extract of the right at small deformations.

In Figure 5.37, data describing the microscopic properties of the links and bonds is plotted. As in the 2D-case, the simulated network has been stretched only up to $\lambda_{\mathrm{max}} = 5.0$ now to impede the occurrence of unphysical end-to-end distances $r > n$ of the links. In contrast to the 2D-case, the stretches, extensions and free energy densities for $\phi = 0.6$ overlap with those for $\phi = 0.4$. The same occurs for $\phi = 0.8$ and $\phi = 0.9$. Moreover, for $\phi = 0.1$, the fractions of broken filler-filler bonds and weakened polymer-filler bonds show a kink as links are extended higher then their contour length. In the 2D-case, this coincidence is not pronounced. Nevertheless, an useful improvement of the model must be the introduction of finite extensibility of the links. The fraction of links with end-to-end distances $r > n$ appears to approach $1/3$ at high filler content and large deformations. This fractions would correspond to the ideal fraction of links oriented along the stretching direction in the 3D-networks. Thus, the links oriented along the stretching direction must be highly extended in agreement with the observations in the snapshots of 2D-networks presented in Figure 5.33. For the remaining bond types, their alignment appears to be not of primary importance for their weakening or breaking. In addition, the comparatively steep incline of the fraction of broken filler-filler bonds at small deformations indicates their importance for the Payne effect. Besides, the other observations which can be made regarding Figure 5.37 are analogous to the 2D-case presented in Figure 5.30.

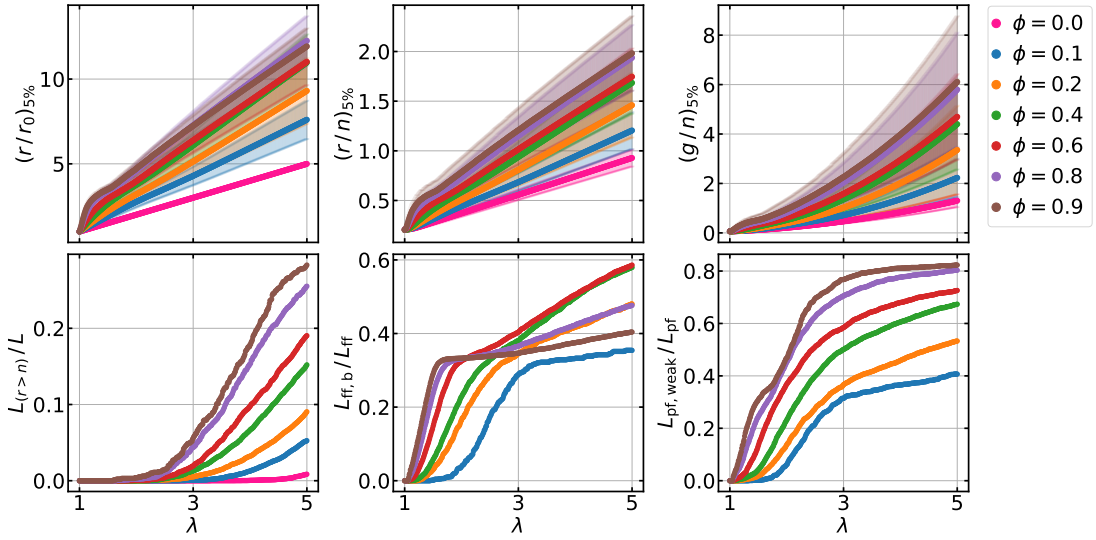

Figure 5.37.: Plots of stretch r/r_0, extension r/n, energy density g/n of links versus the macroscopic stretch λ obtained as averages over the links with the top 5 % values in a non-crystallizing 3D-network consisting of $N = 5832$ nodes with filler content ϕ. The fraction $L_{(r>n)}/L$ of links with $r > n$, the fraction $L_{\mathrm{ff,b}}/L_{\mathrm{ff}}$ of reversibly broken filler-filler bonds and the fraction $L_{\mathrm{pf,weak}}/L_{\mathrm{pf}}$ of reversibly weakened polymer-filler bonds are also plotted versus the stretch λ. The MG was applied for $50 \cdot N$ MC steps and it has been set $R^{\mathrm{ff}} = R^{\mathrm{pf}} = 1.1$, $k^{\mathrm{ff}} = 5.0$, $k^{\mathrm{pf}} = 4.0$ and $k^{\mathrm{pf}}_{\mathrm{weak}} = 1.0$, i.e. the networks are configured analogously to those considered in Figure 5.36.

Figure 5.38 shows stress-stretch curves of non-crystallizing 3D-networks containing different content of finely dispersed filler. The stress-amplification effect of the filler is enhanced compared to flocculated filler. In particular, the stress is already amplified at small stretches by small content of finely dispersed filler.

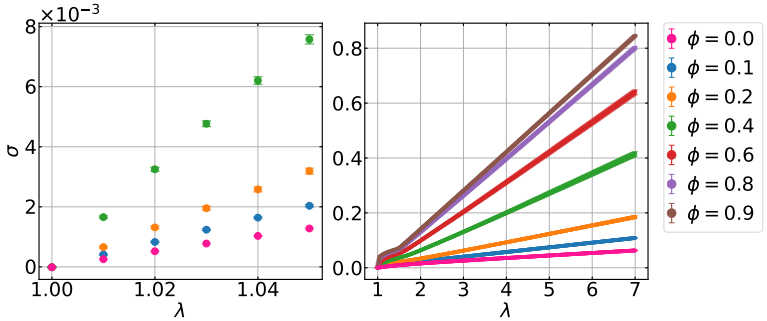

Figure 5.38.: Stress-stretch curves for stretching non-crystallizing 3D-networks consisting of $N = 5832$ nodes with variable filler content ϕ. The filler is randomly distributed. It has been set $R^{\mathrm{ff}} = R^{\mathrm{pf}} = 1.1$, $k^{\mathrm{ff}} = 5.0$, $k^{\mathrm{pf}} = 4.0$ and $k^{\mathrm{pf}}_{\mathrm{weak}} = 1.0$. The left panel shows an extract of the right at small deformations.

In Figure 5.39, information about the links in non-crystallizing 3D-networks containing finely dispersed filler is plotted. The stretches, extensions and free energy densities of the networks with $\phi \geq 0.4$ lay close together and nearly overlap, while, for smaller filler content, these quantities are amplified with increasing filler content. This observation is possibly related to percolation. In addition, the fractions of links with end-to-end distances $r > n$ and of broken filler-filler bonds overlap for $\phi = 0.8$ and $\phi = 0.9$. The fraction of broken filler-filler bonds decreases with increasing filler content for $\phi \geq 0.4$ at larger stretch beyond a cross over region. For $\phi = 0.8$ and $\phi = 0.9$,

the values become even smaller than for $\phi = 0.1$. They saturate at approximately 1/3 which corresponds to the fraction of filler-filler bonds that are ideally aligned with the stretching direction. The data for $\phi = 0.4$ overlaps with that for $\phi = 0.2$ above the cross over. The fractions of weakened polymer-filler bonds show two kinks. First, they level off and, then, they increase again until they appear to saturate if the networks were deformed further, except for the case $\phi = 0.1$. This has not been observed for flocculated filler and is not as pronounced in the corresponding 2D-case. In contrast to the case of flocculated filler, the fraction of weakened polymer-filler bonds at large stretches decreases with increasing filler content for $\phi \geq 0.6$.

Since the 2D- and the 3D-case are very similar and since it is difficult to visualize 3D-networks, snapshots of them will not be considered here.

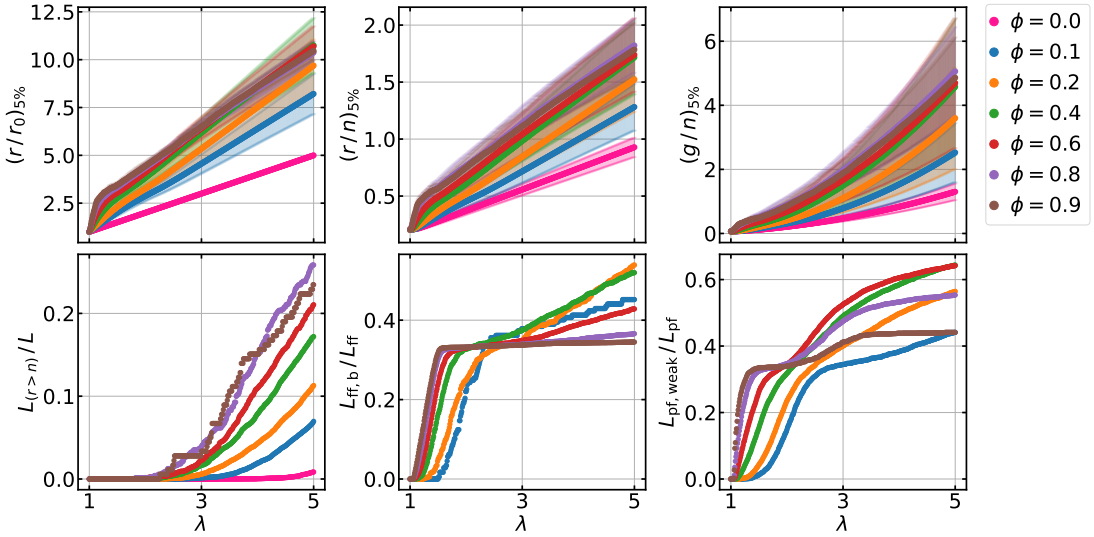

Figure 5.39.: Plots of stretch r/r_0, extension r/n, energy density g/n of links versus the macroscopic stretch λ obtained as averages over the links with the top 5 % values in a non-crystallizing 3D-network consisting of $N = 5832$ nodes with filler content ϕ. The fraction $L_{(r>n)}/L$ of links with $r > n$, the fraction $L_{\mathrm{ff,b}}/L_{\mathrm{ff}}$ of reversibly broken filler-filler bonds and the fraction $L_{\mathrm{pf,weak}}/L_{\mathrm{pf}}$ of reversibly weakened polymer-filler bonds are also plotted versus the stretch λ. The filler is randomly distributed and it has been set $R^{\mathrm{ff}} = R^{\mathrm{pf}} = 1.1$, $k^{\mathrm{ff}} = 5.0$, $k^{\mathrm{pf}} = 4.0$ and $k^{\mathrm{pf}}_{\mathrm{weak}} = 1.0$, i.e. the networks are configured analogously to those considered in Figure 5.38.

In analogy to the 2D-case, the stress-amplification factors are computed now for further quantification. The stress-amplification factors are derived from the linear fits to the data shown in Figure A.28 and Figure A.29 with their parameters given in Table A.6 and Table A.7 for flocculated and finely dispersed filler respectively. They are plotted in Figure 5.40 and the Guth-Gold relation according to Equation 5.6 is fitted.

The data for flocculated filler is well described by the Guth-Gold relation. However, the reduced χ^2-value $\chi^2/ndf = 51.39$ is larger than the ideal value of 1.0 due to the small errors of the data points. The curve is stretched along the ϕ-axis compared to that obtained by Trabelsi *et al.* [18] for CB-filled NR and the amplification effect of the filler appears to be weaker.

For finely dispersed filler, the Guth-Gold relation does not fit the data well. This is also indicated by the reduced χ^2-value $\chi^2/ndf = 895.72$ which is too large. The observations made here are similar to the 2D-case. The data may be described by the Guth-Gold relation up to approximately $\phi = 0.3$ which is in the vicinity of the

percolation threshold, but here are too few data points in this region for a definite conclusion regarding that. For larger filler content, the stress-amplification factor appears to increase more flat.

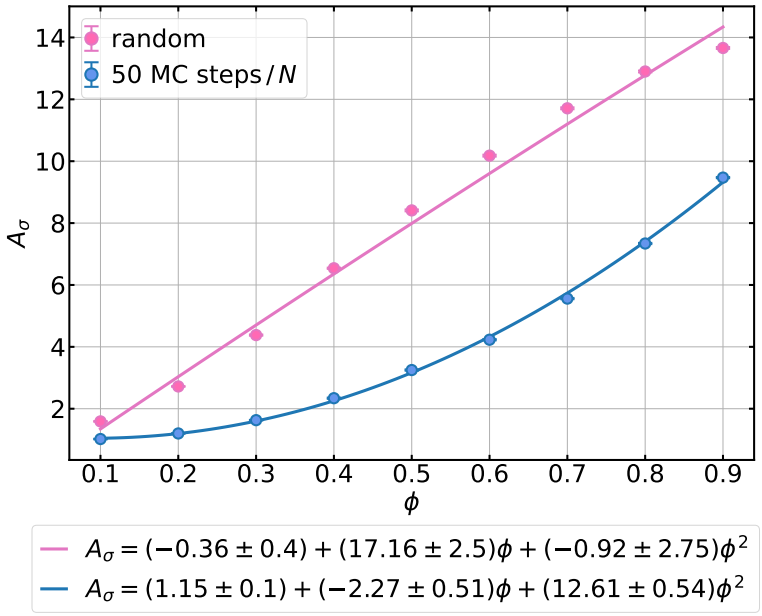

Figure 5.40.: Stress amplification factor A_σ versus filler content ϕ for non-crystallizing 3D-networks consisting of $N = 5832$ nodes for different filler morphologies, i.e. randomly dispersed filler and application of the MG for 50 MC steps$/N$. The data is fitted according to the relation by Guth and Gold given in Equation 5.6.

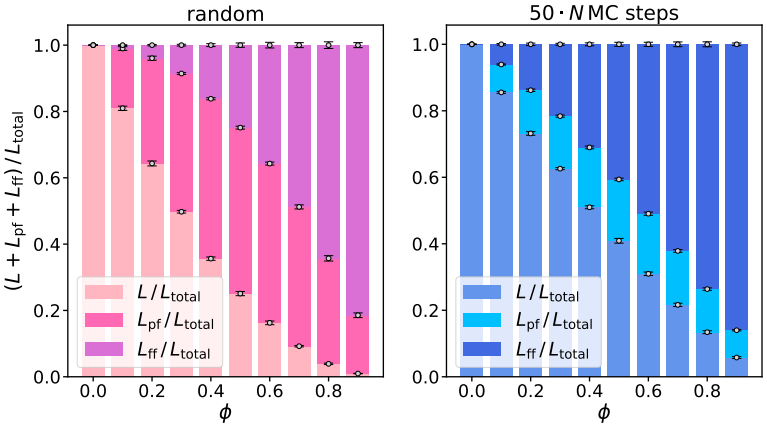

Figure 5.41.: Composition the total number of links and bonds L_{total} of 3D-model networks. The fractions of links L, polymer-filler bonds L_{pf} and filler-filler bonds L_{ff} are shown depending on the filler content ϕ. The data are obtained as averages from 10 independent networks consisting of $N = 5832$ nodes. The dots highlight the contribution of each connection type and their error bars indicate the corresponding standard deviations.

In Figure 5.41, the composition of the total number of links and bonds of the 3D-networks is illustrated for both considered filler dispersions and variable filler content. Analogously to the 2D-case, the variation of the fraction of polymer-filler bonds is smaller in the case of flocculated filler than for finely dispersed filler. Additionally, the fraction of polymer-filler bonds increases up to a certain filler content and decreases afterwards. This filler content appears to be slightly larger than the percolation thresh-

old. However, this is a possible explanation for the behavior of the stress-amplification factor depending on the filler content. The polymer-filler bonds deliver an important contribution to the strength of the model networks because they only weaken but do not break compared to filler-filler bonds. However, the reduction of the fraction of links compensates the reinforcing effect to a comparatively small extend.

Altogether, stress amplification due to the inclusion of filler particles into the model networks can be observed in the 2D- and in the 3D-case. This effect is enhanced if the filler content is increased. In addition, stress amplification is advanced if the filler is finely dispersed because of the increased number of polymer-filler bonds. However, for coarsely dispersed filler, the stress-amplification factor is well described by a Guth-Gold relation, but this does not hold for finely dispersed filler. Furthermore, snapshots of the 2D-networks have shown that the filler particles are tightly bound in aggregates, whereas extension of the links located between these aggregates is promoted.

5.5. Effect of Filler on Strain-Induced Crystallization

In the previous section, the stress amplification due to the inclusion of filler into non-crystallizing 2D- and 3D-networks has been studied for coarsely and finely dispersed filler. In this section, the effect of filler content and filler dispersion on strain-induced crystallization (SIC) and the accompanying mechanical behavior is investigated.

First, flocculated filler is considered, i.e. the MG has been applied for $10 \cdot N$ MC steps in the 2D-case. Figure 5.42 depicts snapshots and corresponding stress-stretch and crystallinity-stretch curves of crystallizing 2D-networks containing a fraction $\phi = 0.2$ of filler. The first links which crystallize are located adjacent to filler aggregates. With increasing stretch, neighboring links of those which are already semi-crystalline crystallize. As SIC continues, crystalline planes emerge perpendicularly to the stretching direction. These structures have also been observed for the unfilled network shown in Figure A.30 which has also been deformed up to $\lambda_{\max} = 5.0$. The semi-crystalline planes are situated between filler aggregates along the direction of the deformation. Crystalline strands traverse the network at the maximum applied stretch due to strain amplification. In the corresponding unfilled network presented in Figure A.30, this phenomenon does not occur because the maximum applied stretch is too small. Nevertheless, it is visible for larger stretches in Figure 5.4 and also for $\phi = 0.1$ at $\lambda_{\max} = 5.0$ which is shown in Figure A.31. Besides, the formation of crystalline strands which traverse the network is prohibited if the filler content is increased such that links do not percolate anymore. This is indicated in Figure A.32. During recovery, in contrast to the unfilled case, the crystallites melt in reverse order with respect to the stretching process here, but a link remains highly crystalline until melting of crystalline segments in this particular link starts.

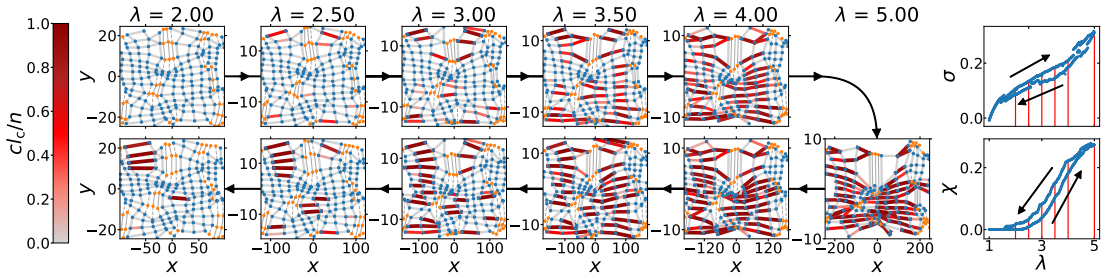

Figure 5.42.: Snapshots of a crystallizing 2D-network which consists of $N = 196$ nodes with filler content $\phi = 0.2$ at certain stretches λ during a strain cycle. The MG ran through $10 \cdot N$ MC steps. It has been set $R^{\mathrm{ff}} = R^{\mathrm{pf}} = 1.1$, $k^{\mathrm{ff}} = 5.0$, $k^{\mathrm{pf}} = 4.0$ and $k^{\mathrm{pf}}_{\mathrm{weak}} = 1.0$. The upper row represents the stretching process, while the lower row shows the contraction of the network. Each column corresponds to a specific stretch such that the plots share the x-axis. The direction of the deformation is along the x-axis. The scaling of the axes mimics the volume conservation. The blue dots stand for the cross links, while the orange dots represent filler. The crystallinity cl_{c}/n of each link is indicated according to the color bar. Links which cross the boundaries due to the periodic boundary conditions are not drawn. Moreover, the corresponding stress-stretch and crystallinity-stretch curves are depicted, where the vertical red lines mark the stretches at which the snapshots have been taken. The black arrows expose stretching and contraction of the network.

In Figure 5.43, stress-stretch and crystallinity-stretch curves are plotted for stretching of crystallizing 2D-networks containing variable fractions of flocculated filler. The stress is amplified like in the non-crystallizing case and the onset of SIC is shifted towards smaller stretches due to the inclusion of filler. The plateau of the stress which forms at the onset of SIC in the unfilled case vanishes as filler is included into the networks. These observations agree with experimental observations for filled NR. However, the stress does not steeply increase at large deformations as it is expected due to strain-hardening. For the unfilled network, the maximum applied stretch is to small. For filled networks, linear forces apparently dominate the stress-stretch behavior. Another reason is that finite chain extensilibility is not considered in the model which mainly causes the increase of the stress of real polymer chains. Furthermore, for $\phi = 0.4$, the crystallinity appears to saturate at the maximum stretch, but the approached value is smaller than 0.5 which would mean that, in the ideal case, all of the links oriented along the stretching direction are fully crystalline.

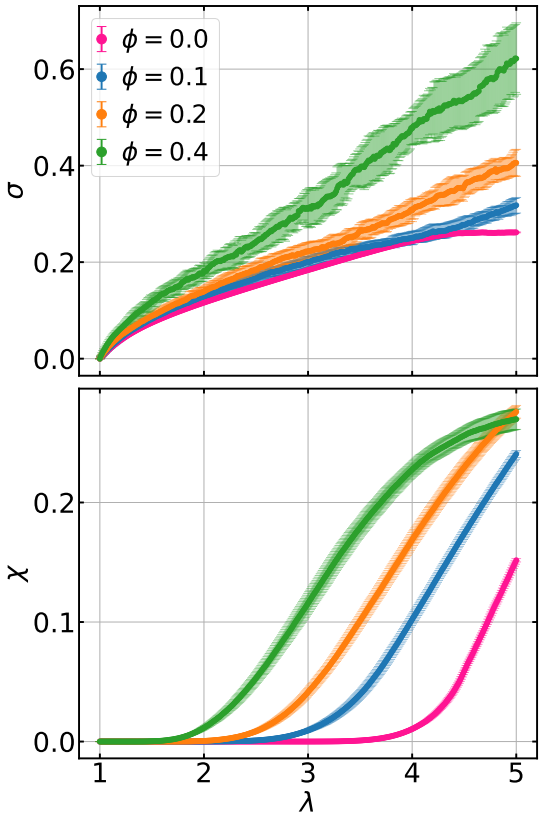

Figure 5.43.: Stress-stretch and crystallinity-stretch curves for stretching crystallizing 2D-networks consisting of $N = 5041$ nodes with variable filler content ϕ. The MG ran through $10 \cdot N$ MC steps. It has been set $R^{\mathrm{ff}} = R^{\mathrm{pf}} = 1.1$, $k^{\mathrm{ff}} = 5.0$, $k^{\mathrm{pf}} = 4.0$ and $k^{\mathrm{pf}}_{\mathrm{weak}} = 1.0$.

In Figure 5.44, the stress-stretch and crystallinity-stretch curves are depicted for entire strain cycles. For each filler content, the stress-stretch curves for both the crystallizing and the corresponding non-crystallizing case are plotted together. For $\phi = 0.1$, the crystallizing networks are softened by the onset of SIC. A plateau which is shorter than in the unfilled case can be observed. This is consistent with experimental observations. In addition, the hysteresis appears to be tighter than in the unfilled case. These phenomena are promoted for $\phi = 0.2$. Additionally, softening of the networks is not pronounced. At large stretches, the stress of the crystallizing networks becomes larger than that for the corresponding non-crystallizing networks. For $\phi = 0.4$, there may be a tendency for the formation of a plateau of the stress at the onset of SIC, but it is not significant. For larger filler contents, the plateau cannot be observed. For $\phi \geq 0.4$, the stress of the crystallizing and corresponding non-crystallizing networks approximately overlap. The hysteresis of the stress already vanishes for $\phi = 0.4$. Although it apparently tightens with increasing filler content, it remains visible for the crystallinity until $\phi = 0.8$. For $\phi = 0.4$ and $\phi = 0.6$, the crystallinity appears to converge to a value close to 0.3. For larger filler content, this value is reached approximately between $\lambda = 3.5$ and $\lambda = 4.0$ and the crystallinity decreases beyond. This is contrary to the expectations since increasing stretch must promote SIC.

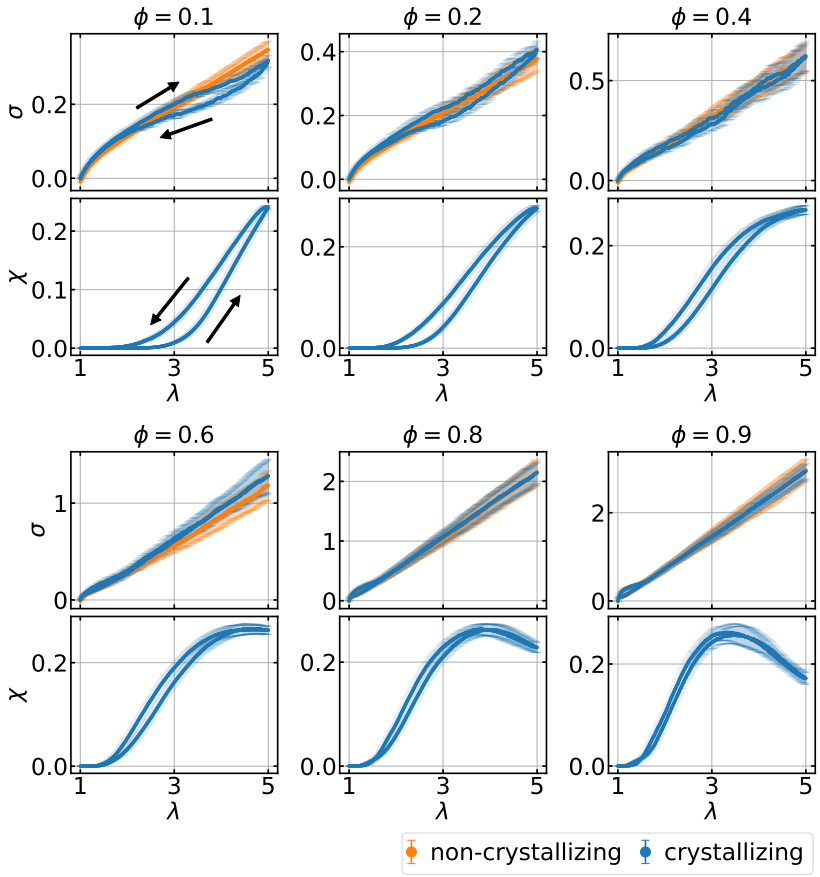

Figure 5.44.: Stress-stretch and crystallinity-stretch curves for a deformation cycle of crystallizing 2D-networks consisting of $N = 5041$ nodes with variable filler content ϕ. The MG ran through $10 \cdot N$ MC steps. It has been set $R^{\mathrm{ff}} = R^{\mathrm{pf}} = 1.1$, $k^{\mathrm{ff}} = 5.0$, $k^{\mathrm{pf}} = 4.0$ and $k^{\mathrm{pf}}_{\mathrm{weak}} = 1.0$. Stress-stretch curves are for corresponding non-crystallizing networks are also plotted. The arrows in the upper left plot indicate stretching and contraction.

Figure 5.45 shows the top-5 % values of the stretch, the extension and the free energy density of the links dependent on the stretch as well as the fraction of links with end-to-end distances $r > n$, the fraction of broken filler-filler bonds and the fraction of weakened polymer-filler bonds for variable filler content.

Regarding the decrease of the crystallinity with increasing stretch mentioned above in the context of Figure 5.44, it appears like the maximum of the crystallinity is located at the stretch at which the fraction of links with end-to-end distances $r > n$ exceeds approximately 0.3. This value is even smaller than the fraction of links which are ideally oriented along the stretching direction and, thus, potentially crystallizing. As it has been discussed in [3], the force of a link is reduced by increasing its crystallinity if its end-to-end distance is smaller than its contour length. If the end-to-end distances becomes $r > n$, the force is increased by increasing the crystallinity. Therefore, it is preferred by the model networks to melt crystallites at large stretches in order to minimize the forces. Large filler content apparently promotes this because filler-filler bonds are stronger than links and bind the filler nodes tightly to each other.

Furthermore, the behavior of the fractions of links with end-to-end distance $r > n$, of broken filler-filler bonds and of weakened polymer-filler bonds behave like for the non-crystallizing case depicted in Figure 5.30. However, the behavior of the stretches, extensions and free energy densities is affected by SIC, in particular for $\phi \leq 0.4$. At certain stretches depending on filler content, SIC impedes the further expansion of

the links for a short stretch interval. The slope of free energy densities is reduced at the onset of SIC, but increases again afterwards. This can be particularly observed for small filler contents. For $\phi = 0.2$, the increase of the free energy density beyond this short plateau is also visible. It is attributed to the extension of the links which simultaneously increases above their contour length.

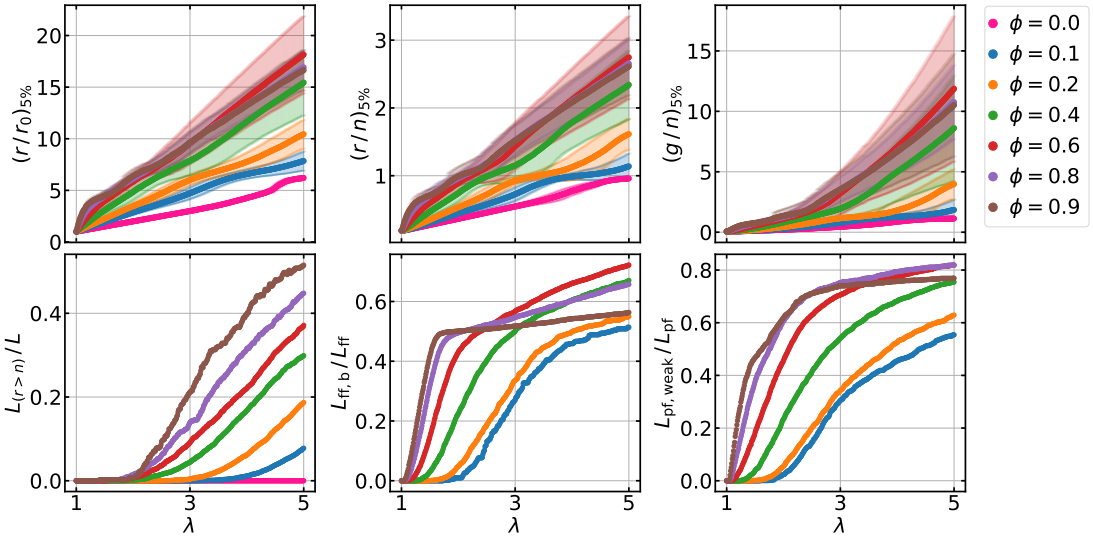

Figure 5.45.: Plots of stretch r/r_0, extension r/n, energy density g/n of links versus the macroscopic stretch λ obtained during stretching as averages over the links with the top 5 % values in a crystallizing 2D-network consisting of $N = 5041$ nodes with filler content ϕ. The fraction $L_{(r>n)}/L$ of links with $r > n$, the fraction $L_{\mathrm{ff,b}}/L_{\mathrm{ff}}$ of reversibly broken filler-filler bonds and the fraction $L_{\mathrm{pf,weak}}/L_{\mathrm{pf}}$ of reversibly weakened polymer-filler bonds are also plotted versus the stretch λ. The MG was applied for $10 \cdot N$ MC steps and it has been set $R^{\mathrm{ff}} = R^{\mathrm{pf}} = 1.1$, $k^{\mathrm{ff}} = 5.0$, $k^{\mathrm{pf}} = 4.0$ and $k^{\mathrm{pf}}_{\mathrm{weak}} = 1.0$, i.e. the networks are configured analogously to those considered in Figure 5.43 and Figure 5.44.

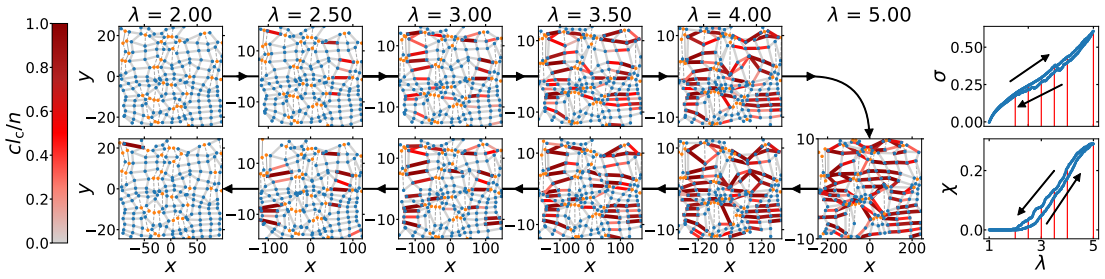

Figure 5.46.: Snapshots of a crystallizing 2D-network which consists of $N = 196$ nodes with filler content $\phi = 0.2$ at certain stretches λ during a strain cycle. The filler is randomly distributed. It is set $R^{\mathrm{ff}} = R^{\mathrm{pf}} = 1.1$, $k^{\mathrm{ff}} = 5.0$, $k^{\mathrm{pf}} = 4.0$ and $k^{\mathrm{pf}}_{\mathrm{weak}} = 1.0$. The upper row represents the stretching process, while the lower row shows the contraction of the network. Each column corresponds to a specific stretch such that the plots share the x-axis. The direction of the deformation is along the x-axis and the scaling of the axes mimics the volume conservation. While the blue dots stand for the cross links, the orange dots represent filler. The crystallinity cl_{c}/n of each link is indicated according to the color bar. Links which cross the boundaries due to the periodic boundary conditions are not drawn. Moreover, the corresponding stress-stretch and crystallinity-stretch curves are depicted, where the vertical red lines mark the stretches at which the snapshots have been taken. The black arrows expose stretching and contraction of the network.

As a next step, finely dispersed, i.e. randomly distributed, filler is considered. Figure 5.46 shows snapshots and corresponding stress-stretch and crystallinity-stretch curves for crystallizing 2D-networks with filler content $\phi = 0.2$. The observations are analogous to the case of flocculated filler depicted in Figure 5.42, but the formation of percolating crystalline strands is impeded due to the filler distribution. Also the formation of crystalline planes is not as pronounced. These effects are enhanced if the filler content is increased as it can be seen in Figure A.33.

Furthermore, the observations regarding the stress-stretch and crystallinity-stretch behavior of 2D-crystallizing network containing finely dispersed filler is analogous to the case of flocculated filler. Nevertheless, the stress amplification is advanced and the onset of SIC is shifted to even smaller stretches according to Figure A.39. Supplemental plots addressing the stress-stretch and crystallinity-stretch behavior of these networks can be found in Figure A.34 and in Figure A.35, but they do not provide further information with respect to the case of flocculated filler.

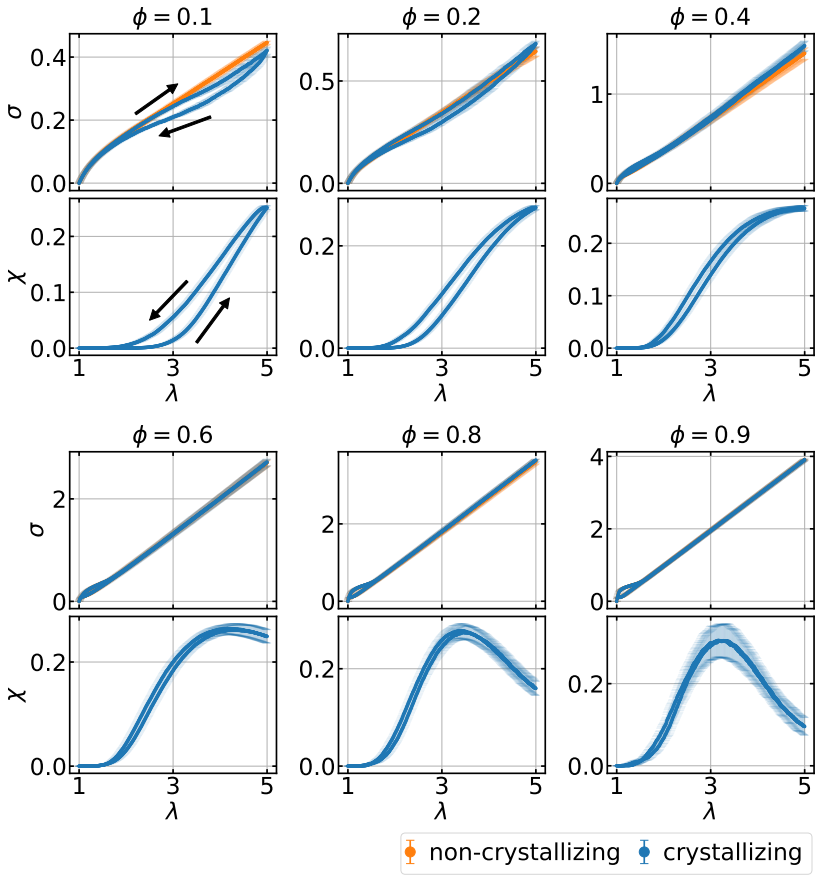

Figure 5.47.: Stress-stretch and crystallinity-stretch curves for a deformation cycle of crystallizing 2D-networks consisting of $N = 5041$ nodes with variable filler content ϕ. The filler is randomly distributed. It has been set $R^{\mathrm{ff}} = R^{\mathrm{pf}} = 1.1$, $k^{\mathrm{ff}} = 5.0$, $k^{\mathrm{pf}} = 4.0$ and $k^{\mathrm{pf}}_{\mathrm{weak}} = 1.0$. Stress-stretch curves are for corresponding non-crystallizing networks are also plotted. The arrows in the upper left plot indicate stretching and contraction.

In order to quantify stress amplification and the shift of the onset of SIC, stress-amplification factors and the onset of SIC are obtained depending on filler content for both considered filler dispersions.

The stress amplification factors are obtained from plots of the stress of the filled network versus the corresponding stress of the unfilled network at identical stretch. The data is fitted with a linear function in the range $\lambda \in [2.0, 3.0]$, but the networks have been stretched until $\lambda_{\mathrm{max}} = 5.0$. Note that this interval is situated above the onset of SIC for filled networks. These plots are depicted in Figure A.36 with the fit parameters given in Table A.8 for flocculated filler and in Figure A.37 with the fit parameters given in Table A.9 for finely dispersed filler. The procedure is analogous to that applied in the previous section for non-crystallizing networks.

In Figure 5.48, the stress-amplification factors for crystallizing 2D-networks are plotted depending on filler content for finely dispersed, i.e. randomly distributed, and flocculated filler, i.e. the MG has been applied for $10 \cdot N$ MC steps. The data is fitted with the Guth-Gold relation given in Equation 5.6. The reduced χ^2-value for the case of flocculated filler amounts to $\chi^2/ndf = 165.32$ which is significantly larger than the ideal value of 1.0 because of the small errors of the stress-amplification factors since they are obtained from linear fits. For the case of finely dispersed filler, the reduced χ^2-value $\chi^2/ndf = 2571.56$ supports the observation that the fitted function is not suitable to describe the data properly. The observations which can be made here are

analogous to the non-crystallizing case discussed in section 5.4, also with respect to the data obtained by Trabelsi *et al.* [18].

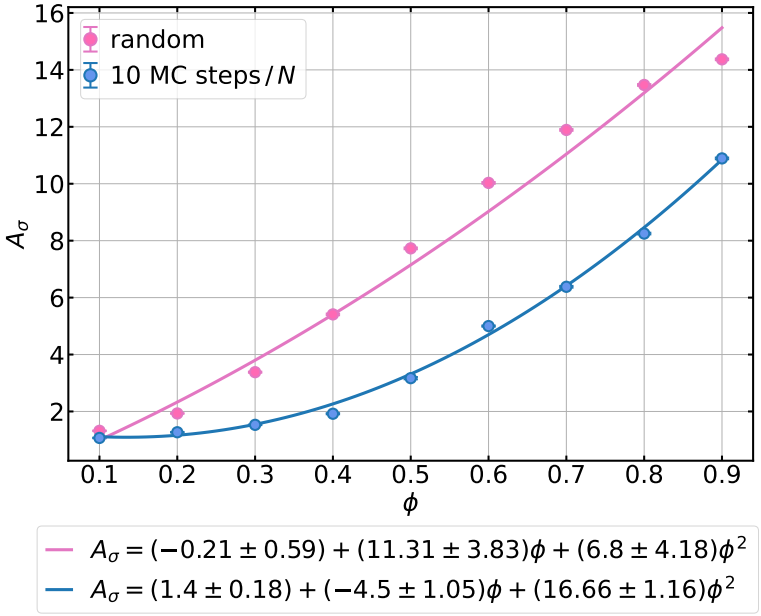

Figure 5.48.: Stress amplification factor A_σ versus filler content ϕ for crystallizing 2D-networks consisting of $N = 5041$ nodes for different filler morphologies, i.e. randomly dispersed filler and application of the MG for 10 MC steps/ N. The data is fitted according to the relation by Guth and Gold.

In Figure 5.49, the onset stretch of SIC λ_{SIC} and the corresponding stress σ_{SIC} at λ_{SIC} are plotted depending on filler content for both filler dispersions. The onset stretch of SIC is obtained as the first stress during stretching of crystallizing networks for which the crystallinity is larger than zero. In the model, even the formation of a single crystalline chain segment in the model is sufficient to cause a non-zero crystallinity. However, a single crystalline segment in an amorphous model network is rather oriented than "crystalline". From an experimental point of view, crystallinity is understood as the formation of a superstructure which, for example, causes a certain pattern in the detected signal during WAXS. Besides, taking for instance Figure 5.4 into account, the occurrence of individual crystalline segments is not sufficient to cause the steep increase of the crystallinity. It just starts as a superstructure, i.e. a crystalline layer, forms.

At first glance, the non-linear decrease of the onset stretch of SIC in Figure 5.49 agrees with the non-linear behavior of the stress-amplification factor, in particular for the case of flucculated filler. For finely dispersed filler, the behavior of the stress-amplification factor plotted in Figure 5.48 suggests that the dependence of the onset stretch of SIC on the filler content should be different compared to flocculated filler. However, the onset stretches of SIC for filled networks lay below the stretch interval considered for obtaining the stress-amplification factors above in any case and, thus, different mechanisms contribute to stress amplification and the shift of the onset of SIC. For instance, links with $r > n$ just occur at stretches larger than the onset of SIC, but within the interval considered for the computation of the stress-amplification factors. In addition, the comparison of Figure 5.45 and Figure A.35 indicates that the fractions of broken filler-filler bonds and weakened polymer-filler bonds as well as the top-5 % values of the stretches and extensions of the links behave very similar for both filler dispersions until the onset of SIC. Therefore, the behavior of the onset of SIC is depending on the filler content is nearly independent of the filler dispersion, but

the small differences at intermediate filler contents arise from the compositions of the networks as they are visualized in Figure 5.35.

Experimentally obtained values for the onset stretch of SIC in NR containing variable content of CB are listed in Table 5.9. For the unfilled networks, the onset of SIC in the model is consistent with the experimentally obtained values for high deformation rates, although the latter tend to be slightly larger. For filled networks, the onsets of SIC in the model are smaller than the experimentally obtained values in any case. The aforementioned definition of crystallinity and, thus, the onset of SIC in the model contributes systematically to this difference.

The stress σ_{SIC} at λ_{SIC} depending on filler content decreases with increasing filler content for finely dispersed filler, while it tends to from a plateau for flocculated filler as the filler content exceeds the percolation threshold. The stress at the onset of SIC is larger for randomly distributed filler until $\phi = 0.7$. The main reason for this behavior is the dependence of the network composition on the filler dispersion which promotes the extension of different types of connections causing different forces. This underlines the stress-amplification effect of the inclusion of filler.

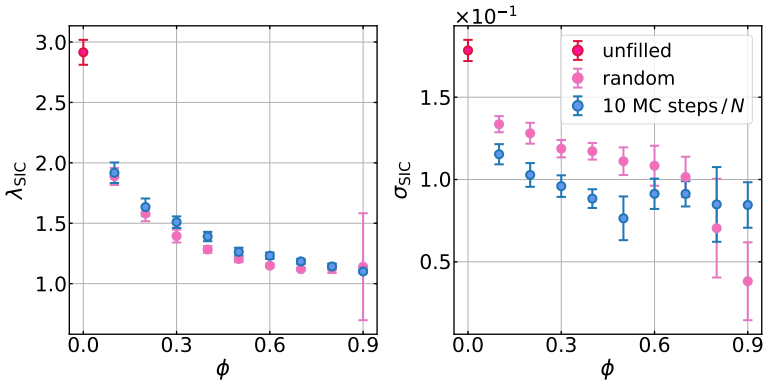

Figure 5.49.: Stretch λ_{SIC} and stress σ_{SIC} at the onset of SIC for variable filler content ϕ. The data has been obtained as averages from 10 independent simulations of stretching 2D-networks which consist of $N = 5041$ nodes. It has been set $R^{\mathrm{ff}} = R^{\mathrm{pf}} = 1.1$, $k^{\mathrm{ff}} = 5.0$, $k^{\mathrm{pf}} = 4.0$ and $k^{\mathrm{pf}}_{\mathrm{weak}} = 1.0$. The data is compiled in Table A.10 and Table A.11.

Table 5.9.: Experimentally obtained onset stretches λ_{SIC} of SIC in CB-filled NR for different filler contents. Unfortunately, the data taken from [259] has not been further specified in the reference.

mass fraction / phr	ϕ	λ_{SIC}	CB type	T	deformation rate	reference
0		4.0		22 °C	1 mm/min	[18]
		3.0		25 °C	10 mm/min	[19]
		3.25			10 mm/min	[259]
20	0.097	2.6	N 339	25 °C	10 mm/min	[19]
		2.75	N 330		10 mm/min	[259]
40	0.177	2.3	N 339	25 °C	10 mm/min	[19]
50	0.2	2	N 375	22 °C	1 mm/min	[18]

Furthermore, the hystereses of the stress-stretch and the crystallinity-stretch curves for complete strain cycles are compared for both filler dispersions depending on filler content. The hysteresis Δ_X of quantity X is calculated as the area between the curves

accounting for the stretching and contraction process by numerical integration of the corresponding curves respectively. The integral accounting for unloading is subtracted from that for loading and the result is normalized by the integral corresponding to stretching. It holds:

$$\Delta_X = \frac{\sum_{i=0}^{\max} \left[X_{\text{stretch}}\left(\lambda_i\right) - X_{\text{contract}}\left(\lambda_i\right)\right] \Delta\lambda}{\sum_{i=0}^{\max} X_{\text{stretch}}\left(\lambda_i\right) \Delta\lambda}, \tag{5.7}$$

where the sums run over all values of the stretch from the initial stretch $\lambda_0 = 1.0$ to the maximum applied stretch $\lambda_{\max}$. The σ- and χ-hysteresis of the stress and the crystallinity, respectively, are plotted depending on the filler content for finely dispersed and flocculated filler in Figure 5.50.

An enormous contribution to the hysteresis is expected to arise from SIC. The hysteresis of the stress for the unfilled networks is smaller than that for networks containing only a small fraction of filler. One possible reason is that SIC cannot fully evolve in this case due to the maximum applied stretch. In addition, the inclusion of filler is expected to provide another contribution to the hysteresis. Nevertheless, the hysteresis decreases beyond $\phi = 0.1$ and $\phi = 0.2$ for finely dispersed and flocculated filler respectively. A possible reason is that the networks are composed of fewer crystallizable links with increasing filler content.

The χ-hysteresis possesses a negative sign because the crystallinity at a fixed stretch is larger during contraction than during stretching. This is reverse to the behavior of the stress. Moreover, the hysteresis of the crystallinity is the smallest for unfilled networks and increases with increasing filler content, i.e. its absolute value decreases. This validates that the inclusion of filler significantly contributes to the σ-hysteresis, particularly for networks containing a small fraction of filler. The absolute value of the χ-hysteresis is smaller for finely dispersed filler than for flocculated filler because of the compositions of the networks. Besides, the decrease of the absolute value of the χ-hysteresis and the simultaneous decrease of the σ-hysteresis indicate that the contribution of SIC to the σ-hysteresis is minor at larger filler content since the fraction of crystallizable links in the networks decreases with increasing filler content. The stress-stretch and crystallinity-stretch curves in Figure 5.44 and Figure 5.47 show that filler mainly contributes to the σ-hysteresis at small deformations, while SIC dominates at intermediate to large deformations.

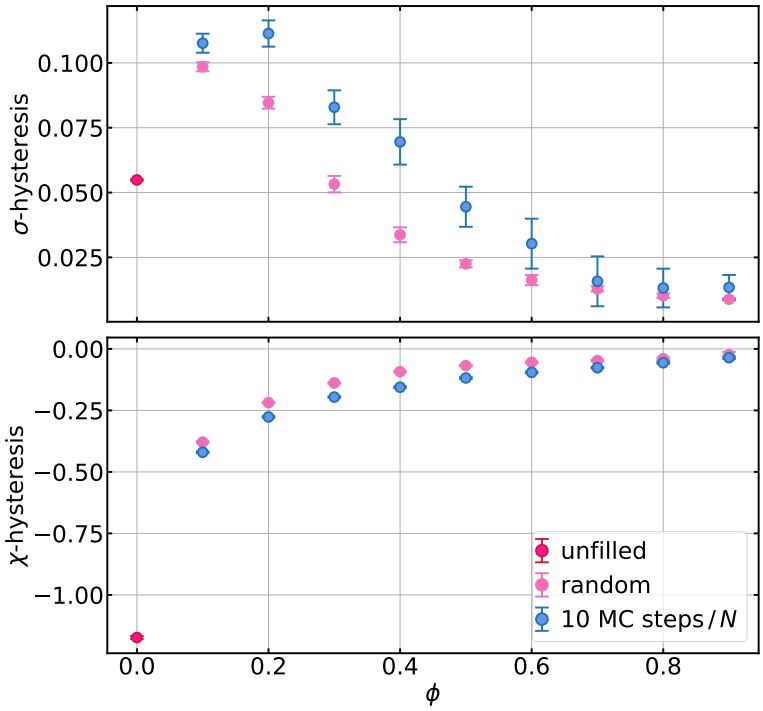

Figure 5.50.: Stress and crystallinity hysteresis versus filler content ϕ. The data has been obtained as averages from 10 independent simulations of 2D-networks which consist of $N = 5041$ nodes. It has been set $R^{\mathrm{ff}} = R^{\mathrm{pf}} = 1.1$, $k^{\mathrm{ff}} = 5.0$, $k^{\mathrm{pf}} = 4.0$ and $k^{\mathrm{pf}}_{\mathrm{weak}} = 1.0$.

As a next step, crystallizing 3D-networks are investigated. In Figure 5.51. stress-stretch and crystallinity-stretch curves are depicted for variable content of flocculated filler. In analogy to the 2D-case, the stress is amplified by the inclusion of filler and the onset of SIC is shifted towards smaller stretches as the filler content is increased. The plateau of the stress is not visible for the filled networks in this plot. What is important to notice here is that the steep increase of the crystallinity in the vicinity of the onset of SIC and the accompanying kink of the stress vanish for filled networks.

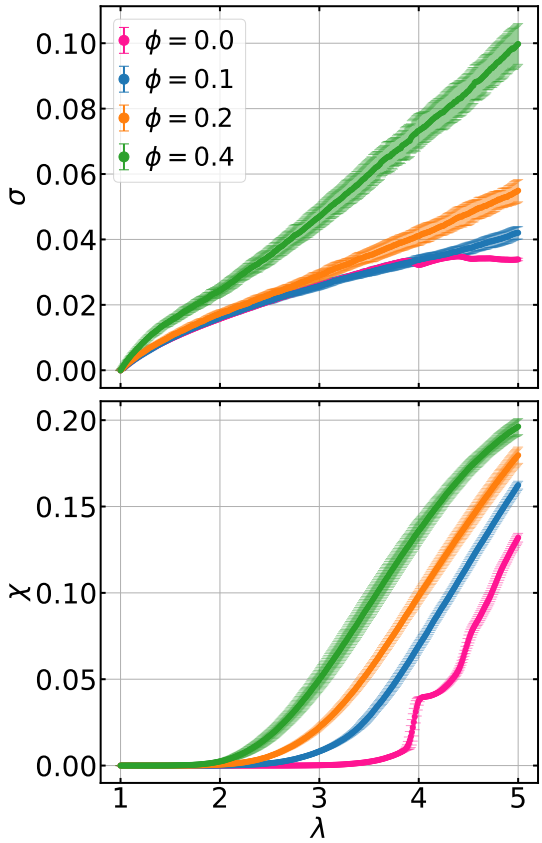

Figure 5.51.: Stress-stretch and crystallinity-stretch curves for stretching crystallizing 3D-networks consisting of $N = 5832$ nodes with variable filler content ϕ. The MG ran through $50 \cdot N$ MC steps. It has been set $R^{\mathrm{ff}} = R^{\mathrm{pf}} = 1.1$, $k^{\mathrm{ff}} = 5.0$, $k^{\mathrm{pf}} = 4.0$ and $k^{\mathrm{pf}}_{\mathrm{weak}} = 1.0$.

In Figure 5.52, stress-stretch and crystallinity-stretch curves of crystallizing and corresponding non-crystalllizing 3D-networks are shown for flocculated filler. The observations which can be made here are analogous to the 2D-case. For $\phi \leq 0.2$, the model networks are softened by SIC. For larger filler contents, the stress-stretch curves for crystallizing networks overlap with that for the corresponding non-crystallizing networks. The hysteresis of the stress and of the crystallinity tighten with increasing filler content. Furthermore, the crystallinity of highly filled networks decreases with increasing filler content. The maximum is reaches approximately at the stretch at which the fraction of links with end-to-end distances $r > n$ becomes 0.15 according to Figure 5.53. The decrease of the crystallinity can still be attributed to this unphysically large extension of a large number of links.

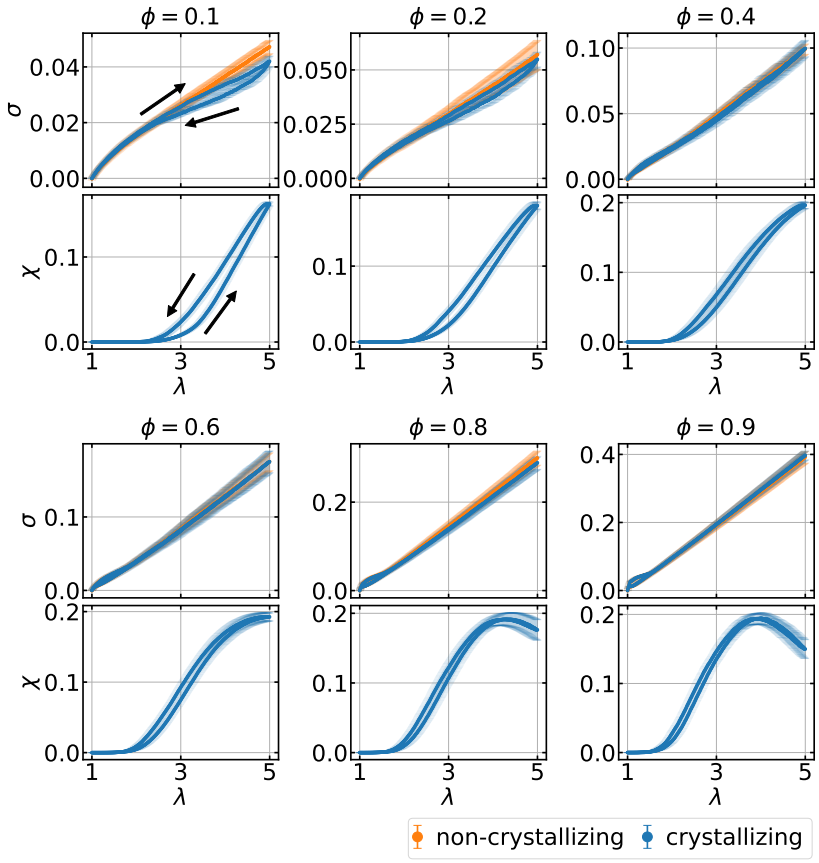

Figure 5.52.: Stress-stretch and crystallinity-stretch curves for a deformation cycle of crystallizing 3D-networks consisting of $N = 5832$ nodes with variable filler content ϕ. The MG ran through $50 \cdot N$ MC steps. It has been set $R^{\mathrm{ff}} = R^{\mathrm{pf}} = 1.1$, $k^{\mathrm{ff}} = 5.0$, $k^{\mathrm{pf}} = 4.0$ and $k^{\mathrm{pf}}_{\mathrm{weak}} = 1.0$. Stress-stretch curves are for corresponding non-crystallizing networks are also plotted. The arrows in the upper left plot indicate stretching and contraction.

Figure 5.53 shows further information about the links and bonds in the networks. Essentially, most of the observations which can be made here are similar to those for non-crystallizing 3D-networks or for crystallizing 2D-networks containing flocculated filler. For the unfilled networks, the top-5 % values of the stretch and extension of the links show a jump at the same stretch as the crystallinity in Figure 5.51. A large number of semi-crystalline segments in the links appear to suddenly become straight rods. The network appears to eventually undergo a phase transition. For filled networks, the behavior of the stretches, the extensions and the free energy densities obey different behavior than in the non-crystallizing case. The behavior apparently changes at the onset of SIC and as the free energy density shows a kink, particularly for $\phi \geq 0.2$. This kink shifts towards smaller stretches with increasing filler content and may also be related to the number of links with end-to-end distances $r > n$.

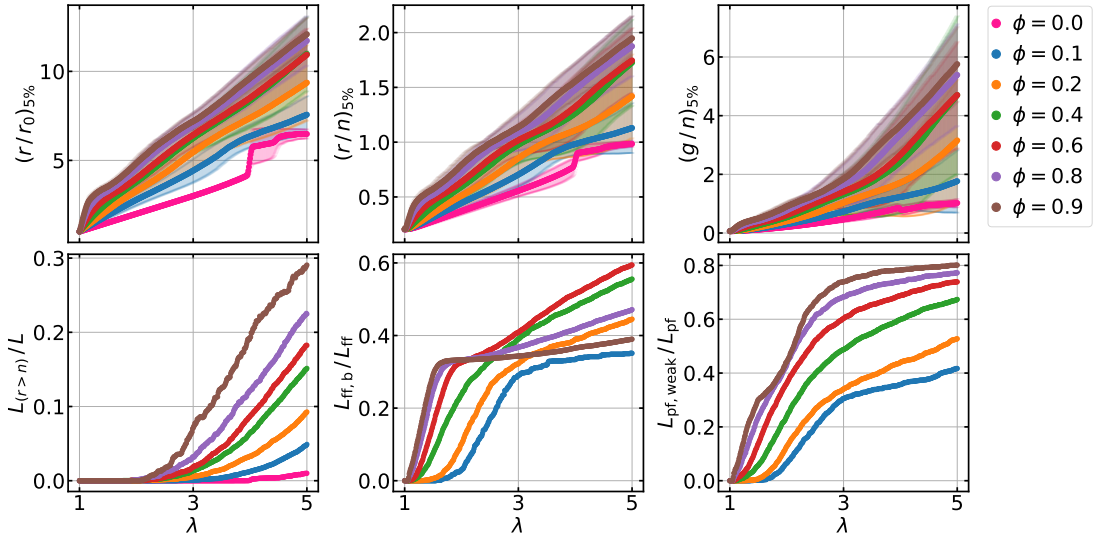

Figure 5.53.: Plots of stretch r/r_0, extension r/n, energy density g/n of links versus the macroscopic stretch λ obtained during stretching as averages over the links with the top 5 % values in a crystallizing 3D-network consisting of $N = 5832$ nodes with filler content ϕ. The fraction $L_{(r>n)}/L$ of links with $r > n$, the fraction $L_{\mathrm{ff,b}}/L_{\mathrm{ff}}$ of reversibly broken filler-filler bonds and the fraction $L_{\mathrm{pf,weak}}/L_{\mathrm{pf}}$ of reversibly weakened polymer-filler bonds are also plotted versus the stretch λ. The MG was applied for $50 \cdot N$ MC steps and it has been set $R^{\mathrm{ff}} = R^{\mathrm{pf}} = 1.1$, $k^{\mathrm{ff}} = 5.0$, $k^{\mathrm{pf}} = 4.0$ and $k^{\mathrm{pf}}_{\mathrm{weak}} = 1.0$, i.e. the networks are configured analogously to those considered in Figure 5.51 and in Figure 5.52.

Plots which are analogous to those discussed for the case of flocculated filler can be found in Figure A.39, in Figure A.41 and in Figure A.40 for 3D-crystallizing networks containing finely dispersed filler. The observations that can be made are either analogous to the case of flocculated filler or to the 2D-case and, thus, not discussed further here.

Now, stress-amplification is quantified by obtaining the stress-amplification factor for 3D-crystallizing networks depending on filler content for finely dispersed and flocculated filler. The procedure is analogous to that for the 2D-case. The stress of the filled networks is plotted for the stress of the unfilled network at identical stretch and the corresponding stress-amplification factor is determined from a linear fit. The corresponding plots are presented in Figure A.38 for flocculated filler and in Figure A.42 for finely dispersed filler. In Figure 5.54, the stress-ampllification factors are plotted versus filler content for both considered filler dispersions and fitted with the Guth-Gold relation according to Equation 5.6.

Analogous to the 2D-case and to the case of non-crystallizing networks, the fitted function describes the data for flocculated filler well, although the reduced χ^2-value $\chi^2/ndf = 174.79$ is again significantly larger than the ideal value of 1.0 due to the small errors of the data points resulting from the method for obtaining them. For finely dispersed filler, the Guth-Gold relation does not fit the data. This is in accordance with the corresponding reduced χ^2-value $\chi^2/ndf = 1038.62$. In comparison to the experimental data obtained by Trabelsi *et al.* [18], the data is still stretched along the ϕ-axis such that the stress-amplification factors obtained here are smaller. Nevertheless, stress amplification is enhanced if the filler in finely dispersed.

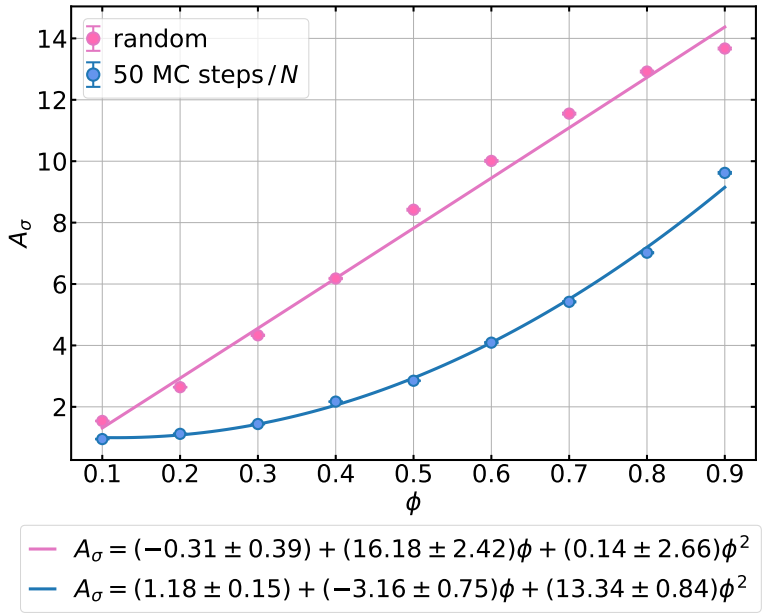

Figure 5.54.: Stress amplification factor A_σ versus filler content ϕ for crystallizing 3D-networks consisting of $N = 5832$ nodes for different filler morphologies, i.e. randomly dispersed filler and application of the MG for 50 MC steps/ N. The data is fitted according to the relation by Guth and Gold.

Figure 5.55 shows the onset stretch λ_{SIC} of SIC in crystallizing 3D-networks and the corresponding stress σ_{SIC} depending on filler content for both considered filler dispersions. The onset stretch decreases with increasing filler content, but the data for both filler dispersions overlap. The stresses at the onset stretch of SIC also overlap for both filler dispersions. They decrease with increasing filler content until approximately $\phi = 0.4$ for finely dispersed filler and $\phi = 0.5$ for flocculated filler and tends to increase beyond. The onset of SIC is not determined by the composition of links and bonds of the networks here. The stress at the onset of SIC is possibly related to the percolation threshold of the filler.

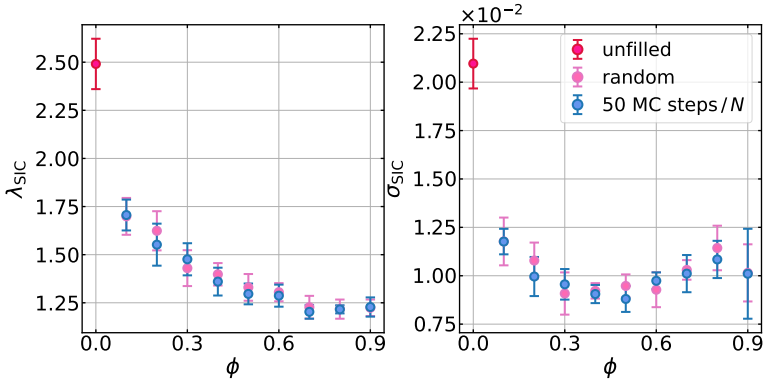

Figure 5.55.: Stretch λ_{SIC} and stress σ_{SIC} at the onset of SIC for variable filler content ϕ. The data has been obtained as averages from 10 independent simulations of stretching 3D-networks which consist of $N = 5832$ nodes. It has been set $R^{\mathrm{ff}} = R^{\mathrm{pf}} = 1.1$, $k^{\mathrm{ff}} = 5.0$, $k^{\mathrm{pf}} = 4.0$ and $k^{\mathrm{pf}}_{\mathrm{weak}} = 1.0$. The data is compiled in Table A.14 and Table A.15.

In Figure 5.56, the hystereses of the stress and the crystallinity are plotted versus filler content for finely dispersed and flocculated filler. The hystereses are computed according to Equation 5.7. In contrast to the 2D-case, the σ-hysteresis is at maximum

for the unfilled networks. A possible explanation is that, in 2D-networks, around 1/2 of the polymer-filler and filler-filler bonds are oriented along the stretching direction and, thus, potentially contribute to the hysteresis. In 3D-networks only around 1/3 of the bonds is aligned with the direction of the deformation. Therefore, the contribution of SIC must be of primary importance here. Nevertheless, in particular for $\phi = 0.2$ and $\phi = 0.3$, the inclusion of filler apparently contributes significantly to the hysteresis of the stress. The differences between the case of finely dispersed and flocculated filler may be attributed to the different compositions of the networks. The decrease of the σ-hysteresis mainly arises from the hysteresis of the crystallinity since the absolute value of the χ-hysteresis also decreases with increasing filler content.

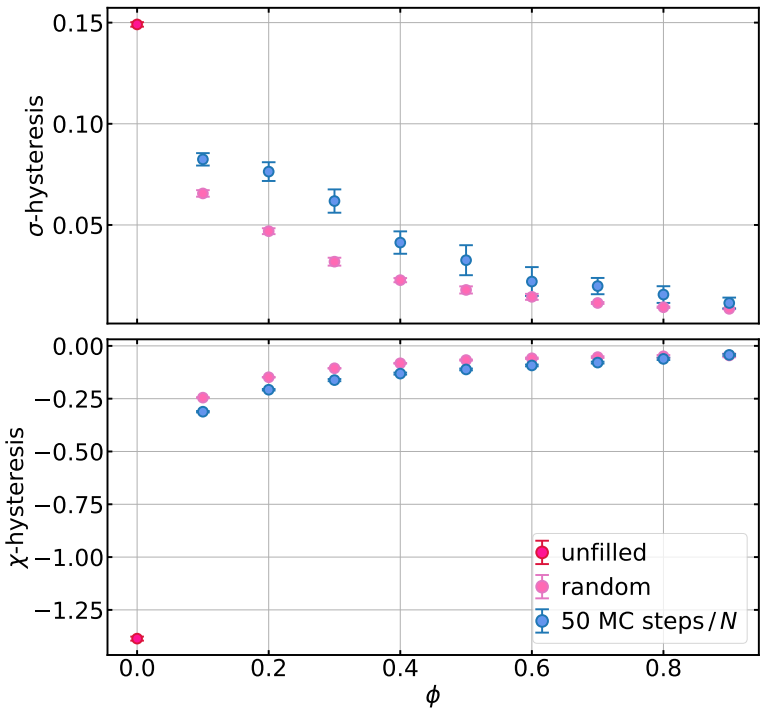

Figure 5.56.: Stress and crystallinity hysteresis versus filler content ϕ. The data has been obtained as averages from 10 independent simulations of 3D-networks which consist of $N = 5832$ nodes. It has been set $R^{\mathrm{ff}} = R^{\mathrm{pf}} = 1.1$, $k^{\mathrm{ff}} = 5.0$, $k^{\mathrm{pf}} = 4.0$ and $k^{\mathrm{pf}}_{\mathrm{weak}} = 1.0$.

Altogether, the onset of SIC is shifted towards smaller stretches due to the inclusion of filler in the 2D- and in the 3D-case. For the 2D-networks, this effects tends to be advanced for finely dispersed filler. In particular, SIC evolves between adjacent filler aggregates since extension of these links is promoted. Additionally, the plateau of the stress vanishes with increasing filler content and the hystereses of the stress-stretch and the crystallinity-stretch curves tighten.

5.6. Critical Free Energy Density

As a first attempt, the rupture criterion for the links in the model networks has been defined by a critical force f_{rupt} [4]. However, since minimization of energy is a more suitable approach to rupture as pointed out in section 2.5, the critical force is now replaced by a critical free energy density $(g/n)_{\mathrm{crit}}$, which is the free energy of a link divided by the number of Kuhn segments which it contains. As mentioned in section 2.2, the process of SIC stores energy in the crystalline segments. Thus, SIC prohibits rupture

since more energy is required to break a crystalline segment than a non-crystalline segment. As a result, it is more suitable to use a critical free energy density instead of a critical force. In addition, applying an energy criterion aligns with Griffith's criterion [154] which has been discussed in section 2.5. The normalization of the energy rupture criterion to the number of Kuhn segments in a link is necessary because otherwise links which consist of more Kuhn segments would break at smaller stretch or smaller stress.

2D-networks

As a first step to obtain the critical free energy density, histograms of the free energy per Kuhn segment, which are computed during a strain cycle, are analyzed. For this purpose, a crystallizing and a non-crystallizing unfilled 2D-network consisting of $N = 5041$ nodes with the parameters given in Table 4.3 are simulated. Although the maximum stretch is set to $\lambda_{\max} = 7.0$ here, it is more appropriate to reduce it to $\lambda_{\max} = 5.0$ because of links with $r > n$, which occur since finite chain extensibility is not considered.

The histograms for the free energy density are shown in Figure 5.57. With increasing stretch, the initial peak of the histogram splits into two peaks around $\lambda = 3.0$ in both the crystallizing and the non-crystallizing case. The one at small energy densities accounts for the links oriented perpendicularly to the direction of the deformation, while the second peak stands for the links oriented along the stretching direction. Until $\lambda = 4.0$ is reached, the histograms for the crystallizing and the non-crystallizing network overlap. At higher stretches, the histogram for the non-crystallizing network flares towards higher stretches compared to that for the crystallizing network. At $\lambda = 6.0$, the maximum of the second peak for the crystallizing network appears to be situated at smaller free energy densities than the analogous peak for the non-crystallizing network. However at $\lambda = 7.0$, a 'plateau' in the histogram for crystallizing network forms beyond the second peak and the crystallizing network contains higher free energy densities than the non-crystallizing network. This is possibly because of the occurrence of unphysical end-to-end distances of the links at such high stretches. During the contraction, the peaks move towards smaller free energy densities until they overlap again around zero. In comparison to the stretching process, the histogram for the crystallizing network still shows two separated peaks at $\lambda = 2.0$. This is because of the hysteresis of SIC.

In order to make crystallizing networks break at higher stretches than non-crystallizing networks, the tail of the histogram for the non-crystallizing network must be cut off by the critical free energy density. These free energy densities are not reached in the crystallizing network in the appropriate range of stretches. Therefore, suitable choices for the critical free energy density are approximately between $g/n = 1.0$ and $g/n = 2.0$. If the maximum stretch and critical free energy density are sufficiently high, the crystallizing network would break at smaller stretches than the non-crystallizing network or the non-crystallizing network might persist compared to the crystallizing network. Moreover, if the critical free energy density is too large, none of the networks would break.

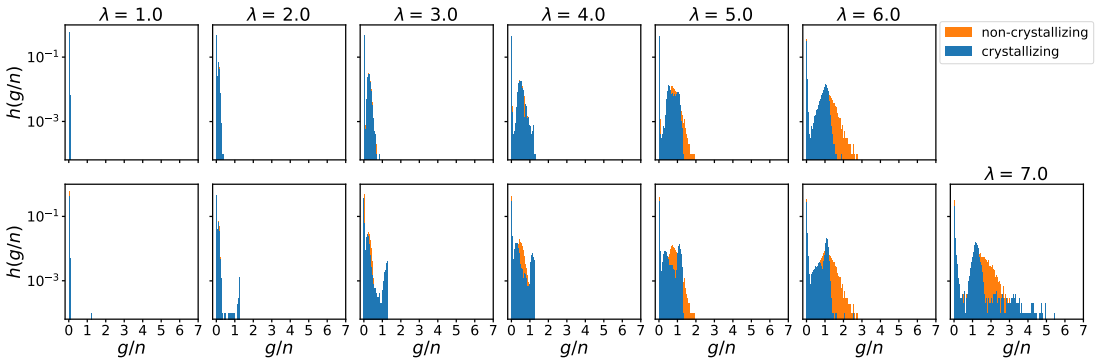

Figure 5.57.: Histograms of the free energy density g/n during a strain cycle with $\lambda_{\max} = 7.0$ and stretch increment $\Delta\lambda = 0.01$. The upper row is for the stretching process and the lower row for the contraction. Each column corresponds to a fixed stretch.

In order to obtain a critical free energy density more precisely, it is checked whether links in a network break and how many of them in the interval of possible critical free energy densities derived from the histograms. For this purpose, stretching of 2D-networks with the parameters given in Table 4.3 is simulated, where breaking of links is enabled. The maximum stretch is set to $\lambda_{\max} = 5.0$ and $(g/n)_{\text{crit}}$ is varied. For each critical free energy density, 10 networks are simulated. The numbers of damaged networks and of failed networks are counted. A network is called damaged if at least one link broke, but the network does not necessarily fail. If a sufficiently high fraction of links broke such that the network is destroyed, it is classified as a failed network. In the real world, this means that the network breaks into two parts which is not possible in the simulation due to the periodic boundary conditions. Failure is indicated by the stress vanishing at the end of the stretching process since it drops to zero at the stretch where the entire network breaks. Based on this definition of failure of the model network, the tensile strength σ_{t} will be obtained as the maximum stress reached in a failed network and the elongation at break λ_{t} as the stretch at which the tensile strength σ_{t} has been reached. Here, it is presumed that the stress monotonically increases until failure. Since the tensile strength and the elongation at break are ultimate properties, they are obtained from the networks which failed. Moreover, the fraction L_{b}/L of links that broke in total of the total number of links[1] is computed as average from the data for all damaged networks where the error is given by the standard deviation.

The results are plotted in Figure 5.58. For small critical free energy densities, both the crystallizing and the non-crystallizing networks break and the fractions of broken links overlap. Previous investigations [4] have shown that these values of the fractions of broken links are sufficient to make a network fail. Around $(g/n)_{\text{crit}} = 1.25$, the fraction of broken links for the crystallizing networks rapidly drops to zero and more of them become stable, while all of the non-crystallizing networks still break. However, the non-crystallizing networks become also stable around $(g/n)_{\text{crit}} = 2.0$. Subsequently, the rupture behavior of crystallizing and non-crystallizing networks must be analyzed. Therefore both types of networks must fail. In addition, it is required that the tensile strength and the elongation at break of crystallizing networks are higher than for non-crystallizing networks. Hence, an appropriate choice for the critical free energy density may be $(g/n)_{\text{crit}} = 1.25$. In this case, both kind of networks fail, but the 'degree of destruction' of crystallizing networks is smaller. Furthermore, both the tensile strength and the elongation at break increase with increasing critical free energy density. For

[1] The total number of links means only connections between two cross links, i.e. polymer chains but not filler-filler or polymer-filler bonds.

failed networks, the tensile strength of crystallizing networks is smaller than that of non-crystallizing networks. The elongation at break of the crystallizing networks steeply inclines in the range of critical free energy densities where the falling edge of the fraction of broken links is located.

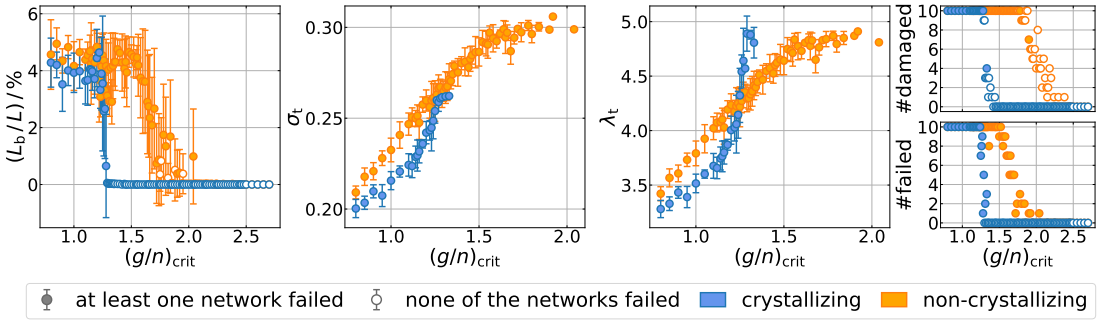

Figure 5.58.: Fraction of broken links L_b/L, tensile strength σ_t, elongation at break λ_t, number of damaged networks and number of failed networks for variable critical free energy densities $(g/n)_{crit}$ obtained from the simulations of 10 unfilled 2D-networks.

3D-networks

The critical free energy density in unfilled 3D-networks can be analyzed analogously to the 2D-case. Figure 5.59 shows free energy density histograms for a crystalllizing and a non-crystallizing unfilled 3D-network which consist of $N = 5832$ nodes. The histograms behave analogously to those for the 2D-networks. The range of the free energy density for an appropriate rupture criterion appears to be also between $g/n = 1.0$ and $g/n = 2.0$.

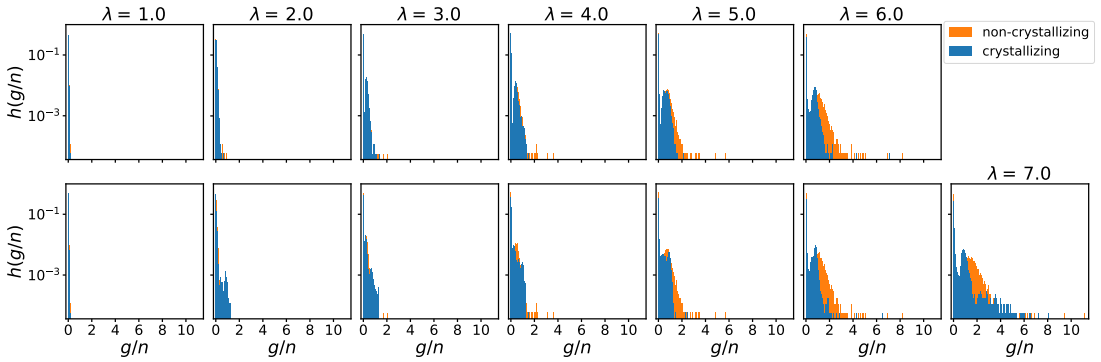

Figure 5.59.: Histograms of the free energy density g/n in a crystallizing and a non-crystallizing 3D-network during a strain cycle with $\lambda_{max} = 7.0$ and stretch increment $\Delta\lambda = 0.01$. The upper row is for the stretching process and the lower row for the contraction. Each column corresponds to a fixed stretch.

As in the 2D-case, the value for the critical free energy density $(g/n)_{crit}$ is now derived from the dependence of the fraction of broken links L_b/L, the tensile strength σ_t, the elongation at break λ_t, the number of damaged networks and the number of networks which failed on the choice of $(g/n)_{crit}$. The corresponding data is plotted in Figure 5.60. The falling edges of the fraction of broken links are located at slightly smaller free energy densities than in the 2D-case. The crystallizing networks do not fail already below $(g/n)_{crit} = 1.25$, but the tensile strength and the elongation at break are always smaller for crystallizing than for non-crystallizing networks if the networks fail. Apparently, there is no choice for the critical free energy density in

the case of unfilled networks which fits the requirements that both crystallizing and non-crystallizing networks fail and that the tensile strength and elongation at break of crystallizing networks are larger. For subsequent studies of filled networks, a sufficiently good choice of the critical free energy density would roughly be between 1.1 and 1.25, but this is elaborated further in the next section.

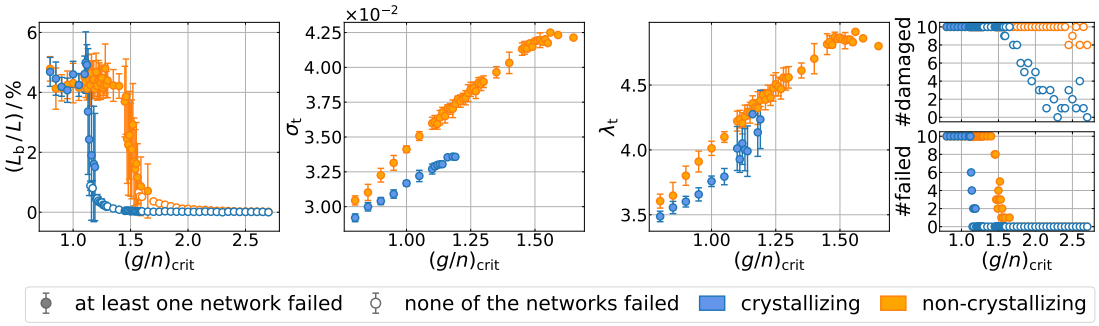

Figure 5.60.: Fraction of broken links L_b/L, tensile strength σ_t, elongation at break λ_t, number of damaged networks and number of networks which failed for variable critical free energy densities $(g/n)_{crit}$ obtained from the simulations of 10 unfilled 3D-networks.

5.6.1. Free Energy Density in Filled Networks

In order to investigate tensile strength not only of unfilled networks, free energy densities in filled networks are analyzed analogous to the unfilled case and the rupture criterion will be examined. For the generation of filled networks, the MG is applied for $10 \cdot N$ MC steps in the 2D-case and for $50 \cdot N$ MC steps in the 3D-case, i.e. the filler is coarsely dispersed, and it is set $R^{ff} = R^{pf} = 1.1$, $k^{ff} = 5.0$, $k^{pf} = 4.0$ and $k^{pf}_{weak} = 1.0$.

2D-networks

First, the free energy density of the links in filled networks is studied. The MG is applied for $10 \cdot N$ MC steps. Figure 5.61 shows free energy density histograms for a crystallizing and a non-crystallizing network with filler content $\phi = 0.1$. The links reach significantly higher free energy densities than in the unfilled networks already for this small filler content. Already at $\lambda = 3.0$, higher free energy densities are reached in the non-crystallizing network than in the crystallizing network. In addition, the free energy densities of the crystallizing networks flare from the second peak towards larger values already at $\lambda = 5.0$ which is at a smaller stretch than in the unfilled case.

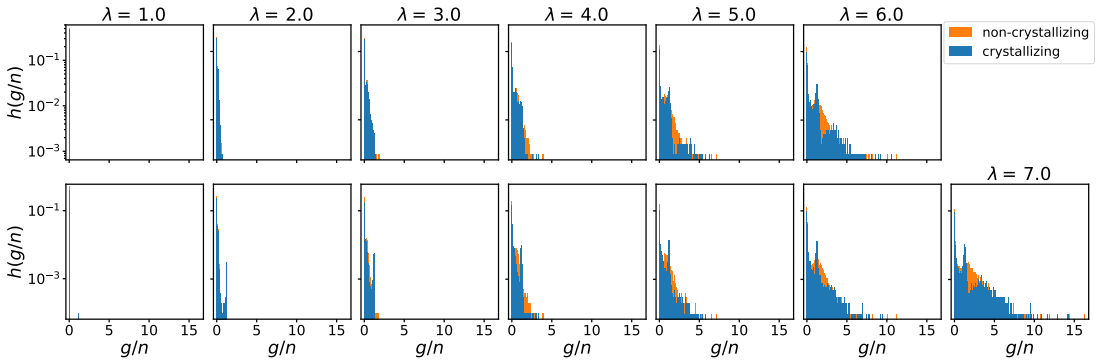

Figure 5.61.: Histograms of the free energy density g/n during a strain cycle with $\lambda_{\max} = 7.0$ and stretch increment $\Delta\lambda = 0.01$. The simulated networks contain a volume fraction $\phi = 0.1$ of filler and it is set $R^{\mathrm{ff}} = R^{\mathrm{pf}} = 1.1$, $k^{\mathrm{ff}} = 5.0$, $k^{\mathrm{pf}} = 4.0$ and $k^{\mathrm{pf}}_{\mathrm{weak}} = 1.0$. The upper row is for the stretching process and the lower row for the contraction. Each column corresponds to a fixed stretch.

In Figure 5.62, mean values of the free energy densities in the crystallizing and in the non-crystallizing network are compared to the unfilled network at different stretches and plotted for various parameterizations of the spring constants and cut-off radii. The links are not breakable here. Since the filler content is very small, i.e. below the percolation threshold, formation of large holes due to softening or rupture of polymer-filler and filler-filler bonds which may lead to failure of the networks is negligible. If the polymer-filler bonds only weaken or are even stable, the mean free energy density is elevated in the filled network compared to the unfilled. The effect enhances if filler-filler bonds are additionally stable. This can be observed especially at large stretches. Nevertheless, the data for the filled networks is situated within the error margins of the data for the unfilled network. The inclusion of filler into the rubber matrix redistributes the stretch. On the one hand, it must not be favorable to stretch filler-filler bonds to a high extend because they possess the largest spring constant. On the other hand, links have the smallest 'spring constant' and, therefore, can be highly extended. If the polymer-filler bonds, i.e. the connection between filler aggregates and polymer, are stable or only weaken, the free energy density of the links is increased in comparison to unfilled networks. However, if this connection breaks, the filler aggregates must not be stretched further because they are rather isolated instead of traversing the network. Thus, the deformation acts on links as in pure rubber.

Figure 5.63 shows analogous data for networks containing a fraction $\phi = 0.5$ of filler. For $\lambda > 1.0$ and if polymer-filler bonds are stable, the mean free energy densities are elevated above the error margins of those for the unfilled networks. The observations which can be made here are analogous to the case $\phi = 0.1$, but the effects of the different parameterizations are more pronounced.

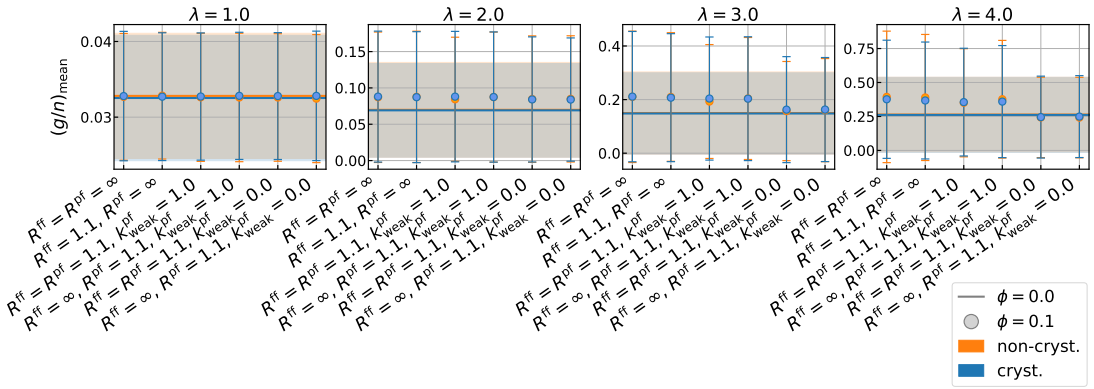

Figure 5.62.: Mean free energy densities of the links in crystallizing and non-crystallizing networks containing a volume fraction $\phi = 0.1$ of filler. The cut-off radii and spring constants for polymer-filler and filler-filler bonds vary.

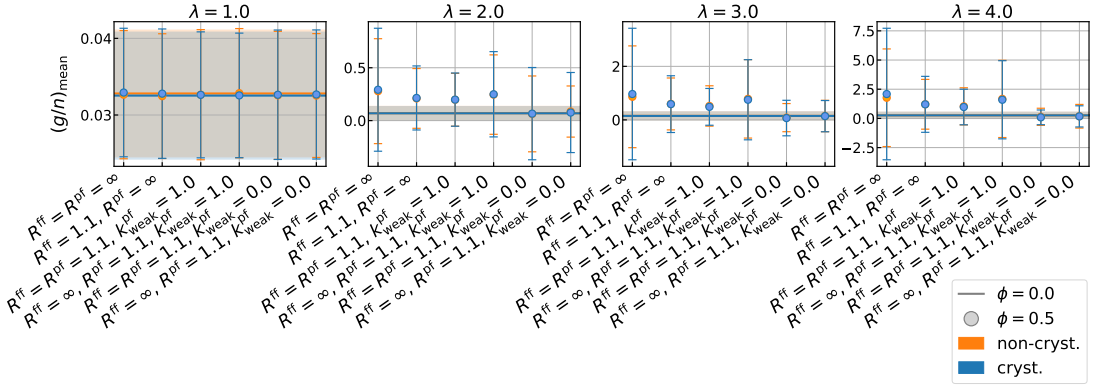

Figure 5.63.: Mean free energy densities of the links in crystallizing and non-crystallizing networks containing a volume fraction $\phi = 0.5$ of filler. The cut-off radii and spring constants for polymer-filler and filler-filler bonds vary.

As a next step, various critical free energy densities are tested on filled networks. Again, the fraction of broken links L_b/L, the tensile strength σ_t and the elongation at break λ_t are computed as explained above and the number of damaged as well as the number of failed networks are counted. The networks are stretched until $\lambda_{max} = 5.0$. The critical free energy densities have been selected from the previous range. Plots of the data can be found in subsection A.8.1 and, for $\phi = 0.1$, in Figure 5.64.

While damage due to rupture of links is prevented in both crystallizing and non-crystallizing unfilled networks approximately beyond $(g/n)_{crit} = 1.5$, most of the filled networks still fail, especially also for small filler content. However, an increasing number of networks does not fail when $\phi \geq 0.3$ as the filler content approaches the percolation threshold, which is around $\phi = 0.5$. In the case of $\phi = 0.1$, an interval of critical free energy densities close to $(g/n)_{crit} = 1.5$ exists in which the fraction of broken links in the crystallizing model networks is larger than for the corresponding non-crystallizing networks, but, simultaneously, both the tensile strength and the elongation at break are larger for the crystallizing case. Similar observations can also be made for $\phi \leq 0.5$ and this is in contrast to the unfilled case. For $\phi \leq 0.3$, the tensile strength and the elongation at break of the crystallizing networks exceeds those of the corresponding non-crystallizing networks for $(g/n)_{crit} \geq 1.5$. This holds in particular for $(g/n)_{crit} = 1.5$ and $(g/n)_{crit} = 1.75$. In comparison to smaller values of the critical free energy density, for which the fraction of broken links is larger for the non-crystallizing networks, the rupture criterion is fulfilled just at higher stretches. Hence, breaking links must be

higher extended. Since finite chain extensibility is not included into the model, links can be stretched beyond their contour length. Although SIC lowers the force of links and simultaneously their energy at end-to-end distances below the contour length, it leads to increased energy above [4]. Therefore, even more links potentially reach the critical free energy density in crystallizing networks compared to non-crystallizing networks. For $\phi = 0.4$, the tensile strength and elongation at break remain larger for the crystallizing than for the non-crystallizing networks for $(g/n)_{\text{crit}} = 1.5$. For higher critical free energy densities, the tensile strengths of crystallizing and non-crystallizing networks overlap. Moreover, the fraction of broken links tends to decrease with increasing critical free energy density for crystallizing networks, but it does not significantly differ for non-crystallizing networks. For $\phi = 0.5$, most of the networks do not fail. Thus, the data for the tensile strength and elongation at break is not meaningful. There are cases in which the crystallizing networks do not fail, but a non-crystallizing network does. As before, the fraction of broken links tends to decrease with increasing critical free energy density, while the data for the crystallizing and the non-crystallizing case overlap. For higher filler content, the fraction of broken links still tends to decrease. It is smaller for the crystallizing networks than for the non-crystallizing at $(g/n)_{\text{crit}} = 1.5$ and $(g/n)_{\text{crit}} = 1.75$, although the error bars of the data points overlap for some filler content. For $\phi \geq 0.7$, none of the networks fails. Since links still break, holes must form, but a percolating structure stabilizes the network. Note that polymer-filler bonds must be crucial for this as they only weaken but do not break. In addition, filler-filler bonds which are oriented perpendicularly to the stretching direction tend to not break at at larger stretches because the volume is conserved in the simulation and, thus, they are rather compressed instead of extended.

Overall, the data indicates that a suitable value for the critical free energy density is $(g/n)_{\text{crit}} = 1.5$ because of the behavior of the tensile strength and the elongation at break of filled model networks. Both quantities are larger for the crystallizing than for the non-crystallizing networks which is required based the phenomenology. Nevertheless, the observations made here suggest that it will be difficult to analyze the rupture behavior of filled model networks around and especially above the percolation threshold since they do not fail beyond it under the given conditions.

By analyzing unfilled networks, $(g/n)_{\text{crit}} = 1.25$ has been determined as an appropriate value for the critical free energy density. For networks with filler content between $\phi = 0.2$ and $\phi = 0.4$, the fraction of broken links tends to be higher in non-crystallizing networks than in the corresponding crystallizing with this value of the critical free energy density. In addition, for $\phi = 0.3$ and $\phi = 0.4$, more of the non-crystallizing networks failed than corresponding crystallizing networks. Both aspects may also be understood as strength of the networks which, in the model, is determined by the choice of the critical free energy density.

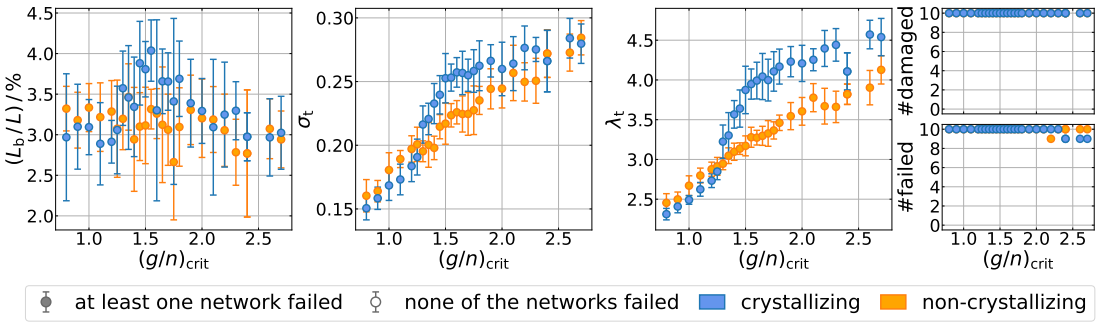

Figure 5.64.: Fraction of broken links L_b/L, tensile strength σ_t, elongation at break λ_t, number of damaged networks and number of networks which failed for variable critical energy densities $(g/n)_{crit}$ obtained from the simulations of 10 2D-networks containing a fraction $\phi = 0.1$ of filler.

3D-networks

Plots of the fraction of broken links L_b/L, tensile strength σ_t, elongation at break λ_t, number of stable networks and number of networks which failed versus the critical free energy density $(g/n)_{crit}$ for variable filler content ϕ are presented in subsection A.8.1 and in Figure 5.65 for $\phi = 0.1$. None of the networks fails for $\phi \geq 0.4$ with the applied maximum stretch $\lambda_{max} = 5.0$.

In contrast to the unfilled case, for $\phi = 0.1$, the fraction of broken links is approximately constant in the non-crystallizing case. For crystallizing networks, it tends to decrease, but shows a maximum approximately at $(g/n)_{crit} = 1.35$ at which the fraction of broken links is larger for the crystallizing networks than for the non-crystallizing networks. Simultaneously, the tensile strength and the elongation at break become larger for crystallizing than for corresponding non-crystallizing networks. In the same region of critical free energy densities for $\phi = 0.2$, the tensile strength and elongation at break of crystallizing networks also exceed those of non-crystallizing networks. The fraction of broken links does not show a clear trend at this filler content. For $\phi = 0.3$, just one crystallizing network breaks at all. However, for this and larger filler contents, the fraction of broken links decreases steeper for crystallizing networks than for non-crystallizing networks approximately between $(g/n)_{crit} = 1.3$ and 1.5. Thus, the 'degree of destruction' is larger for crystallizing networks than for non-crystallizing networks in this interval.

Based on the observations made in this section and for simplicity, the critical free energy density is set to $(g/n)_{crit} = 1.5$ as in the 2D-case. Note that this choice for the threshold value for rupture of links is justified by theoretical considerations made in section 3.5 for non-crystalline links.

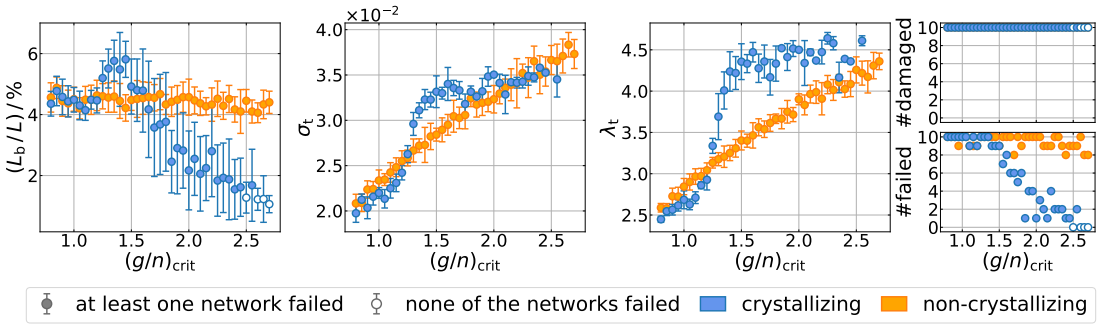

Figure 5.65.: Fraction of broken links L_b/L, tensile strength σ_t, elongation at break λ_t, number of damaged networks and number of networks which failed for variable critical energy densities $(g/n)_{crit}$ obtained from the simulations of 10 3D-networks containing a fraction $\phi = 0.1$ of filler.

5.7. Rupture Behavior

The aim of this section is the microstructural investigation of the rupture behavior of the model networks by applying the critical free energy densities obtained in the previous section as rupture criterion for links. It will be examined which type of linkages, i.e. links, filler-filler bonds or polymer-filler bonds, causes failure of the model networks and how the parametrization of the model networks affects the rupture behavior. In addition, the role of SIC will be discussed. On the one hand, these investigations provide a deeper understanding of the model. On the other hand, they are motivated by experimental observations which have been discussed in section 2.5.

First, the snapshots of unfilled crystallizing and non-crystallizing 2D-networks consisting of $N = 5041$ nodes are analyzed. These networks are stretched until $\lambda_{max} = 5.0$. Figure 5.66 shows snapshots and corresponding stress-stretch curves for the case that the critical free energy density $(g/n)_{crit} = 1.25$ is applied. In the non-crystallizing network, randomly distributed holes occur due to rupture of links. They are round and do not possess sharp edges because of the periodic boundary conditions and modeling of the links as Gaussian chains which collapse according to their entropic elasticity if they are located in the vicinity of a hole. With increasing stretch, the holes grow perpendicularly to the stretching direction. The path along which they grow is not deflected or branched. Additionally, new holes form, in particular near large holes perpendicularly to the stretching direction, i.e. along the direction along which the large hole probably grows. Holes also merge during the rupture process.

In the crystallizing network, the observations which can be made are similar. SIC appears to be promoted at the boundaries of the holes and in their vicinity perpendicular to the direction of deformation. As in the non-destructive case, crystalline layers build up in the model networks. However, these do not prevent failure and do not cause crack deflection or crack branching. The extracts of snapshots of the crystallizing network depicted in Figure 5.67 visualize the formation of the hole which is going to grow such that the model network fails. At $\lambda = 4.0$ a hole is observable on the left side of the extract which is apparently caused by rupture of a single link. The links which are situated adjacent to the broken, i.e. missing, link and perpendicularly to the direction of the deformation are semi-crystalline. There are further semi-crystalline links randomly distributed over the extract of the model network. At $\lambda = 4.55$, which is the first stretch at which the network is plotted in Figure 5.66, a semi-crystalline layer has grown around the hole perpendicularly to the stretching direction. In addition, 4 new holes formed in the center and on the left side of the extract due to rupture of individ-

ual links. These holes are also surrounded by crystalline domains similar to that which has been observed around the first hole at $\lambda = 4.0$. Comparing the extracts at $\lambda = 4.0$ and at $\lambda = 4.55$ indicates that the newly emerging holes result from highly crystalline and comparatively short chains. This observation is in contrast to the expectation that SIC reinforces the material and it has already been made in [3]. Probably, these links reach end-to-end distances which exceed their contour length since finite chain extensibility is not included into the model. Thus, accompanied by their high crystallinity, they preferentially break. At $\lambda = 4.58$, which is the second stretch at which the model network is plotted in Figure 5.66, two of the holes located in the center of the extract of the model network grew perpendicularly to the stretching direction compared to $\lambda = 4.55$ and the crystalline domains further evolved. However, one may wonder why the link situated at the bottom of the large hole does not possess a higher crystallinity like for example the one on its left side. A possible explanation, because of the position of the link, is that it is stretched to an end-to-end distance $r > n$. In this region, at least the conformational part of the free energy of the link is reduced, if the number of crystalline segments is decreased.

Comparing the stress-stretch curves of the crystallizing and non-crystallizing network shows that the elongation at break is increased by SIC, but the tensile strength is nearly unaltered. This is in accordance with the previous investigations. The snapshots are all taken in the range of stretches in which the stretch drops. Thus, this can be associated with fast growth of holes to large size leading to failure. In the crystallizing case, the stress drops in the region of the plateau of the stress in the non-destructive case. The crystallinity has already steeply increased, but it drops to zero as the stress does. On the one hand, rupture of semi-crystalline links contributes for the aforementioned reason. On the other hand, rupture of the network leads to contraction of the Gaussian chains which causes melting of strain-induced crystallites.

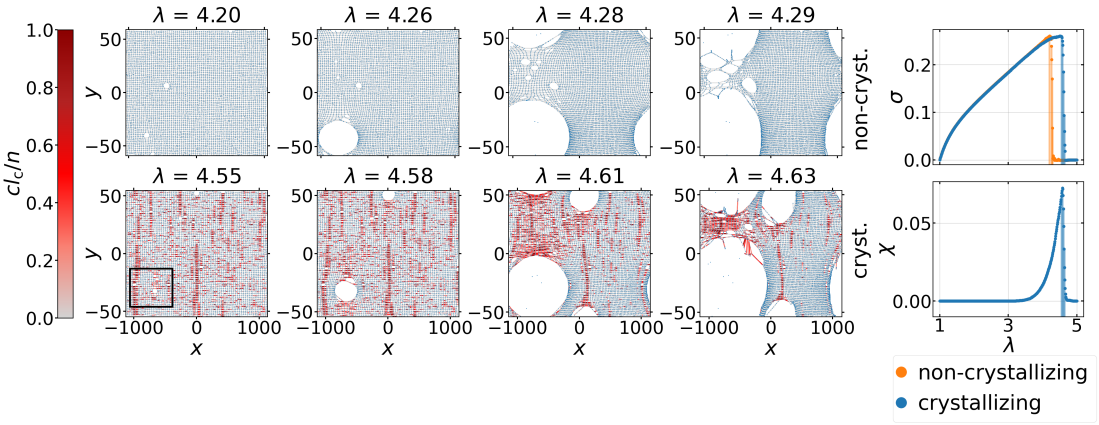

Figure 5.66.: Snapshots of a crystallizing and a non-crystallizing 2D-network which consist of $N = 5041$ nodes at certain stretches λ during a stretching process along the x-axis with the critical free energy density set to $(g/n)_{\text{crit}} = 1.25$. The scaling of the axes mimics the volume conservation. While the blue dots stand for the cross links, the crystallinity cl_c/n of each link is indicated according to the color bar. Links which cross the boundaries due to the periodic boundary conditions are not drawn. Moreover, the corresponding stress-stretch and crystallinity-stretch curves are depicted, where the vertical lines mark the stretches at which the snapshots have been taken. In Figure 5.67, the extract of the crystallizing model network, which is indicated by the black rectangle, is considered.

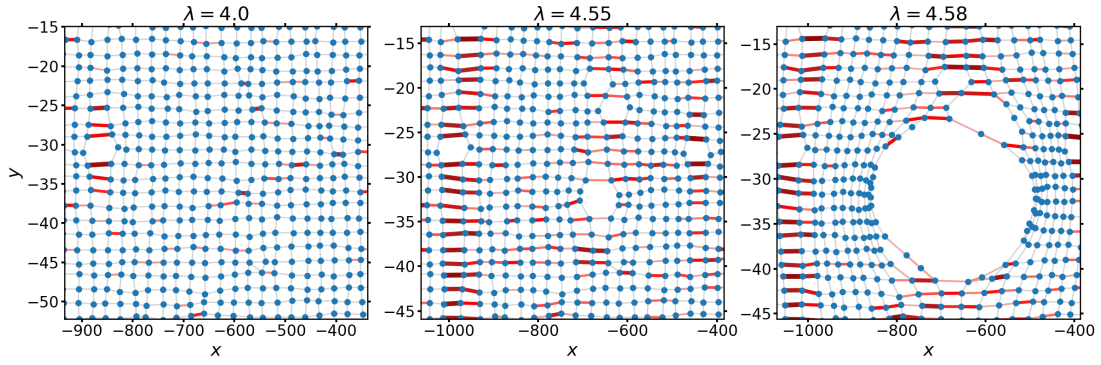

Figure 5.67.: Extracts of the snapshots of a crystallizing 2D-network which consists of $N = 5041$ nodes at certain stretches λ during a stretching along the x-axis. The critical free energy density is set to $(g/n)_{\mathrm{crit}} = 1.25$. The scaling of the axes mimics the volume conservation. The blue dots stand for the cross links, while the crystallinity cl_{c}/n of each link is indicated according to the color bar. The extract is that indicated by the rectangle in the snapshot of the crystallizing network at $\lambda = 4.55$ in Figure 5.66.

In Figure 5.68, snapshots and corresponding stress-stretch curves of unfilled crystallizing and non-crystallizing 2D-networks are shown during stretching with $(g/n)_{\mathrm{crit}} = 1.5$. The observations which can be made here are analogous to the previous case, but the crystallizing network does not fail and not even a single link in this network breaks. However, this is in accordance with the previous investigations of the tensile strength and the elongation at break depending on the critical free energy density.

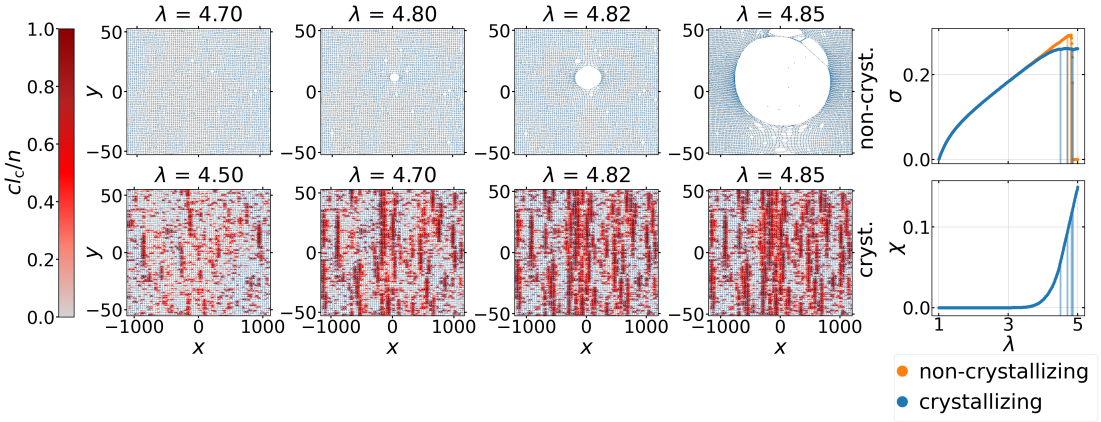

Figure 5.68.: Snapshots of a crystallizing and a non-crystallizing 2D-network which consist of $N = 5041$ nodes at certain stretches λ during a stretching process along the x-axis with the critical free energy density set to $(g/n)_{\mathrm{crit}} = 1.5$. The scaling of the axes mimics the volume conservation. While the blue dots stand for the cross links, the crystallinity cl_{c}/n of each link is indicated according to the color bar. Links which cross the boundaries due to the periodic boundary conditions are not drawn. Moreover, the corresponding stress-stretch and crystallinity-stretch curves are depicted, where the vertical lines mark the stretches at which the snapshots have been taken.

In the following it is clarified which type of linkages acts as actuator of hole formation and causes failure of filled networks. It will be investigated how the parametrization of filler-filler and polymer-filler bonds affects the rupture behavior. In addition, the role of SIC will be pointed out.

For this purpose, 8 different combinations of cut-off radii R^{ff} and R^{pf}, values of the

spring constant $k_{\mathrm{weak}}^{\mathrm{pf}}$ and filler morphologies inside the rubber matrix are applied for variable filler content ϕ of the model networks. They are given for instance in the legend of Figure 5.69 and in Table A.16. If the cut-off radii of filler-filler or polymer-filler bonds are infinitely large, the corresponding spring constant for the interaction is constant, i.e. independent of the distance between the nodes involved, and the corresponding bonds cannot break or weaken. In this case, the spring constant $k_{\mathrm{weak}}^{\mathrm{pf}}$ is not specified. Setting $k_{\mathrm{weak}}^{\mathrm{pf}} = 0.0$ means that polymer-filler bonds break reversibly. If the filler morphology is not specified, the MG is applied for $10 \cdot N$ MC steps. The annotation "random" means that the filler is randomly distributed, i.e. the MG is not applied. The remaining parameters are set to their default values.

For each configuration, 10 independent simulations of 2D-model networks consisting of $N = 5041$ nodes are conducted. The number of networks which failed is counted and the elongation at break λ_{t} is obtained as average. The elongation at break is defined as the stretch at which the maximum of the stress occurs if a network fails, i.e. the stress vanishes at the end of the simulation. In addition, the fraction of broken links L_{b}/L, the fraction of broken or weakened, depending on the parametrization, polymer-filler bonds $L_{\mathrm{pf,b/w}}/L_{\mathrm{pf}}$ and the fraction of broken filler-filler bonds $L_{\mathrm{ff,b}}/L_{\mathrm{ff}}$ are obtained as averages at different stretches λ. In particular, if at least one of the networks failed, these quantities are determined as averages at the elongation at break λ_{t} which itself depends on the parametrization. Note that the considered stretch $\lambda = 4.75$ is larger than the elongation at break of all networks which fail.

Figure 5.69 shows the data for non-crystallizing networks where $(g/n)_{\mathrm{crit}} = 1.25$ is applied. The reduction of the number of networks which failed beyond a certain filler content compared to the unfilled case indicates reinforcement by filler. The elongation at break of networks which fail is also decreased in almost every case by the inclusion of filler according to the expectation from experimental observations. Overall, the number of networks which failed and the elongation at break decrease with increasing filler content. Only if the filler-filler bonds cannot break but the polymer-filler bonds can break, the elongation at break does not show a clear dependence on filler content. However, the dependence of the elongation at break on the filler content will be elaborated further for certain network configurations in the subsequent section.

If the cut-off radii of both filler-filler and polymer-filler bonds are infinitely large, i.e. configuration 0 is considered, failure of the model networks is solely caused by rupture of links. Increasing the filler content promotes this, in particular at small deformations. Nevertheless, the networks only fail for comparatively small filler contents.

In the case that filler-filler bonds can break but polymer-filler bonds neither weaken nor break, i.e. configuration 1 is taken into account, at $\lambda = 1.5$, the fraction of broken links is reduced and a comparatively large fraction of filler-filler bonds breaks already at small deformations. Simultaneously, the fraction of broken links is decreased compared to the previous case. Like rupture of links, breaking of filler-filler bonds is advanced with increasing filler content. This still holds at the elongation at break for networks which fail. At $\lambda = 4.75$, the fraction of broken filler-filler bonds just increases until $\phi = 0.6$ and, then, decreases with increasing filler content. The fraction of broken links still increases with increasing filler content at this stretch. Note that the fraction of broken filler-filler bonds becomes larger than 0.5 at large stretches and for comparatively high filler contents. Due to the regular structure of the networks, this indicates that also filler-filler bonds break which are not aligned with the stretching direction and rather oriented perpendicularly to it. Comparatively large fractions of filler-filler bonds break already at small stretches which suggests that this process triggers the formation of holes in the model networks. However, failure is apparently governed by rupture of

links because failure just occurs for small filler contents. Overall, the fraction of broken links at the elongation at break is still comparatively small, but it is enhanced at larger stretches, i.e. after fracture. In networks which fail, breaking filler-filler bonds can be reversed due to the definition of the bonds because the network of Gaussian chains collapses during rupture which decreases the distances between interaction partners.

If filler-filler bonds can break and polymer-filler bonds can weaken, i.e. configuration 2 is considered, the fraction of broken links and broken filler-filler bonds are reduced compared to configuration 1 at $\lambda = 1.5$. At larger stretches, the fraction of broken links for configuration 2 is larger for high filler contents. At the elongation at break, the fraction of broken filler-filler bonds decreases with increasing filler content in configuration 2 in contrast to configuration 1. The fraction of weakened polymer-filler bonds also decreases with increasing filler content, but the fraction of broken links increases. Therefore, the formation of holes is possibly triggered by both breaking of filler-filler bonds and weakening of polymer-filler bonds here. Weakening of polymer-filler bonds does not cause a hole due to rupture of the bond itself, but it promotes rupture of adjacent links which bear the load. In order to examine whether filler-filler or polymer-filler bonds predominantly contribute to fracture and failure, snapshots of the model networks must be evaluated.

If the filler is now randomly distributed, i.e. configuration 3 is taken into account, both the fractions of weakened polymer-filler bonds and of broken filler-filler bonds are increased compared to configuration 2 at $\lambda = 1.5$, while the fraction of broken links is increased. The fractions of weakened polymer-filler bonds and the fractions of broke filler-filler bonds appear to be of similar magnitude. At the elongation at break, the fractions of weakened polymer-filler bonds and broken filler-filler bonds significantly decrease with increasing filler content, but they are still enhanced compared to configuration 2. In analogy to the previous case, filler-filler and polymer-filler bonds trigger the formation of holes. Nevertheless, the random distribution of filler increases the number of polymer-filler bonds which can prevent failure of the networks by building up a percolating structure. This is visualized in snapshots of model networks which will be presented in the following.

If filler-filler bonds cannot break and polymer-filler bonds can weaken, i.e. configuration 4 is considered, the fractions of broken links at $\lambda = 1.5$ are increased compared to configuration 1 and similar to those for configuration one. The fraction of weakened polymer-filler bonds is also increased compared to the previous configurations. At the elongation at break, the fraction of weakened polymer-filler bonds is comparable to configuration 2 or slightly smaller. This suggests that weakening of polymer-filler bonds promotes rupture of links.

If both filler-filler and polymer-filler bonds can break, i.e. configuration 5 is taken into account, all of the networks fail. In this case, no definite conclusion can be made on which type of linkages causes failure based on the given data. The same holds for configuration 6 in which bonds are parametrized by the same values but the filler is randomly distributed. However, at $\lambda = 1.5$, the fraction of broken links is increased compared to configurations 2 and 3, respectively, which are analogous except that polymer-filler bonds can weaken. In addition, the fractions of broken filler-filler and polymer-filler bonds are reduced.

If filler-filler bonds cannot break but polymer-filler bonds can, i.e. configuration 7 is considered, the fraction of broken polymer-filler bonds monotonically increases with increasing filler content at $\lambda = 1.5$, whereas, at $\lambda = 2.5$ and at the elongation at break, it apparently decreases until a certain filler content and increases beyond. In contrast, the fraction of broken links just increases until a certain filler content and decreases beyond at any stretch. In comparison to configuration 1, the fraction of broken links

at fixed filler content is smaller for stretches $\lambda > 1.5$. The fraction of broken filler-filler bonds in the case of configuration 1 and the fraction of broken polymer-filler bonds in configuration 7 are similar at $\lambda = 1.5$. At larger stretches, the relation depends on the filler content. In comparison to configuration 4 in which polymer-filler bonds can only weaken but not break, the fraction of broken links and the fraction of broken polymer-filler bonds is increased at the elongation at break in configuration 7. The formation of holes is apparently triggered by breaking of polymer-filler bonds which promotes rupture of links.

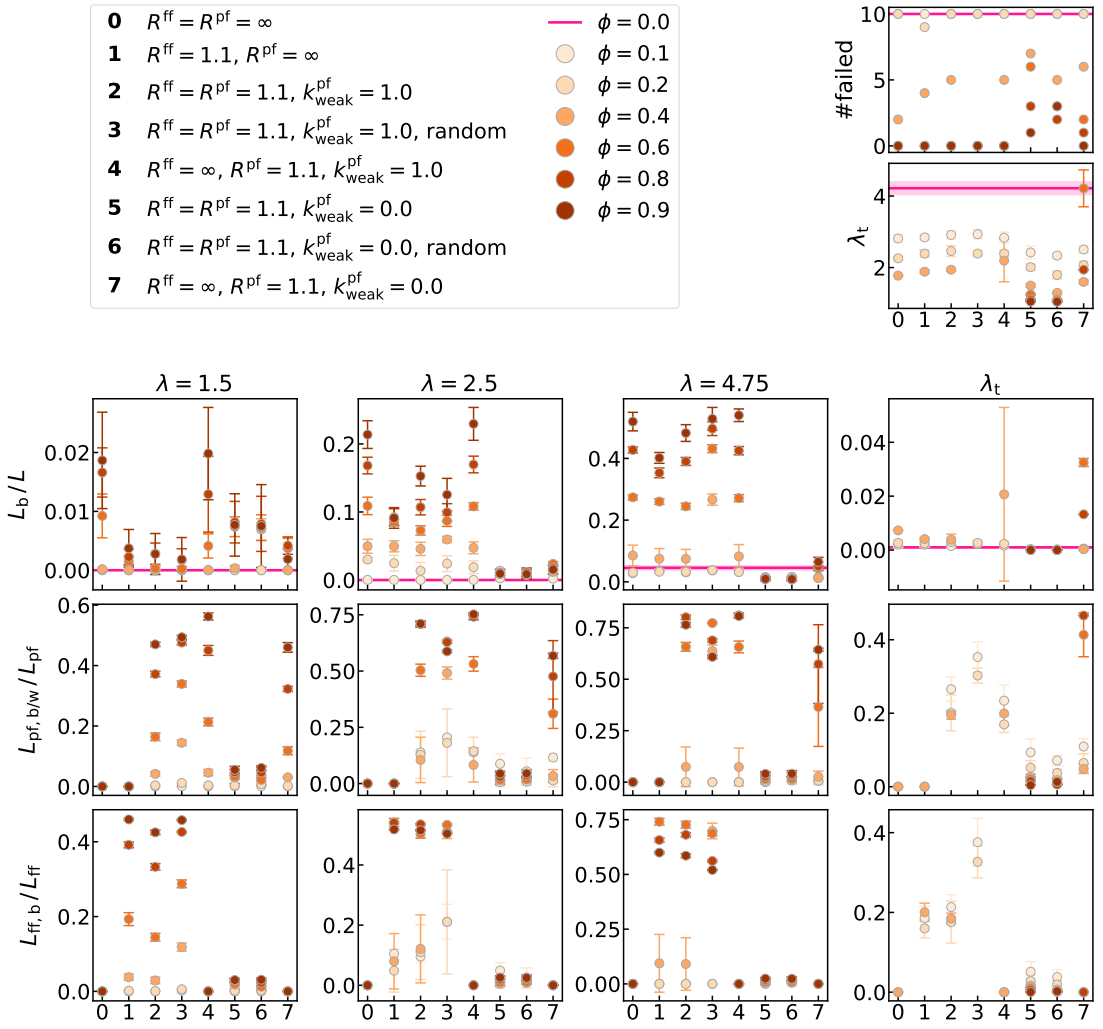

Figure 5.69.: Fraction of broken links L_b/L, fraction of broken or weakened polymer-filler bonds $L_{pf,b/w}/L_{pf}$ and fraction of broken filler-filler bonds $L_{ff,b}/L_{ff}$ obtained as averages at different stretches λ for non-crystallizing 2D-networks with variable filler content ϕ and critical free energy density $(g/n)_{crit} = 1.25$. Different combinations of parametrizations, i.e. configurations 0-7, of the cut-off radii R^{ff} and R^{pf}, the spring constant k^{pf}_{weak} and the filler morphology have been applied. The number of networks which failed and the elongation at break λ_t are also shown.

Note that Figure 5.69 is very complex, which makes some information not easily accessible, but it facilitates the direct comparison of different configurations and filler contents. In subsection A.8.2, supplemental plots of the evolution of the fraction of broken links, the fraction of broken or weakened polymer-filler bonds and the fraction of broken filler-filler bonds with increasing stretch are depicted, except for configurations 2 and

3 which are shown and discussed in the following, since the focus on the investigations in the subsequent section will be on networks with $R^{\mathrm{ff}} = R^{\mathrm{pf}} = 1.1$ and $k^{\mathrm{pf}}_{\mathrm{weak}} = 1.0$. Essentially, the supplemental plots indicate that filler-filler and polymer-filler bonds weaken or break, depending on their parametrization, at smaller stretches than the links. The onset of softening or breaking of links and bonds decreases with increasing filler content. Altogether, the weakening or breaking of filler-filler and polymer-filler bonds apparently triggers the rupture process and rupture of links may cause ultimate failure. Nevertheless, snapshots of the model networks must still be analyzed in order to draw definite conclusions regarding that.

In the case of configuration 2, the data is depicted in Figure 5.70, i.e. the MG has been applied for $10 \cdot N$ MC steps. Breaking of filler-filler bonds and weakening of polymer-filler bonds starts at smaller stretches than rupture of links. This supports the statement from above that these two effects trigger the formation of holes. They apparently start at similar stretches. Thus, still no definite conclusion can be drawn on which type of bonds is predominantly causing the formation of holes. For $\phi \leq 0.4$, as the fraction of broken links begins to steeply increase, the networks start to fail. This is indicated by the elongation at break. Both the fraction of broken filler-filler bonds and weakened polymer-filler bonds decrease immediately. The fraction of broken links rises further until it reaches a plateau value which suggests that one or several holes that have been formed grow. The formation of the plateau means that the network totally failed. In experiments, the material would be torn apart into two pieces, but this cannot happen here because of the application of periodic boundary conditions in the simulation. As already mentioned above the network of Gaussian chains collapses during fracture. Thus, broken filler-filler bonds and weakened polymer-filler bonds can establish again according to their definition. When $\phi = 0.4$, the plateau of the fraction of broken links is not clearly observable because more than half of the networks which have been considered in the computation of the mean fraction of broken links did not fail. This also holds for the behavior of the data for the fraction of broken filler-filler bonds and the fraction of weakened polymer-filler bonds. For $\phi = 0.6$ and $\phi = 0.8$, all quantities increase with increasing stretch. When the fraction of broken links increases, the increase of the fraction of broken filler-filler bonds and the fraction of weakened polymer-filler bonds is impeded.

Figure 5.71 shows analogous data for randomly distributed filler. Altogether the observations which can be made here are analogously to the case of flocculated filler.

Moreover, non-crystallizing 2D-networks are studied for the critical free energy density $(g/n)_{\mathrm{crit}} = 1.5$. The investigations conducted are analogously to the previous. The corresponding plots are included in subsection A.8.2. The fraction of broken links, broken or weakened polymer-filler bonds and broken filler-filler bonds for each configuration with variable filler content at different stretches is plotted in Figure A.66.

The evolution of the fraction of broken links, the fraction of weakened polymer-filler bonds and the fraction of broken filler-filler bonds during stretching is monitored for the configurations 2 and 3, i.e. it is set $R^{\mathrm{ff}} = R^{\mathrm{pf}} = 1.1$,$k^{\mathrm{pf}}_{\mathrm{weak}} = 1.0$ and the MG is applied for $10 \cdot N$ MC steps or for $0 \cdot N$ MC steps. The data is shown in Figure A.67 and Figure A.68, respectively. Altogether, the observations which can be made here are analogous to the case $(g/n)_{\mathrm{crit}} = 1.25$ which has been discussed above.

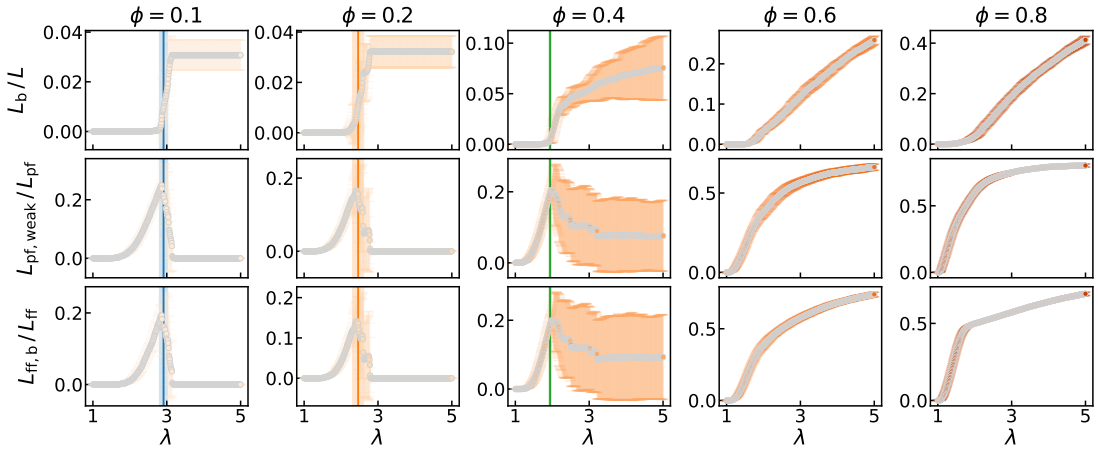

Figure 5.70.: Evolution of the fraction of broken links L_b/L, the fraction of weakened polymer-filler bonds $L_{pf,weak}/L_{pf}$ and the fraction of broken filler-filler bonds $L_{ff,b}/L_{ff}$ during stretching of non-crystallizing 2D-networks consisting of $N = 5041$ nodes with different filler content ϕ. The MG has been applied for $10 \cdot N$ MC steps and it has been set $\lambda_{max} = 5.0$ and $(g/n)_{crit} = 1.25$. The data are obtained as averages from 10 independent simulations. Moreover, the vertical lines mark the mean values of elongation at break, obtained from the networks which failed, with the standard deviation indicated by the shaded area.

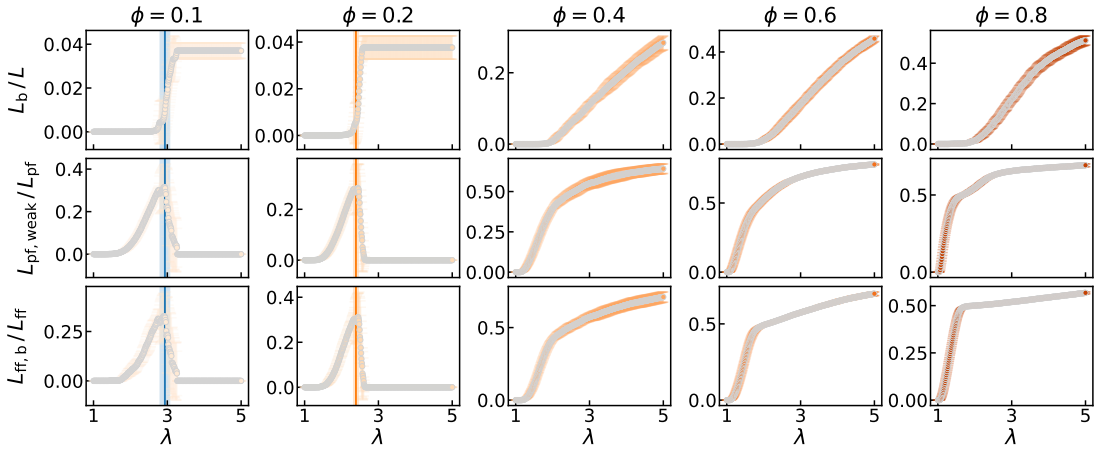

Figure 5.71.: Evolution of the fraction of broken links L_b/L, the fraction of weakened polymer-filler bonds $L_{pf,weak}/L_{pf}$ and the fraction of broken filler-filler bonds $L_{ff,b}/L_{ff}$ during stretching of non-crystallizing 2D-networks consisting of $N = 5041$ nodes with different filler content ϕ. The filler is randomly distributed and it has been set $\lambda_{max} = 5.0$ and $(g/n)_{crit} = 1.25$. The data are obtained as averages from 10 independent simulations. Moreover, the vertical lines mark the mean values of elongation at break, obtained from the networks which failed, with the standard deviation indicated by the shaded area.

As a next step, crystallizing networks are considered with critical free energy density $(g/n)_{crit} = 1.25$. First, the impact of the parametrization of the cut-off radii R^{ff} and R^{pf} and of the spring constant k^{pf}_{weak} on the fraction of broken links, the fraction of broken or weakened polymer-filler bonds and the fraction of broken filler-filler bonds is studied. The filler dispersion is considered as well. Figure 5.72 shows analogous data to that which has been presented for non-crystallizing networks in Figure 5.69. The observations which can be made here are analogous to the non-crystallizing case.

In Figure 5.73 and Figure 5.74, the evolution of the fraction of broken links, the

fraction of weakened polymer-filler bonds and the fraction of broken filler-filler bonds are plotted for configurations 2 and 3, respectively, for different filler contents. The observations which can be made here are also analogous to the non-crystallizing case which have been discussed in the context of Figure 5.70 and Figure 5.71, respectively.

Like for the non-crystallizing case, supplemental plots of evolution of the fraction of broken links, the fraction of broken or weakened polymer-filler bonds and the fraction of broken filler-filler bonds are depicted in subsection A.8.2. The conclusions which can be drawn are also analogous.

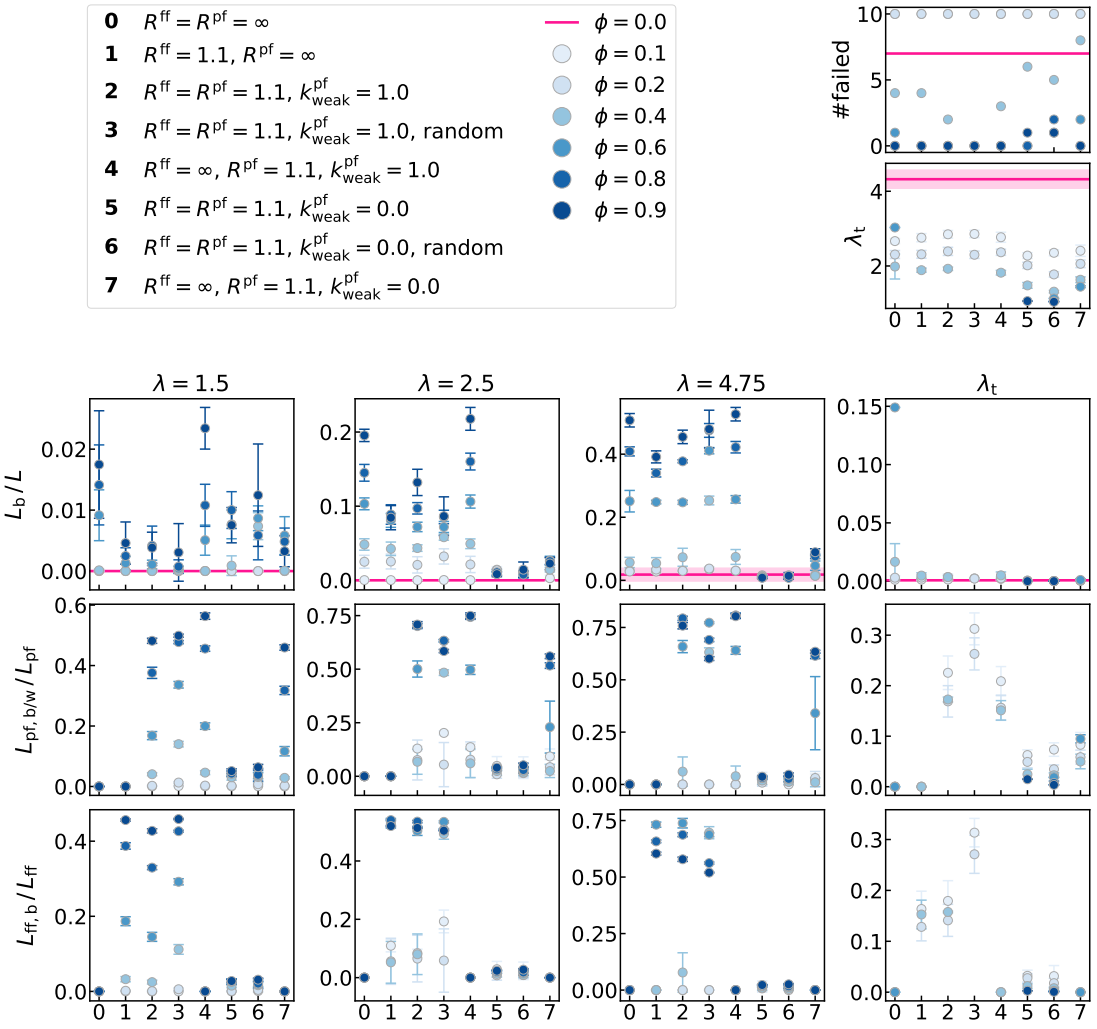

Figure 5.72.: Fraction of broken links L_b/L, fraction of broken or weakened polymer-filler bonds $L_{pf,b/w}/L_{pf}$ and fraction of broken filler-filler bonds $L_{ff,b}/L_{ff}$ obtained as averages at different stretches λ for crystallizing 2D-networks with variable filler content ϕ and critical free energy density $(g/n)_{crit} = 1.25$. Different combinations of parametrizations, i.e. configurations 0-7, of the cut-off radii R^{ff} and R^{pf}, the spring constant k^{pf}_{weak} and the filler morphology have been applied. The number of networks which failed and the elongation at break λ_t are also shown.

Now, the critical free energy density $(g/n)_{crit} = 1.5$ is applied to crystallizing networks and corresponding plots are included in subsection A.8.2. In Figure A.75, the fraction of broken links, the fraction of broken or weakened polymer-filler bonds and the fraction of broken filler-filler bonds are plotted for each configuration and different filler contents.

For the configurations 2 and 3, i.e. it is set $R^{ff} = R^{pf} = 1.1$,$k^{pf}_{weak} = 1.0$ and the MG is

applied for $10 \cdot N$ MC steps or for $0 \cdot N$ MC steps, the evolution of the fraction of broken links, the fraction of weakened polymer-filler bonds and the fraction of broken filler-filler bonds with increasing stretch are obtained. The data is presented in Figure A.76 and Figure A.77, respectively. The observations which can be made here are analogous to the case $(g/n)_{\text{crit}} = 1.25$.

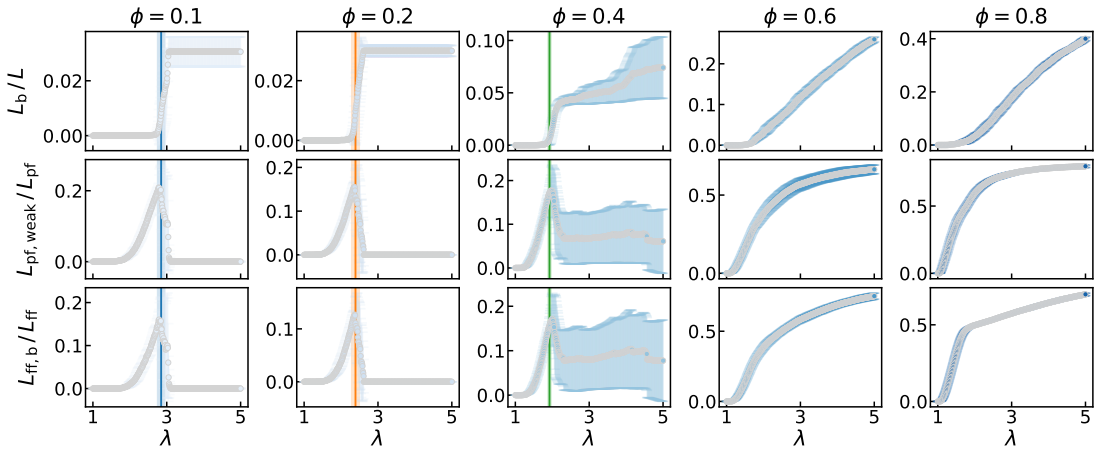

Figure 5.73.: Evolution of the fraction of broken links L_{b}/L, the fraction of weakened polymer-filler bonds $L_{\text{pf,weak}}/L_{\text{pf}}$ and the fraction of broken filler-filler bonds $L_{\text{ff,b}}/L_{\text{ff}}$ during stretching of crystallizing 2D-networks consisting of $N = 5041$ nodes with different filler content ϕ. The MG has been applied for $10 \cdot N$ MC steps and it has been set $\lambda_{\text{max}} = 5.0$ and $(g/n)_{\text{crit}} = 1.25$. The data are obtained as averages from 10 independent simulations. Moreover, the vertical lines mark the mean values of elongation at break, obtained from the networks which failed, with the standard deviation indicated by the shaded area.

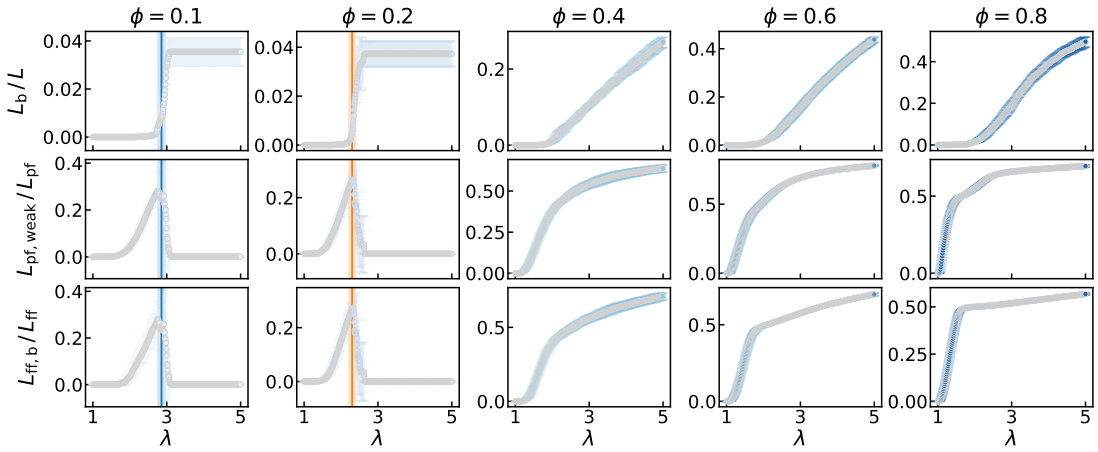

Figure 5.74.: Evolution of the fraction of broken links L_{b}/L, the fraction of weakened polymer-filler bonds $L_{\text{pf,weak}}/L_{\text{pf}}$ and the fraction of broken filler-filler bonds $L_{\text{ff,b}}/L_{\text{ff}}$ during stretching of crystallizing 2D-networks consisting of $N = 5041$ nodes with different filler content ϕ. The filler is randomly distributed and it has been set $\lambda_{\text{max}} = 5.0$ and $(g/n)_{\text{crit}} = 1.25$. The data are obtained as averages from 10 independent simulations. Moreover the vertical lines indicate the mean values of elongation at break, obtained from the networks which failed, with the standard deviation indicated by the shaded area.

The figures addressing the microstructural phenomena in the model networks presented up to this point have not yet allowed for definite conclusions regarding the

rupture process. For validation of the statements made above, snapshots of model networks with configurations 2 and 3 are considered now.

First, non-crystallizing networks with coarsely dispersed filler, i.e. configuration 2, are analyzed. Snapshots at different stretches during stretching for different filler contents with corresponding stress-stretch curves are depicted in Figure 5.75. Extracts visualizing the formation of holes in the model networks more clearly are presented in Figure 5.76 The critical free energy density is set to $(g/n)_{\mathrm{crit}} = 1.25$. At small stretches, the filler particles are apparently bound tightly to each other or to adjacent cross links because of the parametrization of filler-filler bonds. Those links which are located between two filler aggregates along the stretching direction are highly extended. With increasing stretch, holes predominantly form due to rupture of these links. Since the links are modeled as Gaussian chains, links located in the vicinity of the hole along the stretching direction retract, while the links which are oriented in the stretching direction but located perpendicular to it, adjacent to the hole, appear to be stretched even more. As the networks are stretched further, more holes occur and some of them grow. This is apparently dominated by rupture of links. In contrast to the unfilled case, the growth direction is not strictly perpendicularly to the stretching direction, but tends to deviate depending on the location of links and filler aggregates. A possible reason for the deflection of the growth direction are the polymer-filler bonds. They can only weaken but not break by definition and, thus, the holes have to circumvent them in order to grow. Besides, several small holes can merge into larger holes. For small filler contents, growth of the holes causes failure of the model networks, while, for larger filler contents, failure is prevented by the formation of a percolating structure of links and bonds. For $\phi = 0.5$, the sizes of the holes at maximum stretch suggest that the networks would fail if the maximum stretch is increased. For larger filler contents, the size of the holes at maximum stretch decreases. In the case $\phi = 0.9$, the filler nodes appear to build up strands of high node concentration which traverse the model network along the stretching direction. During stretching, the model networks are compressed perpendicularly to the stretching direction because of volume conservation. Since the energetically optimum end-to-end distance of filler-filler bonds is given by their non-zero equilibrium, this kind of displacements of the filler nodes probably minimizes the energy of the highly filled system.

Furthermore, the onset of rupture is marked in the stress-stretch curves. It is defined as the stretch at which the first link breaks. For $\phi = 0.1$, the stress shows a small kink, but, for $\phi = 0.3$, the stress does not possess a specific feature at the onset of rupture. Overall, the formation of small holes appears to not significantly affect the stress, while their successive growth until failure makes the stress drop. In addition, the stress-stretch curves suggest that the inclusion of filler impedes the rupture process since the stress does not drop abruptly from its maximum to zero but it shows oscillations for $\phi = 0.3$. Moreover, the tensile strength and the elongation at break of the network with $\phi = 0.1$ are larger than for the network with $\phi = 0.3$. This is in contrast to expectations from experimental observations, but it will be evaluated further in the next section. Note that, here, the tensile strength is understood as the maximum stress which is reached. The elongation at break is the corresponding stretch.

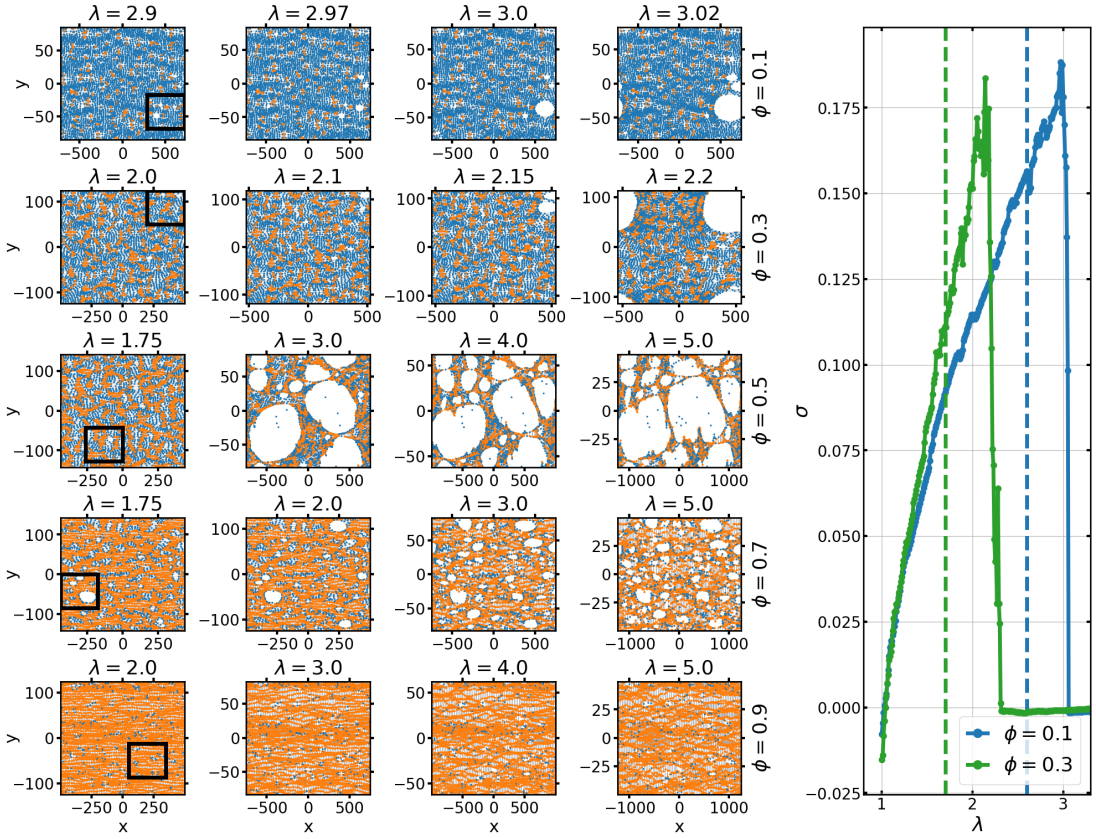

Figure 5.75.: Snapshots of non-crystallizing 2D-networks which consist of $N = 5041$ nodes with different filler content ϕ at certain stretches λ during a stretching process. The MG is applied for $10 \cdot N$ MC steps and $R^{\mathrm{ff}} = R^{\mathrm{pf}} = 1.1$, $k^{\mathrm{ff}} = 5.0$, $k^{\mathrm{pf}} = 4.0$, and $k^{\mathrm{pf}}_{\mathrm{weak}} = 1.0$, i.e. configuration 2 is considered, with $(g/n)_{\mathrm{crit}} = 1.25$ as the critical free energy density. The stretching direction is the x-axis and the scaling of the axes mimics the volume conservation. While the blue dots stand for the cross links, the orange dots represent filler. The black rectangles indicate the regions which are depicted in the extracts of the snapshots in Figure 5.76. On the right side, the corresponding stress-stretch curves of networks which failed are shown, where the data points are connected for the eye and the onset of rupture in each case is indicated by a dashed line.

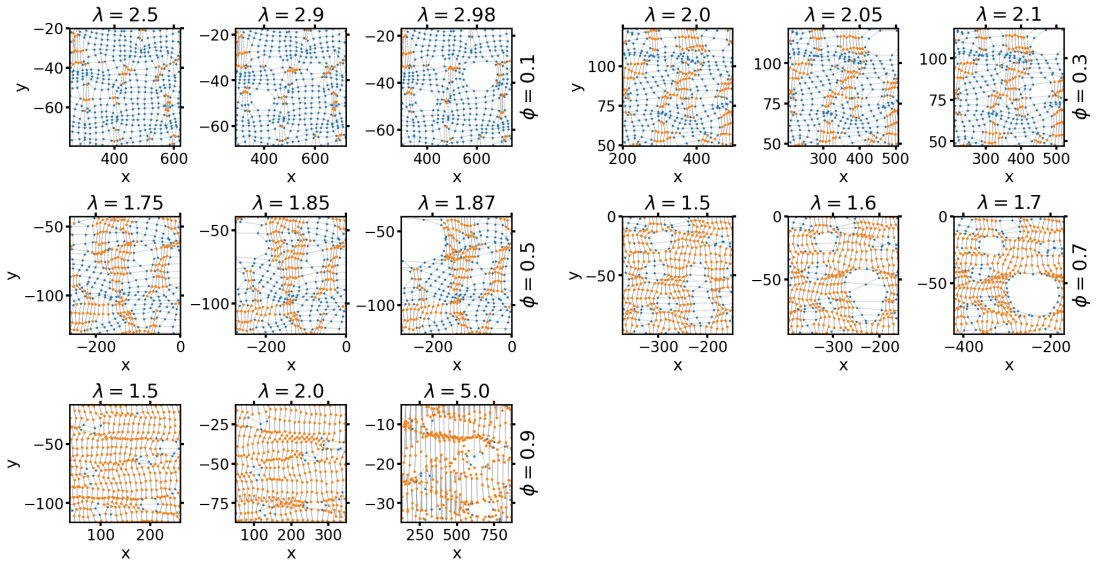

Figure 5.76.: Extracts of snapshots of the model networks depicted in Figure 5.75 in the regions indicated by the rectangles in there.

For configuration 3, in which the filler is randomly distributed, snapshots and extracts of them are presented in Figure 5.77 and Figure 5.78, respectively. Essentially, the observations which can be made here are analogous to the case of configuration 2 in which the MG is applied for $10 \cdot N$ MC steps. However, for $\phi = 0.5$, it appears like a larger number of smaller holes have formed at the maximum stretch in comparison to coarsely dispersed filler. The reason is that, for coarsely dispersed filler in contrast to finely dispersed filler, there are larger domains which only contain links and, thus, are potential holes. Moreover, for $\phi = 0.3$, the oscillations in the decrease of the stress as failure of the network is approached are more pronounced than in the case of finely dispersed filler. In addition, the stress just vanishes at larger stretch than in the case $\phi = 0.1$, although the process of rupture leading to failure starts at a significantly smaller stretch where the maximum of the stress is situated. Thus, failure is impeded. Nevertheless, this raises the question whether the quantities describing the ultimate mechanical properties of the model networks are well-defined.

Snapshots and corresponding stress-stretch curves for non-crystallizing 2D-networks with $(g/n)_{\text{crit}} = 1.5$ are presented in subsection A.8.3 in Figure A.78 to Figure A.81. Altogether, the observations which can be made there are analogous to the case $(g/n)_{\text{crit}} = 1.25$. Note that the non-crystallizing network containing a fraction $\phi = 0.3$ of finely dispersed filler does not fail, even though the holes become very large. Possibly, the maximum applied stretch is not sufficient here to cause failure. In addition, the stress significantly drops around $\lambda = 2.5$ to approximately half of its maximum value. The stress increases again beyond the sharp decrease because the network is mainly deformed but not destructed. According to this stress-stretch curve, stretching of the links and, then, their rupture dominates at small to intermediate stretches. At larger stretches, although the stress shows oscillations due to further destruction, the deformation of polymer-filler bonds appears to mainly contribute. The stress reflects their linear behavior and they are the bonds which can stabilize the network because they cannot break by definition.

Overall, the snapshots invalidate the following statement which is based on the evaluation of the evolution of the fraction of broken links, the fraction of weakened polymer-

filler bonds and the fraction of broken filler-filler bonds: The formation of holes in the model networks is initiated from breaking of filler-filler bonds. For small filler contents, the snapshots prove that the formation of holes and ultimate failure are governed by rupture of links. Although filler-filler and polymer-filler bonds do not directly cause hole formation, regions of high stress are generated by the inclusion of filler in which rupture of links is fostered. For large filler contents, percolating structures of links and bonds traverse the networks along the stretching direction which prevent failure.

Nevertheless, one may ask why the rupture of such a large fraction of filler-filler bonds optically appears to not contribute to the formation of holes. A possible explanation is that the filler-filler bond oriented along the stretching direction already break at small stretches by definition. In practice, the bond energy or the force of these bonds becomes zero. Therefore, displacing two disconnected filler nodes along the direction of the deformation during stretching, apart from the transformation of the node position at each deformation step in the simulation algorithm, would not minimize the total energy further if the bonds remain broken.

Moreover, the polymer-filler bonds also do not significantly contribute to the formation of holes. If they were highly extended, also adjacent links laying in the same plane perpendicularly to the stretching direction would be highly deformed which promotes rupture of these links. However, this is not observed here. Even if a polymer-filler bond is weakened, its energy is larger than that of a link with the same end-to-end distance. Therefore, extension of links is still preferred.

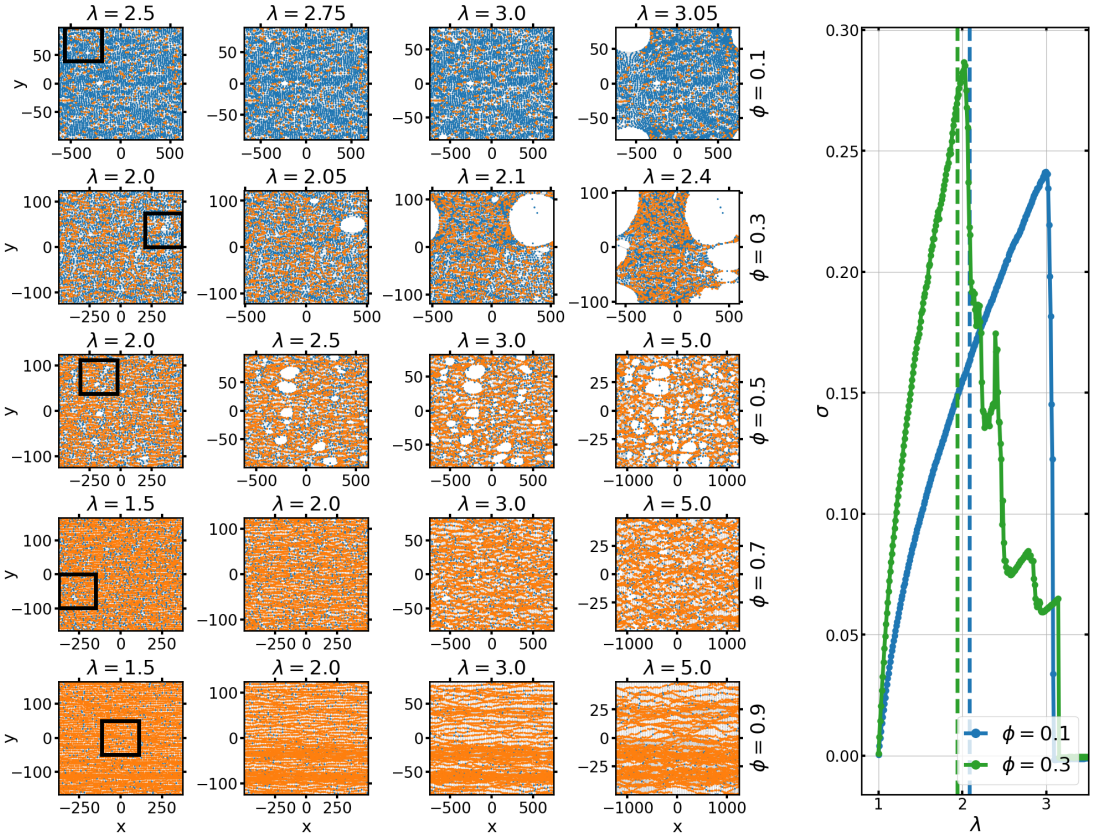

Figure 5.77.: Snapshots of non-crystallizing 2D-networks which consist of $N = 5041$ nodes with different filler content ϕ at certain stretches λ during a stretching process. The filler is randomly distributed, i.e. the MG ran through $0 \cdot N$ MC steps. It has been set $R^{\mathrm{ff}} = R^{\mathrm{pf}} = 1.1$, $k^{\mathrm{ff}} = 5.0$, $k^{\mathrm{pf}} = 4.0$ and $k^{\mathrm{pf}}_{\mathrm{weak}} = 1.0$, i.e. configuration 3 is considered, with $(g/n)_{\mathrm{crit}} = 1.25$ as the critical free energy density. The stretching direction is the x-axis. The scaling of the axes mimics the volume conservation. The blue dots stand for the cross links, while the orange dots represent filler. The black rectangles indicate the regions which are depicted in the extracts of the snapshots in Figure 5.78. On the right side, the corresponding stress-stretch curves of networks which failed are shown, where the data points are connected for the eye and the onset of rupture in each case is indicated by a dashed line.

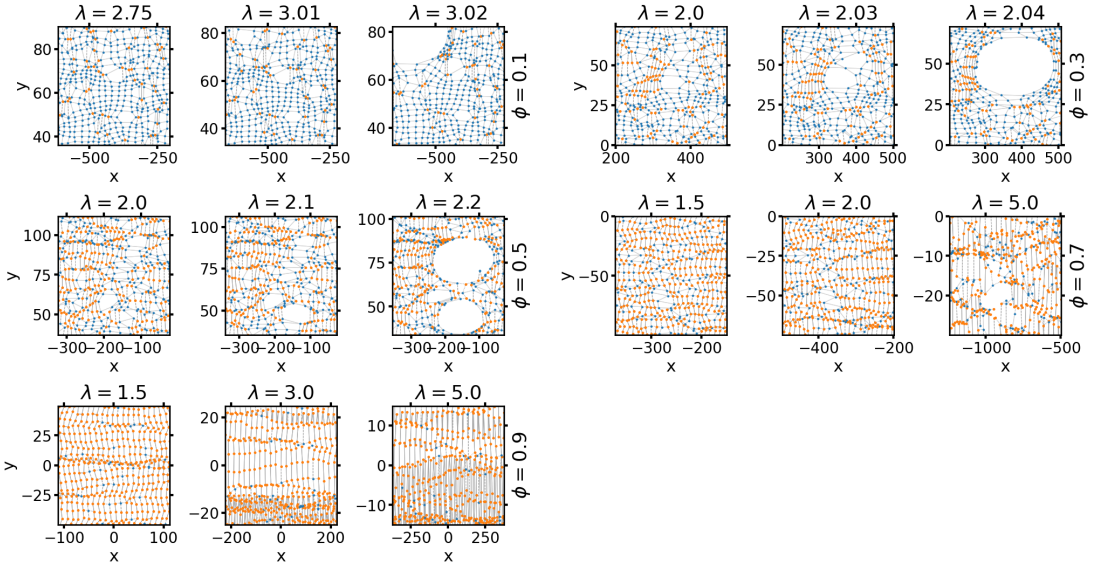

Figure 5.78.: Extracts of snapshots of the model networks depicted in Figure 5.77 in the regions indicated by the rectangles in there.

As a next step, crystallizing model networks are taken into account with critical free energy density $(g/n)_{\text{crit}} = 1.25$. For configuration 2, i.e. the MG has been applied for $10 \cdot N$ MC steps, snapshots and corresponding stress-stretch curves are shown in Figure 5.79 and extracts of snapshots can be found in Figure 5.80. Like in the non-crystallizing case, the formation of holes is initiated by rupture of links located between two adjacent filler aggregates. This happens before larger crystalline domains have build in the model networks. SIC is apparently promoted in links which are located at the boundaries of a hole and stretched further due to previous bond breaking. Nevertheless, SIC does not prevent the growth of holes in the model networks. The reason is that the end-to-end distances of the links can exceed their contour length because finite chain extensibility is not included into the model. In the region of end-to-end distances which are larger than the contour length, the energy of a link is increased with increasing crystallinity which fosters the link to reach the critical free energy density for rupture. The remaining observations which can be made here are analogous to the non-crystallizing case.

The onset of SIC which is marked in the stress-stretch curves is defined as the stretch at which the first segment of a link becomes crystalline here. It is located below the onset of rupture which indicates that SIC can reinforce the model networks.

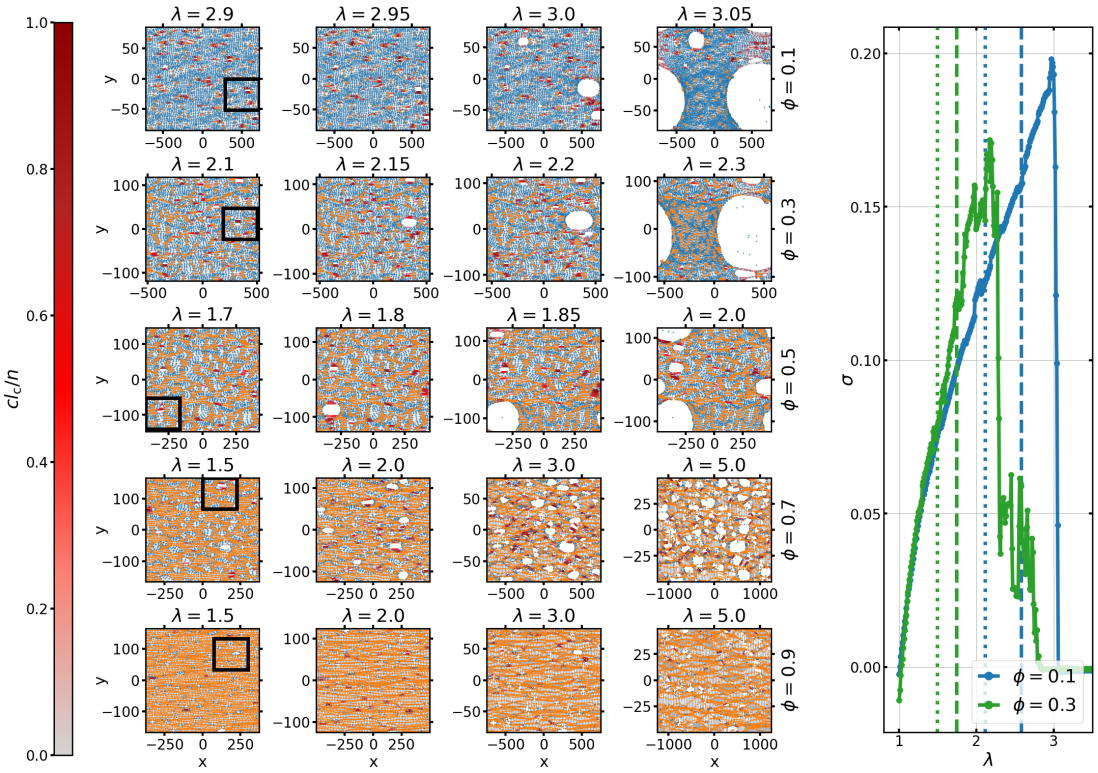

Figure 5.79.: Snapshots of crystallizing 2D-networks which consist of $N = 5041$ nodes with different filler content ϕ at certain stretches λ during a stretching process. The MG ran through $10 \cdot N$ MC steps. It has been set $R^{\mathrm{ff}} = R^{\mathrm{pf}} = 1.1$, $k^{\mathrm{ff}} = 5.0$, $k^{\mathrm{pf}} = 4.0$ and $k^{\mathrm{pf}}_{\mathrm{weak}} = 1.0$, i.e. configuration 2 is considered, with $(g/n)_{\mathrm{crit}} = 1.25$ as the critical free energy density. The stretching direction is the x-axis and the scaling of the axes mimics the volume conservation. While the blue dots stand for the cross links, the orange dots represent filler. The crystallinity cl_c/n of each link is indicated according to the color bar. In Figure 5.80, the extracts of the snapshots are depicted, which are indicated by the black rectangles. On the right side, corresponding stress-stretch curves of networks which failed are shown, where the data points are connected for the eye. The onset of SIC in each case is marked by a dotted line and the onset of rupture is indicated by a dashed line.

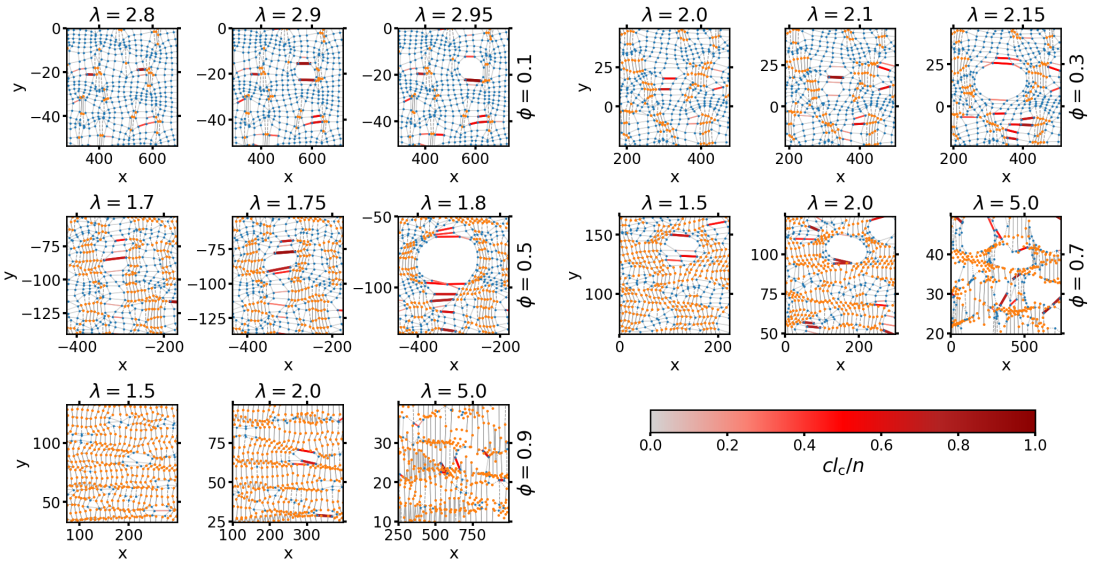

Figure 5.80.: Extracts of snapshots of the model networks depicted in Figure 5.79 in the regions indicated by the rectangles in there.

For configuration 3, i.e. randomly distributed filler, corresponding plots are depicted in Figure 5.81 and Figure 5.82. In comparison to configuration 2, SIC appears to be more advanced in this case. This agrees with the case in which rupture of links is not considered. For $\phi \geq 0.5$, it appears like a larger number of smaller holes forms. Further observations which can be made here are analogous to the case of configuration 2 and the non-crystallizing case.

In the case that the critical free energy density is set to $(g/n)_{\text{crit}} = 1.5$, snapshots and extracts of snapshots of crystallizing 2D-networks with configuration 2 and 3 are included in subsection A.8.3 in Figure A.82 to Figure A.85. The observations in this case are analogous to the previous.

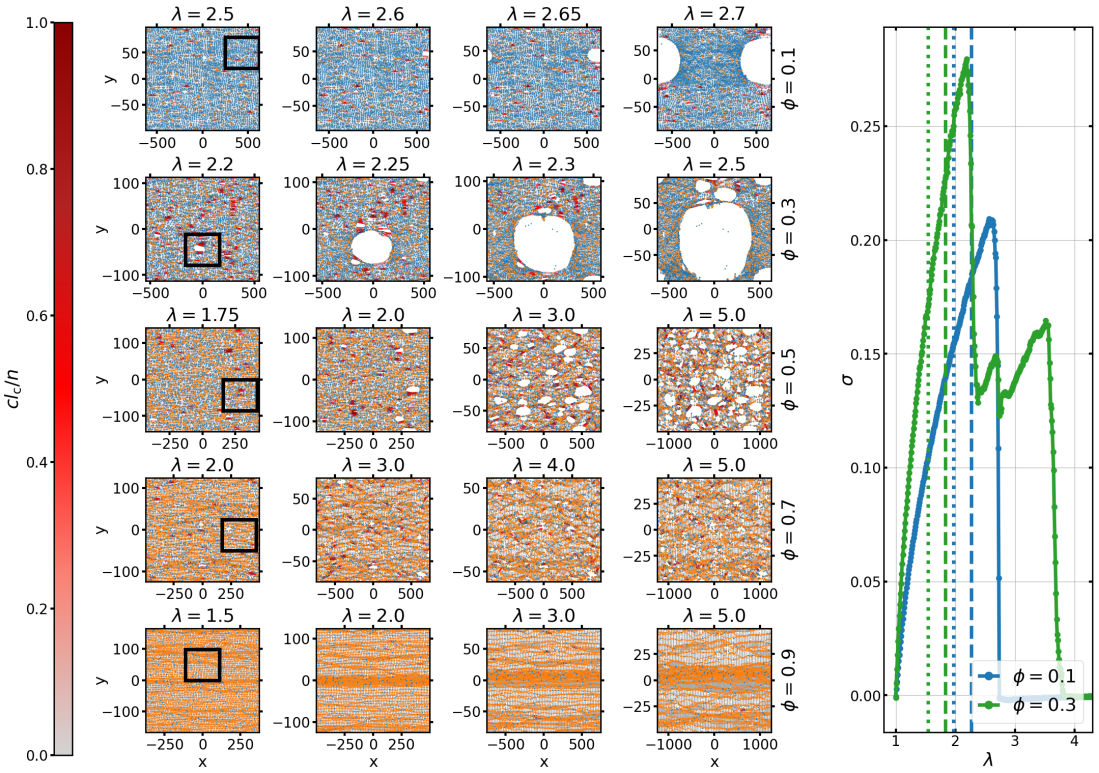

Figure 5.81.: Snapshots of crystallizing 2D-networks which consist of $N = 5041$ nodes with different filler content ϕ at certain stretches λ during a stretching. The filler is randomly distributed, i.e. the MG ran through $0 \cdot N$ MC steps. It has been set $R^{\mathrm{ff}} = R^{\mathrm{pf}} = 1.1$, $k^{\mathrm{ff}} = 5.0$, $k^{\mathrm{pf}} = 4.0$ and $k^{\mathrm{pf}}_{\mathrm{weak}} = 1.0$, i.e. configuration 3 is considered, with $(g/n)_{\mathrm{crit}} = 1.25$ as the critical free energy density. The stretching direction is the x-axis and the scaling of the axes mimics the volume conservation. While the blue dots stand for the cross links, the orange dots represent filler. The crystallinity cl_{c}/n of each link is indicated according to the color bar. In Figure 5.82, the extracts of the snapshots are depicted, which are indicated by the black rectangles. On the right side, the corresponding stress-stretch curves of networks which failed are shown, where the data points are connected for the eye. The onset of SIC in each case is marked by a dotted line and the onset of rupture is indicated by a dashed line.

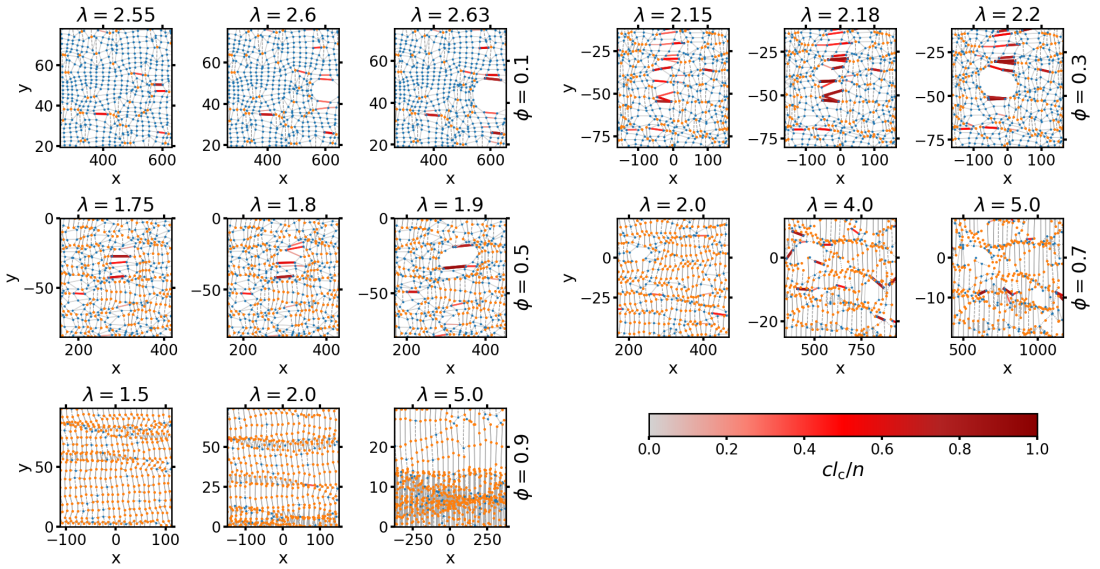

Figure 5.82.: Extracts of snapshots of the model networks depicted in Figure 5.81 in the regions indicated by the rectangles in there.

Furthermore, it is useful to check in detail whether breaking of links or SIC starts at smaller stretches because SIC is expected to act reinforcing which means crystals must evolve in order to prevent rupture of links. For this purpose, the onset stretch of rupture λ_b, which is the stretch at which the first link breaks, is plotted versus the onset stretch of SIC λ_{SIC}, which is the stretch at which the first segment of a link in the model network becomes crystalline. In Figure 5.83, this is done for configurations 2 and 3 and the critical free energy density is $(g/n)_{crit} = 1.25$. Note that the error margins of the data points are comparatively large. They result from the random factors involved when setting up the model networks. For randomly distributed, i.e. finely dispersed, filler, both the onset of rupture and the onset of SIC are decreased by the inclusion of a fraction $\phi \leq 0.2$ of filler into the networks. This agrees with stress amplification. In contrast to the unfilled case, rupture starts before SIC for these small filler contents. Since SIC has not evolved as rupture begins, it cannot retard it compared to the non-crystallizing case. For larger filler contents, both the onset of rupture and the onset of SIC become larger than for $\phi = 0.1$. This is possibly related to the filler morphology inside the rubber matrix because filler-filler bonds appear to preferentially break. While the onset of rupture and the onset of SIC are approximately equal for $\phi = 0.3$, the onset of rupture becomes larger for higher filler contents. However, this does not mean that there are no holes in the the model networks since they can also occur due to breaking of filler-filler bonds. Nevertheless, SIC could retard or even prevent failure of the model networks in this case. Both the onset of rupture and the onset of SIC are approximately constant for high filler contents.

For coarsely dispersed filler, i.e. the MG has been applied for $10 \cdot N$ MC steps, the observations and the conclusions which can be drawn are similar to the case of finely dispersed filler. Here, the onset of rupture and the onset of SIC decrease until $\phi = 0.3$ and the onset stretch of SIC is larger than the onset of rupture. For $\phi = 0.4$, both quantities are increased and approximately equal as it has been observed for $\phi = 0.3$ in the case of finely dispersed filler, but, here, there are still networks which fail. As the filler content is increased, the onset stretch of rupture tends to be larger than the onset of SIC which possibly contributes to the prevention of failure of the model networks. In addition, these data points are independent of the filler content.

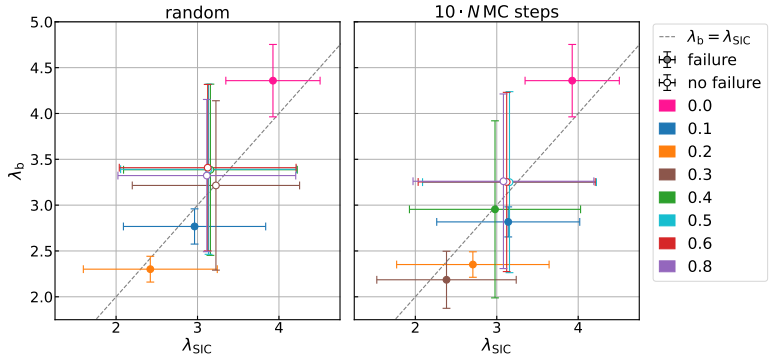

Figure 5.83.: Plots of the onset stretch of rupture λ_b versus the onset stretch of SIC λ_{SIC} for different filler content ϕ. The data has been obtained from 10 independent simulations of crystallizing 2D-networks consisting of $N = 5041$ nodes with $(g/n)_{crit} = 1.25$. In the left panel, the filler is finely dispersed, while it is coarsely dispersed in the right panel. The line for $\lambda_b = \lambda_{SIC}$ is drawn as a guide to the eye.

In Figure 5.84, analogous data for $(g/n)_{crit} = 1.5$ is shown. For finely dispersed filler, the onset stretch of rupture is larger or equal to the onset of SIC for any filler content. Therefore, SIC can possibly retard or prevent destruction of the model networks. Both quantities reach their minimum at $\phi = 0.2$. For $\phi > 0.3$, the data points are independent of the filler content. For coarsely dispersed filler, the onset of SIC is approximately independent of the filler content for $\phi > 0.1$. The onset of rupture decreases until $\phi = 0.3$ and increases then until the data points become nearly constant for $\phi \geq 0.5$. For $\phi < 0.5$, except for $\phi = 0.1$, the onset stretch of rupture is smaller than the onset of SIC.

Overall, the relation between the onset stretch of rupture and the onset stretch of SIC and indicate the ability of SIC to retard or prevent rupture. For several cases with small filler contents, rupture starts before SIC. For sufficiently large filler content, the relation is constant and SIC begins before rupture. The relation between the onset of rupture and the onset of SIC is apparently optimized for prospective retardation of rupture if the filler is finely dispersed and the critical free energy density is set to $(g/n)_{crit} = 1.5$.

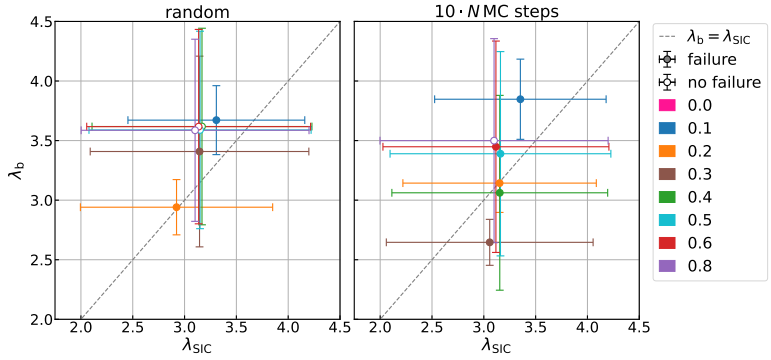

Figure 5.84.: Plots of the onset stretch of rupture λ_b versus the onset of SIC λ_{SIC} for different filler content ϕ. The data has been obtained from 10 independent simulations of crystallizing 2D-networks consisting of $N = 5041$ nodes with $(g/n)_{crit} = 1.5$. In the left panel, the filler is finely dispersed, while it is coarsely dispersed in the right panel. The line for $\lambda_b = \lambda_{SIC}$ is drawn as a guide to the eye. Note that there is no data point for $\phi = 0.0$ because no link breaks in these networks.

For the sake of completeness, snapshots of crystallizing 2D-networks with the other configurations for the parametrization of filler-filler and polymer-filler bonds are included in subsection A.8.3. All configurations are defined in Table A.16.

If filler-filler bonds cannot break and polymer-filler bonds cannot weaken or break, i.e. configuration 0 is considered which is depicted in Figure A.86, holes form between adjacent filler aggregates for small filler contents as it has been observed above. In this regions, also SIC preferentially occurs. However, SIC does not prevent rupture. Furthermore, strain-induced crystallites oriented along the stretching direction evolve at the boundaries of the holes perpendicularly to the direction of the deformation. The holes grow due to further rupture of links. If the filler content becomes sufficiently large, i.e. around $\phi = 0.5$, links and especially bonds apparently build up a percolating structure which persists during the deformation. Domains purely composed of links appear to become holes during the deformation. The remaining links appear to attach to the filler network. This can be attributed to the particular modeling of the links.

For the case of configuration 1, where the filler-filler bonds can break but polymer-filler bonds cannot weaken or break, the snapshots are shown in Figure A.87. The observations which can be made here are analogous to the case that the polymer-filler bonds weaken or not change at all. Breaking of filler-filler bonds apparently does not change the process of hole formation. Nevertheless, for $\phi = 0.5$, the holes in this network at the maximum stretch appear to be larger than for configuration 0. Therefore, breaking of filler-filler bonds possibly contributes to the rupture process in particular if a percolating filler structure traverses the polymer.

The snapshots for configuration 4 where the filler-filler bonds cannot break but filler-filler bonds can weaken are depicted in Figure A.88. The observations do not change in this case.

If both filler-filler and polymer-filler bonds can break, i.e. configuration 5 is considered, the initiation of hole formation changes. Corresponding snapshots of the model networks are shown in Figure A.89. While holes formed in domains of links for the previously considered parametrizations of filler-filler and polymer-filler bonds, hole formation is now appears to be preferentially initiated by breaking of filler-filler bonds or by breaking of polymer-filler bonds. The former effect means that holes emerge inside filler aggregates, but the study of configurations 1 to 3 proves that breaking of filler-filler bonds is not sufficient to cause failure of highly filled model networks. The latter effect triggers the formation of holes directly at the polymer-filler interface. These observations demonstrate the importance of a strong polymer-filler interface for the persistence and strength of filled elastomers.

The snapshots for configuration 6, which is analogous to configuration 5 but with randomly distributed filler, are depicted in Figure A.90. The observations are analogous to those made for configuration 5. However, since the fraction of polymer-filler bonds is increased now due to the morphology, they are also more involved in the process of hole formation now.

If filler-filler bonds cannot break but polymer-filler bonds can, i.e configuration 7, snapshots of the model networks are shown in Figure A.91. In this case, holes predominantly form due to breaking of polymer-filler bonds. In addition, the snapshots indicate that also breaking of polymer-filler bonds is not sufficient to cause failure of highly filled model networks.

Altogether, the snapshots of the model networks indicate that the parametrization of polymer-filler bonds determines whether holes preferentially form in domains consisting of solely of links or at the polymer-filler interface. Moreover, the investigations prove that neither breaking of filler-filler bonds or breaking of polymer-filler bonds alone can cause failure of highly filled model networks. Both types of bonds must be breakable

to initiate this phenomenon.

In this section, the fraction of broken filler-filler bonds, broken or weakened polymer-filler bonds and broken links in the model networks during stretching and snapshots of them have been obtained. Although large fractions of filler-filler and polymer-filler bonds break or weaken respectively for the configurations 2 and 3 which are of special interest, rupture of links initiates the formation of holes. It is also crucial for failure of the model networks. Nevertheless, rupture of links occurs preferentially between adjacent filler aggregates because the stress of links located in this regions appears to be amplified. SIC preferentially occurs at the boundaries of the holes as it is expected. However, if these links become highly crystalline and they are stretched beyond their contour length, they cannot prevent the growth of holes or cause crack deflection because they tend to break as finite chain extensibility is not included into the model. In addition, SIC only starts before rupture depending on the filler content, filler dispersion and critical free energy density.

5.8. Tensile Strength and Elongation at Break

The previous section dealt with local phenomena inside the model networks during rupture. As a next step, the tensile strength and the elongation at break of the model networks, which are macroscopic quantities describing the ultimate mechanical properties, are studied. The impact of the filler content and, in particular, the filler dispersion on the tensile strength and the elongation at break is investigated. The role of the choice of the critical free energy density for rupture of links will also be pointed out. Additionally, the impact of the parametrization of filler filler and polymer-filler bonds is considered.

2D-networks

Since the analysis of unfilled networks indicated $(g/n)_{\mathrm{crit}} = 1.25$ as suitable critical free energy density while the investigation of filled networks suggested $(g/n)_{\mathrm{crit}} = 1.5$, both values will be applied subsequently.

Figure 5.85 shows plots of the fraction of broken links L_{b}/L, the tensile strength σ_{t}, the elongation at break λ_{t} the number of damaged networks and the number of failed networks versus filler content ϕ for 2D-networks with critical free energy density $(g/n)_{\mathrm{crit}} = 1.25$. The filler is coarsely dispersed and the networks are stretched up to $\lambda_{\mathrm{max}} = 5.0$. For obtaining the desired quantities for each configuration from the simulations, the same procedure as in section 5.6, where the critical free energy density has been derived from these values, is applied.

All of the simulated networks are damaged, but the number of networks which fail decreases as the percolation threshold around $\phi = 0.5$ is approached. The corresponding filler content tends to be slightly smaller for crystallizing networks. In addition, the number of unfilled networks which failed is smaller in the crystallizing case. This suggests an increased general strength of crystallizing networks. The fractions of broken links do not significantly differ for crystallizing and non-crystallizing networks. It is approximately constant until $\phi = 0.3$, but increases beyond, in particular also when the networks do not fail. A possible explanation is that the polymer-filler bonds foster the formation of a percolating structure of links and bonds traversing the polymer along the stretching direction which fosters rupture of links. Network which do not fail possess maximum strength under the applied conditions. Note that applying a larger

maximum stretch could possibly change the observations.

The maximum value of the tensile strength occurs for the unfilled networks. This is in contrast to experimental observations. It is expected that the tensile strength increases until a maximum is reached at certain filler content and decreases beyond it [13, 14, 24–27]. The location of this maximum depends on temperature and may coincide with the percolation threshold at room temperature [24, 25]. However, there is a dependence on the properties of the filler itself [13, 14]. In addition, against the expectations, the tensile strength of networks which fail decreases with increasing filler content. At first glance, this suggests that the filler is comparatively lumpy such that it potentially acts as crack precursor due to its size which is experimentally observed for agglomerates with linear dimension of the order of 10 to 100 µm [167, 184, 260, 261]. This explains why finely dispersed filler or small filler particles are preferred when rubber composites are manufactured. However, the aggregates in the model networks are at least 2 orders of magnitude smaller. Therefore, the origin of this phenomenon must be of different nature. The decrease of the tensile strength, in particular compared to the unfilled case, is caused by accelerated initiation of hole formation due stress amplification and the absence of a percolating structure of links and bonds which can stabilize the model networks. In Figure 5.75 and Figure 5.79, it has been observed for this configuration that holes first occur between adjacent filler aggregates.

Furthermore, the elongation at break is at maximum for the unfilled networks. Experiments show that a maximum should be reached for very small filler content [26], but this range may not be resolved here. The decrease with increasing filler content is consistent with experiments. In the model networks, the decrease of the elongation at break agrees with the stress amplification due to the inclusion of filler.

Both, the tensile strength and the elongation at break tend to be higher for non-crystallizing than for crystallizing networks. This is mainly attributed to the choice of the critical free energy density according to conclusions drawn during the definition of this threshold value for rupture of links.

Converting the units applied here to SI-units by using the Kuhn length $b = 9.34\,\text{Å}$ [108] of *cis*-polyisoprene and the temperature $T = 300\,\text{K}$ yields for the tensile strength of the unfilled crystallizing network $\sigma_{\text{t,SI}} = (1.27 \pm 0.03)\,\text{MPa}$. Comparing this value with those for vulcanized NR given in Table A.3 shows significant differences. Although the deformation applied in the simulation is expected to be slow, it cannot be translated to a certain strain rate which is used in experiments. The tensile strength is closest to that obtained by Savetlana *et al.* [27] at a comparatively high strain rate for the sample vulcanized with 6 phr of sulfur, but still twice as large. Nevertheless, the corresponding measured elongation at break is only slightly smaller than the value obtained from the simulation. According to the considerations made in section 2.3, the mesh size of this experimental sample is $a \approx 5.9\,\text{nm} - 9.8\,\text{nm}$ which agrees well with the initial lattice spacing of the model networks. Moreover, the tensile strength obtained in the simulation is about an order of magnitude smaller than the experimentally obtained value determined by Ostad-Movahed *et al.* [178] at comparatively low strain rate and the value presented in Figure 2.21. These two experimental samples contain a smaller amount of sulfur and, thus, must have larger mesh size than the model networks. Another possible explanation for the discrepancies of the tensile strengths is that stretches larger than $\lambda_{\text{max}} = 5.0$ are reached until failure occurs in these experiments. If rupture of links is involved in the model, the stress of the model networks does not reach the stretch range of the steep increase which is observed in the experimental data because of the choice of the critical free energy density. In addition, finite chain extensibility which causes this incline is not incorporated into the model. Furthermore, the model

networks considered up to this point are 2D in contrast to real samples which are 3D-systems. Thus, the 2D-model does not provide a reliable quantitative prediction of the tensile strength.

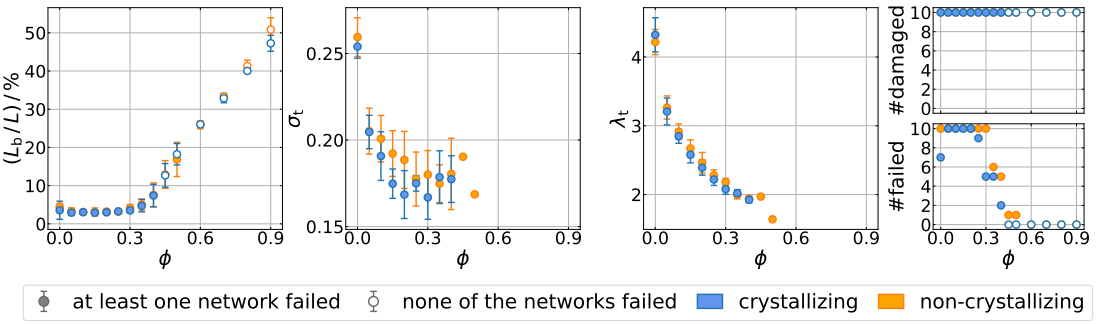

Figure 5.85.: Fraction of broken links L_b/L, tensile strength σ_t, elongation at break λ_t, number of damaged networks and number of networks which failed for variable filler content ϕ obtained from the simulations of 10 2D-networks with critical free energy density $(g/n)_{crit} = 1.25$. It is set $R^{ff} = R^{pf} = 1.1$, $k^{ff} = 5.0$, $k^{pf} = 4.0$ and $k^{pf}_{weak} = 1.0$. The MG ran through $10 \cdot N$ MC steps.

At this point, a remark regarding the identification of failure of the model networks is useful because the number of failed networks is not just 0 or 10 for each configuration. On the one hand, a certain network is characterized by 'randomness' introduced when the initial configuration is set up. Indeed, there are networks which, in comparison to others, do not fail because of the formation of a percolating structure by links and bonds as explained above. On the other hand, false positive identification of networks which do not fail possibly occurs. This means that a model network may not fail according to the definition of failure applied in this analysis, but failure of it may be observed in snapshots. As explained above, failure of the model networks is defined by stress $\sigma \leq 0.0$ at the maximum stretch. This threshold value for the stress is possibly too strict. Snapshots of all the networks simulated here have not been obtained since saving the necessary data requires a lot of storage.

In subsection A.8.4, exemplary stress-stretch curves of some of the networks simulated for Figure 5.85 are presented, but also stress-stretch curves of networks simulated for the subsequent Figures 5.86, 5.89, and 5.90 are shown. These raw stress-stretch curves visualize the described difficulties. Additionally, in particular in Figure A.93, there are networks for which the stress becomes zero at intermediate stretches, but it is significantly enhanced when the maximum stretch is reached. The origin of this behavior is not absolutely clear. A reason could be that the network did not fail when the stress became zero. Another possible explanation is that the structure remaining after failure is deformed. In contrast to links, filler-filler and polymer-filler bonds do not collapse during the rupture process because they have a non-zero equilibrium end-to-end distance.

In order to avoid the false positive identification of networks which do not fail, the definition and procedure for the identification of failure must be adapted. One possibility is to increase the threshold of the stress at maximum stretch in the criterion for failure implemented in the analysis. However, it may be difficult to justify a certain choice for this value because the stress of the model networks can also be decreased by the formation of holes even though failure does not occur. Another, more advanced possibility is to implement the identification of failure into the simulation algorithm. This would also solve the issue of the fixed maximum stretch because the simulation could be terminated at failure instead. For instance, an occupation grid of the simulation box could be constructed or a so-called Voronoi analysis could be executed as it

is done for the detection of voids in MD simulations, for example in [43]. In the latter case, each atom belongs to a cell and a void is defined by a certain size of this cell. In this model, a suitable criterion for the definition of failure based on occupation would be that the empty space along the axis perpendicular to the stretching direction must equal the length of the simulation box along this axis.

Nevertheless, for simplicity and as a first approach, the failure criterion that the stress must be $\sigma \leq 0.0$ at maximum stretch is applied also in the following.

As a next step, finely dispersed filler is considered. For this purpose, the MG is not applied to the initial configuration such that the filler is randomly distributed all over the rubber matrix. It is set $R^{\mathrm{ff}} = R^{\mathrm{pf}} = 1.1$, $k^{\mathrm{ff}} = 5.0$, $k^{\mathrm{pf}} = 4.0$ and $k^{\mathrm{pf}}_{\mathrm{weak}} = 1.0$ again. The corresponding plots, which are analogous to the previous, are depicted in Figure 5.86. In contrast to the previous results, the crystallizing networks stop to fail already for $\phi = 0.25$ which is below the percolation threshold, while the non-crystallizing networks also do not fail beyond. Although the tensile strength for the unfilled networks is higher than for poorly filled networks, the tensile strength tends to increase with increasing filler content if only filled networks are considered. A possible explanation is an increased number of polymer-filler bonds because finely dispersed filler possesses more polymer-filler interfaces than a coarse filler morphology. Since polymer-filler bonds only weaken but do not break, they can enhance the tensile strength by holding the network together. Nevertheless, the expected maximum of the tensile strength cannot be observed. In addition, the tensile strength of non-crystallizing networks is higher than for corresponding crystallizing networks. This is still be attributed to the choice of the critical free energy density. As for the previous filler morphology, the elongation at break decreases, but does not reach a maximum at small filler content. It may not be resolved here. Furthermore, the behavior of the fraction of broken links changed. For the previous morphology, it is approximately constant and starts to increase apparently linearly around the percolation threshold. Now, the data for the fraction of broken links possesses a rather s-like shape. Since the rupture of links in the model networks could be related to stress-amplification, the s-like shape of the fraction of broken links possibly reflects that of the stress-amplification factor for the networks containing finely dispersed filler to a certain extend.

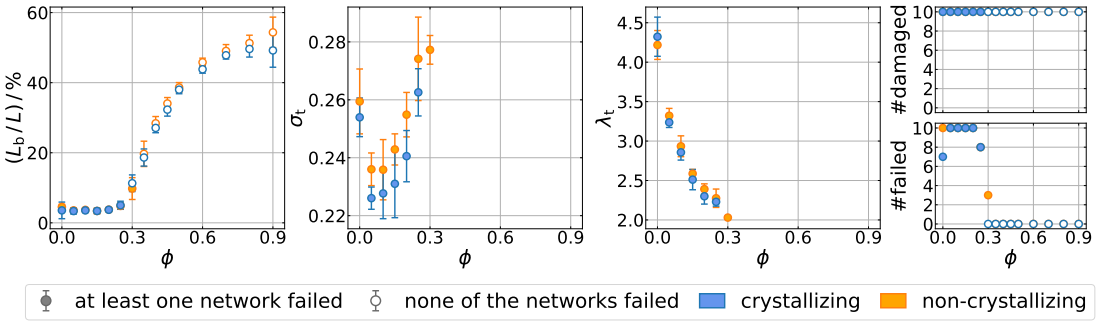

Figure 5.86.: Fraction of broken links L_b/L, tensile strength σ_t, elongation at break λ_t, number of damaged networks and number of networks which failed for variable filler content ϕ obtained from the simulations of 10 2D-networks with critical free energy density $(g/n)_{\mathrm{crit}} = 1.25$. It is set $R^{\mathrm{ff}} = R^{\mathrm{pf}} = 1.1$, $k^{\mathrm{ff}} = 5.0$, $k^{\mathrm{pf}} = 4.0$ and $k^{\mathrm{pf}}_{\mathrm{weak}} = 1.0$. In contrast to the other cases, the morphology generator is not applied here, i.e. the filler morphology is random.

According to the comparison of the rather coarse filler morphology with the randomly distributed filler, the tensile strength is elevated the finer the filler is dispersed due to an increased number of polymer-filler bonds. To validate this statement, the MG is

adapted in order to maximize the number of polymer-filler interfaces. For this purpose, the sign in the exponential function in the Metropolis criterion in Equation 4.6 is inverted:

$$\min\left(1, \exp\left[-\Delta W\right]\right) \geq \zeta. \tag{5.8}$$

The evolution of the energy and the corresponding filler morphology is presented in Figure 5.87. The incline of the energy implies that the number of polymer-filler interfaces increases as demanded. While there are coarser aggregates in the initial morphology with randomly distributed filler, the overall dispersion becomes finer with increasing number of MC steps. In the following, the adjusted MG is set to run through $100 \cdot N$ MC steps.

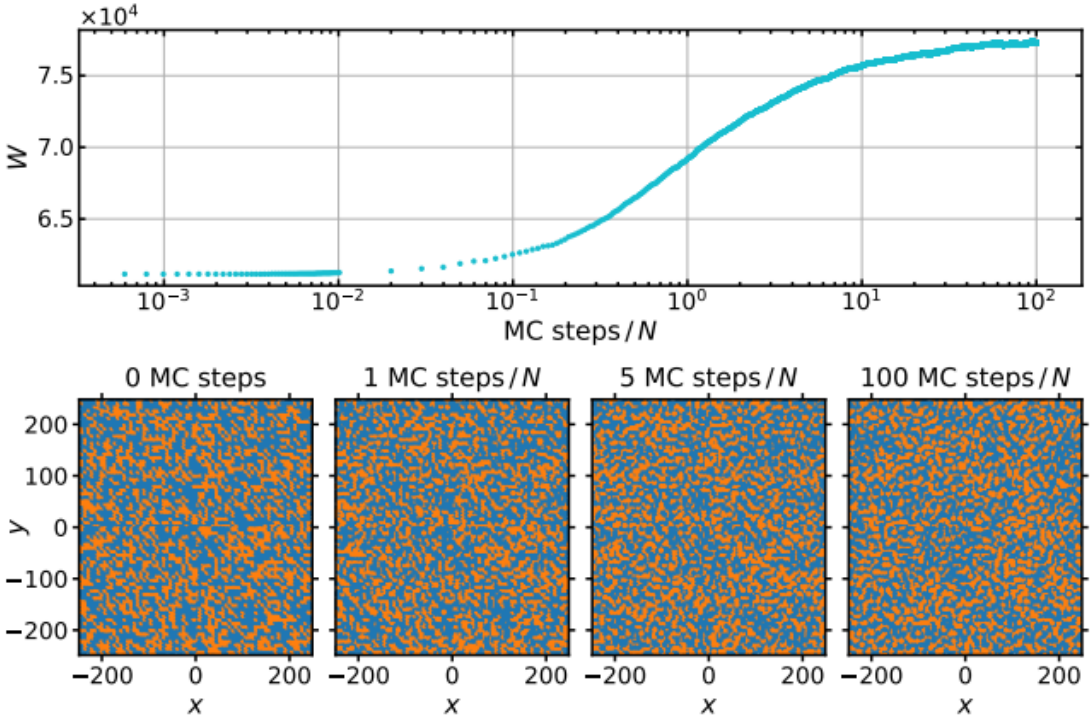

Figure 5.87.: Evolution of the energy W and the filler morphology generated with the adapted Metropolis criterion given in Equation 5.8 for a 2D-networks consisting of $N = 5041$ nodes and containing a fraction $\phi = 0.4$ of filler. The radius for setting up the neighbor list is set as $r_{\mathrm{morph}} = 2\, d_{\mathrm{init}}$.

In Figure 5.88, the fraction of broken links L_{b}/L, the tensile strength σ_{t}, the elongation at break λ_{t} the number of damaged networks and the number of failed networks are plotted versus filler content ϕ for 2D-networks with critical free energy density $(g/n)_{\mathrm{crit}} = 1.25$. As for the other filler morphologies, the tensile strength of poorly filled networks is smaller than that of the unfilled network. The difference is increased compared to randomly distributed filler. Taking the data for coarsely dispersed filler into account, this effect is enhanced when the filler becomes finer. In addition, the reduction of the tensile strength here with respect to the case of randomly distributed filler is systematic. Until the filler content at which the networks do not fail anymore is reached, the tensile strength increases as for the previous morphology. It appears like the slope of the data does not significantly change due to the new filler morphology. In addition, the elongation at break behaves analogously to the previous case. Nevertheless, the number of failed networks in the crystallizing case already begins to decrease for $\phi = 0.2$. Furthermore, the fraction of broken links steeply inclines between $\phi = 0.25$

and $\phi = 0.4$. Beyond this incline, the fraction of broken links is elevated compared to the case of randomly distributed filler. This is possibly related to the increased number of polymer-filler bonds.

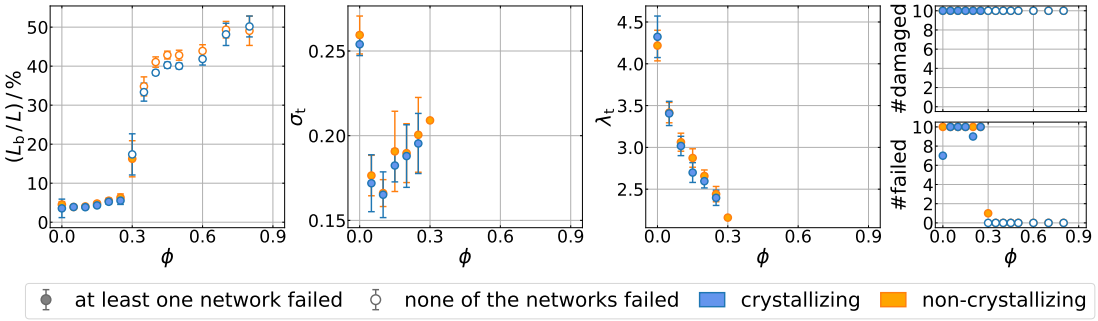

Figure 5.88.: Fraction of broken links L_b/L, tensile strength σ_t, elongation at break λ_t, number of damaged networks and number of networks which failed for variable filler content ϕ obtained from the simulations of 10 2D-networks with critical free energy density $(g/n)_{crit} = 1.25$. It is set $R^{ff} = R^{pf} = 1.1$, $k^{ff} = 5.0$, $k^{pf} = 4.0$ and $k^{pf}_{weak} = 1.0$. In contrast to the other cases, the morphology generator is configured such that the number of polymer-filler interfaces is maximized.

Up to this point, the critical free energy density $(g/n)_{crit} = 1.25$ which has been obtained in section 5.6 as rupture criterion from the analysis of unfilled networks has been combined with different filler morphologies. The investigation of the dependence of the tensile strength on the filler content has shown that the morphology affects the behavior. However, in any case, the tensile strength of crystallizing networks is smaller or at least equal to that of the corresponding non-crystallizing networks which is in contradictory to experimental observations. Analogous observations are made for the elongation at break. Therefore, the higher value for the critical free energy density $(g/n)_{crit} = 1.5$ is applied in the following. This value has been derived from the dependence of the tensile behavior of filled networks on the critical free energy density.

In Figure 5.89, the fraction of broken links L_b/L, the tensile strength σ_t, the elongation at break λ_t, the number of damaged networks and the number of networks which failed are plotted versus filler content ϕ for 2D-networks with critical free energy density $(g/n)_{crit} = 1.5$. Here, the original MG ran through $10 \cdot N$ MC steps. The elevated critical free energy density has the desired effect. Both the tensile strength and the elongation at break of crystallizing networks are higher than for the corresponding non-crystallizing networks. However, the higher critical free energy density does not improve the overall behavior of the tensile strength and the elongation at break. The tensile strength decreases until $\phi = 0.3$ and increases afterwards until the networks do not fail anymore which is at $\phi > 0.6$ for the crystallizing and at $\phi > 0.5$ for the non-crystallizing networks. This does not fit experimental observations. The elongation at break decreases as expected until $\phi = 0.45$, but it tends to increase above. This can be attributed to the formation of structures of links and bonds which stabilize the networks to a certain extend. Furthermore, in particular for the unfilled case, none of the crystallizing networks is damaged, while most of the non-crystallizing networks fail. Possibly, a larger maximum stretch is required for damage of the crystallizing networks. In any filled case, the number of failed networks behaves similar in the crystallizing and in the non-crystallizing case. Moreover, above the percolation threshold, the fraction of broken links in the non-crystallizing networks becomes higher than in the crystallizing networks which indicates a higher degree of destruction.

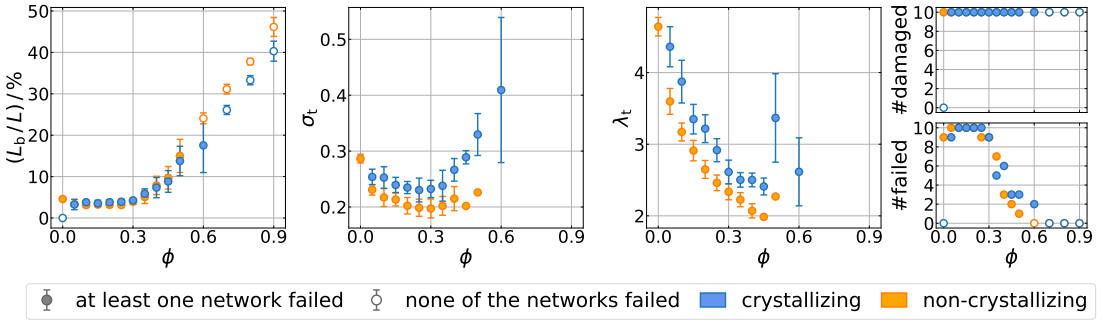

Figure 5.89.: Fraction of broken links L_b/L, tensile strength σ_t, elongation at break λ_t, number of damaged networks and number of networks which failed for variable filler content ϕ obtained from the simulations of 10 2D-networks with critical free energy density $(g/n)_{crit} = 1.5$. It is set $R^{ff} = R^{pf} = 1.1$, $k^{ff} = 5.0$, $k^{pf} = 4.0$ and $k^{pf}_{weak} = 1.0$. The MG ran through $10 \cdot N$ MC steps.

In Figure 5.90, the results are plotted for networks containing randomly distributed filler. The behavior of the fraction of broken links behaves as in the case of $(g/n)_{crit} = 1.25$. The tensile strength of poorly filled networks is still smaller than for unfilled networks, but it shows the expected increase if only filled networks are considered. This is the desired behavior and it confirms that the filler dispersion determines the behavior of the tensile strength depending on filler content. For $\phi > 0.35$, none of the crystallizing networks fails, while this threshold is at $\phi = 0.3$ for non-crystallizing networks. The elongation at break decreases as expected until this point. In addition, both the tensile strength and the elongation at break are higher for crystallizing than for non-crystallizing networks which agrees with experiments.

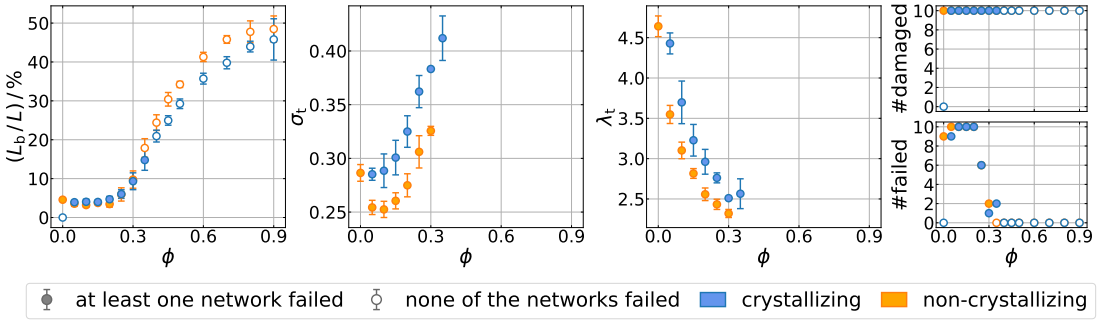

Figure 5.90.: Fraction of broken links L_b/L, tensile strength σ_t, elongation at break λ_t, number of damaged networks and number of networks which failed for variable filler content ϕ obtained from the simulations of 10 2D-networks with critical free energy density $(g/n)_{crit} = 1.5$. It is set $R^{ff} = R^{pf} = 1.1$, $k^{ff} = 5.0$, $k^{pf} = 4.0$ and $k^{pf}_{weak} = 1.0$. In contrast to the other cases, the morphology generator is not applied here, i.e. the filler morphology is random.

In Figure 5.91, analogous plots are presented for networks in which the filler morphology has been generated by the adapted MG. Due to the change in the Metropolis criterion given in Equation 5.8, the number of polymer-filler interfaces is maximized by the algorithm. None of the non-crystallizing networks fails anymore already for $\phi > 0.25$, while this happens for $\phi > 0.3$ for crystallizing networks. This means that the strength of the non-crystallizing networks is higher than that of the corresponding crystallizing networks for $\phi = 0.3$. The tensile strength of the unfilled networks is still higher than that of poorly filled networks. However, the tensile strength still tends to increase and the elongation at break decreases.

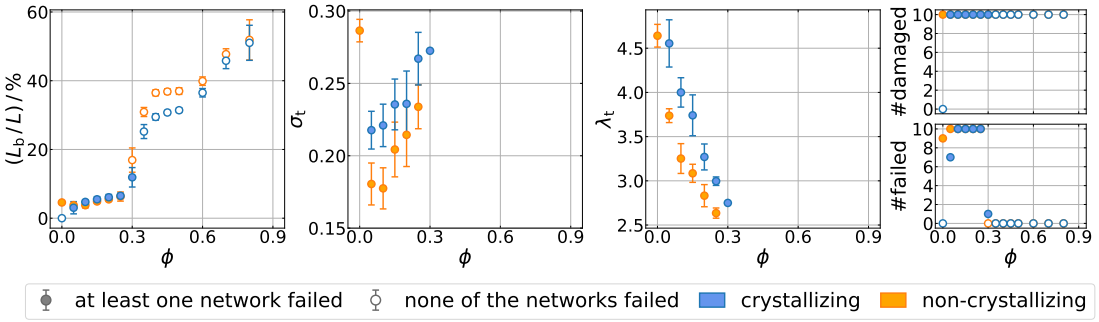

Figure 5.91.: Fraction of broken links L_b/L, tensile strength σ_t, elongation at break λ_t, number of damaged networks and number of networks which failed for variable filler content ϕ obtained from the simulations of 10 2D-networks with critical free energy density $(g/n)_{crit} = 1.5$. It is set $R^{ff} = R^{pf} = 1.1$, $k^{ff} = 5.0$, $k^{pf} = 4.0$ and $k^{pf}_{weak} = 1.0$. In contrast to the other cases, the morphology generator is configured such that the number of polymer-filler interfaces is maximized.

As indicated above, it is expected that increasing the maximum stretch increases the number of networks which fail. Therefore, networks containing randomly distributed filler are considered again and the critical free energy density is set to $(g/n)_{crit} = 1.5$, but the networks are now stretched up to $\lambda_{max} = 7.0$. The corresponding results are presented in Figure 5.92. Although the behavior of the tensile strength and the elongation at break is not affected by increasing the maximum applied stretch, the number of networks which fail is identical for crystallizing and non-crystallizing networks and starts to decrease for $\phi = 0.2$. This is expected according to the corresponding snapshots of the model networks. For networks which contain a comparatively small filler content and which do not fail when the maximum stretch $\lambda_{max} = 5.0$ is applied, large holes have evolved and a comparatively small number of links and bonds holds the networks together. It has been expected that further stretching leads to failure. However, note that stretching of the links beyond their contour length is promoted by increased stretch. For larger filler contents, the holes which have formed at $\lambda_{max} = 5.0$ are comparatively small due to percolating structures of links and bonds and, thus, it is expected that the networks also do not fail for $\lambda_{max} = 7.0$

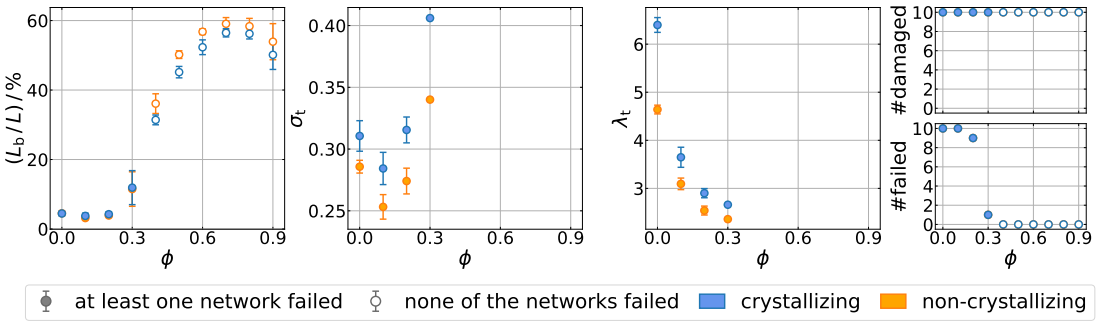

Figure 5.92.: Fraction of broken links L_b/L, tensile strength σ_t, elongation at break λ_t, number of damaged networks and number of networks which failed for variable filler content ϕ obtained from the simulations of 10 2D-networks with critical free energy density $(g/n)_{crit} = 1.5$. It is set $R^{ff} = R^{pf} = 1.1$, $k^{ff} = 5.0$, $k^{pf} = 4.0$ and $k^{pf}_{weak} = 1.0$. The filler is randomly distributed. The network is stretched up to $\lambda_{max} = 7.0$.

Overall, the filler morphology determines the behavior of the tensile strength depending on filler content, while the choice of the critical free energy density determines the relation between the quantities describing the ultimate properties of crystallizing

and corresponding non-crystallizing networks. Both aspects affect the filler content for which failure of the networks terminates. Dependent on the filler morphology, the networks become stable below or at the percolation threshold. For finely dispersed filler, an increase of the tensile strength can be observed, but it does not show a maximum because it cannot be computed if the networks do not fail. The elongation at break behaves according to experimental data under the consideration that the region of small filler content is possibly not highly resolved. However, the tensile strength of the unfilled model networks does not agree with experimental data because it is higher than for networks with small filler content. Altogether, the simulated networks for $(g/n)_{\mathrm{crit}} = 1.5$ and randomly distributed filler yield the optimum results for tensile strength and elongation at break with regard to experimental data.

In order to gain insights into the dependence of the ultimate properties on the parametrization of filler-filler and polymer-filler bonds, plots of the fraction of broken links L_{b}/L, the tensile strength σ_{t}, the elongation at break λ_{t} the number of damaged networks and the number of network which failed versus filler content ϕ are presented in subsection A.8.5. The configurations which have been analyzed in section 5.7 and are defined in Table A.16 are considered. Configuration 2 and 3 have already been discussed in detail above.

For the case that both filler-filler and polymer-filler bonds do not weaken or break, i.e. configuration 0, the data is shown in Figure A.96 and in Figure A.97. The tensile strength and the elongation at break possess very similar behavior to that observed for configuration 2 in Figure 5.85 and in Figure 5.89 where the filler is coarsely dispersed and filler-filler bonds break but polymer-filler bonds weaken. In particular, the tensile strength and the elongation at break are elevated for crystallizing networks compared to non-crystallizing networks when the critical free energy density is set to $(g/n)_{\mathrm{crit}} = 1.5$.

If the filler-filler bonds can break but the polymer-filler bonds cannot weaken or break, i.e. configuration 1 in considered, the behavior of the tensile strength and the elongation at break is still similar and no significant differences can be observed. The corresponding data is depicted in Figure A.98 and Figure A.99.

For the case that filler-filler bonds do not break but the polymer-filler bonds weaken, i.e. configuration 4, the data is shown in Figure A.100 and in Figure A.101. The tensile strength and the elongation at break behave still analogously.

However, if both the filler-filler and the polymer-filler bonds can break, i.e. configuration 5 is considered, the observations change. The corresponding data is depicted in Figure A.102 and in Figure A.103. Both crystallizing and non-crystallizing networks fail above the percolation threshold, but there are still cases in which none of the crystallizing networks fails. Due to the parametrization of the bonds, none of the type of links and bonds can stabilize the network along the stretching direction by being permanently active. The tensile strength tends to decrease until $\phi = 0.6$. In the other cases, the minimum of the tensile strength occurred around $\phi = 0.3$. The elongation at break decreases further with increasing filler content. The fraction of broken links also decreases with increasing filler content which indicates that rupture is governed by breaking of filler-filler and polymer-filler bonds. The analysis of snapshots of corresponding model networks has shown that breaking of filler-filler and polymer-filler bonds initiates the formation of holes. To what extend this contributes to failure has not obtained. What is also different in this case is that the fraction of broken links, the tensile strength and the elongation at break for crystallizing and non-crystallizing networks still overlap when the critical free energy density is increased from $(g/n)_{\mathrm{crit}} = 1.25$ to $(g/n)_{\mathrm{crit}} = 1.5$.

If the filler is randomly distributed instead of coarsely dispersed now, i.e. config-

uration 6 is considered, the onset of the increase of the tensile strength is shifted to approximately $\phi = 0.5$. The corresponding data is presented in Figure A.104 and in Figure A.105. This shift can possibly be related to the fraction of polymer-filler bonds depending on the filler morphology.

For the case that filler-filler bonds cannot break but polymer-filler bonds can, i.e. configuration 7, the data is plotted in Figure A.106 and in Figure A.107. The observations are similar to those made for configuration 2. In comparison to configuration 1, where filler-filler bonds can break but polymer-filler bonds cannot, the filler content at which most of the networks do not break anymore is increased here. This can be attributed to the smaller fraction of polymer-filler bonds compared to filler-filler bonds in the respective networks. If the critical free energy density is increased from $(g/n)_{\text{crit}} = 1.25$ to $(g/n)_{\text{crit}} = 1.5$, the tensile strength and the elongation at break of crystallizing and non-crystallizing networks still overlap. Furthermore, the behavior of the fraction of broken links for configuration 7 is different compared to the other configurations. For $(g/n)_{\text{crit}} = 1.25$, it tends to decrease until $\phi = 0.4$ and increases afterwards. While the increase continues in the crystallizing case, the fraction of broken links in the non-crystallizing case levels off at $\phi = 0.7$. For $(g/n)_{\text{crit}} = 1.5$, the fraction of broken links in the non-crystallizing case behavior similar as for $(g/n)_{\text{crit}} = 1.25$, but, in the crystallizing case, the fraction of broken links becomes even smaller and nearly constant for $\phi > 0.6$.

Another point which requires some attention is that, on the one hand, most of the model networks, which have been analyzed in this section, do not fail if the filler content is sufficiently large. On the other hand, if the parametrization of filler-filler or polymer-filler bonds is changed such that failure occurs also at large filler contents, the tensile strength decreases with increasing filler content until a certain point and just increases beyond. Therefore, some attempts are made to generate an increase of the tensile strength at small deformations until a maximum is reached and a decrease beyond. This is the behavior expected from experimental observations. For this purpose, configuration 3 is combined with breaking of polymer-filler bonds. In configuration 3, the filler is randomly distributed, filler-filler bonds can break and polymer-filler bonds can weaken. Breaking of polymer-filler bonds is now introduced at cut-off distances larger than that which is still applied for weakening. Hence, breaking of polymer-filler bonds is expected to occur at large deformations.

Corresponding plots of the fraction of broken links L_{b}/L, the tensile strength σ_{t}, the elongation at break λ_{t} the number of damaged networks and the number of network which failed versus filler content ϕ are included in subsection A.8.5. The modification of the parametrization of polymer-filler bonds does not have the desired effect. In any case, the tensile strength decreases at small filler contents until most of the networks do not fail anymore. If some of the networks fail at filler contents $\phi > 0.6$, the tensile strength tends to increase with increasing filler content.

In conclusion, these final investigations demonstrate that the parametrization of filler-filler and polymer-filler bonds also plays a crucial role for the reinforcing ability of the filler and, thus, for the behavior of the tensile strength depending on filler content. In particular, they highlight the importance of the polymer-filler interface.

3D-networks

In this subsection, 3D-model networks consisting of $N = 5832$ nodes are considered. Based on the analysis of the fraction of broken links, the tensile strength, the elon-

gation at break, the number of damaged networks and the number of networks which failed depending on the choice of the critical free energy density for filled networks, $(g/n)_{\mathrm{crit}} = 1.5$ is set as a suitable value. For the parametrization of filler-filler and polymer-filler bonds, it is set $R^{\mathrm{ff}} = R^{\mathrm{pf}} = 1.1$, $k^{\mathrm{ff}} = 5.0$, $k^{\mathrm{pf}} = 4.0$ and $k^{\mathrm{pf}}_{\mathrm{weak}} = 1.0$. In the following, coarsely dispersed filler, i.e. the MG is applied for $50 \cdot N$ MC steps. and finely dispersed, i.e. randomly distributed, filler are considered. The networks are stretched until $\lambda_{\mathrm{max}} = 5.0$.

For the case of coarsely dispersed filler, the fraction of broken links L_{b}/L, tensile strength σ_{t}, elongation at break λ_{t}, number of damaged networks and number of networks which failed are plotted versus filler content ϕ in Figure 5.93. First of all, the behavior of the model networks appears to be determined by their percolation threshold. In the 3D-case it is between $\phi = 0.3$ and $\phi = 0.4$. Therefore, the networks do not fail already for smaller filler contents than in the 2D-case. The tensile strength decreases with increasing filler content up to this point. For non-crystallizing networks, the tensile strength is at maximum for the unfilled case. These observations are consistent with the corresponding 2D-case, for which the data is depicted in Figure 5.85 and Figure 5.85. In the crystallizing case, none of the networks fails for $\phi \leq 0.05$. Thus, it cannot be observed whether the maximum of the tensile strength occurs for the unfilled case or for poorly filled networks. This can be attributed to the choice of the critical free energy density or to the applied maximum stretch. Both the tensile strength and the elongation at break are larger for the crystallizing networks than for the corresponding non-crystallizing networks as it is expected. The elongation at break decreases nearly linearly with increasing filler content. Furthermore, the behavior of the fraction of broken links differs from that observed in the 2D-case. For small filler contents, it is larger for the non-crystallizing network than for the crystallizing networks, but the observation is the opposite as the crystallizing networks start to fail and the fraction of broken links in them steeply increases. As $\phi = 0.3$ is approached, the fraction of broken links becomes again larger for the non-crystallizing networks and increases further in both cases, although the networks to not fail.

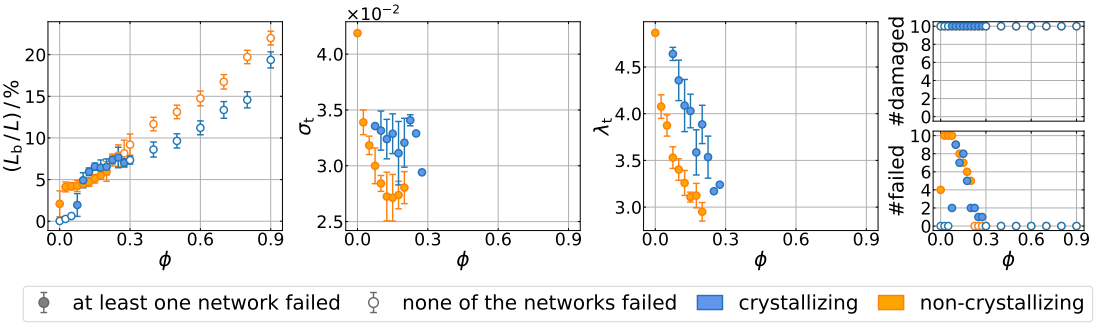

Figure 5.93.: Fraction of broken links L_{b}/L, tensile strength σ_{t}, elongation at break λ_{t}, number of damaged networks and number of networks which failed for variable filler content ϕ obtained from the simulations of 10 3D-networks with critical free energy density $(g/n)_{\mathrm{crit}} = 1.5$. It is set $R^{\mathrm{ff}} = R^{\mathrm{pf}} = 1.1$, $k^{\mathrm{ff}} = 5.0$, $k^{\mathrm{pf}} = 4.0$ and $k^{\mathrm{pf}}_{\mathrm{weak}} = 1.0$. The MG ran through $50 \cdot N$ MC steps.

Figure 5.94 shows the corresponding data for the case of finely dispersed filler. In this case, nearly none of the crystallizing networks fails. However, the tensile strength tends to increase with increasing filler content which has also been observed in the 2D-case in Figure 5.86 and Figure 5.90. The elongation at break still tends to decrease with increasing filler content. The networks do not fail anymore already for smaller

filler contents than in the case of coarsely dispersed filler. Furthermore, the fraction of broken links behaves similar to the case of coarsely dispersed filler.

In the previous subsection, the tensile strength of unfilled crystallizing 2D-networks has been compared to experimental data for vulcanized NR. In the 3D-case, the tensile strength of the unfilled crystallizing networks cannot be obtained since none of these networks fails under the conditions applied in the simulations. However, for $(g/n)_{\mathrm{crit}} = 1.5$, the tensile strength in SI-units of unfilled non-crystallizing 3D-model networks is $\sigma_{\mathrm{t,SI}} = (0.21 \pm 0.01)\,\mathrm{MPa}$, while it is $\sigma_{\mathrm{t,SI}} = (1.43 \pm 0.04)\,\mathrm{MPa}$ for 2D-networks. The value for the 3D-network is smaller by a factor of roughly 7. The deviation of this order of magnitude of the stress between the 2D- and 3D-case is systematic. Hence, the stresses of filled crystallizing networks which failed are significantly smaller than the experimentally measured data given in Table A.3.

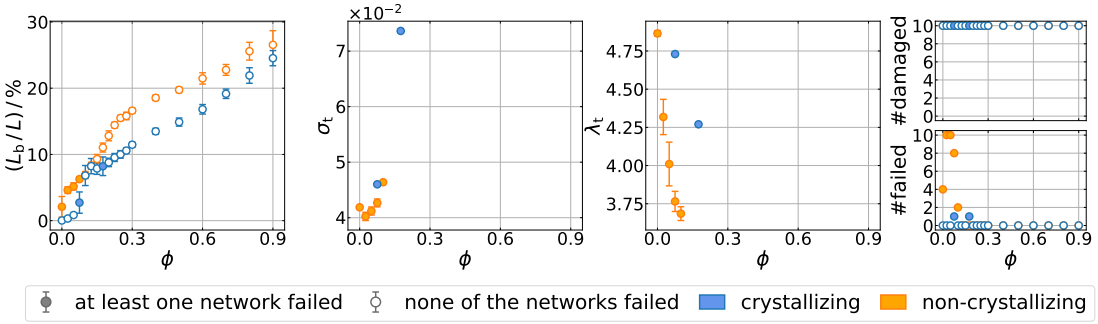

Figure 5.94.: Fraction of broken links L_{b}/L, tensile strength σ_{t}, elongation at break λ_{t}, number of damaged networks and number of networks which failed for variable filler content ϕ obtained from the simulations of 10 3D-networks with critical free energy density $(g/n)_{\mathrm{crit}} = 1.5$. It is set $R^{\mathrm{ff}} = R^{\mathrm{pf}} = 1.1$, $k^{\mathrm{ff}} = 5.0$, $k^{\mathrm{pf}} = 4.0$ and $k^{\mathrm{pf}}_{\mathrm{weak}} = 1.0$. The filler is randomly distributed.

Since the crystallizing model networks do not fail if they are poorly filled or unfilled, smaller critical free energy densities are additionally considered. For the case that the critical free energy density is $(g/n)_{\mathrm{crit}} = 1.35$ and the filler is coarsely dispersed, the data is presented in Figure A.111 in subsection A.8.5. For finely dispersed filler, the data is shown in Figure A.112. In both cases the observation which can be made are analogous to the case of $(g/n)_{\mathrm{crit}} = 1.5$.

Reducing the critical free energy density further to $(g/n)_{\mathrm{crit}} = 1.3$ yields the data depicted in Figure 5.95 for coarsely dispersed filler and in Figure 5.96 for finely dispersed filler. In this case, the behavior of the tensile strength and the elongation at break is still analogous depending on filler content, but the difference due to SIC is reduced with respect to the case of $(g/n)_{\mathrm{crit}} = 1.5$. Therefore, smaller values of the critical free energy density are not tested. Moreover, in particular for finely dispersed filler, crystallizing networks still fail at larger filler contents than non-crystallizing networks. Nevertheless, unfilled and poorly filled networks still do not fail here.

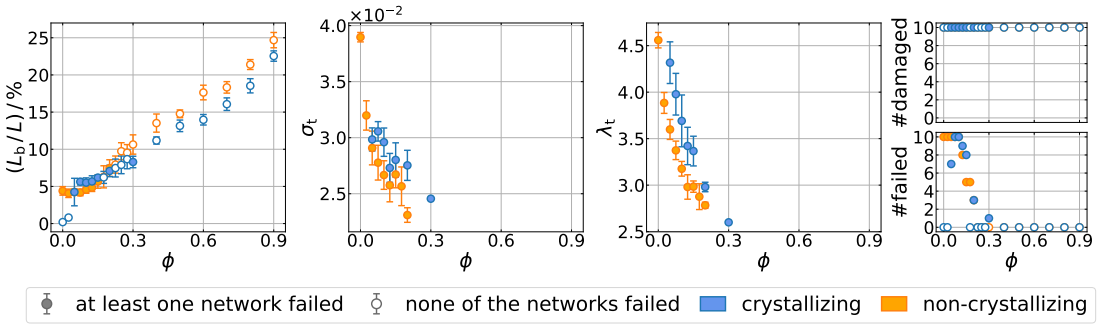

Figure 5.95.: Fraction of broken links L_b/L, tensile strength σ_t, elongation at break λ_t, number of damaged networks and number of networks which failed for variable filler content ϕ obtained from the simulations of 10 3D-networks with critical free energy density $(g/n)_{crit} = 1.3$. It is set $R^{ff} = R^{pf} = 1.1$, $k^{ff} = 5.0$, $k^{pf} = 4.0$ and $k^{pf}_{weak} = 1.0$. The MG ran through $50 \cdot N$ MC steps.

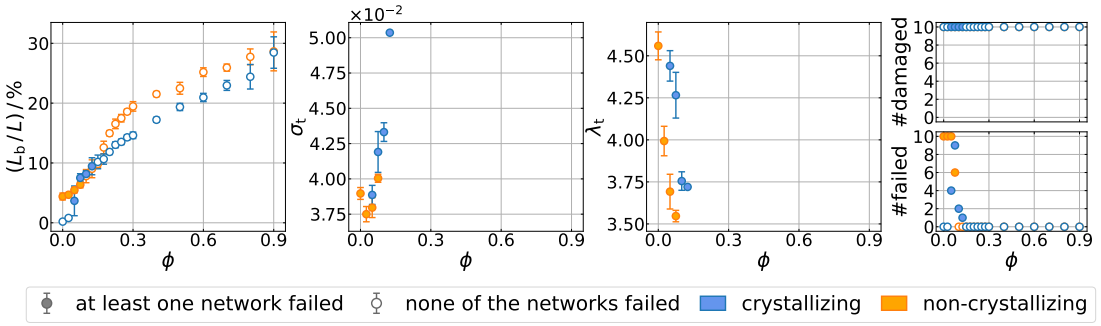

Figure 5.96.: Fraction of broken links L_b/L, tensile strength σ_t, elongation at break λ_t, number of damaged networks and number of networks which failed for variable filler content ϕ obtained from the simulations of 10 3D-networks with critical free energy density $(g/n)_{crit} = 1.3$. It is set $R^{ff} = R^{pf} = 1.1$, $k^{ff} = 5.0$, $k^{pf} = 4.0$ and $k^{pf}_{weak} = 1.0$. The filler is randomly distributed.

Because changing the critical free energy density mainly affects the difference between the tensile strength of the crystallizing and the corresponding non-crystallizing networks, the networks containing randomly distributed filler are now stretched up to $\lambda_{max} = 7.0$. It is expected that more of the networks fail in particular for small filler contents. For the critical free energy density $(g/n)_{crit} = 1.5$, the results are depicted in Figure 5.92. Increasing the maximum applied stretch has the desired effect. In contrast to the case of $\lambda_{max} = 5.0$, for which the results are presented in Figure 5.94, all of the unfilled non-crystallizing networks fail here. The corresponding crystallizing networks still do not fail. For $\phi = 0.025$, none of the crystallizing networks failed previously, but one fails now. The overall number of networks which failed is enhanced in both the crystallizing and the non-crystallizing case of poorly filled networks. The tensile strength of crystallizing networks tends to decrease until $\phi = 0.05$, but increases for larger filler contents. At every filler content, it is larger for the crystallizing networks than for the non-crystallizing networks as expected. The elongation at break of crystallizing networks is also enhanced compared to non-crystallizing networks. In addition, the number of networks which failed is larger for the non-crystallizing networks. Therefore, the strength of the model networks must be advanced by SIC. However, there is an interval of the fraction of broken links in which it is larger for crystallizing networks than for non-crystallizing networks and all of those crystallizing networks failed. Due to the increased applied stretch, SIC is favored, but, simultaneously, it is promoted that the end-to-end distance of links exceeds their contour length. Since the free energy

density of highly crystalline links is increased as their end-to-end distance exceeds their contour length, rupture of these links is promoted.

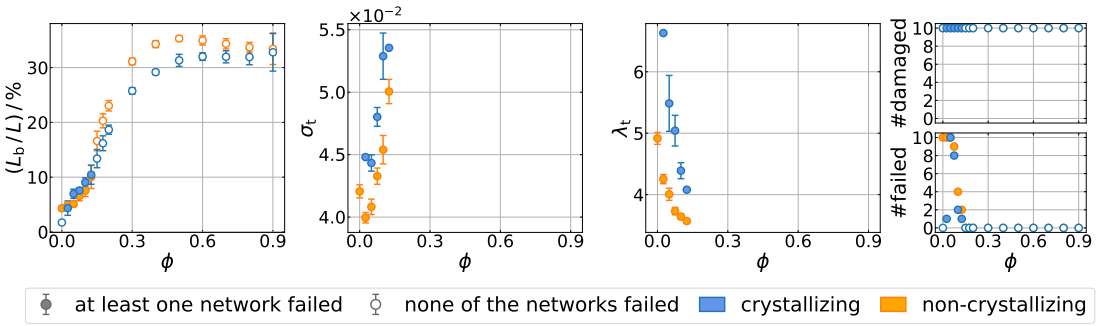

Figure 5.97.: Fraction of broken links L_b/L, tensile strength σ_t, elongation at break λ_t, number of damaged networks and number of networks which failed for variable filler content ϕ obtained from the simulations of 10 3D-networks with critical free energy density $(g/n)_{crit} = 1.5$ and $\lambda_{max} = 7.0$. It is set $R^{ff} = R^{pf} = 1.1$, $k^{ff} = 5.0$, $k^{pf} = 4.0$ and $k^{pf}_{weak} = 1.0$. The filler is randomly distributed.

Altogether, the investigation of the tensile strength and the elongation at break of 3D-networks depending on the filler dispersion, the filler content and the applied critical free energy density shows similar results to the 2D-case. The filler dispersion determines the dependence of the tensile strength on the filler loading, while the choice of the critical free energy density governs the relation between the values for crystallizing and corresponding non-crystallizing networks. If the filler is finely dispersed, the tensile strength increases with increasing filler content with exception of the unfilled case. As the percolation of the model networks is approached, which is at smaller filler content for 3D-networks than for 2D-networks, the model networks do not fail. However, the values for the tensile strength obtained via simulations of 3D-networks are significantly smaller than in the 2D-case and than experimentally measured values.

5.9. Fatigue

In this section, the fatigue life of the model networks is studied. For simplicity, this is done based on the crack nucleation approach, according to the considerations made in section 2.5. The crack growth approach, however, requires information about the crack that causes failure or a measure for the growth rate and the computation of the energy release rate if a crack is inserted initially into a model network. The crack growth approach is more controlled and, thus, yields less scattered data because void formation due to the randomness of the model networks is relevant for crack nucleation but less important for the growth of a macroscopic crack. Networks into which a crack has been inserted artificially in the initial configuration have been studied qualitatively with tensile test simulations in [3].

In order to study the fatigue behavior of the model networks, Wöhler curves are obtained by plotting the maximum stretch λ_{max} versus the fatigue life N_{fail}, i.e. the number of the strain cycle in which the network fails, in a log-log plot. Note that in general the stress amplitude is applied as fixed quantity instead of the stretch. In the simulations, the stretch is the quantity that is fixed, whereas the stress is the response of a certain model network to the deformation. It is expected that, if λ_{max} is sufficiently large, the networks fail at some point. Beyond this maximum stretch at which failure occurs first, the number of the strain cycles which a networks resist is expected to decrease or, for the model networks, it must at least be constant. In general, the decrease

is linear. A sketch of a Wöhler curve for filled NR can be found in Figure 2.25. If the applied maximum stretch is sufficiently high, a network is expected to fail already in the first strain cycle.

Since simulations for multiple strain cycles are computationally very expensive, 2D-networks consisting of only $N = 196$ nodes and 3D-networks consisting of $N = 216$ nodes are investigated here, but they are deformed for up to 1000 strain cycles for each maximum stretch $\lambda_{\max}$. Note that this maximum number of strain cycles is still small compared to the number of strain cycles which can be performed in an experiment and to the number of strain cycles which the material applied in a damping element must persist. For each filler content ϕ, a fixed initial network configuration is set up. This partly eliminates the randomness in the data. The filler is randomly distributed and the spring constants and cut-off radii are set as given in Table 5.7.

For obtaining the fatigue life based on the stress-stretch curves, it is presumed that the model networks fail during stretching or in the vicinity of the maximum stretch. It has been observed that some networks can start to fail at the maximum stretch, but it takes some deformation steps at the beginning of the contraction until the stress reaches vanishingly small values. For instance, this can be observed for the network with $\phi = 0.1$ in Figure 5.98 for $\lambda_{\max} = 3.6$. In addition, not all of the networks are expected to fail in the first strain cycle and the stress is expected to be lowered in the next strain cycles. In general, failure can occur at a stretch which differs from the stretch at total maximum stress. Thus, the procedure for the identification of failure of the model networks which has been applied above to the data obtained from simulation of tensile tests is not suitable here. In addition, as pointed out earlier in the context of the tensile tests, the identification of failure of the model networks based on their stress-stretch curves bears some difficulties.

In the following, the fatigue life N_{fail} is the strain cycle in which the stress during stretching or in the vicinity of the maximum stretch strongly decreases such that it becomes smaller than a threshold value. The stress during further stretching, subsequent contraction and in the next strain cycles must be on average smaller than this threshold value.

In order to gain first insights into the mechanical behavior of the model networks during cyclic deformation, Figure 5.98 shows stress-stretch curves for all of the strain cycles for non-crystallizing 2D-networks containing different fractions of filler and for different maximum stretches. Because a large amount of data overlaps in these plots, the stress at maximum stretch $\sigma_{\max} \equiv \sigma(\lambda_{\max})$ is additionally considered as an identifier for fatigue. For each case included in Figure 5.98, $\sigma_{\max}/\sigma_{\max,1}$ is plotted versus the number of the strain cycles in Figure 5.99 with $\sigma_{\max,1}$ as the stress at maximum stretch in the first strain cycle.

In the case of the unfilled network, the stress is lowered with increasing number of strain cycles, but the network does not fail. This is a kind of fatigue is expected to occur due to rearrangements in the material. In the model, it can only be induced by rupture of links, since applied deformation is quasi-static such that the unfilled system is in an equilibrium state at each stretch. Therefore, the deformation would be reversible if links cannot break as it can be observed in Figure 5.4 by the example of one strain cycle of an unfilled model network. However, Figure 5.99 shows that the maximum stretch is only decreased once after a number of approximately 250 strain cycles which appears to be independent of the maximum applied stretch. This suggests that the decrease of the stress may be of computational origin.

For $\phi = 0.1$, the stress is lowered analogously after a certain number of strain cycles

for small maximum stretch. As the applied maximum stretch is increased to $\lambda_{\max} = 3.5$, the stress is lowered at small deformations, but it is enhanced at large deformations. This behavior can also be observed in the plot of the maximum stretch versus the strain cycle. In filled networks, rearrangements occur at small stretches because of breaking and weakening of filler-filler and polymer-filler bonds which determine the stress-stretch behavior. The increase of the stress at maximum stress possibly originates from further stretching of polymer-filler bonds which cannot break by definition. As the maximum applied stretch becomes sufficiently high, the network fails already in the first strain cycle. Since the network fails during the first steps of the contraction in the first strain cycle, $\sigma_{\max}/\sigma_{\max,1}$ is very small in the subsequent strain cycles. For $\lambda_{\max} = 3.75$, the network fails before the maximum stretch is reached in the first strain cycle reminding of the simple tensile test. Thus, $\sigma_{\max}/\sigma_{\max,1}$ is significantly enhanced after multiple strain cycles. Note that the strain cycles after failure are not physically relevant.

If the filler content is increased to $\phi = 0.3$, $\sigma_{\max}/\sigma_{\max,1}$ behaves analogous to the previous cases for $\lambda_{\max} = 1.25$, but the decrement is located at a smaller number of strain cycles now. For $\lambda_{\max} = 2.5$, the stress significantly decreases as the 1000th strain cycle is approached, in particular at maximum stretch. This behavior indicates fatigue of the model network. Due the inclusion of filler, the stress is amplified such that rupture of links is promoted which itself leads to rearrangements in the material. Hence, holes in the model networks can accumulate over several strain cycles. Nevertheless, the model network does not fail in this case. As the maximum stretch is increased to $\lambda_{\max} = 2.75$, the stress falls at a certain stretch in the first strain cycle, but it does not vanish. A hole apparently grows which does not become sufficiently large to cause failure. The ratio $\sigma_{\max}/\sigma_{\max,1}$ decreases already at a smaller number of strain cycles than in the previous case. Additionally, the stress also becomes vanishingly small which indicates failure of the model network. However, failure is not identified according to the classification described above because the stress increases again in the next strain cycles until it approaches its original level. This behavior is contradictory to fatigue. In order to check whether the model network truly fails in the strain cycle for which the stress vanishes, snapshots of the model network during the entire deformation process must be considered. They would also provide further insights why the stress increases in some strain cycles compared to the previous. Since the simulations of 1000 strain cycles are computationally very expensive and would require for the storage of a large amount of data, this is not done here. An alternative is to advance the identification of failure by the implementation of an occupation grid into the simulation algorithm. As the maximum stretch is further increased, the network fails already in the first strain cycle before the maximum stretch is reached. Although the stress for $\lambda_{\max} = 4.0$ decreases at the stretch at which it started to fall for $\lambda_{\max} = 2.75$, it does not immediately reach zero. After this comparatively slow decrease, it increases again until the network fails.

Furthermore, for $\phi = 0.5$ and $\lambda_{\max} = 1.5$, the stress decreases as number of strain cycles approaches 1000, but the network does not fail analogous to the case $\lambda_{\max} = 2.5$ for $\phi = 0.3$. However, as the maximum stretch becomes sufficiently large, the stress-stretch behavior becomes almost independent and linear for large numbers of strain cycles. In contrast to smaller filler contents, the stress does not approach zero with increasing number of strain cycles. A possible explanation is that large holes already grow during the first strain cycles due to rupture of links. Therefore, the stress-stretch behavior at larger number of strain cycles obeys the linear relation of filler-filler and polymer-filler bonds. According to the data presented in Figure A.68, breaking of filler-filler bonds is promoted at small deformations and for large filler contents. When rupture of links begins, or even at smaller stretches, filler-filler bonds establish again because their breaking is reversible and the network is compressed perpendicularly to

the stretching direction due to volume conservation. Thus, filler-filler bonds can stabilize the network in addition to polymer-filler bonds if the applied stretch is sufficiently large. Note that for very small stretches like $\lambda_{\max} = 1.5$, pure stress amplification which promotes rupture of links may be of minor importance. According to the plot in Figure A.68 showing the fraction of broken links depending on the stretch during a tensile test, links begin to break at larger stretches. This validates the statement above that rearrangements in filled model elastomer networks cause accumulation of damage. Nevertheless, investigations of snapshots of the model networks are necessary to draw definite conclusions.

For $\phi = 0.7$ and $\lambda_{\max} = 1.25$, the stress shows a distinct hysteresis due to reversible breaking and weakening of filler-filler and polymer-filler bonds. When the maximum stretch is increased to $\lambda_{\max} = 1.5$ or $\lambda_{\max} = 3.5$, the ratio $\sigma_{\max}/\sigma_{\max,1}$ shows a kink at a certain number of strain cycles which is smaller for the larger maximum stretch. The decrease indicates fatigue. Although the ratio does not reach zero and failure is not identified, further investigations are required to prove this. Analogous to $\phi = 0.5$, the stress-stretch behavior becomes nearly linear for sufficiently large maximum stretch.

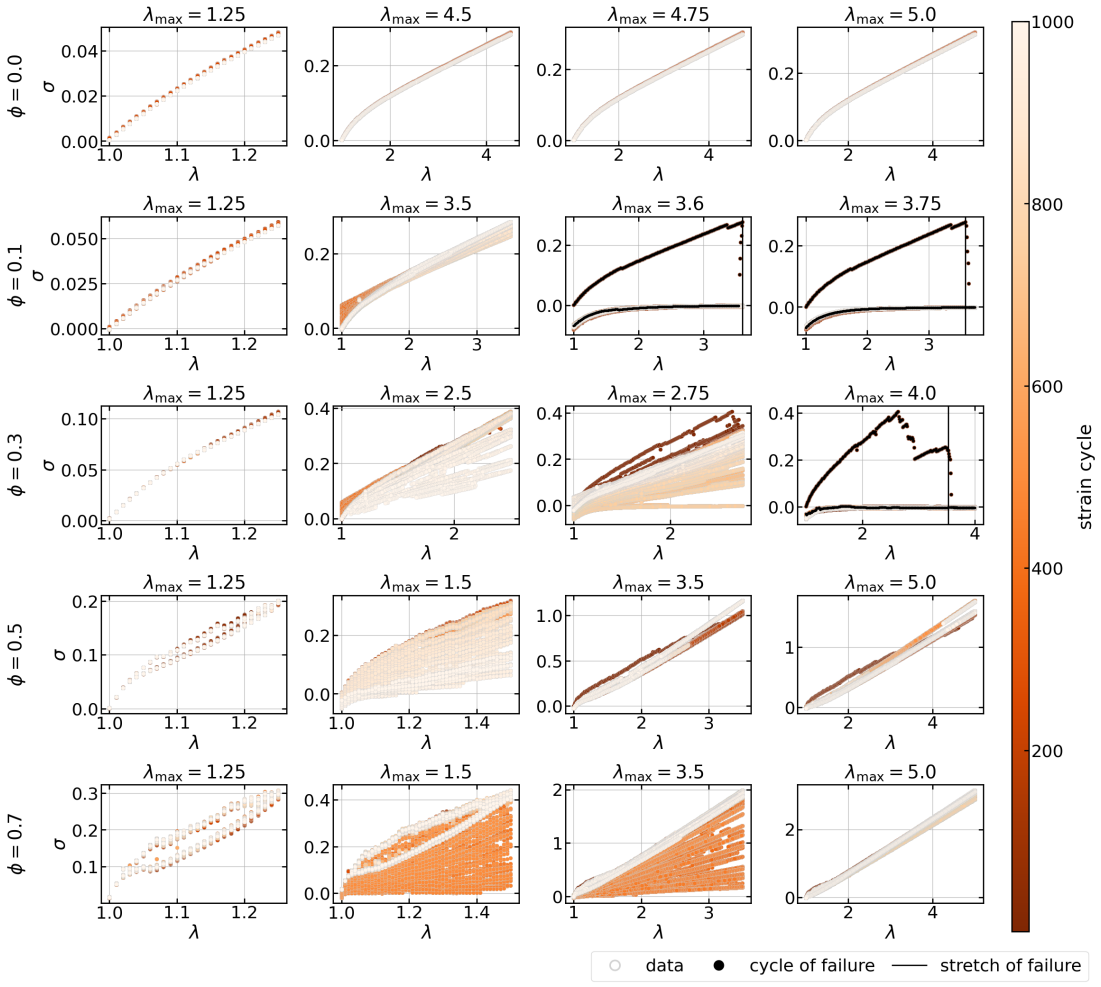

Figure 5.98.: Stress-stretch curves for strain cycles of non-crystallizing 2D-networks consisting of $N = 196$ nodes with variable filler content ϕ and with $(g/n)_{\text{crit}} = 1.5$ as the critical free energy density. The filler is randomly distributed and the initial configurations of the networks for fixed filler content are identical. For each maximum stretch $\lambda_{\max}$, the networks have been deformed for up to 1000 cycles.

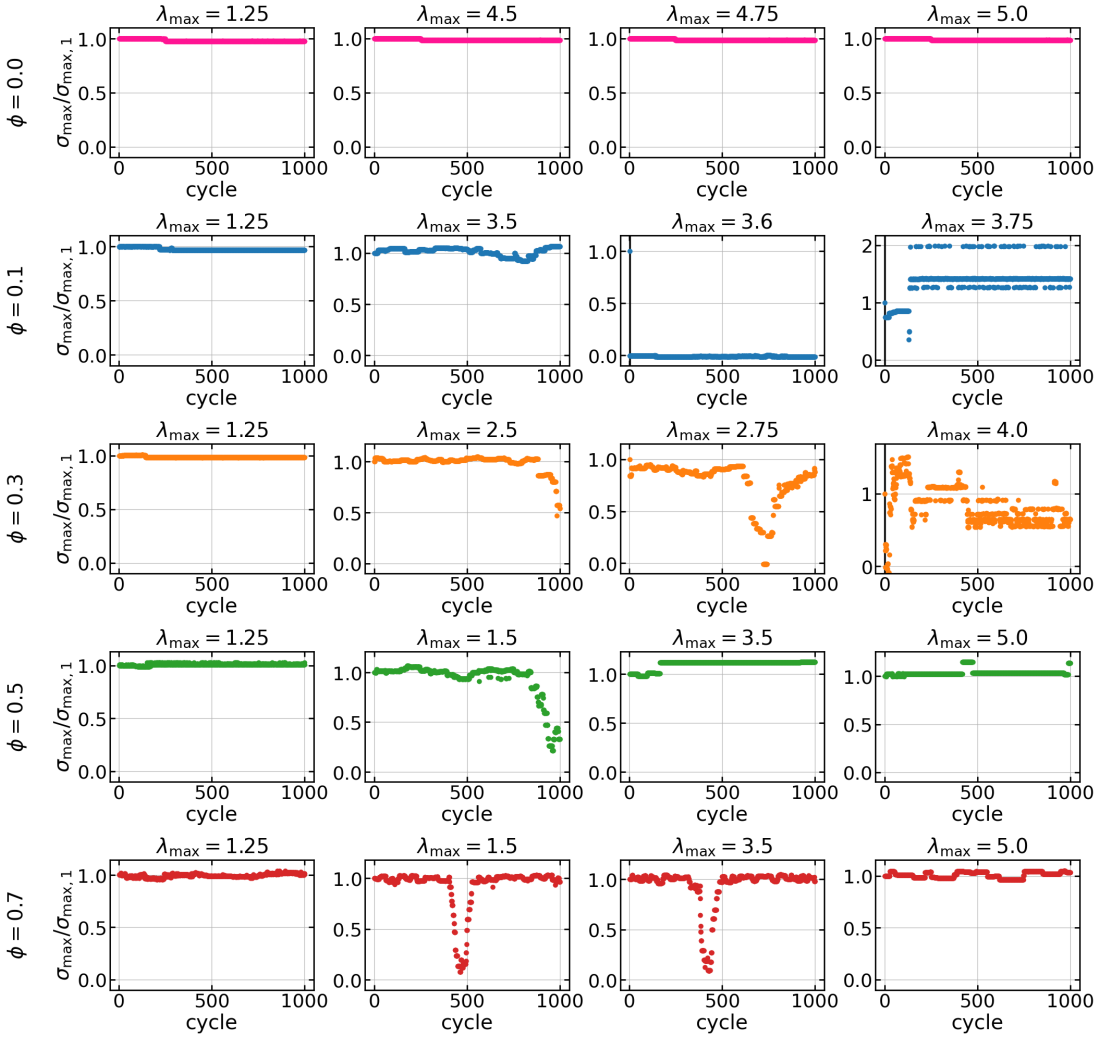

Figure 5.99.: Plots of $\sigma_{max}/\sigma_{max,1}$ versus the number of the strain cycle for non-crystallizing 2D-networks consisting of $N = 196$ nodes with variable filler content ϕ and with $(g/n)_{crit} = 1.5$ as the critical free energy density. The filler is randomly distributed and the initial configurations of the networks for fixed filler content are identical. For each maximum stretch λ_{max}, the networks have been deformed for up to 1000 cycles.

For crystallizing 2D-networks with different filler contents, the stress-stretch curves for cyclic deformation with variable maximum stretches λ_{max} are depicted in Figure 5.100, while the plots of the ratio $\sigma_{max}/\sigma_{max,1}$ are shown in Figure 5.101. The observations that can be made are analogous to the non-crystallizing case. For the unfilled network, $\sigma_{max}/\sigma_{max,1}$ shows very small variations because SIC affects the microstructure of the model networks and causes a hysteresis of the stress. In particular for poorly filled networks, the stress oscillates in the range of stretches where the typical plateau or the increase beyond it evolve due to SIC. Therefore, the decreases can be explained by rupture of highly crystalline links which are extended to end-to-end distances beyond their contour length.

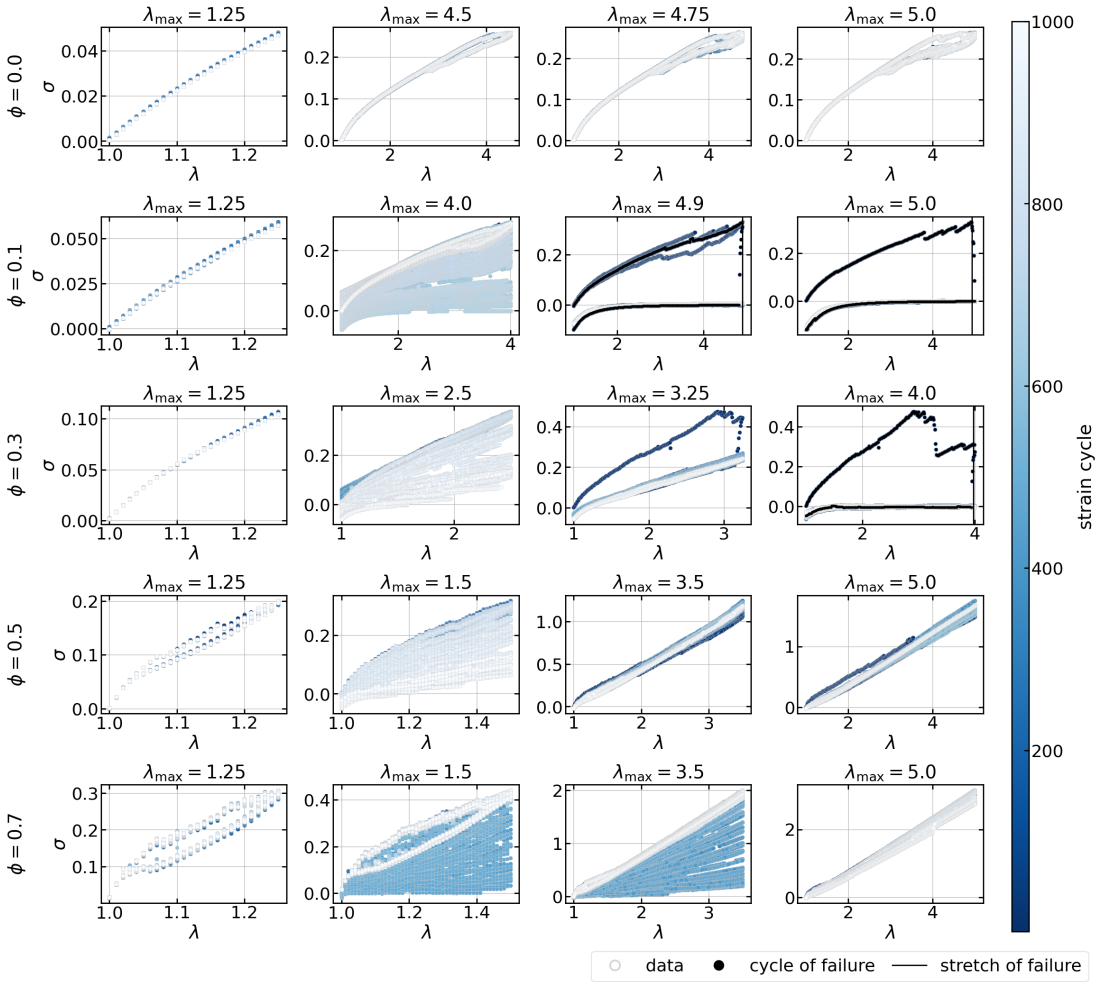

Figure 5.100.: Stress-stretch curves for strain cycles of crystallizing 2D-networks consisting of $N = 196$ nodes with variable filler content ϕ and with $(g/n)_{\text{crit}} = 1.5$ as the critical free energy density. The filler is randomly distributed and the initial configurations of the networks for fixed filler content are identical. For each maximum stretch λ_{max}, the networks have been deformed for up to 1000 cycles.

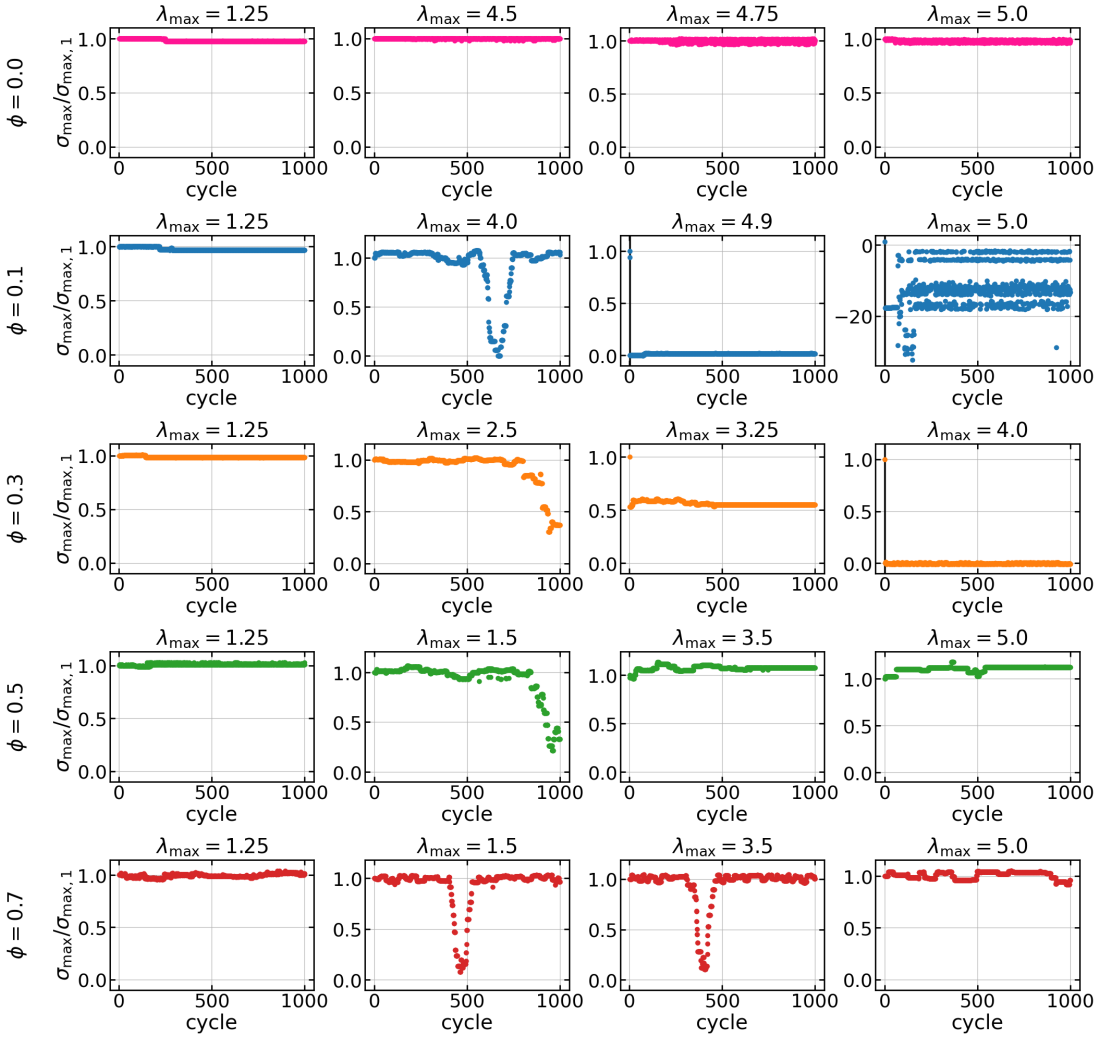

Figure 5.101.: Plots of $\sigma_{max}/\sigma_{max,1}$ versus the number of the strain cycle for crystallizing 2D-networks consisting of $N = 196$ nodes with variable filler content ϕ and with $(g/n)_{crit} = 1.5$ as the critical free energy density. The filler is randomly distributed and the initial configurations of the networks for fixed filler content are identical. For each maximum stretch λ_{max}, the networks have been deformed for up to 1000 cycles.

In Figure 5.102, the Wöhler curves of the non-crystallizing and crystallizing 2D-networks are plotted for variable filler contents. For better visibility, they are additionally presented in Figure A.113 and Figure A.114 for each filler content separately. If the networks are unfilled or contain only a very small fraction of filler, they do not fail according to the applied classification which has been explained above. Nevertheless, the reason is probably not the classification method here. According to the stress-stretch curves presented above, the networks truly do not fail because the applied maximum stretches are too small to trigger failure or the critical free energy density for rupture of links is too large. This is consistent with the observations made for the tensile tests.

As the filler content is increased, the non-crystallizing networks fail in the first strain cycle. The applied maximum stretch at which the transition occurs tends to decrease with increasing filler content and then increases until the networks do not fail anymore. This reduction agrees with the dependence of the elongation at break on the filler content in a tensile test which is shown in Figure 5.90. Only for $\phi = 0.3$ and $\phi = 0.35$, there is a maximum stretch between 'no failure' and 'failure in the first strain cycle' at which the network fails. As the percolation threshold of the 2D-networks is approached,

which is around $\phi = 0.5$ for the 2D-networks, the networks do not fail. However, for $\phi = 0.9$, the network fails after multiple strain cycles when the maximum stretch is applied. Taking into account the stress-stretch curves, which have been discussed above, suggests that potential failure due to fatigue at these large filler contents is not detected by the applied identification method.

In the case of crystallizing networks, analogous observations can be made, except that the network with $\phi = 0.9$ does not fail under any of the applied conditions. Failure of the crystallizing networks requires for higher maximum stretches than in the case of non-crystallizing networks. This aligns with the results of the tensile tests. For $\phi = 0.1$ and $\phi = 0.15$, the fatigue life is increased at one point as the maximum stretch is increased. A possible origin of this deviation from the expectation is the method for the identification of failure.

Altogether, the expected linear behavior of the Wöhler curves cannot be observed. In particular, for most of the considered filler contents, there is only a sharp transition between 'no failure' and 'failure in the first strain cycle' instead of a broader range of fatigue lives. Fatigue, in the way it is indicated by the stress-stretch curves in Figure 5.98 and Figure 5.100, is not captured in these Wöhler curves. On the one hand, only specific network configurations are investigated here and further networks with the same parameters must be studied to get more reliable results by obtaining averages of the fatigue life N_{fail}. On the other hand, the method for the identification of failure must be improved. It only captures failure in the form in which it is known from tensile tests, but it does not identify failure if it occurs due to accumulation of damage in subsequent strain cycles. In the latter case, the stress of an entire strain cycle decreases with respect to the previous strain cycle with increasing number of strain cycles. Nevertheless, it must be validated whether this decrease of the stress is truly failure or whether this is of another origin. For this purpose, an optimization can be achieved by the implementation of an occupation grid into the simulation algorithm.

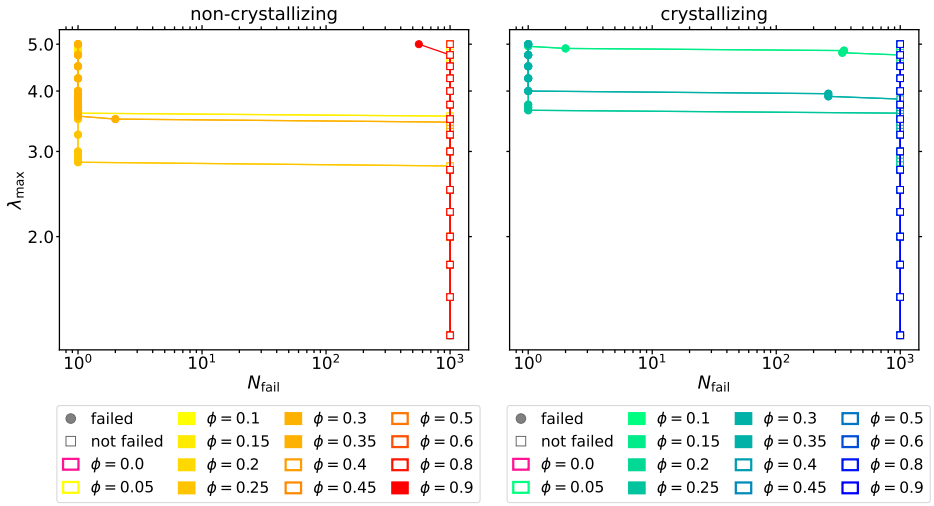

Figure 5.102.: Wöhler curves for non-crystallizing and crystallizing 2D-networks consisting of $N = 196$ nodes with variable filler content ϕ. The filler is randomly distributed and the critical free energy density is $(g/n)_{\text{crit}} = 1.5$. For fixed filler content, the initial configurations of the networks are identical and, for each maximum stretch λ_{max}, the networks have been deformed for up to 1000 cycles. The data points are connected for the eye.

As a next step, cyclic deformation of 3D-networks is studied. The stress-stretch curves for non-crystallizing networks containing various contents of filler ϕ and for different maximum stretches λ_{max} are depicted in Figure 5.103. In Figure 5.104, the ratio

$\sigma_{\max}/\sigma_{\max,1}$ is plotted versus the number of the strain cycle. For the unfilled network, the stress at is decreased as the number of strain cycles increases. In contrast to the 2D-case, the stress at maximum stretch varies differently for each maximum stretch and the decrease does not occur at a constant number of strain cycles. Particularly, the decrement of the stress tends to occur at a smaller number of strain cycles as the maximum stretch is increased. This suggests that the network shows fatigue due to internal rearrangements caused by rupture of links, although the network does not fail.

For $\phi = 0.1$ and $\lambda_{\max} = 1.25$, the stress is significantly reduced after a certain number of strain cycles, but the decrement at maximum stretch remains constant as the cyclic deformation proceeds. Although the stress reduction is not gradually, this observation is an indication of fatigue of the model network. For $\lambda_{\max} = 3.5$, the reduction of the stress is smaller and the stress at maximum stretch is increased in a certain intermediate interval. When the maximum stretch is increased to $\lambda_{\max} = 3.75$, the method utilized for the identification of failure does not discern the steep decrease in the stress associated with failure in the first strain cycle as it occurs during the contraction of the network. As the maximum stretch is incremented, the model networks fails during stretching in the first strain cycle.

For $\phi = 0.3$ and $\lambda_{\max} = 1.25$, the stress is enhanced with increasing number of strain cycles due to rearrangements in the network associated with the inclusion of filler. This does not align with fatigue as it is expected. In particular for the last strain cycles, a hysteresis of the stress can be observed which is attributed to breaking and weakening of filler-filler and polymer-filler bonds. When the maximum stretch is increased to $\lambda_{\max} = 3.0$, the stress at maximum stretch oscillates. A possible explanation is that rupture of links and recombination of bonds, which both affect the microstructure of the model networks, alternate on the scale of strain cycles. Rupture of links does not cause failure here, only softening. However, snapshots of the model networks must be investigated to draw definite conclusions on the effects causing this behavior. Increasing the maximum stretch to $\lambda_{\max} = 3.5$ initially decreases the stress at maximum stretch and, then, increases it. The stress-stretch curves for all strain cycles behave analogously, but thus suggests reinforcement contrary to the expected fatigue. The observation is reversed for $\lambda_{\max} = 5.0$. The stress increases with increasing number of strain cycles, reaches a plateau and decreases stepwise afterwards. Thus, fatigue can be observed after a sufficient number of cyclic deformations.

For $\phi = 0.5$ and comparatively small maximum stretches, the stress is enhanced for small numbers of strain cycles, but it gradually decreases with proceeding cyclic deformation. At larger maximum stretches, the stress-stretch curves become nearly linear as the cyclic deformation continues. Simultaneously, the stress at maximum is slightly enhanced beyond a certain number of strain cycles. These observations result from the filler-filler and polymer-filler bonds as explained above for the 2D-networks.

When the filler content is $\phi = 0.7$, for small maximum stretches, the stress at maximum stretch varies around its original value. In addition, the stress-stretch curves possess a distinct hysteresis. As the maximum stretch is increased to $\lambda_{\max} = 2.5$, the stress at maximum stretch tends to decrease which indicates fatigue during the cyclic deformation. If the maximum stretch is large, the stress at maximum stretch is enhanced at a certain number of strain cycles due to filler-filler and polymer-filler bonds, but it scatters.

Note that, for 2D-networks, for example the non-crystallizing network containing a fraction $\phi = 0.3$ of filler that has been stretched up to $\lambda_{\max} = 2.5$, the stress at maximum stretch falls down towards zero as the maximum number of strain cycles is approached. For other parametrizations of 2D-networks, similar reductions of the stress with a subsequent increase occur already at smaller numbers of strain cycles.

These decreases are fast in comparison to the stepwise decrements of the stress at maximum stretch observed for the 3D-networks. Thus, fatigue is impeded in the 3D-case, whereas reinforcement due to the inclusion of filler apparently dominates the mechanical behavior during cyclic deformation.

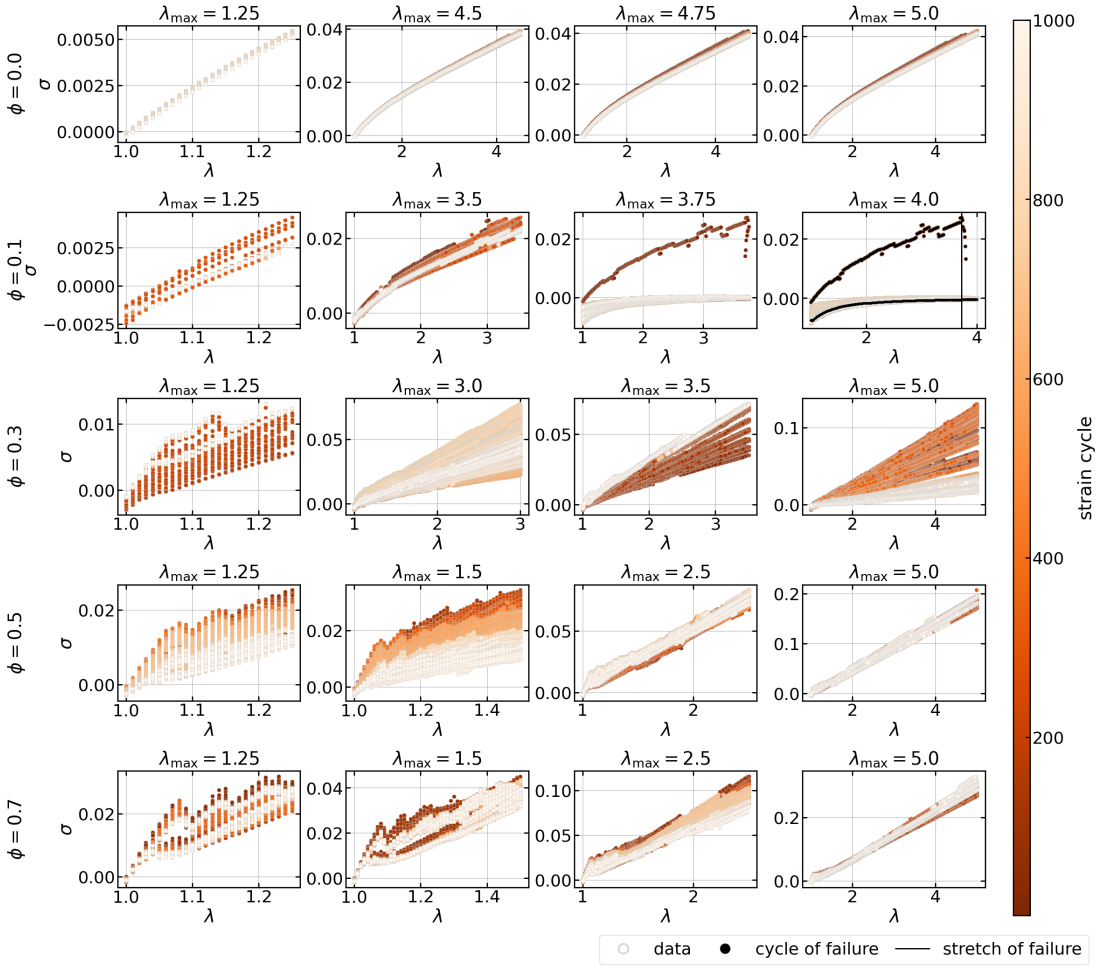

Figure 5.103.: Stress-stretch curves for strain cycles of non-crystallizing 3D-networks consisting of $N = 216$ nodes with variable filler content ϕ and with $(g/n)_{\text{crit}} = 1.5$ as the critical free energy density. The filler is randomly distributed and the initial configurations of the networks for fixed filler content are identical. For each maximum stretch λ_{max}, the networks have been deformed for up to 1000 cycles.

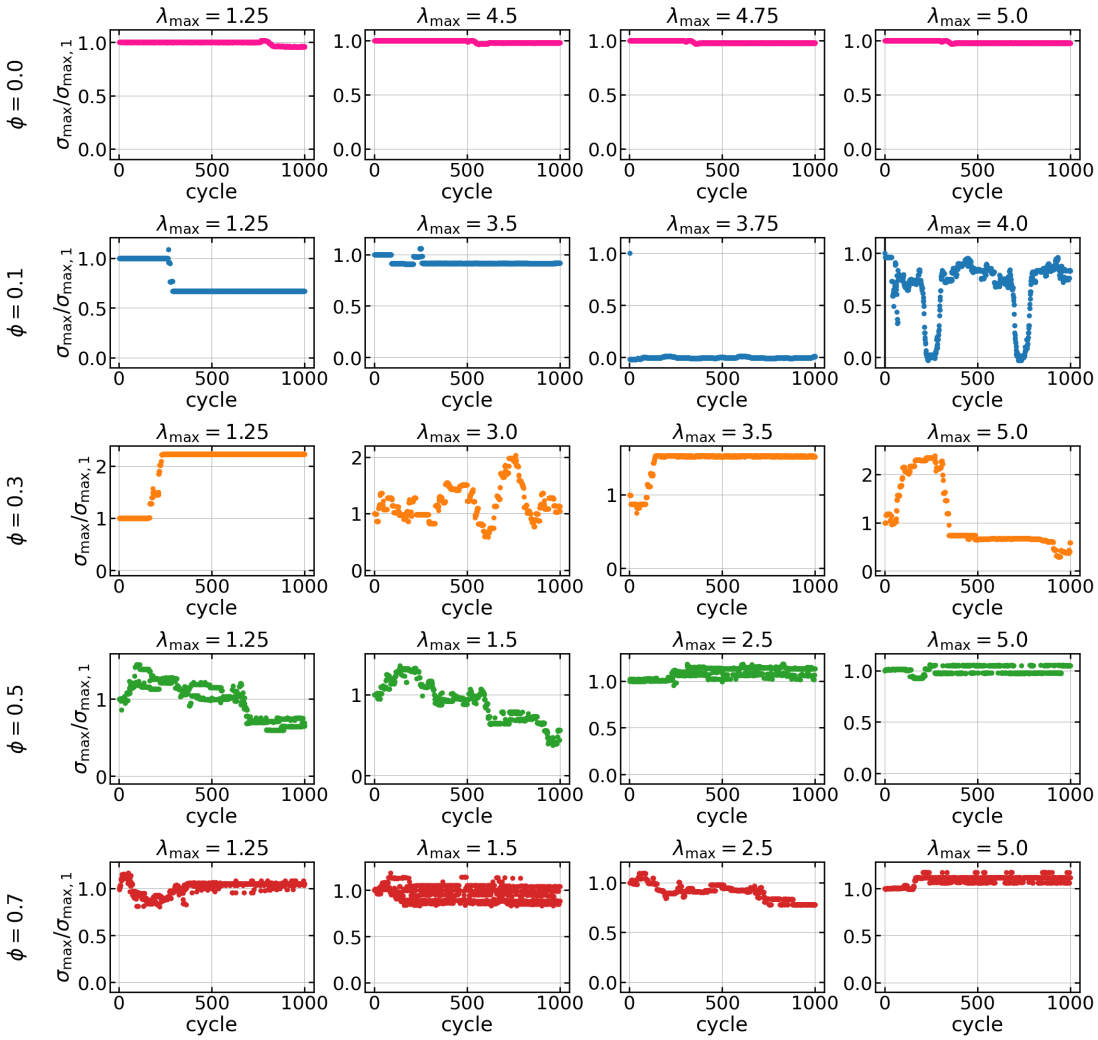

Figure 5.104.: Plots of $\sigma_{max}/\sigma_{max,1}$ versus the number of the strain cycle for non-crystallizing 3D-networks consisting of $N = 216$ nodes with variable filler content ϕ and with $(g/n)_{crit} = 1.5$ as the critical free energy density. The filler is randomly distributed and the initial configurations of the networks for fixed filler content are identical. For each maximum stretch λ_{max}, the networks have been deformed for up to 1000 cycles.

Analogous plots of the stress-stretch curves and the ratio $\sigma_{max}/\sigma_{max,1}$ for crystallizing 3D-networks are included in Figure 5.105 and Figure 5.106, respectively. The observations which can be made are similar to the non-crystallizing case. Note that the stress at maximum stretch behaves identical for $\lambda_{max} = 1.25$ in the crystallizing and in the non-crystallizing case because SIC evolves at larger deformations.

SIC causes a hysteresis of the stress of the unfilled network as expected. If the maximum stretch is sufficiently large, the decrement of the stress at maximum stretch is larger and shifted towards a smaller number of strain cycles compared to the non-crystallizing case. The reason is that rupture of highly crystalline links is promoted compared to non-crystalline links if their end-to-end distance exceeds their contour length. For the same reason the reduction of the stress at maximum stretch is larger in the crystallizing case for $\phi = 0.1$ and $\lambda_{max} = 3.5$. At this filler content, failure of the model networks is prevented, but the stress at maximum stretch is still reduced which indicates fatigue. Nevertheless, in the range of the plateau which is associated with SIC, the stress appears to be enhanced with increasing number of strain cycles, even in the unfilled case. A possible explanation is that rupture of certain links enforces extension

of surrounding links which must bear the load. If these links are highly crystalline, their force increases even more as end-to-end distances beyond the contour length are reached.

If the filler content is $\phi = 0.3$, the model network is rather reinforced by the inclusion of filler than showing fatigue in comparison to the non-crystallizing network. For $\phi = 0.5$, fatigue is advanced with respect to the non-crystallizing case for comparatively large maximum stretches since the stress at maximum stretch is reduced as the final strain cycle is approached. This observation may be attributed to the rupture of highly crystalline links which form preferentially due to stress amplification. Nevertheless, as already stated above, the study of snapshots of the model network is necessary for a detailed analysis of fatigue of the model networks based on their stress-stretch behavior during cyclic deformation.

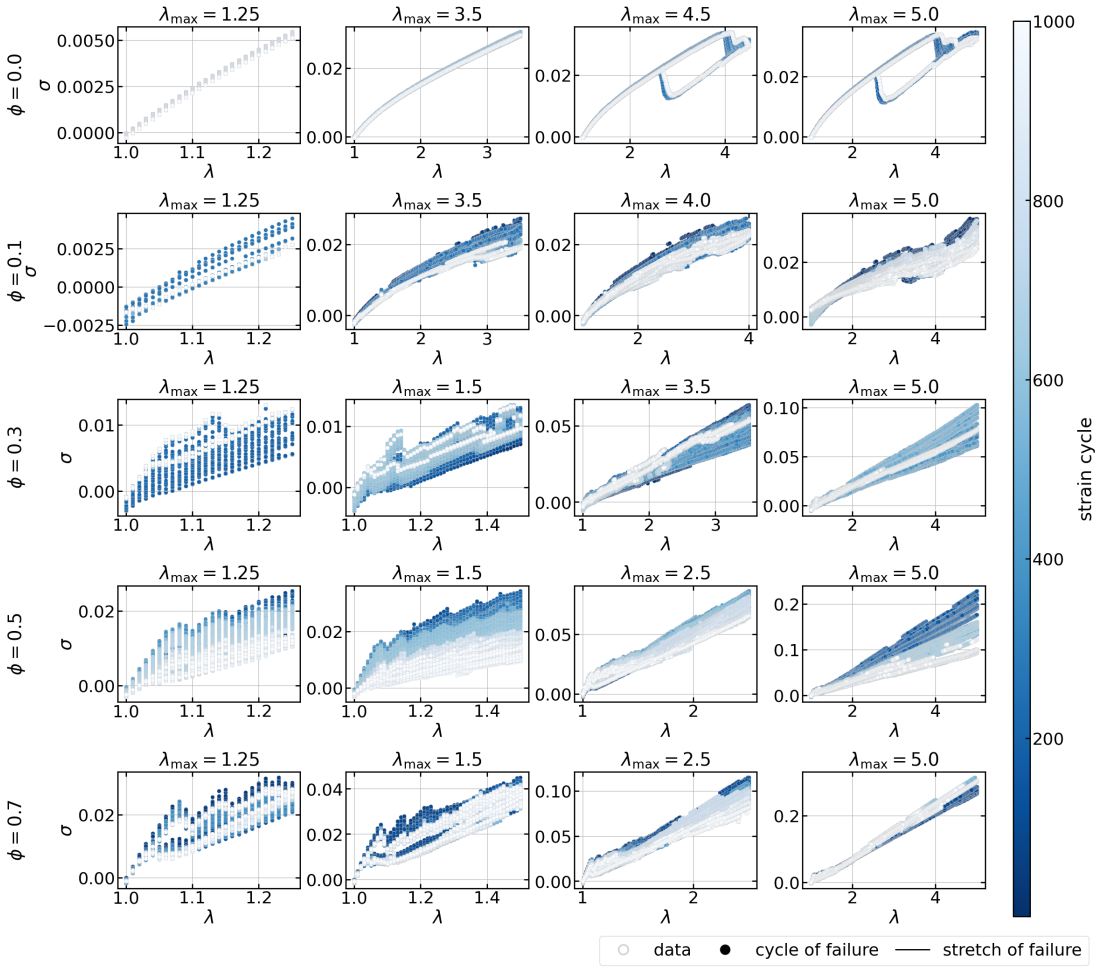

Figure 5.105.: Stress-stretch curves for strain cycles of crystallizing 3D-networks consisting of $N = 216$ nodes with variable filler content ϕ and with $(g/n)_{crit} = 1.5$ as the critical free energy density. The filler is randomly distributed and the initial configurations of the networks for fixed filler content are identical. For each maximum stretch λ_{max}, the networks have been deformed for up to 1000 cycles.

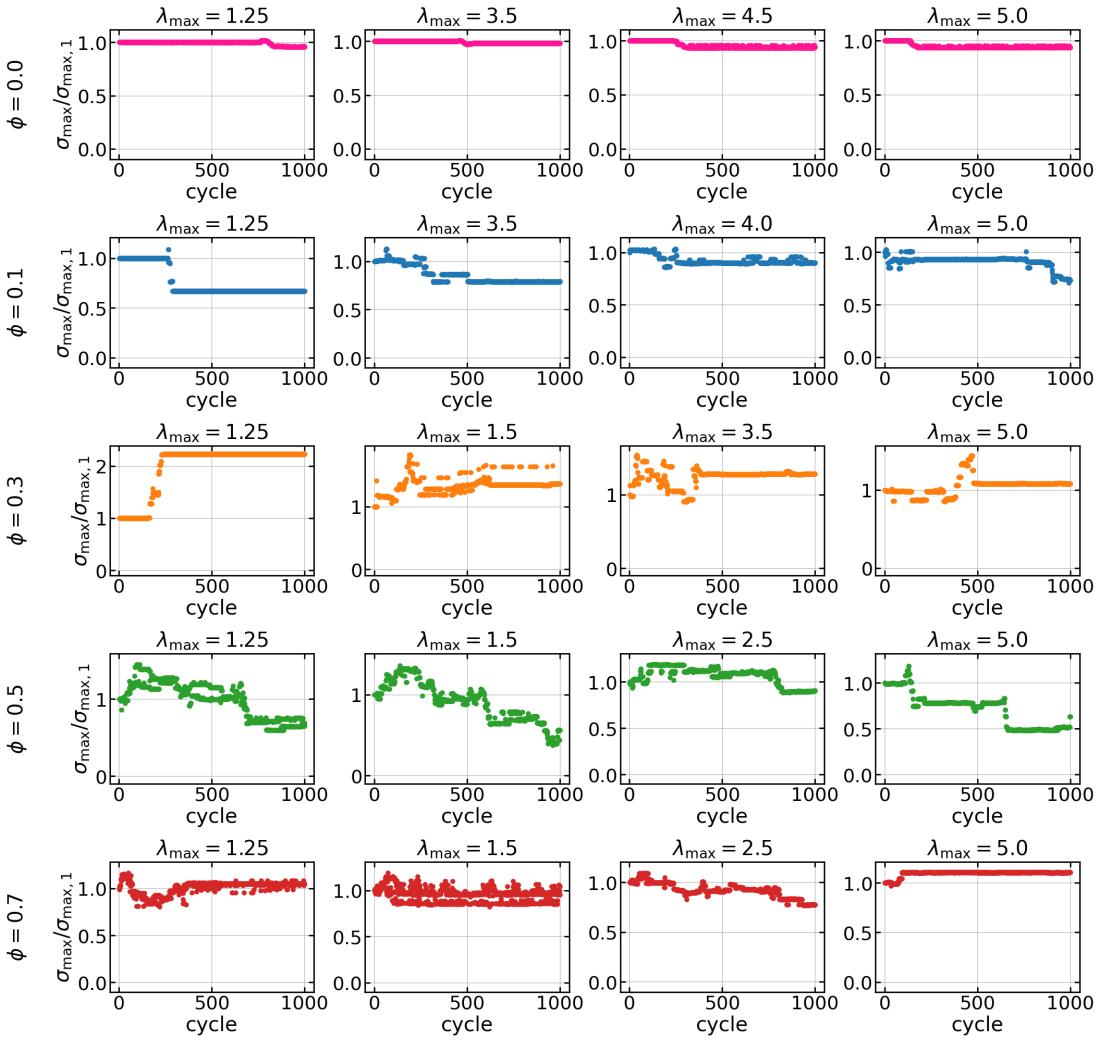

Figure 5.106.: Plots of $\sigma_{max}/\sigma_{max,1}$ versus the number of the strain cycle for crystallizing 3D-networks consisting of $N = 216$ nodes with variable filler content ϕ and with $(g/n)_{crit} = 1.5$ as the critical free energy density. The filler is randomly distributed and the initial configurations of the networks for fixed filler content are identical. For each maximum stretch λ_{max}, the networks have been deformed for up to 1000 cycles.

In Figure 5.107, the Wöhler curves of non-crystallizing and crystallizing 3D-networks are depicted and they are also plotted separately for each filler content in Figure A.115 and Figure A.116, respectively. Analogously to the 2D-networks, the 3D-networks do not fail if they are unfilled or just poorly filled. As the filler content is increased in the non-crystallizing case, the fatigue life N_{fail} immediately switches from 'no failure' to 'failure in the first strain cycle'. The maximum stretch of this transition is decreased and takes an additional intermediate value when the filler content is further incremented until the networks do not fail at all again. However, the expected linear behavior of the curve cannot be observed. Failure of the networks terminates as the percolation threshold, which is around $\phi = 0.3$ for the 3D-networks, is approached. SIC apparently advances the fatigue life for small filler contents because fewer of the networks fail and the transition of the fatigue life is located at higher maximum stretch. In addition, the transition region is broader.

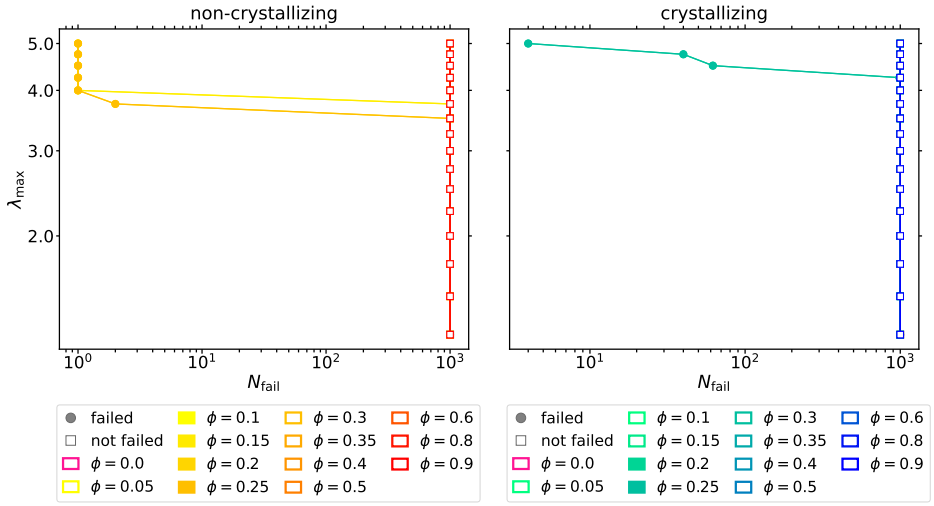

Figure 5.107.: Wöhler curves for non-crystallizing and crystallizing 3D-networks consisting of $N = 216$ nodes with variable filler content ϕ. The filler is randomly distributed and the critical free energy density is $(g/n)_{\text{crit}} = 1.5$. for fixed filler content, the initial configurations of the networks are identical and, for each maximum stretch λ_{max}, the networks have been deformed for up to 1000 cycles. The data points are connected for the eye.

Altogether, the investigations presented in this section do not yet provide quantitative results for fatigue of filled and strain-crystallizing elastomer networks. The Wöhler curves only show sharp transitions of the fatigue life but not the expected linear behavior. The predominant states are 'no failure' and 'failure in the first strain cycle'. To obtain more reliable data for the Wöhler curves, the method for the identification of failure must be advanced. For this purpose, an occupation grid could be implemented into the simulation algorithm. However, the dependence of the Wöhler curve on the filler content and SIC agrees with the results obtained from the tensile tests that have been presented in the previous section.

Although it is difficult to monitor fatigue of the model networks with the employed method for the identification of failure and the Wöhler curves, the study of the stress-stretch curves provides some insights into fatigue in terms of stress softening. Nevertheless, fatigue of the model networks due to rearrangements in the model networks associated with the inclusion of filler is accompanied by reinforcement. The reason for this deviation from the expectation may be the particular modeling of filler-filler and polymer-filler bonds in the model. A definite conclusion regarding that requires for the analysis of snapshots of the model networks during cyclic deformation. This also enables clarification of the relation between the microstructure of the model networks and fatigue.

6. Conclusion

The objective of this thesis is the investigation of reinforcement in strain-crystallizing elastomers containing particulate fillers using computer modeling. For this purpose, the model for SIC in elastomers proposed by Plagge & Hentschke [1] is combined with the morphology generator (MG) developed by Viktorova *et al.* [2]. The MG is an algorithmic approach to generating different filler dispersions inside a polymer matrix based on the experimental interface tensions of the rubber components. In addition, a rupture criterion for the model polymer links between two cross links is integrated into this new material model allowing to simulate tensile tests, i.e. the stress and the elongation at break. Although this new material model applies quite generally to filled elastomers, the focus is on natural rubber (NR) as the polymer. This is because chemically cross-linked NR possesses outstanding mechanical properties even without additional filler reinforcement, which makes it the polymer of choice in high performance rubber applications.

A brief summary of the new material model is the following: Unfilled model elastomer networks consist of nodes, which represent chemical cross links, and links, which are the polymer chains that connect two cross links. The latter are modeled as freely-jointed chains. Physical entanglements are not included. Initially, the nodes are placed on a simple square or cubic lattice. It is assumed that the strain-induced crystallites, forming within in the links, are strictly aligned along the stretching direction. The model networks are deformed in small increments. This means that a model network is either stretched to a maximum elongation or stretched and subsequently relaxed during one or several strain cycles. At each incremental global strain change, the network is relaxed with respect to the node positions and, subsequently, local free energy minimizations with respect to SIC are carried out throughout the network. This ensures that SIC is modeled as a non-equilibrium phenomenon in accordance with reality. Stretching as well as relaxation are conducted under 'quasi-static' conditions. This means that the typical time scale of crystal formation is short compared to the time during which a significant material deformation occurs. Dynamic conditions are not taken into account. For modeling filled networks, a given fraction of the network nodes represents coarse grained filler particles. Initially, the filler is randomly distributed throughout the network. Subsequently, the filler morphology is or can be modified via the MG. Accordingly, filler-filler and polymer-filler bonds are introduced between two filler nodes and between cross link nodes and adjacent filler nodes, respectively. These are modeled as harmonic springs. The parametrization of the springs reflects the nature and strength of the different interfaces, i.e. filler-filler or polymer-filler. Here 'strength' is measured relative to the elastic restoring force of the links. Most of the computer experiments in this thesis are based on 2D-networks, which allows a larger linear dimension of the network. However, based on the 2D-data, selective studies on 3D-networks are included and discussed as well.

The new material model has been tested extensively with the following main results: The stress-stretch and crystallinity-stretch behavior of unfilled non-crystallizing and crystallizing networks obtained by Plagge & Hentschke [1] as well as in [3, 4] are validated. At the onset of SIC, the stress in crystallizing model networks is reduced

compared to the non-crystallizing case and shows a plateau which indicates softening. The strong increase of the stress beyond the plateau in experimental samples is attributed to the finite chain extensibility. Even tough the latter is not part of the Gaussian links in our material model, the stress increases strongly - in accordance with the experiment - as a consequence of the particular modeling of SIC employed here. Due to the separation of the deformation of the network from the local energy minimization which causes SIC, the crystallinity-stress curves show a hysteresis resulting in an attendant hysteresis in the stress-stretch plane. Both the plateau and the hysteresis are typical features of the mechanical behavior of strain-crystallizing elastomers. At the onset of SIC, the crystallites are randomly distributed throughout the network serving as nuclei. With increasing stretch, however, new model crystallites spawn adjacent to the already present nuclei. Initially, this occurs perpendicular to the global elongation direction. Subsequently, continuous bands of crystallites traverse the network parallel to this direction. These structures are influenced by the regularity of the studied networks, e.g. the networks studied here lack in isotropy and do not contain lattice defects in contrast to real elastomer networks. During contraction, crystalline and non-crystalline layers alternate, while the crystalline links appear to compress the non-crystalline links in order to reduce the external force.

For the modeling of filled networks, the MG is parameterized by comparing the generated filler morphologies with TEM images of carbon black (CB) structures in rubber. Initially, the filler is randomly distributed, i.e. finely dispersed, throughout the network. Subsequent application of the MG leads to filler flocculation. The morphology of the flocculated filler, i.e. 'lumpy' or 'fractal-like', depends on the interactions between the components. Most of the morphologies studied here are of the former type. In contrast to [2], only two-component systems are studied here. In this case, the surface tensions which are applied in the MG to characterize the components are of minor importance for the algorithm. Therefore, the MG in its present form is not able to distinguish different combinations of two component types and the resulting filler morphology depends on the remaining parameters here. Of course, the filler morphology depends in particular on the filler content, i.e. on the filler volume fraction in the polymer network. Above the percolation threshold, a filler network traverses the polymer.

The parameters for filler-filler and polymer-filler bonds are obtained from the investigation of the mechanical behavior of non-crystallizing model networks at small deformations. Note that parametrization here is guided by general rather than system-specific experimental observations. This is because most of the results reported here are obtained for two-dimensional networks, whose specific interactions, e.g. polymer-filler, are different in different dimensions. The derivative of the stress-stretch curve, which is proportional to the elastic modulus, is obtained for variable filler content and fitted with a power law. The parameters are set such that the derivative of the stress-stretch curve increases with increasing filler content according to experimental data. The spring constants of both the filler-filler and polymer-filler bonds are larger than those of the links at small strain. The filler-filler bonds are characterized by the highest spring constant compared to the remaining linkages and thus reinforce the model rubber networks. While filler-filler bonds break reversibly beyond a certain bond length, polymer-filler bonds weaken reversibly.

Already the comparison of plots of the derivative of the stress-stretch curve versus filler content for different filler dispersions shows that the reinforcing effect of finely dispersed filler is higher than that of lumpy filler distributions. This result, which is in accordance with experimental observations, can be attributed to the total number of filler-filler and polymer-filler bonds. Indeed, the number of polymer-filler bonds is increased compared to the number of filler-filler bonds if the filler is finely dispersed in

the elastomer matrix. This increases the total length of the polymer-filler interface in contrast to a coarse filler dispersion and enhances reinforcement by bound rubber.

Furthermore, the derivatives of the stress-stretch curves of non-crystallizing networks with variable filler content are examined for the Payne effect. Viktorova *et al.* [2] have already demonstrated that their model for filled elastomers includes this characteristic phenomenon. Since stretching experiments are conducted here instead of shearing, an additional geometry induced spurious reduction of the modulus has to be eliminated. As the filler content exceeds the percolation threshold, the Payne effect can be observed. Here, it is mainly caused by breaking of filler-filler bonds. This is shown by selectively allowing or prohibiting the aforementioned breaking or softening of the filler-filler and polymer-filler bonds.

At larger deformations, the stress at fixed stretch increases with increasing filler content as expected for both non-crystallizing and crystallizing 2D- and 3D-networks. This stress-amplification effect is advanced for finely dispersed filler because of the larger number of polymer-filler bonds compared to coarsely dispersed filler. For coarsely dispersed filler, the stress-amplification factor is well described by a Guth-Gold relation, whereas, for finely dispersed filler, its dependence on the filler content shows a s-like transition at the percolation threshold. In addition, the onset of SIC is shifted towards smaller stretches due to the inclusion of filler. For 2D-networks, the onset of SIC tends to smaller network extension if the filler is finely dispersed than if it is more coarsely dispersed. The plateau of the stress which is characteristic for strain-crystallizing elastomers vanishes with increasing filler content and the typical hysteresis tightens. These results also agree with experimental observations. In this context, snapshots of the model networks have shown that the filler nodes are tightly bound in aggregates. Since extending the links located between adjacent filler aggregates is promoted, SIC in these domains is fostered.

In this work, the simulation of tensile properties characterizing material failure focuses on the tensile strength and the elongation at break. Here, non-crystallizing and crystallizing networks are compared. When the networks are filled, this comparison includes the filler volume fraction as well as filler dispersion. The criterion for the failure of an individual link is based on its free energy density. If the free energy density of a link exceeds a critical value, the link breaks and it is removed from the network. The parametrization of the threshold free energy density is guided by the following principle: A suitable range of critical free energy densities is derived from the comparison of free energy density histograms for an unfilled non-crystallizing and an unfilled crystallizing network. Due to SIC, the local free energy density in the crystallizing network is on average smaller than in the non-crystallizing network. In order to be consistent with the experimental observation that crystallizing elastomers possess a higher tensile strength than non-crystallizing elastomers, the critical free energy density is chosen in the range of comparatively high values, which is reached mainly by links of the non-crystallizing network. In particular, a threshold value can be identified below which the tensile strength of non-crystallizing networks is higher than that of crystallizing networks. Above this threshold, the tensile strength of crystallizing networks is higher than that of the corresponding non-crystallizing networks. The behavior in the latter region is in accordance with experimental observations.

If the tensile strength of non-crystallizing and crystallizing networks are compared at low filler contents, it appears that crystallizing networks are stronger than non-crystallizing networks for a sufficiently high critical free energy density. If the critical free energy density is too small, the tensile strengths show the opposite relation, i.e. non-crystallizing networks are apparently stronger. These observations are independent of the filler dispersion and only made for low filler content because the networks do not

fail if the filler content is sufficiently high.

This statement that networks "do not fail" requires explanation. First, there is a maximum stretch used in all simulated tensile tests. Secondly, the polymer-filler bonds can weaken, which is motivated by the physical nature of the interface, but there is no criterion as to when a weakened polymer-filler bond will break. This in turn means that a percolating filler network will not break at all - which of course is an artifact of the model.

In real polymer networks, close to the elongation at break, a significant fraction of polymer backbone segments and their bonds are aligned with the external force. This fraction of aligned bonds, which increases in the presence of SIC, is thought to ultimately determine the tensile strength and the elongation at break. In the current model, the high degree of orientational order is implied by the underlying lattice in contrast to self-organization in realistic polymer networks. This orientational order due to the underlying lattice is implicitly considered in the choice of the critical free energy density because the peaks in the free energy density histograms, which are analyzed for the determination of the threshold value for rupture of the links, account for links with different orientation. Hence, if the critical free energy density is too small, differences caused by different degrees of bond-alignment in non-crystallizing versus crystallizing networks cannot be observed.

In accordance with experimental observations, the elongation at break decreases with increasing filler content. This is observed for both coarsely and finely dispersed filler. The behavior of the tensile strength predicted by the model is more complex. Even a small addition of filler will decrease the tensile strength of the network compared to the corresponding unfilled network. This finding, which is contrary to the general experimental observation, may be explained as follows. In filled model networks, the spring constants of filler-filler and polymer-filler bonds are higher than the corresponding spring constants of the links. Therefore, it is preferred to extend the links instead of the other bonds first, in particular when they are located between adjacent filler aggregates. Consequently, the free energy density of these links is increased. Therefore, the links break at smaller macroscopic stress.

Although large fractions of filler-filler bonds and polymer filler bonds in the model networks break or weaken, hole formation is initiated by rupture of links. SIC is promoted at the boundaries of these holes, but it cannot prevent their growth in this model. Nevertheless, SIC impedes failure of the model networks.

It is important to note that the decrease of the tensile strength at the 'transition' from an unfilled to a filled network depends on the filler dispersion. If the filler is finely dispersed, the decrease of the tensile strength is reduced. In addition, further increase of the filler volume fraction leads to an increase of the tensile strength, eventually exceeding the tensile strength of the unfilled network in accordance with experimental observations. Is the dispersion coarse instead, however, the tensile strength continues to decrease monotonously with increasing filler volume fraction. It is in accordance with experimental data that the tensile strength tends to increase if the filler is more finely dispersed [262]. In experimental data, the tensile strength increases at small filler content until a maximum is reached and decreases beyond, but this does not occur in the simulated data. Instead, independent of the filler dispersion, the networks do not fail beyond a certain filler content below the percolation threshold. Polymer-filler bonds apparently stabilize the networks because they weaken but do not break. Moreover, the applied maximum stretch is possibly not sufficiently high to lead to failure as explained above.

Under cyclic deformation, fatigue of the model networks occurs in terms of stress-softening. In contrast to experimental observations, it is also observed that the stress

is increased over several strain cycles which is attributed to the particular modeling of filler-filler and polymer filler bonds in combination with the formation of holes in the model networks. According to obtained Wöhler curves in which the applied maximum stretch is plotted versus the fatigue life, fatigue is suppressed for very small filler contents and for filler contents above the percolation threshold. In addition, the fatigue life is enhanced by SIC. However, the expected linear behavior of the Wöhler curves cannot be observed and the results only cover specific network configurations. To draw more reliable conclusions regarding fatigue of the model networks, the method for the identification of failure must be advanced, for example by implementing an occupation grid into the simulation algorithm. An additional analysis of snapshots of the model networks is required to capture rearrangements in the model networks.

The objective of this thesis has been the investigation of distinguishing and common aspects of reinforcement by SIC and by filler in elastomers. An essential difference which the model incorporated is that filler particles are permanently present in the rubber matrix due to the manufacturing process, while strain-induced crystallites spawn and melt depending on the state of deformation. The model shows that both SIC and filler aggregate and form percolating structures if their 'content' in the elastomer matrix is sufficiently high. In contrast to filler particles, strain-induced crystallites form layers perpendicularly to the direction of the elongation and align along this direction. This is related to the structure of the underlying network. While SIC advances with increasing stretch, filler aggregates are getting destroyed in the model. However, filler particles act reinforcing over the entire range of deformations, whereas SIC just becomes relevant at high stretches. Filler particles increase the stress as soon as they are included into the elastomer matrix, while SIC reduces the stress at its onset until hardening occurs. These aspects are reproduced by the model in accordance with experimental observations. In the model, the increase of the tensile strength due to SIC depends on the choice of the critical free energy density, but it is independent on the filler content. In contrast, the impact of filler on the tensile strength depends on the filler content and, additionally, on the filler dispersion.

A general difficulty in the application of the model is that it does not include an explicit temperature or time dependence. However, a variable temperature for SIC might be taken into account by varying the energy which has to be overcome for SIC. Different strain rates can be partly approximated by a variable stretch increment for the strain cycles.

An aspect of reinforcement due to SIC, which is incorporated into the model, is that higher energy is required for the rupture of crystallites than for the rupture of non-crystalline chains segments due to storage of energy in crystalline segments. This is realized by a 'penalty' which has to be overcome to make SIC energetically favorable. However, the contribution of the amorphous chains segments surrounding the crystallites to the resistance to crack initiation and propagation is not considered, because the crystalline segments within a link are not localized. The model relies on the assumption that crystalline chain segments are strictly oriented along the stretching direction and this possibly contributes to reinforcement by SIC, but the model does not explicitly involve the alignment of polymer backbones. However, for the regular lattices underlying the model networks, the choice of the critical free energy density implicitly incorporates the alignment of the links along the direction of the deformation which is thought to generate reinforcement in experiments.

The model reproduces characteristic features of filler reinforcement, but their origins are all united in the parametrization of filler-filler and polymer-filler bonds. Even

though shape and size of the filler particles are not considered in the model, hydrodynamic reinforcement is included since the response to external forces of filler-filler and polymer-filler bonds differs from that of the links. Thus, the mechanical behavior of a filled model network differs from that of an unfilled model network. In addition, the surface properties of the filler particles, which characterize their specific type in experiments, are neglected in the model. However, modeling of different filler-filler and polymer-filler interactions dependent on the types of the components is possible by adjusting the spring constants. Nevertheless, the model is rather crude in this respect. For instance, chemical bonds and adsorption cannot be distinguished. Weakening the polymer-filler bonds allows for reversible formation of bonds similar to the slippage mechanism which means that polymer chains attach and detach from the filler surface during the deformation. However, the contact sites are fixed, i.e. a bond cannot slip from one filler node to an adjacent filler node of the same aggregate. Moreover, the model does not take into account the concept of bound rubber which mainly contributes to filler reinforcement in experiments. Due to the choice of the spring constants, polymer chains in filled model networks experience an advanced stretch compared to polymer chains in unfilled networks which amplifies the stress.

The new material model in this thesis makes predictions which are in accord with experimental observations - but also predictions which are not. One reason for the latter is regular structure of the model elastomers studied here which is an oversimplification. Irregular and thus isotropic networks need to be studied more thoroughly. Likewise, the number of Kuhn segments in a link also is a parameter, which needs additional investigation. The model for filler is also kept very simple. The number of interaction sites on a filler particle in the model is small, and perhaps too small, since it is defined by the coordination number of the underlying regular lattice. Randomizing the underlying lattice will also improve this weak point. In order to analyze crack formation and propagation more realistically, still larger lattices are needed. This of course increases the computational cost.

As already mentioned, an issue of the simulation algorithm when simulating tensile tests is that a given maximum stretch determines the termination of the stretching process. An improvement would be to consider failure of the network in the criterion for the termination of the stretching process in order to capture failure in ideally any case. For example, the behavior of the stress can be monitored since it vanishes when the network fails. Another possibility is to implement an occupation grid into the simulation algorithm that allows to to monitor the size of the holes and, thus, enables the identification of failure. However, a sufficiently high amount of polymer-filler bonds integrated into an advantageous network structure could still prevent the network from failing beyond a certain filler content due to their parametrization. This threshold of the filler content is probably situated around the percolation threshold. Therefore, a criterion for breaking of polymer-filler bonds in the relevant range of deformations could be introduced in addition to softening at small deformations.

Model networks containing an artificially inserted crack in their initial configuration are interesting as well. In the real world this is a common type of experiment. Of course and as already mentioned, fracture experiments are highly rate-dependent. At the moment it is not clear how to implement such a feature into the model. It might also be useful to adapt the boundary conditions. In addition, the impact of the cross link density in the model networks is an issue. For this purpose, the functionality of the nodes of the underlying lattices can be increased, on the one hand, and, on the other hand, the spacing of the initial lattice or the mean length of the links can be varied. Furthermore, different stretching protocols could be introduced and the model could

be generalized to study multi-axial deformation.

Another improvement of the model is the introduction of finite chain extensibility. This was actually tried using the Langevin function to describe the force in a link at large extensions. However, this leads to instabilities in the energy minimization during the simulation because of the steep increase of the force. This problem can possibly be circumvented by including a permanent rupture criterion for the polymer chains in terms of a critical force and a critical extension. This is done in [158], but the authors apply a modified freely-jointed chain model which considers both entropic and energetic stiffness. The latter accounts for elongation of the bonds between the constituents when the chain reaches its contour length.

A. Appendix

A.1. A Model for the Temperature Dependence of the Mechanical Behavior

Due to the viscoelastic behavior of elastomers, the mechanical properties of rubber depend on time and temperature. The phenomenological model for viscoelasticity presented in subsection 2.4.1 does not incorporate temperature but focuses solely on frequency. The material has to be examined on the molecular scale in order to get an insight into the connection of temperature and frequency.

Below the glass transition temperature or glass temperature T_g, the movement of the polymer chain segments is frozen such that the material is in a glassy state [107]. Above the glass temperature, polymer chains can be highly extended because of the rotational freedom of carbon-carbon bonds along their backbone. In this case, additional free volume is provided which enables rotation of the bonds in the polymer backbone. Elastomers are in particular defined by their glass temperature below room temperature.

The relaxation time spectrum of the material characterizes its mechanical behavior and also the glass transition. Below the glass transition, most relaxation times are very long and the material appears to be frozen over the time of the observation. The relaxation process of a polymer chain on the molecular level can be described by a site-exchange model [107]. It relies on the assumption of three rotational isomeric states, i.e. trans, gauche-plus and gauche-minus, for each carbon atom in the polymer backbone. These states are separated by approximately the same energy barrier of height U_0 if no external mechanical force acts in the polymer chain. The C-atoms with thermal energy $k_B T$ oscillate in a minimum of the potential defined by one of the rotational isomeric states.

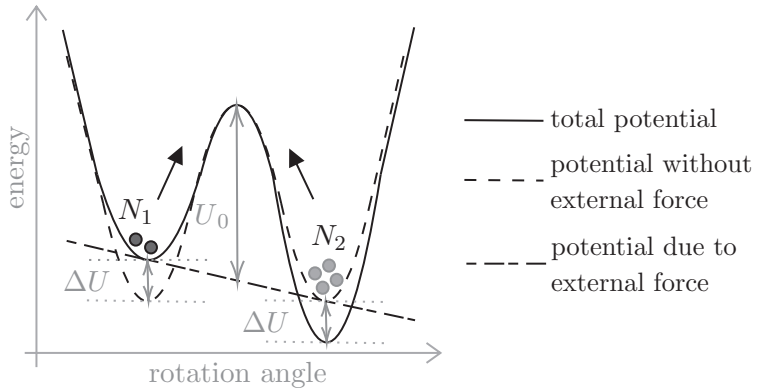

Figure A.1.: Illustration of the potential for the site exchange model. This figure is inspired by Figure 3.38 in [107].

Figure A.1 shows the potential energy for different rotation angles. There are two possible states for an atom. First, the potential without an external force is considered. If the atom gains sufficient thermal energy, it can transfer from a state 1 to another state 2. The number of site exchanges per time interval according to Boltzmann's

statistics is:

$$\Gamma^{1\to 2} = \Gamma^{2\to 1} = \Gamma = g\nu_0 \exp\left(-\frac{U_0}{k_\mathrm{B}T}\right),$$

where g denotes the number of possibilities for the atom to leave its current state and ν_0 is frequency of the oscillation of the atom in the potential minimum. In the equilibrium state, the number of atoms per state is equal, i.e. $N_1 = N_2 = N/2$. If an external force is applied to the polymer chain, the potential changes. The equilibrium state is newly defined and will be reached after a certain relaxation time. Since the different minima of the potential energy account for different rotational isomeric states, the conformation of the chain changes and, therefore, the 'shape' of the sample. Thus, also the modulus varies.

For the site-exchange model with two possible states, this may mean that the potential barrier for state 1 is increased by ΔU and decreased by ΔU for state 2. The probability for a site exchange is then:

$$\Gamma_{2\to 1}^{1\to 2} = \nu_0 \exp\left(-\frac{U_0 \pm \Delta U}{k_\mathrm{B}T}\right) \approx \Gamma\left(1 \pm \frac{\Delta U}{k_\mathrm{B}T}\right)$$

The site exchange from state 1 to state 2 is favored. Thus, the change of the number of atoms in state 1 per time interval can be computed:

$$\dot{N}_1(t) = N_2(t)\,\Gamma^{2\to 1} - N_1(t)\,\Gamma^{1\to 2} = -\dot{N}_2(t)$$

Therefore, the equation of state for the site-exchange model can be derived:

$$\frac{1}{2\Gamma}\frac{d}{dt}\Delta N(t) = -\Delta N(t) + \frac{\Delta U}{k_\mathrm{B}T}N$$

with $\Delta N(t) = N_2(t) - N_1(t)$ and $N = N_1(t) + N_2(t)$. Under the initial condition that both states are equally occupied, the equation of state is solved by

$$\Delta N(t) = N\frac{\Delta U}{k_\mathrm{B}T}\left(1 - \exp\left(-\frac{t}{\tau}\right)\right)$$

with the relaxation time

$$\tau = \tau(U_0, T) = \frac{1}{2\Gamma} = \frac{1}{2\nu_0}\exp\left(\frac{U_0}{k_\mathrm{B}T}\right). \tag{A.1}$$

The latter equation is the Arrhenius relation. The relaxation time relates time and temperature. An increase of the temperature increases the kinetic energy of the C-atoms such that the probability for a site exchange rises. Therefore, the relaxation time is decreased.

Note that it can be checked whether a relaxation process can be described by the site-exchange model by measuring for example the modulus at variable frequencies and variable temperature. In an Arrhenius plot, $-\log\tau$ is plotted versus $\log 1/T$. If the relation is linear, the site-exchange model can be applied for the explanation of the mechanical behavior of the macroscopic material and the energy barrier can be computed from the slope.

The Arrhenius relation in Equation A.1 might be applied to derive an equation for a shift factor for time-temperature superposition analogous to the WLF-Equation 2.20 by obtaining an equation for the viscosity dependent on temperature. This is convenient when approaching the glass transition temperature, but this region is not relevant for the applications of the materials discussed here. Both equations would describe time-temperature relations which account for different relaxation processes within the material and, thus, differ [120]. However, for sufficiently high temperature, the relation between time and temperature derived from the Arrhenius approach coincides with the WLF-Equation 2.20.

A.2. Rupture and Tensile Strength of Elastomers - Supplemental Data

Table A.1.: Compositions of the CB N121 filled NR specimens which have been investigated for the plots depicted in Figure 2.21. All numbers are given in phr ('per hundred rubber'). "CBS" stands for N-cyclohexyl-2-benzothiazole sulfenamides. The row with the title "Material" contains the CB N121 content as identifier.

Material	0	10	20	25	30	35	40	50	60	70	80
NR	100	100	100	100	100	100	100	100	100	100	100
CB N121	0	10	20	25	30	35	40	50	60	70	80
ZnO	2.5	2.5	2.5	2.5	2.5	2.5	2.5	2.5	2.5	2.5	2.5
Stearic acid	2.5	2.5	2.5	2.5	2.5	2.5	2.5	2.5	2.5	2.5	2.5
CBS	1.1	1.1	1.1	1.1	1.1	1.1	1.1	1.1	1.1	1.1	1.1
Sulphur	1.1	1.1	1.1	1.1	1.1	1.1	1.1	1.1	1.1	1.1	1.1

Table A.2.: Compositions of the filled NR specimens which have been investigated for the plots depicted in Figure A.2 and Figure A.4. All numbers are given in phr ('per hundred rubber'). "CBS" stands for N-cyclohexyl-2-benzothiazole sulfenamides. The row with the title "Material" contains the filler content and the filler type as identifiers.

Material	0	20 N121	30 N121	40 N121	50 N121	20 N339	30 N339	40 N339	50 N339
NR	100	100	100	100	100	100	100	100	100
CB N121	0	20	30	40	50	-	-	-	-
CB N339	0	-	-	-	-	20	30	40	50
CB N660	0	-	-	-	-	-	-	-	-
ZnO	2.5	2.5	2.5	2.5	2.5	2.5	2.5	2.5	2.5
Stearic acid	2.5	2.5	2.5	2.5	2.5	2.5	2.5	2.5	2.5
CBS	1.1	1.1	1.1	1.1	1.1	1.1	1.1	1.1	1.1
Sulfur	1.1	1.1	1.1	1.1	1.1	1.1	1.1	1.1	1.1

Material	40 N660	50 N660	60 N660	70 N660
NR	100	100	100	100
CB N121	-	-	-	-
CB N339	-	-	-	-
CB N660	40	50	60	70
ZnO	2.5	2.5	2.5	2.5
Stearic acid	2.5	2.5	2.5	2.5
CBS	1.1	1.1	1.1	1.1
Sulfur	1.1	1.1	1.1	1.1

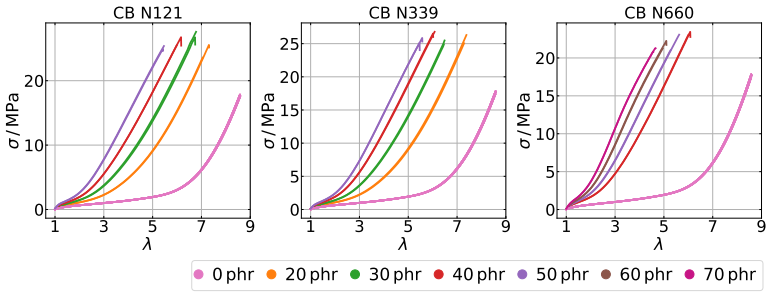

Figure A.2.: Stress-stretch curves of NR filled with variable content of different types of CB. The data has been obtained from a uniaxial tensile test at room temperature with a strain rate of 500 mm/min. For each filler type, stress-stretch curves of several specimens with the same composition are depicted. The compositions of the rubbers are listed in Table A.2. The data has been provided by Dr. Frank Fleck from Continental Reifen Deutschland GmbH.

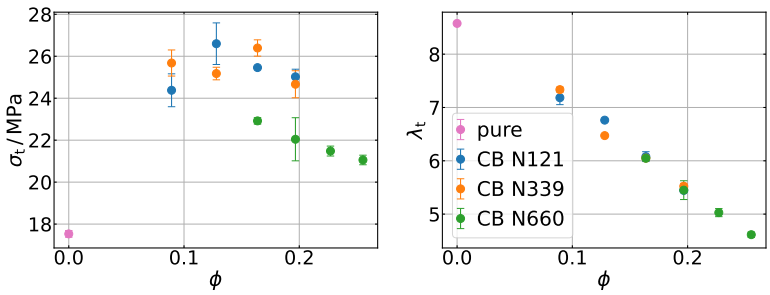

Figure A.3.: Tensile strength and elongation at break of CB-filled NR versus filler volume fraction ϕ for different CB types. The data has been obtained as averages from the stress-stretch curves shown in Figure A.2. The error bars are given by the standard deviations. The mass fractions of filler corresponding to the volume fractions are listed in Table 2.3.

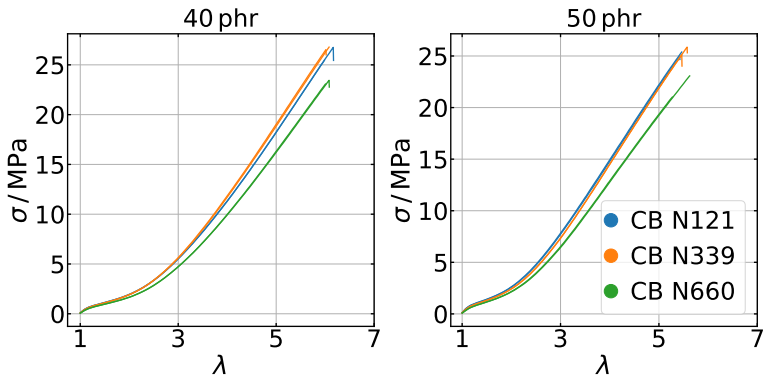

Figure A.4.: Stress-stretch curves of NR filled with different types of CB. The data has been obtained from a uniaxial tensile test at room temperature with a strain rate of 500 mm/min. For each filler type, stress-stretch curves of several specimens with the same composition are depicted. The compositions of the rubbers are listed in Table A.2. The data has been provided by Dr. Frank Fleck from Continental Reifen Deutschland GmbH.

Table A.3 shows experimental data for the tensile strength and elongation at break for NR filled with different types and contents of CB. Ostad-Movahed *et al.* [178] have obtained the data using dumbbell specimens for tensile tests with cross-head

speed 50 mm/min at 21 °C. Savetlana *et al.* [27] and Warasitthinon & Robertson [263] have measured the data according to the ASTM D412 standard with a tensile rate of 500 mm/min at 23 °C. Ürögiová *et al.* [264] have obtained the data according to the ISO 527 standard with a cross-head speed of 200 mm/min. Both the tensile strength and the elongation at break depend on whether the sample is vulcanized, on the filler loading and on the filler type. The measurement method and experimental conditions also play an important role.

Ostad-Movahed *et al.* [178] have also determined the tensile strength and elongation at break of IR to be $\sigma_t = 1.2\,\text{MPa}$ and $\varepsilon_t = 139\,\%$. These values are significantly smaller than the corresponding values for NR. This difference is mainly attributed to SIC which is advanced in NR compared to IR.

Table A.3.: Experimentally obtained tensile strength σ_t and strain at break $\varepsilon_t = \lambda_t - 1$ of filled NR. If the samples are vulcanized, the mass fraction of sulfur m_S is given.

m_S / phr	filler	m_f / phr	ϕ	σ_t / MPa	ε_t / %	reference
-	-			0.437	442.2	[27]
2	-			0.494	383.7	[27]
4	-			0.618	397.2	[27]
6	-			0.637	377.2	[27]
1.5	-			18	1100	[178]
4	CB N220	20		1.216	163.4	[27]
-	CB N330	20		1.189	42.5	[27]
4	CB N330	20		0.836	137.0	[27]
4	CB N550	20		0.610	183.4	[27]
4	CB N660	20		1.210	199.8	[27]
-	CB N330	25		0.916	25.2	[27]
-	CB N330	30		0.565	6.7	[27]
1	CB E250		0.05	27.15	1297.7	[264]
1	CB E250		0.1	32.62	1241.6	[264]
1	CB E250		0.15	31.06	1108.4	[264]
1.8	CB N234	40	0.155	20.6	574	[263]
1.8	CB N234	50	0.186	23.5	515	[263]
1.8	CB N234	60	0.216	23.6	458	[263]
1.8	CB N234	80	0.268	20.1	292	[263]

A.3. Morphology Generation - Supplemental Data

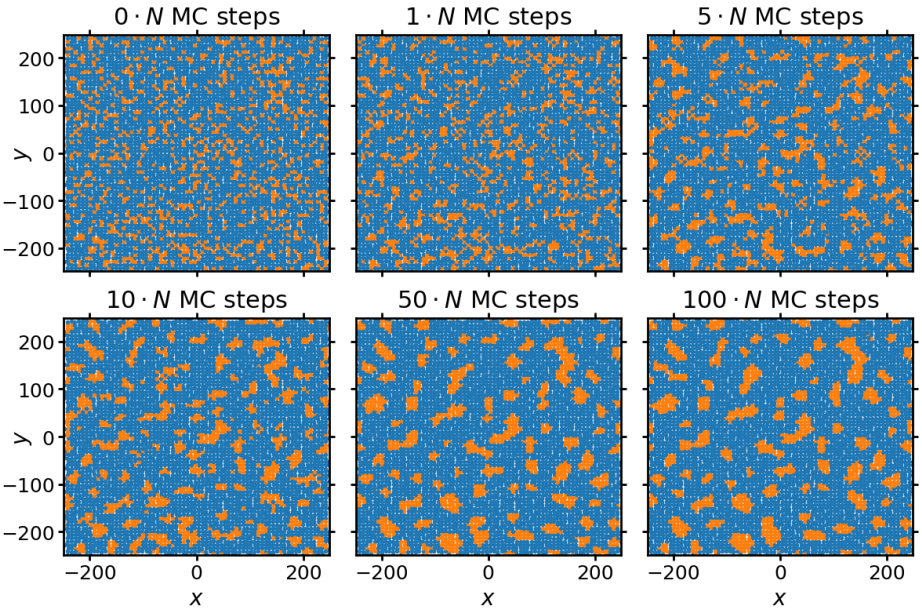

Figure A.5.: Evolution of the filler morphology during the application of the morphology generator at different number of MC steps. The blue dots are cross links, while the orange dots indicate filler. A 2D-network consisting of $N = 5041$ nodes and containing a fraction $\phi = 0.2$ of CB N339 has been simulated with $r_{\mathrm{MG}} = 2.0\, d_{\mathrm{i}}$. The corresponding plot of the total energy W versus the MC attempts per node is presented in Figure 5.7.

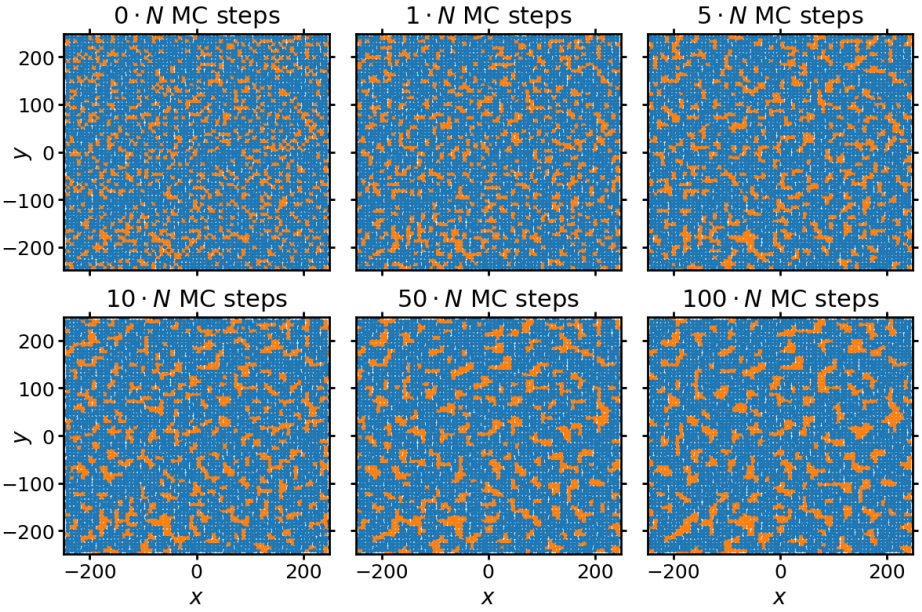

Figure A.6.: Evolution of the filler morphology during the application of the morphology generator at different number of MC steps. The blue dots are cross links, while the orange dots indicate filler. A 2D-network consisting of $N = 5041$ nodes and containing a fraction $\phi = 0.2$ of CB N339 has been simulated. For the neighbor list, it is set $r_{\mathrm{MG}} = 1.205\, d_{\mathrm{i}}$, which corresponds to the radius in which the nearest neighbors (on average 4) are located.

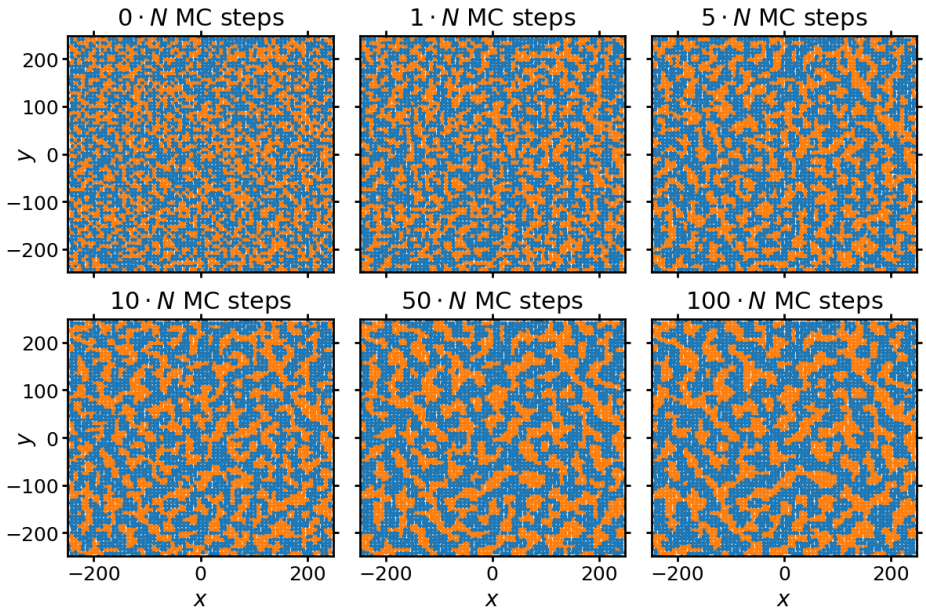

Figure A.7.: Evolution of the filler morphology during the application of the morphology generator at different number of MC steps. The blue dots are cross links, while the orange dots indicate filler. A 2D-network consisting of $N = 5041$ nodes and containing a fraction $\phi = 0.4$ of CB N339 has been simulated. For the neighbor list, it is set $r_{\mathrm{MG}} = 1.205\, d_{\mathrm{i}}$, which corresponds to the radius in which the nearest neighbors (on average 4) are located.

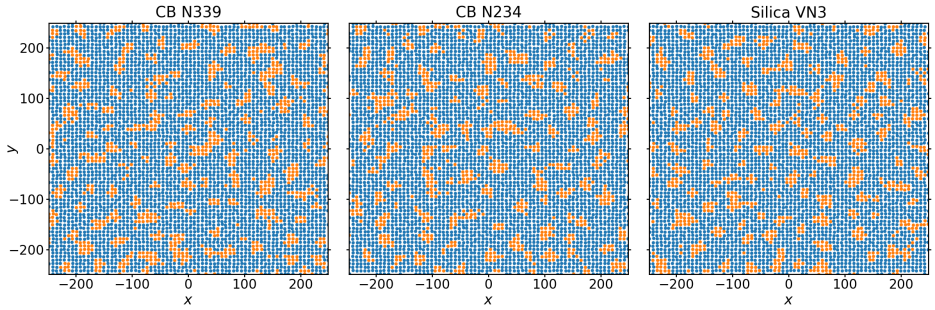

Figure A.8.: Snapshots of 2D-networks after 10 MC steps/N of morphology generation for NR containing different types of filler with the surface tensions given in Table 4.1. The networks which have been simulated consist of $N = 5041$ nodes and contain a fraction $\phi = 0.2$ of filler.

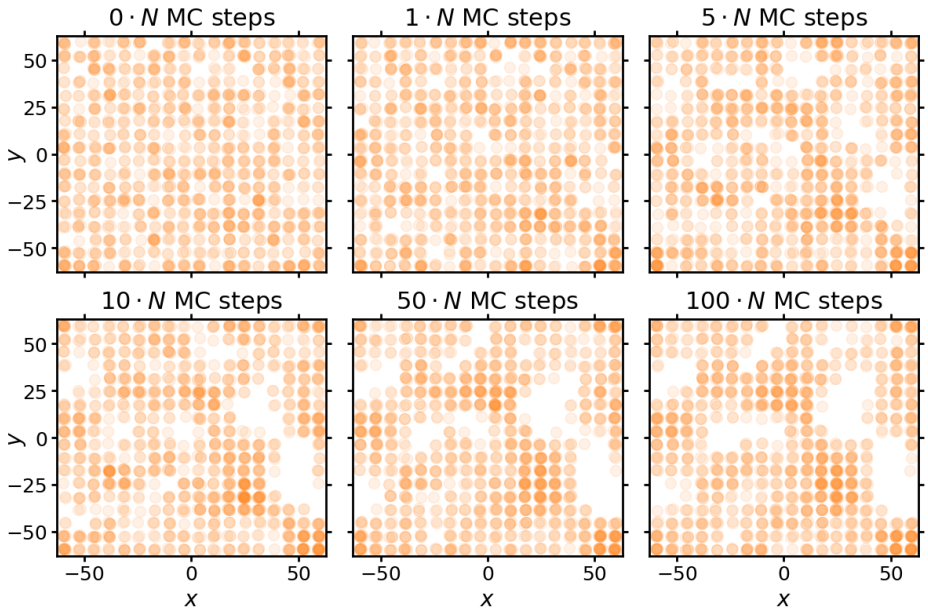

Figure A.9.: Evolution of the filler morphology during the application of the morphology generator at different number of MC steps. The blue dots are cross links, while the orange dots indicate filler. 3D-networks consisting of $N = 5832$ nodes and containing a fraction $\phi = 0.2$ of filler have been simulated with $r_{\text{morph}} = 2.0\, d_{\text{init}}$.

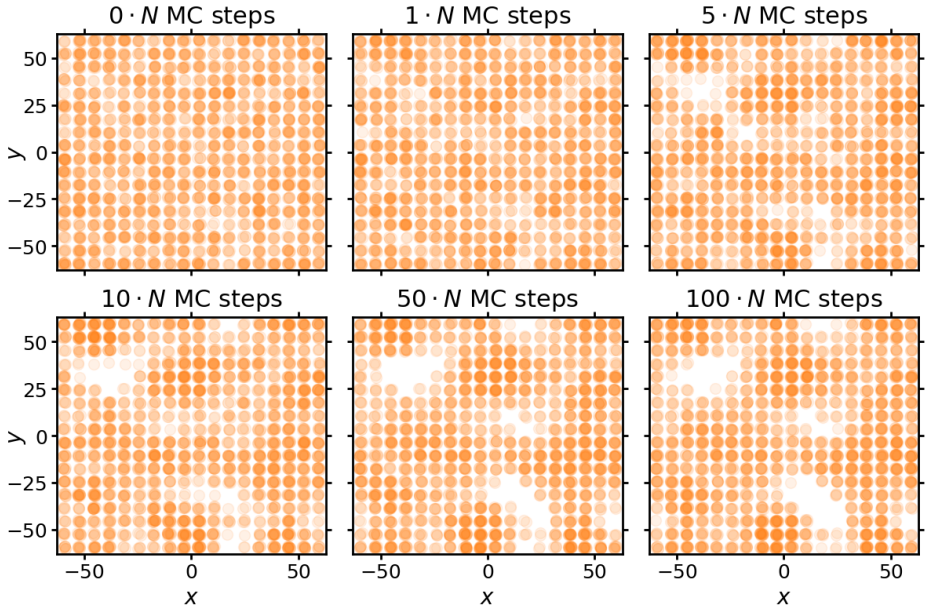

Figure A.10.: Evolution of the filler morphology during the application of the morphology generator at different number of MC steps. The blue dots are cross links, while the orange dots indicate filler. 3D-networks consisting of $N = 5832$ nodes and containing a fraction $\phi = 0.4$ of filler have been simulated with $r_{\text{morph}} = 2.0\, d_{\text{init}}$.

A.4. Parametrization of Filler-Filler and Polymer-Filler Bonds - Details

This section includes supplemental information regarding the parametrization of filler-filler and polymer-filler bonds which is addressed in subsection 5.2.2. As the stress-

stretch curves are discussed first in there, the impact of the limit of slow deformation on the stress-stretch curves and the original offset of the stress of filled networks are discussed. Afterwards, the specification of the spring constants of filler-filler and polymer-filler bonds given by Equation 3.78 is discussed.

A.4.1. Impact of the Limit of Slow Deformation

In order to analyze the impact of the slow deformation limit on the results, analogous simulations for various fractions of filler ϕ are executed, where the reversible bond breaking is included into the energy minimization by the FIRE algorithm. The stretch stress-curves for the non-crystallizing networks are shown in Figure A.11.

In contrast to the limit of slow deformation, the maximum stress increases until $\phi = 0.2$ and decrease thereafter with increasing filler content. This behavior might be related to the percolation threshold of the network. Furthermore, the incline of the stress appears to decrease with increasing filler content, but the regime of small stretches is not resolved here.

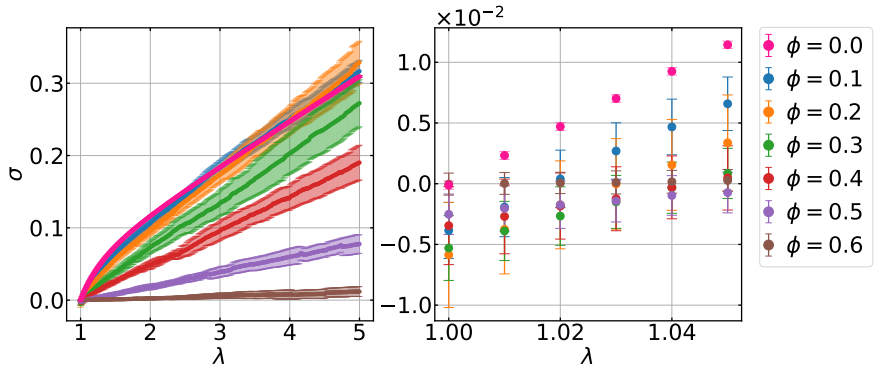

Figure A.11.: Stress-stretch curves obtained as averaged from 10 simulations of non-crystallizing 2D-networks consisting of $N = 5041$ nodes containing different fractions ϕ of filler.

A.4.2. Investigations Regarding the Offset of the Stress in Filled Networks

For further analysis, the initial stress and the forces and extensions of the polymer-filler and filler-filler links dependent on their orientation is investigated. Networks consisting of $N = 196$ nodes with $\kappa = 0.1$ are simulated with variable filler content ϕ. The data refers to the state of the network after the energy minimization by the FIRE algorithm. At this point, usually, the stress is computed, but, additionally, the stress before the energy minimization by the FIRE algorithm is calculated, i.e. immediately after setting up the initial configuration. The data points are obtained as averages from 10 independent simulations and the error bars correspond to the standard deviations.

Because of the overlapping error bars, Figure A.12 does not allow for a definitive conclusion on whether a spatial direction is preferred by filler over the other. Additionally, no conclusive observation can be made regarding the impact of the FIRE algorithm on the negative stresses. However, note that the effect of the filler content might be related to the percolation threshold. Although the links are unable to break reversibly, most of the filler-filler and polymer-filler bonds are extended to $r > r_0$. Nevertheless, it is expected from the symmetry of the potential energy that links stretched to a lower and to a higher extend than the equilibrium distance r_0 occur equally distributed.

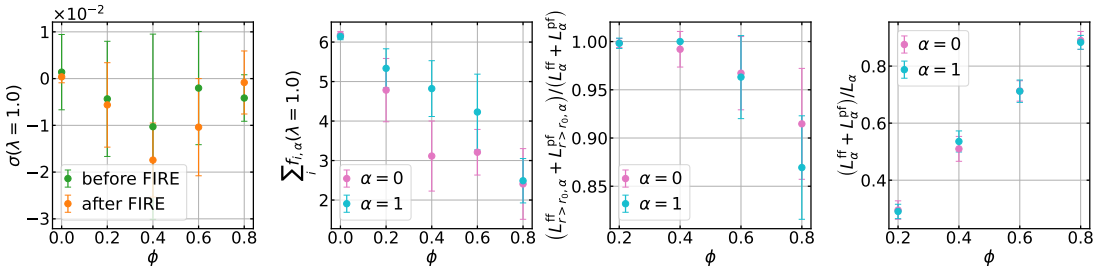

Figure A.12.: From upper left to lower right panel: Stress σ, sum of the components of the forces, fraction of polymer-filler and filler-filler bonds which are extended such that $r > r_0$ and fraction of polymer-filler and filler-filler bonds versus filler content ϕ. The latter are obtained for each spatial direction. The morphology generator ran through $10 \cdot N$ MC steps.

In order to investigate the impact of the filler alignment in the network on the stress, networks consisting of $N = 196$ nodes are simulated with $\kappa = 0.05$ and $n = 49$ Kuhn segments in each link, i.e. the number of Kuhn segments is not randomly drawn from a Gaussian distribution as it has been done previously. Therefore, the network structure is comparatively homogenous. Nevertheless, rectangulary shaped filler aggregates are embedded into the network. They contain $\Phi_0 \times \Phi_1$ filler nodes. For the examined filler morphologies, it holds $\phi\,(\Phi_0/\Phi_1) = \phi\,(\Phi_1/\Phi_0)$. Examples are presented in Figure A.13.

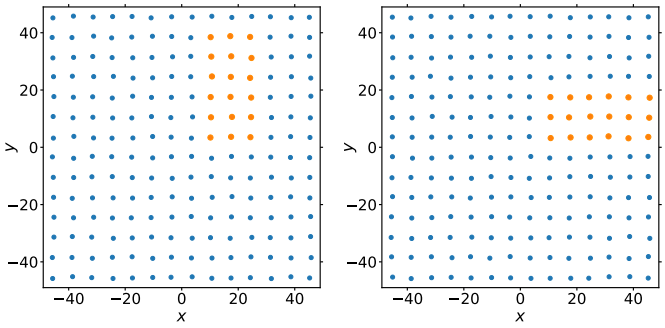

(a) $\Phi_0/\Phi_1 = 0.5$ **(b)** $\Phi_0/\Phi_1 = 2$

Figure A.13.: Examples for filler morphologies generated for the data obtained in Figure A.14. The blue dots represent cross links, while the orange dots are filler. Here, x corresponds to the direction 0, while y corresponds to direction 1.

Figure A.14 shows that all of the filler-filler and polymer-filler bonds are extended above their equilibrium distance. Furthermore, it indicates that the force along the spatial direction with higher number of polymer-filler and filler-filler bonds tends to be higher than in the other direction, but the error bars of the data points overlap.

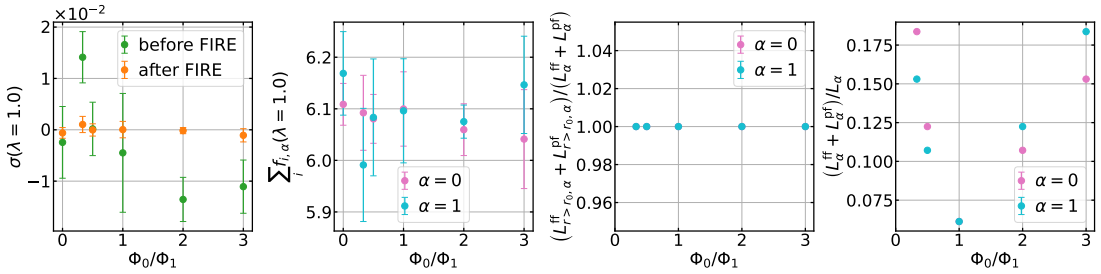

Figure A.14.: From upper left to lower right panel: Stress σ, sum of the components of the forces, fraction of polymer-filler and filler-filler bonds which are extended such that $r > r_0$ and fraction of polymer-filler and filler-filler bonds versus the aspect ratio Φ_0/Φ_1 of the filler aggregate. The latter are obtained for each spatial direction.

The initially negative stress might result from the definition of the equilibrium distances of the bonds. Since the forces of polymer-filler and filler-filler bonds are set to zero, there are non-vanishing contributions to the stress. Therefore, the equilibrium distances are subsequently defined based on an equilibrated pure polymer network as described in section 4.1.

Nevertheless, this modification has not lead to the desired improvement because the initial stress still became negative after a subsequent energy minimization by the FIRE algorithm. This is shown in Figure A.15 and Figure A.16. Therefore, in order to eliminate negative initial stress, the stress-stretch curves for crystallizing networks are shifted by the initial stretch of an unfilled network.

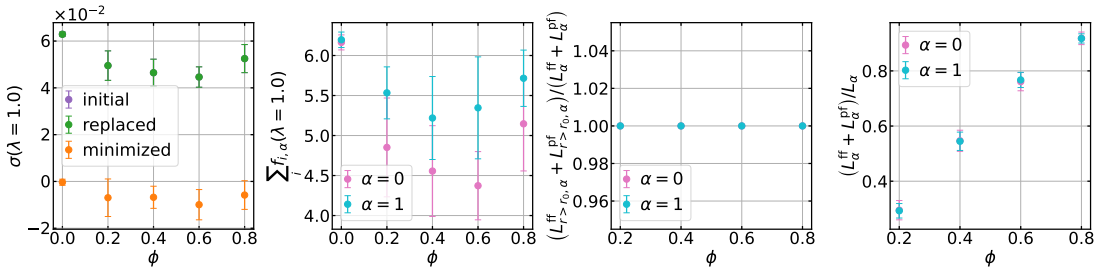

Figure A.15.: From upper left to lower right panel: Stress σ, sum of the components of the forces, fraction of polymer-filler and filler-filler bonds which are extended such that $r > r_0$ and fraction of polymer-filler and filler-filler bonds versus the aspect ratio Φ_0/Φ_1 of the filler aggregate. The latter are obtained for each spatial direction. The "initial" data overlaps with the data after replacing links by filler-filler and polymer-filler bonds according to the generated morphology.

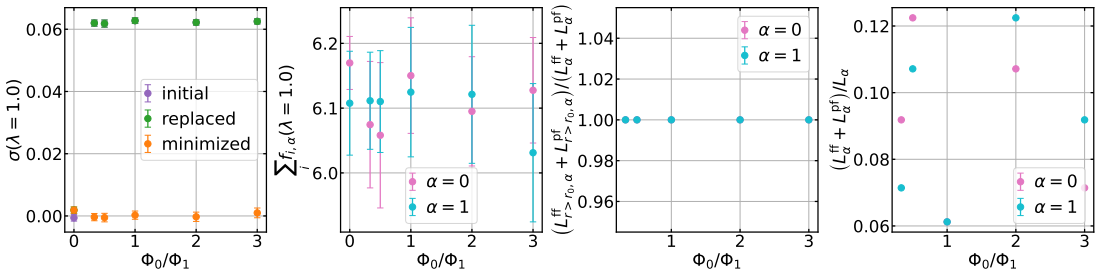

Figure A.16.: From upper left to lower right panel: Stress σ, sum of the components of the forces, fraction of polymer-filler and filler-filler bonds which are extended such that $r > r_0$ and fraction of polymer-filler and filler-filler bonds versus the aspect ratio Φ_0/Φ_1 of the filler aggregate. The latter are obtained for each spatial direction. The morphology generator ran through $10 \cdot N$ MC steps and the "initial" data overlaps with the data after replacing links by filler-filler and polymer-filler bonds according to the generated morphology.

A.4.3. Specification of the Spring Constants

Subsequently, the spring constants for filler-filler and filler-polymer bonds are specified according to Equation 5.2. The spring constant for polymer-filler interaction $k^{\mathrm{pf}} = 4.0$ is fixed, while k^{ff} and $k^{\mathrm{pf}}_{\mathrm{weak}}$ are to be determined. For this purpose, 2D-networks consisting of $N = 5041$ nodes are simulated with variable filler content ϕ. If not stated differently, the MGis applied for $10 \cdot N$ MC steps. As explained previously, $\partial\sigma/\partial\lambda$ is extracted from the stress-stretch curves in the region of small deformation. Equation 5.3 is fitted to each data set.

First, it is checked how the variation of $k \equiv k^{\mathrm{ff}} = k^{\mathrm{pf}} = k^{\mathrm{pf}}_{\mathrm{weak}}$ affects $\partial\sigma/\partial\lambda$ in the case $R^{\mathrm{ff}} = \infty$. The morphology generator runs through $10 \cdot N$ MC steps. The results are depicted in Figure A.17. At low filler content, the error margins of the data points for different k overlap. For high filler content, $\partial\sigma/\partial\lambda$ appear to increase with k, but the error bars still overlap. The curves fit the data well for small filler content, but the error margins of data points for $\phi = 0.9$ do not contain the fitted functions. The differences for high filer content result from the comparatively large errors of the data points which makes them weighted less for the fit. Furthermore, the obtained exponents y lay within the expected range.

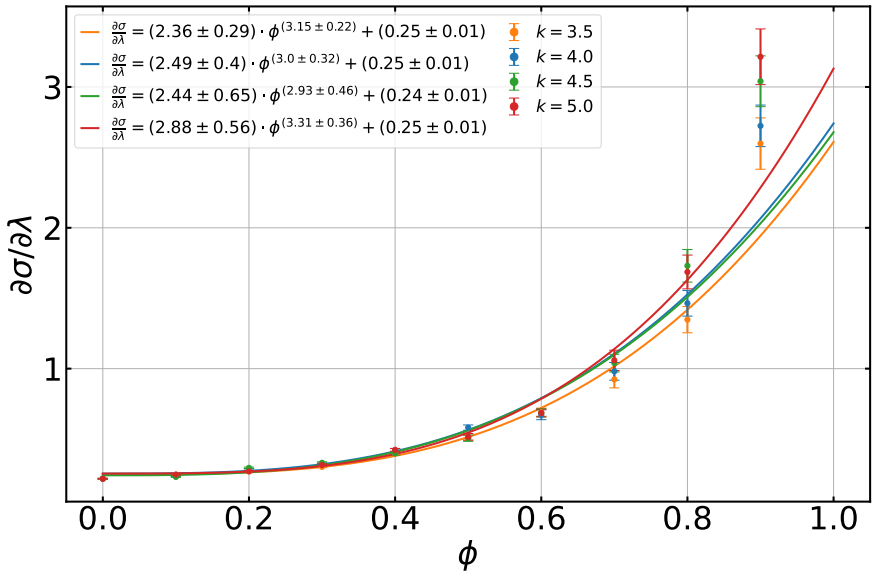

Figure A.17.: $\partial\sigma/\partial\lambda$ versus ϕ for 2D-networks for variable k. The morphology generator ran through $10 \cdot N$ MC steps. It is set $R^{\mathrm{ff}} = \infty$. The data points for $\phi = 0.0$ are not taken into account for the fits.

As a next step, the spring constant for filler-filler interaction k^{ff} is varied, while it is set $k^{\mathrm{pf}} = k^{\mathrm{pf}}_{\mathrm{weak}} = 4.0$ and $R^{\mathrm{ff}} = \infty$. The data is shown in Figure A.18 with the corresponding fitted functions. With increasing k^{ff}, $\partial\sigma/\partial\lambda$ tends to increase. Apparently, $k^{\mathrm{ff}} = 5.0$ is a good choice since it increases $\partial\sigma/\partial\lambda$ relatively to the data for $k^{\mathrm{ff}} = 4.0$ to a higher extend than $k^{\mathrm{ff}} = 4.5$ and $k^{\mathrm{pf}} < k^{\mathrm{ff}}$ is required. Besides, the obtained exponents y are situated within the expected range. Nevertheless, the curves fit the data well for small filler content, but they differ for high filler content due to the comparatively large errors of the data.

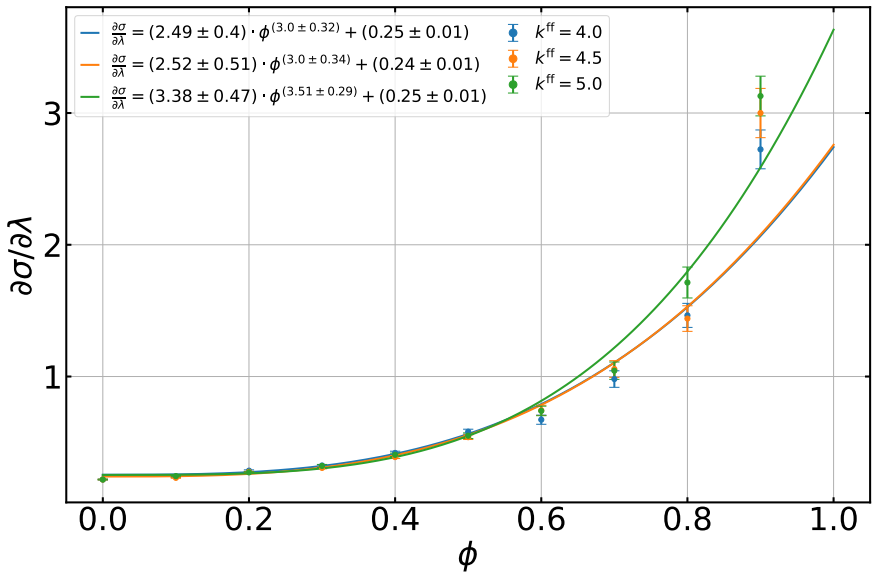

Figure A.18.: $\partial\sigma/\partial\lambda$ versus ϕ for 2D-networks for variable k^{ff}. The morphology generator ran through $10 \cdot N$ MC steps. It is set $k^{\mathrm{pf}} = k^{\mathrm{pf}}_{\mathrm{weak}} = 4.0$ and $R^{\mathrm{ff}} = \infty$. The data points for $\phi = 0.0$ are not taken into account for the fits.

Figure A.19 shows the results for variable $k^{\mathrm{pf}}_{\mathrm{weak}}$ with $R^{\mathrm{pf}} = 1.01$. It is set $k^{\mathrm{ff}} = k^{\mathrm{pf}} = 4.0$ and $R^{\mathrm{ff}} = \infty$. With increasing $k^{\mathrm{pf}}_{\mathrm{weak}}$, $\partial\sigma/\partial\lambda$ increases. For $k^{\mathrm{pf}}_{\mathrm{weak}} \leq 0.1$, the fitted

functions describe the data well, but, for higher $k^{\mathrm{pf}}_{\mathrm{weak}}$, the curves deviate from the data for high filler content. Furthermore, the exponents y become larger than the expected values for the small $k^{\mathrm{pf}}_{\mathrm{weak}}$. For low filler content, the data is approximately constant for $k^{\mathrm{pf}}_{\mathrm{weak}} = 0.1$ and $k^{\mathrm{pf}}_{\mathrm{weak}} = 0.01$. Simultaneously, the stress in these networks is not significantly amplified by small filler content in comparison to the unfilled network. This is illustrated by the stress-stretch curve in Figure A.20, where the stress becomes smaller than in the unfilled network particularly at small stretches. This is in contrast to the expectations. Nevertheless, appears like $k^{\mathrm{pf}}_{\mathrm{weak}} = 0.5$ and $k^{\mathrm{pf}}_{\mathrm{weak}} = 1.0$ are potentially good choices. Note that Viktorova *et al.* [2] have set the spring constant $k^{\mathrm{pf}}_{\mathrm{weak}}$ 4 orders of magnitude smaller than k^{pf}, but apparently it does not make sense to choose this parameter as small here. Therefore, these values are tested in combination with the remaining adjusted parameters. However, the effect of allowing rupture of filler-filler bonds is tested before.

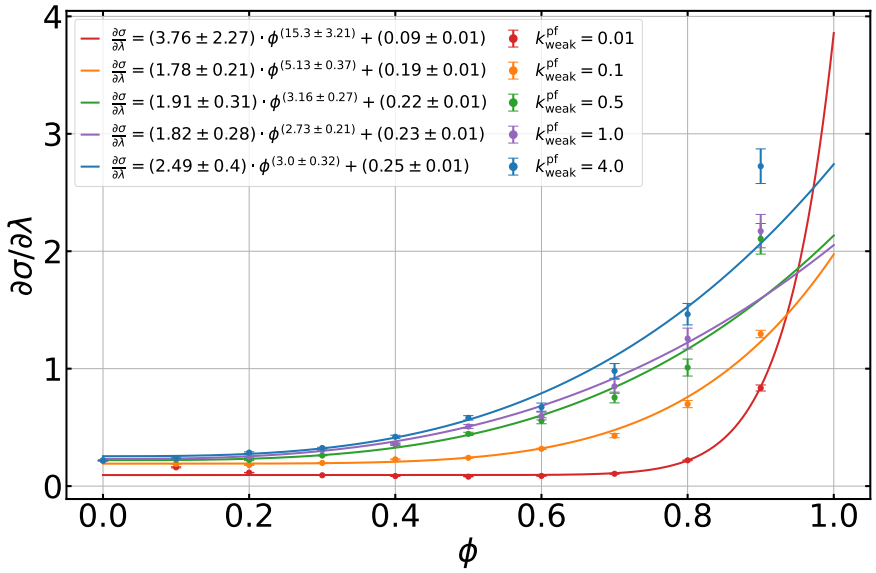

Figure A.19.: $\partial\sigma/\partial\lambda$ versus ϕ for 2D-networks for variable $k^{\mathrm{pf}}_{\mathrm{weak}}$ with $R^{\mathrm{pf}} = 1.01$. The morphology generator ran through $10 \cdot N$ MC steps. It is set $k^{\mathrm{ff}} = k^{\mathrm{pf}} = 4.0$ and $R^{\mathrm{ff}} = \infty$. The data points for $\phi = 0.0$ are not taken into account for the fits.

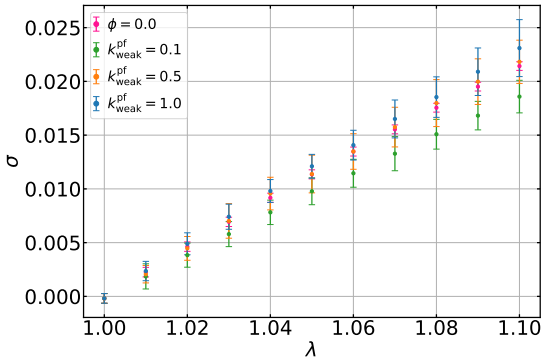

Figure A.20.: Stress-stretch curves for 2D-networks for variable $k^{\mathrm{pf}}_{\mathrm{weak}}$. The networks contain $\phi = 0.1$ of filler and the morphology generator ran through $10 \cdot N$ MC steps.

Setting $R^{\mathrm{ff}} = 1.01$ yields the results depicted in Figure A.21. In contrast to the effect of enabling rupture of filler-filler bonds, decreasing $k^{\mathrm{pf}}_{\mathrm{weak}}$ affects the data more

significant. Therefore, the polymer-filler bonds appear to be dominant compared to the filler-filler bonds.

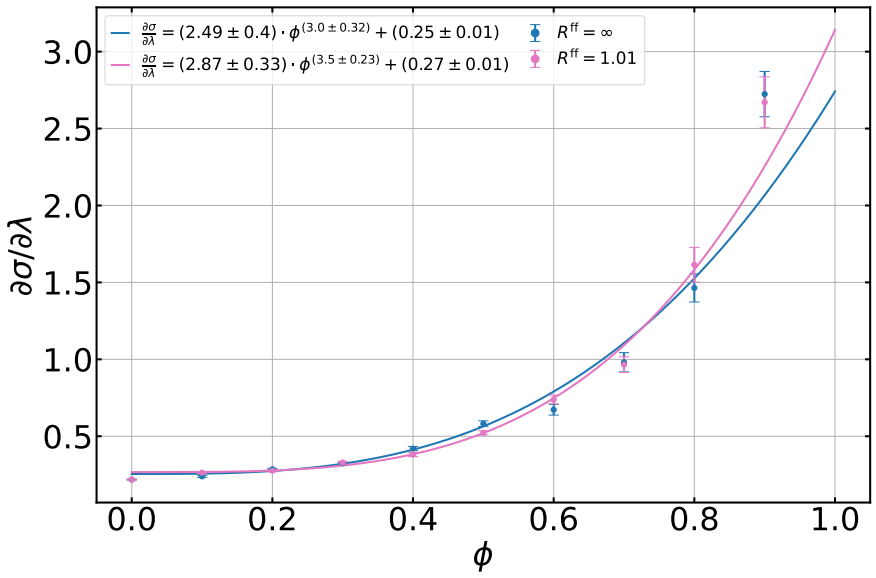

Figure A.21.: $\partial\sigma/\partial\lambda$ versus ϕ for 2D-networks for $R^{\mathrm{ff}} = \infty$ and $R^{\mathrm{ff}} = 1.01$. The morphology generator ran through $10 \cdot N$ MC steps. It is set $k = 4.0$. The data points for $\phi = 0.0$ are not taken into account for the fits.

In the following, $k^{\mathrm{pf}}_{\mathrm{weak}} = 0.5$ and $k^{\mathrm{pf}}_{\mathrm{weak}} = 1.0$ are tested in combination $R^{\mathrm{ff}} = 1.01$, while the cases $k^{\mathrm{ff}} = 4.0$ and $k^{\mathrm{ff}} = 5.0$ are distinguished. The spring constant for polymer-filler interaction $k^{\mathrm{pf}} = 4.0$ is still fixed. The results are depicted in Figure A.22. As previously observed, increasing $k^{\mathrm{pf}}_{\mathrm{weak}}$ increases $\partial\sigma/\partial\lambda$. The data points for fixed $k^{\mathrm{pf}}_{\mathrm{weak}}$ and variable k^{ff} overlap. Considering the fitted curves, it appears like increasing k^{ff} decreases $\partial\sigma/\partial\lambda$, which is in contrast to the results for variable k^{ff} presented in Figure A.18. This might be attributed to rupture of filler-filler bonds, which has been forbidden in the above case. The obtained exponents y are comparatively small, but still consistent with the expected value $y = 2$ for networks with filler content below the percolation threshold.

Figure A.23 shows the stress-stretch curves for $\phi = 0.1$ and $\phi = 0.5$ corresponding to the data presented in Figure A.22. For $\phi = 0.1$ at low stretches, the stress does not appear to be significantly amplified, but it is rather consistent with the data for the unfilled network. However, for higher stretches, the stress becomes larger than for the unfilled network in particular for $k^{\mathrm{pf}}_{\mathrm{weak}} = 1.0$. For $\phi = 0.5$, the stress is significantly increased compared to the unfilled network for all of the choices of the spring constants. In any case, the data for $k^{\mathrm{ff}} = 4.0$ and $k^{\mathrm{ff}} = 5.0$ are consistent. Nevertheless at high stretches, the stress tends to increase with k^{ff}.

In order to meet the relation between the spring constants given in Equation 5.2 and to model stress amplification, it is useful to parameterize the interaction between fillers and between polymer and filler by the parameters summarized in Table 5.6.

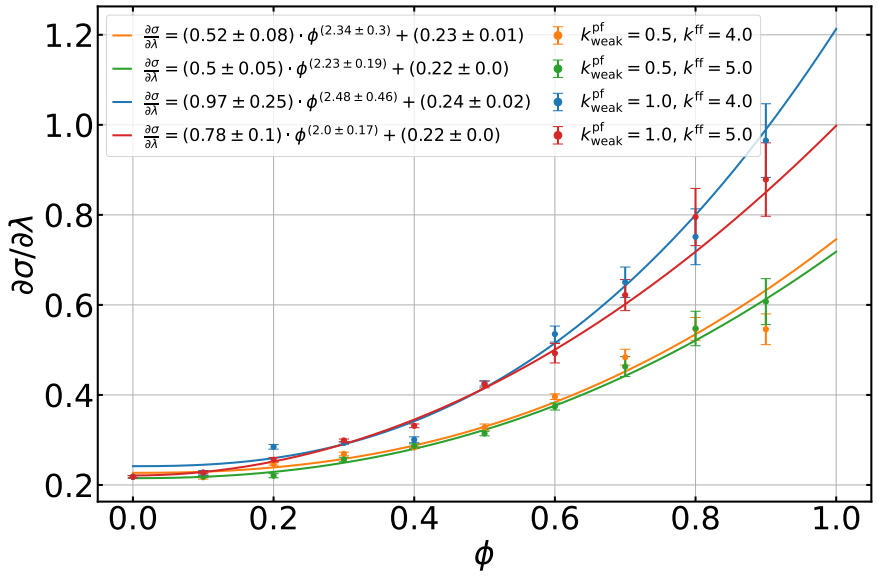

Figure A.22.: $\partial\sigma/\partial\lambda$ versus ϕ for 2D-networks with variable k^{ff} and $k^{\mathrm{pf}}_{\mathrm{weak}}$. It is set $k^{\mathrm{pf}} = 4.0$ and $R^{\mathrm{ff}} = 1.01$. The morphology generator ran through $10 \cdot N$ MC steps. It is set $k = 4.0$. The data points for $\phi = 0.0$ are not taken into account for the fits.

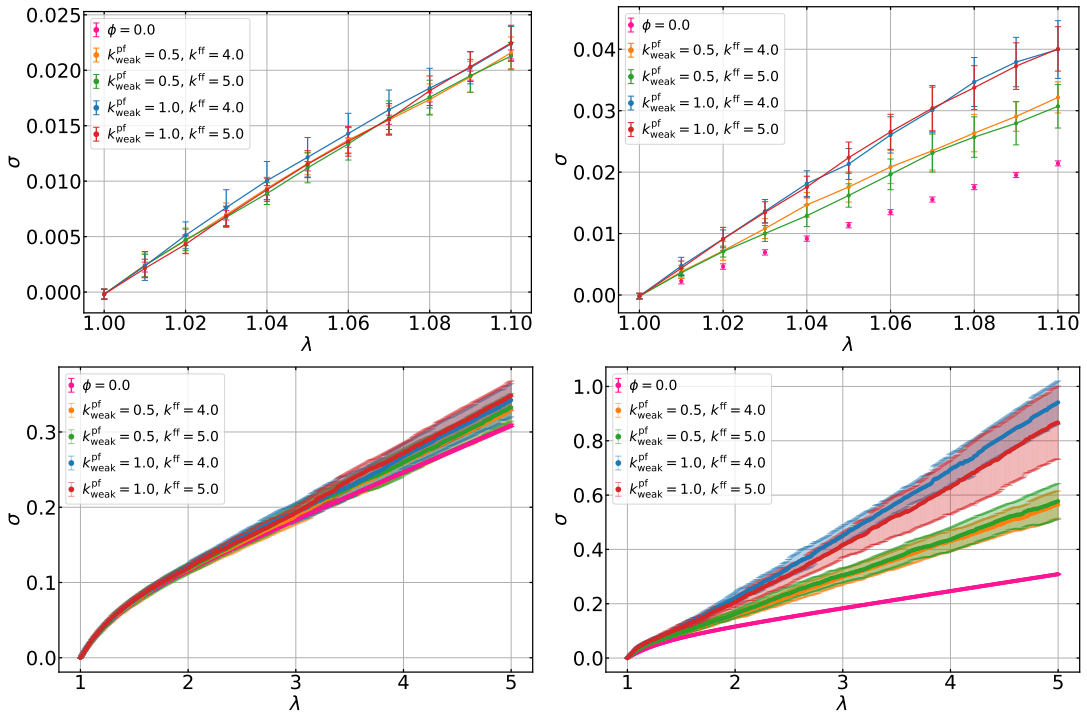

(a) $\phi = 0.1$ **(b)** $\phi = 0.5$

Figure A.23.: Stress-stretch curves for 2D-networks with variable k^{ff} and $k^{\mathrm{pf}}_{\mathrm{weak}}$. It is set $k^{\mathrm{pf}} = 4.0$ and $R^{\mathrm{ff}} = 1.01$. The upper plots show the region of small deformation extracted from the lower plots. The data points are connected for visualization, but this does not have any physical meaning.

A.5. Behavior of Filled Networks at Small Deformations - Supplemental Data

Figure A.24 shows the derivative $\partial\sigma/\partial\lambda$ and the difference of the derivatives $(\partial\sigma/\partial\lambda)_\infty - \partial\sigma/\partial\lambda$ for variable cut-off radii R^{ff} and R^{pf} for filler-filler and polymer-filler bonds, respectively. At very small deformations, the derivatives for $R^{\mathrm{ff}} = R^{\mathrm{pf}} \geq 1.05$ overlap, but that for $R^{\mathrm{ff}} = R^{\mathrm{pf}} = 1.01$ is significantly smaller. As the deformation proceeds, the latter, remains approximately constant, whereas the others for the filled networks, except for $R^{\mathrm{ff}} = R^{\mathrm{pf}} = \infty$, decrease further approaching that for the unfilled case. Only for $R^{\mathrm{ff}} = R^{\mathrm{pf}} \geq 1.05$, the increase of the difference if the derivatives attributed to the Payne Effect can be observed. Since the stretch at which bond breaking starts decreases with decreasing cut-off radius, the onset of the Payne effect is shifted towards smaller stretches analogously. However, for $R^{\mathrm{ff}} = R^{\mathrm{pf}} = 1.01$, the difference of the derivatives decreases until it reaches a plateau value. In this case, the data behaves like for the unfilled case. This suggests that links determine the mechanical behavior because most of the filler-filler bonds break and polymer-filler bonds weaken immediately at the start of the deformation.

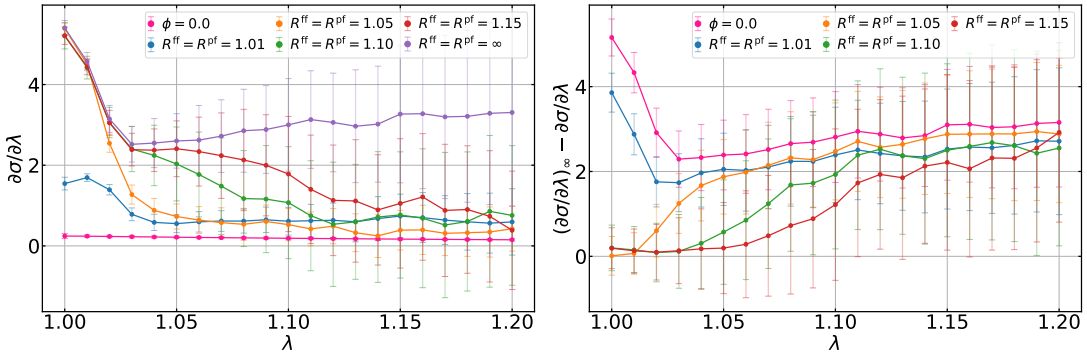

Figure A.24.: $\partial\sigma/\partial\lambda$ and $(\partial\sigma/\partial\lambda)_\infty - \partial\sigma/\partial\lambda$ versus λ for unfilled 2D-networks or 2D-networks with filler content $\phi = 0.9$ for variable cut-off radii R^{ff} and R^{pf}. The data points are connected for the eye, but this does not have any physical meaning.

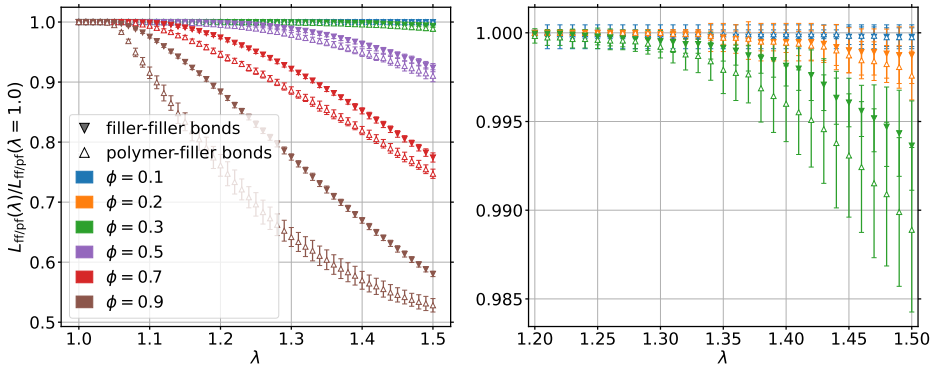

Figure A.25.: Plot of the ratio of the number of filler-filler bonds L_{ff} to the number of filler-filler bonds at the initial stretch $\lambda = 1.0$ as well as the ratio of the number of polymer-filler bonds to the number of polymer-filler bonds L_{pf} at the initial stretch $\lambda = 1.0$ dependent on the stretch λ. The data have been obtained as averages from 10 independent simulations of 2D-networks containing different fractions ϕ of filler with $R^{\mathrm{ff}} = R^{\mathrm{pf}} = 1.1$.

A.6. Behavior of Filled Networks at Large Deformations - Supplemental Data

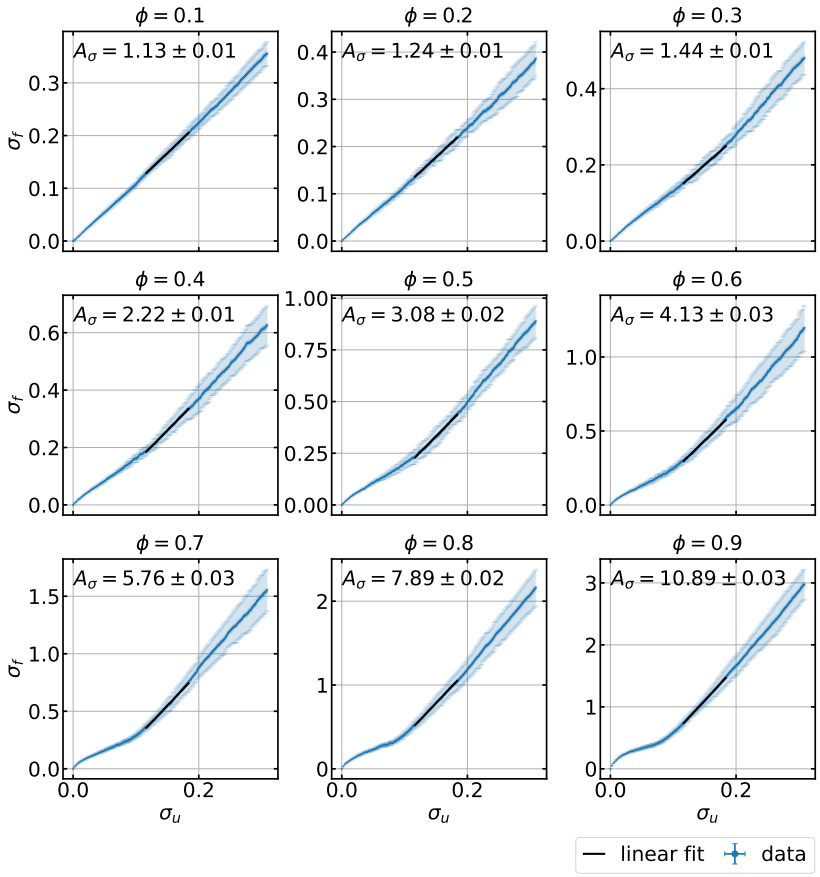

Figure A.26.: Stress in the filled network σ_f versus stress in the unfilled networks σ_u at identical stretches $\lambda \in [1.0, 5.0]$ for different filler contents ϕ. The data has been obtained as averages of 10 independent simulations of non-crystallizing 2D-networks consisting of $N = 5041$ nodes. The MG ran through $10 \cdot N$ MC steps. For $\lambda \in [2.0, 3.0]$, the data has been fitted with a linear function and the resulting stress amplification factors A_σ are given. The corresponding fit parameters are listed in Table A.4.

Table A.4.: Parameters for the linear fits $\sigma_\mathrm{f} = A_\sigma \sigma_\mathrm{u} + B$ shown in Figure A.26.

ϕ	A_σ	B	χ^2/ndf
0.1	1.13 ± 0.01	-0.0 ± 0.01	0.003
0.2	1.24 ± 0.01	-0.01 ± 0.01	0.006
0.3	1.44 ± 0.01	-0.02 ± 0.01	0.011
0.4	2.22 ± 0.01	-0.07 ± 0.01	0.007
0.5	3.08 ± 0.02	-0.13 ± 0.01	0.011
0.6	4.13 ± 0.03	-0.19 ± 0.01	0.01
0.7	5.76 ± 0.03	-0.32 ± 0.01	0.01
0.8	7.89 ± 0.02	-0.4 ± 0.01	0.002
0.9	10.89 ± 0.03	-0.53 ± 0.01	0.003

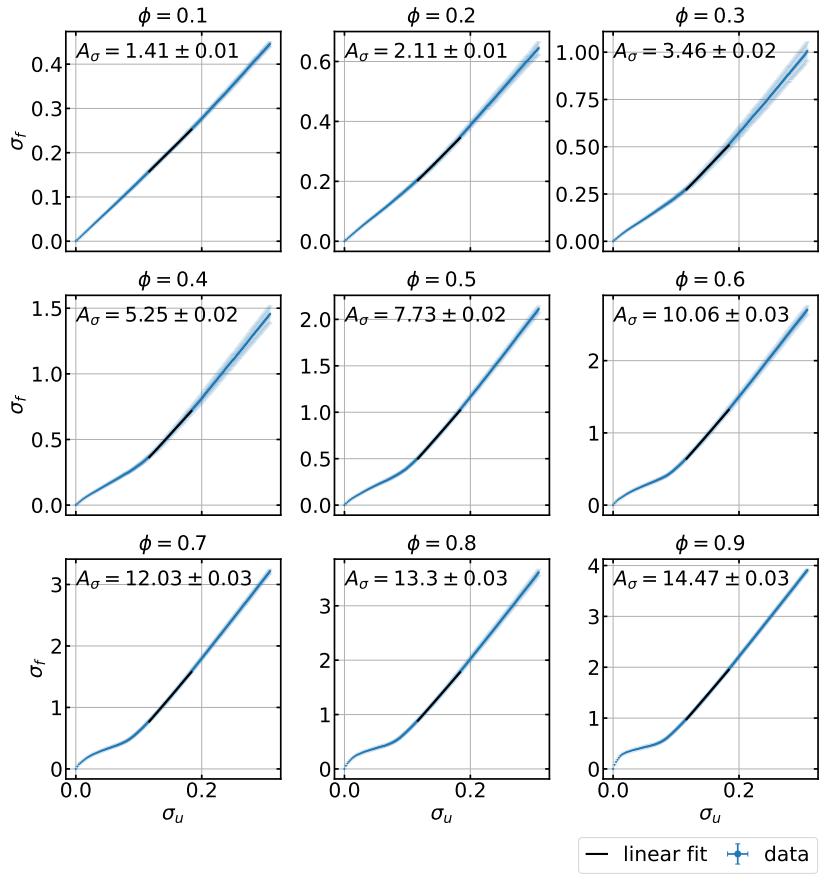

Figure A.27.: Stress in the filled network σ_f versus stress in the unfilled networks σ_u at identical stretches $\lambda \in [1.0, 5.0]$ for different filler contents ϕ. The data has been obtained as averages of 10 independent simulations of non-crystallizing 2D-networks consisting of $N = 5041$ nodes. The filler is randomly distributed. For $\lambda \in [2.0, 3.0]$, the data has been fitted with a linear function and the resulting stress amplification factors A_σ are given. The corresponding fit parameters are listed in Table A.5.

Table A.5.: Parameters for the linear fits $\sigma_\mathrm{f} = A_\sigma \sigma_\mathrm{u} + B$ shown in Figure A.27.

ϕ	A_σ	B	χ^2/ndf
0.1	1.41 ± 0.01	-0.01 ± 0.01	0.02
0.2	2.11 ± 0.01	-0.04 ± 0.01	0.046
0.3	3.46 ± 0.02	-0.13 ± 0.01	0.018
0.4	5.25 ± 0.02	-0.25 ± 0.01	0.027
0.5	7.73 ± 0.02	-0.4 ± 0.01	0.107
0.6	10.06 ± 0.03	-0.53 ± 0.01	0.041
0.7	12.03 ± 0.03	-0.63 ± 0.01	0.151
0.8	13.3 ± 0.03	-0.67 ± 0.01	0.043
0.9	14.47 ± 0.03	-0.71 ± 0.01	0.353

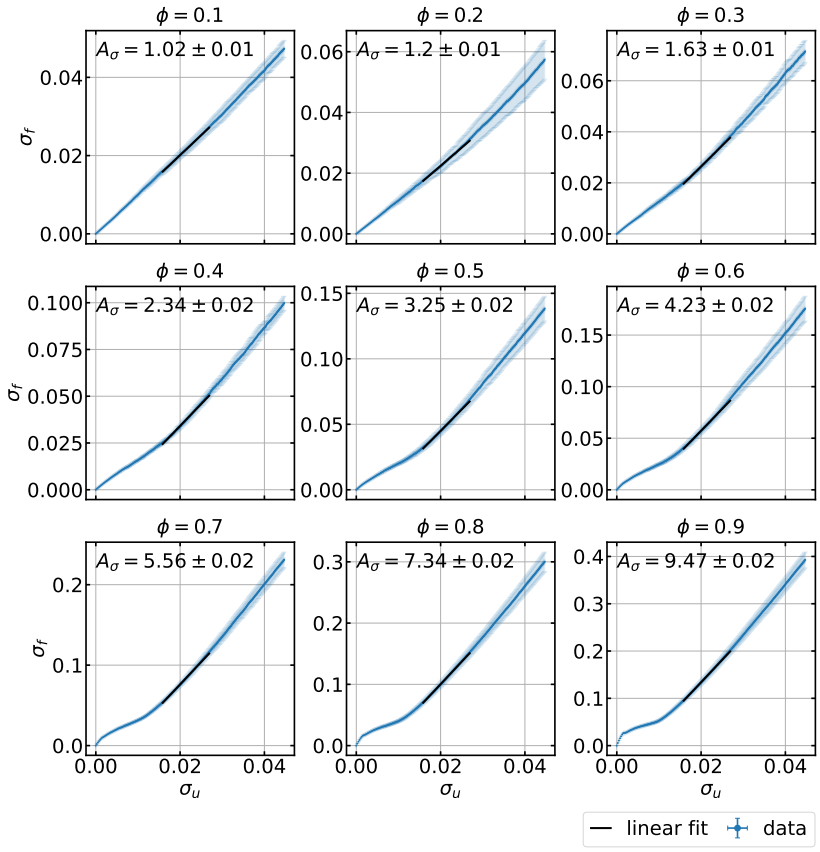

Figure A.28.: Stress in the filled network σ_f versus stress in the unfilled networks σ_u at identical stretches $\lambda \in [1.0, 5.0]$ for different filler contents ϕ. The data has been obtained as averages of 10 independent simulations of non-crystallizing 3D-networks consisting of $N = 5832$ nodes. The MG ran through $10 \cdot N$ MC steps. For $\lambda \in [2.0, 3.0]$, the data has been fitted with a linear function and the resulting stress amplification factors A_σ are given. The corresponding fit parameters are listed in Table A.6.

Table A.6.: Parameters for the linear fits $\sigma_\mathrm{f} = A_\sigma \sigma_\mathrm{u} + B$ shown in Figure A.28.

ϕ	A_σ	B	χ^2/ndf
0.1	1.02 ± 0.01	-0.0 ± 0.01	0.001
0.2	1.2 ± 0.01	-0.0 ± 0.01	0.004
0.3	1.63 ± 0.01	-0.01 ± 0.01	0.026
0.4	2.34 ± 0.02	-0.01 ± 0.01	0.047
0.5	3.25 ± 0.02	-0.02 ± 0.01	0.017
0.6	4.23 ± 0.02	-0.03 ± 0.01	0.015
0.7	5.56 ± 0.02	-0.04 ± 0.01	0.03
0.8	7.34 ± 0.02	-0.05 ± 0.01	0.01
0.9	9.47 ± 0.02	-0.06 ± 0.01	0.01

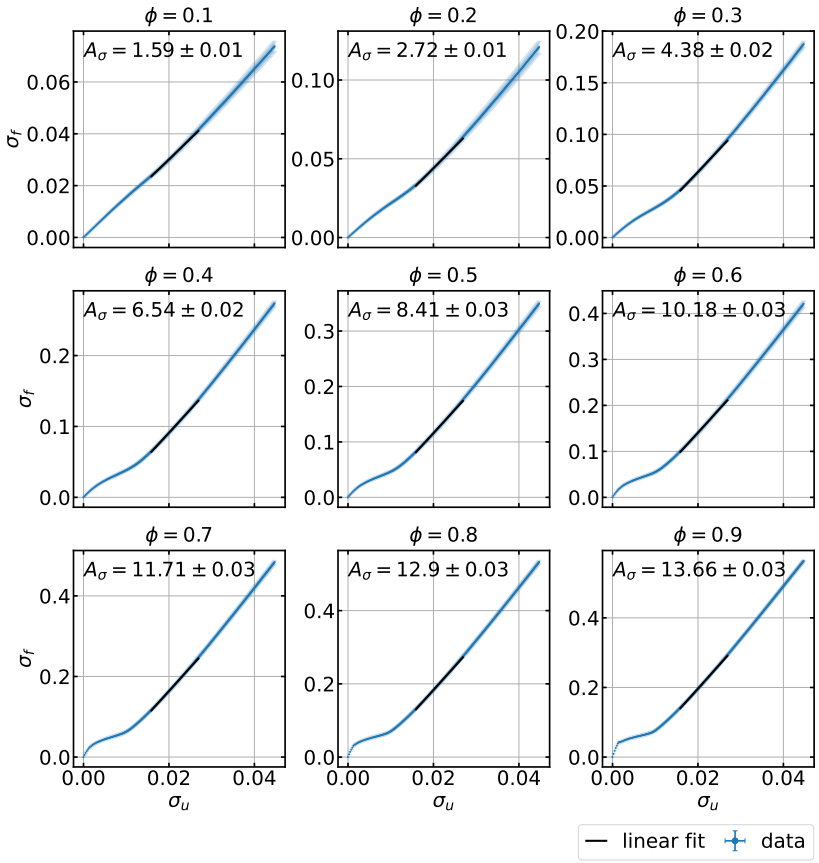

Figure A.29.: Stress in the filled network σ_f versus stress in the unfilled networks σ_u at identical stretches $\lambda \in [1.0, 5.0]$ for different filler contents ϕ. The data has been obtained as averages of 10 independent simulations of non-crystallizing 3D-networks consisting of $N = 5832$ nodes. The filler is randomly distributed. For $\lambda \in [2.0, 3.0]$, the data has been fitted with a linear function and the resulting stress amplification factors A_σ are given. The corresponding fit parameters are listed in Table A.7.

Table A.7.: Parameters for the linear fits $\sigma_\mathrm{f} = A_\sigma \sigma_\mathrm{u} + B$ shown in Figure A.29.

ϕ	A_σ	B	χ^2/ndf
0.1	1.59 ± 0.01	-0.0 ± 0.01	0.047
0.2	2.72 ± 0.01	-0.01 ± 0.01	0.048
0.3	4.38 ± 0.02	-0.02 ± 0.01	0.233
0.4	6.54 ± 0.02	-0.04 ± 0.01	0.117
0.5	8.41 ± 0.03	-0.05 ± 0.01	0.098
0.6	10.18 ± 0.03	-0.06 ± 0.01	0.086
0.7	11.71 ± 0.03	-0.07 ± 0.01	0.219
0.8	12.9 ± 0.03	-0.07 ± 0.01	0.218
0.9	13.66 ± 0.03	-0.08 ± 0.01	1.284

A.7. Impact of Filler on Strain-Induced Crystallization - Supplemental Data

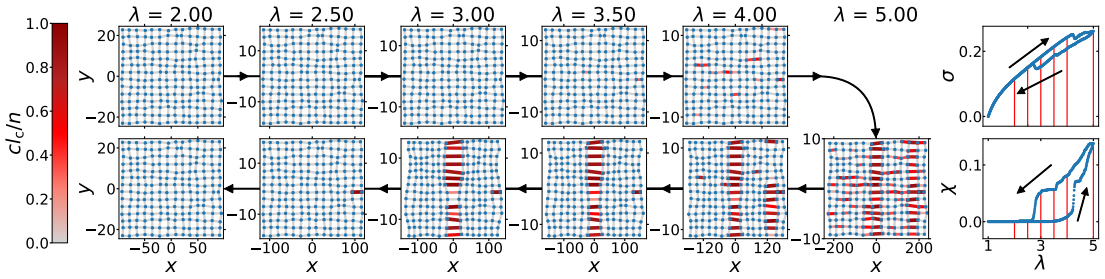

Figure A.30.: Snapshots of an unfilled crystallizing 2D-network which consists of $N = 196$ nodes at certain stretches λ during a strain cycle. The upper row represents the stretching process, while the lower row shows the contraction of the network. Each column corresponds to a specific stretch such that the plots share the x-axis. The direction of the deformation is along the x-axis. The scaling of the axes mimics the volume conservation. The blue dots stand for the cross links, while the crystallinity cl_c/n of each link is indicated according to the color bar. Links which cross the boundaries due to the periodic boundary conditions are not drawn. Moreover, the corresponding stress-stretch and crystallinity-stretch curves are depicted, where the vertical red lines mark the stretches at which the snapshots have been taken. The black arrows expose stretching and contraction of the network. In contrast to Figure 5.4, it is set $\lambda_{\max} = 5.0$ here.

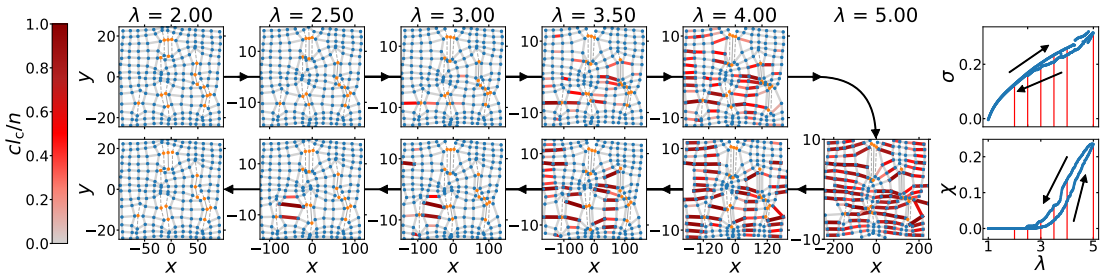

Figure A.31.: Snapshots of a crystallizing 2D-network which consists of $N = 196$ nodes with filler content $\phi = 0.1$ at certain stretches λ during a strain cycle. The MG ran through $10 \cdot N$ MC steps. It has been set $R^{\mathrm{ff}} = R^{\mathrm{pf}} = 1.1$, $k^{\mathrm{ff}} = 5.0$, $k^{\mathrm{pf}} = 4.0$ and $k^{\mathrm{pf}}_{\mathrm{weak}} = 1.0$. The upper row represents the stretching process, while the lower row shows the contraction of the network. Each column corresponds to a specific stretch such that the plots share the x-axis. The direction of the deformation is along the x-axis. The scaling of the axes mimics the volume conservation. The blue dots stand for the cross links, while the orange dots represent filler. The crystallinity cl_c/n of each link is indicated according to the color bar. Links which cross the boundaries due to the periodic boundary conditions are not drawn. Moreover, the corresponding stress-stretch and crystallinity-stretch curves are depicted, where the vertical red lines mark the stretches at which the snapshots have been taken. The black arrows expose stretching and contraction of the network.

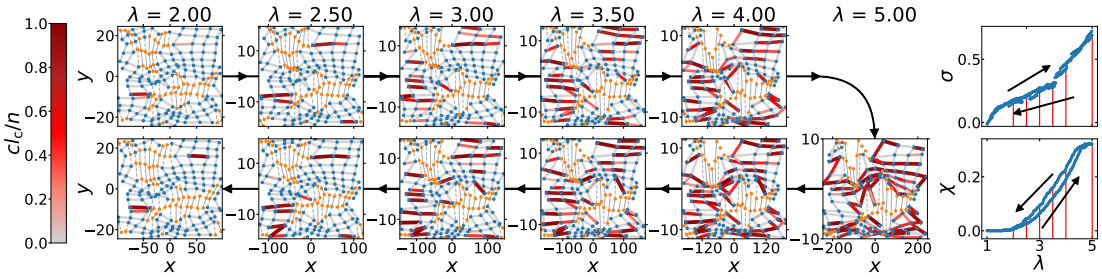

Figure A.32.: Snapshots of a crystallizing 2D-network which consists of $N = 196$ nodes with filler content $\phi = 0.3$ at certain stretches λ during a strain cycle. The MG ran through $10 \cdot N$ MC steps. It has been set $R^{\mathrm{ff}} = R^{\mathrm{pf}} = 1.1$, $k^{\mathrm{ff}} = 5.0$, $k^{\mathrm{pf}} = 4.0$ and $k^{\mathrm{pf}}_{\mathrm{weak}} = 1.0$. The upper row represents the stretching process, while the lower row shows the contraction of the network. Each column corresponds to a specific stretch such that the plots share the x-axis. The direction of the deformation is along the x-axis. The scaling of the axes mimics the volume conservation. The blue dots stand for the cross links, while the orange dots represent filler. The crystallinity cl_c/n of each link is indicated according to the color bar. Links which cross the boundaries due to the periodic boundary conditions are not drawn. Moreover, the corresponding stress-stretch and crystallinity-stretch curves are depicted, where the vertical red lines mark the stretches at which the snapshots have been taken. The black arrows expose stretching and contraction of the network.

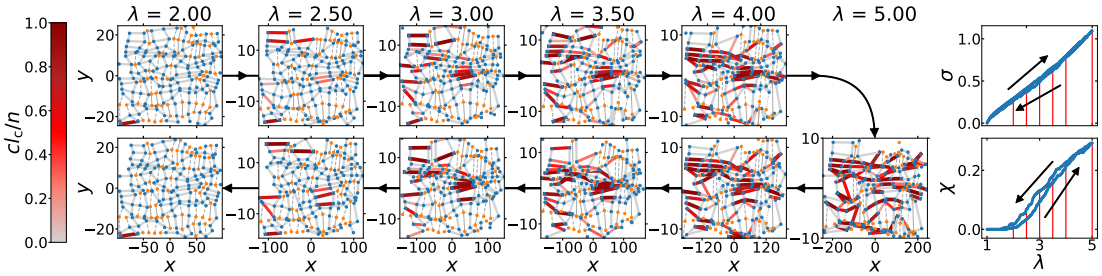

Figure A.33.: Snapshots of a crystallizing 2D-network which consists of $N = 196$ nodes with filler content $\phi = 0.3$ at certain stretches λ during a strain cycle. The filler is randomly distributed. It has been set $R^{\mathrm{ff}} = R^{\mathrm{pf}} = 1.1$, $k^{\mathrm{ff}} = 5.0$, $k^{\mathrm{pf}} = 4.0$ and $k^{\mathrm{pf}}_{\mathrm{weak}} = 1.0$. The upper row represents the stretching process, while the lower row shows the contraction of the network. Each column corresponds to a specific stretch such that the plots share the x-axis. The direction of the deformation is along the x-axis. The scaling of the axes mimics the volume conservation. The blue dots stand for the cross links, while the orange dots represent filler. The crystallinity cl_c/n of each link is indicated according to the color bar. Links which cross the boundaries due to the periodic boundary conditions are not drawn. Moreover, the corresponding stress-stretch and crystallinity-stretch curves are depicted, where the vertical red lines mark the stretches at which the snapshots have been taken. The black arrows expose stretching and contraction of the network.

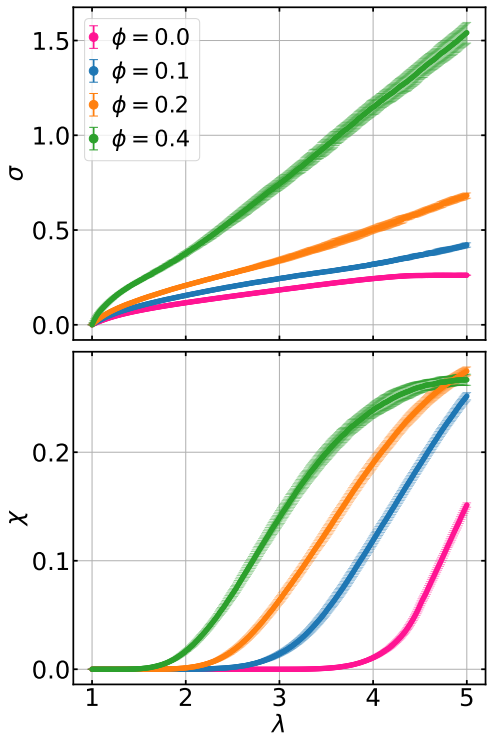

Figure A.34.: Stress-stretch and crystallinity-stretch curves for stretching crystallizing 2D-networks consisting of $N = 5041$ nodes with variable filler content ϕ. The filler is randomly distributed. It has been set $R^{\mathrm{ff}} = R^{\mathrm{pf}} = 1.1$, $k^{\mathrm{ff}} = 5.0$, $k^{\mathrm{pf}} = 4.0$ and $k^{\mathrm{pf}}_{\mathrm{weak}} = 1.0$.

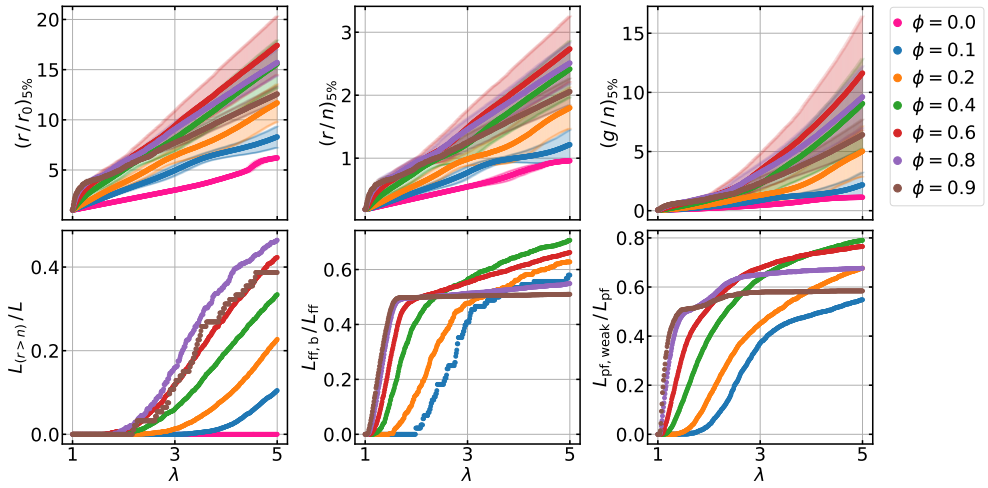

Figure A.35.: Plots of stretch r/r_0, extension r/n, energy density g/n of links versus the macroscopic stretch λ obtained during stretching as averages over the links with the top 5 % values in a crystallizing 2D-network consisting of $N = 5041$ nodes with filler content ϕ. The fraction $L_{(r>n)}/L$ of links with $r > n$, the fraction $L_{\mathrm{ff,b}}/L_{\mathrm{ff}}$ of reversibly broken filler-filler bonds and the fraction $L_{\mathrm{pf,weak}}/L_{\mathrm{pf}}$ of reversibly weakened polymer-filler bonds are also plotted versus the stretch λ. The filler is randomly distributed and it has been set $R^{\mathrm{ff}} = R^{\mathrm{pf}} = 1.1$, $k^{\mathrm{ff}} = 5.0$, $k^{\mathrm{pf}} = 4.0$ and $k^{\mathrm{pf}}_{\mathrm{weak}} = 1.0$, i.e. the networks are configured analogously to those considered in Figure A.34 and in Figure 5.47.

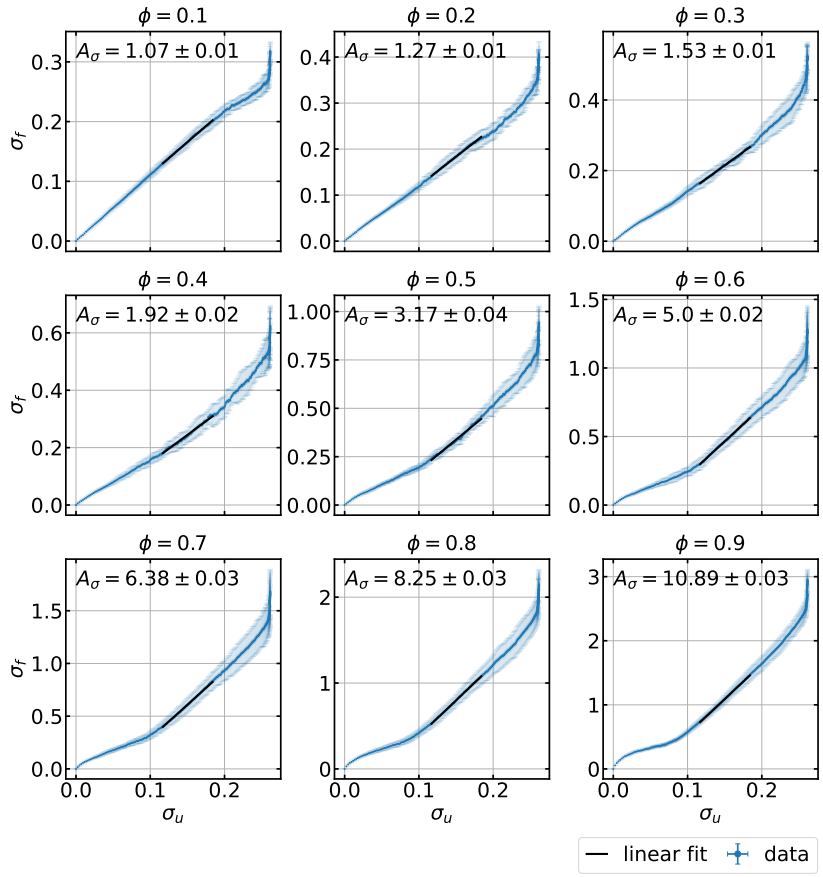

Figure A.36.: Stress in the filled network σ_f versus stress in the unfilled networks σ_u at identical stretches $\lambda \in [1.0, 5.0]$ for different filler contents ϕ. The data has been obtained as averages of 10 independent simulations of crystallizing 2D-networks consisting of $N = 5051$ nodes. The MG ran through $10 \cdot N$ MC steps. For $\lambda \in [2.0, 3.0]$, the data has been fitted with a linear function and the resulting stress amplification factors A_σ are given. The corresponding fit parameters are listed in Table A.8.

Table A.8.: Parameters for the linear fits $\sigma_\mathrm{f} = A_\sigma \sigma_\mathrm{u} + B$ shown in Figure A.36.

ϕ	A_σ	B	χ^2/ndf
0.1	1.07 ± 0.01	0.0 ± 0.01	0.008
0.2	1.27 ± 0.01	-0.01 ± 0.01	0.007
0.3	1.53 ± 0.01	-0.01 ± 0.01	0.014
0.4	1.92 ± 0.02	-0.04 ± 0.01	0.026
0.5	3.17 ± 0.04	-0.14 ± 0.01	0.054
0.6	5.0 ± 0.02	-0.29 ± 0.01	0.004
0.7	6.38 ± 0.03	-0.35 ± 0.01	0.005
0.8	8.25 ± 0.03	-0.44 ± 0.01	0.003
0.9	10.89 ± 0.03	-0.54 ± 0.01	0.007

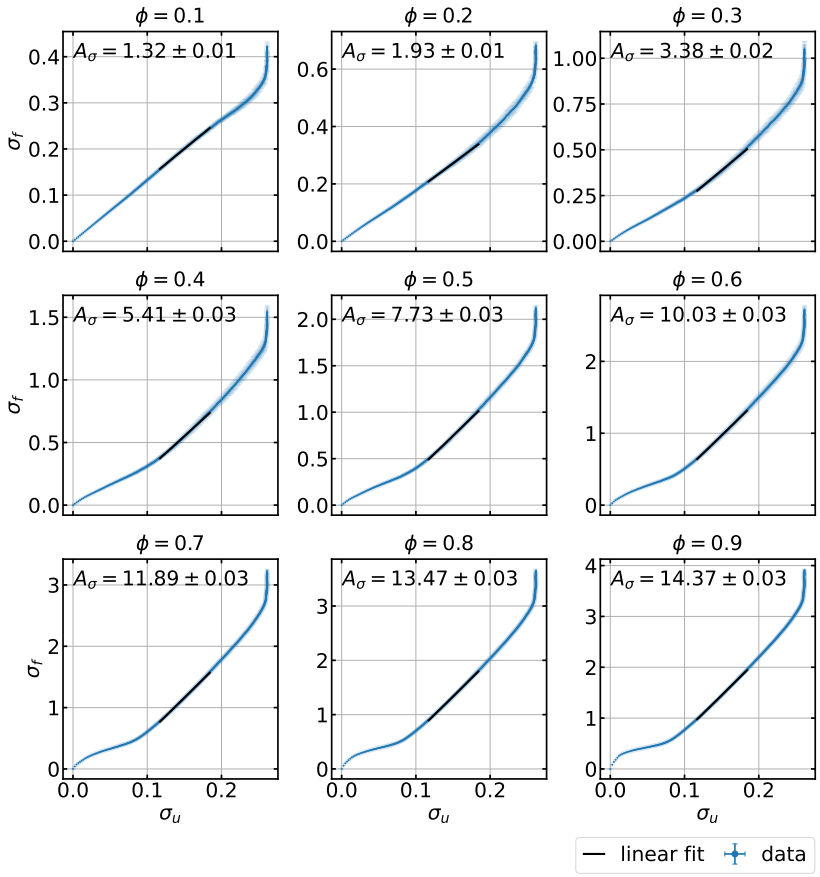

Figure A.37.: Stress in the filled network σ_f versus stress in the unfilled networks σ_u at identical stretches $\lambda \in [1.0, 5.0]$ for different filler contents ϕ. The data has been obtained as averages of 10 independent simulations of crystallizing 2D-networks consisting of $N = 5051$ nodes. The filler is randomly distributed. For $\lambda \in [2.0, 3.0]$, the data has been fitted with a linear function and the resulting stress amplification factors A_σ are given. The corresponding fit parameters are listed in Table A.9.

Table A.9.: Parameters for the linear fits $\sigma_\mathrm{f} = A_\sigma \sigma_\mathrm{u} + B$ shown in Figure A.37.

ϕ	A_σ	B	χ^2/ndf
0.1	1.32 ± 0.01	0.0 ± 0.01	0.042
0.2	1.93 ± 0.01	-0.02 ± 0.01	0.015
0.3	3.38 ± 0.02	-0.12 ± 0.01	0.055
0.4	5.41 ± 0.03	-0.26 ± 0.01	0.07
0.5	7.73 ± 0.03	-0.41 ± 0.01	0.121
0.6	10.03 ± 0.03	-0.53 ± 0.01	0.035
0.7	11.89 ± 0.03	-0.62 ± 0.01	0.118
0.8	13.47 ± 0.03	-0.69 ± 0.01	0.111
0.9	14.37 ± 0.03	-0.71 ± 0.01	0.472

Table A.10.: Stretch λ_{SIC} and stress σ_{SIC} at the onset of SIC for variable filler content ϕ. The data has been obtained as averages from 10 independent simulations of stretching 2D-networks which consist of $N = 5041$ nodes. It has been set $R^{\mathrm{ff}} = R^{\mathrm{pf}} = 1.1$, $k^{\mathrm{ff}} = 5.0$, $k^{\mathrm{pf}} = 4.0$ and $k^{\mathrm{pf}}_{\mathrm{weak}} = 1.0$. The MG ran through $10 \cdot N$ MC steps. The data is plotted in Figure 5.49.

ϕ	λ_{SIC}	σ_{SIC}
0.0	2.92 ± 0.1	0.179 ± 0.007
0.1	1.92 ± 0.09	0.116 ± 0.007
0.2	1.63 ± 0.07	0.103 ± 0.008
0.3	1.51 ± 0.05	0.096 ± 0.007
0.4	1.39 ± 0.04	0.089 ± 0.006
0.5	1.26 ± 0.03	0.077 ± 0.014
0.6	1.23 ± 0.03	0.092 ± 0.010
0.7	1.18 ± 0.02	0.092 ± 0.008
0.8	1.14 ± 0.02	0.085 ± 0.023
0.9	1.1 ± 0.01	0.085 ± 0.014

Table A.11.: Stretch λ_{SIC} and stress σ_{SIC} at the onset of SIC for variable filler content ϕ. The data has been obtained as averages from 10 independent simulations of stretching 2D-networks which consist of $N = 5041$ nodes. It has been set $R^{\mathrm{ff}} = R^{\mathrm{pf}} = 1.1$, $k^{\mathrm{ff}} = 5.0$, $k^{\mathrm{pf}} = 4.0$ and $k^{\mathrm{pf}}_{\mathrm{weak}} = 1.0$. The filler is randomly distributed. The data is plotted in Figure 5.49.

ϕ	λ_{SIC}	σ_{SIC}
0.0	2.92 ± 0.1	0.179 ± 0.007
0.1	1.89 ± 0.07	0.134 ± 0.005
0.2	1.58 ± 0.06	0.129 ± 0.007
0.3	1.39 ± 0.05	0.119 ± 0.006
0.4	1.28 ± 0.03	0.118 ± 0.006
0.5	1.2 ± 0.03	0.112 ± 0.009
0.6	1.15 ± 0.02	0.109 ± 0.013
0.7	1.12 ± 0.01	0.102 ± 0.013
0.8	1.13 ± 0.04	0.071 ± 0.030
0.9	1.14 ± 0.44	0.039 ± 0.024

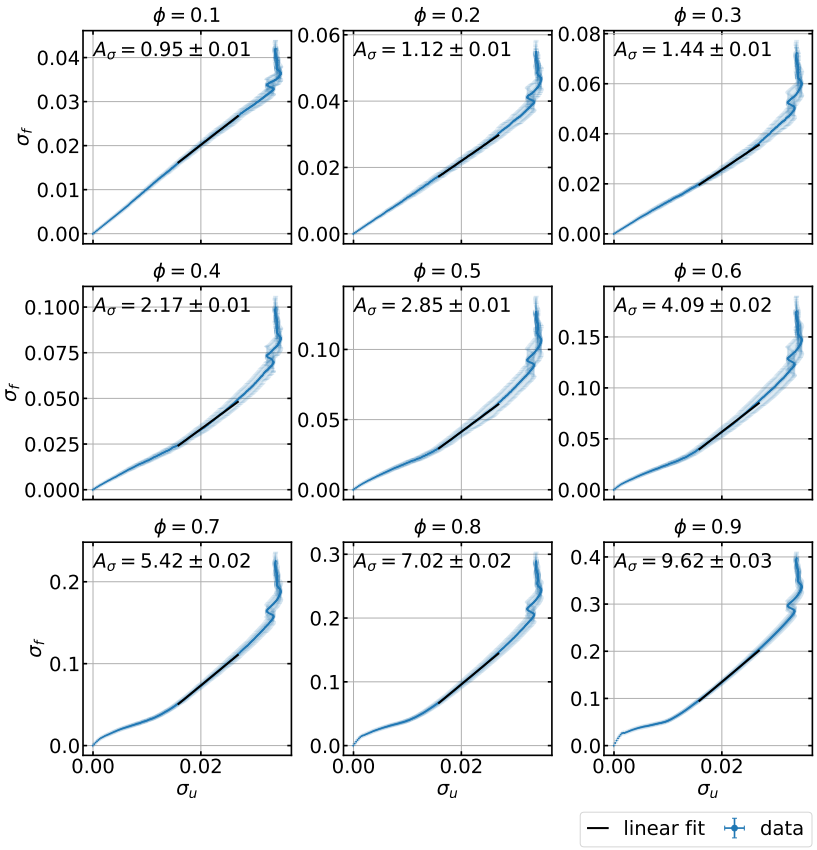

Figure A.38.: Stress in the filled network σ_f versus stress in the unfilled networks σ_u at identical stretches $\lambda \in [1.0, 5.0]$ for different filler contents ϕ. The data has been obtained as averages of 10 independent simulations of crystallizing 3D-networks consisting of $N = 5832$ nodes. The MG ran through $50 \cdot N$ MC steps. For $\lambda \in [2.0, 3.0]$, the data has been fitted with a linear function and the resulting stress amplification factors A_σ are given. The corresponding fit parameters are listed in Table A.12.

Table A.12.: Parameters for the linear fits $\sigma_\mathrm{f} = A_\sigma \sigma_\mathrm{u} + B$ shown in Figure A.38.

ϕ	A_σ	B	χ^2/ndf
0.1	0.95 ± 0.01	0.0 ± 0.01	0.01
0.2	1.12 ± 0.01	-0.0 ± 0.01	0.008
0.3	1.44 ± 0.01	-0.0 ± 0.01	0.018
0.4	2.17 ± 0.01	-0.01 ± 0.01	0.013
0.5	2.85 ± 0.01	-0.02 ± 0.01	0.003
0.6	4.09 ± 0.02	-0.02 ± 0.01	0.009
0.7	5.42 ± 0.02	-0.04 ± 0.01	0.008
0.8	7.02 ± 0.02	-0.04 ± 0.01	0.006
0.9	9.62 ± 0.03	-0.06 ± 0.01	0.038

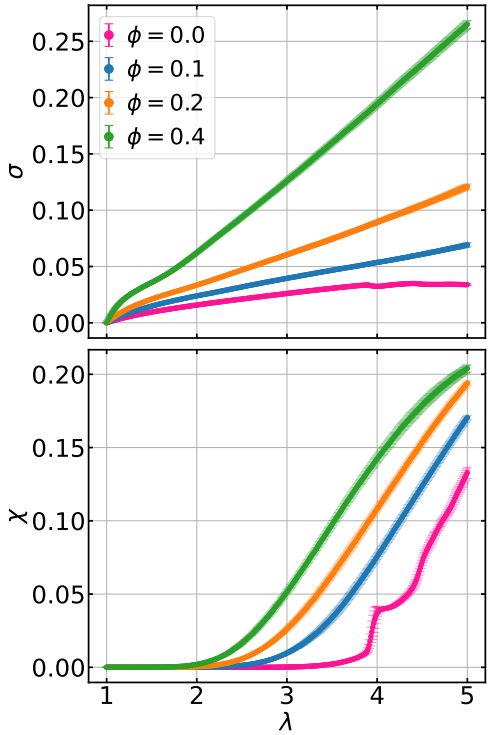

Figure A.39.: Stress-stretch and crystallinity-stretch curves for stretching crystallizing 3D-networks consisting of $N = 5832$ nodes with variable filler content ϕ. The filler is randomly distributed. It has been set $R^{\mathrm{ff}} = R^{\mathrm{pf}} = 1.1$, $k^{\mathrm{ff}} = 5.0$, $k^{\mathrm{pf}} = 4.0$ and $k^{\mathrm{pf}}_{\mathrm{weak}} = 1.0$.

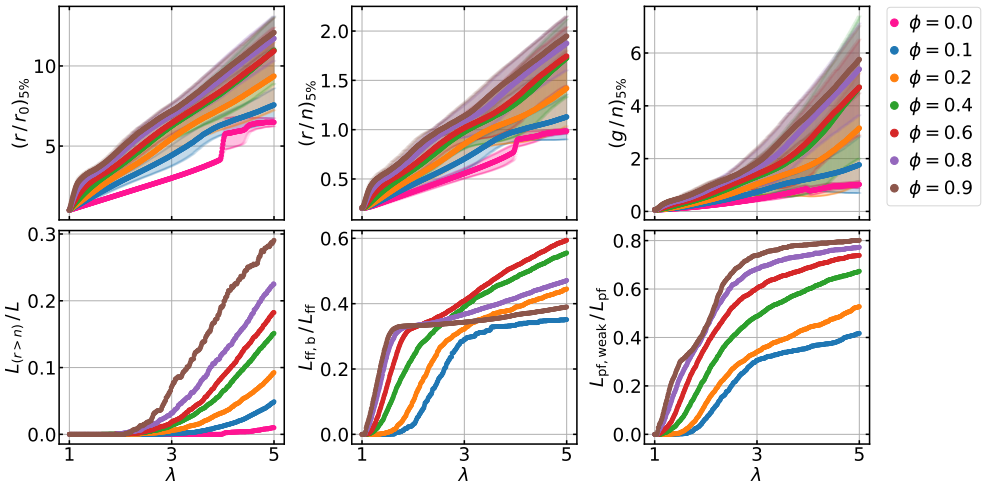

Figure A.40.: Plots of stretch r/r_0, extension r/n, energy density g/n of links versus the macroscopic stretch λ obtained during stretching as averages over the links with the top 5 % values in a crystallizing 3D-network consisting of $N = 5832$ nodes with filler content ϕ. The fraction $L_{(r>n)}/L$ of links with $r > n$, the fraction $L_{\mathrm{ff,b}}/L_{\mathrm{ff}}$ of reversibly broken filler-filler bonds and the fraction $L_{\mathrm{pf,weak}}/L_{\mathrm{pf}}$ of reversibly weakened polymer-filler bonds are also plotted versus the stretch λ. The filler is randomly distributed and it has been set $R^{\mathrm{ff}} = R^{\mathrm{pf}} = 1.1$, $k^{\mathrm{ff}} = 5.0$, $k^{\mathrm{pf}} = 4.0$ and $k^{\mathrm{pf}}_{\mathrm{weak}} = 1.0$, i.e. the networks are configured analogously to those considered in Figure A.39 and in Figure A.41.

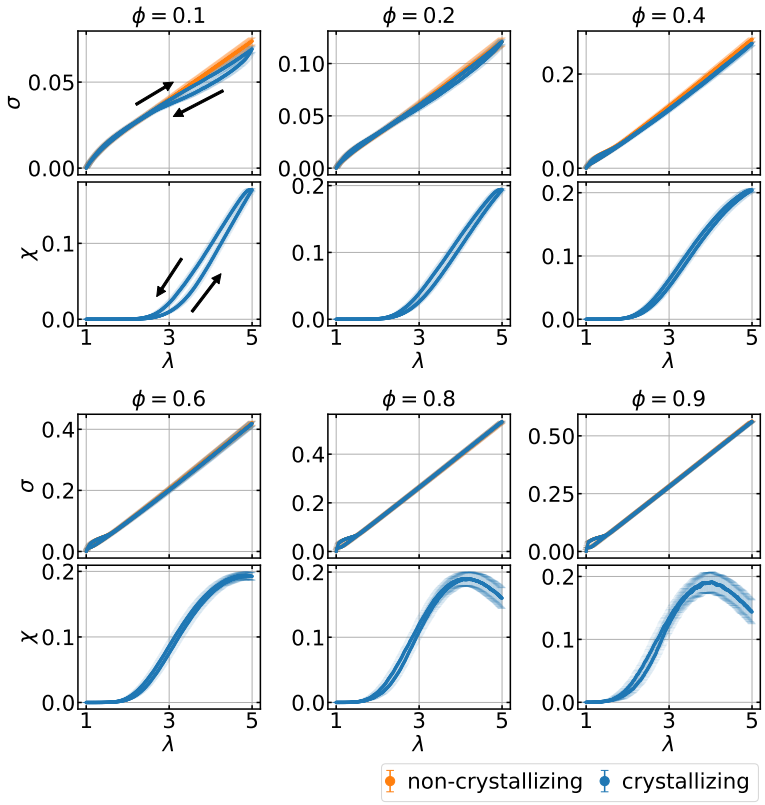

Figure A.41.: Stress-stretch and crystallinity-stretch curves for a deformation cycle of crystallizing 3D-networks consisting of $N = 5832$ nodes with variable filler content ϕ. The filler is randomly distributed. It has been set $R^{\mathrm{ff}} = R^{\mathrm{pf}} = 1.1$, $k^{\mathrm{ff}} = 5.0$, $k^{\mathrm{pf}} = 4.0$ and $k^{\mathrm{pf}}_{\mathrm{weak}} = 1.0$. Stress-stretch curves are for corresponding non-crystallizing networks are also plotted. The arrows in the upper left plot indicate stretching and contraction.

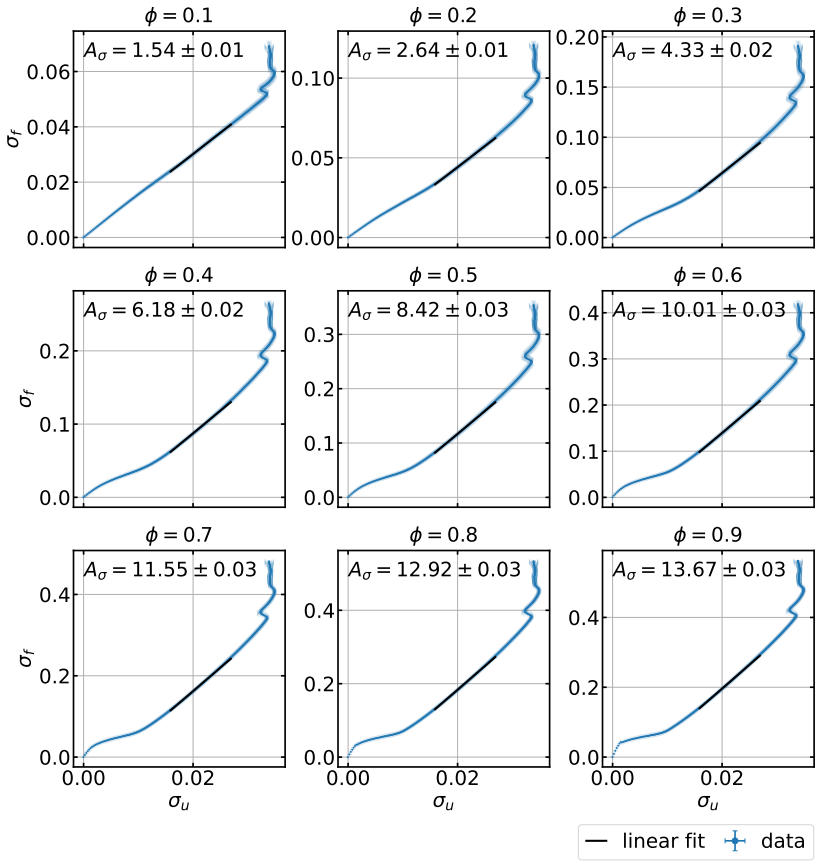

Figure A.42.: Stress in the filled network σ_f versus stress in the unfilled networks σ_u at identical stretches $\lambda \in [1.0, 5.0]$ for different filler contents ϕ. The data has been obtained as averages of 10 independent simulations of crystallizing 3D-networks consisting of $N = 5832$ nodes. The filler is randomly distributed. For $\lambda \in [2.0, 3.0]$, the data has been fitted with a linear function and the resulting stress amplification factors A_σ are given. The corresponding fit parameters are listed in Table A.13.

Table A.13.: Parameters for the linear fits $\sigma_\mathrm{f} = A_\sigma \sigma_\mathrm{u} + B$ shown in Figure A.42.

ϕ	A_σ	B	χ^2/ndf
0.1	1.54 ± 0.01	-0.0 ± 0.01	0.029
0.2	2.64 ± 0.01	-0.01 ± 0.01	0.058
0.3	4.33 ± 0.02	-0.02 ± 0.01	0.048
0.4	6.18 ± 0.02	-0.04 ± 0.01	0.201
0.5	8.42 ± 0.03	-0.05 ± 0.01	0.058
0.6	10.01 ± 0.03	-0.06 ± 0.01	0.077
0.7	11.55 ± 0.03	-0.07 ± 0.01	0.487
0.8	12.92 ± 0.03	-0.07 ± 0.01	0.714
0.9	13.67 ± 0.03	-0.08 ± 0.01	3.134

Table A.14.: Stretch λ_{SIC} and stress σ_{SIC} at the onset of SIC for variable filler content ϕ. The data has been obtained as averages from 10 independent simulations of stretching 3D-networks which consist of $N = 5832$ nodes. It has been set $R^{\mathrm{ff}} = R^{\mathrm{pf}} = 1.1$, $k^{\mathrm{ff}} = 5.0$, $k^{\mathrm{pf}} = 4.0$ and $k^{\mathrm{pf}}_{\mathrm{weak}} = 1.0$. The MG ran through $50 \cdot N$ MC steps. The data is plotted in Figure 5.55.

ϕ	λ_{SIC}	σ_{SIC}
0.0	2.49 ± 0.13	0.021 ± 0.002
0.1	1.71 ± 0.08	0.012 ± 0.001
0.2	1.55 ± 0.11	0.010 ± 0.002
0.3	1.48 ± 0.08	0.010 ± 0.001
0.4	1.36 ± 0.07	0.010 ± 0.001
0.5	1.3 ± 0.05	0.009 ± 0.001
0.6	1.29 ± 0.06	0.010 ± 0.001
0.7	1.2 ± 0.04	0.011 ± 0.001
0.8	1.22 ± 0.02	0.011 ± 0.001
0.9	1.23 ± 0.05	0.011 ± 0.003

Table A.15.: Stretch λ_{SIC} and stress σ_{SIC} at the onset of SIC for variable filler content ϕ. The data has been obtained as averages from 10 independent simulations of stretching 3D-networks which consist of $N = 5832$ nodes. It has been set $R^{\mathrm{ff}} = R^{\mathrm{pf}} = 1.1$, $k^{\mathrm{ff}} = 5.0$, $k^{\mathrm{pf}} = 4.0$ and $k^{\mathrm{pf}}_{\mathrm{weak}} = 1.0$. The filler is randomly distributed. The data is plotted in Figure 5.55.

ϕ	λ_{SIC}	σ_{SIC}
0.0	2.49 ± 0.13	0.021 ± 0.002
0.1	1.7 ± 0.1	0.012 ± 0.002
0.2	1.62 ± 0.1	0.011 ± 0.001
0.3	1.43 ± 0.09	0.010 ± 0.002
0.4	1.4 ± 0.06	0.010 ± 0.001
0.5	1.33 ± 0.07	0.010 ± 0.001
0.6	1.31 ± 0.05	0.010 ± 0.001
0.7	1.23 ± 0.06	0.011 ± 0.001
0.8	1.22 ± 0.05	0.012 ± 0.002
0.9	1.22 ± 0.04	0.011 ± 0.002

A.8. Rupture Behavior - Supplemental Data

In this section, supplemental data regarding the rupture behavior of the model networks is included starting with data required for the definition of the critical free energy density. Data addressing the rupture behavior as well as the tensile strength and the elongation at break is also shown.

A.8.1. Critical Free Energy Density

In the following, plots of the fraction of broken links L_{b}/L, the tensile strength σ_{t}, the elongation at break λ_{t}, the number of damaged as well as the number of failed networks versus the critical free energy density $(g/n)_{\mathrm{crit}}$ are presented for 2D- and 3D-networks with different filler content ϕ. It is set $R^{\mathrm{ff}} = R^{\mathrm{pf}} = 1.1$, $k^{\mathrm{ff}} = 5.0$, $k^{\mathrm{pf}} = 4.0$ and $k^{\mathrm{pf}}_{\mathrm{weak}} = 1.0$. The networks have been stretched until $\lambda_{\mathrm{max}} = 5.0$.

2D-networks

The 2D-networks consist of $N = 5041$ nodes and the MG ran through $10 \cdot N$ MC steps.

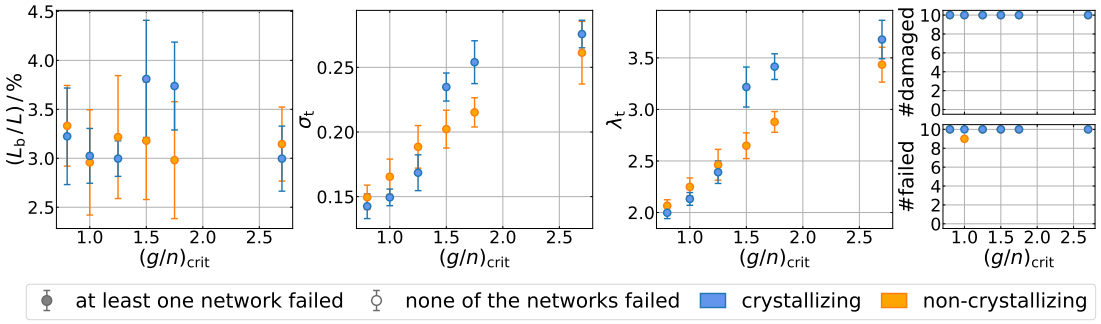

Figure A.43.: Fraction of broken links L_b/L, tensile strength σ_t, elongation at break λ_t, number of damaged networks and number of networks which failed for variable critical energy densities $(g/n)_{crit}$ obtained from the simulations of 10 2D-networks containing a fraction $\phi = 0.2$ of filler.

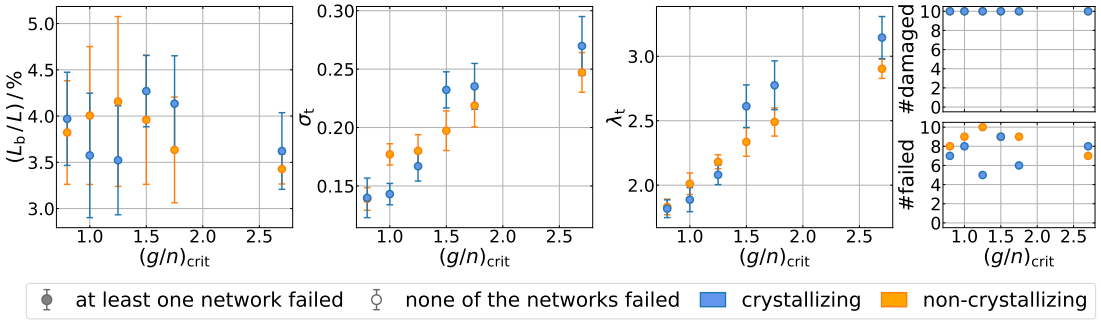

Figure A.44.: Fraction of broken links L_b/L, tensile strength σ_t, elongation at break λ_t, number of damaged networks and number of networks which failed for variable critical energy densities $(g/n)_{crit}$ obtained from the simulations of 10 2D-networks containing a fraction $\phi = 0.3$ of filler.

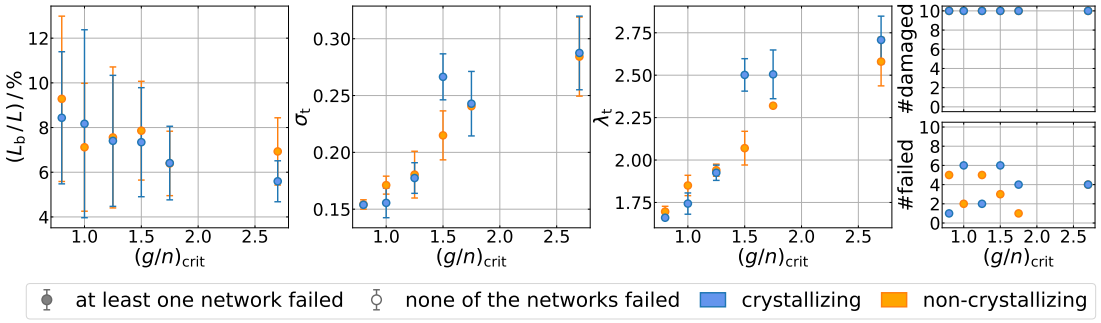

Figure A.45.: Fraction of broken links L_b/L, tensile strength σ_t, elongation at break λ_t, number of damaged networks and number of networks which failed for variable critical energy densities $(g/n)_{crit}$ obtained from the simulations of 10 2D-networks containing a fraction $\phi = 0.4$ of filler.

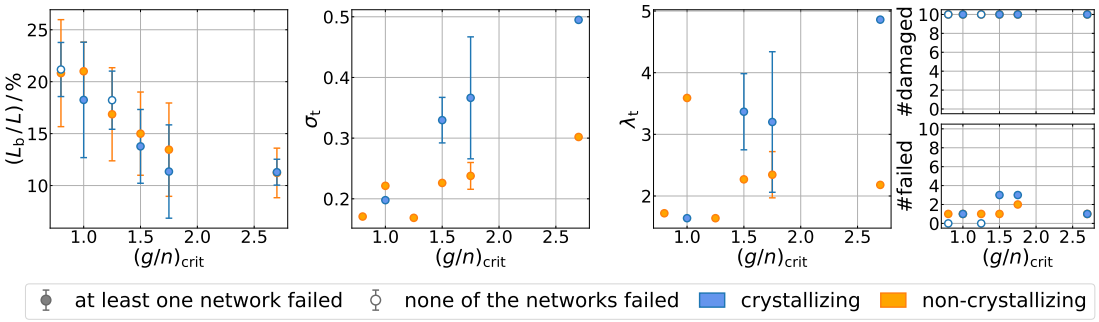

Figure A.46.: Fraction of broken links L_b/L, tensile strength σ_t, elongation at break λ_t, number of damaged networks and number of networks which failed for variable critical energy densities $(g/n)_{crit}$ obtained from the simulations of 10 2D-networks containing a fraction $\phi = 0.5$ of filler.

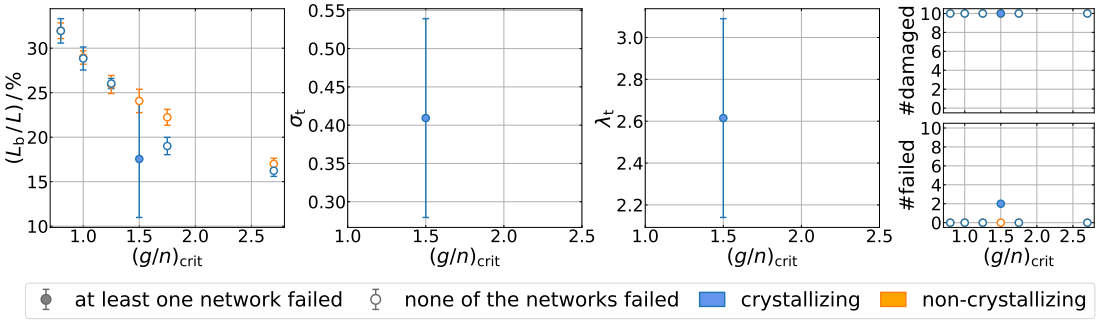

Figure A.47.: Fraction of broken links L_b/L, tensile strength σ_t, elongation at break λ_t, number of damaged networks and number of networks which failed for variable critical energy densities $(g/n)_{crit}$ obtained from the simulations of 10 2D-networks containing a fraction $\phi = 0.6$ of filler.

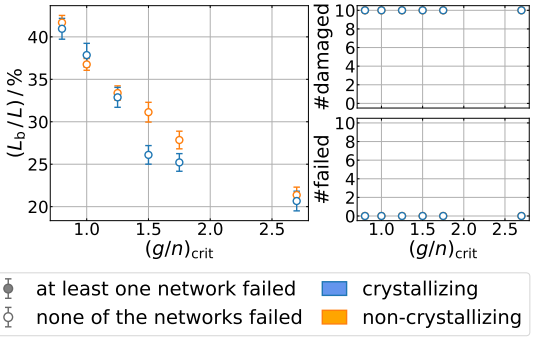

Figure A.48.: Fraction of broken links L_b/L, number of damaged networks and number of networks which failed for variable critical energy densities $(g/n)_{crit}$ obtained from the simulations of 10 2D-networks containing a fraction $\phi = 0.7$ of filler.

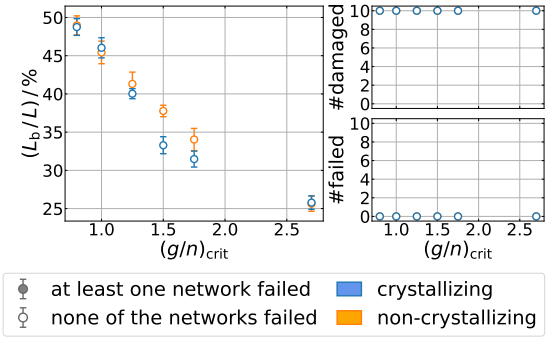

Figure A.49.: Fraction of broken links L_b/L, number of damaged networks and number of networks which failed for variable critical energy densities $(g/n)_{crit}$ obtained from the simulations of 10 2D-networks containing a fraction $\phi = 0.8$ of filler.

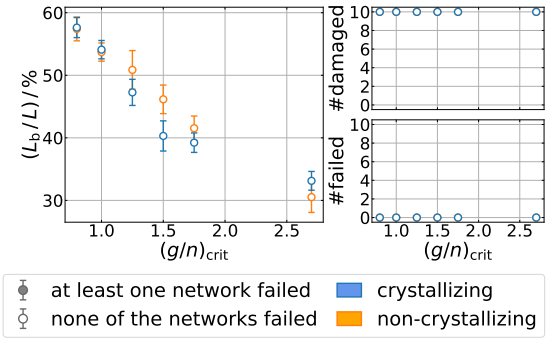

Figure A.50.: Fraction of broken links L_b/L, number of damaged networks and number of networks which failed for variable critical energy densities $(g/n)_{crit}$ obtained from the simulations of 10 2D-networks containing a fraction $\phi = 0.9$ of filler.

3D-networks

The 3D-networks consist of $N = 5832$ nodes and the MG ran through $50 \cdot N$ MC steps.

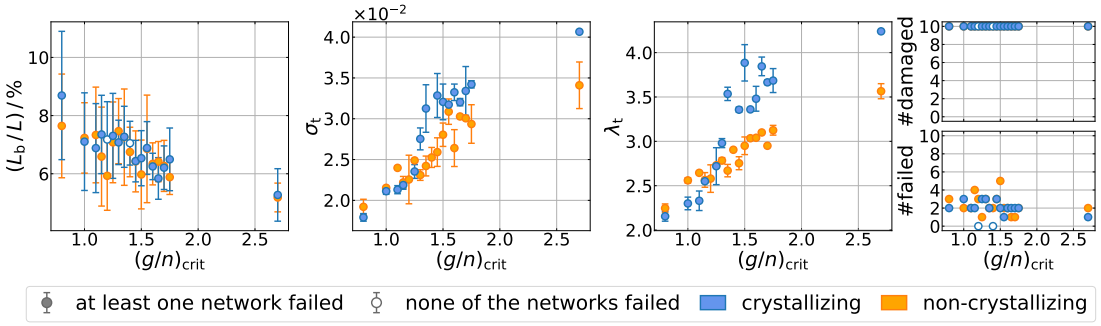

Figure A.51.: Fraction of broken links L_b/L, tensile strength σ_t, elongation at break λ_t, number of damaged networks and number of networks which failed for variable critical energy densities $(g/n)_{crit}$ obtained from the simulations of 10 3D-networks containing a fraction $\phi = 0.2$ of filler.

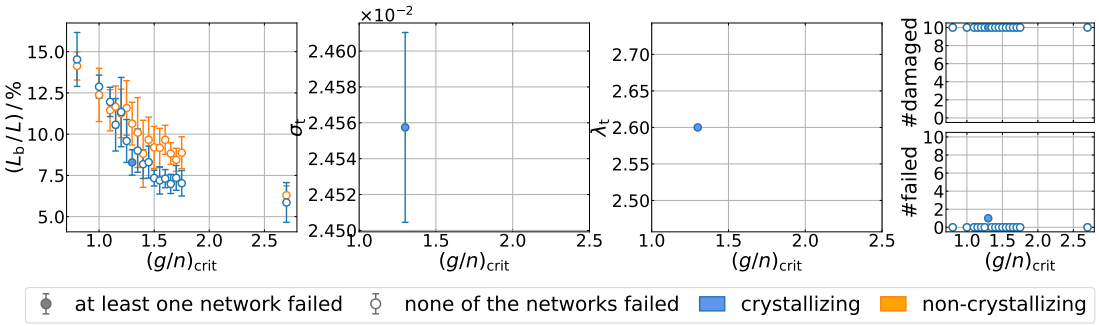

Figure A.52.: Fraction of broken links L_b/L, tensile strength σ_t, elongation at break λ_t, number of damaged networks and number of networks which failed for variable critical energy densities $(g/n)_{crit}$ obtained from the simulations of 10 3D-networks containing a fraction $\phi = 0.3$ of filler.

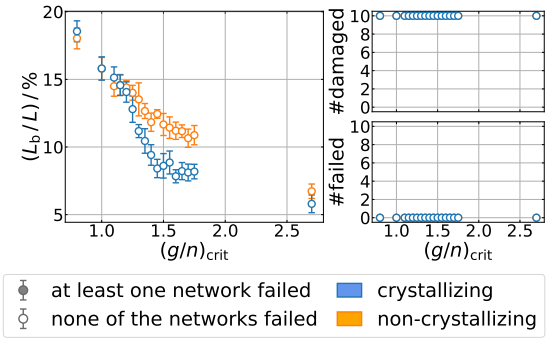

Figure A.53.: Fraction of broken links L_b/L, tensile strength σ_t, elongation at break λ_t, number of damaged networks and number of networks which failed for variable critical energy densities $(g/n)_{crit}$ obtained from the simulations of 10 3D-networks containing a fraction $\phi = 0.4$ of filler.

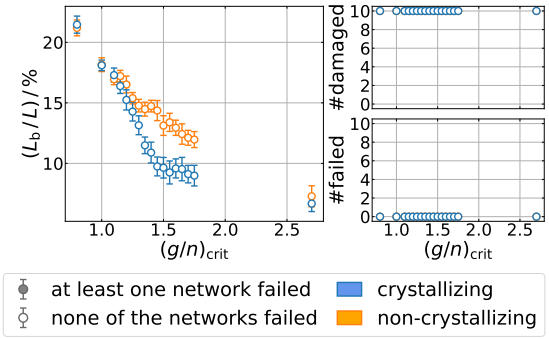

Figure A.54.: Fraction of broken links L_b/L, tensile strength σ_t, elongation at break λ_t, number of damaged networks and number of networks which failed for variable critical energy densities $(g/n)_{crit}$ obtained from the simulations of 10 3D-networks containing a fraction $\phi = 0.5$ of filler.

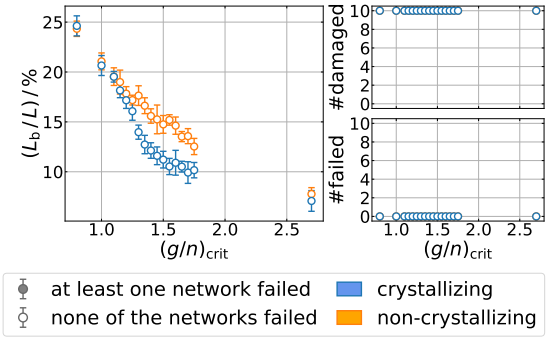

Figure A.55.: Fraction of broken links L_b/L, tensile strength σ_t, elongation at break λ_t, number of damaged networks and number of networks which failed for variable critical energy densities $(g/n)_{crit}$ obtained from the simulations of 10 3D-networks containing a fraction $\phi = 0.6$ of filler.

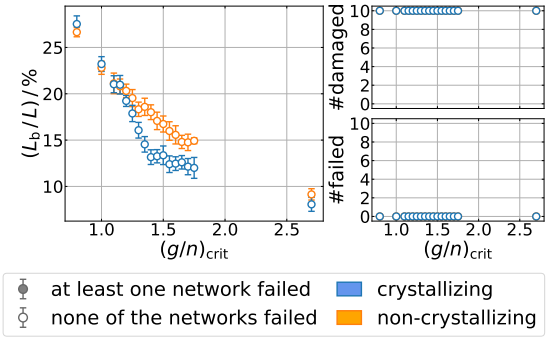

Figure A.56.: Fraction of broken links L_b/L, tensile strength σ_t, elongation at break λ_t, number of damaged networks and number of networks which failed for variable critical energy densities $(g/n)_{crit}$ obtained from the simulations of 10 3D-networks containing a fraction $\phi = 0.7$ of filler.

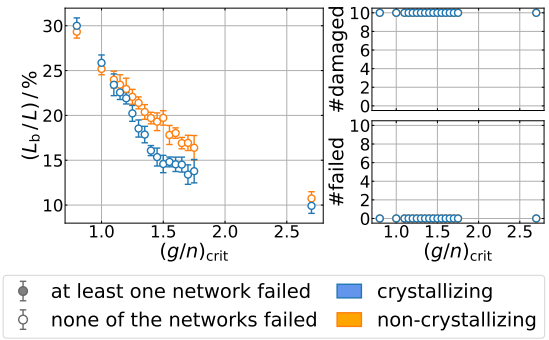

Figure A.57.: Fraction of broken links L_b/L, tensile strength σ_t, elongation at break λ_t, number of damaged networks and number of networks which failed for variable critical energy densities $(g/n)_{crit}$ obtained from the simulations of 10 3D-networks containing a fraction $\phi = 0.8$ of filler.

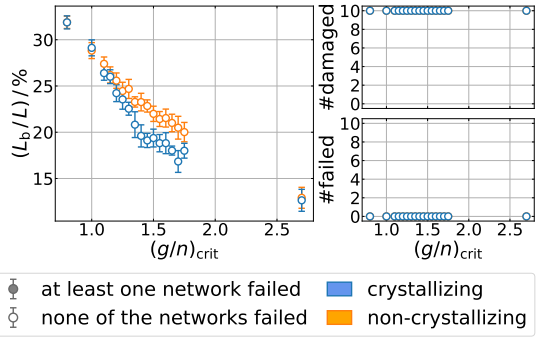

Figure A.58.: Fraction of broken links L_b/L, tensile strength σ_t, elongation at break λ_t, number of damaged networks and number of networks which failed for variable critical energy densities $(g/n)_{crit}$ obtained from the simulations of 10 3D-networks containing a fraction $\phi = 0.9$ of filler.

A.8.2. Parametrization of Filler-Filler and Polymer-Filler Bonds

In this section, supplemental plots addressing the impact of the parametrization of filler-filler and polymer-filler bonds on the rupture behavior are presented as they are discussed in section 5.7. The definitions of each considered configuration are clarified in Table A.16. The focus is on the study of crystallizing and non-crystallizing 2D-networks consisting of $N = 5041$ nodes with variable filler content.

Table A.16.: Parametrization of the cut-off radii R^{ff} and R^{pf} of filler filler and polymer-filler bonds, of the spring constant k^{pf}_{weak} and number of MC steps of the MG for each defined configuration.

configuration	R^{ff}	R^{pf}	k^{pf}_{weak}	MG
0	∞	∞	-	$10 \cdot N$ MC steps
1	1.1	∞	-	$10 \cdot N$ MC steps
2	1.1	1.1	1.0	$10 \cdot N$ MC steps
3	1.1	1.1	1.0	random or $0 \cdot N$ MC steps
4	∞	1.1	1.0	$10 \cdot N$ MC steps
5	1.1	1.1	0.0	$10 \cdot N$ MC steps
6	1.1	1.1	0.0	random or $0 \cdot N$ MC steps
7	∞	1.1	0.0	$10 \cdot N$ MC steps

For the following figures, the critical free energy density $(g/n)_{crit} = 1.25$ is applied. Figure A.59 shows the number of networks which failed and the elongation at break for each configuration for different filler contents. The data corresponds to that in the upper right of Figure 5.69 and Figure 5.72, respectively, but it is reprinted here in order to provide all the necessary information.

For non-crystallizing networks with different filler contents, Figure A.60 to Figure A.65 depict the evolution of the fraction of broken links, the fraction of broken or weakened polymer-filler bonds and the fraction of broken filler-filler bonds with increasing stretch. Corresponding plots for configuration 2 and 3 can be found in Figure 5.70 and Figure 5.71.

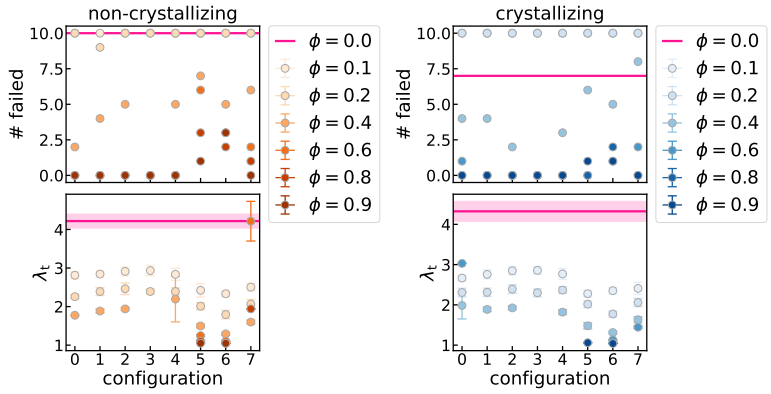

Figure A.59.: Number of networks which failed and elongation at break λ_t for each of the configurations listed in Table A.16 obtained from the simulation of 2D-networks consisting of $N = 5041$ nodes with variable filler content ϕ. It has been set $(g/n)_{crit} = 1.25$.

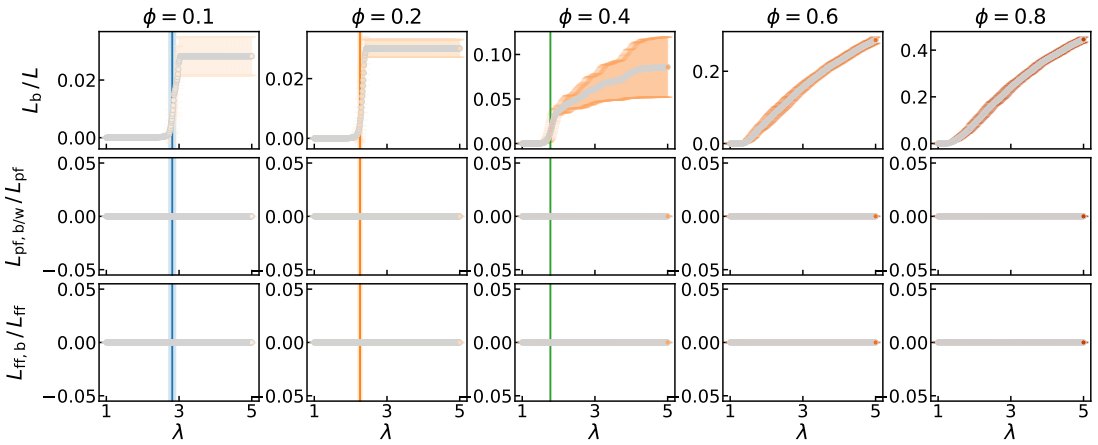

Figure A.60.: Evolution of the fraction of broken links L_b/L, the fraction of broken or weakened polymer-filler bonds $L_{pf,b/w}/L_{pf}$ and the fraction of broken filler-filler bonds $L_{ff,b}/L_{ff}$ during stretching of non-crystallizing 2D-networks consisting of $N = 5041$ nodes with different filler content ϕ. Configuration 0 from Table A.16 is considered. The data are obtained as averages from 10 independent simulations. Moreover, the vertical lines mark the mean values of elongation at break, obtained from the networks which failed, with the standard deviation indicated by the shaded area. It has been set $\lambda_{max} = 5.0$ and $(g/n)_{crit} = 1.25$.

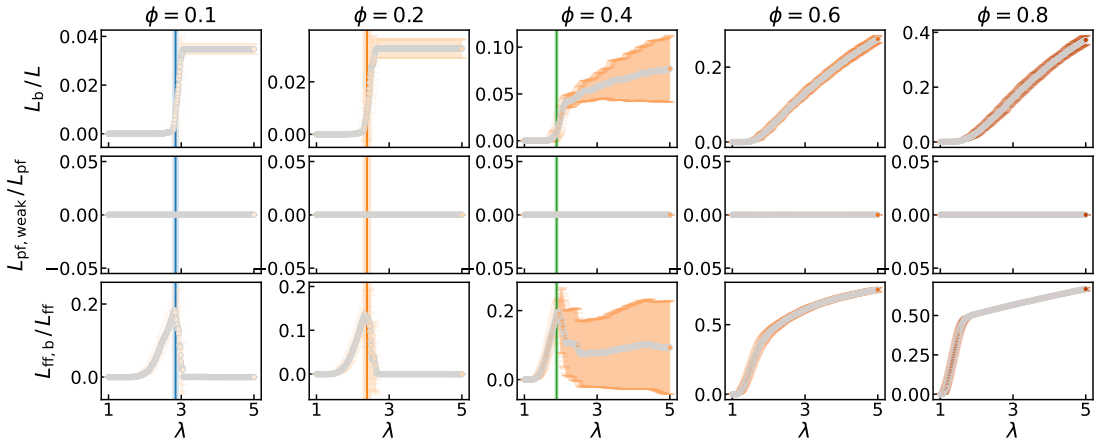

Figure A.61.: Evolution of the fraction of broken links L_b/L, the fraction of broken or weakened polymer-filler bonds $L_{pf,b/w}/L_{pf}$ and the fraction of broken filler-filler bonds $L_{ff,b}/L_{ff}$ during stretching of non-crystallizing 2D-networks consisting of $N = 5041$ nodes with different filler content ϕ. Configuration 1 from Table A.16 is considered. The data are obtained as averages from 10 independent simulations. Moreover, the vertical lines mark the mean values of elongation at break, obtained from the networks which failed, with the standard deviation indicated by the shaded area. It has been set $\lambda_{max} = 5.0$ and $(g/n)_{crit} = 1.25$.

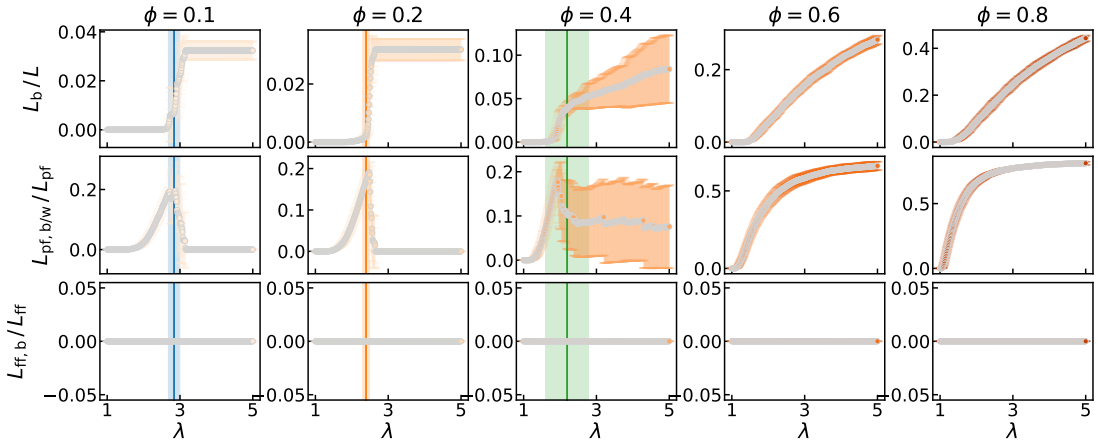

Figure A.62.: Evolution of the fraction of broken links L_b/L, the fraction of weakened polymer-filler bonds $L_{pf,b/w}/L_{pf}$ and the fraction of broken filler-filler bonds $L_{ff,b}/L_{ff}$ during stretching of non-crystallizing 2D-networks consisting of $N = 5041$ nodes with different filler content ϕ. Configuration 4 from Table A.16 is considered. The data are obtained as averages from 10 independent simulations. Moreover, the vertical lines mark the mean values of elongation at break, obtained from the networks which failed, with the standard deviation indicated by the shaded area. It has been set $\lambda_{max} = 5.0$ and $(g/n)_{crit} = 1.25$.

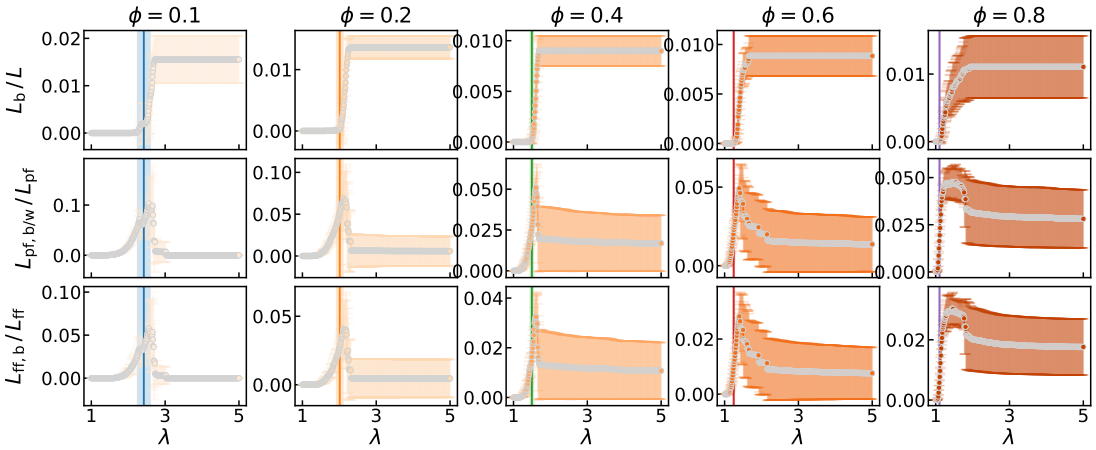

Figure A.63.: Evolution of the fraction of broken links L_b/L, the fraction of broken polymer-filler bonds $L_{\mathrm{pf,b/w}}/L_\mathrm{pf}$ and the fraction of broken filler-filler bonds $L_{\mathrm{ff,b}}/L_\mathrm{ff}$ during stretching of non-crystallizing 2D-networks consisting of $N = 5041$ nodes with different filler content ϕ. Configuration 5 from Table A.16 is considered. The data are obtained as averages from 10 independent simulations. Moreover, the vertical lines mark the mean values of elongation at break, obtained from the networks which failed, with the standard deviation indicated by the shaded area. It has been set $\lambda_\mathrm{max} = 5.0$ and $(g/n)_\mathrm{crit} = 1.25$.

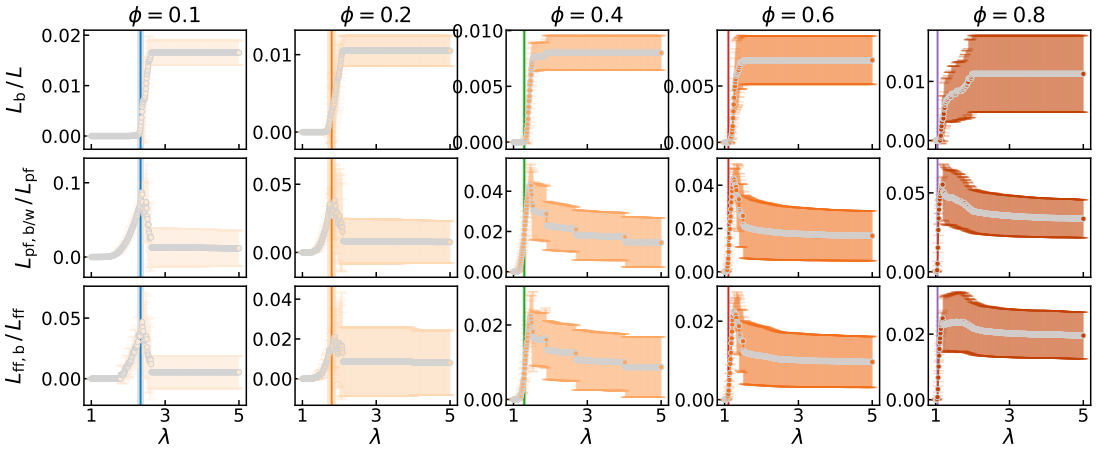

Figure A.64.: Evolution of the fraction of broken links L_b/L, the fraction of broken polymer-filler bonds $L_{\mathrm{pf,b/w}}/L_\mathrm{pf}$ and the fraction of broken filler-filler bonds $L_{\mathrm{ff,b}}/L_\mathrm{ff}$ during stretching of non-crystallizing 2D-networks consisting of $N = 5041$ nodes with different filler content ϕ. Configuration 6 from Table A.16 is considered. The data are obtained as averages from 10 independent simulations. Moreover, the vertical lines mark the mean values of elongation at break, obtained from the networks which failed, with the standard deviation indicated by the shaded area. It has been set $\lambda_\mathrm{max} = 5.0$ and $(g/n)_\mathrm{crit} = 1.25$.

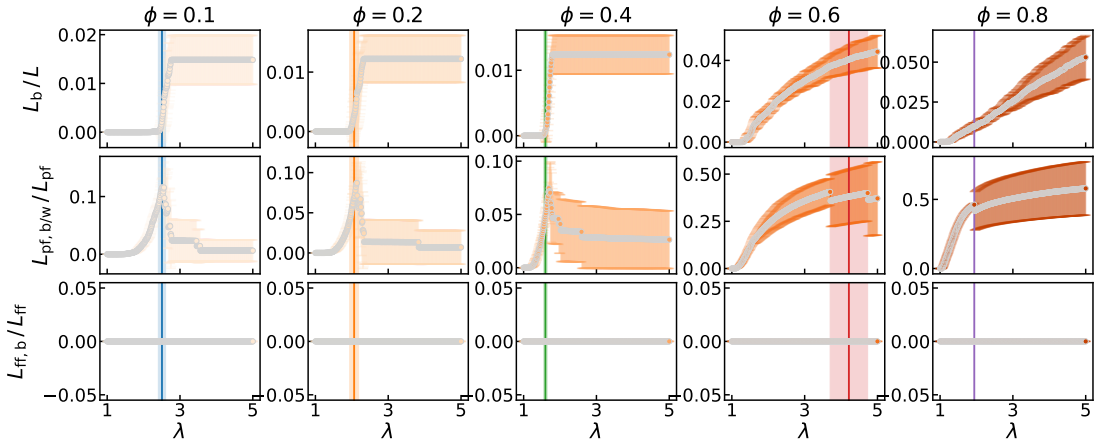

Figure A.65.: Evolution of the fraction of broken links L_b/L, the fraction of broken polymer-filler bonds $L_\mathrm{pf,b/w}/L_\mathrm{pf}$ and the fraction of broken filler-filler bonds $L_\mathrm{ff,b}/L_\mathrm{ff}$ during stretching of non-crystallizing 2D-networks consisting of $N = 5041$ nodes with different filler content ϕ. Configuration 7 from Table A.16 is considered. The data are obtained as averages from 10 independent simulations. Moreover, the vertical lines mark the mean values of elongation at break, obtained from the networks which failed, with the standard deviation indicated by the shaded area. It has been set $\lambda_\mathrm{max} = 5.0$ and $(g/n)_\mathrm{crit} = 1.25$.

In the following, the critical free energy density $(g/n)_\mathrm{crit} = 1.5$ is applied. For the non-crystallizing case, the fraction of broken links L_b/L, fraction of broken or weakened polymer-filler bonds $L_\mathrm{pf,b/w}/L_\mathrm{pf}$ and fraction of broken filler-filler bonds $L_\mathrm{ff,b}/L_\mathrm{ff}$ are plotted for each configuration combined with different filler contents ϕ at different stretches in Figure A.66. The number of failed networks and their elongation at break are also depicted. For configuration 2 and 3, the evolution of the fraction of broken links, the fraction of weakened polymer-filler bonds and the fraction of broken links with increasing stretch are shown in Figure A.67 and Figure A.68, respectively.

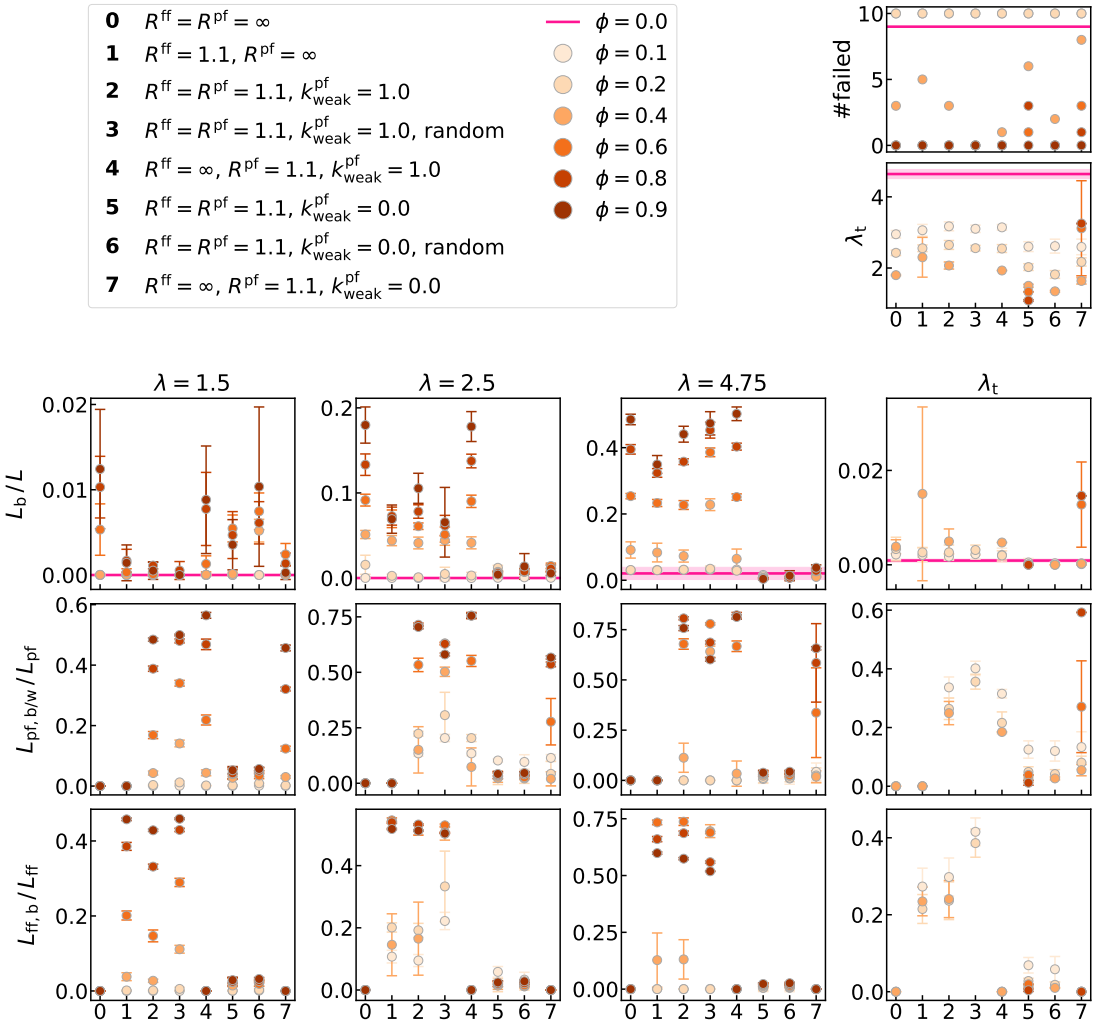

Figure A.66.: Fraction of broken links L_b/L, fraction of broken or weakened polymer-filler bonds $L_{pf,b/w}/L_{pf}$ and fraction of broken filler-filler bonds $L_{ff,b}/L_{ff}$ obtained as averages at different stretches λ for non-crystallizing 2D-networks with variable filler content ϕ and critical free energy density $(g/n)_{crit} = 1.5$. Different combinations of parametrizations, i.e. configurations 0-7, of the cut-off radii R^{ff} and R^{pf}, the spring constant k^{pf}_{weak} and the filler morphology have been applied. The number of networks which failed and the elongation at break λ_t are also shown.

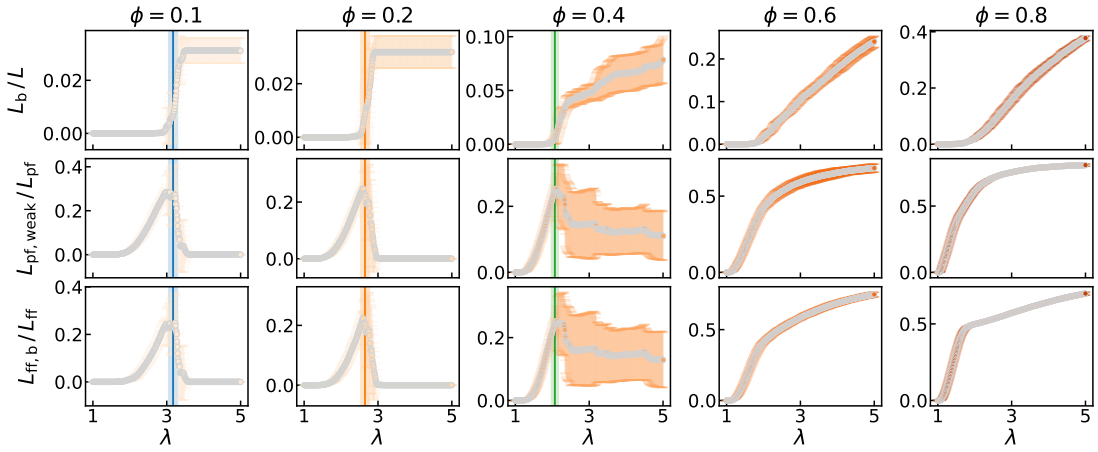

Figure A.67.: Evolution of the fraction of broken links L_b/L, the fraction of weakened polymer-filler bonds $L_{pf,weak}/L_{pf}$ and the fraction of broken filler-filler bonds $L_{ff,b}/L_{ff}$ during stretching of non-crystallizing 2D-networks consisting of $N = 5041$ nodes with different filler content ϕ. Configuration 2 from Table A.16 is considered and, in particular, the MG has been applied for $10 \cdot N$ MC steps. It has been set $\lambda_{max} = 5.0$ and $(g/n)_{crit} = 1.5$. The data are obtained as averages from 10 independent simulations. Moreover, the vertical lines mark the mean values of elongation at break, obtained from the networks which failed, with the standard deviation indicated by the shaded area.

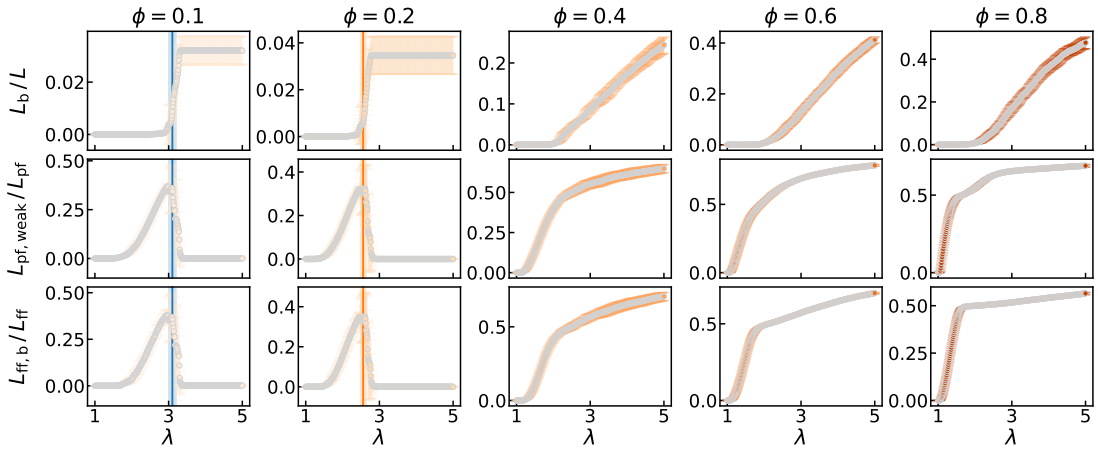

Figure A.68.: Evolution of the fraction of broken links L_b/L, the fraction of weakened polymer-filler bonds $L_{pf,weak}/L_{pf}$ and the fraction of broken filler-filler bonds $L_{ff,b}/L_{ff}$ during stretching of non-crystallizing 2D-networks consisting of $N = 5041$ nodes with different filler content ϕ. Configuration 3 from Table A.16 is considered and, in particular, the filler is randomly distributed. It has been set $\lambda_{max} = 5.0$ and $(g/n)_{crit} = 1.5$. The data are obtained as averages from 10 independent simulations. Moreover, the vertical lines mark the mean values of elongation at break, obtained from the networks which failed, with the standard deviation indicated by the shaded area.

As a next step, crystallizing networks are considered. First, the critical free energy density is set to $(g/n)_{crit} = 1.25$. The evolution of the fraction of broken links, the fraction of broken or weakened polymer-filler bonds and the fraction of broken filler-filler bonds with increasing stretch is shown in Figure A.69 to Figure A.74. Corresponding plots for configuration 2 and 3 can be found in Figure 5.73 and Figure 5.74, respectively.

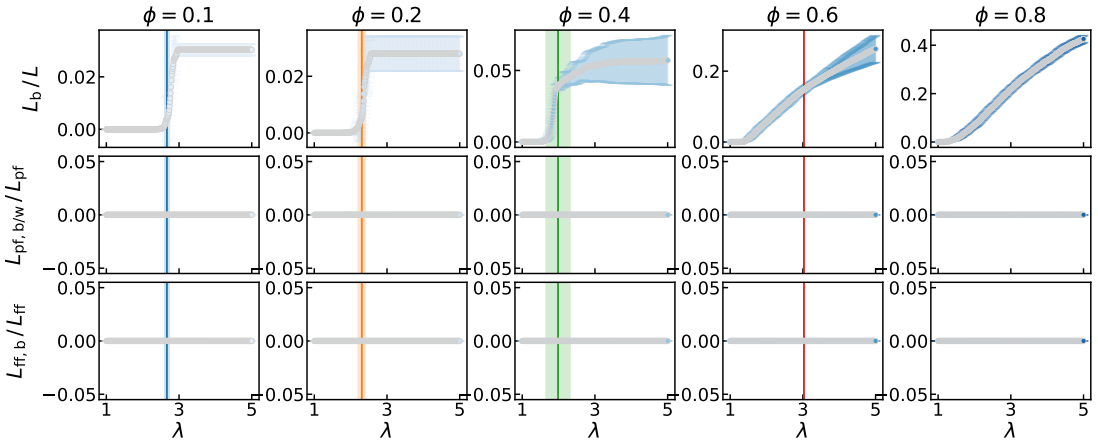

Figure A.69.: Evolution of the fraction of broken links L_b/L, the fraction of broken or weakened polymer-filler bonds $L_{pf,b/w}/L_{pf}$ and the fraction of broken filler-filler bonds $L_{ff,b}/L_{ff}$ during stretching of crystallizing 2D-networks consisting of $N = 5041$ nodes with different filler content ϕ. Configuration 0 from Table A.16 is considered. It has been set $\lambda_{max} = 5.0$ and $(g/n)_{crit} = 1.25$. The data are obtained as averages from 10 independent simulations. Moreover, the vertical lines mark the mean values of elongation at break, obtained from the networks which failed, with the standard deviation indicated by the shaded area.

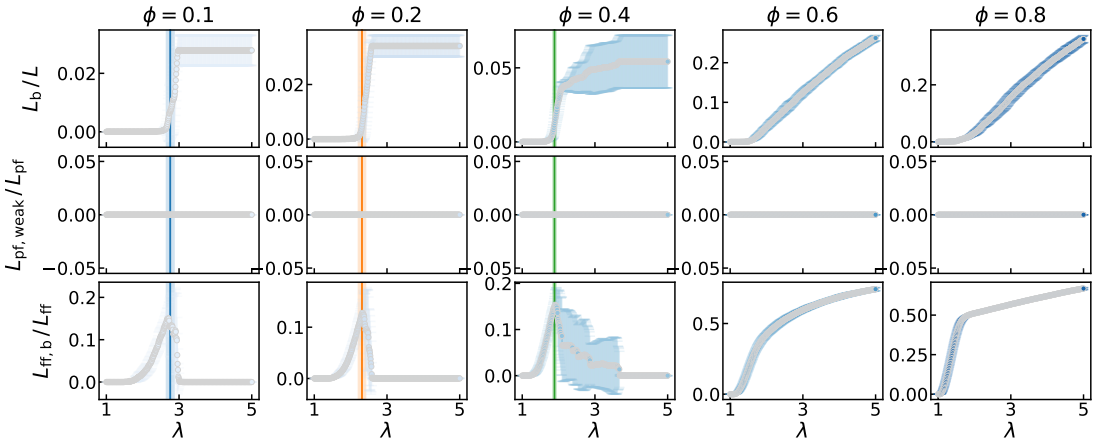

Figure A.70.: Evolution of the fraction of broken links L_b/L, the fraction of broken or weakened polymer-filler bonds $L_{pf,b/w}/L_{pf}$ and the fraction of broken filler-filler bonds $L_{ff,b}/L_{ff}$ during stretching of crystallizing 2D-networks consisting of $N = 5041$ nodes with different filler content ϕ. Configuration 1 from Table A.16 is considered. It has been set $\lambda_{max} = 5.0$ and $(g/n)_{crit} = 1.25$. The data are obtained as averages from 10 independent simulations. Moreover, the vertical lines mark the mean values of elongation at break, obtained from the networks which failed, with the standard deviation indicated by the shaded area.

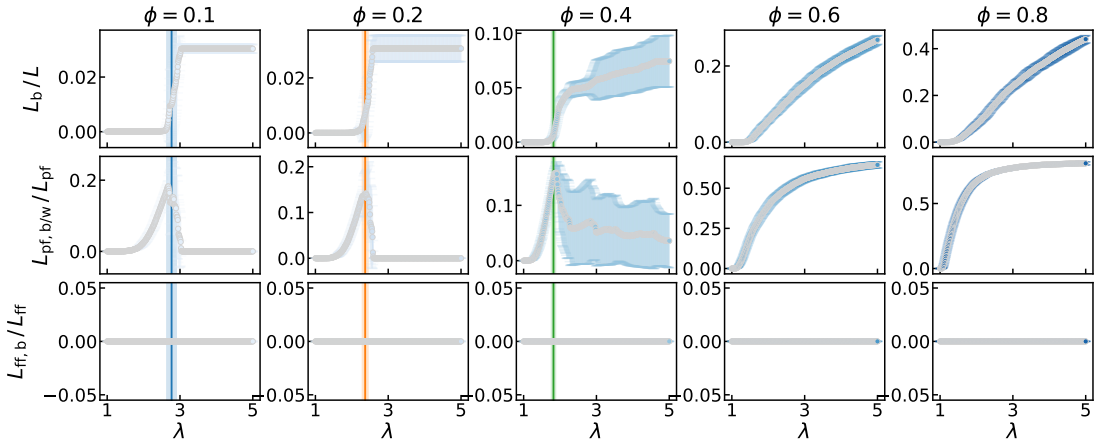

Figure A.71.: Evolution of the fraction of broken links L_b/L, the fraction of weakened polymer-filler bonds $L_{pf,b/w}/L_{pf}$ and the fraction of broken filler-filler bonds $L_{ff,b}/L_{ff}$ during stretching of crystallizing 2D-networks consisting of $N = 5041$ nodes with different filler content ϕ. Configuration 4 from Table A.16 is considered. It has been set $\lambda_{max} = 5.0$ and $(g/n)_{crit} = 1.25$. The data are obtained as averages from 10 independent simulations. Moreover, the vertical lines mark the mean values of elongation at break, obtained from the networks which failed, with the standard deviation indicated by the shaded area.

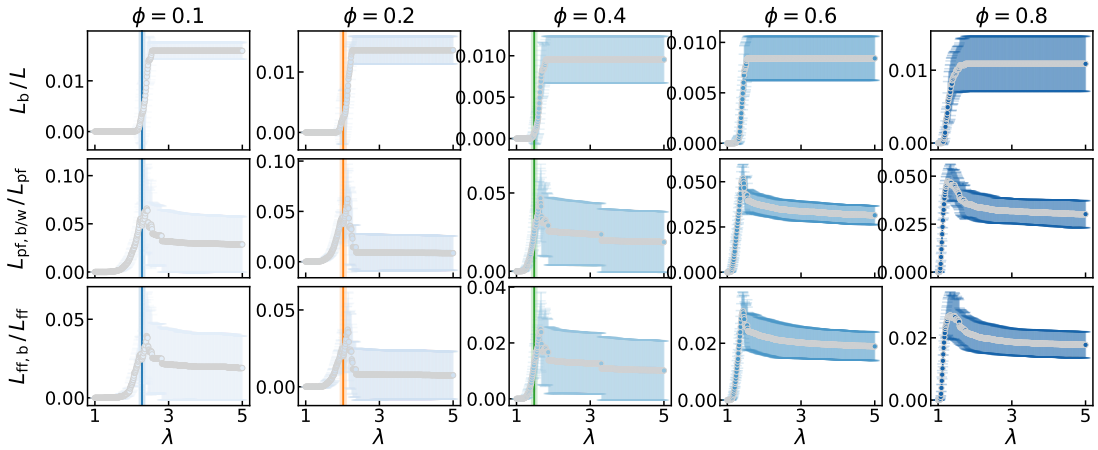

Figure A.72.: Evolution of the fraction of broken links L_b/L, the fraction of broken polymer-filler bonds $L_{pf,b/w}/L_{pf}$ and the fraction of broken filler-filler bonds $L_{ff,b}/L_{ff}$ during stretching of crystallizing 2D-networks consisting of $N = 5041$ nodes with different filler content ϕ. Configuration 5 from Table A.16 is considered. It has been set $\lambda_{max} = 5.0$ and $(g/n)_{crit} = 1.25$. The data are obtained as averages from 10 independent simulations. Moreover, the vertical lines mark the mean values of elongation at break, obtained from the networks which failed, with the standard deviation indicated by the shaded area.

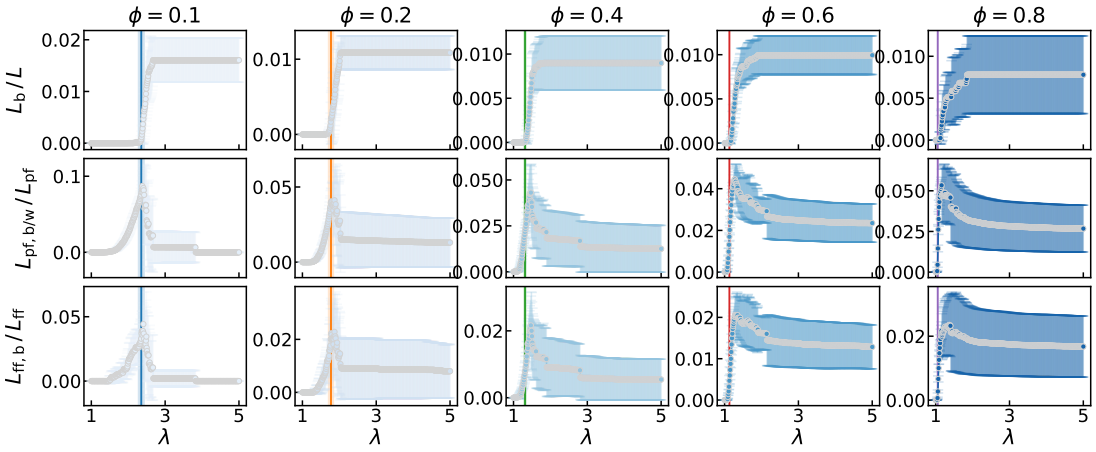

Figure A.73.: Evolution of the fraction of broken links L_b/L, the fraction of broken polymer-filler bonds $L_\mathrm{pf,b/w}/L_\mathrm{pf}$ and the fraction of broken filler-filler bonds $L_\mathrm{ff,b}/L_\mathrm{ff}$ during stretching of crystallizing 2D-networks consisting of $N = 5041$ nodes with different filler content ϕ. Configuration 6 from Table A.16 is considered. It has been set $\lambda_\mathrm{max} = 5.0$ and $(g/n)_\mathrm{crit} = 1.25$. The data are obtained as averages from 10 independent simulations. Moreover, the vertical lines mark the mean values of elongation at break, obtained from the networks which failed, with the standard deviation indicated by the shaded area.

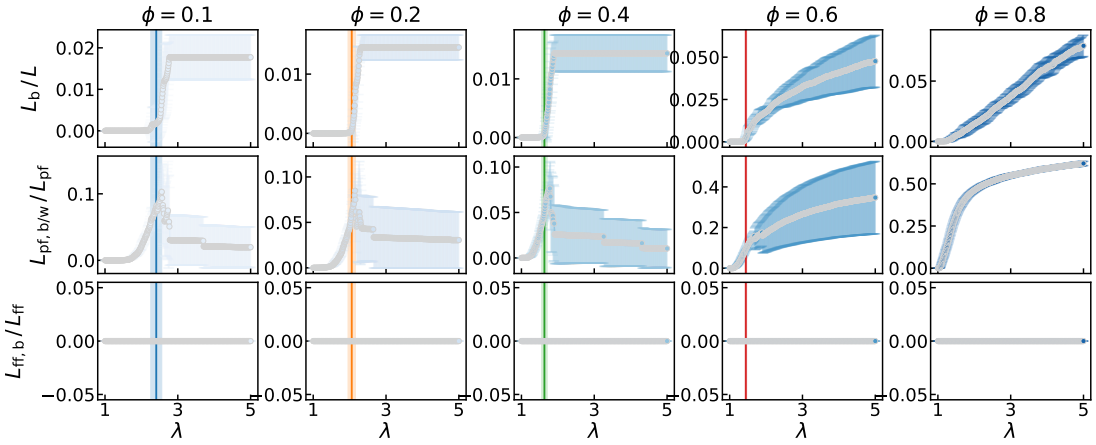

Figure A.74.: Evolution of the fraction of broken links L_b/L, the fraction of broken polymer-filler bonds $L_\mathrm{pf,b/w}/L_\mathrm{pf}$ and the fraction of broken filler-filler bonds $L_\mathrm{ff,b}/L_\mathrm{ff}$ during stretching of crystallizing 2D-networks consisting of $N = 5041$ nodes with different filler content ϕ. Configuration 7 from Table A.16 is considered. It has been set $\lambda_\mathrm{max} = 5.0$ and $(g/n)_\mathrm{crit} = 1.25$. The data are obtained as averages from 10 independent simulations. Moreover, the vertical lines mark the mean values of elongation at break, obtained from the networks which failed, with the standard deviation indicated by the shaded area.

For the critical free energy density $(g/n)_\mathrm{crit} = 1.5$, the fraction of broken links, fraction of broken or weakened polymer-filler bonds and fraction of broken filler-filler bonds are plotted for each configuration combined with different filler contents at different stretches in Figure A.75. The evolution of these quantities during stretching for configuration 2 and 3 is depicted in Figure A.76 and Figure A.77, respectively.

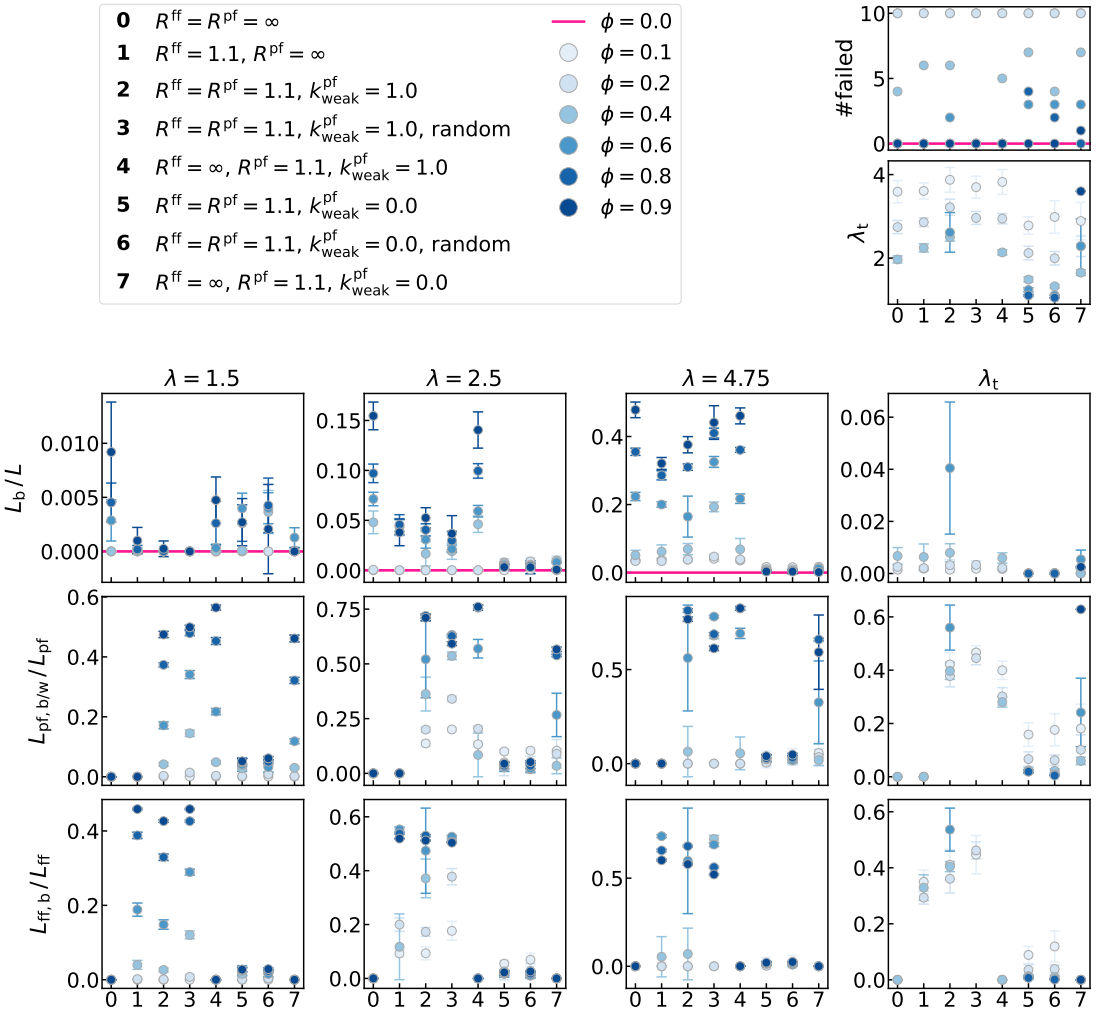

Figure A.75.: Fraction of broken links L_b/L, fraction of broken or weakened polymer-filler bonds $L_{pf,b/w}/L_{pf}$ and fraction of broken filler-filler bonds $L_{ff,b}/L_{ff}$ obtained as averages at different stretches λ for crystallizing 2D-networks with variable filler content ϕ and critical free energy density $(g/n)_{crit} = 1.5$. Different combinations of parametrizations, i.e. configurations 0-7, of the cut-off radii R^{ff} and R^{pf}, the spring constant k^{pf}_{weak} and the filler morphology have been applied. The number of networks which failed and the elongation at break λ_t are also shown.

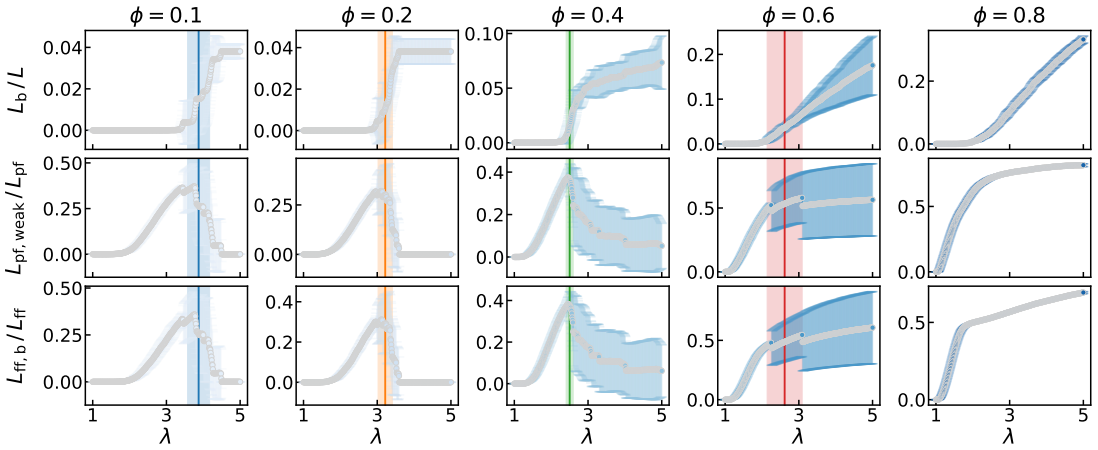

Figure A.76.: Evolution of the fraction of broken links L_b/L, the fraction of weakened polymer-filler bonds $L_\mathrm{pf,weak}/L_\mathrm{pf}$ and the fraction of broken filler-filler bonds $L_\mathrm{ff,b}/L_\mathrm{ff}$ during stretching of crystallizing 2D-networks consisting of $N = 5041$ nodes with different filler content ϕ. Configuration 2 from Table A.16 is considered and, in particular, the MG has been applied for $10 \cdot N$ MC steps. It has been set $\lambda_\mathrm{max} = 5.0$ and $(g/n)_\mathrm{crit} = 1.5$. The data are obtained as averages from 10 independent simulations. Moreover, the vertical lines indicate the mean values of elongation at break, obtained from the networks which failed, with the standard deviation indicated by the shaded area.

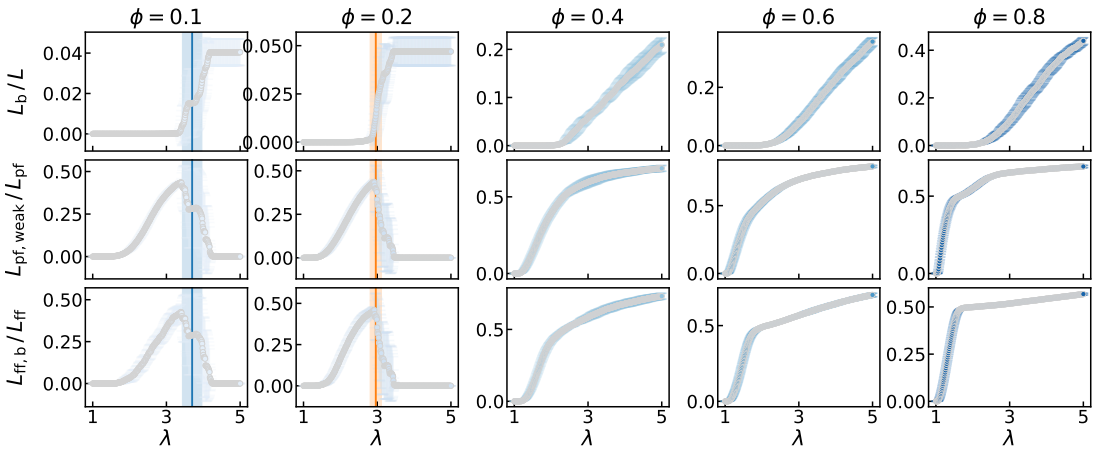

Figure A.77.: Evolution of the fraction of broken links L_b/L, the fraction of weakened polymer-filler bonds $L_\mathrm{pf,weak}/L_\mathrm{pf}$ and the fraction of broken filler-filler bonds $L_\mathrm{ff,b}/L_\mathrm{ff}$ during stretching of crystallizing 2D-networks consisting of $N = 5041$ nodes with different filler content ϕ. Configuration 3 from Table A.16 is considered and, in particular, the filler is randomly distributed. It has been set $\lambda_\mathrm{max} = 5.0$ and $(g/n)_\mathrm{crit} = 1.5$. The data are obtained as averages from 10 independent simulations. Moreover, the vertical lines indicate the mean values of elongation at break, obtained from the networks which failed, with the standard deviation indicated by the shaded area.

A.8.3. Evolution of the Networks during Rupture

In this subsection, the rupture process of crystallizing and non-crystallizing model networks with different parametrizations and filler content is presented. Hence, 2D-networks which consist of $N = 5041$ nodes with different filler content ϕ are stretched up to $\lambda_\mathrm{max} = 5.0$ and snapshots of them are plotted at certain stretches λ during stretching. For each figure, the stretching direction is the x-axis. The scaling of the

axes mimics the volume conservation. Note that periodic boundary conditions are applied. The blue dots stand for the cross links, while the orange dots represent filler. If crystallizing networks are considered, the crystallinity cl_c/n of each link is indicated according to the color bar. The configurations regarding the parametrization of filler-filler and polymer-filler bonds are defined in Table A.16. The corresponding stress-stretch curves of networks which failed are also shown and the data points are connected for the eye.

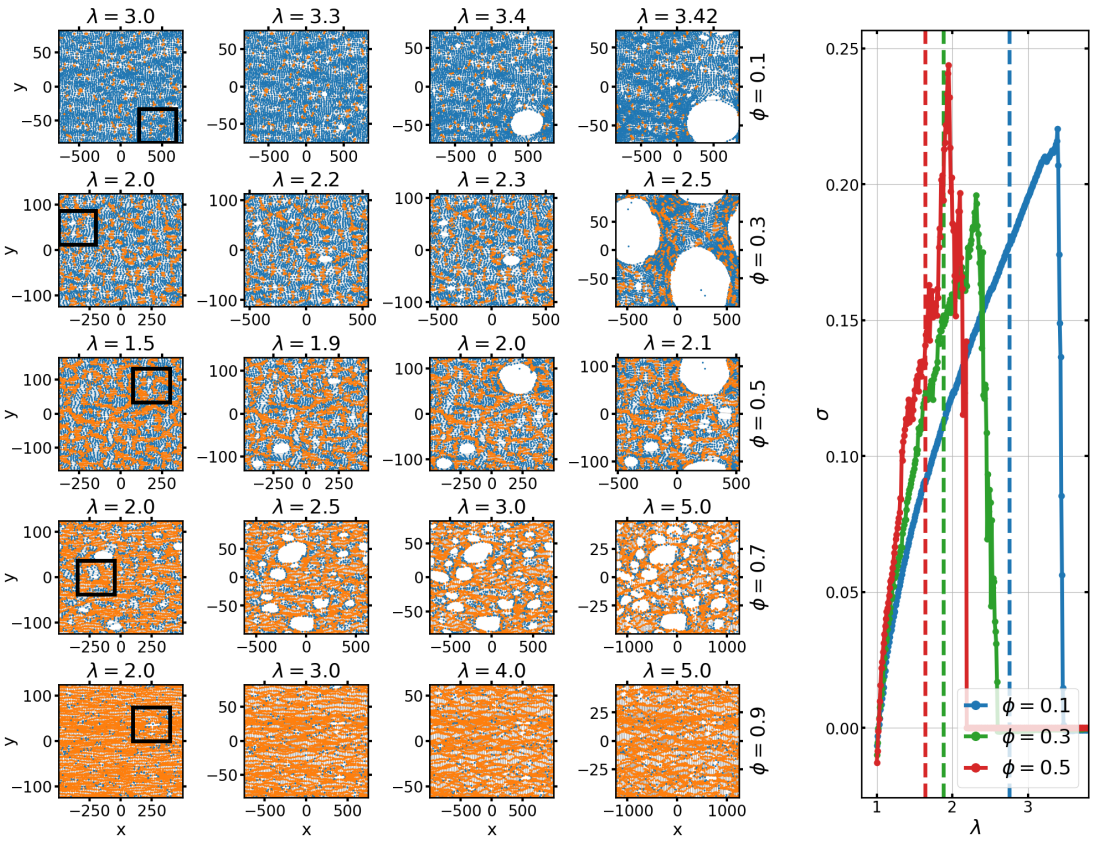

Figure A.78.: Snapshots of non-crystallizing networks with configuration 2: The MG ran through $10 \cdot N$ MC steps and it has been set $R^{\mathrm{ff}} = R^{\mathrm{pf}} = 1.1$, $k^{\mathrm{ff}} = 5.0$, $k^{\mathrm{pf}} = 4.0$ and $k^{\mathrm{pf}}_{\mathrm{weak}} = 1.0$. The critical free energy density is $(g/n)_{\mathrm{crit}} = 1.5$. The black rectangles indicate the regions which are depicted in the extracts of the snapshots in Figure A.79. In the plot of the stress-stretch curves, the onset of rupture in each case is indicated by a dashed line.

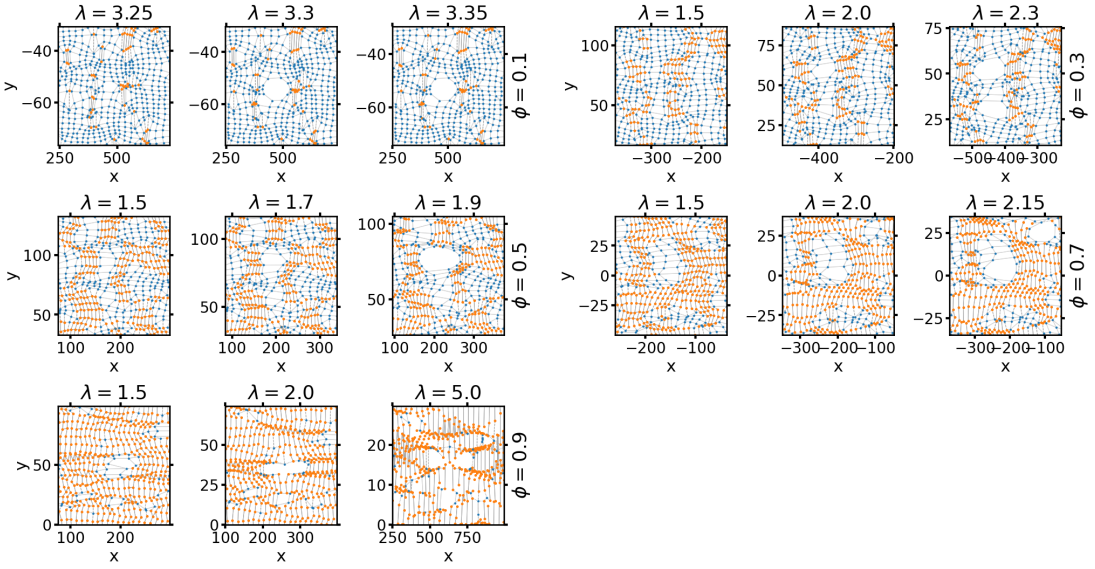

Figure A.79.: Extracts of snapshots of the model networks depicted in Figure A.78 in the regions indicated by the rectangles in there.

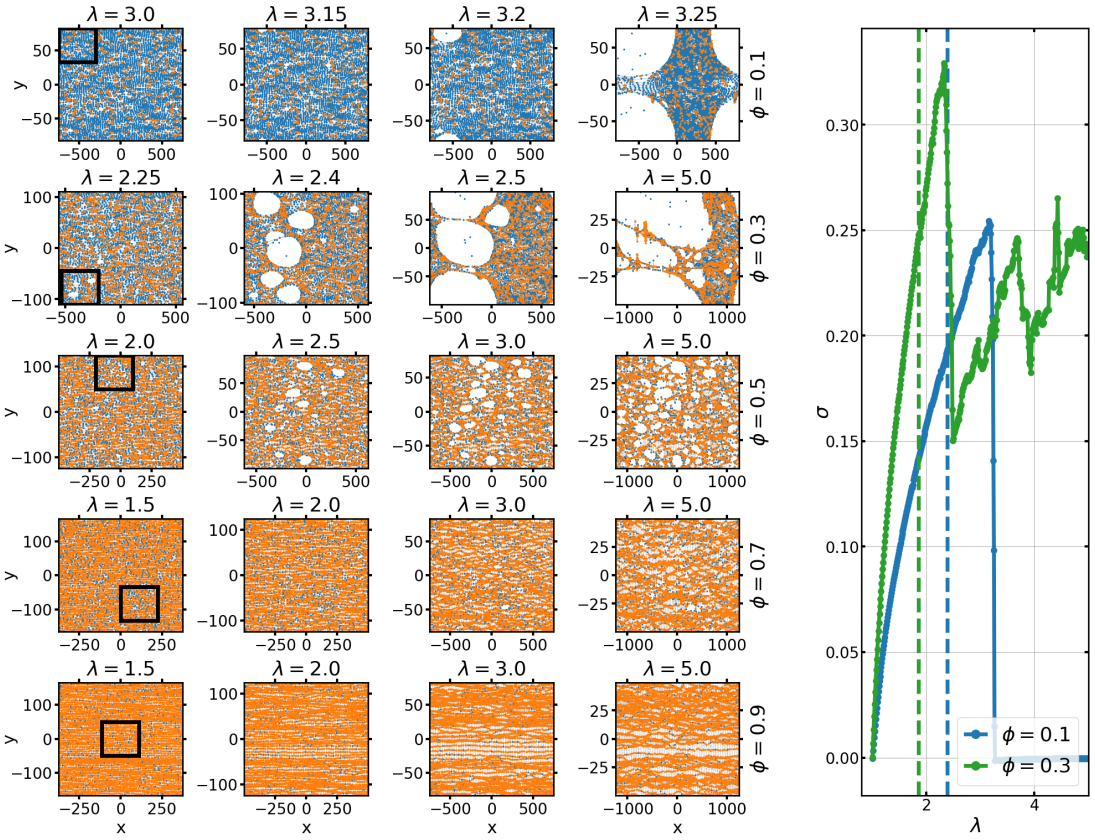

Figure A.80.: Snapshots of non-crystallizing networks with configuration 4: The filler is randomly distributed, i.e. the MG ran through $0 \cdot N$ MC steps and, it has been set $R^{\mathrm{ff}} = R^{\mathrm{pf}} = 1.1$, $k^{\mathrm{ff}} = 5.0$, $k^{\mathrm{pf}} = 4.0$ and $k^{\mathrm{pf}}_{\mathrm{weak}} = 1.0$. The critical free energy density is $(g/n)_{\mathrm{crit}} = 1.5$. The black rectangles indicate the regions which are depicted in the extracts of the snapshots in Figure A.81. For networks with $\phi = 0.1$ and $\phi = 0.2$, the corresponding stress-stretch curves are also shown, where the onset of rupture in each case is indicated by a dashed line.

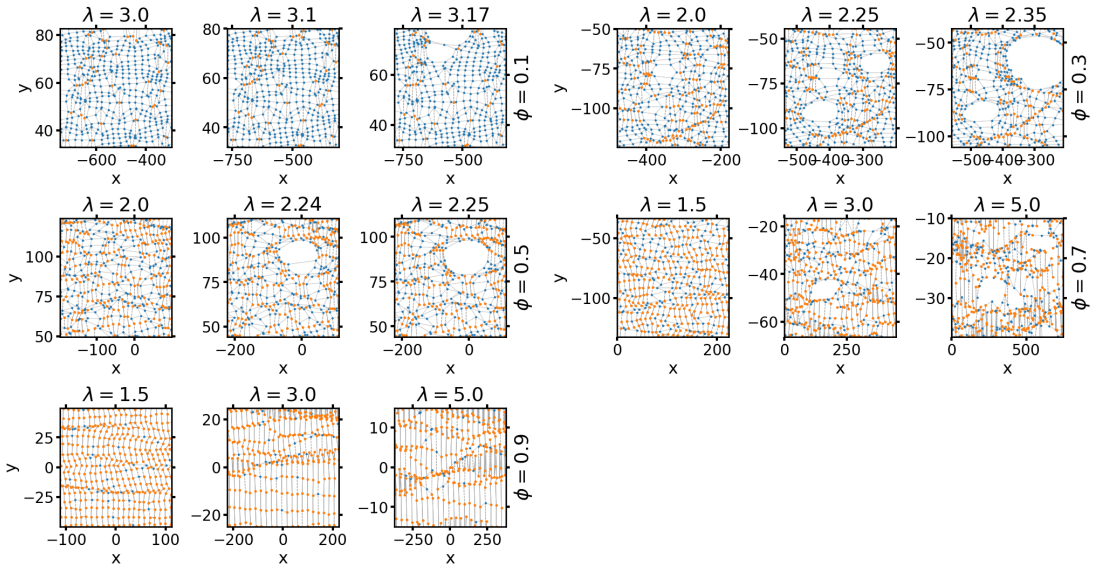

Figure A.81.: Extracts of snapshots of the model networks depicted in Figure A.80 in the regions indicated by the rectangles in there.

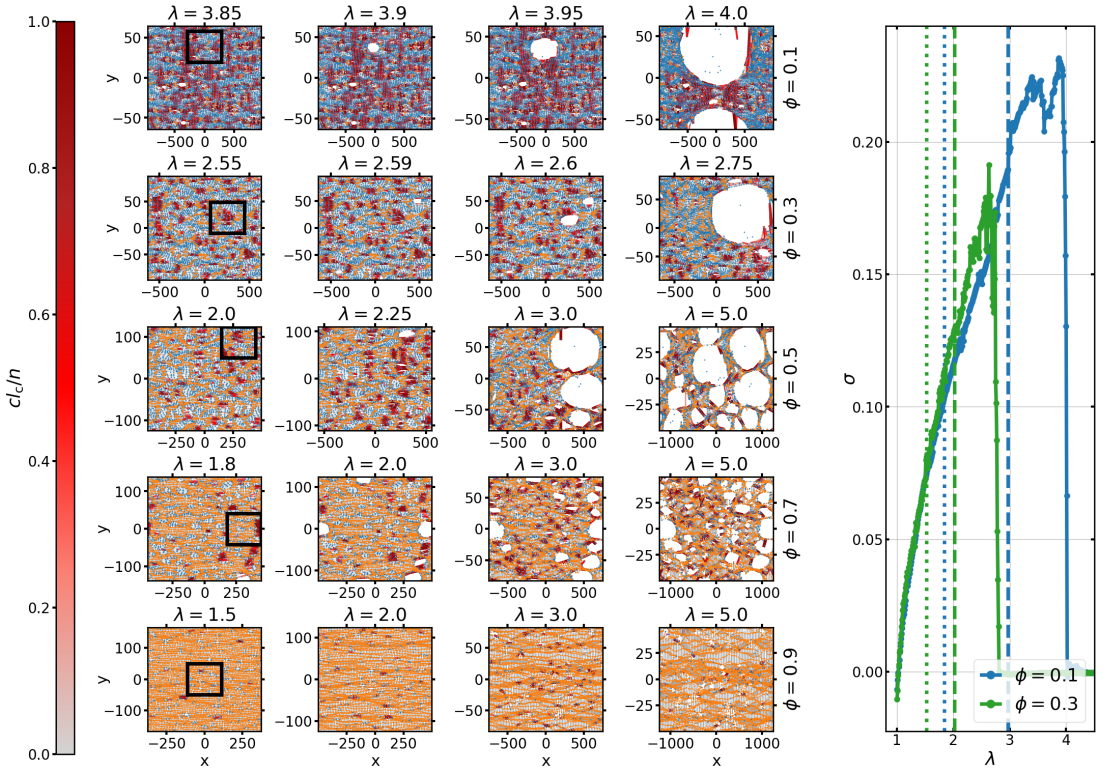

Figure A.82.: Snapshots of crystallizing networks with configuration 2: The MG ran through $10 \cdot N$ MC steps. It has been set $R^{\mathrm{ff}} = R^{\mathrm{pf}} = 1.1$, $k^{\mathrm{ff}} = 5.0$, $k^{\mathrm{pf}} = 4.0$ and $k^{\mathrm{pf}}_{\mathrm{weak}} = 1.0$ with $(g/n)_{\mathrm{crit}} = 1.5$ as the critical free energy density. The black rectangles indicate the regions which are depicted in the extracts of the snapshots in Figure A.83. In the plot of the stress-stretch curves, the onset of SIC in each case is marked by a dotted line and the onset of rupture is indicated by a dashed line.

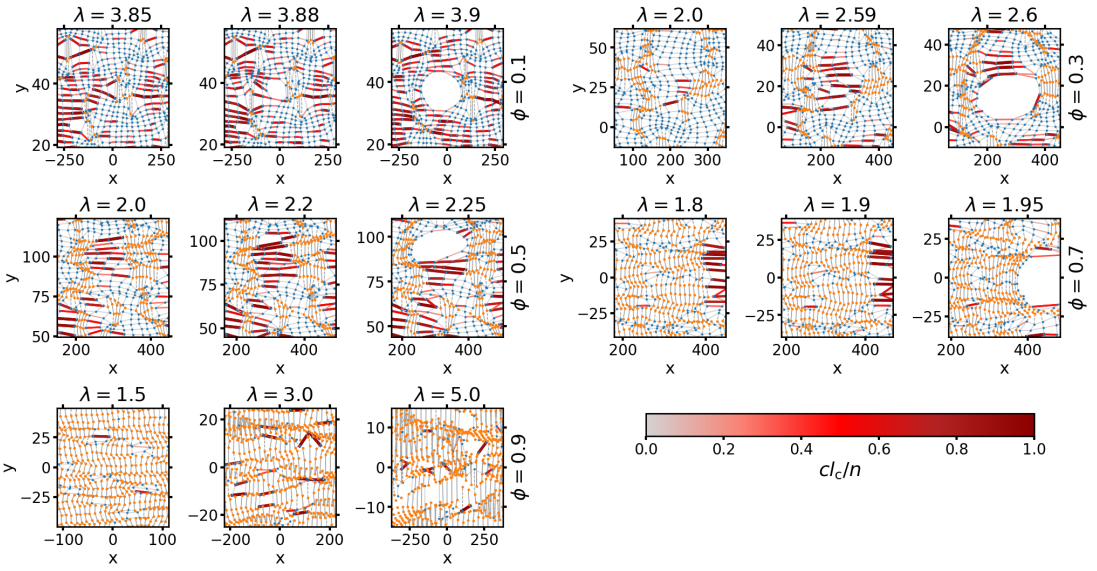

Figure A.83.: Extracts of snapshots of the model networks depicted in Figure A.82 in the regions indicated by the rectangles in there.

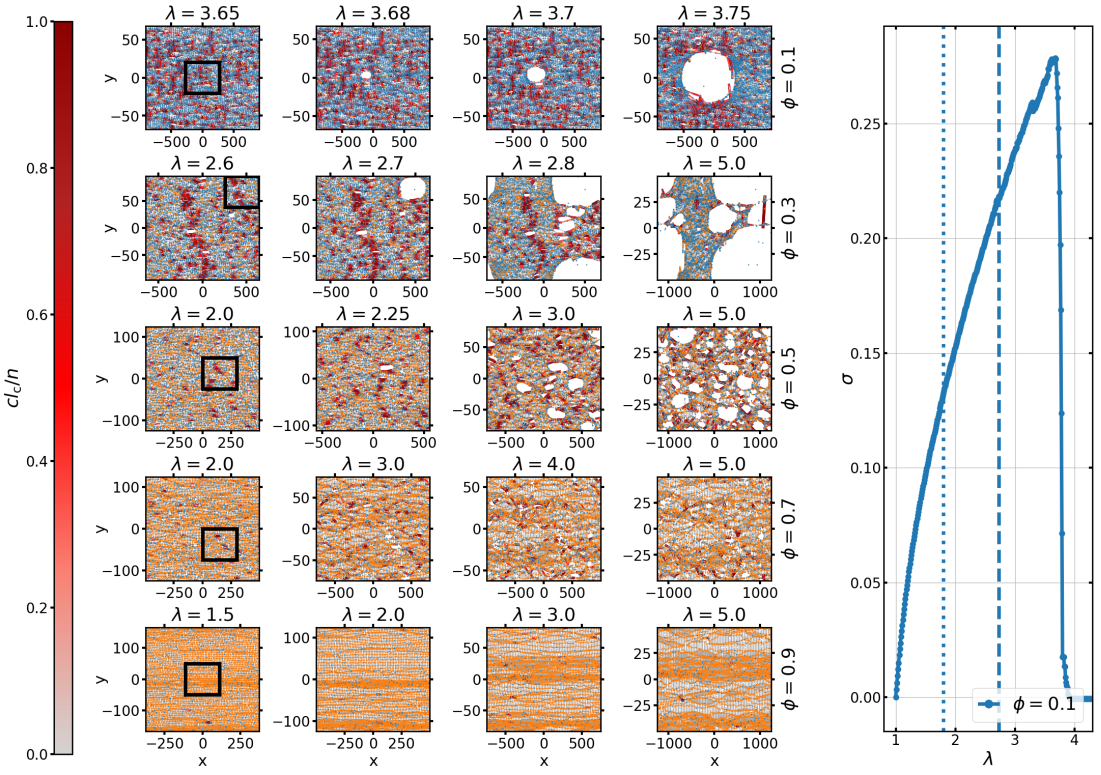

Figure A.84.: Snapshots of crystallizing networks with configuration 3: The filler is randomly distributed, i.e. MG ran through $0 \cdot N$ MC steps, and it has been set $R^{\mathrm{ff}} = R^{\mathrm{pf}} = 1.1$, $k^{\mathrm{ff}} = 5.0$, $k^{\mathrm{pf}} = 4.0$ and $k^{\mathrm{pf}}_{\mathrm{weak}} = 1.0$ with $(g/n)_{\mathrm{crit}} = 1.5$ as the critical free energy density. The black rectangles indicate the regions which are depicted in the extracts of the snapshots in Figure A.85. In the plot of the stress-stretch curves, the onset of SIC in each case is marked by a dotted line and the onset of rupture is indicated by a dashed line.

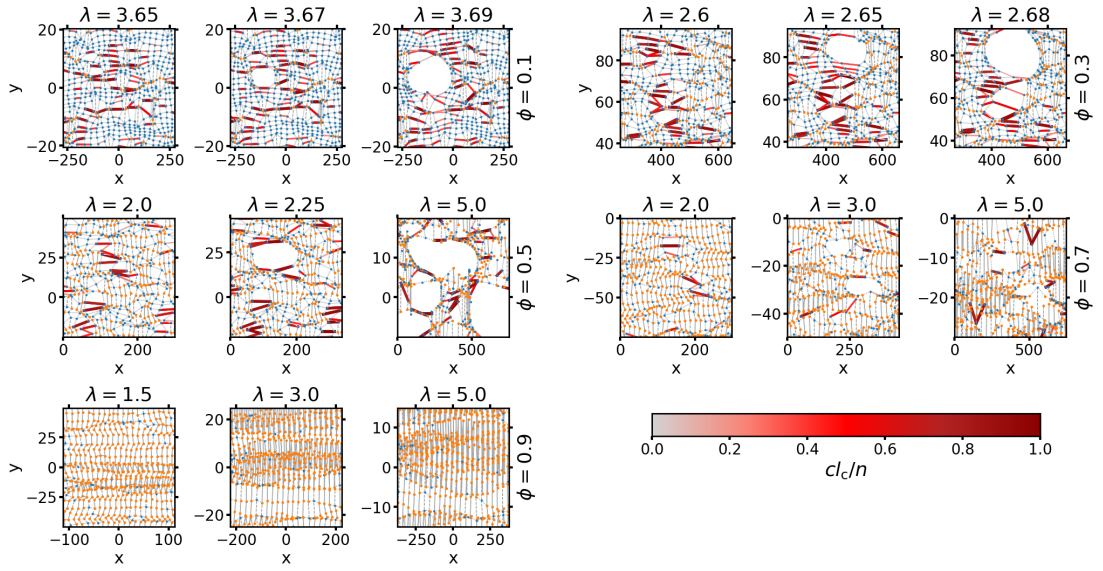

Figure A.85.: Extracts of snapshots of the model networks depicted in Figure A.84 in the regions indicated by the rectangles in there.

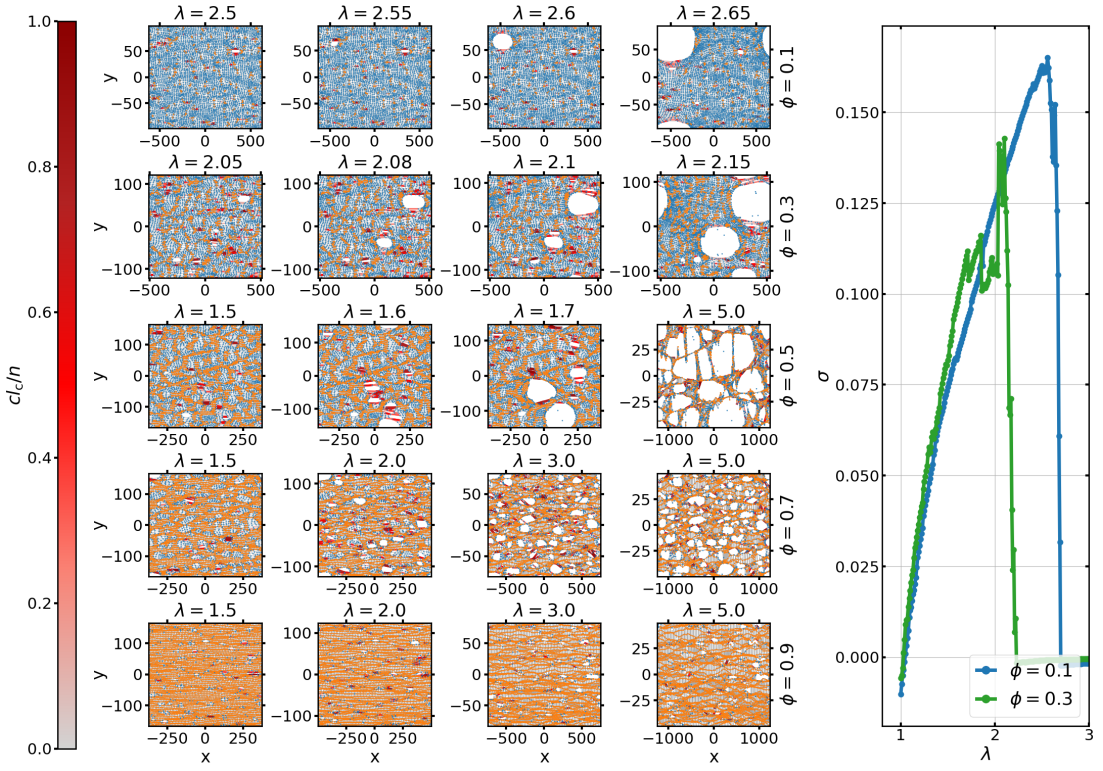

Figure A.86.: Snapshots of crystallizing networks with configuration 0: The MG ran through $10 \cdot N$ MC steps and it has been set $R^{\mathrm{ff}} = R^{\mathrm{pf}} = \infty$, $k^{\mathrm{ff}} = 5.0$ and $k^{\mathrm{pf}} = 4.0$. The critical free energy density is $(g/n)_{\mathrm{crit}} = 1.25$.

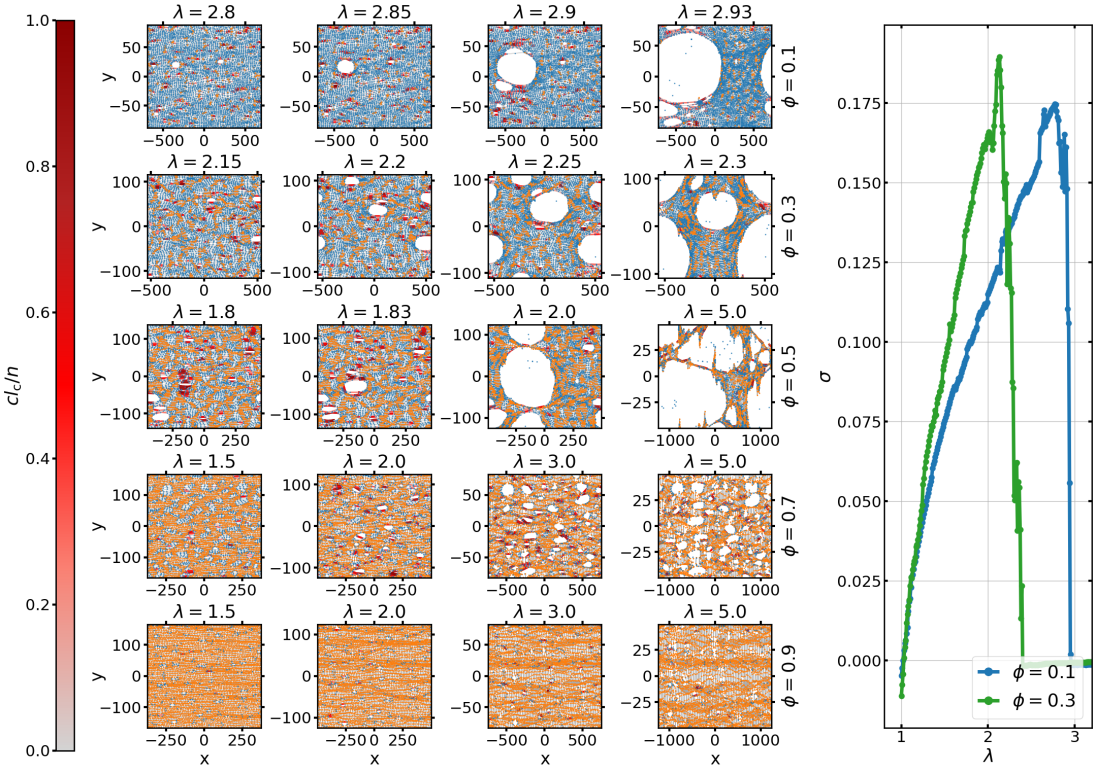

Figure A.87.: Snapshots of crystallizing networks with configuration 1: The MG ran through $10 \cdot N$ MC steps and it has been set $R^{\mathrm{ff}} = 1.1$, $R^{\mathrm{pf}} = \infty$, $k^{\mathrm{ff}} = 5.0$ and $k^{\mathrm{pf}} = 4.0$. The critical free energy density is $(g/n)_{\mathrm{crit}} = 1.25$

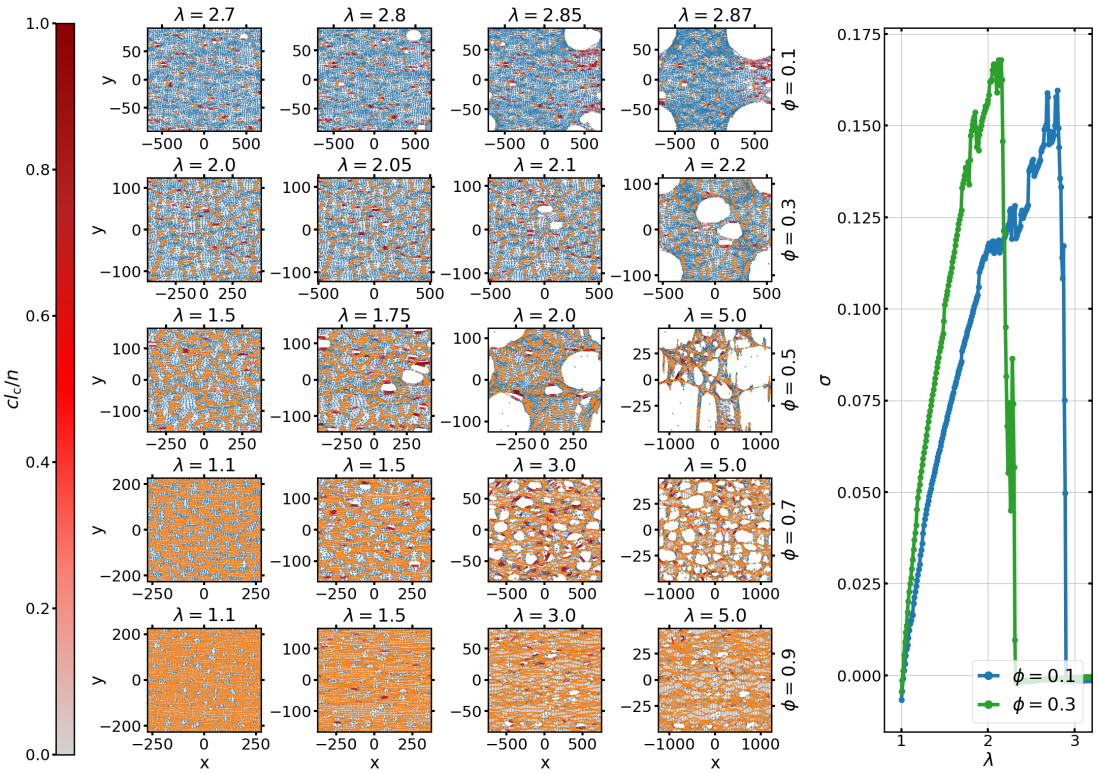

Figure A.88.: Snapshots of crystallizing networks with configuration 4: The MG ran through $10 \cdot N$ MC steps and it has been set $R^{\mathrm{ff}} = \infty$, $R^{\mathrm{pf}} = 1.1$, $k^{\mathrm{ff}} = 5.0$, $k^{\mathrm{pf}} = 4.0$ and $k^{\mathrm{pf}}_{\mathrm{weak}} = 1.0$. The critical free energy density is $(g/n)_{\mathrm{crit}} = 1.25$.

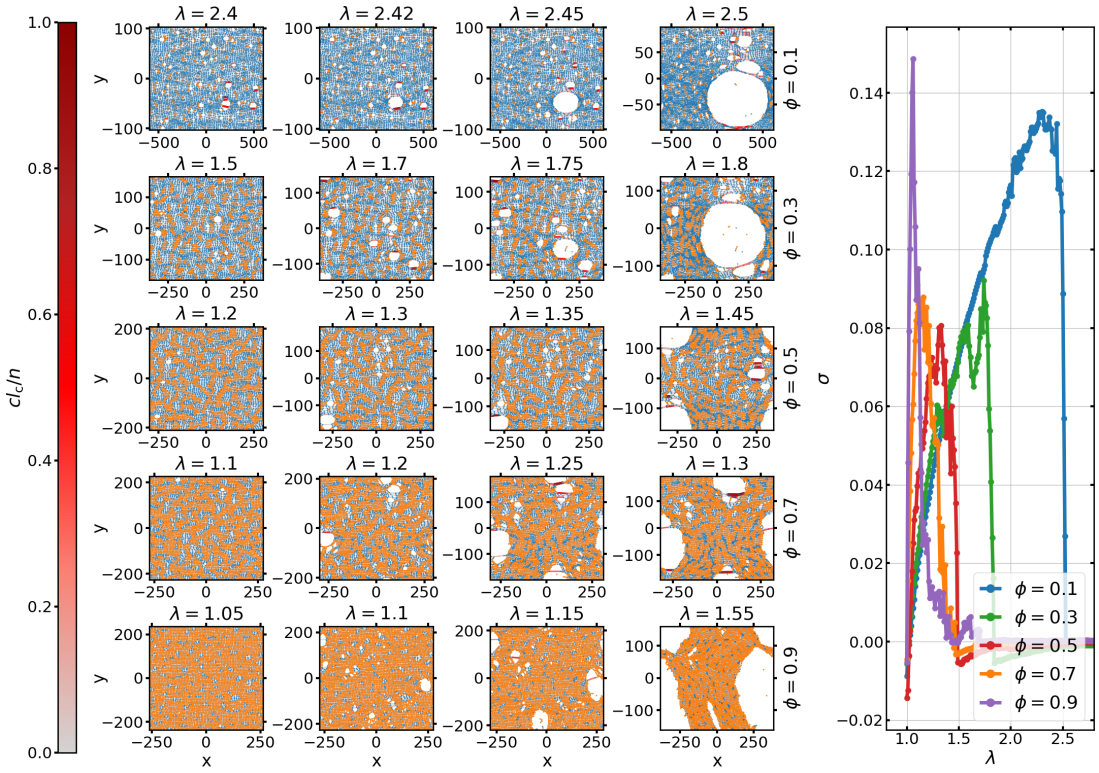

Figure A.89.: Snapshots of crystallizing networks with configuration 5: The MG ran through $10 \cdot N$ MC steps and it has been set $R^{\mathrm{ff}} = R^{\mathrm{pf}} = 1.1$, $k^{\mathrm{ff}} = 5.0$, $k^{\mathrm{pf}} = 4.0$ and $k^{\mathrm{pf}}_{\mathrm{weak}} = 0.0$. The critical free energy density is $(g/n)_{\mathrm{crit}} = 1.25$.

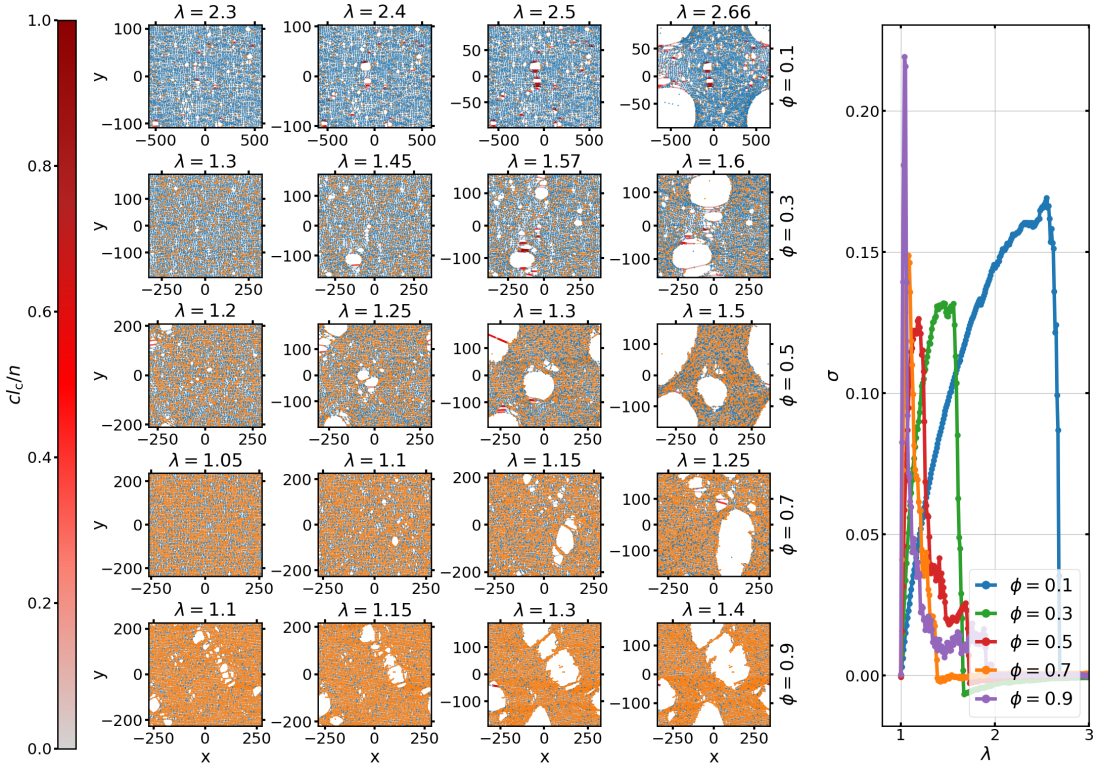

Figure A.90.: Snapshots of crystallizing networks with configuration 6: The filler is randomly distributed and it has been set $R^{\mathrm{ff}} = R^{\mathrm{pf}} = 1.1$, $k^{\mathrm{ff}} = 5.0$, $k^{\mathrm{pf}} = 4.0$ and $k^{\mathrm{pf}}_{\mathrm{weak}} = 0.0$. The critical free energy density is $(g/n)_{\mathrm{crit}} = 1.25$.

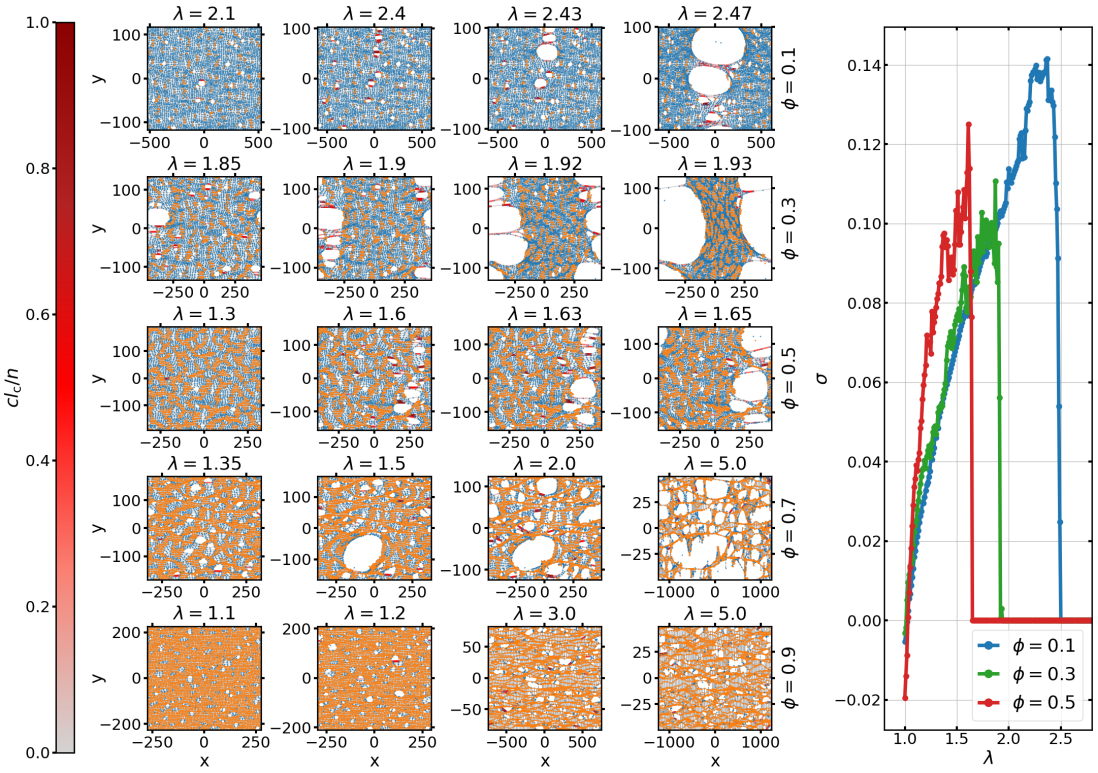

Figure A.91.: Snapshots of crystallizing networks with configuration 7: The MG ran through $10 \cdot N$ MC steps and it has been set $R^{\mathrm{ff}} = \infty$, $R^{\mathrm{pf}} = 1.1$, $k^{\mathrm{ff}} = 5.0$, $k^{\mathrm{pf}} = 4.0$ and $k^{\mathrm{pf}}_{\mathrm{weak}} = 0.0$. The critical free energy density is $(g/n)_{\mathrm{crit}} = 1.25$.

A.8.4. Stress-Stretch Curves

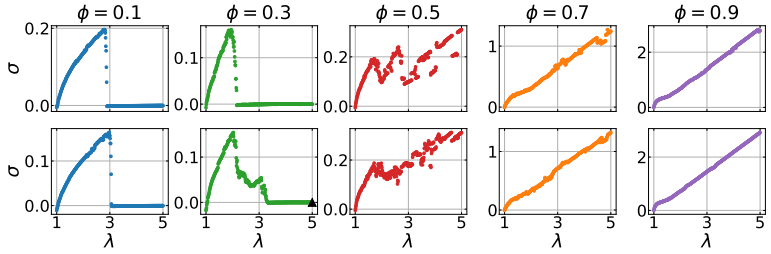

(a) Crystallizing.

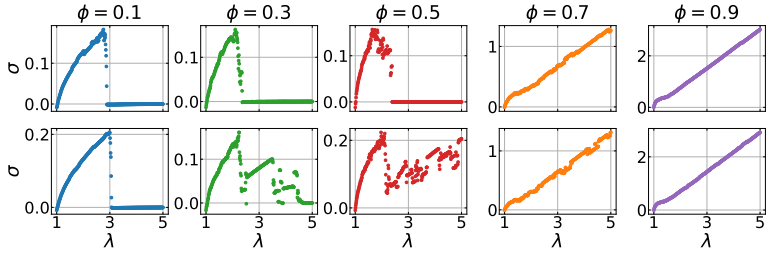

(b) Non-crystallizing.

Figure A.92.: Exemplary raw stress-stretch curves of crystallizing and non-crystallizing networks simulated for Figure 5.85. Each column belongs to a certain filler content ϕ and, in each row, the stress-stretch curve of a different network is depicted. The black rectangle indicates that the stress at the maximum stretch $\lambda_{\mathrm{max}} = 5.0$ is larger than zero.

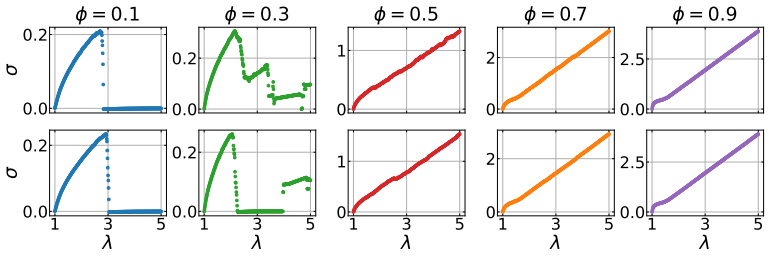

(a) Crystallizing.

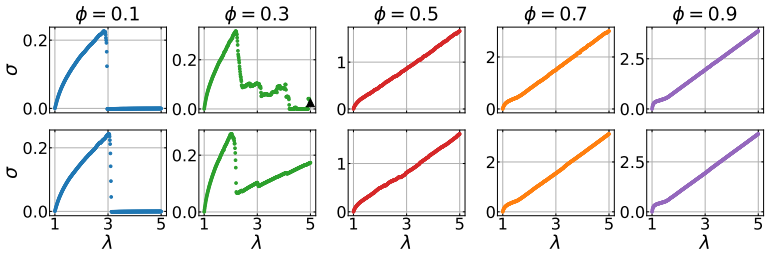

(b) Non-crystallizing.

Figure A.93.: Exemplary raw stress-stretch curves of crystallizing and non-crystallizing networks simulated for Figure 5.86. Each column belongs to a certain filler content ϕ and, in each row, the stress-stretch curve of a different network is depicted. The black rectangle indicates that the stress at the maximum stretch $\lambda_{\max} = 5.0$ is larger than zero.

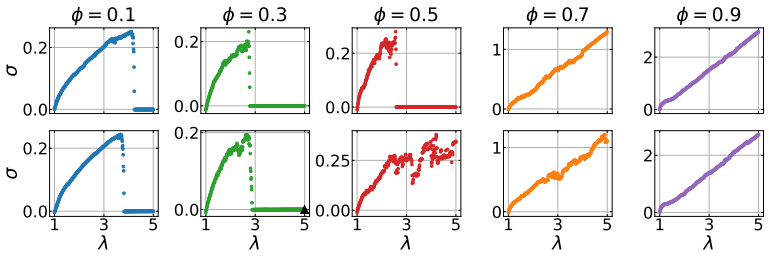

(a) Crystallizing.

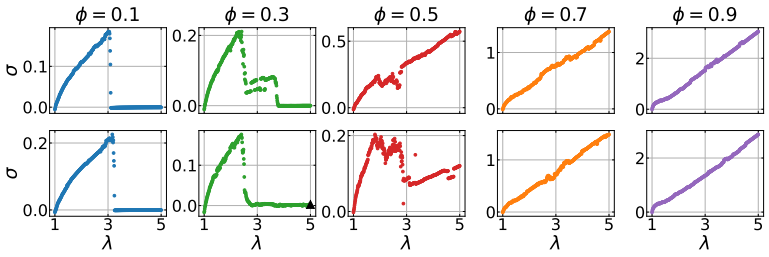

(b) Non-crystallizing.

Figure A.94.: Exemplary raw stress-stretch curves of crystallizing and non-crystallizing networks simulated for Figure 5.89. Each column belongs to a certain filler content ϕ and, in each row, the stress-stretch curve of a different network is depicted. The black rectangles indicate that the stress at the maximum stretch $\lambda_{\max} = 5.0$ is larger than zero.

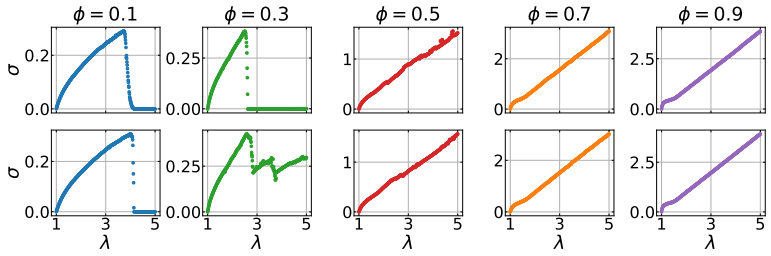

(a) Crystallizing.

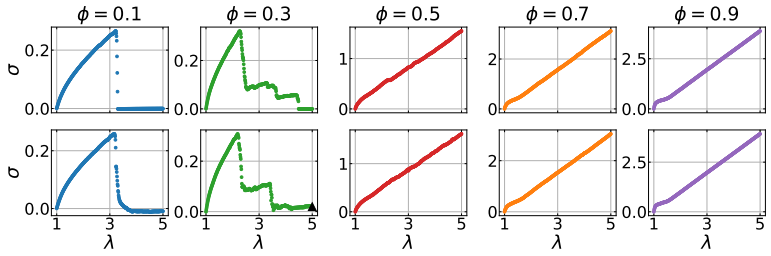

(b) Non-crystallizing.

Figure A.95.: Exemplary raw stress-stretch curves of crystallizing and non-crystallizing networks simulated for Figure 5.90. Each column belongs to a certain filler content ϕ and, in each row, the stress-stretch curve of a different network is depicted. The black rectangle indicates that the stress at the maximum stretch $\lambda_{\max} = 5.0$ is larger than zero.

A.8.5. Tensile Strength and Elongation at Break

In the following, plots of the fraction of broken links L_b/L, the tensile strength σ_t, the elongation at break λ_t, the number of damaged as well as the number of failed networks versus the filler content ϕ are presented for 2D-networks consisting of $N = 5041$ nodes. Unless otherwise specified, the MG ran through $10 \cdot N$ MC steps. The spring constants and cut-off radii of filler-filler and polymer-filler bonds are varied. The networks have been stretched until $\lambda_{\max} = 5.0$.

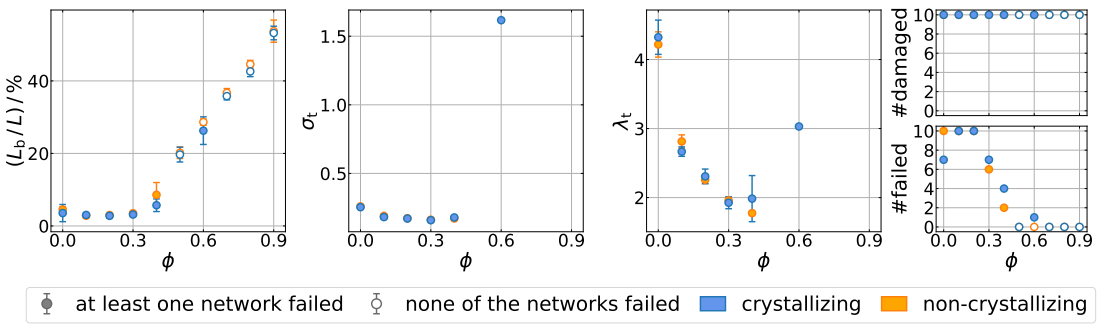

Figure A.96.: Fraction of broken links L_b/L, number of damaged networks and number of networks which failed for variable filler content ϕ obtained from the simulations of 10 2D-networks with critical free energy density $(g/n)_{\text{crit}} = 1.25$. It is set $R^{\text{ff}} = R^{\text{pf}} = \infty$, $k^{\text{ff}} = 5.0$ and $k^{\text{pf}} = 4.0$, which is configuration 0 in Table A.16.

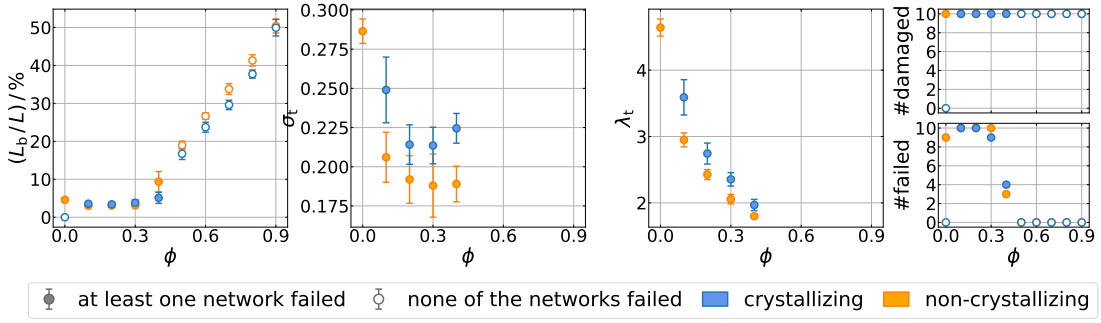

Figure A.97.: Fraction of broken links L_b/L, number of damaged networks and number of networks which failed for variable filler content ϕ obtained from the simulations of 10 2D-networks with critical free energy density $(g/n)_{crit} = 1.5$. It is set $R^{ff} = R^{pf} = \infty$, $k^{ff} = 5.0$ and $k^{pf} = 4.0$, which is configuration 0 in Table A.16.

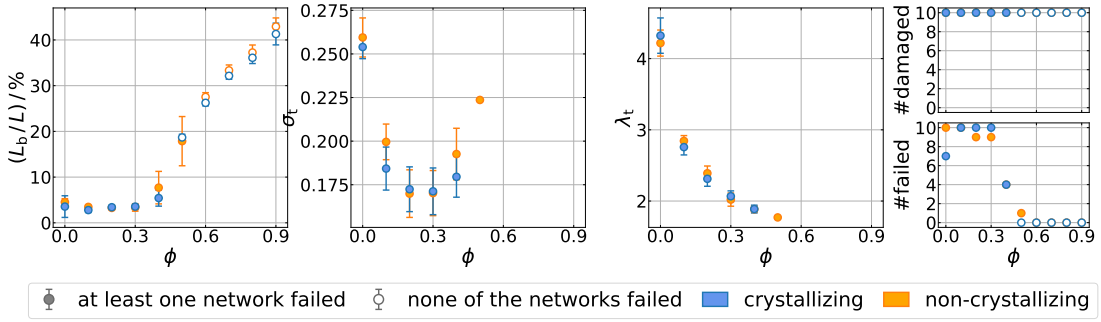

Figure A.98.: Fraction of broken links L_b/L, number of damaged networks and number of networks which failed for variable filler content ϕ obtained from the simulations of 10 2D-networks with critical free energy density $(g/n)_{crit} = 1.25$. It is set $R^{ff} = 1.1$, $R^{pf} = \infty$, $k^{ff} = 5.0$ and $k^{pf} = 4.0$, which is configuration 1 in Table A.16.

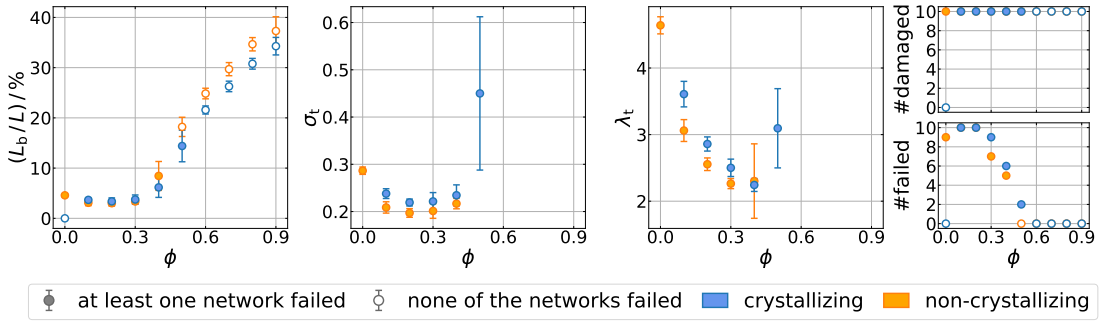

Figure A.99.: Fraction of broken links L_b/L, number of damaged networks and number of networks which failed for variable filler content ϕ obtained from the simulations of 10 2D-networks with critical free energy density $(g/n)_{crit} = 1.5$. It is set $R^{ff} = 1.1$, $R^{pf} = \infty$, $k^{ff} = 5.0$ and $k^{pf} = 4.0$, which is configuration 1 in Table A.16.

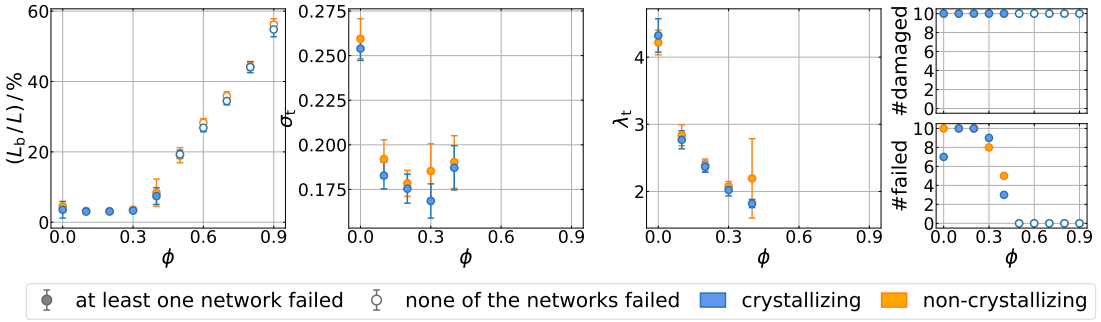

Figure A.100.: Fraction of broken links L_b/L, number of damaged networks and number of networks which failed for variable filler content ϕ obtained from the simulations of 10 2D-networks with critical free energy density $(g/n)_{crit} = 1.25$. It is set $R^{ff} = \infty$, $R^{pf} = 1.1$, $k^{ff} = 5.0$, $k^{pf} = 4.0$ and $k^{pf}_{weak} = 1.0$, which is configuration 4 in Table A.16.

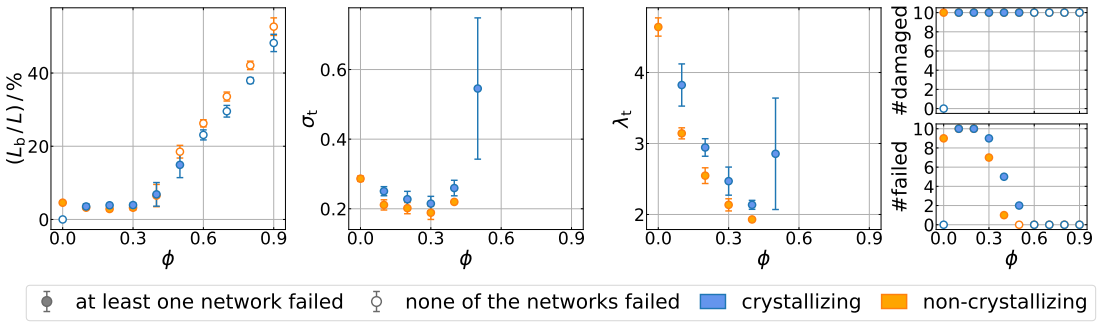

Figure A.101.: Fraction of broken links L_b/L, number of damaged networks and number of networks which failed for variable filler content ϕ obtained from the simulations of 10 2D-networks with critical free energy density $(g/n)_{crit} = 1.5$. It is set $R^{ff} = \infty$, $R^{pf} = 1.1$, $k^{ff} = 5.0$, $k^{pf} = 4.0$ and $k^{pf}_{weak} = 1.0$, which is configuration 4 in Table A.16.

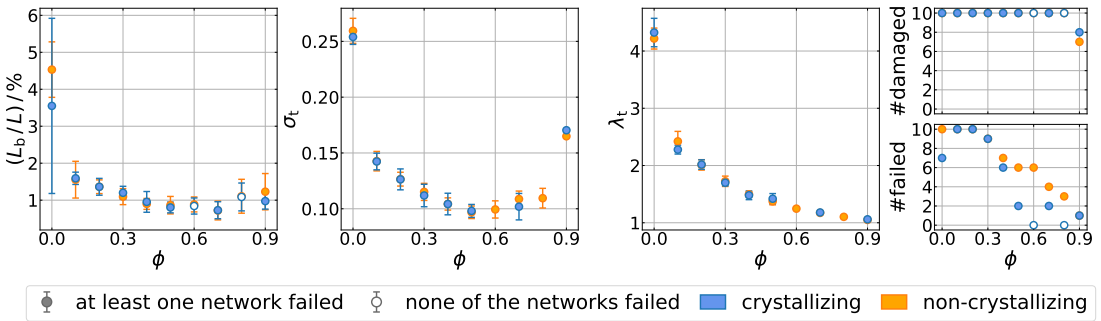

Figure A.102.: Fraction of broken links L_b/L, number of damaged networks and number of networks which failed for variable filler content ϕ obtained from the simulations of 10 2D-networks with critical free energy density $(g/n)_{crit} = 1.25$. It is set $R^{ff} = R^{pf} = 1.1$, $k^{ff} = 5.0$, $k^{pf} = 4.0$ and $k^{pf}_{weak} = 0.0$, which is configuration 5 in Table A.16.

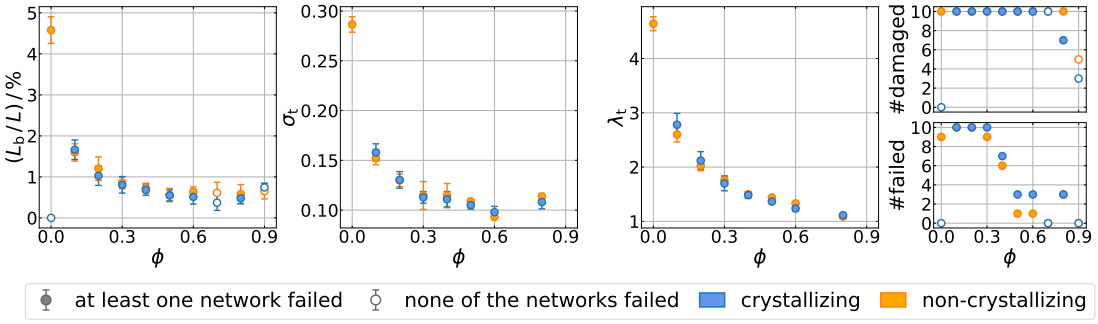

Figure A.103.: Fraction of broken links L_b/L, number of damaged networks and number of networks which failed for variable filler content ϕ obtained from the simulations of 10 2D-networks with critical free energy density $(g/n)_{crit} = 1.5$. It is set $R^{ff} = R^{pf} = 1.1$, $k^{ff} = 5.0$, $k^{pf} = 4.0$ and $k^{pf}_{weak} = 0.0$, which is configuration 5 in Table A.16.

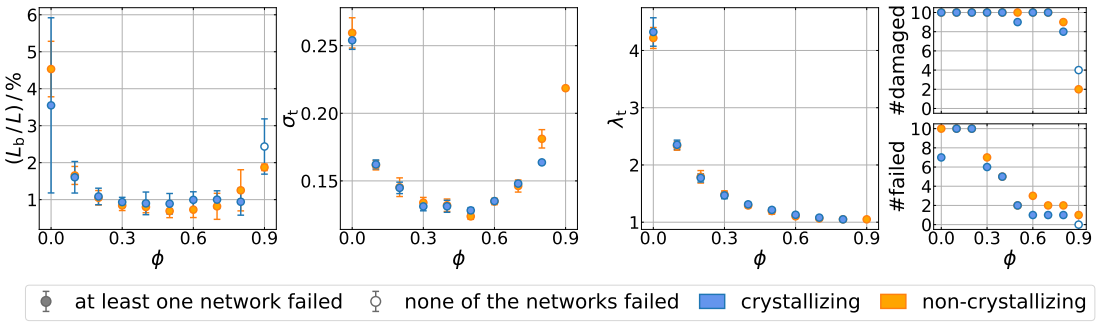

Figure A.104.: Fraction of broken links L_b/L, number of damaged networks and number of networks which failed for variable filler content ϕ obtained from the simulations of 10 2D-networks with critical energy density $(g/n)_{crit} = 1.25$. It is set $R^{ff} = R^{pf} = 1.1$, $k^{ff} = 5.0$, $k^{pf} = 4.0$ and $k^{pf}_{weak} = 0.0$, which is configuration 6 in Table A.16. In contrast to the other cases, the morphology generator is not applied here, i.e. the filler is randomly distributed.

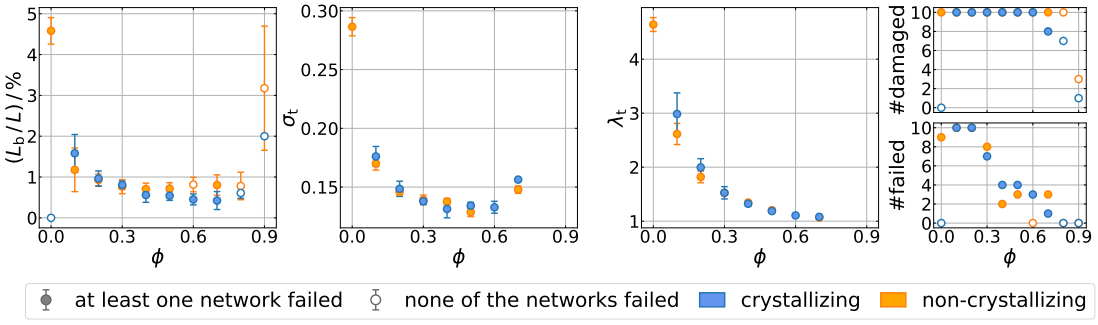

Figure A.105.: Fraction of broken links L_b/L, number of damaged networks and number of networks which failed for variable filler content ϕ obtained from the simulations of 10 2D-networks with critical energy density $(g/n)_{crit} = 1.5$. It is set $R^{ff} = R^{pf} = 1.1$, $k^{ff} = 5.0$, $k^{pf} = 4.0$ and $k^{pf}_{weak} = 0.0$, which is configuration 6 in Table A.16. In contrast to the other cases, the morphology generator is not applied here, i.e. the filler is randomly distributed.

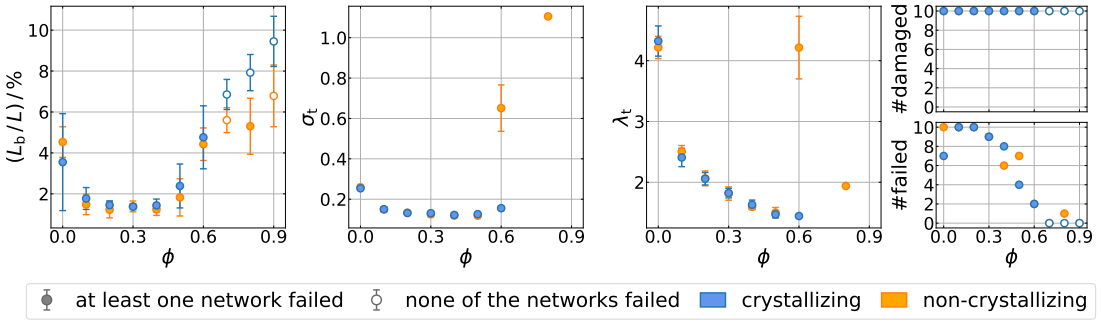

Figure A.106.: Fraction of broken links L_b/L, number of damaged networks and number of networks which failed for variable filler content ϕ obtained from the simulations of 10 2D-networks with critical free energy density $(g/n)_{crit} = 1.25$. It is set $R^{ff} = \infty$, $R^{pf} = 1.1$, $k^{ff} = 5.0$, $k^{pf} = 4.0$ and $k^{pf}_{weak} = 0.0$, which is configuration 7 in Table A.16.

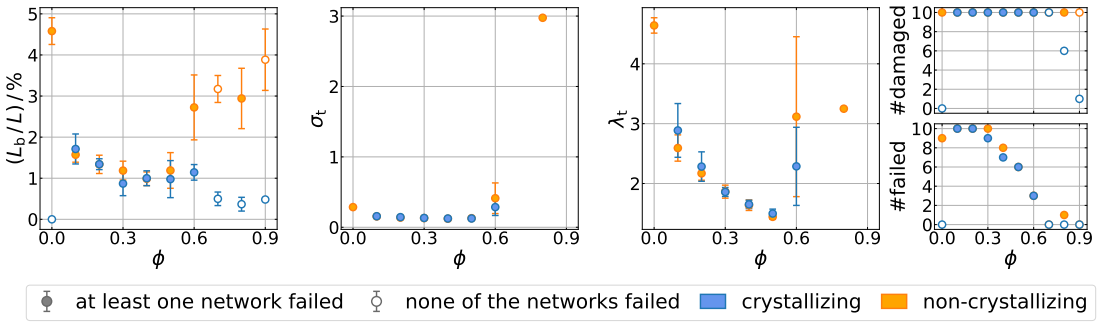

Figure A.107.: Fraction of broken links L_b/L, number of damaged networks and number of networks which failed for variable filler content ϕ obtained from the simulations of 10 2D-networks with critical free energy density $(g/n)_{crit} = 1.5$. It is set $R^{ff} = \infty$, $R^{pf} = 1.1$, $k^{ff} = 5.0$, $k^{pf} = 4.0$ and $k^{pf}_{weak} = 0.0$, which is configuration 7 in Table A.16.

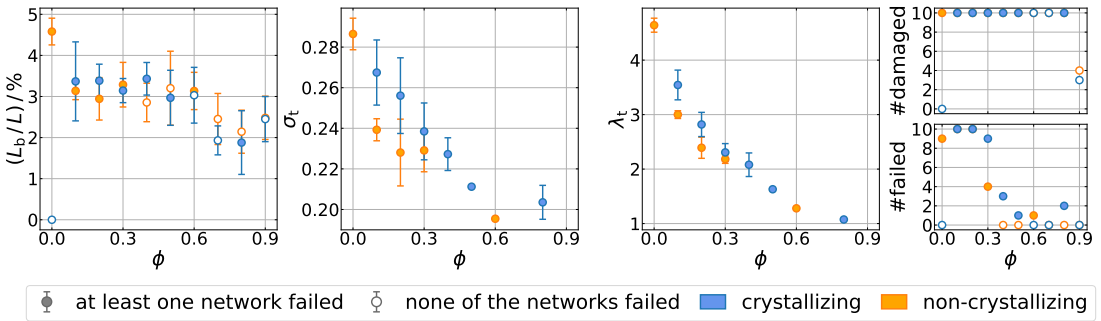

Figure A.108.: Fraction of broken links L_b/L, tensile strength σ_t, elongation at break λ_t, number of damaged networks and number of networks which failed for variable filler content ϕ obtained from the simulations of 10 2D-networks with critical energy density $(g/n)_{crit} = 1.5$. It is set $R^{ff} = R^{pf} = 1.1$, $k^{ff} = 5.0$, $k^{pf} = 4.0$ and $k^{pf}_{weak} = 1.0$. Polymer-Filler bonds break reversibly at $r_i = R^{pf}_{break} r_{0,i}$ with $R^{pf}_{break} = 5.0$. The filler is randomly distributed.

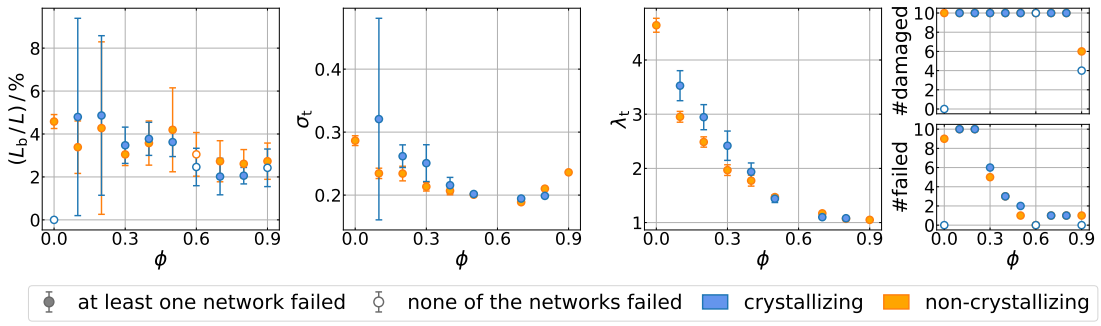

Figure A.109.: Fraction of broken links L_b/L, tensile strength σ_t, elongation at break λ_t, number of damaged networks and number of networks which failed for variable filler content ϕ obtained from the simulations of 10 2D-networks with critical energy density $(g/n)_{crit} = 1.5$. It is set $R^{ff} = R^{pf} = 1.1$, $k^{ff} = 5.0$, $k^{pf} = 4.0$ and $k^{pf}_{weak} = 1.0$. Polymer-Filler bonds break reversibly at $r_i = R^{pf}_{break} r_{0,i}$ with $R^{pf}_{break} = 10.0$. The filler is randomly distributed.

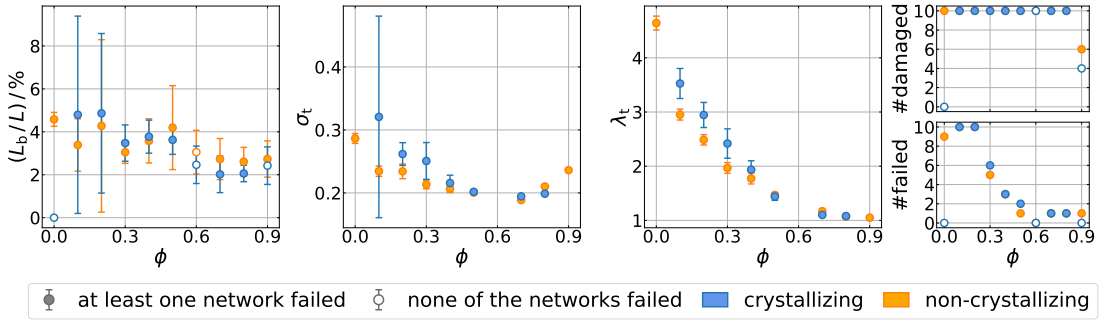

Figure A.110.: Fraction of broken links L_b/L, tensile strength σ_t, elongation at break λ_t, number of damaged networks and number of networks which failed for variable filler content ϕ obtained from the simulations of 10 2D-networks with critical energy density $(g/n)_{crit} = 1.5$. It is set $R^{ff} = R^{pf} = 1.1$, $k^{ff} = 5.0$, $k^{pf} = 4.0$ and $k^{pf}_{weak} = 1.0$. Polymer-Filler bonds break reversibly at $r_i = R^{pf}_{break} r_{0,i}$ with $R^{pf}_{break} = 50.0$. The filler is randomly distributed.

Figure A.111 and Figure A.112 show plots of the fraction of broken links L_b/L, the tensile strength σ_t, the elongation at break λ_t, the number of damaged as well as the number of failed networks versus the filler content ϕ for 3D-networks consisting of $N = 5832$ nodes. To generate coarsely dispersed filler, the MG ran through $50 \cdot N$ MC steps. For the parametrization of filler-filler and polymer-filler bonds, it is set $R^{ff} = R^{pf} = 1.1$, $k^{ff} = 5.0$, $k^{pf} = 4.0$ and $k^{pf}_{weak} = 1.0$. The networks have been stretched until $\lambda_{max} = 5.0$ and the critical free energy density is set to $(g/n)_{crit} = 1.35$.

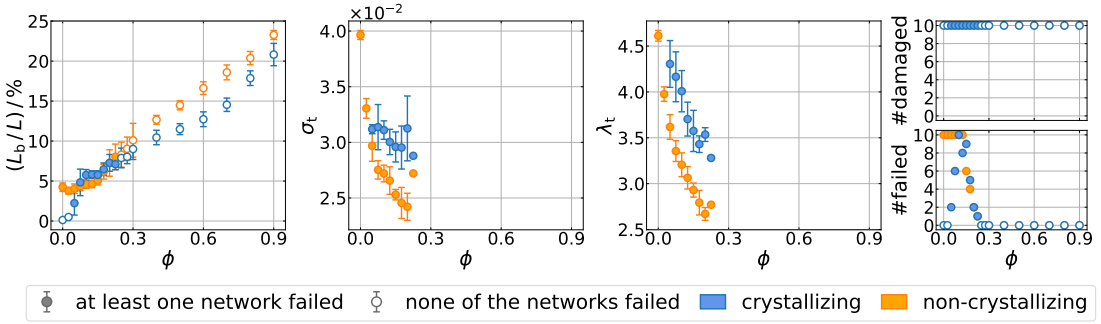

Figure A.111.: Fraction of broken links L_b/L, tensile strength σ_t, elongation at break λ_t, number of damaged networks and number of networks which failed for variable filler content ϕ obtained from the simulations of 10 3D-networks with critical free energy density $(g/n)_{crit} = 1.35$. It is set $R^{ff} = R^{pf} = 1.1$, $k^{ff} = 5.0$, $k^{pf} = 4.0$ and $k^{pf}_{weak} = 1.0$. The MG ran through $50 \cdot N$ MC steps.

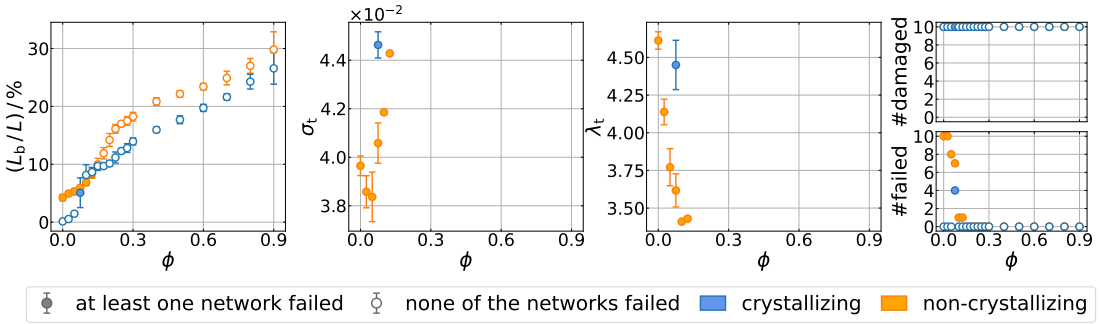

Figure A.112.: Fraction of broken links L_b/L, tensile strength σ_t, elongation at break λ_t, number of damaged networks and number of networks which failed for variable filler content ϕ obtained from the simulations of 10 3D-networks with critical free energy density $(g/n)_{crit} = 1.35$. It is set $R^{ff} = R^{pf} = 1.1$, $k^{ff} = 5.0$, $k^{pf} = 4.0$ and $k^{pf}_{weak} = 1.0$. The filler is randomly distributed.

A.8.6. Fatigue

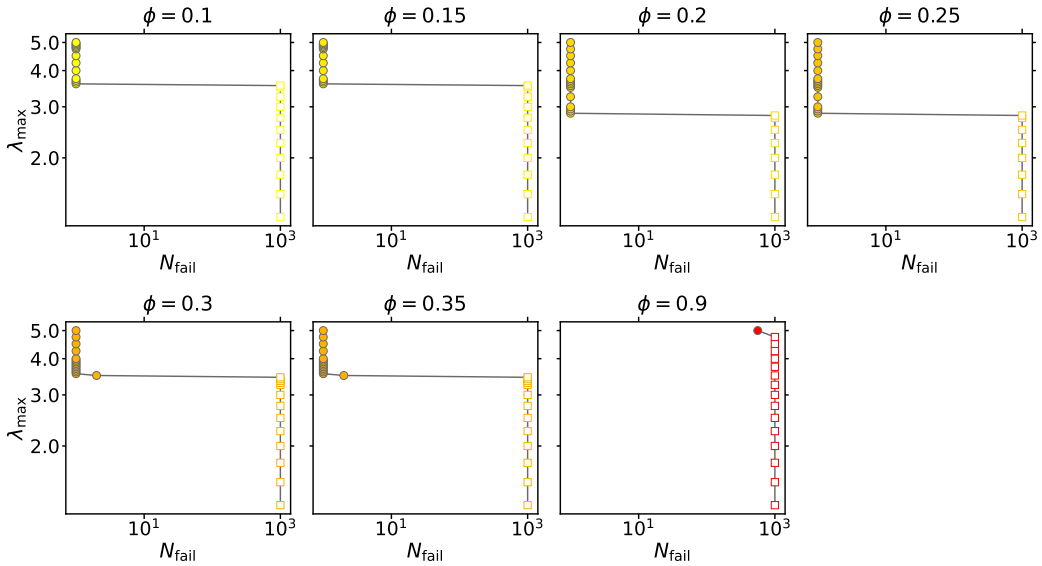

Figure A.113.: Wöhler curves for non-crystallizing 2D-networks consisting of $N = 196$ nodes with variable filler content ϕ. The filler is randomly distributed and the critical free energy density is $(g/n)_{crit} = 1.5$. For fixed filler content, the initial configurations of the networks are identical and, for each maximum stretch λ_{max}, the networks have been deformed for up to 1000 cycles. The data points are connected for the eye.

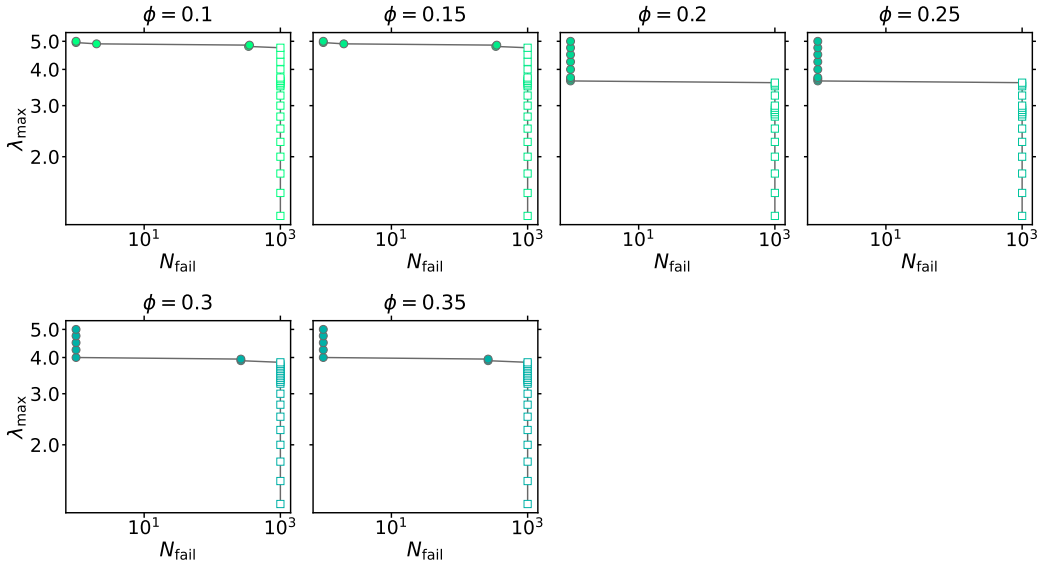

Figure A.114.: Wöhler curves for crystallizing 2D-networks consisting of $N = 196$ nodes with variable filler content ϕ. The filler is randomly distributed and the critical free energy density is $(g/n)_{crit} = 1.5$. For fixed filler content, the initial configurations of the networks are identical and, for each maximum stretch λ_{max}, the networks have been deformed for up to 1000 cycles. The data points are connected for the eye.

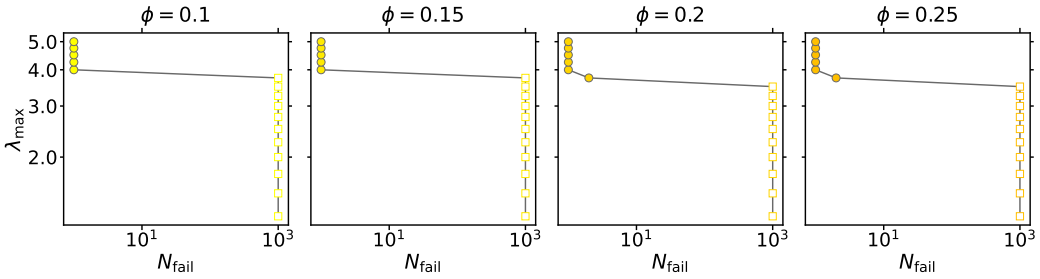

Figure A.115.: Wöhler curves for non-crystallizing 3D-networks consisting of $N = 216$ nodes with variable filler content ϕ. The filler is randomly distributed and the critical free energy density is $(g/n)_{crit} = 1.5$. For fixed filler content, the initial configurations of the networks are identical and, for each maximum stretch λ_{max}, the networks have been deformed for up to 1000 cycles. The data points are connected for the eye.

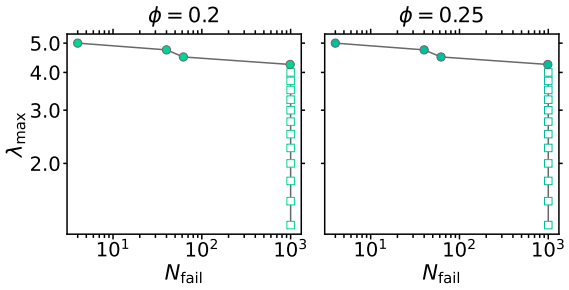

Figure A.116.: Wöhler curves for crystallizing 3D-networks consisting of $N = 216$ nodes with variable filler content ϕ. The filler is randomly distributed and the critical free energy density is $(g/n)_{crit} = 1.5$. For fixed filler content, the initial configurations of the networks are identical and, for each maximum stretch λ_{max}, the networks have been deformed for up to 1000 cycles. The data points are connected for the eye.

A.9. Finite Chain Extensibility

In the model applied in course of this work, Gaussian chains are implemented. Since these model polymer chains can be extended beyond their contour length, some unwanted effects occurred like rupture of highly crystalline links.

However, Gaussian statistics for the freely jointed chain is only valid for end-to-end distances $R \ll R_{max} = Nb$ [55]. Thus, finite chain extensibility must be considered for large deformations.

Note that, in the current version of the model, the nodes and therefore the links are displaced by an affine deformation. In real networks, this is not valid in the non-Gaussian regime, i.e. the regime of high stretches. Nevertheless, the energy minimization by the FIRE algorithm must compensate the application of the affine deformation during stretching.

A.9.1. Fundamental Principles

The conformational entropy of a polymer chain is determined by the probability $P(R)$ that the end-to-end distance of the polymer chain is R:

$$S(R) - S(0) = k_B \ln P(R) - k_B \ln P(0). \tag{A.2}$$

From this equation, the Gibbs free energy and consequently the force on a chain during stretching can be derived.

Thinking of a freely jointed chain with a fixed end-to-end distance R and the start point of the chain located at the origin of the coordinate system and the end point at $(0,0,R)^\intercal$, all values for the orientation angle ϑ, i.e. the angle between the direction of the segment and the z-axis, are not equally probable anymore [265]. The probability $P(R)$ is determined by the distribution of the angles ϑ and φ. The *a priori* probability that the orientation of a randomly chosen segment is in the interval $[\vartheta, \vartheta + \mathrm{d}\vartheta]$ is given as

$$\frac{1}{2} \sin\vartheta \, \mathrm{d}\vartheta. \tag{A.3}$$

Therefore, the number of segments with an orientation angle in the interval $[\vartheta, \vartheta + \mathrm{d}\vartheta]$ is

$$\mathrm{d}N_{\vartheta,\varphi} = \frac{N}{4\pi} \sin\vartheta \, \mathrm{d}\varphi \, \mathrm{d}\vartheta, \tag{A.4}$$

where N denotes the number of Kuhn segments in the polymer chain and the factor 4π results from the range $[0, \pi]$ of possible values for ϑ. Since the angle φ can take values in the interval $[0, 2\pi]$, it holds:

$$\mathrm{d}N_{\vartheta} = \frac{N}{2} \sin\vartheta \, \mathrm{d}\vartheta. \tag{A.5}$$

It is now searched for the most probable angular distribution of the N segments for the fixed end-to-end distance R. For this purpose, the range of ϑ is divided into j small subintervals $\Delta\vartheta_1, \Delta\vartheta_2, \ldots, \Delta\vartheta_j$ and it is searched for the most probable occupation numbers $n_1^0, n_2^0, \ldots, n_j^0$ for these subintervals.
The probability for a set $n_1, n_2, \ldots, n_j$ of occupation numbers for these subintervals of the orientation angle is given as:

$$W = \left[\prod_{i=1}^{j} \left(\frac{1}{2} \sin\vartheta_i \Delta\vartheta_i \right)^{n_i} \right] \frac{N!}{\prod\limits_{i=1}^{j} n_i!}. \tag{A.6}$$

The second factor accounts for the number of distinguishable permutations among the n_i [56]. The problem is solved by computing the logarithm of Equation A.6 with the help of Stirling's formula

$$\ln W \approx \sum_{i=1}^{j} n_i \ln\left(\frac{\sin\vartheta_i \Delta\vartheta_i}{2} \right) + N \ln N - N - \sum_{i=1}^{j} n_i \ln n_i + \sum_{i=1}^{j} n_i, \tag{A.7}$$

and maximizing it under the side conditions:

$$\sum_{i=1}^{j} n_i = N, \tag{A.8}$$

$$\sum_{i=1}^{j} n_i \cdot b \cos\vartheta_i = R. \tag{A.9}$$

The first side condition means that the polymer chain consists of N segments and each of them belongs to one of the $\Delta\vartheta_i$. The second condition describes the fixed end-to-end

distance R, where $b\cos\vartheta_i$ is the projection of the corresponding n_i segments onto the z-axis. For the maximization of Equation A.7, the method of Lagrange multipliers is employed. A variation respective n_i is conducted and the arbitrary constants α and $\frac{\beta}{b}$ are introduced:

$$\delta \ln W = \sum_{i=1}^{j} \frac{\partial \ln W}{\partial n_i} \delta n_i = 0, \tag{A.10}$$

$$\alpha \sum_{i=1}^{j} \delta n_i = 0, \tag{A.11}$$

$$\beta \sum_{i=1}^{j} \cos\vartheta_i \delta n_i = 0. \tag{A.12}$$

Adding up these equations yields:

$$\sum_{i=1}^{j} \left(\frac{\partial \ln W}{\partial n_i} + \alpha + \beta \cos\vartheta_i \right) \delta n_i = 0, \tag{A.13}$$

where the δn_i are independent of each other and it holds:

$$\frac{\partial \ln W}{\partial n_i} + \alpha + \beta \cos\vartheta_i = 0 \quad \forall\ i. \tag{A.14}$$

The first term can be rewritten by employing Equation A.7:

$$\ln\left(\frac{\sin\vartheta_i \Delta\vartheta_i}{2} \right) - \ln n_i + \alpha + \beta\cos\vartheta_i = 0. \tag{A.15}$$

This equation is satisfied by the most probable occupation numbers n_i^0 such that it holds:

$$n_i^0 = \mathrm{e}^{\alpha} \mathrm{e}^{\beta\cos\vartheta_i} \frac{\sin\vartheta_i \Delta\vartheta_i}{2}. \tag{A.16}$$

This yields for infinitesimally small intervals $\Delta\vartheta_i$:

$$\mathrm{d}N_\vartheta = \mathrm{e}^{\alpha} \mathrm{e}^{\beta\cos\vartheta} \frac{\sin\vartheta}{2}\, \mathrm{d}\vartheta. \tag{A.17}$$

The constants α and β can be obtained from

$$N = \frac{1}{2} \int_0^{\pi} \mathrm{e}^{\alpha} \mathrm{e}^{\beta\cos\vartheta} \sin\vartheta\, \mathrm{d}\vartheta = \frac{\mathrm{e}^{\alpha}}{\beta} \sinh\beta, \tag{A.18}$$

$$R = \frac{1}{2} \int_0^{\pi} \mathrm{e}^{\alpha} \mathrm{e}^{\beta\cos\vartheta} \sin\vartheta\, b\cos\vartheta\, \mathrm{d}\vartheta = b\frac{\mathrm{e}^{\alpha}}{\beta^2} \left(\beta\cosh\beta - \sinh\beta\right). \tag{A.19}$$

The first condition determines the parameter α. Dividing Equation A.19 through Equation A.18 allows for obtaining the parameter β:

$$\frac{R}{Nb} = \coth\beta - \frac{1}{\beta} = \mathcal{L}(\beta) \tag{A.20}$$

$$\Rightarrow \quad \beta = \mathcal{L}^{-1}\left(\frac{R}{Nb} \right), \tag{A.21}$$

where $\mathcal{L}(\beta)$ is the Langevin function. Consequently, the most probable distribution of the orientation angle ϑ is given as:

$$\mathrm{d}N_\vartheta = \frac{N\beta}{\sinh\beta}\mathrm{e}^{\beta\cos\vartheta}\frac{\sin\vartheta}{2}\,\mathrm{d}\vartheta. \tag{A.22}$$

From this equation, the logarithm of the probability density $p(R)$ can be derived [56]:

$$\ln p(R) = -N\left(\frac{R}{Nb}\beta + \ln\frac{\beta}{\sinh\beta}\right) + \text{const.} \tag{A.23}$$

Therefore, the conformational entropy of the polymer chain is given as

$$S(R) - S(0) = -k_\mathrm{B}\frac{R}{b}\mathcal{L}^{-1}\left(\frac{R}{Nb}\right). \tag{A.24}$$

Thus, it holds for the conformational contribution to the Gibbs free energy g and for the force f on the polymer chain:

$$g = -T\left(S(R) - S(0)\right) = \frac{k_\mathrm{B}T}{b}R\cdot\mathcal{L}^{-1}\left(\frac{R}{Nb}\right) \tag{A.25}$$

$$\vec{f} = -\frac{\partial g}{\partial\vec{R}} = -f\cdot\vec{e}_R \tag{A.26}$$

$$f = \frac{k_\mathrm{B}T}{b}\mathcal{L}^{-1}\left(\frac{R}{Nb}\right). \tag{A.27}$$

Connecting to SIC

In the following, it is anticipated that cl_c Kuhn segments in a the polymer chain are crystalline and oriented in the direction of the deformation which for instance is the z-direction. The number of Kuhn segments which are required to establish a crystalline segment is the so-called crystal length l_c and c denotes the number of crystalline segments. Hence, the end-to-end vector of the resulting crystalline chain segment is $\vec{c} = (0{,}0{,}cl_\mathrm{c}b)^\intercal$. The conformation of the crystalline chain segment is restricted to straightening along the stretching direction according to the theory for SIC by Flory [46]. Therefore, the crystalline segments to not contribute to the conformational entropy of a semi-crystalline polymer chain, but the $n-cl_\mathrm{c}$ amorphous segments do. Consequently, the modified conformational entropy for a semi-crystalline polymer chain is given as:

$$S\left(|\vec{R}-\vec{c}|\right) - S(0) = -k_\mathrm{B}\frac{|\vec{R}-\vec{c}|}{b}\mathcal{L}^{-1}\left(\frac{|\vec{R}-\vec{c}|}{(N-cl_\mathrm{c})\,b}\right). \tag{A.28}$$

Approximation of the Inverse Langevin Function

The inverse Langevin function is required for the computation of the Gibbs free energy and the force of a semi-crystalline link. Since it does not exist in a closed form, it can be obtained from numerical methods or approximations [266]. Either Taylor expansions or Padé approximations can be employed. The first are suitable for the approximation around zero, while the latter describe the asymptotic behavior for large extension in the vicinity of one properly. Jedynak [266] proposed a rounded N-point Padé approximation formula for the inverse Langevin function with a comparatively high accuracy which is given as follows:

$$\mathcal{L}^{-1}(y) \approx y\frac{3.0 - 2.6y + 0.7y^2}{1 - 0.9y - 0.1y^2} \tag{A.29}$$

Applying this approximation to the conformational contribution to the Gibbs free energy and the force of a semi-crystalline polymer chain yields:

$$g \approx \frac{k_\mathrm{B}T}{b}|\vec{R}-\vec{c}| \cdot \frac{|\vec{R}-\vec{c}|}{(N-cl_\mathrm{c})\,b} \frac{3.0-2.6\frac{|\vec{R}-\vec{c}|}{(N-cl_\mathrm{c})b}+0.7\left(\frac{|\vec{R}-\vec{c}|}{(N-cl_\mathrm{c})b}\right)^2}{1-0.9\frac{|\vec{R}-\vec{c}|}{(N-cl_\mathrm{c})b}-0.1\left(\frac{|\vec{R}-\vec{c}|}{(N-cl_\mathrm{c})b}\right)^2} \tag{A.30}$$

$$f \approx \frac{k_\mathrm{B}T}{b} \cdot \frac{|\vec{R}-\vec{c}|}{(N-cl_\mathrm{c})\,b} \frac{3.0-2.6\frac{|\vec{R}-\vec{c}|}{(N-cl_\mathrm{c})b}+0.7\left(\frac{|\vec{R}-\vec{c}|}{(N-cl_\mathrm{c})b}\right)^2}{1-0.9\frac{|\vec{R}-\vec{c}|}{(N-cl_\mathrm{c})b}-0.1\left(\frac{|\vec{R}-\vec{c}|}{(N-cl_\mathrm{c})b}\right)^2}. \tag{A.31}$$

Note that this approximation yields the free energy and force for the case of Gaussian chains in the limit of small end-to-end distances.

In the following, energies are given in units of $k_\mathrm{B}T$ and lengths in units of the Kuhn length b and it is set $k_\mathrm{B}T = 1$ and $b = 1$. Under the constraint that the end-to-end vector of the semi-crystalline polymer chain is oriented in the same direction as the end-to-end vector of the crystalline segments, i.e. the z-direction, it holds:

$$g = (r-cl_\mathrm{c}) \cdot \frac{r-cl_\mathrm{c}}{N-cl_\mathrm{c}} \frac{3.0-2.6\frac{r-cl_\mathrm{c}}{N-cl_\mathrm{c}}+0.7\left(\frac{r-cl_\mathrm{c}}{N-cl_\mathrm{c}}\right)^2}{1-0.9\frac{r-cl_\mathrm{c}}{N-cl_\mathrm{c}}-0.1\left(\frac{r-cl_\mathrm{c}}{N-cl_\mathrm{c}}\right)^2} \tag{A.32}$$

$$f = \frac{r-cl_\mathrm{c}}{N-cl_\mathrm{c}} \frac{3.0-2.6\frac{r-cl_\mathrm{c}}{N-cl_\mathrm{c}}+0.7\left(\frac{r-cl_\mathrm{c}}{N-cl_\mathrm{c}}\right)^2}{1-0.9\frac{r-cl_\mathrm{c}}{N-cl_\mathrm{c}}-0.1\left(\frac{r-cl_\mathrm{c}}{N-cl_\mathrm{c}}\right)^2}. \tag{A.33}$$

These expressions can be applied for the simulation of a strain-crystallizing elastomer network.

A.9.2. Testing the Model

In order to validate the model for a finite-extensible unfilled network, a 2D-network consisting of $N = 196$ nodes is simulated and the corresponding stress-stretch curves for the crystallizing and the non-crystallizing case and the crystallinity-stretch curve are plotted in Figure A.117. For comparison, the curves for corresponding Gaussian networks are also shown. In addition, snapshots of the finite-extensible crystallizing network are presented in Figure A.118.

In the case of the finite-extensible networks, the stress-stretch curve for the non-crystallizing network shows the expected increase due to the finite extensibility. In the finite-extensible network, crystallization starts at small stretch $\lambda \approx 1.7$, whereas begins at $\lambda \approx 3$ in the case of Gaussian chains. The reason is that the finite-extensible network is not as sensitive to the value of the penalty θ_0 which determines the onset of SIC. In experiments, the onset of SIC is also obtained at higher stretches. The increase in the crystallinity is linear. At the maximum stretch $\lambda = 5$, the crystallinity amounts to $\chi = 0.3$. This value is a result from the small maximum stretch at which a significant amount of links may not be extended sufficiently. The crystallinity has not completely vanished when the sample returned to its original shape. The stress-stretch curve for the crystallizing finite-extensible network levels of in a plateau as crystallization begins. However, the steep increase which can be observed at high stretches for the Gaussian chains does not occur. This verifies that the upturn in the case of Gaussian chains originates from unphysical end-to-end distances of the links which exceed their contour length, i.e. $r > n$. By comparison with the Gaussian network, it is found that the upturn in the stress-stretch curve for the crystallizing network starts around $\lambda = 6.0$

which is the stretch around which the FIRE algorithm does not converge anymore in the case of chains with finite extensibility. Moreover, a hysteresis can be observed in both the stress-stretch and the crystallinity-stretch curve.

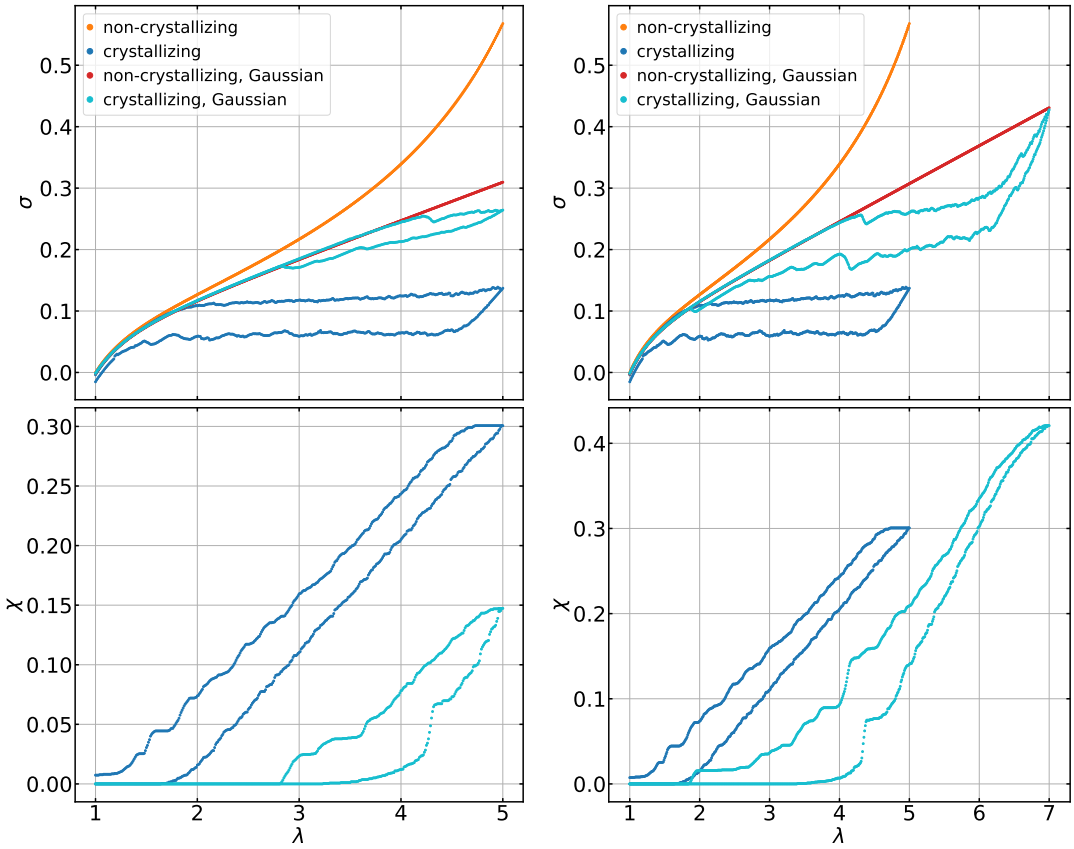

Figure A.117.: Stress-stretch curves for a network of Gaussian chains and a network consisting of chains with finite extensibility obtained from the simulation of 2D-networks of $N = 196$ nodes with $\kappa = 0.1$, $\mu = 49$ and $\sigma_\mu = \mu/5$.

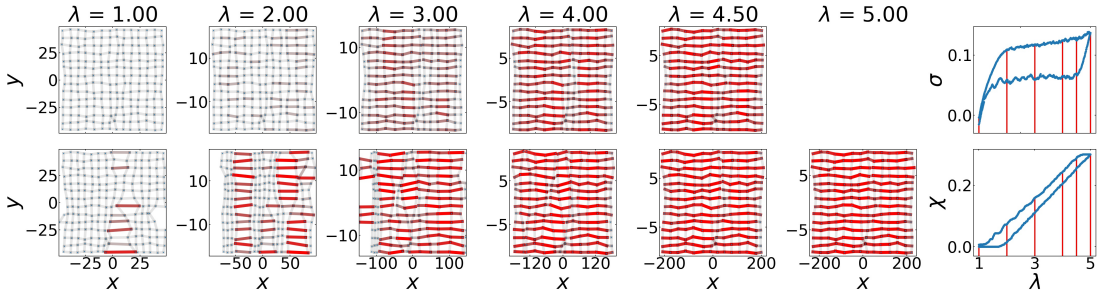

Figure A.118.: Snapshots of a finite-extensible 2D-network of $N = 196$ nodes during a strain cycle and corresponding stress-stretch and crystallinity-stretch curves. The upper row corresponds to the stretching along the x-axis and the lower row to the contraction of the network. The redder and the thicker a link is drawn, the higher is its crystallinity. Moreover, the vertical lines in the stress-stretch and crystallinity-stretch curves mark the stretches at which the snapshots are taken.

Choosing a larger value for $\lambda_{\max}$, for instance $\lambda_{\max} = 6.0$ or $\lambda_{\max} = 7.0$, inhibits the FIRE algorithm from convergence at high stretches λ. This occurs also for larger networks, e.g. $N = 1032$. Nevertheless, this observation is consistent since the number

of Kuhn segments for each link is drawn from a Gaussian distribution with $\mu = 49$ and $\sigma_\mu = \mu/5$. Therefore, the network contains a significant number of links with fewer than $\mu = 49$ Kuhn segments. These shorter links cannot be as highly expanded. Note that the inverse Langevin function and its approximation in Equation A.29 possess a singularity at $r/n = 1$.

In order to capture the increase of the stress beyond the plateau for crystallizing finite-extensible model networks, the parameters of the FIRE algorithm have been adapted, the original FIRE algorithm has been replaced by an advanced version of it proposed by Guénolé *et al.* [267], and the applied MD integrator has been changed from the velocity-Verlet algorithm to the implicit Euler method. With these adjustments, convergence of the algorithm has been achieved in the non-crystallizing case until $\lambda_{\max} = 6.0$, but, for the crystallizing networks, there are still instabilities. Figure A.119 shows exemplary stress-stretch curves for crystallizing and non-crystallizing networks consisting of $N = 196$ nodes for which the FIRE 2.0 algorithm converges at any stretch in both cases.

To improve this approach further, a rupture criterion for the links may be implemented such that links break if their end-to-end distance is sufficiently close to their contour length. This possibly avoids the convergence issues.

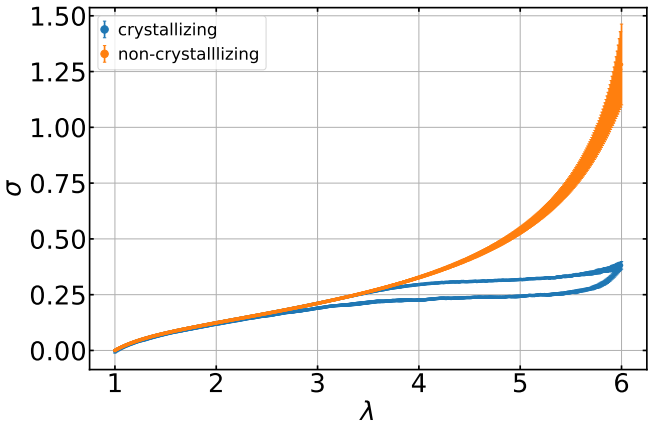

Figure A.119.: Stress-stretch curves for crystallizing and a non-crystallizing finite-extensible 2D-networks consisting of $N = 196$ nodes obtained as averages of 10 simulations. The FIRE 2.0 algorithm with the implicit Euler method as MD integrator is implemented and it is set $\Delta t_{\max} = 0.05$ and $\theta_0 = 3.5$.

References

1. Plagge, J. & Hentschke, R. Microphase Separation in Strain-Crystallizing Rubber. *Macromolecules* **54,** 5629–5635. doi:10.1021/acs.macromol.1c00757 (2021).
2. Viktorova, M. *et al.* Mesoscopic Model for the Simulation of Dynamic Mechanical Properties of Filled Elastomers: Model Construction and Parameterization. *ACS Applied Polymer Materials* **2,** 5521–5532. doi:10.1021/acsapm.0c00868 (2020).
3. Tarrach, L. *Modelling Study of Reinforcement and Crack Formation in Strain-Crystallizing Elastomer Networks* Master Thesis. Bergische Universität Wuppertal (unpublished). Mar. 2022.
4. Tarrach, L., Hentschke, R. & Weilert, J. Modelling Study of Reinforcement and Rupture in Strain-Crystallizing Elastomer Networks. *Kautschuk Gummi Kunststoffe KGK* **3,** 62–71 (2023).
5. Röthemeyer, F. & Sommer, F. *Kautschuktechnologie* ISBN: 978-3-446-43776-0 (Carl Hanser Verlag, München, 2013).
6. Huneau, B. STRAIN-INDUCED CRYSTALLIZATION OF NATURAL RUBBER: A REVIEW OF X-RAY DIFFRACTION INVESTIGATIONS. *Rubber Chemistry and Technology* **84,** 425–452. ISSN: 0035-9475. doi:10.5254/1.3601131 (2011).
7. Trabelsi, S., Albouy, P.-A. & Rault, J. Crystallization and Melting Processes in Vulcanized Stretched Natural Rubber. *Macromolecules* **36,** 7624–7639. doi:10.1021/ma030224c (2003).
8. Chenal, J.-M. *et al.* Molecular weight between physical entanglements in natural rubber: A critical parameter during strain-induced crystallization. *Polymer* **48,** 1042–1046. ISSN: 0032-3861. doi:10.1016/j.polymer.2006.12.031 (2007).
9. Candau, N. *et al.* Strain-Induced Crystallization of Natural Rubber and Cross-Link Densities Heterogeneities. *Macromolecules* **47,** 5815–5824. doi:10.1021/ma5006843 (2014).
10. Toki, S. *et al.* Entanglements and Networks to Strain-Induced Crystallization and Stress–Strain Relations in Natural Rubber and Synthetic Polyisoprene at Various Temperatures. *Macromolecules* **46,** 5238–5248. doi:10.1021/ma400504k (2013).
11. Wang, M.-J. & Morris, M. *Rubber Reinforcement with Particulate Fillers* ISBN: 978-1-56990-719-1 (Carl Hanser Verlag GmbH & Co. KG, 2021).
12. Payne, A. R. & Whittaker, R. E. Low Strain Dynamic Properties of Filled Rubbers. *Rubber Chemistry and Technology* **44,** 440–478. ISSN: 0035-9475. doi:10.5254/1.3547375 (1971).
13. Sambrook, R. W. Influence of Temperature on the Tensile Strength of Carbon Filled Vulcanizates. *Rubber Chemistry and Technology* **44,** 728–743. ISSN: 0035-9475. doi:10.5254/1.3544789 (1971).
14. Boonstra, B. Role of particulate fillers in elastomer reinforcement: a review. *Polymer* **20,** 691–704. ISSN: 0032-3861. doi:10.1016/0032-3861(79)90243-X (1979).
15. Tunnicliffe, L. B. *et al.* Flocculation and Viscoelastic Behaviour in Carbon Black-Filled Natural Rubber. *Macromolecular Materials and Engineering* **299,** 1474–1483. doi:10.1002/mame.201400117 (2014).
16. Stöckelhuber, K. W. *et al.* Impact of Filler Surface Modification on Large Scale Mechanics of Styrene Butadiene/Silica Rubber Composites. *Macromolecules* **44,** 4366–4381. doi:10.1021/ma1026077 (2011).
17. Hentschke, R. The Payne effect revisited. *Express Polymer Letters* **11,** 278–292. doi:10.3144/expresspolymlett.2017.28 (2017).

18. Trabelsi, S., Albouy, P.-A. & Rault, J. Effective Local Deformation in Stretched Filled Rubber. *Macromolecules* **36,** 9093–9099. doi:10.1021/ma0303566 (2003).

19. Poompradub, S. *et al.* Mechanism of strain-induced crystallization in filled and unfilled natural rubber vulcanizates. *Journal of Applied Physics* **97,** 103529. doi:10.1063/1.1900927 (2005).

20. Chenal, J.-M. *et al.* Parameters governing strain induced crystallization in filled natural rubber. *Polymer* **48,** 6893–6901. ISSN: 0032-3861. doi:10.1016/j.polymer.2007.09.023 (2007).

21. Candau, N. *et al.* Compared abilities of filled and unfilled natural rubbers to crystallize in a large strain rate domain. *Composites Science and Technology* **108,** 9–15. ISSN: 0266-3538. doi:10.1016/j.compscitech.2014.12.014 (2015).

22. Rault, J. *et al.* Stress-Induced Crystallization and Reinforcement in Filled Natural Rubbers: ^{2}H NMR Study. *Macromolecules* **39,** 8356–8368. doi:10.1021/ma0608424 (2006).

23. Spratte, T. *et al.* Investigation of strain-induced crystallization of carbon black and silica filled natural rubber composites based on mechanical and temperature measurements. *Polymer* **115,** 12–20. ISSN: 0032-3861. doi:10.1016/j.polymer.2017.03.019 (2017).

24. Azura, A. R., Ghazali, S. & Mariatti, M. Effects of the filler loading and aging time on the mechanical and electrical conductivity properties of carbon black filled natural rubber. *Journal of Applied Polymer Science* **110,** 747–752. doi:10.1002/app.28517 (2008).

25. Plagge, J. Mastering of Filled Rubber Strength beyond WLF: Competition of Temperature, Time, Crack Deflection and Bond Breaking. *Polymers* **14.** ISSN: 2073-4360. doi:10.3390/polym14040765 (2022).

26. A. M. Sadequl, B. T. P. & Ishiaku, U. S. Effect of Filler Loading on the Mechanical Properties of Epoxidized Natural Rubber (ENR 25) Compared with Natural Rubber (SMR L). *International Journal of Polymeric Materials and Polymeric Biomaterials* **43,** 261–278. doi:10.1080/00914039908009689 (1999).

27. Savetlana, S. *et al.* The effect of carbon black loading and structure on tensile property of natural rubber composite. *IOP Conference Series: Materials Science and Engineering* **223,** 012009. doi:https://dx.doi.org/10.1088/1757-899X/223/1/012009 (2017).

28. Azura, A. & Leow, S. Effect of carbon black loading on mechanical, conductivity and ageing properties of Natural Rubber composites. *Materials Today: Proceedings* **17.** 6th International Conference on Recent Advances in Materials, Minerals & Environment (RAMM) 2018, 27 - 29 November 2018, Penang, Malaysia, 1056–1063. ISSN: 2214-7853. doi:10.1016/j.matpr.2019.06.512 (2019).

29. Boyce, M. C. & Arruda, E. M. Constitutive Models of Rubber Elasticity: A Review. *Rubber Chemistry and Technology* **73,** 504–523. ISSN: 0035-9475. doi:10.5254/1.3547602 (2000).

30. Marckmann, G. & Verron, E. Comparison of Hyperelastic Models for Rubber-Like Materials. *Rubber Chemistry and Technology* **79,** 835–858. ISSN: 0035-9475. doi:10.5254/1.3547969 (2006).

31. Dal, H., Açıkgöz, K. & Badienia, Y. On the Performance of Isotropic Hyperelastic Constitutive Models for Rubber-Like Materials: A State of the Art Review. *Applied Mechanics Reviews* **73,** 020802. ISSN: 0003-6900. doi:10.1115/1.4050978 (2021).

32. Smith, S. M. & Simmons, D. S. HORIZONS FOR DESIGN OF FILLED RUBBER INFORMED BY MOLECULAR DYNAMICS SIMULATION. *Rubber Chemistry and Technology* **90,** 238–263. ISSN: 0035-9475. doi:10.5254/rct.17.82668 (2017).

33. Xie, B.-G. *et al.* A combined simulation and experiment study on polyisoprene rubber composites. *Composites Science and Technology* **200,** 108398. ISSN: 0266-3538. doi:10.1016/j.compscitech.2020.108398 (2020).

34. Yang, H. *et al.* Micromechanics models of particulate filled elastomer at finite strain deformation. *Composites Part B: Engineering* **45,** 881–887. ISSN: 1359-8368. doi:10.1016/j.compositesb.2012.07.011 (2013).

35. Lopez-Pamies, O., Goudarzi, T. & Nakamura, T. The nonlinear elastic response of suspensions of rigid inclusions in rubber: I—An exact result for dilute suspensions. *Journal of the Mechanics and Physics of Solids* **61,** 1–18. doi:10.1016/j.jmps.2012.08.010 (2013).

36. Yao, Y. *et al.* An alternative constitutive model for elastic particle-reinforced hyperelastic matrix composites with explicitly expressed Eshelby tensor. *Composites Science and Technology* **221,** 109343. doi:10.1016/j.compscitech.2022.109343 (2022).

37. Hagita, K., Morita, H. & Takano, H. Molecular dynamics simulation study of a fracture of filler-filled polymer nanocomposites. *Polymer* **99,** 368–375. ISSN: 0032-3861. doi:10.1016/j.polymer.2016.07.030 (2016).

38. Viktorova, M. *et al.* Simulation of elastomer nanocomposites: Interfacial stresses and strains related to filler dispersion, global deformation and the Payne effect. *Computational Materials Science* **223,** 112144. ISSN: 0927-0256. doi:10.1016/j.commatsci.2023.112144 (2023).

39. Knauert, S. T., Douglas, J. F. & Starr, F. W. The effect of nanoparticle shape on polymer-nanocomposite rheology and tensile strength. *Journal of Polymer Science Part B: Polymer Physics* **45,** 1882–1897. doi:10.1002/polb.21176 (2007).

40. Hanson, D. E. & Barber, J. L. The theoretical strength of rubber: numerical simulations of polyisoprene networks at high tensile strains evidence the role of average chain tortuosity. *Modelling and Simulation in Materials Science and Engineering* **21,** 075013. doi:10.1088/0965-0393/21/7/075013 (2013).

41. Arash, B., Park, H. S. & Rabczuk, T. Tensile fracture behavior of short carbon nanotube reinforced polymer composites: A coarse-grained model. *Composite Structures* **134,** 981–988. ISSN: 0263-8223. doi:10.1016/j.compstruct.2015.09.001 (2015).

42. Koyanagi, J. *et al.* Molecular dynamics simulation for the quantitative prediction of experimental tensile strength of a polymer material. *Composites Part C: Open Access* **2,** 100041. ISSN: 2666-6820. doi:10.1016/j.jcomc.2020.100041 (2020).

43. David, A. *et al.* Fracture in Silica/Butadiene Rubber: A Molecular Dynamics View of Design–Property Relationships. *ACS Polymers Au* **1,** 175–186. doi:10.1021/acspolymersau.1c00023 (2021).

44. Dargazany, R. *et al.* Constitutive modeling of strain-induced crystallization in filled rubbers. *Phys. Rev. E* **89,** 022604. doi:10.1103/PhysRevE.89.022604 (2 2014).

45. Chen, Q. *et al.* Manipulating the mechanical properties of cis-polyisoprene nanocomposites via molecular dynamics simulation. *Polymer* **256,** 125233. ISSN: 0032-3861. doi:10.1016/j.polymer.2022.125233 (2022).

46. Flory, P. J. Thermodynamics of Crystallization in High Polymers. I. Crystallization Induced by Stretching. *The Journal of Chemical Physics* **15,** 397–408. doi:10.1063/1.1746537 (1947).

47. Laghmach, R. *et al.* Phase field modelling of strain induced crystal growth in an elastic matrix. *The Journal of Chemical Physics* **142,** 244905. ISSN: 0021-9606. doi:10.1063/1.4923226 (2015).

48. Guo, Q., Zaïri, F. & Guo, X. Thermodynamics and mechanics of stretch-induced crystallization in rubbers. *Phys. Rev. E* **97,** 052501. doi:10.1103/PhysRevE.97.052501 (5 2018).

49. Khiêm, V. N. & Itskov, M. Analytical network-averaging of the tube model: Strain-induced crystallization in natural rubber. *Journal of the Mechanics and Physics of Solids* **116,** 350–369. ISSN: 0022-5096. doi:10.1016/j.jmps.2018.04.003 (2018).

50. Tarrach, L. & Hentschke, R. A mesoscopic computer model for reinforcement in filled and strain-crystallizing elastomer networks. *Computational Materials Science* **246,** 113374. doi:10.1016/j.commatsci.2024.113374 (2025).

51. IUPAC. in *Compendium of Chemical Terminology. The Gold Book* (eds McNaught, A. D. & Wilkinson, A.) 2nd ed. (Blackwell Scientific Publications, Oxford, 1997). ISBN: 0-9678550-9-8. https://doi.org/10.1351/goldbook.

52. Lechner, M. D., Gehrke, K. & Nordmeier, E. H. *Makromolekulare Chemie* https://doi.org/10.1007/978-3-642-41769-6 (Springer Spektrum, Berlin, Heidelberg, 2014).

53. Sircar, A. K. *et al.* Glass Transition of Elastomers Using Thermal Analysis Techniques. *Rubber Chemistry and Technology* **72,** 513–552. ISSN: 0035-9475. doi:10.5254/1.3538816 (1999).

54. Makhiyanov, N. & Khasanov, M. N. Glass Transition Parameters of Polyisoprene Rubbers: Differential Scanning Calorimetry Study. *Polymer Science, Series A* **63,** 220–227. doi:10.1134/S0965545X21030093 (2021).

55. Rubinstein, M. & Colby, R. H. *Polymer Physics* (Oxford University Press, 2003).

56. Treloar, L. R. G. *The Physics of Rubber Elasticity* 3rd ed. (Clarendon Press, Oxford, 2005).

57. Wall, F. T. & Flory, P. J. Statistical Thermodynamics of Rubber Elasticity. *J. Chem. Phys.* **19,** 1435. doi:10.1063/1.1748098 (1951).

58. De Gennes, P.-G. *Scaling Concepts in Polymer Physics* (Cornell University Press, 1979).

59. Mark, J. E. Rubber elasticity. *Journal of Chemical Education* **58,** 898. doi:10.1021/ed058p898 (1981).

60. Hentschke, R. *Thermodynamics. For Physicists, Chemists and Materials Scientists* 2nd ed. doi:https://doi.org/10.1007/978-3-030-93879-6 (Springer Cham, 2022).

61. Smallwood, H. M. Limiting Law of the Reinforcement of Rubber. *Journal of Applied Physics* **15,** 758–766. doi:10.1063/1.1707385 (1944).

62. Einstein, A. Eine neue Bestimmung der Moleküldimensionen. *Annalen der Physik* **324,** 289–306. doi:10.1002/andp.19063240204 (1906).

63. Einstein, A. Berichtigung zu meiner Arbeit: „Eine neue Bestimmung der Moleküldimensionen". *Annalen der Physik* **339,** 591–592. doi:10.1002/andp.19113390313 (1911).

64. Guth, E. Theory of Filler Reinforcement. *Journal of Applied Physics* **16,** 20–25. doi:10.1063/1.1707495 (1945).

65. Omnès, B. *et al.* Effective properties of carbon black filled natural rubber: Experiments and modeling. *Composites Part A: Applied Science and Manufacturing* **39,** 1141–1149. ISSN: 1359-835X. doi:10.1016/j.compositesa.2008.04.003 (2008).

66. Chanda, J. *et al.* Fatigue crack growth behavior and morphological analysis of natural rubber compounds with varying particle size and structure of carbon black. *Polymer Engineering & Science* **62,** 743–757. doi:10.1002/pen.25881 (2022).

67. Guth, E. & Simha, R. Untersuchungen über die Viskosität von Suspensionen und Lösungen. 3. Über die Viskosität von Kugelsuspensionen. *Kolloid-Zeitschrift* **74,** 266–275. doi:10.1007/BF01428643 (1936).

68. Guth, E. & Gold, O. Viscosity and Electroviscous Effect of the AgI Sol. II. Influence of the Concentration of AgI and of Electrolyte on the Viscosity. *Phys. Rev.* **53,** 322 (1938).

69. Vand, V. Viscosity of Solutions and Suspensions. I. Theory. *The Journal of Physical and Colloid Chemistry* **52,** 277–299. doi:10.1021/j150458a001 (1948).

70. Saitô, N. Concentration dependence of the viscosity of high polymer solutions. I. *Journal of the Physical Society of Japan* **5,** 4–8 (1950).

71. Mooney, M. The viscosity of a concentrated suspension of spherical particles. *Journal of Colloid Science* **6,** 162–170. ISSN: 0095-8522. doi:10.1016/0095-8522(51)90036-0 (1951).

72. Roscoe, R. The viscosity of suspensions of rigid spheres. *British Journal of Applied Physics* **3,** 267. doi:10.1088/0508-3443/3/8/306 (1952).

73. Batchelor, G. K. & Green, J. T. The determination of the bulk stress in a suspension of spherical particles to order c^2. *Journal of Fluid Mechanics* **56,** 401–427. doi:10.1017/S0022112072002435 (1972).

74. Russel, W. B. & Gast, A. P. Nonequilibrium statistical mechanics of concentrated colloidal dispersions: Hard spheres in weak flows. *The Journal of Chemical Physics* **84,** 1815–1826. ISSN: 0021-9606. doi:10.1063/1.450428 (1986).

75. Felderhof, B. U. *Hydrodynamics of Suspensions* in *Fundamental Problems in Statistical Mechanics VII. Proceedings of the 1989 Altenberg Summer School* (ed van Beijeren, H.) (North-Holland, 1990), 225–254.

76. Hess, W. M. & McDonald, G. C. Improved Particle Size Measurements on Pigments for Rubber. *Rubber Chemistry and Technology* **56,** 892–917. ISSN: 0035-9475. doi:10.5254/1.3538171 (1983).

77. Vilgis, T. A., Heinrich, G. & Klüppel, M. *Reinforcement of Polymer Nano-Composites* (Cambridge University Press, Cambridge, 2009).

78. Marangoni, A. & Wesdorp, L. *Structure and Properties of Fat Crystal Networks* 2nd ed. 10.1201/b12883 (CRC Press, 2012).

79. Buscall, R. *et al.* Scaling behaviour of the rheology of aggregate networks formed from colloidal particles. *J. Chem. Soc., Faraday Trans. 1* **84,** 4249–4260. doi:http://dx.doi.org/10.1039/F19888404249 (12 1988).

80. Weitz, D. A. & Oliveria, M. Fractal Structures Formed by Kinetic Aggregation of Aqueous Gold Colloids. *Phys. Rev. Lett.* **52,** 1433–1436. doi:10.1103/PhysRevLett.52.1433 (16 1984).

81. Brown, W. D. & Ball, R. C. Computer simulation of chemically limited aggregation. *Journal of Physics A: Mathematical and General* **18,** L517. doi:10.1088/0305-4470/18/9/006 (1985).

82. Meakin, P. Formation of Fractal Clusters and Networks by Irreversible Diffusion-Limited Aggregation. *Phys. Rev. Lett.* **51,** 1119–1122. doi:10.1103/PhysRevLett.51.1119 (13 1983).

83. Kolb, M., Botet, R. & Jullien, R. Scaling of Kinetically Growing Clusters. *Phys. Rev. Lett.* **51,** 1123–1126. doi:10.1103/PhysRevLett.51.1123 (13 1983).

84. Mandelbrot, B. B. *Fractals: Form, Chance and Dimension* (W. H. Freeman and Co., New York, 1977).

85. Mandelbrot, B. B. *The Fractal Geometry of the Nature* (W. H. Freeman and Co., New York, 1982).

86. Meakin, P., Donn, B. & Mulholland, G. W. Collisions between Point Masses and Fractal Aggregates. *Langmuir* **5,** 510 (1989).

87. Meakin, P. Fractal aggregates. *Advances in Colloid and Interface Science* **28,** 249–331. ISSN: 0001-8686. doi:10.1016/0001-8686(87)80016-7 (1987).

88. Xi, H. & Hentschke, R. The Influence of Structure on Mechanical Properties of Filler Networks Via Coarse-Grained Modeling. *Macromolecular Theory and Simulations* **23,** 373–382. doi:10.1002/mats.201400009 (2014).

89. Maier, P. & Göritz, D. Molecular Interpretation of the Payne effect. *Kautschuk Gummi Kunststoffe* **49** (1996).

90. Wang, M.-J. The Role of Filler Networking in Dynamic Properties of Filled Rubber. *Rubber Chemistry and Technology* **72,** 430–448. ISSN: 0035-9475. doi:10.5254/1.3538812 (1999).

91. Luginsland, H.-D., Fröhlich, J. & Wehmeier, A. *Reinforcement of Silica-Filled Rubber Compounds* (DEGUSSA, Technical Report: 819, 2001).

92. Klüppel, M., Schuster, R. H. & Heinrich, G. Structure and Properties of Reinforcing Fractal Filler Networks in Elastomers. *Rubber Chemistry and Technology* **70,** 243–255. ISSN: 0035-9475. doi:10.5254/1.3538429 (1997).

93. Payne, A. R. The Elasticity of Carbon Black Networks. *Journal of Colloid Science* **19,** 744–754 (1964).

94. Hentschke, R. in *Constitutive Models for Rubber VIII. Proceedings of the 8th European Conference on Constitutive Models for Rubbers* (eds Gil-Negrete, N. & Alonso, A.) 299–304 (CRC Press, 2013). ISBN: 978-1-138-00072-8.

95. Israelachvili, J. N. *Intermolecular & Surface Forces* 2nd ed. (Academic Press, 1991).

96. Ouyang, G. Modulus, hysteresis and the Payne effect. *Kautschuk Gummi Kunststoffe KGK* **59,** 332–343 (2006).

97. Hentschke, R., Hager, J. & Hojdis, N. W. Molecular modeling approach to the prediction of mechanical properties of silica-reinforced rubbers. *Journal of Applied Polymer Science* **131.** doi:10.1002/app.40806 (2014).

98. Donnet, J.-B. & Custodero, E. in *The Science and Technology of Rubber (Fourth Edition)* (eds Mark, J. E., Erman, B. & Roland, C. M.) Fourth Edition, 383–416 (Academic Press, Boston, 2013). ISBN: 978-0-12-394584-6. doi:10.1016/B978-0-12-394584-6.00008-X.

99. Dannenberg, E. M. The Effects of Surface Chemical Interactions on the Properties of Filler-Reinforced Rubbers. *Rubber Chemistry and Technology* **48,** 410–444. ISSN: 0035-9475. doi:10.5254/1.3547460 (1975).

100. Mitchell, G. A wide-angle X-ray study of the development of molecular orientation in crosslinked natural rubber. *Polymer* **25,** 1562–1572. ISSN: 0032-3861. doi:10.1016/0032-3861(84)90148-4 (1984).

101. Sainumsai, W. *et al.* DEPENDENCE OF THE ONSET OF STRAIN-INDUCED CRYSTALLIZATION OF NATURAL RUBBER AND ITS SYNTHETIC ANALOGUE ON CROSSLINK AND ENTANGLEMENT BY USING SYNCHROTRON X-RAY. *Rubber Chemistry and Technology* **90,** 728–742. ISSN: 0035-9475. doi:10.5254/rct.18.82693 (2017).

102. Gros, A. *et al.* Dominating factor of strain-induced crystallization in natural rubber. *Polymer* **76,** 230–236. ISSN: 0032-3861. doi:10.1016/j.polymer.2015.08.058 (2015).

103. Brüning, K. *et al.* Kinetics of Strain-Induced Crystallization in Natural Rubber Studied by WAXD: Dynamic and Impact Tensile Experiments. *Macromolecules* **45,** 7914–7919. doi:10.1021/ma3011476 (2012).

104. Luch, D. & Yeh, G. S. Y. Morphology of strain-induced crystallization of natural rubber. I. Electron microscopy on uncrosslinked thin film. *Journal of Applied Physics* **43,** 4326–4338. ISSN: 0021-8979. doi:10.1063/1.1660923 (1972).

105. Ferry, J. D. *Viscoelastic Properties of Polymers* 3rd (John Wiley & Sons, 1980).

106. Strobl, G. *The Physics of Polymers* 3rd. ISBN: 978-3-540-68411-4. https://doi.org/10.1007/978-3-540-68411-4 (Springer Berlin, Heidelberg, 2007).

107. Wrana, C. *Polymerphysik* ISBN: 978-3-642-45075-4. doi:10.1007/978-3-642-45076-1 (Springer Sprektrum, Berlin, Heidelberg, 2014).

108. Fetters, L. J., Lohse, D. J. & Colby, R. H. in *Physical Properties of Polymers Handbook* (ed Mark, J. E.) 447–454 (Springer New York, New York, NY, 2007). ISBN: 978-0-387-69002-5. doi:10.1007/978-0-387-69002-5_25.

109. Fetters, L. J. *et al.* Packing Length Influence in Linear Polymer Melts on the Entanglement, Critical, and Reptation Molecular Weights. *Macromolecules* **32,** 6847–6851. doi:10.1021/ma990620o (1999).

110. National Institute of Standards and Technology. *NIST Cheministry WebBook, SRD 69. Isoprene* https://webbook.nist.gov/cgi/cbook.cgi?ID=C78795&Mask=200 (2023).

111. National Institute of Standards and Technology. *NIST Cheministry WebBook, SRD 69. sulfur* https://webbook.nist.gov/cgi/inchi?ID=C7704349&Mask=40 (2023).

112. Flory, P. J. & Rehner John, J. Statistical Mechanics of Cross-Linked Polymer Networks II. Swelling. *The Journal of Chemical Physics* **11,** 521–526. doi:10.1063/1.1723792 (1943).

113. ASTM-D1765. Standard Classification System for Carbon Blacks Used in Rubber Products. doi:10.1520/D1765-23A.

114. Bera, M., Gupta, P. & Maji, P. K. in *Carbon-Containing Polymer Composites* (eds Rahaman, M., Khastgir, D. & Aldalbahi, A. K.) 457–502 (Springer Singapore, Singapore, 2019). ISBN: 978-981-13-2688-2. doi:10.1007/978-981-13-2688-2_13.

115. Fei, Z. *et al.* Influence of Carbon Black on Crosslink Density of Natural Rubber. *Journal of Macromolecular Science, Part B* **51,** 1208–1217. doi:10.1080/00222348.2012.664494 (2012).

116. Medalia, A. I. Effective Degree of Immobilization of Rubber Occluded within Carbon Black Aggregates. *Rubber Chemistry and Technology* **45,** 1171–1194. ISSN: 0035-9475. doi:10.5254/1.3544731 (1972).

117. Wolff, S. & Donnet, J.-B. Characterization of Fillers in Vulcanizates According to the Einstein-Guth-Gold Equation. *Rubber Chemistry and Technology* **63,** 32–45. ISSN: 0035-9475. doi:10.5254/1.3538240 (1990).

118. Menard, K. P. & Menard, N. *Dynamic Mechanical Analysis* 3rd ed. doi:10.1201/9780429190308 (CRC Press, 2020).

119. Hentschke, R. *ClassicalMechanics: Including an Introduction to the Theory of Elasticity* https://doi.org/10.1007/978-3-319-48710-6 (Springer, 2017).

120. Hentschke, R. *A concise Introduction to Polymer Physics - Theoretical Concepts and Applications* Lecture Notes. April 8, 2024. https://constanze.materials.uni-wuppertal.de/fileadmin/physik/theochemphysik/Skripten/rsc-polymerphysics.pdf.

121. Doolittle, A. K. Studies in Newtonian Flow. II. The Dependence of the Viscosity of Liquids on Free-Space. *Journal of Applied Physics* **22,** 1471–1475. ISSN: 0021-8979. doi:10.1063/1.1699894 (1951).

122. Williams, M. L., Landel, R. F. & Ferry, J. D. The Temperature Dependence of Relaxation Mechanisms in Amorphous Polymers and Other Glass-forming Liquids. *Journal of the American Chemical Society* **77,** 3701–3707. doi:10.1021/ja01619a008 (1955).

123. Hu, X.-L. *et al.* Temperature and frequency dependent rheological behaviour of carbon black filled natural rubber. *Plastics, Rubber and Composites* **42,** 416–420. doi:10.1179/1743289813Y.0000000060 (2013).

124. Tanaka, Y. Structural Characterization of Natural Polyisoprenes: Solve the Mystery of Natural Rubber Based on Structural Study. *Rubber Chemistry and Technology* **74,** 355–375. ISSN: 0035-9475. doi:10.5254/1.3547643 (2001).

125. Amnuaypornsri, S. *et al.* The effects of endlinking network and entanglement to stress–strain relation and strain-induced crystallization of un-vulcanized and vulcanized natural rubber. *Polymer* **53,** 3325–3330. ISSN: 0032-3861. doi:10.1016/j.polymer.2012.05.020 (2012).

126. Zhang, X. *et al.* Visualization and Quantification of the Microstructure Evolution of Isoprene Rubber during Uniaxial Stretching Using AFM Nanomechanical Mapping. *Macromolecules* **53,** 3082–3089. doi:10.1021/acs.macromol.9b02656 (2020).

127. Albouy, P.-A., Marchal, J. & Rault, J. Chain orientation in natural rubber, Part I: The inverse yielding effect. *The European Physical Journal E* **17,** 247–259. doi:10.1140/epje/i2004-10145-6 (2005).

128. Tosaka, M. *et al.* Effect of Network-Chain Length on Strain-Induced Crystallization of NR and IR Vulcanizates. *Rubber Chemistry and Technology* **77,** 711–723. ISSN: 0035-9475. doi:10.5254/1.3547846 (2004).

129. Candau, N. *et al.* A comparison of the abilities of natural rubber (NR) and synthetic polyisoprene cis-1,4 rubber (IR) to crystallize under strain at high strain rates. *Phys. Chem. Chem. Phys.* **18,** 3472–3481. doi:http://dx.doi.org/10.1039/C5CP06383C (5 2016).

130. Trabelsi, S., Albouy, P.-A. & Rault, J. Stress-Induced Crystallization Properties of Natural and Synthetic CIS-Polyisoprene. *Rubber Chemistry and Technology* **77,** 303–316. ISSN: 0035-9475. doi:10.5254/1.3547825 (2004).

131. Gent, A. N., Kawahara, S. & Zhao, J. Crystallization and Strength of Natural Rubber and Synthetic cis-1,4-Polyisoprene. *Rubber Chemistry and Technology* **71,** 668–678. ISSN: 0035-9475. doi:10.5254/1.3538496 (1998).

132. Che, J. *et al.* Crystal and Crystallites Structure of Natural Rubber and Synthetic cis-1,4-Polyisoprene by a New Two Dimensional Wide Angle X-ray Diffraction Simulation Method. I. Strain-Induced Crystallization. *Macromolecules* **46,** 4520–4528. doi:10.1021/ma400420k (2013).

133. Chen, Q. *et al.* Structure–Mechanics Relation of Natural Rubber: Insights from Molecular Dynamics Simulations. *ACS Applied Polymer Materials* **4,** 3575–3586. doi:10.1021/acsapm.2c00147 (2022).

134. Candau, N. *et al.* Influence of strain rate and temperature on the onset of strain induced crystallization in natural rubber. *European Polymer Journal* **64,** 244–252. ISSN: 0014-3057. doi:10.1016/j.eurpolymj.2015.01.008 (2015).

135. Candau, N. *et al.* Characteristic time of strain induced crystallization of crosslinked natural rubber. *Polymer* **53,** 2540–2543. ISSN: 0032-3861. doi:10.1016/j.polymer.2012.04.027 (2012).

136. Candau, N. *et al.* Temperature dependence of strain-induced crystallization in natural rubber: On the presence of different crystallite populations. *Polymer* **60,** 115–124. ISSN: 0032-3861. doi:10.1016/j.polymer.2015.01.029 (2015).

137. Ikeda, Y. *et al.* Comparative Study on Strain-Induced Crystallization Behavior of Peroxide Cross-Linked and Sulfur Cross-Linked Natural Rubber. *Macromolecules* **41,** 5876–5884. doi:10.1021/ma800144u (2008).

138. Mullins, L. & Tobin, N. R. Stress softening in rubber vulcanizates. Part I. Use of a strain amplification factor to describe the elastic behavior of filler-reinforced vulcanized rubber. *Journal of Applied Polymer Science* **9,** 2993–3009. doi:10.1002/app.1965.070090906 (1965).

139. Harwood, J. A. C. & Payne, A. R. Stress softening in natural rubber vulcanizates. Part III. Carbon black-filled vulcanizates. *Journal of Applied Polymer Science* **10,** 315–324. doi:10.1002/app.1966.070100212 (1966).

140. Harwood, J. A. C., Mullins, L. & Payne, A. R. Stress softening in natural rubber vulcanizates. Part II. Stress softening effects in pure gum and filler loaded rubbers. *Journal of Applied Polymer Science* **9,** 3011–3021. doi:10.1002/app.1965.070090907 (1965).

141. Carretero-Gonzalez, J. *et al.* Real-Time Crystallization of Organoclay Nanoparticle Filled Natural Rubber under Stretching. *Macromolecules* **41,** 2295–2298. doi:10.1021/ma7028506 (2008).

142. Candau, N. *et al.* Strain induced crystallization in vulcanized natural rubber containing ground tire rubber particles with reinforcement and nucleation abilities. *Polymer Testing* **101,** 107313. ISSN: 0142-9418. doi:10.1016/j.polymertesting.2021.107313 (2021).

143. Barrera, C. S. & Tardiff, J. L. Static and dynamic properties of eggshell filled natural rubber composites for potential application in automotive vibration isolation and damping. *Journal of Cleaner Production* **353,** 131656. doi:10.1016/j.jclepro.2022.131656 (2022).

144. Mullins, L. Softening of Rubber by Deformation. *Rubber Chemistry and Technology* **42,** 339–362. ISSN: 0035-9475. doi:10.5254/1.3539210 (1969).

145. Diani, J., Fayolle, B. & Gilormini, P. A review on the Mullins effect. *European Polymer Journal* **45,** 601–612. ISSN: 0014-3057. doi:10.1016/j.eurpolymj.2008.11.017 (2009).

146. Bueche, F. Molecular basis for the mullins effect. *Journal of Applied Polymer Science* **4,** 107–114. doi:10.1002/app.1960.070041017 (1960).

147. Dannenberg, E. M. & Brennan, J. J. Strain Energy as a Criterion for Stress Softening in Carbon-Black-Filled Vulcanizates. *Rubber Chemistry and Technology* **39,** 597–608. doi:10.5254/1.3544867 (1966).

148. Kraus, G., Childers, C. W. & Rollmann, K. W. Stress softening in carbon black-reinforced vulcanizates. Strain rate and temperature effects. *Journal of Applied Polymer Science* **10,** 229–244. doi:10.1002/app.1966.070100205 (1966).

149. Hanson, D. E. *et al.* Stress softening experiments in silica-filled polydimethylsiloxane provide insight into a mechanism for the Mullins effect. *Polymer* **46,** 10989–10995. ISSN: 0032-3861. doi:10.1016/j.polymer.2005.09.039 (2005).

150. Fukahori, Y. New progress in the theory and model of carbon black reinforcement of elastomers. *Journal of Applied Polymer Science* **95,** 60–67. doi:10.1002/app.20802 (2005).

151. Le Cam, J.-B. *et al.* Strain-induced crystallisation of reinforced elastomers using surface calorimetry. *Polymer Testing* **131,** 108341. ISSN: 0142-9418. doi:10.1016/j.polymertesting.2024.108341 (2024).

152. Le Cam, J.-B. Energy storage due to strain-induced crystallization in natural rubber: The physical origin of the mechanical hysteresis. *Polymer* **127,** 166–173. ISSN: 0032-3861. doi:10.1016/j.polymer.2017.08.059 (2017).

153. Yin, B. *et al.* Frequency- and temperature-dependent Payne effect and hysteresis loss of carbon black filled rubbers: Experimental study and model prediction. *Materials Today Communications* **33,** 104920. ISSN: 2352-4928. doi:10.1016/j.mtcomm.2022.104920 (2022).

154. Griffith, A. A. VI. The phenomena of rupture and flow in solids. *Philosophical Transactions of the Royal Society of London. Series A, Containing Papers of a Mathematical or Physical Character* **221,** 163–198. doi:http://doi.org/10.1098/rsta.1921.0006 (1921).

155. Mars, W. & Fatemi, A. A literature survey on fatigue analysis approaches for rubber. *International Journal of Fatigue* **24,** 949–961. ISSN: 0142-1123. doi:10.1016/S0142-1123(02)00008-7 (2002).

156. Lake, G. J. & Thomas, A. G. The strength of highly elastic materials. *Proc. R. Soc. Lond. A* **300,** 108–119. doi:http://doi.org/10.1098/rspa.1967.0160 (1967).

157. Rivlin, R. S. & Thomas, A. G. Rupture of rubber. I. Characteristic energy for tearing. *Journal of Polymer Science* **10,** 291–318. doi:10.1002/pol.1953.120100303 (1953).

158. Deng, B. *et al.* Nonlocal Intrinsic Fracture Energy of Polymerlike Networks. *Phys. Rev. Lett.* **131,** 228102. doi:10.1103/PhysRevLett.131.228102 (22 2023).

159. Volokh, K. Y. REVIEW OF THE ENERGY LIMITERS APPROACH TO MODELING FAILURE OF RUBBER. *Rubber Chemistry and Technology* **86,** 470–487. ISSN: 0035-9475. doi:10.5254/rct.13.87948 (2013).

160. Wang, S.-Q. *et al.* Fracture Behavior of Polymers in Plastic and Elastomeric States. *Macromolecules* **57,** 3875–3900. doi:10.1021/acs.macromol.3c01952 (2024).

161. Elmukashfi, E. An experimental method for estimating the tearing energy in rubber-like materials using the true stored energy. *Scientific Reports* **11,** 16229. doi:10.1038/s41598-021-95151-y (2021).

162. Rice, J. R. A Path Independent Integral and the Approximate Analysis of Strain Concentration by Notches and Cracks. *Journal of Applied Mechanics* **35,** 379–386. ISSN: 0021-8936. doi:10.1115/1.3601206 (1968).

163. Cherepanov, G. Crack propagation in continuous media: PMM vol. 31, no. 3, 1967, pp. 476–488. *Journal of Applied Mathematics and Mechanics* **31,** 503–512. ISSN: 0021-8928. doi:10.1016/0021-8928(67)90034-2 (1967).

164. Lee, D. & Donovan, J. Critical J-integral and tearing energies for fracture of reinforced natural rubber. *Theoretical and Applied Fracture Mechanics* **4,** 137–147. ISSN: 0167-8442. doi:10.1016/0167-8442(85)90018-7 (1985).

165. Brüning, K., Schneider, K. & Heinrich, G. in *Fracture Mechanics and Statistical Mechanics of Reinforced Elastomeric Blends* (eds Grellmann, W. *et al.*) 43–80 (Springer Berlin Heidelberg, Berlin, Heidelberg, 2013). ISBN: 978-3-642-37910-9. doi:10.1007/978-3-642-37910-9_2.

166. Saintier, N., Cailletaud, G. & Piques, R. Crack initiation and propagation under multiaxial fatigue in a natural rubber. *International Journal of Fatigue* **28,** 61–72. ISSN: 0142-1123. doi:10.1016/j.ijfatigue.2005.03.006 (2006).

167. Huneau, B. *et al.* FATIGUE CRACK INITIATION IN A CARBON BLACK–FILLED NATURAL RUBBER. *Rubber Chemistry and Technology* **89,** 126–141. ISSN: 0035-9475. doi:10.5254/rct.15.84809 (2016).

168. Schneider, K. *et al.* Fatigue crack propagation of silica and carbon black filled natural rubber at elevated temperatures. *International Journal of Fatigue* **177,** 107968. ISSN: 0142-1123. doi:10.1016/j.ijfatigue.2023.107968 (2023).

169. Lindley, P. B. Relation between hysteresis and the dynamic crack growth resistance of natural rubber. *Int. J. Fract.* **9,** 449–462. doi:10.1007/BF00036325 (4 1973).

170. Lee, D. J. & Donovan, J. A. Microstructural Changes in the Crack Tip Region of Carbon-Black-Filled Natural Rubber. *Rubber Chemistry and Technology* **60,** 910–923. ISSN: 0035-9475. doi:10.5254/1.3536164 (1987).

171. Trabelsi, S., Albouy, P.-A. & Rault, J. Stress-Induced Crystallization around a Crack Tip in Natural Rubber. *Macromolecules* **35,** 10054–10061. doi:10.1021/ma021106c (2002).

172. Xiang, F. *et al.* Competition between Strain-Induced Crystallization and Cavitation at the Crack Tip of Unfilled and Carbon Black-Filled Natural Rubber. *Macromolecules* **55,** 10682–10693. doi:10.1021/acs.macromol.2c01038 (2022).

173. Hamed, G. R., Kim, H. J. & Gent, A. N. Cut Growth in Vulcanizates of Natural Rubber, cis-Polybutadiene, and a 50/50 Blend during Single and Repeated Extension. *Rubber Chemistry and Technology* **69,** 807–818. ISSN: 0035-9475. doi:10.5254/1.3538404 (1996).

174. Saintier, N., Cailletaud, G. & Piques, R. Cyclic loadings and crystallization of natural rubber: An explanation of fatigue crack propagation reinforcement under a positive loading ratio. *Materials Science and Engineering: A* **528,** 1078–1086. ISSN: 0921-5093. doi:10.1016/j.msea.2010.09.079 (2011).

175. Medalia, A. I. Effect of Carbon Black on Ultimate Properties of Rubber Vulcanizates. *Rubber Chemistry and Technology* **60,** 45–61. ISSN: 0035-9475. doi:10.5254/1.3536121 (1987).

176. Zhang, H. P. *et al.* Toughening Effect of Strain-Induced Crystallites in Natural Rubber. *Phys. Rev. Lett.* **102,** 245503. doi:10.1103/PhysRevLett.102.245503 (24 2009).

177. Gadaree, K. P. & Salee, G. Fatigue crack propagation in composites with spherical fillers—part 1. *Polymer Composites* **4,** 19–25. doi:10.1002/pc.750040104 (1983).

178. Ostad-Movahed, S. *et al.* Comparing effects of silanized silica nanofiller on the crosslinking and mechanical properties of natural rubber and synthetic polyisoprene. *Journal of Applied Polymer Science* **109,** 869–881. doi:10.1002/app.28144 (2008).

179. Kohls, D. & Beaucage, G. Rational design of reinforced rubber. *Current Opinion in Solid State and Materials Science* **6,** 183–194. ISSN: 1359-0286. doi:10.1016/S1359-0286(02)00073-6 (2002).

180. Poh, B., Ismail, H. & Tan, K. Effect of filler loading on tensile and tear properties of SMR L/ENR 25 and SMR L/SBR blends cured via a semi-efficient vulcanization system. *Polymer Testing* **21,** 801–806. ISSN: 0142-9418. doi:10.1016/S0142-9418(02)00014-4 (2002).

181. Rattanasom, N., Saowapark, T. & Deeprasertkul, C. Reinforcement of natural rubber with silica/carbon black hybrid filler. *Polymer Testing* **26,** 369–377. ISSN: 0142-9418. doi:10.1016/j.polymertesting.2006.12.003 (2007).

182. Scotti, R. *et al.* Shape controlled spherical (0D) and rod-like (1D) silica nanoparticles in silica/styrene butadiene rubber nanocomposites: Role of the particle morphology on the filler reinforcing effect. *Polymer* **55.** Special Issue of Polymer Membranes, 1497–1506. ISSN: 0032-3861. doi:10.1016/j.polymer.2014.01.025 (2014).

183. Choi, S.-S., Nah, C. & Jo, B.-W. Properties of natural rubber composites reinforced with silica or carbon black: influence of cure accelerator content and filler dispersion. *Polymer International* **52,** 1382–1389. doi:10.1002/pi.1232 (2003).

184. Robertson, C. G. *et al.* Characterizing Distributions of Tensile Strength and Crack Precursor Size to Evaluate Filler Dispersion Effects and Reliability of Rubber. *Polymers* **12.** ISSN: 2073-4360. doi:10.3390/polym12010203 (2020).

185. Tee, Y. L., Loo, M. S. & Andriyana, A. Recent advances on fatigue of rubber after the literature survey by Mars and Fatemi in 2002 and 2004. *International Journal of Fatigue* **110,** 115–129. ISSN: 0142-1123. doi:10.1016/j.ijfatigue.2018.01.007 (2018).

186. Marco, Y. *et al.* Prediction of fatigue properties of natural rubber based on the descriptions of the cracks population and of the dissipated energy. *Polymer Testing* **59,** 67–74. ISSN: 0142-9418. doi:10.1016/j.polymertesting.2017.01.015 (2017).

187. Lee, Y.-L. *Fatigue testing and analysis: theory and practice* ISBN: 1417544449 (Elsevier Butterworth-Heinemann [NetLibrary], Burlington, Mass [Boulder, Colo], 2005).

188. Roos, E., Maile, K. & Seidenfuß, M. *Werkstoffkunde für Ingenieure: Grundlagen, Anwendung, Prüfung* 7th ed. ISBN: 9783662647325. doi:10.1007/978-3-662-64732-5 (Springer Berlin Heidelberg, Imprint: Springer Vieweg, Berlin, Heidelberg, 2022).

189. Rösler, J., Harders, H. & Bäker, M. *Mechanisches Verhalten der Werkstoffe* 6. Aufl. ISBN: 9783658137953. doi:10.1007/978-3-658-13795-3 (Springer Fachmedien Wiesbaden, Imprint: Springer Vieweg, Wiesbaden, 2019).

190. Mars, W. V. & Fatemi, A. Fatigue crack nucleation and growth in filled natural rubber. *Fatigue & Fracture of Engineering Materials & Structures* **26,** 779–789. doi:10.1046/j.1460-2695.2003.00678.x (2003).

191. Dong, B., Liu, C. & Wu, Y.-P. Fracture and fatigue of silica/carbon black/natural rubber composites. *Polymer Testing* **38,** 40–45. ISSN: 0142-9418. doi:10.1016/j.polymertesting.2014.06.004 (2014).

192. Rong, J. *et al.* Characteristic Tearing Energy and Fatigue Crack Propagation of Filled Natural Rubber. *Polymers* **13.** ISSN: 2073-4360. doi:10.3390/polym13223891 (2021).

193. Lake, G. J. & Lindley, P. B. The mechanical fatigue limit for rubber. *Journal of Applied Polymer Science* **9,** 1233–1251. doi:10.1002/app.1965.070090405 (1965).

194. Steck, J. *et al.* Multiscale stress deconcentration amplifies fatigue resistance of rubber. *Nature* **624,** 303–308. doi:10.1038/s41586-023-06782-2 (2023).

195. Beurrot-Borgarino, S. *et al.* Strain-induced crystallization of carbon black-filled natural rubber during fatigue measured by in situ synchrotron X-ray diffraction. *International Journal of Fatigue* **47,** 1–7. ISSN: 0142-1123. doi:10.1016/j.ijfatigue.2012.07.001 (2013).

196. Gartner, T. E. I. & Jayaraman, A. Modeling and Simulations of Polymers: A Roadmap. *Macromolecules* **52,** 755–786. doi:10.1021/acs.macromol.8b01836 (2019).

197. Yuan, B. *et al.* Effects of silica/carbon black hybrid nanoparticles on the dynamic modulus of uncrosslinked cis-1,4-polyisoprene rubber: Coarse-grained molecular dynamics. *Polymer* **238,** 124400. ISSN: 0032-3861. doi:10.1016/j.polymer.2021.124400 (2022).

198. Uddin, M. S. & Ju, J. Multiscale modeling of a natural rubber: Bridging a coarse-grained molecular model to the rubber network theory. *Polymer* **101,** 34–47. ISSN: 0032-3861. doi:10.1016/j.polymer.2016.08.037 (2016).

199. Viktorova, M. *et al.* A mesoscopic model for the simulation of dynamic mechanical properties of filled elastomers: Filled binary polymer blends. *Computational Materials Science* **212,** 111597. ISSN: 0927-0256. doi:10.1016/j.commatsci.2022.111597 (2022).

200. Li, X. *et al.* Role of a nanoparticle network in polymer mechanical reinforcement: insights from molecular dynamics simulations. *Phys. Chem. Chem. Phys.* **23,** 21797–21807. doi:http://dx.doi.org/10.1039/D1CP03153H (38 2021).

201. Pavlov, A. S. & Khalatur, P. G. Fully atomistic molecular dynamics simulation of nanosilica-filled crosslinked polybutadiene. *Chemical Physics Letters* **653,** 90–95. ISSN: 0009-2614. doi:10.1016/j.cplett.2016.04.061 (2016).

202. Hagita, K. *et al.* Coarse-Grained Molecular Dynamics Simulation of Filled Polymer Nanocomposites under Uniaxial Elongation. *Macromolecules* **49,** 1972–1983. doi:10.1021/acs.macromol.5b02799 (2016).

203. Shi, R. *et al.* Tensile performance and viscoelastic properties of rubber nanocomposites filled with silica nanoparticles: A molecular dynamics simulation study. *Chemical Engineering Science* **267,** 118318. ISSN: 0009-2509. doi:10.1016/j.ces.2022.118318 (2023).

204. Zhang, Z. *et al.* Molecular dynamics simulation of the impact of the surface topology of carbon black on the mechanical properties of elastomer nanocomposites. *Phys. Chem. Chem. Phys.* **25,** 5602–5612. doi:http://dx.doi.org/10.1039/D2CP04996A (7 2023).

205. Payal, R. S. *et al.* Molecular mechanism of material deformation and failure in butadiene rubber: Insight from all-atom molecular dynamics simulation using a bond breaking potential model. *Polymer* **170,** 113–119. ISSN: 0032-3861. doi:10.1016/j.polymer.2019.03.006 (2019).

206. Morozov, I. A., Komar, L. A. & Lauke, B. Structural–mechanical model of filled rubber: Influence of filler arrangement. *International Journal of Mechanical Sciences* **107,** 160–169. ISSN: 0020-7403. doi:10.1016/j.ijmecsci.2016.01.013 (2016).

207. Dargazany, R. & Itskov, M. A network evolution model for the anisotropic Mullins effect in carbon black filled rubbers. *International Journal of Solids and Structures* **46,** 2967–2977. ISSN: 0020-7683. doi:10.1016/j.ijsolstr.2009.03.022 (2009).

208. Hu, F. *et al.* Molecular dynamics simulation study of the fracture properties of polymer nanocomposites filled with grafted nanoparticles. *Phys. Chem. Chem. Phys.* **21,** 11320–11328. doi:http://dx.doi.org/10.1039/C8CP07668E (21 2019).

209. Yuan, B. *et al.* Coarse-grained molecular dynamics simulation of cis-1,4-polyisoprene with silica nanoparticles under extreme uniaxial tension. *Modelling and Simulation in Materials Science and Engineering* **29,** 055013. doi:10.1088/1361-651x/abfeae (2021).

210. Cobeña-Reyes, J. *et al.* Probabilistic Approach to Low Strain Rate Atomistic Simulations of Ultimate Tensile Strength of Polymer Crystals. *Journal of Chemical Theory and Computation* **19,** 6326–6331. doi:10.1021/acs.jctc.3c00570 (2023).

211. Zhao, X. *et al.* Uncovering the rupture mechanism of carbon nanotube filled cis-1,4-polybutadiene via molecular dynamics simulation. *RSC Adv.* **8,** 27786–27795. doi:http://dx.doi.org/10.1039/C8RA04469D (49 2018).

212. Behnke, R. *et al.* in *Fracture Mechanics and Statistical Mechanics of Reinforced Elastomeric Blends* (eds Grellmann, W. *et al.*) 167–226 (Springer Berlin Heidelberg, Berlin, Heidelberg, 2013). ISBN: 978-3-642-37910-9. doi:10.1007/978-3-642-37910-9_5.

213. Aygün, S. & Klinge, S. Continuum mechanical modeling of strain-induced crystallization in polymers. *International Journal of Solids and Structures* **196-197,** 129–139. ISSN: 0020-7683. doi:10.1016/j.ijsolstr.2020.04.017 (2020).

214. Hentschke, R. & Plagge, J. Strain-induced self-assembly of crystallites in elastomers. *Phys. Rev. E* **104,** 014502. doi:10.1103/PhysRevE.104.014502 (1 2021).

215. Sotta, P. & Albouy, P.-A. Strain-Induced Crystallization in Natural Rubber: Flory's Theory Revisited. *Macromolecules* **53,** 3097–3109. doi:10.1021/acs.macromol.0c00515 (2020).

216. Khiêm, V. *et al.* Thermodynamics of strain-induced crystallization in filled natural rubber under uni- and biaxial loadings, Part II: Physically-based constitutive theory. *Journal of the Mechanics and Physics of Solids* **159,** 104712. ISSN: 0022-5096. doi:10.1016/j.jmps.2021.104712 (2022).

217. Khiêm, V. *et al.* Thermodynamics of strain-induced crystallization in filled natural rubber under uni- and biaxial loadings, Part I: Complete energetic characterization and crystallinity evaluation. *Journal of the Mechanics and Physics of Solids* **159,** 104701. ISSN: 0022-5096. doi:10.1016/j.jmps.2021.104701 (2022).

218. Landau, L. D. & Lifschitz, E. M. *Lehrbuch der theoretischen Physik. VII. Elastizitätstheorie* (eds Schöpf, H.-G. & Ziesche, P.) (Verlag Harri Deutsch, 1991).

219. Kuhn, W. Über die Gestalt fadenförmiger Moleküle in Lösungen. *Kolloid-Zeitschrift,* 2–15. doi:10.1007/BF01451681 (68 1934).

220. Kuhn, W. & Kuhn, H. Die Frage nach der Aufrollung von Fadenmolekeln in strömenden Lösungen. *Helvetica Chimica Acta* **26,** 1394–1465. doi:10.1002/hlca.19430260514 (1943).

221. Hentschke, R. *Statistische Mechanik: Eine Einführung für Physiker, Chemiker und Materialwissenschaftler* (Wiley-VCH, Weinheim, 2004).

222. van der Waals forces. doi:10.1351/goldbook.V06597 (2019).

223. London, F. Zur Theorie und Systematik der Molekularkräfte. *Zeitschrift für Physik* **63,** 245–279. doi:10.1007/BF01421741 (1930).

224. Hamaker, H. The London—van der Waals attraction between spherical particles. *Physica* **4,** 1058–1072. ISSN: 0031-8914. doi:10.1016/S0031-8914(37)80203-7 (1937).

225. Robertson, C. G. & Hardman, N. J. Nature of Carbon Black Reinforcement of Rubber: Perspective on the Original Polymer Nanocomposite. *Polymers* **13.** ISSN: 2073-4360. doi:10.3390/polym13040538 (2021).

226. Marchand, A. *et al.* Why is surface tension a force parallel to the interface? *American Journal of Physics* **79,** 999–1008. ISSN: 0002-9505. doi:10.1119/1.3619866 (2011).

227. Schrader, M. E. Young-Dupre Revisited. *Langmuir* **11,** 3585–3589. doi:10.1021/la00009a049 (1995).

228. Owens, D. K. & Wendt, R. C. Estimation of the surface free energy of polymers. *Journal of Applied Polymer Science* **13,** 1741–1747. doi:10.1002/app.1969.070130815 (1969).

229. Rabel, W. Einige Aspekte der Benetzungstheorie und ihre Anwendung auf die Untersuchung und Veränderung der Oberflächeneigenschaften von Polymeren. *Farbe und Lack* **77,** 997–1005 (1971).

230. Kaelble, D. H. Dispersion-Polar Surface Tension Properties of Organic Solids. *The Journal of Adhesion* **2,** 66–81. doi:10.1080/0021846708544582 (1970).

231. Fowkes, F. M. ATTRACTIVE FORCES AT INTERFACES. *Industrial & Engineering Chemistry* **56,** 40–52. doi:10.1021/ie50660a008 (1964).

232. Stöckelhuber, K. W. *et al.* Contribution of physico-chemical properties of interfaces on dispersibility, adhesion and flocculation of filler particles in rubber. *Polymer* **51,** 1954–1963. ISSN: 0032-3861. doi:10.1016/j.polymer.2010.03.013 (2010).

233. Klat, D., Karimi-Varzaneh, H. A. & Lacayo-Pineda, J. Phase Morphology of NR/SBR Blends: Effect of Curing Temperature and Curing Time. *Polymers* **10.** ISSN: 2073-4360. doi:10.3390/polym10050510 (2018).

234. Miyaji, K. *et al.* Study on Homogeneity in Sulfur Cross-Linked Network Structures of Isoprene Rubber by TD-NMR and AFM – Zinc Stearate System. *Macromolecules* **53,** 8438–8449. doi:10.1021/acs.macromol.0c01266 (2020).

235. Hentschke, R. *et al. Molekulares Modellieren mit Kraftfeldern. Eine Einführung in die Theorie und Praxis der Computersimulation molekularer Systeme* https://constanze.materials.uni-wuppertal.de/fileadmin/physik/theochemphysik/Skripten/MolModell.pdf.

236. Gundlach, N. & Hentschke, R. Modelling Filler Dispersion in Elastomers: Relating Filler Morphology to Interface Free Energies via SAXS and TEM Simulation Studies. *Polymers* **10.** ISSN: 2073-4360. doi:10.3390/polym10040446 (2018).

237. Gundlach, N. *Modeling Filler Flocculation in Elastomers: an Approach Based on Surface Free Energies and Monte Carlo Simulation* Dissertation (Bergische Universität Wuppertal, Wuppertal, 2019). doi:{10.25926/pq5r-qx14}.

238. Press, W. H. *et al. Numerical Recipes in C: The Art of Scientific Computing* 2nd ed. ISBN: 0-521-43108-5 (Cambridge University Press, Cambridge, USA, 1992).

239. Bitzek, E. *et al.* Structural Relaxation Made Simple. *Phys. Rev. Lett.* **97,** 170201. doi:10.1103/PhysRevLett.97.170201 (17 2006).

240. Verlet, L. Computer "Experiments" on Classical Fluids. I. Thermodynamical Properties of Lennard-Jones Molecules. *Phys. Rev.* **159,** 98–103. doi:10.1103/PhysRev.159.98 (1 1967).

241. Swope, W. C. *et al.* A computer simulation method for the calculation of equilibrium constants for the formation of physical clusters of molecules: Application to small water clusters. *The Journal of Chemical Physics* **76,** 637–649. ISSN: 0021-9606. doi:10.1063/1.442716 (1982).

242. Albouy, P.-A. *et al.* A stroboscopic X-ray apparatus for the study of the kinetics of strain-induced crystallization in natural rubber. *Polymer* **53,** 3313–3324. ISSN: 0032-3861. doi:10.1016/j.polymer.2012.05.042 (2012).

243. Gundlach, N., Hentschke, R. & Karimi-Varzaneh, H. A. Filler flocculation in elastomer blends - an approach based on measured surface tensions and monte carlo simulation. *Soft Materials* **17,** 283–296. doi:10.1080/1539445X.2019.1568261 (2019).

244. Klüppel, M. in *Filler-Reinforced Elastomers Scanning Force Microscopy* (eds Capella, B. *et al.*) 1–86 (Springer Berlin Heidelberg, Berlin, Heidelberg, 2003). ISBN: 978-3-540-36438-2. doi:10.1007/b11054.

245. Viktorova, M. *From Microscopic Interactions to Macroscopic Mechanical Properties of Filled Elastomers* Dissertation (Bergische Universität Wuppertal, Wuppertal, 2022).

246. Stauffer, D. in *On Growth and Form. Fractal and Non-Fractal Patterns in Physics* (eds Stanley, H. E. & Ostrowsky, N.) 79–100 (Martinus Nijhoff Publishers, 1986). ISBN: 0-89838-850-3.

247. Stauffer, D. & Aharony, A. *Introduction to Percolation Theory* Revised Second Edition (Taylor & Francis, London, 1994).

248. Christensen, K. *Percolation Theory* https://web.mit.edu/ceder/publications/Percolation.pdf.

249. Zhukov, D., Andrianova, E. & Lesko, S. The Influence of a Network's Spatial Symmetry, Topological Dimension, and Density on Its Percolation Threshold. *Symmetry* **11,** 920. doi:10.3390/sym11070920 (2019).

250. Xue, Q. The influence of particle shape and size on electric conductivity of metal–polymer composites. *European Polymer Journal* **40,** 323–327. ISSN: 0014-3057. doi:10.1016/j.eurpolymj.2003.10.011 (2004).

251. Markov, A., Fiedler, B. & Schulte, K. Electrical conductivity of carbon black/fibres filled glass-fibre-reinforced thermoplastic composites. *Composites Part A: Applied Science and Manufacturing* **37,** 1390–1395. ISSN: 1359-835X. doi:10.1016/j.compositesa.2005.07.009 (2006).

252. Kalaitzidou, K., Fukushima, H. & Drzal, L. T. A Route for Polymer Nanocomposites with Engineered Electrical Conductivity and Percolation Threshold. *Materials* **3,** 1089–1103. ISSN: 1996-1944. doi:10.3390/ma3021089 (2010).

253. Vieira, L. d. S. *et al.* A review concerning the main factors that interfere in the electrical percolation threshold content of polymeric antistatic packaging with carbon fillers as antistatic agent. *Nano Select* **3,** 248–260. doi:10.1002/nano.202100073 (2022).

254. Schueler, R. *et al.* Agglomeration and electrical percolation behavior of carbon black dispersed in epoxy resin. *Journal of Applied Polymer Science* **63,** 1741–1746. doi:10.1002/(SICI)1097-4628(19970328)63:13<1741::AID-APP5>3.0.CO;2-G (1997).

255. Krupa, I. & Chodák, I. Physical properties of thermoplastic/graphite composites. *European Polymer Journal* **37,** 2159–2168. ISSN: 0014-3057. doi:10.1016/S0014-3057(01)00115-X (2001).

256. Park, S.-J., Kim, H.-C. & Kim, H.-Y. Roles of Work of Adhesion between Carbon Blacks and Thermoplastic Polymers on Electrical Properties of Composites. *Journal of Colloid and Interface Science* **255,** 145–149. ISSN: 0021-9797. doi:10.1006/jcis.2002.8481 (2002).

257. Miyasaka, K. *et al.* Electrical conductivity of carbon-polymer composites as a function of carbon content. *Journal of Materials Science* **17,** 1610–1616. doi:10.1007/BF00540785.

258. Wrana, C. *Introduction to Polymer Physics* (LANXESS AG, Leverkusen, Germany, 2009).

259. Ozbas, B. *et al.* Strain-induced crystallization and mechanical properties of functionalized graphene sheet-filled natural rubber. *Journal of Polymer Science Part B: Polymer Physics* **50,** 718–723. doi:10.1002/polb.23060 (2012).

260. Kim, J.-H. & Jeong, H.-Y. A study on the material properties and fatigue life of natural rubber with different carbon blacks. *International Journal of Fatigue* **27,** 263–272. ISSN: 0142-1123. doi:10.1016/j.ijfatigue.2004.07.002 (2005).

261. Tunnicliffe, L. B., Robertson, C. G. & Mars, W. V. A MICROSCOPY INVESTIGATION OF RUBBER COMPOUND CRACK PRECURSORS AND TENSILE FRACTURE SURFACES. *Rubber Chemistry and Technology* **96,** 514–529. ISSN: 0035-9475. doi:10.5254/rct-23.201163 (2023).

262. Boonstra, B. B. & Medalia, A. I. Effect of Carbon Black Dispersion on the Mechanical Properties of Rubber Vulcanizates. *Rubber Chemistry and Technology* **36,** 115–142. ISSN: 0035-9475. doi:10.5254/1.3539530 (1963).

263. Warasitthinon, N. & Robertson, C. G. INTERPRETATION OF THE TANδ PEAK HEIGHT FOR PARTICLE-FILLED RUBBER AND POLYMER NANOCOMPOSITES WITH RELEVANCE TO TIRE TREAD PERFORMANCE BALANCE. *Rubber Chemistry and Technology* **91,** 577–594. ISSN: 0035-9475. doi:10.5254/rct.18.82608 (2018).

264. Ürögiová, E. *et al.* Elastomers Filled with Metal Coated Carbon Black. *Kautschuk Gummi Kunststoffe* **61,** 455–462 (2008).

265. Kuhn, W. & Grün, F. Beziehungen zwischen elastischen Konstanten und Dehnungsdoppelbrechung hochelastischer Stoffe. *Kolloid-Zeitschrift* **101,** 248–271. doi:10.1007/BF01793684 (1942).

266. Jedynak, R. Approximation of the inverse Langevin function revisited. *Rheologica Acta* **54,** 29–39. doi:10.1007/s00397-014-0802-2 (2015).

267. Guénolé, J. *et al.* Assessment and optimization of the fast inertial relaxation engine (FIRE) for energy minimization in atomistic simulations and its implementation in LAMMPS. *Computational Materials Science* **175,** 109584. ISSN: 0927-0256. doi:10.1016/j.commatsci.2020.109584 (2020).

Index

Acknowledgments

At this point, I would like to express my deepest gratitude to all those who have supported and guided me in a personal or academic way throughout the process of completing this dissertation.

First and foremost, I would like to express my sincerest gratitude to my supervisor Prof. Dr. Reinhard Hentschke for his invaluable support and guidance during my time in his research group. His expertise, constructive feedback, and mentorship were indispensable in shaping both this dissertation and my academic development. I am grateful for the time and exceptional effort he dedicated to my work, in particular for always being accessible. The freedom he has given me is very appreciated as well.

I wish to extend my gratitude to Prof. Dr. Nils Hojdis for agreeing to conduct the second review of this dissertation. My gratitude goes as well to Prof. Dr. Michael Karbach for consenting to undertake the third review of this dissertation. I would also like to express my appreciation to Prof. Dr. Dirk Lützenkirchen-Hecht for kindly agreeing to participate in my examination committee.

I am indebted to Dr. Frank Fleck from Continental Reifen Deutschland GmbH, who provided me with experimental data that is part of the foundation of this work.

Furthermore, the friendly and collaborative atmosphere and scientific discussions with the former members of the research group for Theoretical Chemical Physics and my fellow students are deeply appreciated.

I am incredibly thankful to my family, especially to you, Mama, Papa and Lisa, for your support, encouragement, and understanding throughout my academic journey. A special thanks goes to my partner Freddy, whose constant support in every aspect of life was crucial in helping me navigate the challenges during the writing of this dissertation.

Finally, I would like to thank my friends who accompanied me throughout this time for their encouragement. I am grateful to all those who believed in me.

I truly could not have accomplished this without you. Thank you all.